Characterising the *P–T–t* histories and effects of melt loss in high thermal gradient terranes.

LAURA J. MORRISSEY

Geology and Geophysics
School of Physical Sciences
University of Adelaide

This thesis is submitted in fulfilment of the requirements for the degree of Doctor of Philosophy

May 2016

TABLE OF CONTENTS

TABLE OF CONTENTS

ABSTRACT

Zircon U–Pb and Lu–Hf isotopes, in situ U–Pb monazite geochronology and calculated metamorphic phase diagrams are used to explore the tectonic settings of regional high thermal gradient metamorphism as well as the consequences of melt loss on the bulk composition and reactivity of residual rock packages. Case studies are presented from four high thermal gradient terranes: the Windmill Islands in Wilkes Land, east Antarctica; the central Aileron Province in central Australia, the Rayner Complex in east Antarctica and the southern Gawler Craton in South Australia.

The Windmill Islands region records two stages of high thermal gradient metamorphism between c. 1320–1300 Ma and c. 1240–1170 Ma. The first stage of metamorphism occurred at conditions of 3.5–4 kbar and 700–730 ºC and was associated with the formation of a horizontal fabric. The second stage of metamorphism is most strongly recorded in the southern Windmill Islands where it reached conditions of ~4 kbar and 850 ºC, coincident with the emplacement of voluminous isotopically juvenile granitic and charnockitic magmas. The metasedimentary rocks of the Windmill Islands contain both arc- and craton-derived detrital zircon grains, suggesting that they formed in a back-arc setting. An extensional setting is consistent with the high thermal gradients and the formation of a regional horizontal fabric during the first stage of metamorphism. The intrusion of juvenile charnockite further suggests that the overall tectonic regime was extensional and that the crust beneath the Windmill Islands contained little evolved material.

The central Aileron Province records long-lived high thermal gradient anatectic conditions between c. 1590 and 1520 Ma. Peak temperatures were in excess of 850 ºC with pressures of 6.5–7.5 kbar, corresponding to a thermal gradient of >130–140 ºC/kbar. The retrograde evolution involved minor decompression and then slow cooling, culminating with the development of andalusite. The absence of any syn-metamorphic magmatism and the development of contractional structures during metamorphism suggest that long-lived high thermal gradient metamorphism was likely to have been driven to a significant extent by the burial of high heat producing pre-metamorphic granitic rocks that volumetrically dominate the terrane.

The Rayner Complex in east Antarctica was extensively deformed and metamorphosed during the Rayner Orogeny between c. 1020 and 900 Ma. Metamorphism was associated with voluminous granitic and charnockitic magmatism. The earliest phase of metamorphism is recorded in the southern Rayner Complex and involved pressures of >7.5 kbar. Pervasive metamorphism at 950–900 Ma affected the whole Rayner Complex and involved temperatures of 850–880 °C and lower pressures of 6–7 kbar. The Rayner Complex is interpreted to be a back-arc basin that was closed during two-stage collision between the Archean Antarctic cratons to the south and the arc, followed by collision with the Indian Craton.

High thermal gradient metamorphism can occur in both collisional and extensional regimes and in both plate margins and intracontinental settings. The primary thermal driver in the Windmill Islands and the Rayner Complex was likely to have been the thinned lithosphere resulting from back-arc extension, whereas in the central Aileron Province, the primary thermal driver was likely to be anomalously high heat producing crust. However, in all three terranes, the attainment of regional high temperatures was facilitated by the preconditioning (dehydration) of the crust by prior melt loss events and slow erosion rates.

In all four studied terranes, high thermal gradient metamorphism resulted in melt loss that significantly altered the compositions and reactivity of the residual rocks. One implication of melt loss during regional high temperature metamorphism is that it creates a terrane comprising anhydrous, residual rock compositions that are relatively resistant to reworking during subsequent metamorphic events. As demonstration of this, the Rayner Complex records a metamorphic event at c. 540–500 Ma that reached peak conditions of 800–870 °C and 5.5–6.5 kbar. However, high-T mineral growth at 540–500 Ma is only recorded in some locations. The spatial distribution of this mineralogical reworking was controlled by localised rock reactivity that may reflect domains that had undergone hydrous retrogression at the end of the Rayner Orogeny, locally enhancing the responsiveness of the rock mass during the Cambrian.

In the southern Gawler Craton, forward modelling of an Fe-rich phyllite sequence shows that melt loss can also have economic implications by increasing the concentration of iron in the residual rock package, leading to enrichment in Fe-oxide minerals (magnetite and hematite). Muscovite-rich rocks with lower iron content are more fertile, produce more melt and therefore show a more significant increase (up to 35%) in the Fe-oxide content in the residual (melt depleted) rock package. Rocks with primary Fe-rich compositions are less fertile, lose less melt and therefore do not experience the same relative increase in the amount of Fe-oxides in the residuum. The economic implications of the modelling are that the more fertile horizons with lower primary iron contents may be significantly upgraded as a result of melt loss, thereby improving the overall grade of the ore system. In the case of southern Gawler Craton, melt loss-driven Fe enrichment has contributed to the formation of one of Australia's largest known magnetite resource systems.

DECLARATION

I, Laura Morrissey, certify that this work contains no material which has been accepted for the award of any other degree or diploma in my name, in any university or other tertiary institution and, to the best of my knowledge and belief, contains no material previously published or written by another person, except where due reference has been made in the text. In addition, I certify that no part of this work will, in the future, be used in a submission in my name, for any other degree or diploma in any university or other tertiary institution without the prior approval of the University of Adelaide and where applicable, any partner institution responsible for the joint-award of this degree.

I give consent to this copy of my thesis when deposited in the University Library, being made available for loan and photocopying, subject to the provisions of the Copyright Act 1968.

The author acknowledges that copyright of published works contained within this thesis resides with the copyright holder(s) of those works.

I also give permission for the digital version of my thesis to be made available on the web, via the University's digital research repository, the Library Search and also through web search engines, unless permission has been granted by the University to restrict access for a period of time.

LAURA MORRISSEY DATE

Peer reviewed journal articles:

Morrissey, L.J., Payne, J.L., Hand, M., Clark, C., Taylor, R., Kylander-Clark, A., Kirkland, C.L. Linking the Windmill Islands, east Antarctica and the Albany–Fraser Orogen: insights from U–Pb zircon geochronology and Hf isotopes. *Precambrian Research*, under review.

Morrissey, L.J., Hand, M, Lane, K., Kelsey, D.E., Dutch, R.A., 2016. Upgrading iron-rich sequences to economic grade iron-ore deposits by melt loss during granulite-facies metamorphism. *Ore Geology Reviews*, 74, 101–121.

Morrissey, L.J., Hand, M., Kelsey, D.E., Wade, B.P., 2016. Cambrian high-temperature reworking of the Rayner-Eastern Ghats terrane: constraints from the northern Prince Charles Mountains region, east Antarctica. *Journal of Petrology*, 57, 53–92.

Wong, B., **Morrissey, L.J.,** Hand, M., Fields, C., Kelsey, D.E., 2015. Grenvillian-aged reworking of late Paleoproterozoic crust of the southern North Australian Craton, central Australia: implications for the assembly of Mesoproterozoic Australia. *Precambrian Research*, 270, 100–123.

Morrissey, L.J., Hand, M, Kelsey, D.E., 2015. Multi-stage metamorphism in the Rayner–Eastern Ghats terrane: *P–T–t* constraints from the northern Prince Charles Mountains, east Antarctica. *Precambrian Research*, 267, 137–163.

Morrissey, L.J., Hand, M., Raimondo, T., Kelsey, D.E., 2014. Long-lived high-temperature, low-pressure granulite facies metamorphism in the Arunta Region, central Australia. *Journal of Metamorphic Geology*, 32, 25–47.

Morrissey, L.J., Hand, M., Wade, B.P., Szpunar, M., 2013. Early Mesoproterozoic metamorphism in the Barossa Complex, South Australia: links with the eastern margin of Proterozoic Australia. *Australian Journal of Earth Sciences*, 60, 769–795.

Conference presentations:

Morrissey, L., Hand, M., Lane, K., Kelsey, D.E., Dutch, R., 2015. Melt loss and magnetite: improving ore grades during granulite facies metamorphism. Granulites and Granulites 2015, Windhoek, Nambia, July 2015, p. 29.

Morrissey, L., Hand, M., Kelsey, D., Payne, J., 2013. Temporal constraints on the metamorphic evolution of the northern Prince Charles Mountains, east Antarctica. Granulites and Granulites 2013, Hyderabad, January 2013, p. 46.

Morrissey, L., Wong, B., Hand, M., Payne, J., Kelsey, D., Collins, W. J., 2012. Grenvillian-aged reworking in the southern North Australia Craton, central Australia. Proceedings of the 24th International Geological Congress 2012, Brisbane, August 2012.

ACKNOWLEDGEMENTS

Firstly, thank you to my supervisors Martin and Dave who have both provided excellent support and guidance along the way. Both of you have been very generous with your time and knowledge and I have been lucky to have you as supervisors. I would like to thank Martin especially for the chance to pursue opportunities outside my thesis and allowing me to travel to so many interesting locations. I would also like to thank Dave for his unfailing patience and for always being approachable.

I have been very lucky with the places I have visited for fieldwork and for conferences and I have learnt a lot from both. I am indebted to the people who have helped out with fieldwork, in particular the Australian Antarctic Division and the personnel at Casey Station in the 2013–2014 season. The people I met at conferences and the reviewers of various chapters of this thesis also deserve thanks for providing alternative scientific perspectives and ideas, as their comments and suggestions have doubtlessly improved both the manuscripts they reviewed and the subsequent chapters.

Thank you to the staff at Adelaide Microscopy who have been an enormous help with analytical work. Especially thank you to Ben, Aiofe and Angus who have had to repair the laser and the probe many times throughout the course of this PhD, and thank you as well to Ken who has carbon coated many thin sections on short notice.

Thanks to all the other PhD students (and honorary PhDs), including Katherine, Morgan, Naomi, Kat, Bel, Alec, Jade, Bonnie, Dan, Kieran, Lachy and Vicky, as well as old PhDs Katie, Dee and Russell and more recent PhD students Kam, Kiara and Meg, whose friendship has made my PhD and the Mawson Building significantly more enjoyable. Thanks as well to the honours students throughout the last few years who have taught me an awful lot about troubleshooting thermocalc.

Thanks to the coffee shops of Adelaide, without which this thesis may never have been written.

Thank you to my non-geology friends and family for their support and encouragement over the last few years and for never actually voicing the fact that this PhD seemed to take a really long time. Thanks to Kate for listening whenever required and for being my outdoor consultant. A special thank you to my parents for the late night pickups from Adelaide Microscopy and early drop offs at airports, for their assurance that I won't have to pay rent until I'm finished and for their love, patience and encouragement in everything I do. Finally, thank you to Justin, who has alternately provided supervision, moral support, tough love, chocolate and wine as required.

CHAPTER 1

Introduction and thesis outline

1. Introduction to high thermal gradient metamorphism

The thermal structure of the Earth's crust, that is the rate of change of temperature with depth, is characteristic for different geodynamic settings and is encoded by the mineral assemblages that form in metamorphic rocks. Therefore, through the study of metamorphic mineral assemblages and the determination of pressure–temperature (*P–T*) conditions of metamorphic rocks it is possible to make inferences about the tectonic setting of metamorphism in the Earth's past, and to link the changes in metamorphic conditions to secular changes in lithospheric geodynamic regimes (Brown, 2006, 2014).

A number of early papers recognised a distinctive style of regional metamorphism different from the medium pressure,

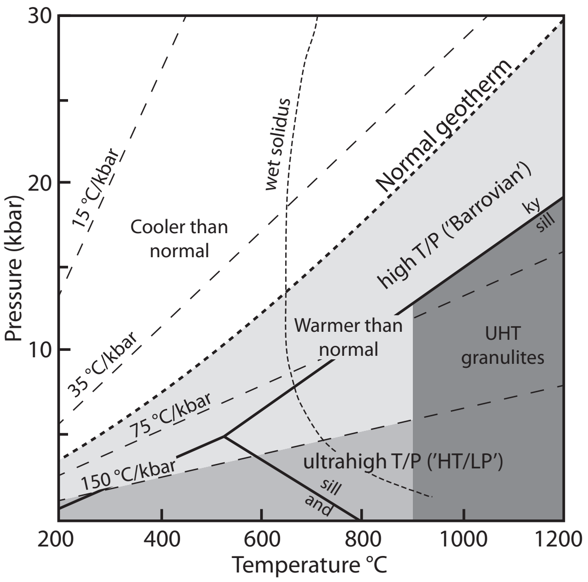

Figure 1: *P–T* diagram showing thermal gradients in relation to a normal crustal geotherm. High to ultrahigh thermal gradients pass through the andalusite and sillimanite fields. Ultrahigh temperature (UHT; >900 °C) metamorphism is the most thermally extreme manifestation of high thermal gradients. Modified after Brown, 2006, 2014 and Kelsey and Hand, 2015.

clockwise *P–T* evolutions that characterise Barrovian-style metamorphism (Fig. 1). This different style of regional metamorphism is characterised by low pressure andalusite- or sillimanite-bearing assemblages that were commonly spatially associated with abundant igneous intrusions (Fig. 1; e.g. Barton and Hanson, 1989; De Yoreo et al., 1991; Lux et al., 1986; Miyashiro, 1961; Zwart, 1967). Metamorphism of this style requires a steep thermal structure (i.e. high to ultrahigh geothermal gradients), and was inferred to occur in a variety of tectonic settings including continent–continent collision zones, regions of extension, magmatic arcs and regions of large aqueous fluid flux above subduction zones (De Yoreo et al., 1991; Loosveld and Etheridge, 1990; Lux et al., 1986; Sandiford and Powell, 1986, 1991; Wickham and Oxburgh, 1985). Despite the variations in inferred tectonic setting, high thermal gradient metamorphism was ultimately interpreted to derive from the advectic transfer of heat by magmatic or aqueous fluids (Barton and Hanson, 1989; Bohlen, 1991; De Yoreo et al., 1991; Lux et al., 1986; Sandiford et al., 1991; Sandiford and Powell, 1991; Wickham and Oxburgh, 1985). The timescales of metamorphism caused by magmatic heat advection are likely to be short (<<10 Myr; e.g. De Yoreo et al., 1991; Rothstein and Hoisch, 1994; Sandiford et al., 1991; Westphal et al., 2003), and therefore high thermal gradient metamorphism was interpreted to reflect transient perturbations of the steady-state thermal structure of the lithosphere. Where high thermal gradient metamorphism was regionally extensive, it was not considered to be synchronous across the whole metamorphic belt and instead was interpreted to result from multiple temporally and spatially localised intrusions (e.g. Barton and Hanson, 1989; De Yoreo et al., 1991). However, two important developments in the investigation of high thermal gradient terranes have required a reassessment of the accepted paradigm of transient heat advection as the driver for metamorphism.

The first development was the recognition of terranes that record regional-scale ultrahigh temperatures (UHT; >900 °C) in crust of relatively normal thickness (Fig. 1; see reviews by Harley, 1998, 2008; Kelsey, 2008; Kelsey and Hand, 2015 and references therein). It is also increasingly recognised that lower-temperature high thermal gradient terranes are likely to be underlain by rocks that record UHT conditions (e.g. Kelsey and Hand, 2015). Although many of these terranes contain large volumes of magmatic rocks, the magmatism is commonly interpreted to be largely the result of metamorphism rather than the cause (e.g. Diener et al., 2013; Halpin et al., 2007a; Korhonen et al., 2015; Smithies et al., 2011). Therefore, the formation of UHT terranes requires a primary thermal driver that is able to generate regionally extensive high temperature metamorphism as well as large-scale melting of the lower crust.

The second development came with the increasing use and sophistication of geochronological techniques. This has given petrologists the ability to link age constraints to segments of the inferred metamorphic P–T path (e.g. Drüppel et al., 2012; Kelsey et al., 2007; Kohn and Malloy, 2004; Reno et al., 2012; Roberts and Finger, 1997; Rubatto et al., 2013), or to directly link trace elements in geochronometers to the growth or breakdown of silicate minerals (e.g. Harley and Kelly, 2007; Hermann and Rubatto, 2003; Johnson et al., 2015; Kelly et al., 2012; Kylander-Clark et al., 2013; Rubatto, 2002; Taylor et al., 2015; Tomkins et al., 2005). A primary result of these endeavours has been the recognition that some terranes record extremely long-lived (>50 Myr) high temperature metamorphic conditions, in contrast to the traditional interpretation that high thermal gradient metamorphism is necessarily short-lived.

These developments have raised a number of questions in the interpretation and understanding of high temperature terranes. The thermal gradients recorded in these terranes are sufficiently steep that they require either mantle heat input or crust with higher than average heat producing capability (e.g. Bohlen, 1991; Clark et al., 2011; Kelsey and Hand, 2015; Sandiford and Hand, 1998). However, despite the knowledge that regional-scale high thermal gradient metamorphism requires an anomalous thermal regime, the tectonic settings and requirements for the generation of high to ultrahigh temperatures are still debated (e.g. Brown, 2014; Chardon et al., 2009; Clark et al., 2011; Gorczyk et al., 2015; Kelsey and Hand, 2015; Santosh and Kusky, 2010; Sizova et al., 2014). In part, this is due to a lack of certainty in how terranes behave during high temperature metamorphism, particularly with respect to the effects of melt generation and loss on crustal rheology and composition (e.g. Diener and Fagereng, 2014; Yakymchuk and Brown, 2014b). Determining the timescales of high thermal gradient metamorphism is also complex, as the ability of a rock to record all, or part, of the metamorphic evolution at high temperatures may depend on the closure temperature of the mineral geochronometer (e.g. U–Pb in zircon and monazite), the presence of melt and the reactivity of the rock (e.g. Kelly et al., 2012; Kelsey, 2008; Phillips et al., 2007, 2009; Yakymchuk and Brown, 2014a). A number of these issues are discussed in more detail below, and form the subject matter of the chapters in this thesis.

2. Thermal drivers and tectonic setting of high thermal gradient metamorphism

The duration of metamorphism is related to the longevity of the heat source and the rates of exhumation, and therefore can provide an important constraint on the tectonic setting. Short-lived (<10 Ma) high thermal gradient metamorphism can be generated by coeval magmatism or rapid exhumation, whereas longer-lived (>10 Ma) high thermal gradient metamorphism is more suggestive of slow erosion rates and crust that is in approximate isostatic equilibrium. A number of studies have attempted to identify the thermal drivers that allow the attainment and maintenance of high thermal gradients on a regional scale, particularly the attainment of UHT conditions (e.g. Brown, 2007, 2014; Clark et al., 2011; Gorczyk et al., 2015; Harley, 2004; Kelsey, 2008; Kelsey and Hand, 2015; Sandiford and Hand, 1998; Sandiford and Powell, 1986, 1991; Santosh and Kusky, 2010; Sizova et al., 2014; Wells, 1980; Wickham and Oxburgh, 1985).

The thermal gradients in most high temperature terranes exceed the conductive limit, assuming normal crustal heat production of <1.5–2.0 μWm^{-3} and mantle heat flow of of ~30 mWm^{-2} (e.g. Kelsey and Hand, 2015). Many authors therefore suggest that the primary thermal driver for high temperature metamorphism is advective addition of mantle heat, either through extension or lithospheric delamination (e.g. Bohlen, 1991; Collins, 2002; Diener et al., 2013; Kemp et al., 2007; Sandiford and Powell, 1986, 1991). A direct link between mantle magmatism and high thermal gradient metamorphism is observed in some terranes (e.g. Clark et al., 2014; Guo et al., 2012; Johnson et al., 2003b; Kemp et al., 2007; Westphal et al., 2003), but many high to ultrahigh temperature terranes do not record field evidence for significant mafic magmatism (e.g. Clark et al., 2011). Nonetheless, extension or thinning of the lithosphere resulting in increased mantle heat flow is commonly proposed as a mechanism to generate high thermal gradient metamorphism (Currie and Hyndman, 2006; De Yoreo et al., 1991; Hyndman et al., 2005; Sandiford and Powell, 1986; Sizova et al., 2014; Wickham and Oxburgh, 1985). In the modern Earth, back-arcs are regions of thinned lithosphere and high surface heat flow that may maintain elevated temperatures for 300 Myr (Currie and Hyndman, 2006; Hyndman et al., 2005). Thickening of back-arc basins or extended crust during subsequent accretion or continental collision has been proposed as a mechanism to augment temperatures by increasing radiogenic heat production in already hot crust (Brown, 2006, 2007; Clark et al., 2011; Collins, 2002; Gorczyk et al., 2015; Kemp et al., 2007; Sizova et al., 2014). 2D geodynamic modelling has shown that shallow slab breakoff and syn-extensional magmatism as a result of decompressional melting of asthenosphic mantle can generate UHT conditions (Sizova et al., 2014), as can thickening of a hot, thin and wide back-arc (Gorczyk et al., 2015). However, other workers have argued that granulite terranes preserve anhydrous mineral assemblages, which are inconsistent with a back-arc setting that is hydrated as a result of fluids from the subducting slab (Santosh and Kusky, 2010). Instead, subduction of an actively spreading ridge is invoked as a mechanism to allow upwelling asthenosphic mantle to come into contact with the base of the overriding plate, generating UHT conditions (Santosh and Kusky, 2010; Santosh et al., 2011, 2012). This mechanism would be likely to generate relatively spatially localised UHT conditions.

An alternative mechanism is the burial of high heat producing basement to mid-crustal depths, which can generate the conditions required for high thermal gradient metamorphism in the overlying sedimentary rocks (Anderson et al., 2013; Clark et al., 2011; Sandiford and Hand, 1998; Sandiford et al., 1998). As heat production is concentrated in the mid-crust, this mechanism can allow high thermal gradient metamorphism in the mid- to upper crust without causing significant melting of a refractory lower crust (Sandiford and Hand, 1998). Radiogenic heat production is a long-lived heat source, allowing high thermal gradients to be maintained for as long as the terrane remains buried (Clark et al., 2011). However, for elevated radioactive heat production to generate high temperatures, erosion must be limited (e.g. by the formation of plateaux or negligible topography) to allow the increased heat production associated with thickened crust time to substantially raise crustal temperatures via conductive heating (Chardon et al., 2009; Clark et al., 2011, 2015). For a typical range of crustal thicknesses, it may take in the order of 30–50 Myr to approach the conductive limit (Clark et al., 2011). Another important consideration in the attainment of high temperatures is the preconditioning (dehydration) of crust as a result of previous metamorphism or a prolonged prograde evolution, which limits the thermal buffering effect of partial melting during subsequent events (Brown and Korhonen, 2009; Clark et al., 2011; Kelsey and Hand, 2015; Stüwe, 1995; Vielzeuf et al., 1990). Therefore, high thermal gradient metamorphism is not limited to regions of high mantle heat flow, but may also occur in regions of continental collision (e.g. large hot orogens such as the Tibetan Plateau) if there is a combination of elevated crustal heat production, slow erosion and preconditioned crust (e.g. Chardon et al., 2009; Clark et al., 2011; Hacker et al., 2000; Jamieson and Beaumont, 2013).

In many terranes, it is likely that a number of these mechanisms operate simultaneously to contribute to the generation of high temperatures. Therefore, detailed geological and metamorphic constraints from high thermal gradient terranes are required to inform the geodynamic models that seek to understand the formation of long-lived, high temperature metamorphism.

Part 1 of this thesis explores the metamorphic evolution of three well-known, long-lived, high thermal gradient terranes: the Windmill Islands, east Antarctica (part of the larger Albany–Fraser–Wilkes Land orogenic system); the central Aileron Province, central Australia; and the Rayner Complex, east Antartctica (Fig. 2). Each of these terranes record very high thermal gradients of >130 °C/kbar with elevated temperatures persisting for more than 80 Myr. As the duration of metamorphism provides an important constraint on the causative mechanisms of high thermal gradient metamorphism, calculated metamorphic phase diagrams are combined with in situ U–Pb monazite geochronology to determine a *P–T–t* path for these terranes and make inferences about the likely tectonic setting of metamorphism. In addition, zircon U–Pb and Lu–Hf isotopes from the Windmill Islands are used to investigate the crustal evolution and provide further constraints on the tectonic setting of metamorphism. Zircon Lu–Hf isotopes from syn-metamorphic magmatic rocks can be used to assess the proportion of juvenile input, and therefore the role of mantle magmatism.

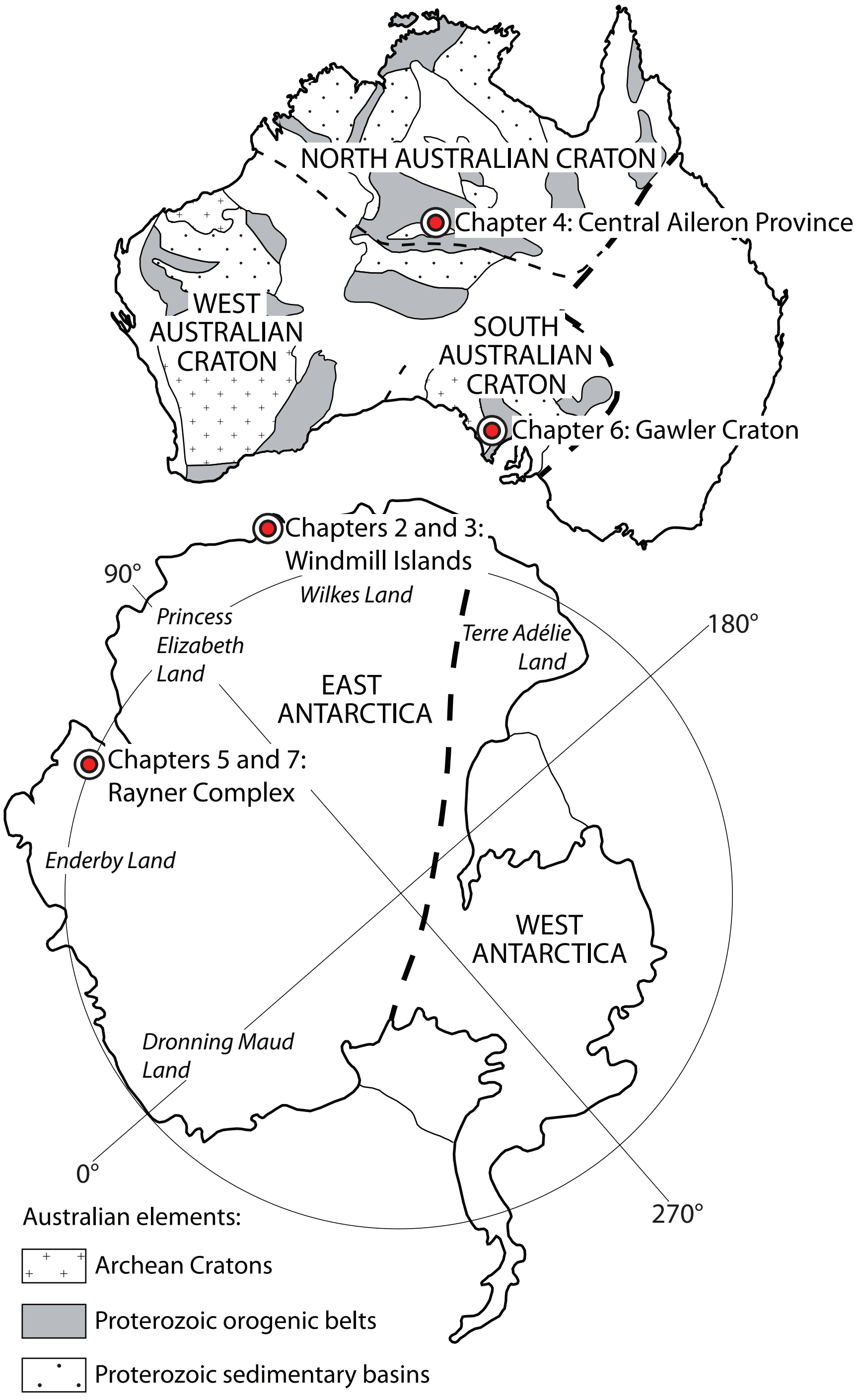

Figure 2: Simplified maps of Australia and Antarctica showing the locations of the high thermal gradient terranes investigated in this thesis.

3. The role of partial melting during high temperature metamorphism

The process of partial melting and melt migration during high temperature metamorphism is the fundamental process that differentiates the continental crust into a residual lower crust and an upper crust that is enriched in incompatible elements (Rudnick and Gao, 2003). It also results in rheological stratification (e.g. Diener and Fagereng, 2014; Handy et al., 2001; Jackson et al., 2004; Yakymchuk and Brown, 2014b). An understanding of the processes of melt generation and melt loss are therefore necessary for the interpretation of residual granulites and migmatites, as well as having implications for *P–T* modelling due to the compositional consequences of melt loss during metamorphism.

3.1. Melt generation and melt extraction

The amount of melting at the fluid-present solidus is commonly thought to be insignificant, unless there is the retention or infiltration of an H_2O-rich fluid (e.g. Johnson et al., 2003a, 2011; Rubatto et al., 2009; Sawyer, 2010; Yakymchuk and Brown, 2014b). Instead, the production of large volumes of melt in the crust is interpreted to occur as a result of suprasolidus fluid-absent dehydration melting. With increasing temperature, melting proceeds via the breakdown of hydrous minerals such as muscovite, biotite and hornblende and by the consumption of quartz and feldspar, depending on protolith composition (e.g. Patiño Douce and Beard, 1995; Patiño Douce and Harris, 1998; Rapp et al., 1991; Vielzeuf and Holloway, 1988). Mineral equilibria modelling in melt-bearing systems has provided a better understanding of the effects of bulk composition and rock fertility on melt production (e.g. Brown and Korhonen, 2009; Johnson et al., 2008; White et al., 2001, 2007; Yakymchuk and Brown, 2014b) whereas experimental and petrological observations have provided further information on the generation and segregation of melt at both grain and outcrop scale (e.g. Brown, 2010; Diener et al., 2014; Guernina and Sawyer, 2003; Handy et al., 2001; Johnson et al., 2001; Marchildon and Brown, 2002; Sawyer, 1994, 2001; Yakymchuk and Brown, 2014b; Yakymchuk et al., 2013). Melting is interpreted to begin at grain boundaries and accumulate until it reaches a critical threshold, where it is then lost episodically from the source rock (Sawyer, 1994; Yakymchuk and Brown, 2014b; Yakymchuk et al., 2013). Each melt loss event modifies the chemical composition of the system that generated the melt, and therefore the fertility of the residual rock (Brown, 2013; Korhonen et al., 2010; Vielzeuf et al., 1990; White and Powell, 2002; Yakymchuk and Brown, 2014b). In a static system, melt loss has been interpreted to occur when the melt connectivity threshold is exceeded, at ~7% melt (Rosenberg and Handy, 2005). However, in a system undergoing deformation this threshold is likely to be much lower (e.g. Brown, 2010; Handy et al., 2001), and melt loss may even be continuous (e.g. Johnson et al., 2011). Therefore, the processes of melt generation and melt loss in high temperature metamorphic rocks remains incompletely understood.

Melt loss has a number of important consequences for tectonics, crustal rheology and the long-term thermal character of the crust (e.g. Brown, 1994; Diener and Fagereng, 2014; Handy et al., 2001; Rapp et al., 1991; Sandiford et al., 2002; Sawyer, 1994; White and Powell, 2002; Yakymchuk and Brown, 2014b). Melt-bearing horizons are extremely weak and may localise strain or flow in response to gravitationally or tectonically-induced stresses (e.g. Beaumont et al., 2001, 2006; Chardon et al., 2009; Diener and Fagereng, 2014; Jamieson and Beaumont, 2013; Rey et al., 2009; Yakymchuk and Brown, 2014b). This has implications for the timescales that rocks reside within collisional orogens (e.g. Chardon et al., 2009). However, the long-term effect of melt loss is to strengthen the residual lower crust relative to the unmelted protoliths by replacing weak mica and quartz with strong garnet and feldspar-bearing assemblages (Diener and Fagereng, 2014). Partial melting also results in the redistribution of heat producing elements to the upper crust, resulting in long-term stabilisation of the lithosphere (Sandiford, 2010; Sandiford and McLaren, 2002; Sandiford et al., 2002). The redistribution of heat producing elements into the upper crust during orogenesis means that they may be more likely to be eroded and incorporated into sedimentary basins. The deposition of detritus enriched in heat producing elements on passive margins has been proposed as a mechanism for generating high thermal gradient terranes during subsequent collision (Clark et al., 2015). Finally, as discussed above, previous melt loss is an important consideration when investigating the *P–T* evolution of high thermal gradient terranes, as melt loss limits further melting reactions and allows the attainment of higher temperatures (e.g. Brown and Korhonen, 2009; Clark et al., 2011; Stüwe, 1995; Vielzeuf et al., 1990).

3.2. Melt and the interpretation of geochronology

Determining the timing of metamorphism is vital for correlating metamorphic events across a terrane, but also for determining the timescale of the high temperature processes. However, in many suprasolidus terranes, the interpretation of monazite and zircon U–Pb geochronology requires an assessment of the effects of fluid and melt-bearing processes. The stability of monazite and zircon in suprasolidus rocks is strongly dependent on the *P–T* conditions of metamorphism and the amount and chemistry of the melt (e.g. Kelsey et al., 2008; Rapp and Watson, 1986; Stepanov et al., 2012; Yakymchuk and Brown, 2014a). In the residual source rock, monazite (and to a lesser extent, zircon) may be partially dissolved into melt by prograde metamorphism to high temperatures (Kelsey et al., 2008; Stepanov et al., 2012; Yakymchuk and Brown, 2014a). Therefore, monazite and zircon ages in high temperature rocks may not record peak conditions, and instead reflect growth during melt crystallisation near the elevated solidus (Brown and Korhonen, 2009; Kelsey et al., 2008; Roberts and Finger, 1997; Stepanov et al., 2012; Yakymchuk and Brown, 2014a). As a result, age variation between samples in high temperature, melt-depleted terranes has been explained by differences in solidus temperatures of the residual rock (Korhonen et al., 2013b; Reno et al., 2012). An array of concordant U–Pb analyses within samples has been interpreted to reflect either Pb-loss as a result of prolonged high temperature, high strain conditions (Halpin et al., 2012), multiple, discrete thermal events within a short timescale (e.g. Robb et al., 1999; Smithies et al., 2011), or continuous growth due to slow cooling from the point where melt begins to crystallise to the temperature of the solidus (Kelsey, 2008; Korhonen et al., 2013b; Walsh et al., 2015; Yakymchuk and Brown, 2014a). The interpretation of monazite geochronology is additionally complicated as monazite is also susceptible to low temperature fluid flow processes (e.g. Harlov et al., 2011; Kelly et al., 2012; Williams et al., 2011), including the release of aqueous fluids as a result of the crystallisation of nearby magmatic rocks or rocks with higher solidi. Therefore, an understanding of the *P–T* conditions and volume of melt generation and melt loss are necessary for the interpretation of geochronology in high temperature terranes.

3.3. Melt loss and implications for P–T modelling

Despite the importance of melt loss for the interpretation of residual granulites and migmatites, quantifying the effects of melt loss remains a significant challenge for metamorphic geologists when inferring the *P–T* evolution of a terrane. The open-system process of melt loss is necessary for the preservation of anhydrous granulite facies mineral assemblages that would otherwise be retrogressed on cooling in a closed system (Brown, 2002; Guernina and Sawyer, 2003; White and Powell, 2002). However, melt loss is likely to significantly modify the composition of the protolith rock, meaning that metamorphic geologists cannot use the residual granulite bulk compositions to quantify the prograde *P–T* evolution of such rocks (e.g. Johnson and White, 2011; Kelsey and Hand, 2015; White and Powell, 2002).

The effects of step-wise melt loss on the chemical composition of the residual rock can be quantified using a series of calculated *P–T* pseudosections (Yakymchuk and Brown, 2014b). This can then be used to assess the effects of melt loss on crustal rheology (Diener and Fagereng, 2014) or the behaviour of geochronometers (Yakymchuk and Brown, 2014a). An inverse process can be used to reconstruct pre-melt loss bulk composition to model the possible prograde history where the composition of the protolith is unknown (Korhonen et al., 2013a).

Part 2 of this thesis uses a sequence of iron-rich metasedimentary rocks in the southern Gawler Craton (Fig. 2) that range in grade from greenschist to granulite facies to model the effects of melt loss in a situation where the bulk composition of both the unmelted protoliths and residual granulites are known. One compositional implication of melt loss is that the residual rock becomes enriched in compatible elements such as iron (e.g. Brown, 2013; Guernina and Sawyer, 2003; Redler et al., 2013; Sawyer, 1994; Vielzeuf et al., 1990; White and Powell, 2002; Yakymchuk and Brown, 2014b). This tendency for compatible element enrichment potentially has economic implications because it can increase the concentration of metals in rock sequences that contain primary metal anomalies to the point where they are economically attractive.

4. Recognising polymetamorphism in high thermal gradient terranes

The traditional approach to determining the tectono-metamorphic evolution of terranes is to use the paragenetic sequence of mineral growth, including mineral reaction microstructures, to interpret a likely *P–T–t* path and to use this to inform tectonic models. However, to interpret a *P–T* path, it is necessary to first establish that the paragenetic sequence records the effects of a single, continuous metamorphic event. This is generally not possible to do on the basis of petrography (or calculated phase diagrams) alone. The increasing use of in situ geochronology has allowed metamorphic geologists to recognise reaction microstructures that record the effects of temporally unrelated events (e.g. Dutch et al., 2005; Goncalves et al., 2004; Hand et al., 1992; Hensen and Zhou, 1995; Kelsey et al., 2007; Korhonen et al., 2012; Yakymchuk et al., 2015). However, recognising polymetamorphism in granulite terranes that have experienced extensive melt loss remains difficult and therefore requires care to unravel. As these terranes typically comprise rocks with refractory, unreactive chemical compositions, the paucity of a fluid hinders the formation of new, overprinting mineral assemblages and the resetting or new growth of high-temperature geochronometers such as monazite and zircon (e.g. Drüppel et al., 2012; Korhonen et al., 2012; Phillips et al., 2007, 2009; Tenczer et al., 2006; White and Powell, 2002). Nonetheless, if an appropriate heat source exists, these terranes are susceptible to high-*T* thermal reworking because they largely avoid the energetic requirements for melting (e.g. Brown and Korhonen, 2009; Clark et al., 2011; Stüwe, 1995; Vielzeuf et al., 1990; Walsh et al., 2015).

Part 3 of this thesis explores the controls on metamorphic reworking and the mechanisms for recognising cryptically recorded polymetamorphism in refractory terranes that have undergone melt loss. The Rayner Complex (Fig. 2) is a terrane that records apparently different *P–T* paths for spatially adjacent areas. In situ monazite geochronology is combined with petrographic interpretation to investigate the record of polymetamorphism in a terrane that generally preserves rocks with residual, metamorphically unreactive chemical compositions.

5. Thesis outline

The central aim of this thesis is to develop a framework for how high thermal gradient terranes behave, from the tectonic setting and mechanisms for attaining high temperatures, their ability to record the prograde to peak metamorphic history, and finally the consequences of high thermal gradient metamorphism for bulk compositions and reactivity during subsequent metamorphic events. As high thermal gradient terranes commonly only record part of their history, this thesis has three main aims:

1. To explore the tectonic settings required to achieve and maintain elevated temperatures using case studies from three terranes that record long-lived high thermal gradient metamorphism.

2. To explore the effect of granulite facies metamorphism and melt loss on the bulk composition, metamorphic reactivity and the way economic mineral systems can be augmented via high temperature metamorphic processes.

3. To explore the way in which metamorphic reworking is recorded in compositionally resistant terranes.

This thesis has been written as a series of individual manuscripts addressing specific aspects of high thermal gradient terranes that address the aims of the study. Many of these manuscripts are published in peer reviewed journals and so have been included in their original published state. This leads to some repetition in the methodology sections and the interpretation of *P–T* modelling and geochronology, but highlights the considerations that are necessary when determining the *P–T–t* evolution of a high temperature terrane. New activity–composition (*a–x*) models for use with the most recent update of the thermodynamic dataset used by THERMOCALC, ds62, were released for public use during the course of this PhD (Holland and Powell, 2011; Powell et al., 2014; White et al., 2014a, 2014b). Therefore, ds62 was used for the calculation of phase equilibria in Chapters 3 and 6, whereas Chapters 4, 5 and 7 use ds55 (Powell and Holland, 1988).

5.1. Part 1: Chapters 2–5

Chapters 2 and 3 provide a case study from the Windmill Islands, east Antarctica. The Windmill Islands region is part of a larger, long-lived, high to ultrahigh temperature orogenic belt that includes the Albany–Fraser Orogen in Western Australia and the Musgrave Province in central Australia. The Windmill Islands record evidence for two stages of metamorphism and voluminous high temperature magmatism. A number of different tectonic scenarios have been proposed for the Windmill Islands region prior to the first stage of metamorphism, ranging from a passive margin that evolves into a foreland basin to thickening of an extensional accretionary orogen. **Chapter 2** uses U–Pb and Lu–Hf isotopic systems in zircon to investigate the crustal evolution of the Windmill Islands. Detrital zircon age data is used to investigate the likely sources of sedimentation and the

Lu–Hf isotopic signature of zircon in magmatic rocks is used to investigate the possible sources of magmatism, with the aim of providing constraints on the tectonic setting. **Chapter 3** uses in situ U–Pb monazite geochronology and calculated metamorphic phase diagrams from samples that record different stages of the overall *P–T* history of the Windmill Islands to unravel the two stages of metamorphism. This is then used to assess the likely tectonic setting of the eastern margin of the Windmill Islands–Albany–Fraser system in the context of the constraints placed on crustal evolution in Chapter 2.

Chapter 2 is under review in *Precambrian Research* as:
Morrissey, L.J., Payne, J.L., Hand, M., Clark, C., Taylor, R., Kirkland, C.L., Kylander-Clark, A. Linking the Windmill Islands, east Antarctica and the Albany–Fraser Orogen: insights from U–Pb zircon geochronology and Hf isotopes.

Chapter 3 is written for submission to *Journal of Metamorphic Geology* as:
Morrissey, L.J., Hand, M., Kelsey, D.E. Assessing tectonic models for Stage I–Stage II metamorphism in the Antarctica segment of the Musgrave–Albany–Fraser Orogen using *P–T* constraints.

Chapter 4 provides a case study from the Reynolds Range in the central Aileron Province, central Australia. The Reynolds Range is an exceptional example of apparently long-lived high thermal gradient granulite facies metamorphism where evidence for coeval magmatism or extension is absent. Existing zircon and monazite U–Pb isotopic age data from the Reynolds Range suggest that anatectic conditions were sustained for up to 30 Myr during the Early Mesoproterozoic and were followed by c. 100 Myr of slow cooling (Buick et al., 1999; Rubatto et al., 2001; Vry and Baker, 2006; Williams et al., 1996). Therefore, a long-lived, non-magmatic heat source is required to sustain the elevated temperatures. In situ U–Pb monazite geochronology from samples recording specific parts of the *P–T* evolution is combined with calculated metamorphic phase diagrams to document the *P–T–t* evolution and constrain the duration of metamorphism in the Reynolds Range. The duration of high temperature metamorphism and the inferred cooling rate provide important constraints on the mechanisms that can generate high thermal gradient metamorphism. They suggest that the Reynolds Range is an example of metamorphism driven by the burial of high heat producing crust.

This chapter is published as:
Morrissey, L.J., Hand, M., Raimondo, T., Kelsey, D.E., 2014. Long-lived high-temperature, low-pressure granulite facies metamorphism in the Arunta Region, central Australia. *Journal of Metamorphic Geology*, **32**, 25–47. doi:10.1111/jmg.12056.

Chapter 5 provides a case study from the Rayner Complex, east Antarctica, which forms part of a vast high thermal gradient terrane that includes the ultrahigh temperature Eastern Ghats Province in India. Detailed *P–T–t* studies from the Eastern Ghats suggest that ultrahigh conditions were sustained for >50 Myr and may have persisted for as long as 200 Myr (Korhonen et al., 2013b). Metamorphism involved an anticlockwise *P–T* path dominated by isobaric cooling and was associated with voluminous granitic and charnockitic magmatism (Korhonen et al., 2013a, 2013b). Charnockitic magmatism in the Rayner Complex appears to be equally long-lived (Halpin et al., 2012). However, the only studies from the Rayner Complex that combine in situ geochronology with modern metamorphic phase equilibria are limited to outcrops along the coast (Halpin et al., 2007a, 2007b). The northern Prince Charles Mountains (nPCM) provide a large region of inland outcrop in the Rayner Complex. **Chapter 5** uses samples of metapelite from the nPCM to place detailed *P–T–t* constraints on metamorphism in the Rayner Complex, which can then inform geodynamic models. The Rayner Complex provides an example of an extremely long-lived high thermal gradient terrane that is likely to be the result of thickening of a wide back-arc, where the maintenance of elevated temperatures was probably assisted by episodic magmatism.

This chapter is published as:
Morrissey, L.J., Hand, M, Kelsey, D.E., 2015. Multi-stage metamorphism in the Rayner–Eastern Ghats Terrane: *P–T–t* constraints from the northern Prince Charles Mountains, east Antarctica. *Precambrian Research*, **267**, 137–163. doi: 10.1016/j.precamres.2015.06.003.

5.2. Part 2: Chapter 6

Chapter 6 explores the process of metamorphism and step-wise melt loss on a sequence of iron-rich metasedimentary rocks in the southern Gawler Craton that range in grade from greenschist facies phyllite to granulite facies gneisses. The greenschist facies phyllites are not economic but the granulite facies gneisses contain economic quantities of magnetite. This chapter uses a series of calculated metamorphic phase diagrams to model the change in composition and proportion of Fe-oxides during high temperature metamorphism of two samples of the greenschist facies protoliths. **Chapter 6** shows that volume reduction as a result of granulite facies melt loss is a mechanism to concentrate iron in the residual rock package up to economic grades.

This chapter is published as:
Morrissey, L.J., Hand, M, Lane, K., Kelsey, D.E., Dutch, R.A., 2016. Upgrading iron-rich sequences to economic grade iron-ore deposits by melt loss during granulite-facies metamorphism. *Ore Geology Reviews*, **74**, 101–121. doi: 10.1016/j.oregeorev.2015.11.012.

5.3. Part 3: Chapter 7

Chapter 7 provides a framework for recognising the effects of high temperature reworking in a refractory residual terrane that has undergone extensive melt loss and metamorphism. The Rayner Complex underwent high temperature metamorphism and melting during the Rayner Orogeny, the conditions of which are constrained in Chapter 5. This is used as basis to assess the metamorphic effects of later reworking of the Rayner Complex during the Cambrian. Detailed petrography is combined with in situ U–Pb geochronology and *P–T* pseudosections to investigate the effect of a second high temperature event on those regions that may have experienced retrogression at the end of the Rayner Orogeny. **Chapter 7** shows that adjacent regions that preserve different *P–T* paths (clockwise versus anticlockwise) can be used in conjunction with geochronology to recognise a second, high temperature metamorphic event that is cryptically recorded.

This chapter is published as:
Morrissey, L.J., Hand, M., Kelsey, D.E., Wade, B.P., 2016. Cambrian high-temperature reworking of the Rayner–Eastern Ghats terrane: constraints from the northern Prince Charles Mountains region, east Antarctica. *Journal of Petrology*, **57**, 53–92. doi: 10.1093/petrology/egv082.

5.4. Key findings and conclusions: Chapter 8

Chapter 8 summarises the key findings of each of the chapters of this thesis and provides some future research directions to further understand the origin and evolution of high thermal gradient terranes.

In addition to the chapters in this thesis, I have authored or co-authored two other manuscripts during the course of my PhD. These are loosely related to the subject matter of this thesis and are referred to in a number of the following chapters. Full text versions of these papers are included in this thesis as **Appendix 1**. The manuscripts are published as:

Morrissey, L.J., Hand, M., Wade, B.P., Szpunar, M., 2013. Early Mesoproterozoic metamorphism in the Barossa Complex, South Australia: links with the eastern margin of Proterozoic Australia. *Australian Journal of Earth Sciences*, **60**, 769–795. doi: 10.1080/08120099.2013.860623.

Wong, B., Morrissey, L.J., Hand, M., Fields, C., Kelsey, D.E., 2015. Grenvillian-aged reworking of late Paleoproterozoic crust of the southern North Australian Craton, central Australia: implications for the assembly of Mesoproterozoic Australia. *Precambrian Research*, **270**, 100–123. doi: 10.1016/j.precamres.2015.09.001.

References

Anderson, J.R., Kelsey, D.E., Hand, M., Collins, W.J., 2013. Conductively driven, high-thermal gradient metamorphism in the Anmatjira Range, Arunta region, central Australia. Journal of Metamorphic Geology 31, 1003–1026.

Barton, M.D., Hanson, R.B., 1989. Magmatism and the development of low-pressure metamorphic belts: Implications from the western United States and thermal modeling. Geological Society of America Bulletin 101, 1051–1065.

Beaumont, C., Jamieson, R.A., Nguyen, M.H., Lee, B., 2001. Himalayan tectonics explained by extrusion of a low-viscosity crustal channel coupled to focused surface denudation. Nature 414, 738–742.

Beaumont, C., Nguyen, M.H., Jamieson, R.A., Ellis, S., 2006. Crustal flow modes in large hot orogens, in: Law, R.D., Searle, M.P., Godin, L. (Eds.), Modelling Channel Flow and Ductile Extrusion Processes. Geological Society, London, Special Publications, pp. 91–145.

Bohlen, S.R., 1991. On the formation of granulites. Journal of Metamorphic Geology 9, 223–229.

Brown, M., 1994. The generation, segregation, ascent and emplacement of granite magma: the migmatite-to-crustally-derived granite connection in thickened orogens. Earth-Science Reviews 36, 83–130.

Brown, M., 2002. Retrograde processes in migmatites and granulites revisited. Journal of Metamorphic Geology 20, 25–40.

Brown, M., 2006. Duality of thermal regimes is the distinctive characteristic of plate tectonics since the Neoarchean. Geology 34, 961–964.

Brown, M., 2007. Metamorphic Conditions in Orogenic Belts: A Record of Secular Change. International Geology Review 49, 193–234.

Brown, M., 2010. The spatial and temporal patterning of the deep crust and implications for the process of melt extraction. Philosophical Transactions of the Royal Society A 368, 11–51.

Brown, M., 2013. Granite: From genesis to emplacement. Geological Society of America Bulletin 125, 1079–1113.

Brown, M., 2014. The contribution of metamorphic petrology to understanding lithosphere evolution and geodynamics. Geoscience Frontiers 5, 553–569.

Brown, M., Korhonen, F.J., 2009. Some Remarks on Melting and Extreme Metamorphism of Crustal Rocks Physics and Chemistry of the Earth's Interior, in: Gupta, A.K., Dasgupta, S. (Eds.). Springer New York, pp. 67–87.

Buick, I.S., Frei, R., Cartwright, I., 1999. The timing of high-temperature retrogression in the Reynolds Range, central Australia: constraints from garnet and epidote Pb–Pb dating. Contributions to Mineralogy and Petrology 135, 244–254.

Chardon, D., Gapais, D., Cagnard, F., 2009. Flow of ultra-hot orogens: A view from the Precambrian, clues for the Phanerozoic. Tectonophysics 477, 105–118.

Clark, C., Fitzsimons, I.C.W., Healy, D., Harley, S.L., 2011. How Does the Continental Crust Get Really Hot? Elements 7, 235–240.

Clark, C., Healy, D., Johnson, T., Collins, A.S., Taylor, R.J., Santosh, M., Timms, N.E., 2015. Hot orogens and supercontinent amalgamation: A Gondwanan example from southern India. Gondwana Research 28, 1310–1328.

Clark, C., Kirkland, C.L., Spaggiari, C.V., Oorschot, C., Wingate, M.T.D., Taylor, R.J., 2014. Proterozoic granulite formation driven by mafic magmatism: An example from the Fraser Range Metamorphics, Western Australia. Precambrian Research 240, 1–21.

Collins, W.J., 2002. Nature of extensional accretionary orogens. Tectonics 21, 1–12.

Currie, C.A., Hyndman, R.D., 2006. The thermal structure of subduction zone back arcs. Journal of Geophysical Research: Solid Earth 111, B08404.

De Yoreo, J.J., Lux, D.R., Guidotti, C.V., 1991. Thermal modelling in low-pressure/high-temperature metamorphic belts. Tectonophysics 188, 209-238.

Diener, J.F.A., Fagereng, Å., 2014. The influence of melting and melt drainage on crustal rheology during orogenesis. Journal of Geophysical Research: Solid Earth 119, 6193–6210.

Diener, J.F.A., White, R.W., Hudson, T.J.M., 2014. Melt production, redistribution and accumulation in mid-crustal source rocks, with implications for crustal-scale melt transfer. Lithos 200–201, 212–225.

Diener, J.F.A., White, R.W., Link, K., Dreyer, T.S., Moodley, A., 2013. Clockwise, low-*P* metamorphism of the Aus granulite terrain, southern Namibia, during the Mesoproterozoic Namaqua Orogeny. Precambrian Research 224, 629–652.

Drüppel, K., Elsäßer, L., Brandt, S., Gerdes, A., 2012. Sveconorwegian Mid-crustal Ultrahigh-temperature Metamorphism in Rogaland, Norway: U–Pb LA-ICP-MS Geochronology and Pseudosections of Sapphirine Granulites and Associated Paragneisses. Journal of Petrology 54, 305–350.

Dutch, R.A., Hand, M., Clark, C., 2005. Cambrian reworking of the southern Australian Proterozoic Curnamona Province: constraints from regional shear-zone systems. Journal of the Geological Society 162, 763–775.

Goncalves, P., Nicollet, C., Montel, J.-M., 2004. Petrology and in situ U–Th–Pb Monazite Geochronology of Ultrahigh-Temperature Metamorphism from the Andriamena Mafic Unit, North–Central Madagascar. Significance of a Petrographical *P–T* Path in a Polymetamorphic Context. Journal of Petrology 45, 1923–1957.

Gorczyk, W., Smithies, H., Korhonen, F., Howard, H., Quentin De Gromard, R., 2015. Ultra-hot Mesoproterozoic evolution of intracontinental central Australia. Geoscience Frontiers 6, 23–37.

Guernina, S., Sawyer, E.W., 2003. Large-scale melt-depletion in granulite terranes: an example from the Archean Ashuanipi Subprovince of Quebec. Journal of Metamorphic Geology 21, 181–201.

Guo, J., Peng, P., Chen, Y., Jiao, S., Windley, B.F., 2012. UHT sapphirine granulite metamorphism at 1.93–1.92 Ga caused by gabbronorite intrusions: Implications for tectonic evolution of the northern margin of the North China Craton. Precambrian Research 222–223, 124–142.

Hacker, B.R., Gnos, E., Ratschbacher, L., Grove, M., McWilliams, M., Sobolev, S.V., Wan, J., Zhenhan, W., 2000. Hot and Dry Deep Crustal Xenoliths from Tibet. Science 287, 2463–2466.

Halpin, J.A., Clarke, G.L., White, R.W., Kelsey, D.E., 2007a. Contrasting *P–T–t* paths for Neoproterozoic metamorphism in MacRobertson and Kemp Lands, east Antarctica. Journal of Metamorphic Geology 25, 683–701.

Halpin, J.A., Daczko, N.R., Milan, L.A., Clarke, G.L., 2012. Decoding near-concordant U–Pb zircon ages spanning several hundred million years: recrystallisation, metamictisation or diffusion? Contributions to Mineralogy and Petrology 163, 67–85.

Halpin, J.A., White, R.W., Clarke, G.L., Kelsey, D.E., 2007b. The Proterozoic *P–T–t* Evolution of the Kemp Land Coast, East Antarctica; Constraints from Si-saturated and Si-undersaturated

Metapelites. Journal of Petrology 48, 1321–1349.

Hand, M., Dirks, P., Powell, R., Buick, I.S., 1992. How well established is isobaric cooling in Proterozoic orogenic belts? An example from the Arunta Inlier, central Australia. Geology 20, 649–652.

Handy, M.R., Mulch, A., Rosenau, M., Rosenberg, C.L., 2001. The role of fault zones and melts as agents of weakening, hardening and differentiation of the continental crust: a synthesis. Geological Society, London, Special Publications 186, 305–332.

Harley, S.L., 1998. Ultrahigh temperature granulite metamorphism (1050 °C, 12 kbar) and decompression in garnet (Mg70)–orthopyroxene–sillimanite gneisses from the Rauer Group, East Antarctica. Journal of Metamorphic Geology 16, 541–562.

Harley, S.L., 2004. Extending our understanding of Ultrahigh temperature crustal metamorphism. Journal of Mineralogical and Petrological Sciences 99, 140–158.

Harley, S.L., 2008. Refining the *P–T* records of UHT crustal metamorphism. Journal of Metamorphic Geology 26, 125–154.

Harley, S.L., Kelly, N.M., 2007. The impact of zircon–garnet REE distribution data on the interpretation of zircon U–Pb ages in complex high-grade terrains: An example from the Rauer Islands, East Antarctica. Chemical Geology 241, 62–87.

Harlov, D.E., Wirth, R., Hetherington, C.J., 2011. Fluid-mediated partial alteration in monazite: the role of coupled dissolution–reprecipitation in element redistribution and mass transfer. Contributions to Mineralogy and Petrology 162, 329–348.

Hensen, B.J., Zhou, B., 1995. Retention of isotopic memory in garnets partially broken down during an overprinting granulite-facies metamorphism: Implications for the Sm–Nd closure temperature. Geology 23, 225–228.

Hermann, J., Rubatto, D., 2003. Relating zircon and monazite domains to garnet growth zones: age and duration of granulite facies metamorphism in the Val Malenco lower crust. Journal of Metamorphic Geology 21, 833–852.

Holland, T.J.B., Powell, R., 2011. An improved and extended internally consistent thermodynamic dataset for phases of petrological interest, involving a new equation of state for solids. Journal of Metamorphic Geology 29, 333–383.

Hyndman, R.D., Currie, C.A., Mazzotti, S.P., 2005. Subduction zone backarcs, mobile belts, and orogenic heat. GSA Today 15, 4–10.

Jackson, J.A., Austrheim, H., McKenzie, D., Priestley, K., 2004. Metastability, mechanical strength, and the support of mountain belts. Geology 32, 625–628.

Jamieson, R.A., Beaumont, C., 2013. On the origin of orogens. Geological Society of America Bulletin 125, 1671–1702.

Johnson, T.E., Brown, M., Solar, G.S., 2003a. Low–pressure subsolidus and suprasolidus phase equilibria in the MnNCKFMASH system: Constraints on conditions of regional metamorphism in western Maine, northern Appalachians. American Mineralogist 88, 624–638.

Johnson, T.E., Clark, C., Taylor, R.J.M., Santosh, M., Collins, A.S., 2015. Prograde and retrograde growth of monazite in migmatites: An example from the Nagercoil Block, southern India. Geoscience Frontiers 6, 373–387.

Johnson, T.E., Gibson, G.M., Brown, M., Buick, I.S., Cartwright, I., 2003b. Partial Melting of Metapelitic Rocks Beneath the Bushveld Complex, South Africa. Journal of Petrology 44, 789–813.

Johnson, T.E., Hudson, N.F.C., Droop, G.T.R., 2001. Melt segregation structures within the Inzie Head gneisses of the northeastern Dalradian. Scottish Journal of Geology 37, 59–72.

Johnson, T.E., White, R.W., 2011. Phase equilibrium constraints on conditions of granulite-facies metamorphism at Scourie, NW Scotland. Journal of the Geological Society 168, 147–158.

Johnson, T.E., White, R.W., Brown, M., 2011. A year in the life of an aluminous metapelite xenolith—The role of heating rates, reaction overstep, H_2O retention and melt loss. Lithos 124, 132–143.

Johnson, T.E., White, R.W., Powell, R., 2008. Partial melting of metagreywacke: a calculated mineral equilibria study. Journal of Metamorphic Geology 26, 837–853.

Kelly, N.M., Harley, S.L., Möller, A., 2012.

Complexity in the behavior and recrystallization of monazite during high-*T* metamorphism and fluid infiltration. Chemical Geology 322–323, 192–208.

Kelsey, D.E., 2008. On ultrahigh-temperature crustal metamorphism. Gondwana Research 13, 1–29.

Kelsey, D.E., Clark, C., Hand, M., 2008. Thermobarometric modelling of zircon and monazite growth in melt-bearing systems: examples using model metapelitic and metapsammitic granulites. Journal of Metamorphic Geology 26, 199–212.

Kelsey, D.E., Hand, M., 2015. On ultrahigh temperature crustal metamorphism: phase equilibria, trace element thermometry, bulk composition, heat sources, timescales and tectonic settings. Geoscience Frontiers 6, 311–356.

Kelsey, D.E., Hand, M., Clark, C., Wilson, C.J.L., 2007. On the application of in situ monazite chemical geochronology to constraining *P–T–t* histories in high-temperature (>850 °C) polymetamorphic granulites from Prydz Bay, East Antarctica. Journal of Geological Society, London 164, 667–683.

Kemp, A.I.S., Shimura, T., Hawkesworth, C.J., EIMF, 2007. Linking granulites, silicic magmatism, and crustal growth in arcs: Ion microprobe (zircon) U–Pb ages from the Hidaka metamorphic belt, Japan. Geology 35, 807–810.

Kohn, M.J., Malloy, M.A., 2004. Formation of monazite via prograde metamorphic reactions among common silicates: implications for age determinations. Geochimica et Cosmochimica Acta 68, 101–113.

Korhonen, F., Brown, M., Clark, C., Foden, J.D., Taylor, R., 2015. Are granites and granulites consanguineous? Geology 43, 991–994.

Korhonen, F.J., Brown, M., Clark, C., Bhattacharya, S., 2013a. Osumilite–melt interactions in ultrahigh temperature granulites: phase equilibria modelling and implications for the *P–T–t* evolution of the Eastern Ghats Province, India. Journal of Metamorphic Geology 31, 881–907.

Korhonen, F.J., Brown, M., Grove, M., Siddoway, C.S., Baxter, E.F., Inglis, J.D., 2012. Separating metamorphic events in the Fosdick migmatite–granite complex, West Antarctica. Journal of Metamorphic Geology 30, 165–192.

Korhonen, F.J., Clark, C., Brown, M., Bhattacharya, S., Taylor, R., 2013b. How long-lived is ultrahigh temperature (UHT) metamorphism? Constraints from zircon and monazite geochronology in the Eastern Ghats orogenic belt, India. Precambrian Research 234, 322–350.

Korhonen, F.J., Saito, S., Brown, M., Siddoway, C.S., 2010. Modeling multiple melt loss events in the evolution of an active continental margin. Lithos 116, 230–248.

Kylander-Clark, A.R.C., Hacker, B.R., Cottle, J.M., 2013. Laser-ablation split-stream ICP petrochronology. Chemical Geology 345, 99–112.

Loosveld, R.J.H., Etheridge, M.A., 1990. A model for low-pressure facies metamorphism during crustal thickening. Journal of Metamorphic Geology 8, 257–267.

Lux, D.R., DeYoreo, J.J., Guldotti, C.V., Decker, E.R., 1986. Role of plutonism in low-pressure metamorphic belt formation. Nature 323, 794–797.

Marchildon, N., Brown, M., 2002. Grain-scale melt distribution in two contact aureole rocks: implications for controls on melt localization and deformation. Journal of Metamorphic Geology 20, 381–396.

Miyashiro, A., 1961. Evolution of Metamorphic Belts. Journal of Petrology 2, 277–311.

Patiño Douce, A.E., Beard, J.S., 1995. Dehydration-melting of Biotite Gneiss and Quartz Amphibolite from 3 to 15 kbar. Journal of Petrology 36, 707–738.

Patiño Douce, A.E., Harris, N., 1998. Experimental Constraints on Himalayan Anatexis. Journal of Petrology 39, 689–710.

Phillips, G., Kelsey, D.E., Corvino, A.F., Dutch, R.A., 2009. Continental Reworking during Overprinting Orogenic Events, Southern Prince Charles Mountains, East Antarctica. Journal of Petrology 50, 2017–2041.

Phillips, G., White, R.W., Wilson, C.J.L., 2007. On the roles of deformation and fluid during rejuvenation of a polymetamorphic terrane: inferences on the geodynamic evolution of the Ruker Province, East Antarctica. Journal of Metamorphic Geology 25, 855–871.

Powell, R., Holland, T., 1988. An internally consistent thermodynamic dataset with uncertainties and correlations: 3. Application methods, worked examples and a computer program. Journal of Metamorphic Geology 6, 173–204.

Powell, R., White, R.W., Green, E.C.R., Holland, T.J.B., Diener, J.F.A., 2014. On parameterizing thermodynamic descriptions of minerals for petrological calculations. Journal of Metamorphic Geology 32, 245–260.

Rapp, R., Watson, E.B., 1986. Monazite solubility and dissolution kinetics: implications for the thorium and light rare earth chemistry of felsic magmas. Contributions to Mineralogy and Petrology 94, 304–316.

Rapp, R.P., Watson, E.B., Miller, C.F., 1991. Precambrian Granitoids Petrogenesis, Geochemistry and Metallogeny Partial melting of amphibolite/eclogite and the origin of Archean trondhjemites and tonalites. Precambrian Research 51, 1–25.

Redler, C., White, R.W., Johnson, T.E., 2013. Migmatites in the Ivrea Zone (NW Italy): Constraints on partial melting and melt loss in metasedimentary rocks from Val Strona di Omegna. Lithos 175-176, 40–53.

Reno, B.L., Piccoli, P.M., Brown, M., Trouw, R.A.J., 2012. In situ monazite (U–Th)–Pb ages from the Southern Brasília Belt, Brazil: constraints on the high-temperature retrograde evolution of *HP* granulites. Journal of Metamorphic Geology 30, 81–112.

Rey, P.F., Teyssier, C., Whitney, D.L., 2009. Extension rates, crustal melting, and core complex dynamics. Geology 37, 391–394.

Robb, L.J., Armstrong, R.A., Waters, D.J., 1999. The History of Granulite-Facies Metamorphism and Crustal Growth from Single Zircon U–Pb Geochronology: Namaqualand, South Africa. Journal of Petrology 40, 1747–1770.

Roberts, M.P., Finger, F., 1997. Do U–Pb zircon ages from granulites reflect peak metamorphic conditions? Geology 25, 319–322.

Rosenberg, C.L., Handy, M.R., 2005. Experimental deformation of partially melted granite revisited: implications for the continental crust. Journal of Metamorphic Geology 23, 19–28.

Rothstein, D.A., Hoisch, T.D., 1994. Multiple intrusions and low-pressure metamorphism in in the central Old Woman Mountains, south-eastern California: constraints from thermal modelling. Journal of Metamorphic Geology 12, 723–734.

Rubatto, D., 2002. Zircon trace element geochemistry: partitioning with garnet and the link between U–Pb ages and metamorphism. Chemical Geology 184, 123–138.

Rubatto, D., Chakraborty, S., Dasgupta, S., 2013. Timescales of crustal melting in the Higher Himalayan Crystallines (Sikkim, Eastern Himalaya) inferred from trace element-constrained monazite and zircon chronology. Contributions to Mineralogy and Petrology 165, 349–372.

Rubatto, D., Hermann, J., Berger, A., Engi, M., 2009. Protracted fluid-induced melting during Barrovian metamorphism in the Central Alps. Contributions to Mineralogy and Petrology 158, 703–722.

Rubatto, D., Williams, I.S., Buick, I.S., 2001. Zircon and monazite response to prograde metamorphism in the Reynolds Range, central Australia. Contributions to Mineralogy and Petrology 140, 458–468.

Rudnick, R.L., Gao, S.X., 2003. Composition of the continental crust, in: Rudnick, R.L. (Ed.), The Crust Volume 3, Treatise on Geochemistry. Elsevier–Pergamon, Oxford, UK, pp. 1–64.

Sandiford, M., 2010. Why are the continents just so…? Journal of Metamorphic Geology 28, 569–577.

Sandiford, M., Hand, M., 1998. Australian Proterozoic high-temperature, low-pressure metamorphism in the conductive limit. Geological Society, London, Special Publications 138, 109–120.

Sandiford, M., Hand, M., McLaren, S., 1998. High geothermal gradient metamorphism during thermal subsidence. Earth and Planetary Science Letters 163, 149–165.

Sandiford, M., Martin, N., Zhao, S., Fraser, G., 1991. Mechanical consequences of granite emplacement during high-*T*, low-*P* metamorphism and the origin of "anticlockwise" *P–T* paths. Earth and Planetary Science Letters 107, 164–172.

Sandiford, M., McLaren, S., 2002. Tectonic feedback and the ordering of heat producing elements within the continental lithosphere. Earth and Planetary Science Letters 204, 133–150.

Sandiford, M., McLaren, S., Neumann, N., 2002. Long-term thermal consequences of the redistribution of heat-producing elements associated with large-scale granitic complexes. Journal of Metamorphic Geology 20, 87–98.

Sandiford, M., Powell, R., 1986. Deep crustal metamorphism during continental extension: modern and ancient examples. Earth and Planetary Science Letters 79, 151–158.

Sandiford, M., Powell, R., 1991. Some remarks on high-temperature—low-pressure metamorphism in convergent orogens. Journal of Metamorphic Geology 9, 333–340.

Santosh, M., Kusky, T., 2010. Origin of paired high pressure–ultrahigh-temperature orogens: a ridge subduction and slab window model. Terra Nova 22, 35–42.

Santosh, M., Kusky, T., Wang, L., 2011. Supercontinent cycles, extreme metamorphic processes, and changing fluid regimes. International Geology Review 53, 1403–1423.

Santosh, M., Liu, S.J., Tsunogae, T., Li, J.H., 2012. Paleoproterozoic ultrahigh-temperature granulites in the North China Craton: Implications for tectonic models on extreme crustal metamorphism. Precambrian Research 222–223, 77–106.

Sawyer, E.W., 1994. Melt segregation in the continental crust. Geology 22, 1019–1022.

Sawyer, E.W., 2001. Melt segregation in the continental crust: distribution and movement of melt in anatectic rocks. Journal of Metamorphic Geology 19, 291–309.

Sawyer, E.W., 2010. Migmatites formed by water-fluxed partial melting of a leucogranodiorite protolith: Microstructures in the residual rocks and source of the fluid. Lithos 116, 273–286.

Sizova, E., Gerya, T., Brown, M., 2014. Contrasting styles of Phanerozoic and Precambrian continental collision. Gondwana Research 25, 522–545.

Smithies, R.H., Howard, H.M., Evins, P.M., Kirkland, C.L., Kelsey, D.E., Hand, M., Wingate, M.T.D., Collins, A.S., Belousova, E., 2011. High-temperature granite magmatism, crust-mantle interaction and the Mesoproterozoic intracontinental evolution of the Musgrave Province, Central Australia. Journal of Petrology 52, 931–958.

Stepanov, A.S., Hermann, J., Rubatto, D., Rapp, R.P., 2012. Experimental study of monazite/melt partitioning with implications for the REE, Th and U geochemistry of crustal rocks. Chemical Geology 300–301, 200–220.

Stüwe, K., 1995. Thermal buffering effects at the solidus. Implications for the equilibration of partially melted metamorphic rocks. Tectonophysics 248, 39–51.

Taylor, R.J.M., Clark, C., Johnson, T.E., Santosh, M., Collins, A.S., 2015. Unravelling the complexities in high-grade rocks using multiple techniques: the Achankovil Zone of southern India. Contributions to Mineralogy and Petrology 169, 1–19.

Tenczer, V., Powell, R., Stüwe, K., 2006. Evolution of H_2O content in a polymetamorphic terrane: the Plattengneiss Shear Zone (Koralpe, Austria). Journal of Metamorphic Geology 24, 281–295.

Tomkins, H.S., Williams, I.S., Ellis, D.J., 2005. In situ U–Pb dating of zircon formed from retrograde garnet breakdown during decompression in Rogaland, SW Norway. Journal of Metamorphic Geology 23, 201–215.

Vielzeuf, D., Clemens, J.D., Pin, C., Moinet, E., 1990. Granites, Granulites, and Crustal Differentiation, in: Vielzeuf, D., Vidal, P. (Eds.), Granulites and Crustal Evolution. Springer Netherlands, pp. 59–85.

Vielzeuf, D., Holloway, J.R., 1988. Experimental determination of the fluid-absent melting relations in the pelitic system. Contributions to Mineralogy and Petrology 98, 257–276.

Vry, J.K., Baker, J.A., 2006. LA-MC-ICPMS Pb–Pb dating of rutile from slowly cooled granulites: Confirmation of the high closure temperature for Pb diffusion in rutile. Geochimica et Cosmochimica Acta 70, 1807–1820.

Walsh, A.K., Kelsey, D.E., Kirkland, C.L., Hand, M., Smithies, R.H., Clark, C., Howard, H.M., 2015. $P-T-t$ evolution of a large, long-lived, ultrahigh-temperature Grenvillian belt in central Australia. Gondwana Research 28, 531–564.

Wells, P.R.A., 1980. Thermal models for the magmatic accretion and subsequent metamorphism of continental crust. Earth and Planetary Science Letters 46, 253–265.

Westphal, M., Schumacher, J.C., Boschert, S., 2003. High-Temperature Metamorphism and the

Role of Magmatic Heat Sources at the Rogaland Anorthosite Complex in Southwestern Norway. Journal of Petrology 44, 1145–1162.

White, R.W., Powell, R., 2002. Melt loss and the preservation of granulite facies mineral assemblages. Journal of Metamorphic Geology 20, 621–632.

White, R.W., Powell, R., Holland, T.J.B., 2001. Calculation of partial melting equilibria in the system Na_2O–CaO–K_2O–FeO–MgO–Al_2O_3–SiO_2–H_2O (NCKFMASH). Journal of Metamorphic Geology 19, 139–153.

White, R.W., Powell, R., Holland, T.J.B., 2007. Progress relating to calculation of partial melting equilibria for metapelites. Journal of Metamorphic Geology 25, 511–527.

White, R.W., Powell, R., Holland, T.J.B., Johnson, T.E., Green, E.C.R., 2014a. New mineral activity–composition relations for thermodynamic calculations in metapelitic systems. Journal of Metamorphic Geology 32, 261–286.

White, R.W., Powell, R., Johnson, T.E., 2014b. The effect of Mn on mineral stability in metapelites revisited: new *a–x* relations for manganese-bearing minerals. Journal of Metamorphic Geology 32, 809–828.

Wickham, S.M., Oxburgh, E.R., 1985. Continental rifts as a setting for regional metamorphism. Nature 318, 330–333.

Williams, I.S., Buick, I.S., Cartwright, I., 1996. An extended episode of early Mesoproterozoic metamorphic fluid flow in the Reynolds Range, central Australia. Journal of Metamorphic Geology 14, 29–47.

Williams, M.L., Jercinovic, M.J., Harlov, D.E., Budzyn, B., Hetherington, C.J., 2011. Resetting monazite ages during fluid-related alteration. Chemical Geology 283, 218–225.

Yakymchuk, C., Brown, M., 2014a. Behaviour of zircon and monazite during crustal melting. Journal of the Geological Society 171, 465–479.

Yakymchuk, C., Brown, M., 2014b. Consequences of open-system melting in tectonics. Journal of the Geological Society 171, 21–40.

Yakymchuk, C., Brown, M., Clark, C., Korhonen, F.J., Piccoli, P.M., Siddoway, C.S., Taylor, R.J.M., Vervoort, J.D., 2015. Decoding polyphase migmatites using geochronology and phase equilibria modelling. Journal of Metamorphic Geology 33, 203–230.

Yakymchuk, C., Brown, M., Ivanic, T.J., Korhonen, F.J., 2013. Leucosome distribution in migmatitic paragneisses and orthogneisses: A record of self-organized melt migration and entrapment in a heterogeneous partially-molten crust. Tectonophysics 603, 136–154.

Zwart, H., 1967. The duality of orogenic belts. Geologie en Mijnbouw 46, 283–309.

CHAPTER 2

This chapter is under review in *Precambrian Research* as:

Morrissey, L.J., Payne, J.L., Hand, M., Clark, C., Taylor, R., Kirkland, C., Kylander-Clark, A. Linking the Windmill Islands, east Antarctica and the Albany–Fraser Orogen: insights from U–Pb zircon geochronology and Hf isotopes.

Statement of Authorship

Title of Paper	Linking the Windmill Islands, east Antarctica and the Albany–Fraser Orogen: insights from U–Pb zircon geochronology and Hf isotopes.
Publication status	☐Published ☐Accepted for publication ☒Submitted for publication ☐Unpublished and unsubmitted work written in manuscript style
Publication Details	Morrissey, L.J., Payne, J.L., Hand, M., Clark, C., Taylor, R., Kirkland, C.L., Kylander-Clark, A. Linking the Windmill Islands, east Antarctica and the Albany–Fraser Orogen: insights from U–Pb zircon geochronology and Hf isotopes. *Precambrian Research*.

Principal Author

Name of Principal Author (Candidate)	Laura Morrissey		
Contribution to the Paper	Project design, fieldwork, sample preparation, LA-ICP-MS data collection, processing and interpretation, manuscript design and composition, creation of figures.		
Overall percentage (%)	80		
Certification:	This paper reports on original research I conducted during the period of my Higher Degree by Research candidature and is not subject to any obligations or contractual agreements with a third party that would constrain its inclusion in this thesis. I am the primary author of this paper.		
Signature		Date	16/05/2016

Co-Author Contributions

By signing the Statement of Authorship, each author certifies that:

i. the candidate's stated contribution to the publication is accurate (as detailed above);
ii. permission is granted for the candidate in include the publication in the thesis; and
iii. the sum of all co-author contributions is equal to 100% less the candidate's stated contribution.

Name of Co-Author	Justin Payne		
Contribution to the Paper	Assistance with sample preparation, assistance with LA-ICP-MS data processing and interpretation, manuscript review.		
Signature		Date	19/05/2016

Name of Co-Author	Martin Hand		
Contribution to the Paper	Guidance with LA-ICP-MS data interpretation, manuscript review.		
Signature		Date	17th May 2016

Name of Co-Author	Chris Clark		
Contribution to the Paper	Guidance with LA-ICP-MS data interpretation, manuscript review.		
Signature		Date	17th May 2016

Name of Co-Author	Richard Taylor		
Contribution to the Paper	Assistance with sample imaging, guidance with LA-ICP-MS data interpretation, manuscript review.		
Signature		Date	17th May 2016

Name of Co-Author	Christopher Kirkland		
Contribution to the Paper	Guidance with LA-ICP-MS data interpretation and tectonic implications, manuscript review.		
Signature		Date	17 - May -16.

Name of Co-Author	Andrew-Kylander Clark		
Contribution to the Paper	Assistance with LA-ICP-MS data collection, manuscript review.		
Signature		Date	17 - may -16

ABSTRACT

U–Pb and Hf isotopic data from metasedimentary and magmatic rocks from the Windmill Islands in Wilkes Land, East Antarctica, confirm age and crustal evolution links between the Albany–Fraser Orogen and this part of East Antarctica. Detrital zircon age data indicate that the protoliths to the metasedimentary rocks of the Windmill Islands were deposited in the interval 1340–1300 Ma. Metamorphic zircon growth at c. 1300 Ma and a crystallisation age of c. 1315 Ma for the protoliths to an orthogneiss that intrudes the metasedimentary rocks provide a minimum depositional age. Significant detrital zircon age components are identified at 1790 Ma, 1595 Ma and 1380 Ma. The 1340–1300 Ma depositional interval and the detrital age components suggest that the Windmill Islands metasedimentary rocks can be linked to metasedimentary rocks of the Arid Basin in the Albany–Fraser Orogen. The sediment sources were likely to be derived from the West Australian Craton as well as a significant component from the c. 1410 Ma Haig Cave Supersuite in the Madura Province. This combination of sources suggests a back-arc setting for the Arid Basin, consistent with the short interval between deposition and high thermal gradient metamorphism. The magmatic rocks in the Windmill Islands have intrusive ages of c. 1315 Ma, 1250–1210 Ma and 1200–1160 Ma. The first phase of magmatism was likely to be derived from melting of Arid Basin metasedimentary rocks, based on abundant inherited zircon with similar ages to the surrounding metasedimentary rocks. The final two phases of magmatism have juvenile $\varepsilon_{Hf}(t)$ values consistent with greater asthenospheric sources within these melts.

1. Introduction

Wilkes Land, in East Antarctica (Fig. 1), was a central component in the formation of the Nuna, Rodinia and Gondwana supercontinents (e.g. Aitken et al., 2014; Boger, 2011; Fitzsimons, 2000, 2003; Payne et al., 2009). There is general agreement in palaeogeographical reconstructions that Wilkes Land and southern Australia were contiguous during the Mesoproterozoic (e.g. Aitken et al., 2014, 2016; Boger, 2011; Fitzsimons, 2003; Li et al., 2008). This reconstruction is supported by existing geochronology that suggests that the Windmill Islands in Wilkes Land record two stages of metamorphism and magmatism between 1340–1300 Ma and 1240–1140 Ma, coeval with Stages I and II of the Albany–Fraser Orogeny in Western Australia and the Mt West and Musgrave Orogenies in the Musgrave Province in central Australia (Clark et al., 2000; Kirkland et al., 2011, 2013b, 2015b; Post et al., 1997; Spaggiari et al., 2015; Zhang et al., 2012). This similarity in geochronology between Wilkes Land, the Albany–Fraser Orogen and the Musgrave Province has previously been used to suggest these regions form part of a vast Mesoproterozoic orogenic system that extended from Antarctica to the Musgrave Province, including perhaps extensions into the Warumpi Province in central Australia (Fig. 1; e.g. Clark et al., 2014; Fitzsimons, 2003; Kirkland et al., 2011; Morrissey et al., 2011; Smits et al., 2014; Walsh et al., 2015; Wong et al., 2015) and even perhaps relics as far westward as the Rudall Province on the margin of the Archean Pilbara Craton (Kirkland et al., 2013a).

Regional airborne geophysical datasets have been used to provide geometric constraints on the original Mesoproterozoic configuration of this vast orogen and to attempt to reconstruct links between the Australian and Antarctic parts of the system (Aitken et al., 2014, 2016). The

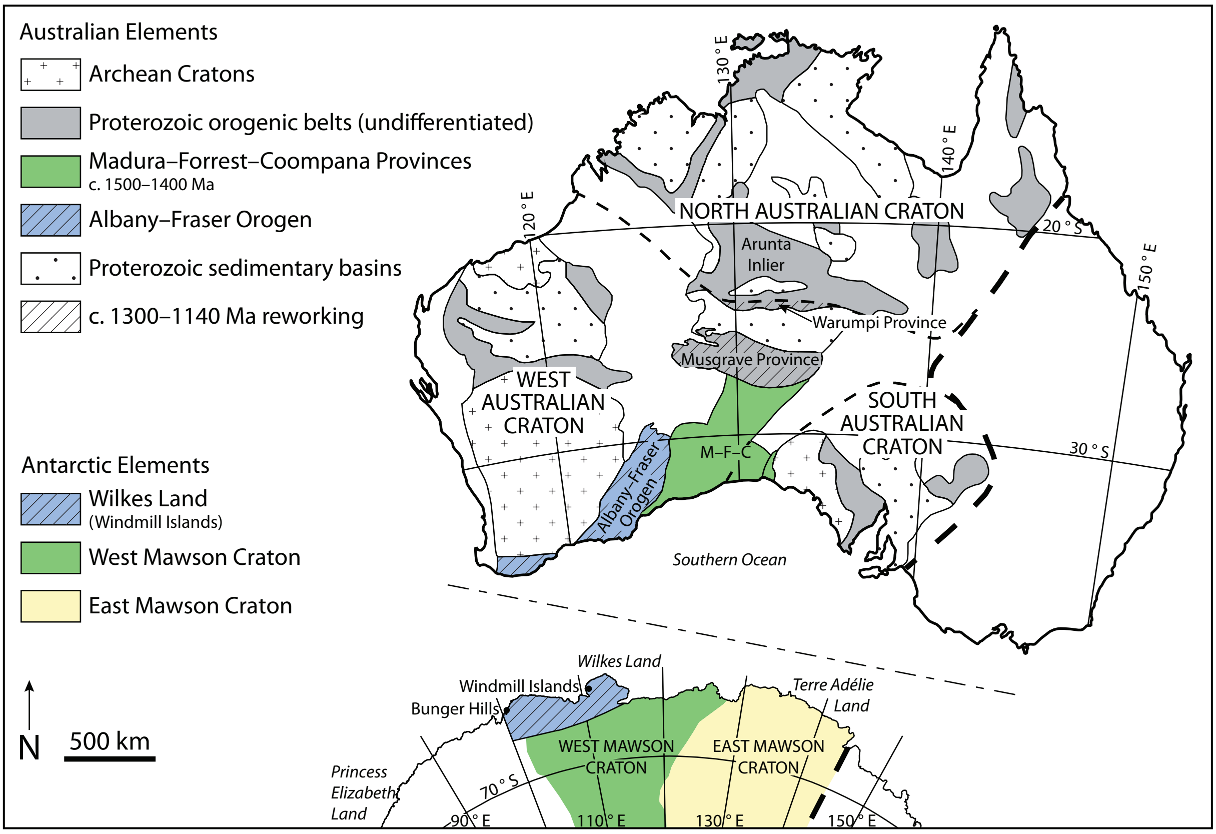

Figure 1: Simplified geological map of Australia and Antarctica showing relevant geological provinces. Australian elements are modified from Kirkland et al. (2011). Tectonic interpretation of basement geology in Antarctica inferred from geophysics by Aitken et al. (2014).

paucity of outcrop within both Antarctica and Australia means there are limited geological constraints on the reconstruction, and the links between each of the components of this large Mesoproterozoic system remain poorly understood (e.g. Kirkland et al., 2013b; Smits et al., 2014). Recent extensive geochronological and isotopic datasets from the Albany–Fraser Orogen and Musgrave Province have been used to constrain the timing and source of sedimentation and the magmatic history of these regions (e.g. Kirkland et al., 2011, 2013b, 2015b; Smithies et al., 2010; Spaggiari et al., 2015; Waddell et al., 2015). These recent studies suggest that despite the temporal similarities in orogenesis and magmatism, the two regions evolved on different basement. The Albany–Fraser Orogen is proposed to have formed on evolved crust that is likely to correspond to the Archean West Australian Craton, whereas the basement to the Musgrave Province is proposed to be younger and more juvenile (Kirkland et al., 2013b, 2015b). The Madura Province to the south appears to share similar isotopic characteristics with the Musgrave Province basement, and the two regions are proposed to be contiguous (Fig. 1; Kirkland et al., 2015b). However, the geochronological and isotopic dataset from Wilkes Land is more limited and there is little information on the basement rocks in this region (Möller et al., 2002; Post, 2000; Post et al., 1997; Zhang et al., 2012). This has hindered attempts to link the geology of Wilkes Land to other components in the Mesoproterozoic orogenic system. A clear understanding of the evolution of each of these regions is therefore pivotal to tectonic reconstructions of both the

Australian and Antarctic continents during the Proterozoic.

This study presents zircon U–Pb and Lu–Hf isotopic results from metasedimentary rocks and structurally constrained magmatic rocks from the Windmill Islands. The Windmill Islands represent the most areally significant region of outcrop in Wilkes Land. There has been very little geochronology and no zircon Lu–Hf data collected from the metasedimentary rocks making up the Windmill Islands. The aim of this study is to assess whether the Windmill Islands form part of the Albany–Fraser Orogen, and therefore whether this component of Wilkes Land has basement corresponding to the West Australian Craton. Isotopic data from the metasedimentary rocks are used to establish the timing and source of deposition and therefore draw lithostratigraphic correlations across the now separate Australo–Antarctic system. Isotopic data from magmatic rocks are used to investigate the timing and character of magmatism and tectonic setting.

2. Geological setting

The Windmill Islands are located on the Wilkes Land Coast and include approximately 400 km^2 of exposed outcrop on peninsulas and islands in the vicinity of the Australian Antarctic Casey Station (Figs. 1 and 2). The outcrops consist of high-grade deformed and migmatised pelitic to psammitic metasedimentary rocks and orthogneisses that have been intruded by a charnockite suite, minor porphyritic granite and late-stage dolerite dykes (Blight and Oliver, 1977; Möller et al., 2002; Post, 2000; Zhang et al., 2012). Approximately 70% of the outcrop is made up of garnet-bearing granitic gneiss or charnockite (Fig. 2; Zhang et al., 2012). Detailed descriptions of each lithology are given in Paul et al. (1995) and Post (2000). The metamorphic grade in the Windmill Islands increases from upper amphibolite facies in the north to granulite facies in the south (Fig. 2; Blight and Oliver, 1977; Möller et al., 2002; Post, 2000). There is no systematic variation in Nd isotopic or geochemical composition of protolith lithologies between the lower and higher grade areas of the Windmill Islands, suggesting they are a single terrane with a common crustal history (Blight and Oliver, 1977; Möller et al., 2002; Post, 2000).

The metasedimentary rocks are intruded by protoliths to the orthogneiss units and therefore are the oldest rocks exposed in the Windmill Islands. The age of the sedimentary protoliths has hitherto been unconstrained. Inherited zircon yielding magmatic crystallization ages of 1450–1350 Ma have previously been found within magmatic rocks in the Windmill Islands. These inherited ages have been interpreted as maximum depositional ages of the sedimentary protoliths or an early phase of igneous activity (Post, 2000; Zhang et al., 2012). The protoliths to the orthogneisses intruded during two periods of magmatic activity at c. 1315 Ma and c. 1250–1210 Ma (Post, 2000; Zhang et al., 2012), the former of which closely corresponds to the timing of magmatic activity during Stage I (1345–1260 Ma) of the Albany–Fraser Orogeny (Bodorkos and Clark, 2004; Clark et al., 2000). The magmatism in Wilkes Land has been correlated to two tectono-metamorphic events: M_1/D_1 between 1340 and 1300 Ma and M_2/D_2 between 1240 and 1140 Ma (Post, 2000; Post et al., 1997; Zhang et al., 2012).

The structural history of the Windmill Islands has been described in detail by previous workers (Paul et al., 1995; Post, 2000). M_1/D_1 involved the formation of a horizontal fabric and isoclinal folds defined by aligned leucosomes (Paul et al., 1995; Post, 2000). Metamorphic conditions associated with this event reached

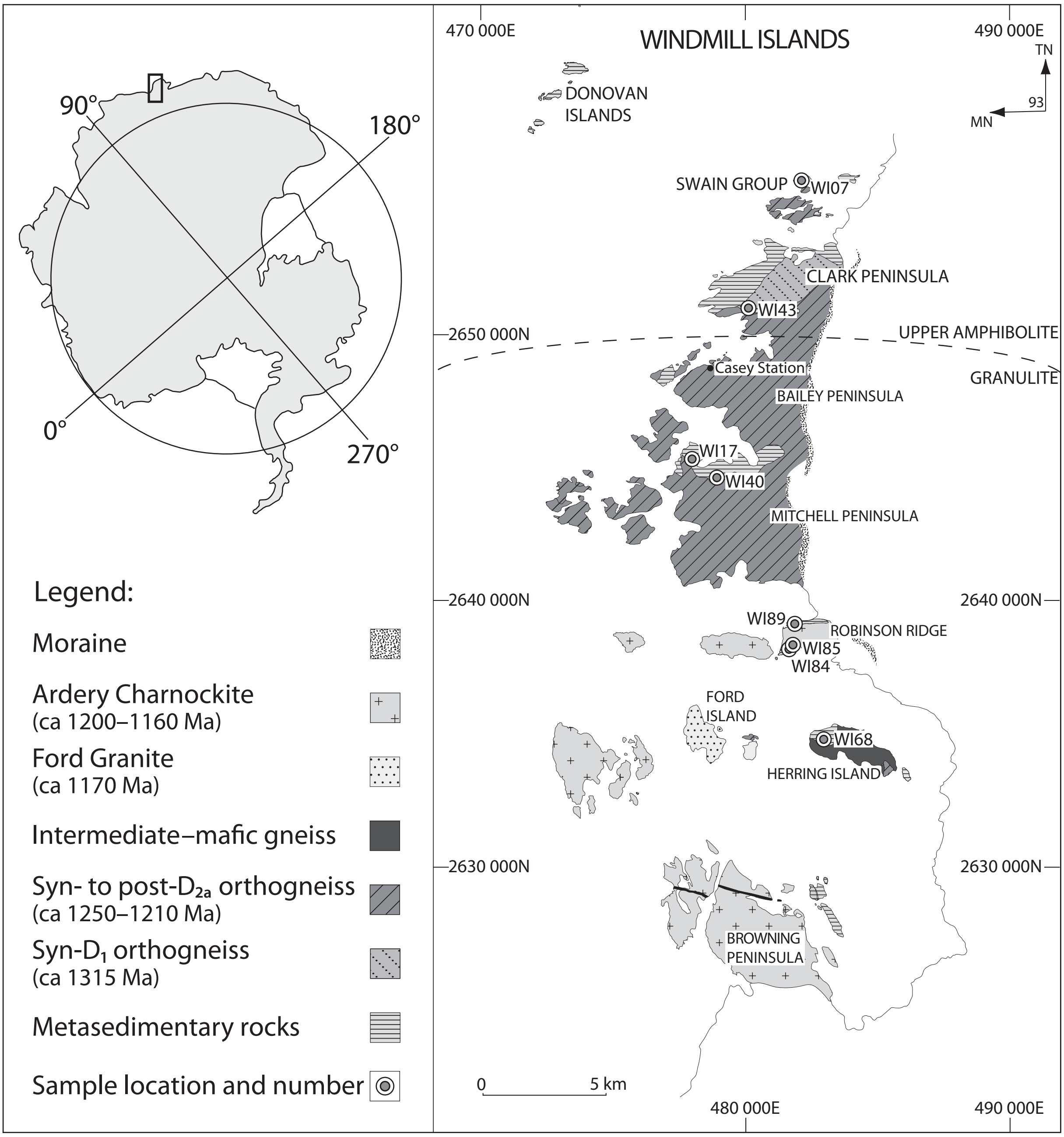

Figure 2: Sketch geological map of the Windmill Islands, from Post (2000). Ages of lithologies are from Post (2000) and Zhang et al. (2012).

upper amphibolite facies, with the formation of sillimanite–biotite–cordierite or biotite–garnet-bearing assemblages in metapelitic rocks (Blight and Oliver, 1977; Paul et al., 1995) and the intrusion of granite on Clark Peninsula at c. 1315 Ma (Fig. 2). The thermal and deformation effects of M_2/D_2 increase progressively to the south, culminating in granulite facies conditions in the southern islands. The event occurred in two stages, D_{2a} and D_{2b}. Garnet and cordierite-bearing leucosomes formed early in M_2 and were folded in tight isoclinal folds during D_{2a} (Blight and Oliver, 1977; Paul et al., 1995; Post, 2000). Voluminous garnet-bearing granite was also intruded during D_{2a} and was weakly deformed (Fig. 2; Post, 2000). Zhang et al. (2012) interpreted samples of garnet-bearing granitic gneiss and foliated garnet-bearing granite to have magmatic ages of 1250–1240 Ma, whereas Post (2000) suggested a younger intrusion age for a syn- to post- D_{2a} orthogneiss of 1214 ± 10 Ma. Deformation during D_{2b} involved tight southeast plunging folds resulting in complex fold interference patterns. Partial melting continued during D_{2b}, with garnet–orthopyroxene–cordierite-bearing leucosomes forming in the axial plane of D_{2b} structures. The final stages of the second metamorphic event involved the intrusion of the Ford Island Granite and the Ardery Charnockite in the southern Windmill Islands (Fig. 2). The Ford Island Granite has an age of 1173 ± 9 Ma and a weak S_{2b} foliation, consistent with intrusion during the waning stages of D_2 (Post, 2000). Zhang et al. (2012) interpreted the Ardery Charnockite to be a syntectonic pluton that contains the regional S_2 foliation, emplaced at c. 1200 Ma. However, Post (2000) interpreted it to still preserve the original igneous flow fabric and to have intruded after the main phase of deformation at 1163 ± 7 Ma.

3. Sampling and Methods

Eight samples were selected for LA-ICP-MS U–Pb and Lu–Hf isotopic analysis from locations throughout the Windmill Islands (Fig. 2; Table 1). Four metasedimentary rocks were sampled with the aim of providing constraints on the provenance and timing of deposition. Four structurally constrained granitic and charnockitic samples were selected to provide constraints on the timing of magmatism and peak metamorphism. The Lu–Hf isotopic signature of dated zircon crystals in these rocks was also investigated to help define source melt compositions.

Zircons were separated from crushed rocks using magnetic and heavy liquid techniques. The separated zircon crystals were hand-picked and mounted in 1 inch epoxy discs. The epoxy disks were polished to half grain thickness to expose grain centres. Mounts were carbon coated and imaged using a cathodoluminescence (CL) detector on a Tescan MIRA3 Field Emission scanning electron microscope (SEM) at Curtin University, Perth, to identify compositional domains for analysis.

3.1. U–Pb geochronology

U–Pb isotopic analyses were done at the University of California Santa Barbara, using a Photon Machines 193 nm nanosecond laser, a HelEx ablation cell and a Nu Plasma high resolution multicollector inductively coupled plasma-mass spectrometer following the

Table 1: Sample locations and lithology.

Sample	Location		Easting	Northing	Rock type
Metasedimentary rocks					
WI07	Cameron Island	49D	482148	2655814	Upper amphibolite facies metasediment
WI40	Mitchell Peninsula	49D	479134	2644765	Granulite facies pelitic gneiss
WI89	Robinson Ridge	49D	481688	2639149	Granulite facies metapelite
WI68	Herring Island	49D	482772	2634855	Granulite facies pelitic gneiss
Magmatic rocks					
WI43	Clark Peninsula	49D	480225	2651026	Syn-D_1 orthogneiss
WI17	Mitchell Peninsula	49D	478144	2645496	Unfoliated biotite granite
WI84	Robinson Ridge	49D	481305	2638236	Coarse-grained Ardery Charnockite
WI85	Robinson Ridge	49D	481332	2638269	Fine-grained Ardery Charnockite

methods of Kylander-Clark et al. (2013). Trace element data were collected in 'split stream' mode with an Agilent 7700s ICP-MS and were used to assist in the assessment of U–Pb data quality. Each analysis was pre-ablated with one laser pulse to remove any surface contamination. The total acquisition time of each analysis was 35 s and included 15 s of background measurement and 20 s of laser ablation. Ablation was performed with a spot size of 20 μm and a repetition rate of 4 Hz. Each analysis involved simultaneous measurement of masses ^{204}(Pb + Hg), ^{206}Pb, ^{207}Pb, ^{208}Pb on ETP discrete-dynode electron multipliers and ^{232}Th and ^{238}U on Faraday cups equipped with 10^{11} ohm resistors.

Iolite version 3.1 was used to reduce raw data and calculate U–Th–Pb isotopic ratios and their uncertainties (Paton et al., 2010, 2011). Uncertainties are quoted at the 2σ level and include contributions from the external reproducibility of the primary reference standard for the ^{207}Pb/^{206}Pb and ^{206}Pb/^{238}U ratios propagated in quadrature. The zircon standard GJ-1 (TIMS normalisation data: ^{207}Pb/^{206}Pb = 608.3 Ma, ^{206}Pb/^{238}U = 600.7 Ma, ^{207}Pb/^{235}U = 602.2 Ma; Jackson et al., 2004) was used to correct for mass bias, elemental fractionation and instrument drift. Analyses of the primary standard GJ-1 over all of the analytical sessions yielded a mean ^{206}Pb/^{238}U age of 600.8 ± 0.8 Ma (n = 94). Data accuracy was monitored using repeated analysis of secondary standards 91500 (^{207}Pb/^{206}Pb age = 1065 Ma; Wiedenbeck et al., 1995), Plešovice (^{206}Pb/^{238}U age = 337.1 ± 0.4 Ma; Sláma et al., 2008) and Mud Tank (732 ± 5 Ma; Black and Gulson, 1978). Throughout the analytical sessions, secondary standard 91500 yielded a ^{207}Pb/^{206}Pb weighted average age of 1064.4 ± 2.6 Ma (n = 82, $2s_T$ = 19), Plešovice yielded a ^{206}Pb/^{238}U weighted mean age of 334.8 ± 1.0 Ma (n = 25, $2s_T$ = 6) and Mud Tank yielded a ^{206}Pb/^{238}U weighted average age of 720.8 ± 1.9 Ma (n = 27, $2s_T$ = 13). U–Pb data were plotted using Isoplot (Ludwig, 2003). Common Pb corrections were not performed but analyses were discarded where significant levels of ^{204}Pb were recognised. Uncertainties provided in brackets (denoted $2s_T$) with each weighted mean age incorporate the systematic uncertainty of the facility indicated by the long-term external reproducibilities of the 91500 secondary standard. These are 0.90% and 0.92% for ^{207}Pb/^{206}Pb and ^{206}Pb/^{238}U, respectively (1SD, n = 220).

3.2. Hf isotopes

The Lu–Hf–Yb isotope compositions were measured with the same MC-ICP-MS at University of California Santa Barbara in later analytical sessions after the collection of U–Pb and trace element data. In an effort to obtain Hf isotope data for the same domains as targeted for U–Pb, laser ablation spots for Lu–Hf–Yb were sited on top of the U–Pb spots. Each analysis was pre-ablated with one laser pulse to remove any surface contamination. The total acquisition time of each analysis was 65 s and included 35 s of background measurement and 30 s of laser ablation. Ablation was performed using a repetition rate of 12 Hz. A spot size of 40 μm was used for the metasedimentary samples and sample WI43, whereas the large grain size in samples WI17, WI84 and WI85 allowed for a correspondingly larger laser spot size of 50 μm. Each analysis involved simultaneous measurement of masses ^{171}Yb, ^{173}Yb, ^{175}Lu, ^{176}Hf (+ Lu + Yb), ^{177}Hf, ^{178}Hf, ^{179}Hf and ^{180}Hf on Faraday cups.

Data were reduced using Iolite version 3.1 (Paton et al., 2011). Hf mass bias was corrected using a natural ^{179}Hf/^{177}Hf ratio of 0.7325. Isobaric interferences of ^{176}Hf by Yb and Lu were corrected using the methods of Woodhead et al. (2004) with direct measurement of $^{171}Yb/^{173}Yb$ fractionation using the Yb isotopic values of Segal et al. (2003). Assuming the same mass bias behaviour as Yb, a correction for Lu isobaric interference on ^{176}Hf used a $^{176}Lu/^{175}Lu$ ratio of 0.02655 (Vervoort et al., 2004).

Instrument performance and stability were monitored by analysis of zircon standards Mud Tank, Plesovice, 91500 and GJ-1. The weighted average $^{176}Hf/^{177}Hf$ value for Mud Tank over all the analytical sessions was 0.282522 ± 9 (2σ, n = 65) which is within uncertainty of the published value of 0.282507 ± 6 (Woodhead and Hergt, 2005). The weighted average $^{176}Hf/^{177}Hf$ values for Plešovice, 91500 and GJ-1 were 0.282482 ± 14, 0.282303 ± 17 and 0.282014 ± 16 respectively (2σ, n = 27). These are within uncertainty of the respective published values of 0.282482 ± 13 (Sláma et al., 2008), 0.282306 ± 8 (Woodhead and Hergt, 2005) and 0.282000 ± 5 (Morel et al., 2008). The initial $^{176}Hf/^{177}Hf$ in zircon is calculated using the ^{176}Lu decay constant of 1.865 x 10^{-11} units (Scherer et al., 2001). Epsilon hafnium values ($\varepsilon_{Hf}(t)$) were calculated using CHUR values of $^{176}Hf/^{177}Hf$ = 0.282785 and $^{176}Lu/^{177}Hf$ = 0.0336 (Bouvier et al., 2008). Model ages were not calculated due to the uncertainties associated with the appropriate mantle and crustal composition (Payne et al., 2016)

4. Results

4.1. U–Pb geochronology of metasedimentary rocks

U–Pb geochronology results for metasedimentary samples are presented as Supplementary Data S2.1. Detailed zircon descriptions for metasedimentary samples are presented as Supplementary Data S2.2. Representative CL images of zircon grains from each metasedimentary sample are presented in Figure 3. $^{207}Pb/^{206}Pb$ data are used for all age determinations in this study. Analyses that are excluded from the calculation of probability density plots are shown on the concordia plots as unfilled, grey dashed ellipses (Fig. 4). Analyses that targeted metamorphic rims or grains are shown as filled ellipses. The large probability density plots in Figure 4 depict analyses that targeted detrital cores and include all detrital analyses that are <10% discordant. However, only those analyses that are within 2σ of concordia are used for the interpretation of maximum depositional ages and metamorphic populations due to the importance of obtaining robust age constraints. The small, inset histograms show concordant analyses that are interpreted to reflect metamorphic zircon based on the CL images.

4.1.1. Sample WI07

Sample WI07 is an amphibolite facies metapelite from the Swain Group in the northern Windmill Islands. The rocks contain fine-grained discontinuous leucosomes that are concordant with the fabric. The sample contains garnet, biotite, K-feldspar, plagioclase, magnetite, ilmenite, quartz and accessory zircon and monazite. Zircon grains in this sample are typically pale pink to pale yellow, up to 300 μm in length and equant to slightly elongate with aspect ratios up to 1:3.5. Four zircon morphologies were recognised in CL images (Fig. 3a). The majority of grains have dark, homogenous rims (morphology 1) that overgrow bright, oscillatory zoned cores (morphology 2). In some cases, there is a thin, bright zone at the boundary between core and rim, possibly representing minor recrystallisation of the core (Fig. 3a). The third morphology is defined as inner rims up to 20 μm in width that have a high CL response and overgrow low CL response cores (Fig.

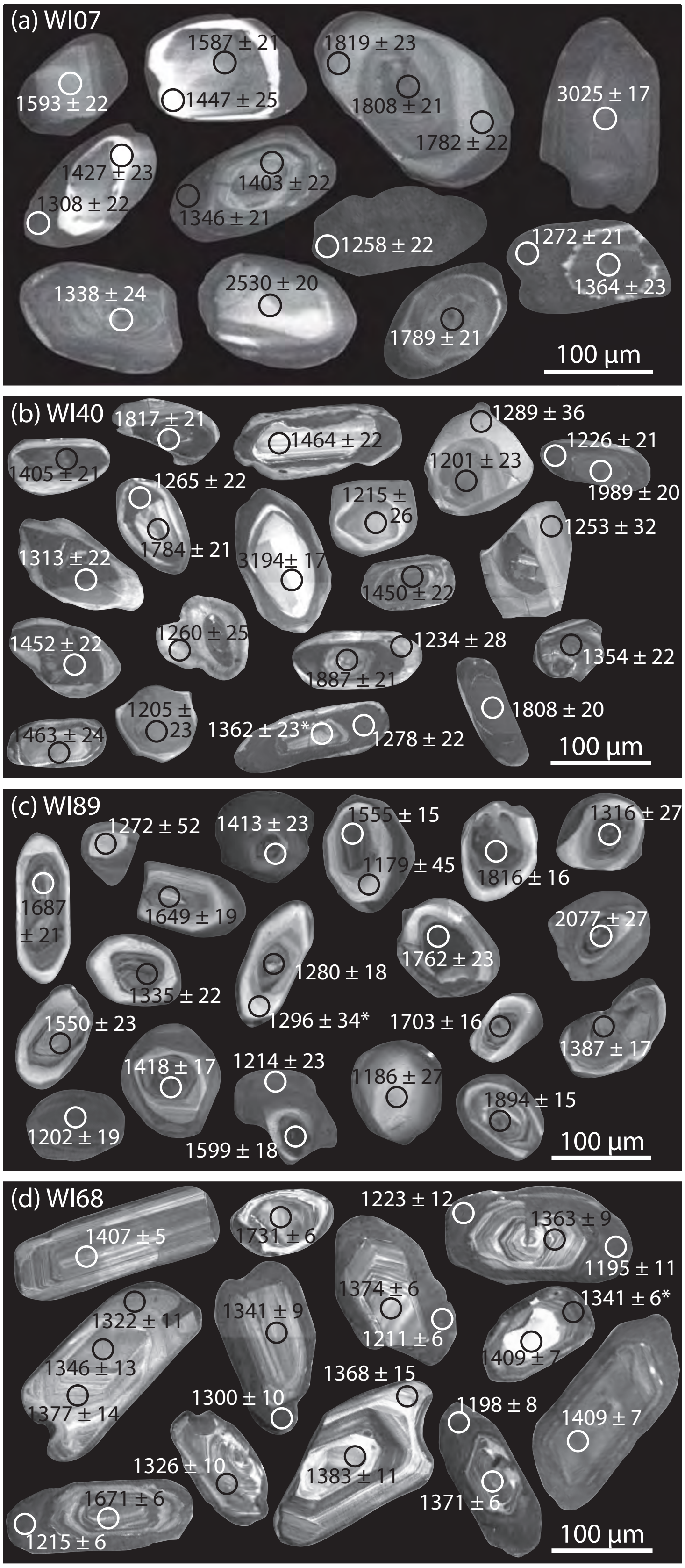

Figure 3: Representative CL images of zircon from metasedimentary rocks. The ages given are the $^{207}Pb/^{206}Pb$ age. Asterisks after the age denote analyses that are >10% discordant. (a) Sample WI07. (b) Sample WI40. (c) Sample WI89. (d) Sample WI68.

3a). Some grains appear dark and broadly homogenous in CL and are interpreted to be equivalent to morphology 1 (Fig. 3a).

Eighty-two U–Pb analyses were collected from 69 grains, targeting both the cores and the dark homogenous rims. Sixty-five cores that are interpreted to be detrital and are <10% discordant yield an array of analyses between c. 3025 and c. 1340 Ma (Fig. 4a). On a probability density plot these ages define three main peaks at c. 1370, c. 1595 and c. 1780 Ma, defined by contributions from 12, 7 and 16 analyses. Eight analyses fall in the range 2300–3025 Ma, with three at c. 2550 Ma. The youngest concordant analysis from an oscillatory zoned core has a $^{207}Pb/^{206}Pb$ age of 1338 ± 24 Ma (Fig. 3a). Of the seven metamorphic rims analysed, only three are concordant and have $^{207}Pb/^{206}Pb$ ages between 1295–1325 Ma (Fig. 4a).

4.1.2. Sample WI40

Sample WI40 is a metapelitic gneiss from Mitchell Peninsula (Fig. 2). The sample contains garnet, cordierite, biotite, K-feldspar, plagioclase, sillimanite, magnetite, spinel, ilmenite and accessory zircon and monazite. A gneissic fabric is defined by biotite-rich layers and quartzofeldspathic leucosomes.

Zircon grains in this sample are typically clear to pale brown, equant to slightly elongate with aspect ratios up to 1:3. CL images can be classified into five zircon morphologies. The first is defined by cores that show oscillatory zoning or are internal domains clearly separated by a thin, high CL response zone and are interpreted as detrital magmatic zircon grains. The second morphology is defined by grains with low CL response, homogenous cores that may contain very small oscillatory zoned relics. These low CL response zones are interpreted to be cores that have either been resorbed/recrystallised or are the result of zircon growth during metamorphism (Fig. 3b). The third morphology is defined by rims that are bright in CL. These bright rims may be overgrown by the fourth morphology, defined by narrow secondary rims or zones of resorption that have little CL response. The fifth morphology is defined by equant grains that display diffuse zoning or sector zoning that may be overgrown by a thin rim (Fig. 3b). These are interpreted to be metamorphic neoblasts.

Seventy-five analyses were collected from 63 grains targeting all zircon morphologies. Twenty-seven cores that are interpreted to be detrital and are <10% discordant define five $^{207}Pb/^{206}Pb$ age peaks at c. 1370 Ma, c. 1410 Ma, c. 1460 Ma, c. 1750 Ma and c. 1800 Ma, defined by 3, 3, 4, 3, and 8 analyses (Fig. 4b). This sample also yields single, analyses at around 1900 Ma, 2000 Ma and 3200 Ma (Fig. 4b). The youngest concordant oscillatory zoned zircon core in this sample yields a $^{207}Pb/^{206}Pb$ age of 1354 ± 22 Ma (Fig. 3b).

Metamorphic zircon in this sample occurs in a range from 1310 Ma to 1180 Ma. A probability plot of the $^{207}Pb/^{206}Pb$ ages of concordant zircon broadly defines three peaks at c. 1310 Ma, 1250 Ma and 1210 Ma. Age groupings based on the CL images do not yield single populations and cannot be used to define these age peaks further.

4.1.3. Sample WI89

Sample WI89 is a coarse-grained garnet–cordierite-bearing horizon located along the contact with the Ardery Charnockite on Robinson Ridge (Fig. 2). At outcrop scale, the garnet–cordierite gneiss is cross-cut by leucosomes that contain garnet up to several centimetres in diameter. The sample contains garnet, cordierite, plagioclase, K-feldspar,

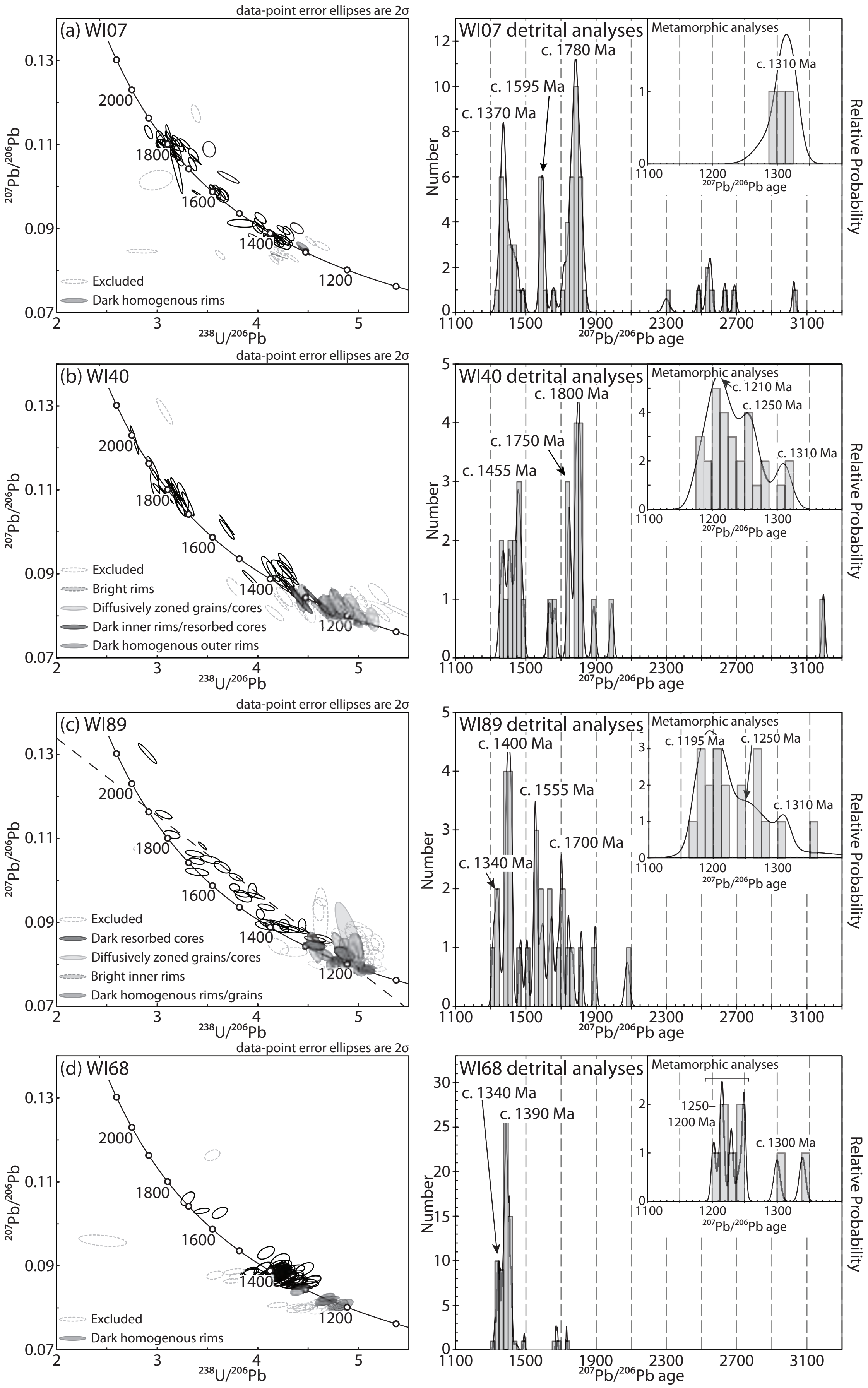

data-point error ellipses are 2σ
(a) WI07
Excluded
Dark homogenous rims
WI07 detrital analyses
c. 1780 Ma
c. 1595 Ma
c. 1370 Ma
Metamorphic analyses
c. 1310 Ma
(b) WI40
Excluded
Bright rims
Diffusively zoned grains/cores
Dark inner rims/resorbed cores
Dark homogenous outer rims
WI40 detrital analyses
c. 1800 Ma
c. 1750 Ma
c. 1455 Ma
c. 1210 Ma
c. 1250 Ma
c. 1310 Ma
(c) WI89
Excluded
Dark resorbed cores
Diffusively zoned grains/cores
Bright inner rims
Dark homogenous rims/grains
WI89 detrital analyses
c. 1400 Ma
c. 1555 Ma
c. 1700 Ma
c. 1340 Ma
c. 1195 Ma
c. 1250 Ma
c. 1310 Ma
(d) WI68
Excluded
Dark homogenous rims
WI68 detrital analyses
c. 1340 Ma
c. 1390 Ma
1250–
1200 Ma
c. 1300 Ma
^{207}Pb/^{206}Pb
^{238}U/^{206}Pb
Number
^{207}Pb/^{206}Pb age
Relative Probability

Figure 4 (previous page): U–Pb gechronology from metasedimentary rocks. U–Pb Tera–Wasserburg plots (on the left) and probability plots (on the right) are presented for each sample. On the Tera–Wasserburg plots the dashed grey ellipses denote analyses that are excluded on the basis of discordance. Interpreted detrital analyses are shown as black unfilled ellipses. Newly grown metamorphic or recrystallised zircon analyses are shown as filled ellipses, with varying shades of grey representing different zircon morphologies. Probability density plots are calculated using the $^{207}Pb/^{206}Pb$ age. The large probability density plots only include detrital analyses (<10% discordant), determined on the basis of zircon morphology. The inset probability density plots include concordant metamorphic and reset analyses. (a) Sample WI07. (b) Sample WI40. (c) Sample WI89; (d) Sample WI68.

quartz, ilmenite, magnetite and late biotite with accessory tourmaline, zircon and monazite.

Zircon grains in this sample are typically clear to pale pink. They are commonly small (<100 μm in diameter) equant and rounded to subrounded in shape. Rarely, grains may be slightly elongate with ratios of 1:2.5. In CL, zircon grains commonly have a core that is of variable size and morphology but may be very small (<20 μm). These cores are interpreted to be detrital magmatic zircon. They are overgrown by an inner rim with bright CL response and a second rim that has a dark, homogenous response in CL (Fig. 3c). Both the bright inner rim and darker outer rim are interpreted to be metamorphic. Where grains have a bright core with diffuse or no zoning that is overgrown by a dark rim, the bright core is also interpreted to be metamorphic (Fig 3c). Dark, weakly zoned to unzoned zircon cores that may have small detrital relics also occur in this sample, and are interpreted to be partially to completely resorbed cores.

Seventy four analyses were collected from 63 grains. Twenty-seven analyses are interpreted to reflect detrital grains and are <10% discordant. Many of the analyses in this sample are slightly to moderately discordant and scatter towards a lower intercept on concordia of around c. 1200 Ma, the same age as metamorphic zircon overgrowths. This is consistent with radiogenic-Pb mobility at the same time as new zircon precipitation was occurring. Two main peaks occur at c. 1400 Ma and c. 1550 Ma, defined by 8 and 3 analyses respectively. Although precises ages of detrital components in this rock are challenging to determine, there is clear evidence of a substantial older detrital component. The youngest concordant oscillatory zoned core yields a $^{207}Pb/^{206}Pb$ age of 1399 ± 20 Ma.

Concordant metamorphic zircon in this sample ranges from 1310 Ma to 1170 Ma. A probability plot of the $^{207}Pb/^{206}Pb$ ages of concordant zircon broadly defines two peaks at c. 1310 Ma and 1190 Ma with a broad shoulder peak at c. 1250 Ma (Fig. 4c). Age groupings based on the CL images do not yield single populations and cannot be used to define these age peaks further.

4.1.4. Sample WI68

Sample WI68 is an orthopyroxene–cordierite-bearing gneiss from Herring Island in the southern Windmill Islands. The sample was collected from a lens of metapelite within a large area of nebulitic migmatite. It contains orthopyroxene, cordierite, K-feldspar, plagioclase, quartz, magnetite, minor biotite and accessory zircon and monazite.

Zircon grains in this sample are typically pale pink to pale yellow, equant to slightly elongate, and 70–200 μm in length. In CL images, the majority of zircon grains have well preserved high-CL response cores that display strong oscillatory or fir-tree zoning. They are overgrown by low-CL response homogenous rims of variable thickness which truncate core zonation (Fig. 3d). Rare discrete grains are dark with homogenous CL response.

Ninety-two analyses were collected from 71 grains, targeting both the cores and the dark homogenous rims. Sixty-five core analyses are interpreted to be detrital and <10% discordant. Three core analyses yielded ages between c. 1730–1670 Ma. The majority of cores yielded ages between c. 1400–1340 Ma. The two youngest concordant oscillatory zoned grains yield ages of 1322 ± 11 Ma and 1331 ± 15 Ma that may provide a maximum depositional age for this sample. The concordant dark rims yield $^{207}Pb/^{206}Pb$ ages between 1250–1200 Ma, with the exception of one dark rim that yields an age of 1300 ± 10 Ma (Fig. 3d). This suggests that the majority of metamorphic zircon records the M_2 event, at 1250–1200 Ma.

4.2. U–Pb geochronology of magmatic rocks

U–Pb geochronology results for magmatic samples are presented as Supplementary Data S2.1. Tera–Wasserburg concordia plots and representative CL images of zircon grains from each magmatic sample are presented in Figure 5. Only analyses that are concordant (within 2σ of concordia) are used for the calculation of weighted average ages. Analyses that are excluded appear as unfilled, grey dashed ellipses.

4.2.1. Sample WI43

Sample WI43 is from an orthogneiss on Clark Peninsula (Fig. 2). It contains a weak S_1 foliation and has previously been interpreted to have intruded the metasedimentary rocks during D_1. The orthogneiss comprises large K-feldspar augen, plagioclase, quartz and biotite.

Zircon grains in this sample are typically honey brown to light yellow, 150–250 μm in length and have aspect ratios that vary from 1:1.5 (stubby grains) to 1:4 (elongate grains). In CL images, many of the larger, stubby zircon grains contain high-CL response cores that show weak oscillatory zoning or diffuse zoning (Fig. 5a). These cores are overgrown by zircon that appears dark in CL. The smaller, elongate zircons appear either weakly concentrically zoned or unzoned in CL (Fig. 5a).

Thirty analyses were collected from 28 grains. Ten analyses are discordant. The remaining 20 analyses yield ages between 1400–1300 Ma (Fig. 5a). It is not possible to determine a clear crystallisation age for this sample. The older analyses are consistent with the strong c. 1380 Ma detrital peak in the surrounding metasedimentary rocks and therefore may be inherited, with the younger age recording the timing of magmatism. An alternative interpretation is that protolith to the orthogneiss has a c. 1400 Ma crystallisation age, with the younger ages resulting from metamorphism. Zircon morphology does not provide a clear interpretation of the crystallisation age, as the bright cores and darker rims or grains do not yield consistent ages. Similarly, there are no consistent differences in trace element ratios

Figure 5 (facing page): U–Pb geochronology and CL images from igneous rocks. U–Pb Tera–Wasserburg plots (on the left) and representative CL images (on the right) are presented for each sample. On the Tera–Wasserburg plots the dashed grey ellipses denote analyses that have been excluded from the calculations on the basis of discordance. Uncertainties provided in brackets (denoted $2s_T$) incorporate the systematic uncertainty. The ages given on the CL images are the $^{207}Pb/^{206}Pb$ age. (a) Sample WI43. (b) Sample WI17. (c) Sample WI84. (d) Sample WI85.

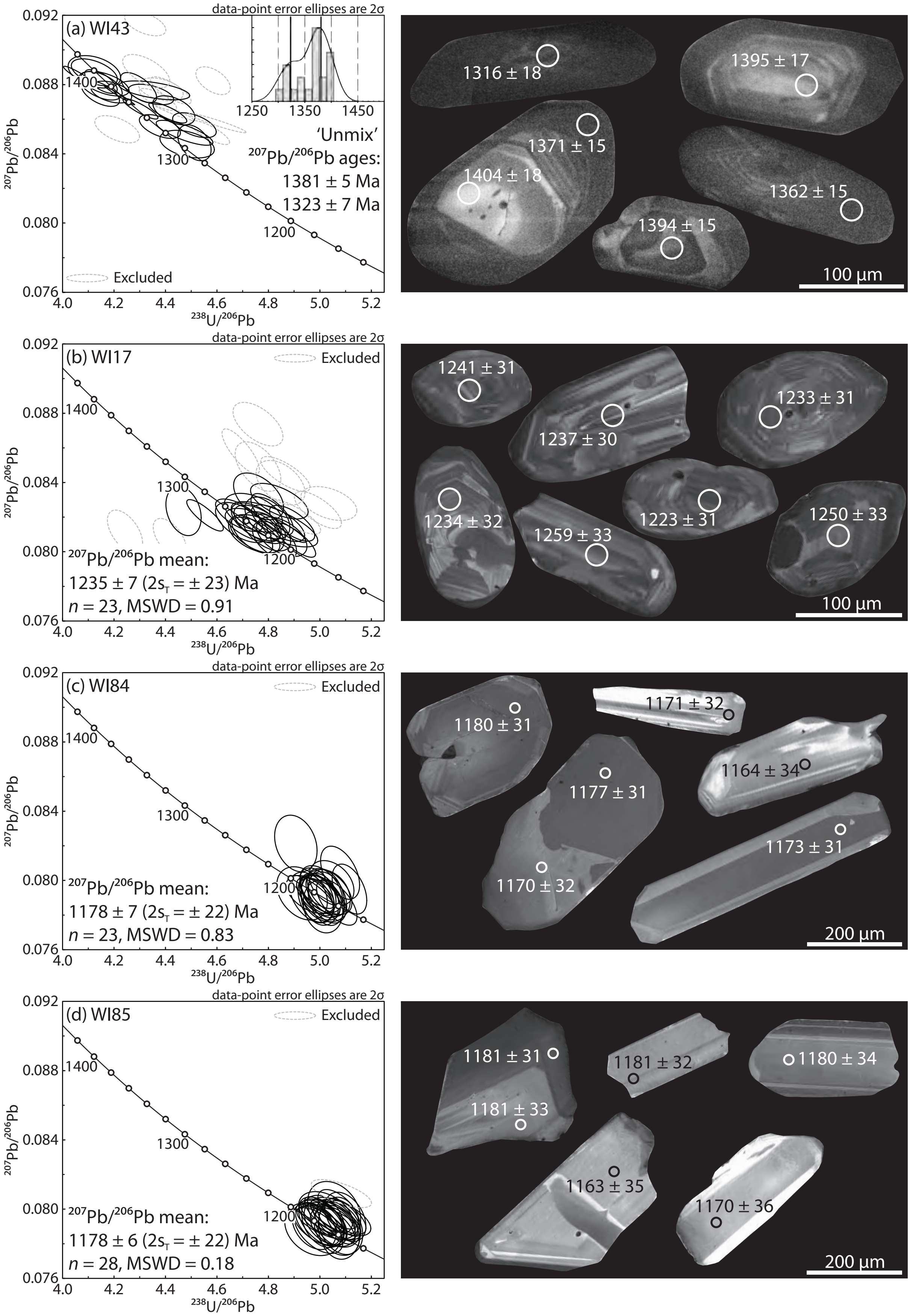
data-point error ellipses are 2σ
(a) WI43
1250 1350 1450
'Unmix'
207Pb/206Pb ages:
1381 ± 5 Ma
1323 ± 7 Ma
1400
1300
1200
Excluded
207Pb/206Pb
238U/206Pb
1316 ± 18
1395 ± 17
1371 ± 15
1404 ± 18
1362 ± 15
1394 ± 15
100 µm
(b) WI17
Excluded
207Pb/206Pb mean:
1235 ± 7 (2sT = ± 23) Ma
n = 23, MSWD = 0.91
1241 ± 31
1237 ± 30
1233 ± 31
1234 ± 32
1259 ± 33
1223 ± 31
1250 ± 33
100 µm
(c) WI84
207Pb/206Pb mean:
1178 ± 7 (2sT = ± 22) Ma
n = 23, MSWD = 0.83
1180 ± 31
1171 ± 32
1164 ± 34
1177 ± 31
1173 ± 31
1170 ± 32
200 µm
(d) WI85
207Pb/206Pb mean:
1178 ± 6 (2sT = ± 22) Ma
n = 28, MSWD = 0.18
1181 ± 31
1181 ± 32
1180 ± 34
1181 ± 33
1163 ± 35
1170 ± 36
200 µm

between the cores and rims. The dark rims and dark, unzoned acicular grains commonly were not analysed in this study as they are uranium rich and contain high concentrations of ^{206}Pb, resulting in tripping of ion counters during analysis. As no chemical or morphological difference can be used to define age coherent groupings, we apply a statistical approach as an exploratory exercise to resolve potentially significant zircon growth events. We use the 'Unmix ages' function in Isoplot (Sambridge and Compston, 1994) to statistically identify two peaks at 1381 ± 5 Ma and 1323 ± 7 Ma (relative misfit = 0.527; fractions of 0.65 and 0.35 respectively). Post (2000) interpreted U–Pb SIMS data from a similar syn-D_1 orthogneiss to suggest crystallisation age of c. 1315 ± 6 Ma and inherited xenocrystic zircon in the range 1487–1350 Ma, consistent with the age peaks in this sample. The range in xenocrystic zircon ages in that sample may suggest that the c. 1400 Ma age peak in sample WI43 is more likely to reflect inheritance from the surrounding metasedimentary rocks rather than a c. 1400 Ma crystallisation age.

4.2.2. Sample WI17

Sample WI17 is from an unfoliated biotite granite that intruded granulite facies metasedimentary rocks on Mitchell Peninsula. This sample contains quartz, K-feldspar, biotite and plagioclase.

The zircon grains extracted from this sample are typically pale amber to honey brown, 50–250 μm and equant to elongate with aspect ratios from 1:1 up to 4:1. They show complex zoning in CL images, with bright oscillatory or sector zoned grains truncated by zones with a dark CL response (Fig. 5b).

Thirty-three analyses were collected from 30 grains. All concordant analyses yield a ^{207}Pb/^{206}Pb weighted average age of 1235 ± 7 Ma (Fig. 5b; n = 23, MSWD = 0.91), interpreted to be the crystallisation age of this sample.

4.2.3. Sample WI84

The Ardery Charnockite outcrops extensively in the southern Windmill Islands. It has been interpreted to comprise a complex of multiple intrusions with subtle differences in grain size and mineral abundances (Blight and Oliver, 1977; Zhang et al., 2012). The Ardery Charnockite typically contains coarse-grained K-feldspar, plagioclase, orthopyroxene and quartz and may contain hornblende, biotite and magnetite. It is interpreted to postdate D_{2b} and preserves a weak igneous flow fabric (Post, 2000). WI84 is a sample of coarse-grained Ardery Charnockite from Robinson Ridge.

Zircon grains are typically clear to pale brown in colour, large (up to ~600 μm in length) and elongate, with aspect ratios varying from 1:2 to 1:6. In CL images, zircons are bright and display complex zoning patterns but commonly show oscillatory zoning. This zoning may be resorbed or overprinted by zones that have low CL response (Fig. 5c). Some grains appear in CL as weakly zoned to unzoned dark grains.

Twenty-five analyses were collected from 24 grains. There is no correlation between zircon morphology and age. The ^{207}Pb/^{206}Pb weighted average age of concordant analyses 1178 ± 7 Ma (Fig. 5c; n = 23, MSWD = 0.83), interpreted as the age of crystallisation of the charnockite.

4.2.4. Sample WI85

Sample WI85 is a sample of fine-grained Ardery Charnockite from Robinson Ridge. The morphology of zircon grains in this sample is very similar to that of sample WI84, though the zircons analysed in this sample are commonly less elongate.

Twenty-nine analyses were collected from 28 grains in sample WI85. The $^{207}Pb/^{206}Pb$ weighted average age of concordant analyses discordant is 1178 ± 6 Ma (Fig. 5d; n = 28, MSWD = 0.18). This age is identical to sample WI84 and is interpreted to be the age of magmatic crystallisation.

4.3. Hf isotopes of metasedimentary rocks

All Hf isotope data for metasedimentary rocks are provided in Supplementary Data S2.3. Hf isotope analyses were collected from detrital cores with U–Pb ages that are <10% discordant and are large enough to fit a 40 µm analysis spot; therefore not all detrital analyses have corresponding Hf isotope analyses.

A number of the detrital analyses in this study form discordant U–Pb arrays, suggesting that these samples have experienced ancient Pb-loss and therefore some grains may yield misleading $^{207}Pb/^{206}Pb$ ages (Fig. 4). To assist in identifying the presence of ancient Pb-loss, Hf isotope data for metasedimentary rocks are presented as initial $^{176}Hf/^{177}Hf$ versus U–Pb age (Fig. 6), as it is widely recognised that the Hf isotopic system has greater resistance to overprinting events than the U–Pb system. Horizontal

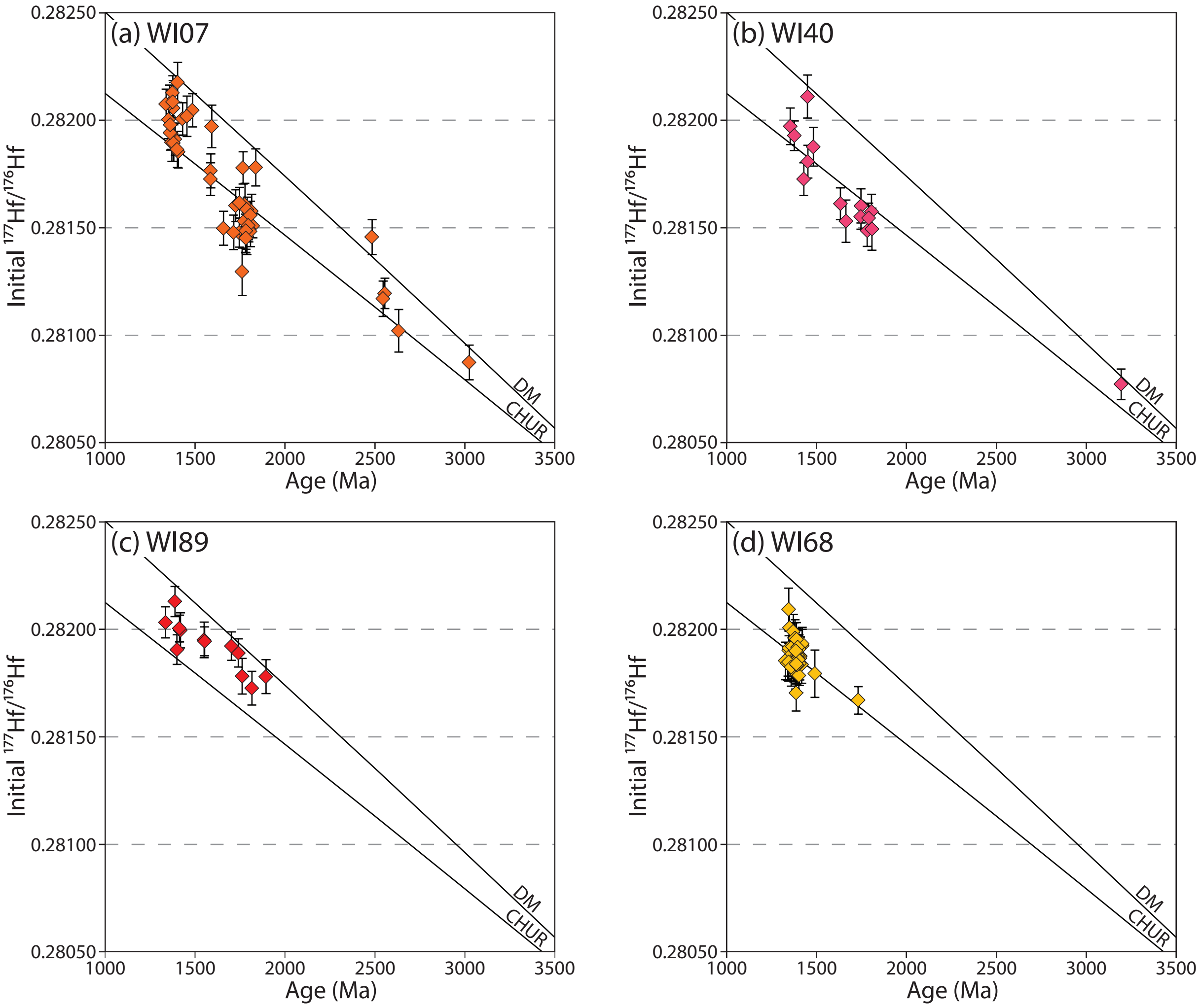

Figure 6: Initial $^{177}Hf/^{176}Hf$ ratios of metasedimentary samples. The ratios are plotted against the $^{207}Pb/^{206}Pb$ age. The error bars are 2SE. (a) Sample WI07. (b) Sample WI40. (c) Sample WI89. (d) Sample WI68.

trends in the Hf evolution plots may suggest age variation of zircons with a consistent initial Hf isotope composition (e.g. of potentially initially the same age), and therefore allow for an assessment of the likelihood of ancient Pb-loss.

4.3.1. Sample WI07

Forty-seven Hf isotope analyses of zircon cores were collected from sample WI07 (Fig. 6a). Analyses with ages between 1490–1340 Ma have initial $^{176}Hf/^{177}Hf$ in the range 0.281853 to 0.282176, corresponding to $\varepsilon_{Hf}(t)$ of -1 to +10 (n = 18). Three analyses with ages of 1595–1585 Ma have a range of initial $^{176}Hf/^{177}Hf$ values of 0.281765 to 0.281971 with a corresponding $\varepsilon_{Hf}(t)$ range of -2 to +7. Twenty-one analyses between 1840 and 1660 Ma in sample WI07 have initial $^{176}Hf/^{177}Hf$ in the range 0.281295–0.281780, corresponding to $\varepsilon_{Hf}(t)$ of -13 to +6. A single analysis with an age of 2428 Ma has initial $^{176}Hf/^{177}Hf$ of 0.281457 ($\varepsilon_{Hf}(t)$ = +9). Four analyses with ages between 2555 and 3025 Ma have initial $^{176}Hf/^{177}Hf$ between 0.281195 and 0.280873, corresponding to $\varepsilon_{Hf}(t)$ of -3 to +2.

4.3.2. Sample WI40

Fifteen Hf isotope analyses of zircon cores were collected from sample WI40 (Fig. 6b). Six analyses with ages between 1480 and 1350 Ma have initial $^{176}Hf/^{177}Hf$ in the range in the range 0.281726 to 0.282110 with a corresponding $\varepsilon_{Hf}(t)$ range of -5 to +9. Analyses in the age range 1810–1630 Ma (including a number of partially discordant analyses) have similar initial $^{176}Hf/^{177}Hf$ of 0.281493–0.281612, corresponding to $\varepsilon_{Hf}(t)$ of -7 to -2 (n = 8). One older analysis with an age of 3194 Ma has initial $^{176}Hf/^{177}Hf$ of 0.280772 ($\varepsilon_{Hf}(t)$ = +2).

4.3.3. Sample WI89

Thirteen Hf isotope analyses of zircon cores were collected from sample WI89 (Fig. 6c). Six core analyses with ages between 1420–1320 Ma in sample WI89 have initial $^{176}Hf/^{177}Hf$ between 0.281905 and 0.282130, corresponding to $\varepsilon_{Hf}(t)$ between 0 and +8. Two analyses with ages of c. 1555 Ma have initial $^{176}Hf/^{177}Hf$ of 0.281951 ($\varepsilon_{Hf}(t)$ = +5). The remaining five analyses range in age from 1900–1700 Ma and have initial $^{176}Hf/^{177}Hf$ 0.281726 to 0.281922, corresponding to $\varepsilon_{Hf}(t)$ of +3 to +8.

4.3.4. Sample WI68

Forty-two Hf isotopes analyses of zircon cores were collected from sample WI68 (Fig. 6d). Of these, 40 analyses fall in the age range 1420–1330 Ma and yield initial $^{176}Hf/^{177}Hf$ values between 0.281702–0.282092, corresponding to $\varepsilon_{Hf}(t)$ of -7 to +6 (Fig. 6d). One analysis with a $^{207}Pb/^{206}Pb$ age of 1491 ± 9 Ma has a similar initial $^{176}Hf/^{177}Hf$ of 0.281793 ($\varepsilon_{Hf}(t)$ = -1.6). An older analysis with a $^{207}Pb/^{206}Pb$ age of 1731 ± 6 Ma has an initial $^{176}Hf/^{177}Hf$ of value of 0.281669 ($\varepsilon_{Hf}(t)$ = -0.5).

4.4. Hf isotopes of magmatic rocks

Hf isotope data for magmatic rocks are given in Supplementary Data S2.3. Hf isotope analyses for magmatic rocks are calculated using the corresponding $^{207}Pb/^{206}Pb$ age for each analysis.

4.4.1. Sample WI43

The initial $^{176}Hf/^{177}Hf$ ranges between 0.281839 and 0.282088 with a corresponding $\varepsilon_{Hf}(t)$ of -3 to + 6 (Fig. 7; n = 24). The older and younger ages show the same range in initial $^{176}Hf/^{177}Hf$.

4.4.2. Sample WI17

Hf isotopic analyses from sample WI17 have a range of initial $^{176}Hf/^{177}Hf$ values between 0.282010 and 0.282123 (Fig. 7; n = 17). $\varepsilon_{Hf}(t)$ ranges from +1 to +4 with a weighted average of 1.9 ± 1.2 (MSWD = 0.11).

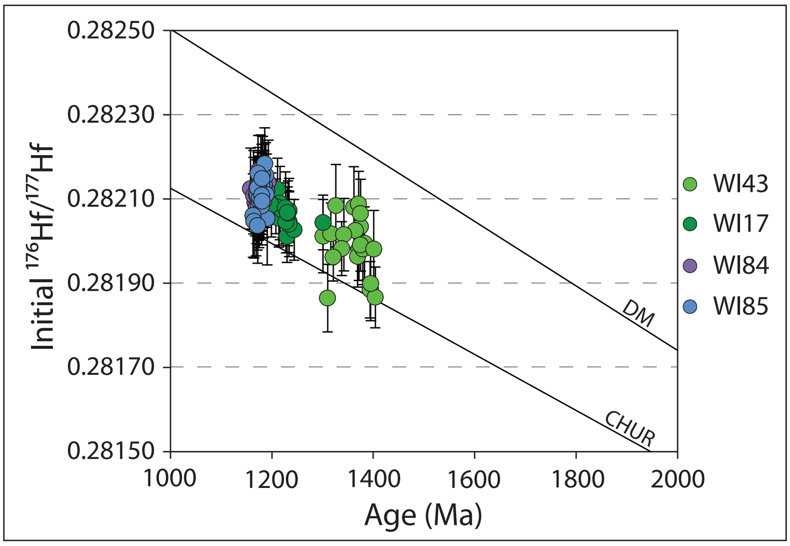

Figure 7: Initial $^{177}Hf/^{176}Hf$ ratios of magmatic rocks. The ratios are plotted against the $^{207}Pb/^{206}Pb$ age for each analysis. The error bars are 2SE.

4.4.3. Sample WI84

Hf isotope analyses from sample WI84 yield a range of initial $^{176}Hf/^{177}Hf$ between 0.282062 and 0.282166 (Fig. 7; n = 22). $\varepsilon_{Hf}(t)$ ranges from +1 to +4 with a weighted average of 2.4 ± 1.2 (MSWD = 0.13).

4.4.4. Sample WI85

Hf isotopic analyses from sample WI85 yield initial $^{176}Hf/^{177}Hf$ ratios in the range 0.282036 to 0.282184 (Fig. 7; n = 28). $\varepsilon_{Hf}(t)$ ranges from 0 to + 5 with a weighted average of 2.6 ± 1.1 (MSWD = 0.21).

5. Discussion

5.1. Age and provenance of the metasedimentary rocks of the Windmill Islands

This study provides new constraints on the timing of deposition of the metasedimentary rocks in the Windmill Islands. The youngest concordant oscillatory zoned cores, interpreted to reflect magmatic genesis, in this study range in age between 1354–1322 Ma. These cores are commonly overgrown by metamorphic zircon rims that yield ages younger than 1300 Ma (Fig. 3). This suggests that deposition of the sedimentary protoliths occurred in the interval 1350–1300 Ma. All samples have similar maximum depositional ages, suggesting they could reflect components of the same depositional system.

The metasedimentary samples from the Windmill Islands each show slightly different age distributions. However, the granulite facies samples in the southern Windmill Islands also display U–Pb discordance indicative of ancient radiogenic Pb-loss, which may be the source of some of the observed differences in detrital spectra. Sample WI07 is an amphibolite facies metasedimentary rock that appears to better preserve detrital zircon populations and is therefore used a framework to aid in the interpretation of the discordant analyses from other samples. Three peaks are defined by concordant analyses at c. 1380 Ma, c. 1595 Ma and c. 1790 Ma with minor older components between c. 3200–1900 Ma (Fig. 4). These peaks are used to assess the likely provenance of the Windmill Islands metasedimentary rocks with reference to neighbouring terrains (Fig. 1; Fig. 8a).

All metasedimentary samples in this study contain a significant population of oscillatory zoned cores with ages between 1420–1330 Ma. Inherited populations in magmatic rocks between 1450–1350 Ma have been noted elsewhere in the Windmill Islands (Post, 2000; Zhang et al., 2012), consistent with the widespread occurrence of this age component. The $\varepsilon_{Hf}(t)$ signature of the 1490–1330 Ma detritus in the Windmill Islands metasediments is between -7 to +10, but dominantly in the range -4 to +6 (Fig. 8a). Zircons of this age have no known source within the West Australian Craton, but are consistent with derivation from the c. 1410 Ma Loongana Arc in the Madura Province (Fig. 1), which has $\varepsilon_{Hf}(t)$ between -2.5 and +11.5 (Fig. 8a; Spaggiari et al., 2014, 2015).

Sample WI07 contains a concordant zircon population at c. 1595 Ma (*n* = 7). Sample WI89 contains discordant analyses in the range 1590–1550 Ma (*n* = 5) that are likely to correspond to this population (Fig. 4a and c). As many of the 1610–1500 Ma aged domains were small, only five Hf isotope analyses were collected from this population. Three analyses have $\varepsilon_{Hf}(t)$ ranges of +5 to +7 and two analyses have CHUR-like values, however, due to the small number of analyses it is difficult to assign significance to the $\varepsilon_{Hf}(t)$ range (Fig. 8a). Zircons between 1600–1550 Ma are uncommon in the West Australia Craton. However, one source could be the along-strike Musgrave Province, which contains orthogneiss and metagranites with 1600–1550 Ma protolith ages (Camacho and Fanning, 1995; Edgoose et al., 2004; Howard et al., 2015). These are interpreted to have formed in a juvenile arc setting and have $\varepsilon_{Nd}(t)$ values of -1.2 to 0.9, broadly consistent with the juvenile $\varepsilon_{Hf}(t)$ data from this study (Fig. 8a; Wade et al., 2006, 2008). An alternative source for the c. 1595 Ma detritus in the Windmill Islands may be the 1595–1575 Hiltaba Suite and coeval (c. 1590 Ma) Gawler

Figure 8 (facing page): Hf evolution diagrams for the Windmill Islands. Part (a): Detrital zircon samples from this study are plotted as diamonds in shades of red–yellow. Detrital zircon from Arid Basin metasedimentary units (SDF: Snowys Dam Formation, GCG: Gwynne Creek Gneiss, MM: Malcolm Metamorphics) are plotted as open circles in shades of blue for comparison, from Spaggiari et al. (2015). The age and isotopic character of detrital zircon from the Wirku Metamorphics (WM) in the Musgrave Province is also shown for comparison, from Woodhouse et al. (available from GSWA's online geochronology database at http://dmp.wa.gov.au/geochron). The <1400 Ma magmatic rocks of the Musgrave Province have isotopic signatures that fall within the most radiogenic array of the Wirku Metamorphics. The other filled areas denote the age and isotopic character of possible source regions. LA: Loongana Arc, from Spaggiari et al. (2015); BZ: Biranup Zone, from Kirkland et al. (2015b); YC: Yilgarn Craton, from Wyche et al. (2012) and Ivanic et al. (2012); MP: Musgrave Province 1600–1550 Ma orthogneisses, $\varepsilon_{Nd}(t)$ data from Wade et al. (2006) converted to $\varepsilon_{Hf}(t)$ values using the crustal array equation $\varepsilon_{Hf}(t) = 1.35\ \varepsilon_{Nd}(t) + 2.82$ of Vervoort et al. (1999). Part (b): Magmatic samples from this study are plotted as circles in shades of blue–green. Detrital zircon from this study with ages <2000 Ma are plotted as diamonds in shades of red–yellow for comparison with the magmatic samples. Unfilled squares are $\varepsilon_{Hf}(t)$ magmatic analyses from Zhang et al. (2012). The light grey filled squares are $\varepsilon_{Nd}(t)$ whole rock data for Windmill Islands magmatic rocks from Zhang et al. (2012) and Möller et al. (2002) converted to $\varepsilon_{Hf}(t)$values. The dark grey filled squares are $\varepsilon_{Nd}(t)$ data whole rock data for Windmill Islands metasedimentary rocks from Möller et al. (2002) converted to $\varepsilon_{Hf}(t)$ values. The dark purple and blue filled areas represent the age and $\varepsilon_{Hf}(t)$ values for zircon from the Recherche and Esperance Supersuites respectively, from Kirkland et al. (2015b). The light purple and blue filled areas represent whole rock $\varepsilon_{Nd}(t)$ values of the Recherche and Esperance Supersuites from Smithies et al. (2015a) converted to $\varepsilon_{Hf}(t)$ values. The dark grey filled area represents whole rock $\varepsilon_{Nd}(t)$ values of the Moodini Supersuite in the Madura Province from Smithies et al. (2015b), converted to $\varepsilon_{Hf}(t)$values.

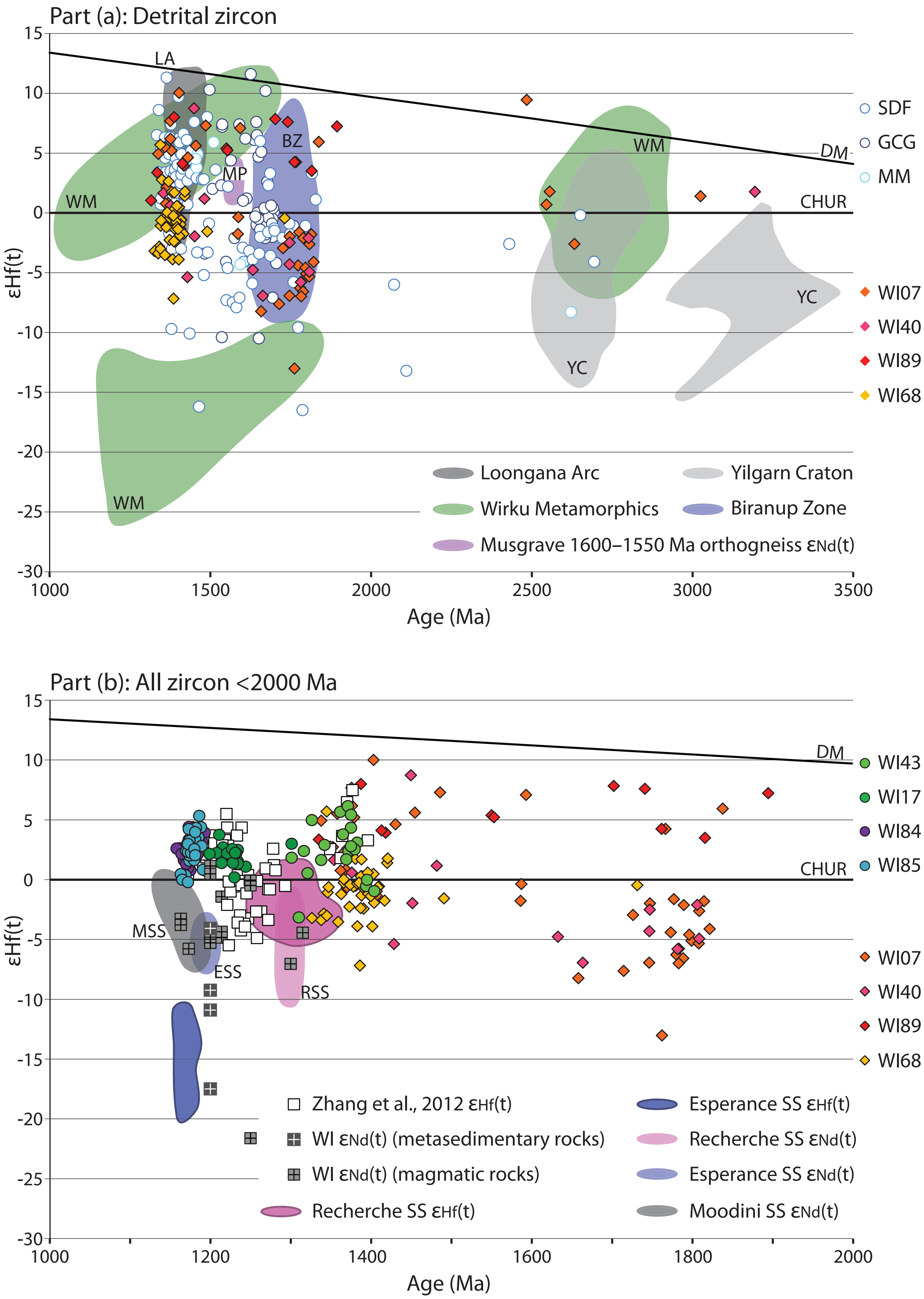
Part (a): Detrital zircon
εHf(t)
Age (Ma)
LA
WM
BZ
MP
YC
DM
CHUR
SDF
GCG
MM
WI07
WI40
WI89
WI68
Loongana Arc
Yilgarn Craton
Wirku Metamorphics
Biranup Zone
Musgrave 1600–1550 Ma orthogneiss εNd(t)
Part (b): All zircon <2000 Ma
MSS
ESS
RSS
WI43
WI17
WI84
WI85
Zhang et al., 2012 εHf(t)
WI εNd(t) (metasedimentary rocks)
WI εNd(t) (magmatic rocks)
Recherche SS εHf(t)
Esperance SS εHf(t)
Recherche SS εNd(t)
Esperance SS εNd(t)
Moodini SS εNd(t)

Range Volcanics (Blissett et al., 1993; Daly et al., 1998; Hand et al., 2007) within the Gawler Craton. However, modern stream detrital zircon data from the Gawler Craton shows that the c. 1595 Ma zircons have an $\varepsilon_{Hf}(t)$ peak at -2.3 (Belousova et al., 2009), which is not consistent with the more juvenile $\varepsilon_{Hf}(t)$ values for 1600–1550 Ma detrital zircons in this study.

Samples WI07 and WI40 have a significant detrital populations aged between 1800–1770 Ma. Although it is now discordant, it is likely that sample WI89 also contains this population. The zircons within this age range have bimodal $\varepsilon_{Hf}(t)$ distributions. The detrital zircons from samples WI07 and WI40 dominantly have $\varepsilon_{Hf}(t)$ between -2 and -7, whereas sample WI89 and two analyses from sample WI07 have $\varepsilon_{Hf}(t)$ between +3 and +8 (Fig. 8a). This suggests that magmatism in the source terrain may have involved both juvenile input and reworking of an Archean component. Magmatic rocks between 1800–1700 Ma are found in the Biranup and Nornalup zones in the Albany–Fraser Orogen (Fig. 9), and the $\varepsilon_{Hf}(t)$ of detrital zircons from the Windmill Islands isotopically overlaps with magmatic zircons from these regions (Fig. 8a).

The source of the minor 3000–1900 Ma detrital components is unclear. In particular, 2550–2450 Ma ages are rare within the Yilgarn Craton (Spaggiari et al., 2015), and the $\varepsilon_{Hf}(t)$ of these analyses in the Windmill Islands samples commonly plots outside the isotopic envelope of the Yilgarn Craton (Fig. 8a). Similarly-aged detritus is found within the Big Red Paragneiss in the c. 1815–1600 Ma Barren Basin in the Albany–Fraser Orogen (Spaggiari et al., 2015), suggesting detritus recycled from the Barren Basin may have been a source for the Windmill Islands metasedimentary rocks. The original source of this detritus is still uncertain. If the source of the 2550–2450 Ma detritus was proximal during deposition of the Barren Basin, it has since been eroded or has not as yet been identified. A more distal source may be the 2555–2430 Ma granitic gneisses of the Glenburgh Terrane, on the northern margin of the Yilgarn Craton (Johnson et al., 2011), although this is not supported by the Hf isotopic signature of the zircon. Alternatively, magmatism from 2555 Ma to 2460 Ma is common within the Sleaford and Mulgathing Complexes in the Gawler Craton (Reid et al., 2014).

The Windmill Islands metasedimentary rocks appear likely to be derived from a combination of the West Australian Craton, including the Yilgarn Craton and the Albany–Fraser Orogen, and regions in proximity of the Albany–Fraser Orogen, such as the Musgrave Province and the Loongana Arc of the Madura Province. The location of the Windmill Islands between the West Australian Craton and Loongana Arc is consistent with these regions being contiguous at the time of sediment deposition.

5.2. Age and isotopic character of the magmatic rocks of the Windmill Islands

A range of ages have previously been obtained for the magmatic rocks of the Windmill Islands (Post, 2000; Post et al., 1997; Zhang et al., 2012). Four structurally constrained granitic and charnockitic samples were selected to provide further constraints on the timing and isotopic character of magmatism in the Windmill Islands.

5.2.1. Timing and style of M_1/D_1 magmatism

Sample WI43 is an orthogneiss whose protolith is interpreted to have intruded into metasedimentary rocks on Clark Peninsula based on field relationships (Post, 2000). Although it was not possible to determine an unequivocal magmatic age from sample WI43,

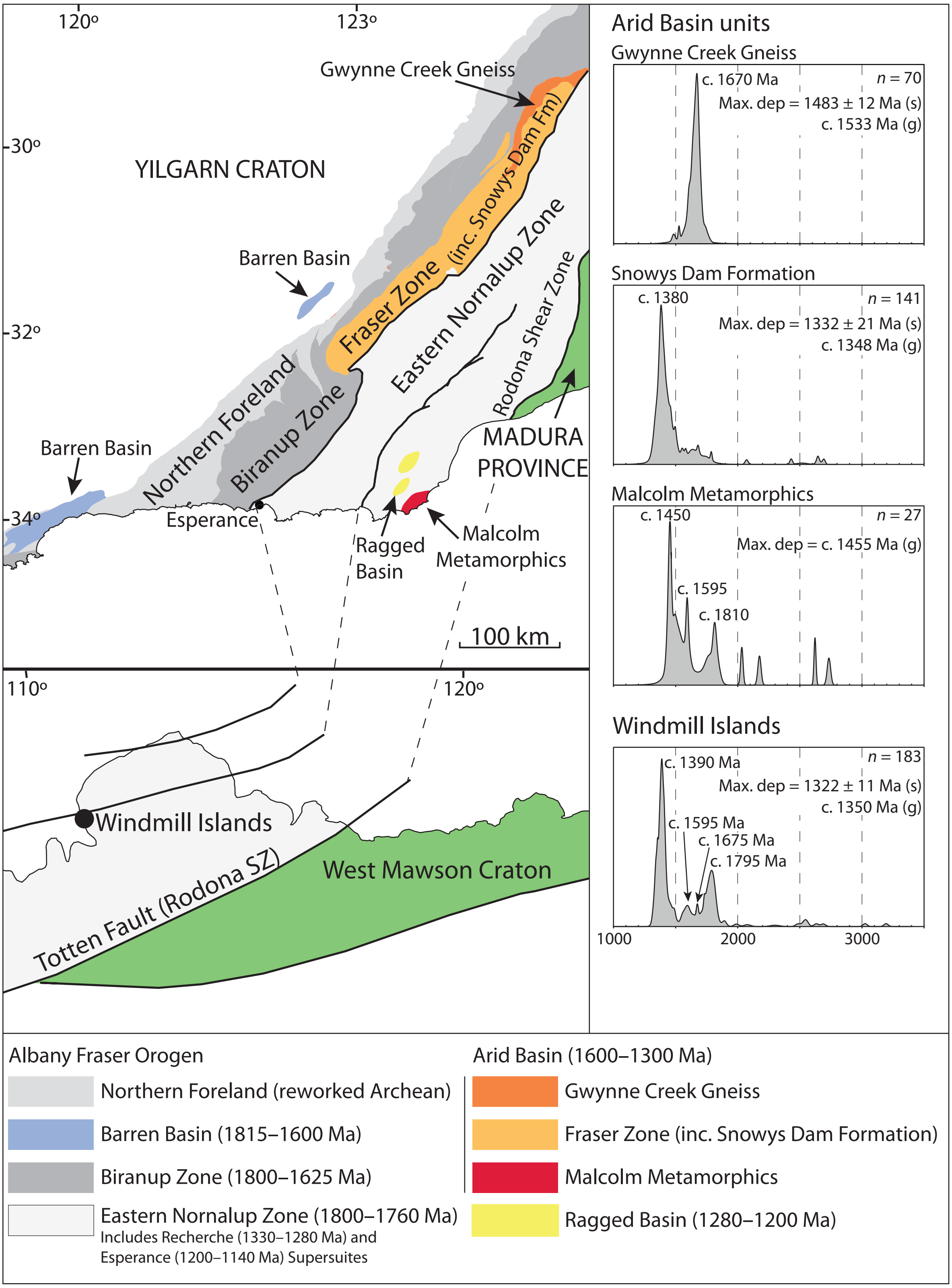

Figure 9: Comparison of detrital zircon spectra and interpreted tectonic elements for the Albany–Fraser Orogen (Arid Basin) and the Windmill Islands. Inferred paleogeographic reconstruction from Aitken et al. (2016). Geology of the Albany–Fraser Orogen modified after Spaggiari et al. (2014). Detrital zircon data is from Adams (2012) and Spaggiari et al. (2015). Maximum depositional age for each unit is given as the youngest single analysis (s) and youngest group (g).

the 'Unmix' age of 1326 ± 5 Ma for sample WI43 (Fig. 4) is broadly consistent with the oldest metamorphic ages in this study and the interpreted magmatic age of 1315 ± 6 Ma by Post (2000). The older zircons in both sample WI43 and the sample dated by Post (2000) range in age between 1490–1350 Ma, suggesting that the younger age is likely to be the magmatic age. This suggests that magmatism associated with D_1/M_1 occurred very shortly after the deposition of the sediments, and provides a minimum depositional age for the protoliths of the sedimentary rocks in the Windmill Islands. The syn-D_1 orthogneiss has $\varepsilon_{Hf}(t)$ between -3 and +6, which falls within the range in $\varepsilon_{Hf}(t)$ of the c. 1400–1350 Ma detrital zircons (Fig. 8b). The $\varepsilon_{Nd}(1315)$ value for the sample dated by Post (2000) is -5.4 (Fig. 8b; Möller et al., 2002). The large number of older zircons, combined with the similarity in $\varepsilon_{Hf}(t)$ between the orthogneiss and detrital zircons, suggests that the orthogneiss is crustally derived from a source rich in c. 1400–1350 Ma zircons, or is extremely crustally contaminated. Although a mantle component cannot be ruled out, on the basis of comparison to the detrital zircon data this is likely to be limited.

5.2.2. Timing and style of M_2/D_2 magmatism

The M_2 biotite granite in this study (sample WI17) is unfoliated, does not contain garnet, and yields a crystallisation age of 1235 ± 7 Ma, with juvenile $\varepsilon_{Hf}(t)$ between 0 and +4 (Figs 7 and 8b). Zhang et al. (2012) dated two samples of garnet-bearing granitic gneiss and one sample of garnet-bearing foliated granite (syn-D_2) and suggested similar crystallisation ages of 1250–1240 Ma, with $\varepsilon_{Hf}(t)$ values falling into two groups of -5 to -3 and -1 to +1 (Fig. 8b). The sample of garnet-bearing granite and one of the granitic gneisses yields $\varepsilon_{Nd}(t)$ values of -2.5 and -2.2 respectively. A second sample of granitic gneiss yields $\varepsilon_{Nd}(t)$ of -18.1, interpreted to reflect significant assimilation of the surrounding metasedimentary rocks (Fig. 8b; Zhang et al., 2012). A weakly foliated, garnet-bearing sample of syn- to post-D_{2a} orthogneiss has a younger crystallisation age of 1214 ± 10 Ma (Post, 2000). $\varepsilon_{Nd}(1215)$ data from three similar samples yield values between -5.7 and -3.1 (Fig. 8b; Möller et al., 2002). The range in ages, Hf isotope values and mineralogy between samples suggests that the D_2 granites have multiple, distinct intrusive phases.

The syn- to post-D_{2a}, garnet-bearing orthogneisses have high silica values and have been previously interpreted to have formed from the partial melting of Paleoproterozoic crust (Zhang et al., 2012). Additionally, Zhang et al. (2012) found inherited igneous zircon at c. 1370 Ma in these samples and suggested that this may have been the age of an earlier magmatic event in the Windmill Islands. However, as in the case of the syn-D_1 orthogneiss, these ages may instead be derived from the Windmill Islands metasedimentary rocks. This suggests that the D_2 granites contain a significant crustal component. However, the range in $\varepsilon_{Nd}(t)$ data between -5.7 and -2.2 is more juvenile than that of four samples of metasedimentary gneiss that yield $\varepsilon_{Nd}(1200)$ of -15.1 to -5.1 (Fig. 8b; Möller et al., 2002). This, in combination with the juvenile $\varepsilon_{Hf}(t)$ values for sample WI17, suggests that magmatism was associated with varying degrees of juvenile input and is not solely the result of crustal melting.

The Ardery Charnockite has been interpreted to intrude late in M_2 (Paul et al., 1995; Post, 2000) and is the most juvenile rock suite in the terrane. The two samples of Ardery Charnockite in this study (samples WI84 and WI85) have indistinguishable ages of 1175 ± 7 Ma and 1178 ± 6 Ma and the same range in $\varepsilon_{Hf}(t)$ of 0 to +5 (Figs. 7 and, 8b). Two nearby samples of Ardery Charnockite dated by Zhang et al. (2012) yield ages between 1230 and 1170 Ma, with weighted average ages of c. 1200 Ma, but an identical ε_{Hf}(t) range from 0 to +5 and whole rock ε_{Nd}(t) of -1.6 and -1.1 (Fig. 8b; Zhang et al., 2012). SHRIMP data from Post (2000) suggests a younger age of 1163 ± 7 Ma for a sample of Ardery Charnockite, with slightly more evolved ε_{Nd}(1163) between -4.5 and -4.9 (Fig. 8b; Möller et al., 2002).

There is a slight increase in ε_{Hf}(t) values between the M_2 biotite granite (sample WI17) and the charnockite samples in this study (samples WI84 and WI85). This trend in ε_{Hf}(t) is observed more strongly in the samples of Zhang et al. (2012), and similarly, there is a minor increase in ε_{Nd}(t) between the charnockites and the granitic gneisses (Möller et al., 2002; Zhang et al., 2012). This suggests that to form the more juvenile Ardery Charnockite, there must have been either mafic input or melting of a more juvenile lower crust. The geochemistry of the Ardery Charnockite has been interpreted to have been produced by partial melting of a mafic lower crust by underplated basaltic magmas (Kilpatrick and Ellis, 1992; Zhang et al., 2012), consistent with the interpretation that the charnockites are the most isotopically 'juvenile' rock type in the Windmill Islands. This lower crust may have been generated during the preceding D_2 granitoid magmatism that incorporated mantle-derived melts.

5.3. Tectonic setting of the Wilkes Land–Albany–Fraser system

Palaeogeographical reconstructions based on geophysics place the Windmill Islands within the Nornalup Zone of the eastern Albany–Fraser Orogen to the west of the Rodona Shear Zone (Aitken et al., 2014, 2016), which is interpreted to be a suture zone separating the Madura Province of oceanic affinity from the West Australian Craton (Fig. 9; Kirkland et al., 2015b; Spaggiari et al., 2015). Therefore, the new data obtained in this study allows for testing the proposed tectonic models for the Albany–Fraser Orogen.

5.3.1. Magmatism within the Wilkes Land–Albany–Fraser system

The likely timing of M_1 magmatism in the Windmill Islands was coeval with intrusion of the c. 1330–1280 Ma Recherche Supersuite granites and the coeval Fraser Zone gabbros during Stage I of the Albany–Fraser Orogeny (Kirkland et al., 2015b). The Recherche Supersuite granites have been divided into two types, the Gora Hill Suite and the Southern Hills Suite (Smithies et al., 2015a). The Gora Hill Suite (ε_{Nd}(t) = -5.88 to -4.32) is interpreted to be derived from a regionally extensive, lower crustal hot zone that involved mingling of mafic magmas with partial melts derived from Biranup Zone or Northern Foreland sources (Smithies et al., 2015a). The Southern Hills Suite comprises synogranites with geochemistry that suggests they were derived from partial melting of metasedimentary rocks (Smithies et al., 2015a). These synogranites have ε_{Nd}(t) of -3.01 to -7.8, consistent with derivation from metasedimentary rocks with a significant radiogenic c. 1400 Ma detrital component (Smithies et al., 2015a) .The syn-D1 orthogneiss in the Windmill Islands contains a large number of inherited zircon grains and has an ε_{Nd}(t) value of -5.5, within the range of the Southern Hills Suite. Therefore, although no whole rock geochemistry is available for the syn-D_1 orthogneiss from the Windmill Islands, its isotopic signature and age is consistent with a correlation to the Southern Hills Suite (Fig. 8b).

There is no magmatism between the intrusion of the 1330–1280 Ma Recherche Supersuite granites and the 1200–1140 Ma Esperance Supersuite in the Albany–Fraser Orogen (Clark et al., 2000; Kirkland et al., 2011, 2015b). Therefore the 1250–1210 Ma, syn- to post-D_2 granites in the Windmill Islands have no known equivalents in the Albany–Fraser Orogen and their tectonic significance is difficult to determine. Minor inheritance in some samples, combined with field observations of metasedimentary rafts included in the orthogneisses, suggest that there is some crustal derivation or assimilation. However, the relatively juvenile $\varepsilon_{Hf}(t)$ signature of magmatic zircons of -5 to +4 (this study; Zhang et al., 2012) requires either a significant mantle component, or that the lower crust of the Windmill Islands was at this stage dominantly composed of juvenile material with limited volumes of older, evolved material.

The 1200–1160 Ma Ardery Charnockite temporally corresponds to the Esperance Suite magmatism in the Albany–Fraser Orogen. Coeval magmatism also occurs in the Musgrave Province with the 1220–1150 Ma Pitjantjatjara Supersuite and in the Madura Province at 1225–1130 Ma with the Moodini Supersuite. Each of these suites have similar geochemical characteristics and are interpreted to be derived from high temperature melting of anhydrous lower crust, likely associated with significant juvenile mantle input as a result of extension (Kilpatrick and Ellis, 1992; Smithies et al., 2015a; Zhang et al., 2012). Hf isotopic data is only available from one sample of the Esperance Supersuite from the northeastern Nornalup Zone, which yields nonradiogenic $\varepsilon_{Hf}(t)$ values from -20 to -10 (Fig. 8b; Kirkland et al., 2012a). $\varepsilon_{Nd}(1200)$ from six samples across the Albany–Fraser Orogen ranges from -7.34 to -4.87 (Fig. 8b; Smithies et al., 2015a). The Ardery Charnockite appears to be more radiogenic than the Esperance Suite, with $\varepsilon_{Hf}(t)$ of 0 to +5 and $\varepsilon_{Nd}(1200)$ of -4.6 to -1.1 (Post, 2000; Zhang et al., 2012). However, Smithies et al. (2015b) notes that the Moodini Supersuite granites in the Madura Province show spatial trends in age and isotopic compositions with increasing distance from the margin of the West Australian Craton, with young (1144–1125 Ma), radiogenic ($\varepsilon_{Nd}(1200)$ = -1.85 to -2.7) granites in the eastern Madura Province and older (1181–1172 Ma), less radiogenic ($\varepsilon_{Nd}(1200)$ = -7.34 to -3.7) granites in the west (Smithies et al., 2015b). These older, westernmost granites are similar to the Ardery Charnockite (Fig. 8b).

Both the Ardery Charnockite and the c. 1250–1210 Ma magmatism in the Windmill Islands are relatively juvenile and do not show evidence for significant amounts of evolved crust. As the Windmill Islands are interpreted to be located within the Nornalup Zone in the Albany–Fraser Orogen (Fig. 9; e.g. Aitken et al., 2014, 2016), this suggests that magmatism and metamorphism occurred in crust that was likely to have been significantly modified by prior addition of juvenile material. The more juvenile nature of the Windmill Islands rocks compared to those from the western Albany–Fraser Orogen may relate to increasing volumes of mantle input into attenuated crust with increasing distance from the margin of the West Australian Craton. The juvenile magmatism at c. 1250–1210 Ma may represent an additional phase of extension between Stage I and Stage II of the Albany Fraser Orogeny.

5.3.2. Deposition of the Windmill Islands/Arid Basin sedimentary rocks

The maximum depositional age of the metasedimentary rocks in the Windmill Islands is consistent with the timing of deposition of the youngest units of the c. 1600 to 1305 Ma Arid Basin in the Albany–Fraser Orogen

(Spaggiari et al., 2015), and the Windmill Islands metasedimentary rocks share similar detrital zircon age peaks and $\varepsilon_{Hf}(t)$ values with the Snowys Dam Formation and Malcolm Metamorphics (Figs. 8a and 9; Spaggiari et al., 2014, 2015). Although the metasedimentary rocks in the Windmill Islands share similarities in depositional age and detrital signature with some units of the Wirku Metamorphics in the Musgrave Province, the Hf isotopic array for the Wirku Metamorphics is very different (Fig. 8a). Therefore, the Windmill Islands metasedimentary rocks are interpreted to best correlate with units in the Arid Basin.

The currently proposed tectonic model for the Albany–Fraser Orogen during the Mesoproterozoic involves the formation of a marginal ocean basin on the eastern edge of the Yilgarn Craton after c. 1600 Ma. Continued extension formed an ocean-continent transition in the eastern Nornalup Zone, outboard of the craton margin (Fig. 9; Spaggiari et al., 2015). The Madura Province (Loongana Arc) rocks are interpreted to have formed in an oceanic arc (Kirkland et al., 2015b) that formed via east-dipping subduction of the passive margin of the Albany–Fraser Orogen (Spaggiari et al., 2014, 2015). The Arid Basin is therefore interpreted to have formed in a passive margin setting on the edge of the West Australian Craton, with the exception of the Malcolm Metamorphics that have been interpreted as a forearc basin that formed on the western side of the emergent Loongana Arc (Spaggiari et al., 2015). To account for the large volume of Loongana Arc-derived detritus, the Arid Basin is interpreted to have evolved into a foreland basin after soft collision of the arc with the margin of the Albany–Fraser Orogen at c. 1330 Ma (Spaggiari et al., 2015). However, the interpretation of east dipping subduction appears inconsistent with new data from the Windmill Islands.

Basins containing detrital zircons that are close in age to the depositional age of the sediment are considered likely to have formed in convergent settings (e.g. back-arc, forearc or trench settings), reflecting the significant amount of nearby coeval magmatism in that setting (Cawood et al., 2012). The Windmill Islands and Snowys Dam Formation have similar maximum depositional ages of c. 1350 Ma (Fig. 9; Clark et al., 2014; Spaggiari et al., 2015). Both are dominated by 1400–1375 Ma detrital zircon with $\varepsilon_{Hf}(t)$ values between -2 and +12, interpreted to be derived from the Loongana Arc (Fig. 8a; Spaggiari et al., 2014, 2015), consistent with a convergent setting. The Windmill Islands metasedimentary rocks contain c. 1595 and c. 1790 Ma components which also occur in the Malcolm Metamorphics and may be derived from both the Musgrave Province and the West Australian Craton (Figs. 8a and 9; Adams, 2012; Spaggiari et al., 2014, 2015). Therefore, the detrital zircons in the Windmill Islands metasedimentary rocks suggest that the Arid Basin had to form in a setting that allowed both significant craton-derived and arc-derived detritus. A tectonic setting involving the development of a foreland basin would allow for the older components to be recycled from the Malcolm Metamorphics, although the lack of a substantial c. 1450 Ma component in the Windmill Islands means that this seems unlikely (Fig. 9).

The tectonic setting of the Arid Basin is also constrained by the observed metamorphic conditions (Clark et al., 2014). Although the timing of M_1 metamorphism in the Windmill Islands is not well constrained, all metasedimentary samples as well as sample WI43 contain some concordant zircon rims at c. 1300 Ma (Figs. 4 and 5a), which are interpreted to reflect metamorphic growth. The conditions of M_1 metamorphism are poorly constrained but conventional thermobarometry suggests temperatures of 750 °C at 4 kbar (Post, 2000). In the Malcolm Metamorphics, monazite geochronology suggests M_1 occurred at c. 1310 Ma and identical *P–T* estimates of 4–5 kbar and 750 °C have been proposed (Adams, 2012; Clark et al., 2000). In the model of Spaggiari et al. (2014; 2015), this would require the interpreted forearc basin (Malcolm Metamorphics) and foreland basin (Windmill Islands and Snowys Dam Formation) to have seemingly comparable *P–T–t* evolutions. However, forearc basins are commonly characterised by low thermal gradients (Brown, 2006; Dickinson, 1995), which may be inconsistent with the high thermal conditions recorded by the Malcolm Metamorphics. In the Fraser Zone (Fig. 9), the time interval between deposition of the Snowys Dam Formation and metamorphism is similarly short (Clark et al., 2014). Metamorphism in the Fraser Zone is interpreted to have involved high thermal gradients and was associated with mafic and felsic magmatism (Clark et al., 2014; Kirkland et al., 2011). The gabbros that intrude the Snowys Dam Formation have rare inherited zircons and isotopic signatures consistent with the assimilation of an older, felsic crust that is likely to be derived from the West Australian Craton (Clark et al., 2014; Smithies et al., 2013). Additionally, the geochemical signature of mafic intrusives within the Fraser Zone have been used to suggest a possible back-arc setting for this region during Stage I of the Albany–Fraser Orogeny (Clark et al., 2014; Smithies et al., 2013).

Our preferred interpretation is that the protoliths to the Windmill Islands metasedimentary rocks were deposited in a back-arc basin. A back-arc basin is consistent with the detrital zircon spectra that suggest sediment sourced from both the craton and the arc, the short time interval between deposition and M_1 metamorphism and the attainment of high thermal gradients throughout the region. It is also consistent with previous interpretations of the Fraser Zone as a back-arc or intracontinental rift setting that developed on the margin of the West Australian Craton (Clark et al., 2014; Kirkland et al., 2011; Smithies et al., 2013). The metasedimentary rocks of the Windmill Islands include sequences of psammitic gneiss, pelitic gneiss, calc-silicate, banded iron formation and manganese-rich horizons (Paul et al., 1995; Post, 2000). The Arid Basin comprises similarly variable sequences including interbedded sandstone and mudstone, calcareous rocks or marls, iron rich horizons, and probable volcaniclastic or volcanic successions (Spaggiari et al., 2014, 2015). Additionally, boron-bearing minerals such as tourmaline, kornerupine and dumortierite are common throughout the Windmill Islands (Post, 2000). Similar boron-rich mineral assemblages have been cited as evidence for a back-arc basin or a continental rift setting (e.g. Grew et al., 2013; Slack et al., 1993). The Windmill Islands metasedimentary rocks also contain abundant iron oxides and are enriched in manganese, which is commonly interpreted to reflect an environment with hydrothermal activity (e.g. Ashley et al., 1998; Mücke, 2005). This is consistent with an extensional back-arc setting rather than a compressional foreland basin.

If the Arid Basin was deposited in a back-arc basin setting, this would necessitate west-dipping subduction during creation of the Loongana Arc. The Loongana Arc has previously been proposed to have formed as a result of east-dipping subduction to account for the “juvenile, uncontaminated” chemistry of the mafic-ultra mafic rocks and low-K plagiogranites intersected in drill holes, as well as the lack of tectonic activity in the Albany–Fraser Orogen at this time (Spaggiari et al., 2015). The Rodona Shear Zone has been interpreted as the fundamental suture zone that separates the Albany–Fraser margin from outboard crust of the Loongana Arc. Two drill holes located either side of the Rodona Shear Zone (holes NSD and MAD002) have both intersected crust interpreted to be >1400 Ma with chemical characteristics of EMORB proto-oceanic crust (Smithies et al., 2015b). It is likely that NSD penetrated an over-thrust package, transported back craton-wards (Spaggiari and Tyler, 2014). Nevertheless, the Rodona Shear Zone may not be a fundamental terrane boundary between two separate pieces of crust but rather reflect a broad transition zone to crust of oceanic affinity. The Madura Province therefore represents a region of highly extended crust that has been modified by repeated addition of juvenile material and reflects an ocean continent transition zone (Kirkland et al., 2015a; Smithies et al., 2015b). The Loongana Arc has been defined based on samples from a limited number of drill holes. $\varepsilon_{Hf}(t)$ from these samples ranges from -2.5 to +11.5 (Kirkland et al., 2015b), suggesting a very juvenile source. Nevertheless, even within the Madura Province rare isotopically evolved packages with greater crustal influence can be found (e.g. Burkin Prospect; Kirkland et al., 2012b), likely reflecting rifted fragments of the continental margin. Additionally, detrital zircons between 1420–1340 Ma in this study have $\varepsilon_{Hf}(t)$ as evolved as -7 (Fig. 8a). If zircons of this age are all derived from the magmatic rocks of the Madura Province, this suggests that at least some of the magmatism may have been crustally contaminated, consistent with a component being derived directly (e.g. rifted sliver) off the West Australian Craton. Furthermore, the abundance of c. 1400–1350 Ma detrital zircons in pelitic rocks suggests that there must have been significant volumes of felsic magmatism to generate the zircons. The tectonic setting of the Wilkes Land–Albany–Fraser system at c. 1400–1300 Ma could reflect a long-lived, highly extended margin.

6. Conclusions

U–Pb geochronology from detrital zircon from metasedimentary rocks in the Windmill Islands in Wilkes Land, East Antarctica, suggests that the protoliths were deposited in the interval 1350–1300 Ma. The dominant detrital peaks are c. 1800–1700 Ma, c. 1595 Ma and c. 1380 Ma. These ages correspond to events in neighbouring terrains, including the West Australian Craton, Musgrave Province and the Madura Province (Fig. 1). The location of the Windmill Islands between the West Australian Craton and the Madura Province suggests that they were contiguous at the time of sediment deposition. The metasedimentary rocks have been metamorphosed and intruded by three phases of magmatism at c. 1325–1315 Ma, c. 1250–1210 Ma and c. 1200–1170 Ma. The first phase of magmatism is likely to have been crustally derived, whereas the second and third phases of magmatism are associated with varying amounts of juvenile addition. The relatively juvenile Hf isotopic signature of these magmatic rocks is consistent with the location of the Windmill Islands above relatively thin crust that contains little evolved material. The short interval between deposition of the sediments and high thermal gradient metamorphism, combined with the lack of evolved material in the lower crust, suggests that the Windmill Islands may have formed in a back-arc setting in a highly extended part of the West Australian Craton. This interpretation therefore suggests that the Albany–Fraser Orogen was bounded to the east by west-dipping subduction, represented by the c. 1410–1350 Ma Loongana Arc.

Acknowledgments

This project was completed with funding from Australian Antarctic Science Program Project 4191 and DE120103067 to CC. The authors would like to thank the Australian Antarctic Division and personnel of Casey Station for assistance with logistics and fieldwork.

References

Adams, M., 2012. Structural and geochronological evolution of the Malcolm gneiss, Nornalup Zone, Albany–Fraser Orogen, Western Australia. Geolocial Survey of Western Australia, Record 2012/4, p. 132.

Aitken, A.R.A., Betts, P.G., Young, D.A., Blankenship, D.D., Roberts, J.L., Siegert, M.J., 2016. The Australo–Antarctic Columbia to Gondwana transition. Gondwana Research 29, 136–152.

Aitken, A.R.A., Young, D.A., Ferraccioli, F., Betts, P.G., Greenbaum, J.S., Richter, T.G., Roberts, J.L., Blankenship, D.D., Siegert, M.J., 2014. The subglacial geology of Wilkes Land, East Antarctica. Geophysical Research Letters 41, 2390–2400.

Ashley, P.M., Lottermoser, B.G., Westaway, J.M., 1998. Iron-formations and epigenetic ironstones in the Palaeoproterozoic Willyama Supergroup, Olary Domain, South Australia. Mineralogy and Petrology 64, 187–218.

Belousova, E.A., Reid, A.J., Griffin, W.L., O'Reilly, S.Y., 2009. Rejuvenation vs. recycling of Archean crust in the Gawler Craton, South Australia: Evidence from U–Pb and Hf isotopes in detrital zircon. Lithos 113, 570–582.

Black, L., Gulson, B., 1978. The age of the Mud Tank Carbonatite, Strangways Range, Northern Territory. BMR Journal of Australian Geology and Geophysics 3, 227–232.

Blight, D.F., Oliver, R.L., 1977. The metamorphic geology of the Windmill Islands, Antarctica: A preliminary account. Journal of the Geological Society of Australia 24, 239–262.

Blissett, A.H., Creaser, R.A., Daly, S.J., Flint, R.B., Parker, A.J., 1993. Gawler Craton- Gawler Range Volcanics, in: Drexel, J.F., Preiss, W.V., Parker, A.J. (Eds.), The Geology of South Australia. South Australia Geological Survey, Bulletin 54, pp. 107–124.

Bodorkos, S., Clark, D.J., 2004. Evolution of a crustal-scale transpressive shear zone in the Albany–Fraser Orogen, SW Australia: 1. *P–T* conditions of Mesoproterozoic metamorphism in the Coramup Gneiss. Journal of Metamorphic Geology 22, 691–711.

Boger, S.D., 2011. Antarctica — Before and after Gondwana. Gondwana Research 19, 335–371.

Bouvier, A., Vervoort, J.D., Patchett, P.J., 2008. The Lu–Hf and Sm–Nd isotopic composition of CHUR: Constraints from unequilibrated chondrites and implications for the bulk composition of terrestrial planets. Earth and Planetary Science Letters 273, 48–57.

Brown, M., 2006. Duality of thermal regimes is the distinctive characteristic of plate tectonics since the Neoarchean. Geology 34, 961–964.

Camacho, A., Fanning, C.M., 1995. Some isotopic constraints on the evolution of the granulite and upper amphibolite facies terranes in the eastern Musgrave Block, central Australia. Precambrian Research 71, 155–181.

Cawood, P.A., Hawkesworth, C.J., Dhuime, B., 2012. Detrital zircon record and tectonic setting. Geology 40, 875–878.

Clark, C., Kirkland, C.L., Spaggiari, C.V., Oorschot, C., Wingate, M.T.D., Taylor, R.J., 2014. Proterozoic granulite formation driven by mafic magmatism: An example from the Fraser Range Metamorphics, Western Australia. Precambrian Research 240, 1–21.

Clark, D.J., Hensen, B.J., Kinny, P.D., 2000. Geochronological constraints for a two-stage history of the Albany–Fraser Orogen, Western Australia. Precambrian Research 102, 155–183.

Daly, S.J., Fanning, C.M., Fairclough, M.C., 1998. Tectonic evolution and exploration potential of the Gawler Craton, South Australia. AGSO Journal of Australia Geology and Geophysics 17, 145–168.

Dickinson, W., 1995. Forearc basins, in: Busby, C.J., Ingersoll, R.V. (Eds.), Tectonics of sedimentary basins. Blackwell Science., United States of America, pp. 221–261.

Edgoose, C.J., Scrimgeour, I.R., Close, D.F., 2004. Geology of the Musgrave Block, Northern Territory, Northern Territory Geological Survey, Report 15. Northern Territory Geological Survey, Darwin.

Fitzsimons, I.C.W., 2000. A review of tectonic events in the East Antarctic Shield and their implications for Gondwana and earlier supercontinents. Journal of African Earth Sciences 31, 3–23.

Fitzsimons, I.C.W., 2003. Proterozoic basement provinces of southern and southwestern Australia, and their correlation with Antarctica. Geological Society, London, Special Publications 206, 93–130.

Grew, E.S., Carson, C.J., Christy, A.G., Boger, S.D., 2013. Boron- and phosphate-rich rocks in the Larsemann Hills, Prydz Bay, East Antarctica: tectonic implications. Geological Society, London, Special Publications 383, 73–94.

Hand, M., Reid, A.J., Jagodzinski, E., 2007. Tectonic Framework and Evolution of the Gawler Craton, Southern Australia. Economic Geology 102, 1377–1395.

Howard, H.M., Smithies, R.H., Kirkland, C.L., Kelsey, D.E., Aitken, A., Wingate, M.T.D., Quentin de Gromard, R., Spaggiari, C.V., Maier, W.D., 2015. The burning heart — The Proterozoic geology and geological evolution of the west Musgrave Region, central Australia. Gondwana Research 27, 64–94.

Ivanic, T.J., Van Kranendonk, M.J., Kirkland, C.L., Wyche, S., Wingate, M.T.D., Belousova, E.A., 2012. Zircon Lu–Hf isotopes and granite geochemistry of the Murchison Domain of the Yilgarn Craton: Evidence for reworking of Eoarchean crust during Meso-Neoarchean plume-driven magmatism. Lithos 148, 112–127.

Jackson, S.E., Pearson, N.J., Griffin, W.L., Belousova, E.A., 2004. The application of laser ablation-inductively coupled plasma-mass spectrometry to in situ U–Pb zircon geochronology. Chemical Geology 211, 47–69.

Johnson, S.P., Sheppard, S., Rasmussen, B., Wingate, M.T.D., Kirkland, C.L., Muhling, J.R., Fletcher, I.R., Belousova, E.A., 2011. Two collisions, two sutures: Punctuated pre-1950 Ma assembly of the West Australian Craton during the Ophthalmian and Glenburgh Orogenies. Precambrian Research 189, 239–262.

Kilpatrick, J.A., Ellis, D.J., 1992. C-type magmas: igneous charnockites and their extrusive equivalents. Earth and Environmental Science Transactions of the Royal Society of Edinburgh 83, 155–164.

Kirkland, C., Smithies, H.R., Spaggiari, C.V., Wingate, M.T.D., 2015a. Madura Province: isotopes and crustal evolution, in: Spaggiari, C.V., Smithies, H.R. (Eds.), Eucla basement stratigraphic drilling results release workshop: extended abstracts. Geological Survey of Western Australia, Record 2015/10, pp. 17–28.

Kirkland, C., Wingate, M.T.D., Spaggiari, C.V., 2012a. 182474: granite vein, Big Red prospect., Geochronology Record 1051. Geological Survey of Western Australia, p. 4.

Kirkland, C.L., Johnson, S.P., Smithies, R.H., Hollis, J.A., Wingate, M.T.D., Tyler, I.M., Hickman, A.H., Cliff, J.B., Tessalina, S., Belousova, E.A., Murphy, R.C., 2013a. Not-so-suspect terrane: Constraints on the crustal evolution of the Rudall Province. Precambrian Research 235, 131–149.

Kirkland, C.L., Smithies, R.H., Spaggiari, C.V., 2015b. Foreign contemporaries – Unravelling disparate isotopic signatures from Mesoproterozoic Central and Western Australia. Precambrian Research 265, 218–231.

Kirkland, C.L., Smithies, R.H., Woodhouse, A.J., Howard, H.M., Wingate, M.T.D., Belousova, E.A., Cliff, J.B., Murphy, R.C., Spaggiari, C.V., 2013b. Constraints and deception in the isotopic record; the crustal evolution of the west Musgrave Province, central Australia. Gondwana Research 23, 759–781.

Kirkland, C.L., Spaggiari, C.V., Pawley, M.J., Wingate, M.T.D., Smithies, R.H., Howard, H.M., Tyler, I.M., Belousova, E.A., Poujol, M., 2011. On the edge: U–Pb, Lu–Hf, and Sm–Nd data suggests reworking of the Yilgarn craton margin during formation of the Albany-Fraser Orogen. Precambrian Research 187, 223–247.

Kirkland, C.L., Wingate, M.T.D., Spaggiari, C.V., 2012b. 182485: migmatitic gneiss, Burkin Prospect, Geochronology Record 1140. Geological Survey of Western Australia, p. 4.

Kylander-Clark, A.R.C., Hacker, B.R., Cottle, J.M., 2013. Laser-ablation split-stream ICP petrochronology. Chemical Geology 345, 99–112.

Li, Z.X., Bogdanova, S.V., Collins, A.S., Davidson, A., De Waele, B., Ernst, R.E., Fitzsimons, I.C.W., Fuck, R.A., Gladkochub, D.P., Jacobs, J., Karlstrom, K.E., Lu, S., Natapov, L.M., Pease, V., Pisarevsky, S.A., Thrane, K., Vernikovsky, V., 2008. Assembly, configuration, and break-up history of Rodinia: A synthesis. Precambrian Research 160, 179–210.

Ludwig, 2003. Berkeley Geochronology Centre, Special Publication 4.

Möller, A., Post, N., Hensen, B., 2002. Crustal residence history and garnet Sm–Nd ages of high-grade metamorphic rocks from the Windmill Islands area, East Antarctica. Int J Earth Sci (Geol Rundsch) 91, 993–1004.

Morel, M.L.A., Nebel, O., Nebel-Jacobsen, Y.J., Miller, J.S., Vroon, P.Z., 2008. Hafnium isotope characterization of the GJ-1 zircon reference material by solution and laser-ablation MC-ICPMS. Chemical Geology 255, 231–235.

Morrissey, L., Payne, J.L., Kelsey, D.E., Hand, M., 2011. Grenvillian-aged reworking in the North Australian Craton, central Australia: Constraints from geochronology and modelled phase equilibria. Precambrian Research 191, 141–165.

Mücke, A., 2005. The Nigerian manganese-rich iron-formations and their host rocks—from sedimentation to metamorphism. Journal of African Earth Sciences 41, 407–436.

Paton, C., Hellstrom, J., Paul, B., Woodhead, J., Hergt, J., 2011. Iolite: Freeware for the visualisation and processing of mass spectrometric data. Journal of Analytical Atomic Spectrometry 26, 2508–2518.

Paton, C., Woodhead, J.D., Hellstrom, J.C., Hergt, J.M., Greig, A., Maas, R., 2010. Improved laser ablation U-Pb zircon geochronology through robust downhole fractionation correction. Geochemistry, Geophysics, Geosystems 11, 1–36.

Paul, E., Stüwe, K., Teasdale, J., Worley, B., 1995. Structural and metamorphic geology of the Windmill Islands, east Antarctica: Field evidence for repeated tectonothermal activity. Australian Journal of Earth Sciences 42, 453–469.

Payne, J.L., Hand, M., Barovich, K.M., Reid, A., Evans, D.A.D., 2009. Correlations and reconstruction models for the 2500-1500 Ma evolution of the Mawson Continent. Geological Society, London, Special Publications 323, 319–355.

Payne, J.L., McInerney, D.J., Barovich, K.M., Kirkland, C.L., Pearson, N.J., Hand, M., 2016. Strengths and limitations of zircon Lu-Hf and O isotopes in modelling crustal growth. Lithos 248–251, 175–192.

Post, N.J., 2000. Unravelling Gondwana fragments: An integrated structural, isotopic and petrographic investigation of the Windmill Islands, Antarctica. PhD Thesis, University of New South Wales, p. 213.

Post, N.J., Hensen, B.J., Kinny, P.D., 1997. Two Metamorphic Episodes during a 1340–1180 Convergent Tectonic Event in the Windmill Islands, East Antarctica, in: Ricci, C.A. (Ed.), The Antarctic Region: Geological Evolution and Processes. Terra Antartica Publication, Sienna, pp. 157–161.

Reid, A.J., Jagodzinski, E.A., Fraser, G.L., Pawley, M.J., 2014. SHRIMP U–Pb zircon age constraints on the tectonics of the Neoarchean to early Paleoproterozoic transition within the Mulgathing Complex, Gawler Craton, South Australia. Precambrian Research 250, 27–49.

Sambridge, M.S., Compston, W., 1994. Mixture modeling of multi-component data sets with application to ion-probe zircon ages. Earth and Planetary Science Letters 128, 373–390.

Scherer, E., Münker, C., Mezger, K., 2001. Calibration of the Lutetium-Hafnium Clock. Science 293, 683–687.

Segal, I., Halicz, L., Platzner, I.T., 2003. Accurate isotope ratio measurements of ytterbium by multiple collection inductively coupled plasma mass spectrometry applying erbium and hafnium in an improved double external normalization procedure. Journal of Analytical Atomic Spectrometry 18, 1217–1223.

Slack, J.F., Palmer, M.R., Stevens, B.P.J., Barnes, R.G., 1993. Origin and significance of tourmaline-rich rocks in the Broken Hill District, Australia. Economic Geology 88, 505–541.

Sláma, J., Košler, J., Condon, D.J., Crowley, J.L., Gerdes, A., Hanchar, J.M., Horstwood, M.S.A., Morris, G.A., Nasdala, L., Norberg, N., Schaltegger, U., Schoene, B., Tubrett, M.N., Whitehouse, M.J., 2008. Plešovice zircon - A new natural reference material for U–Pb and Hf isotopic microanalysis. Chemical Geology 249, 1–35.

Smithies, H., Howard, H.M., Evins, P., Kirkland, C., Kelsey, D.E., Hand, M., Wingate, M.T.D., Collins, A.S., Belousova, E.A., Allchurch, S., 2010. Geochemistry, geochronology, and petrogenesis of Mesoproterozoic felsic rocks in the west Musgrave Province, central Australia, and implications for the Mesoproterozoic tectonic evolution of the region. Geological Society of Western Australia, Perth, p. 82.

Smithies, H.R., Spaggiari, C.V., Kirkland, C., 2015a. Building the crust of the Albany–Fraser Orogen: constraints from granite geochemistry. Geological Survey of Western Australia, Report 150, p. 49.

Smithies, H.R., Spaggiari, C.V., Kirkland, C., Howard, H., Maier, W.D., 2013. Petrogenesis of gabbros of the Mesoproterozoic Fraser Zone: constraints on the tectonic evolution of the Albany–Fraser Orogen. Geological Survey of Western Australia, Record 2013/5, p. 29.

Smithies, H.R., Spaggiari, C.V., Kirkland, C., Wingate, M.T.D., England, R.N., 2015b. Madura Province: geochemistry and petrogenesis, in: Spaggiari, C.V., Smithies, H.R. (Eds.), Eucla basement stratigraphic drilling results release workshop: extended abstracts. Geological Survey of Western Australia, Record 2015/10, pp. 17–28.

Smits, R.G., Collins, W.J., Hand, M., Dutch, R., Payne, J.L., 2014. A Proterozoic Wilson cycle identified by Hf isotopes in central Australia: Implications for the assembly of Proterozoic Australia and Rodinia. Geology, 42, 231–234.

Spaggiari, C.V., Kirkland, C., Smith, J., Wingate, M.T.D., 2014. Tectonic links between Proterozoic sedimentary cycles, basin formation and magmatism in the Albany–Fraser Orogen, Western Australia, Record 2014/6. Geological Survey of Western Australia, p. 165.

Spaggiari, C.V., Kirkland, C.L., Smithies, R.H., Wingate, M.T.D., Belousova, E.A., 2015. Transformation of an Archean craton margin during Proterozoic basin formation and magmatism: The Albany–Fraser Orogen, Western Australia. Precambrian Research 266, 440–466.

Spaggiari, C.V., Tyler, I.M., 2014. Albany–Fraser Orogen seismic and magnetotelluric (MT) workshop 2014: extended abstracts. Geological Survey of Western Australia.

Vervoort, J.D., Patchett, P.J., Blichert-Toft, J., Albarède, F., 1999. Relationships between Lu–Hf and Sm–Nd isotopic systems in the global sedimentary system. Earth and Planetary Science Letters 168, 79–99.

Vervoort, J.D., Patchett, P.J., Söderlund, U., Baker, M., 2004. Isotopic composition of Yb and the determination of Lu concentrations and Lu/Hf ratios by isotope dilution using MC–ICPMS. Geochemistry, Geophysics, Geosystems 5, Q11002.

Waddell, P.-J.A., Timms, N.E., Spaggiari, C.V., Kirkland, C.L., Wingate, M.T.D., 2015. Analysis of the Ragged Basin, Western Australia: Insights into syn-orogenic basin evolution within the Albany–Fraser Orogen. Precambrian Research 261, 166–187.

Wade, B., Kelsey, D.E., Hand, M., Barovich, K.M., 2008. The Musgrave Province: Stitching north, west and south Australia. Precambrian Research 166, 370–386.

Wade, B.P., Barovich, K.M., Hand, M., Scrimgeour, I., Close, D.F., 2006. Evidence for Early Mesoproterozoic Arc Magmatism in the Musgrave Block, Central Australia: Implications for Proterozoic Crustal Growth and Tectonic Reconstructions of Australia. Journal of Geology 114, 43–63.

Walsh, A.K., Kelsey, D.E., Kirkland, C.L., Hand, M., Smithies, R.H., Clark, C., Howard, H.M., 2015. $P-T-t$ evolution of a large, long-lived, ultrahigh-temperature Grenvillian belt in central Australia. Gondwana Research 28, 531–564.

Wiedenbeck, M., AllÉ, P., Corfu, F., Griffin, W.L., Meier, M., Oberli, F., Quadt, A.V., Roddick, J.C., Spiegel, W., 1995. Three natural zircon standards for U–Th–Pb, Lu–Hf, Trace Element and REE analyses. Geostandards Newsletter 19, 1–23.

Wong, B.L., Morrissey, L.J., Hand, M., Fields, C.E., Kelsey, D.E., 2015. Grenvillian-aged reworking of late Paleoproterozoic crust of the southern North Australian Craton, central Australia: Implications for the assembly of Mesoproterozoic Australia. Precambrian Research 270, 100–123.

Woodhead, J., Hergt, J., Shelley, M., Eggins, S., Kemp, R., 2004. Zircon Hf-isotope analysis with an excimer laser, depth profiling, ablation of complex geometries, and concomitant age estimation. Chemical Geology 209, 121–135.

Woodhead, J.D., Hergt, J.M., 2005. A Preliminary Appraisal of Seven Natural Zircon Reference Materials for In Situ Hf Isotope Determination. Geostandards and Geoanalytical Research 29, 183–195.

Wyche, S., Kirkland, C.L., Riganti, A., Pawley, M.J., Belousova, E., Wingate, M.T.D., 2012. Isotopic constraints on stratigraphy in the central and eastern Yilgarn Craton, Western Australia. Australian Journal of Earth Sciences 59, 657–670.

Zhang, S.-H., Zhao, Y., Liu, X.-C., Liu, Y.-S., Hou, K.-J., Li, C.-F., Ye, H., 2012. U–Pb geochronology and geochemistry of the bedrocks and moraine sediments from the Windmill Islands: Implications for Proterozoic evolution of East Antarctica. Precambrian Research 206–207, 52–71.

			Isotopic ratios						Age estimates							
Spot name	Th/U	$^{204}Pb/^{206}Pb$	$^{207}Pb/^{206}Pb$	±1σ	$^{206}Pb/^{238}U$	±1σ	$^{207}Pb/^{235}U$	±1σ	$^{207}Pb/^{206}Pb$	±1σ	$^{206}Pb/^{238}U$	±1σ	$^{207}Pb/^{235}U$	±1σ	Conc. (%)	Zircon interpretation
WI07: Cameron Island																
WI07-1	1.48	4.00E-04	0.08787	0.00110	2.84700	0.07300	0.23630	0.00400	1367	19	1367	21	1379	24	99	D
WI07-2	1.94	5.26E-04	0.08691	0.00120	2.80200	0.06500	0.23500	0.00310	1355	17	1360	16	1358	26	100	D
WI07-4	0.03	4.17E-05	0.08490	0.00093	2.75500	0.05300	0.23620	0.00220	1343	14	1367	11	1313	21	104	M
WI07-5	0.89	4.35E-05	0.11007	0.00120	4.65700	0.08900	0.30750	0.00260	1759	16	1728	13	1801	20	96	D
WI07-6	0.74	2.38E-04	0.08830	0.00100	2.91000	0.05700	0.23940	0.00210	1384	15	1383	11	1389	22	100	D
WI07-7	0.52	1.45E-04	0.14640	0.00320	9.59000	0.44000	0.47400	0.01300	2388	44	2498	58	2300	38	109	D
WI07-8	0.20	3.40E-04	0.11736	0.00150	4.80500	0.11000	0.29700	0.00340	1785	18	1676	17	1916	22	87	D
WI07-9	0.86	6.67E-05	0.16275	0.00180	10.38000	0.21000	0.46170	0.00450	2469	19	2447	20	2484	19	98	D
WI07-10	0.81	3.85E-04	0.11134	0.00120	4.94300	0.09600	0.32100	0.00290	1809	16	1794	14	1821	20	99	D
WI07-11	0.81	1.67E-04	0.10915	0.00120	4.77600	0.10000	0.31600	0.00460	1780	18	1770	23	1785	20	99	D
WI07-12	0.64	3.85E-04	0.08914	0.00100	2.90300	0.06200	0.23500	0.00290	1382	16	1360	15	1407	22	97	D
WI07-13	0.07	2.17E-03	0.10140	0.00230	4.73000	0.22000	0.33800	0.01600	1765	40	1870	77	1646	41	114	D
WI07-14	0.88	4.55E-04	0.10685	0.00130	4.41200	0.09100	0.29760	0.00350	1714	17	1679	17	1746	22	96	D
WI07-15	0.01	1.11E-05	0.08199	0.00090	2.73400	0.05400	0.24010	0.00240	1338	15	1387	12	1245	22	111	M
WI07-16	2.33	5.56E-05	0.08769	0.00098	2.94400	0.05800	0.24100	0.00260	1393	15	1392	13	1376	21	101	D
WI07-17	0.02	8.20E-05	0.08254	0.00092	2.74300	0.05800	0.23860	0.00280	1340	16	1379	15	1258	22	110	M
WI07-18	1.12	0.00E+00	0.08601	0.00110	2.85200	0.05900	0.23800	0.00260	1369	16	1376	13	1338	24	103	D/ MD
WI07-19	0.41	6.67E-05	0.08576	0.00098	3.05000	0.06300	0.25530	0.00300	1420	16	1465	15	1333	22	110	D
WI07-20	0.49	8.55E-05	0.10842	0.00120	4.97500	0.10000	0.32920	0.00350	1817	19	1834	17	1773	20	103	D
WI07-21	0.74	7.69E-05	0.22620	0.00250	18.92000	0.38000	0.59970	0.00670	3039	21	3028	27	3025	17	100	D
WI07-22	0.69	0.00E+00	0.10866	0.00120	4.69700	0.09200	0.31020	0.00310	1766	17	1741	15	1777	21	98	D
WI07-24	0.36	8.62E-05	0.18388	0.00210	12.72000	0.29000	0.49660	0.00700	2658	22	2599	30	2688	19	97	D
WI07-25	1.35	0.00E+00	0.10569	0.00130	4.33300	0.09200	0.29530	0.00360	1699	17	1668	18	1726	22	97	D
WI07-26	0.14	2.46E-04	0.08637	0.00095	2.64600	0.05100	0.22080	0.00210	1313	14	1286	11	1346	21	96	M
WI07-27	0.80	3.33E-03	0.08896	0.00100	3.05100	0.06900	0.24680	0.00310	1420	17	1422	16	1403	22	101	D
WI07-28	0.10	4.98E-04	0.09105	0.00120	3.27100	0.11000	0.26010	0.00810	1472	25	1489	41	1447	25	103	D
WI07-29	0.47	1.03E-04	0.09805	0.00110	3.70200	0.07500	0.27320	0.00270	1571	16	1557	14	1587	21	98	D
WI07-30	0.65	4.76E-04	0.08739	0.00100	2.93200	0.06100	0.24320	0.00270	1390	16	1403	14	1369	22	103	D
WI07-31	0.66	8.33E-04	0.09024	0.00100	3.11000	0.06300	0.25010	0.00260	1435	16	1439	14	1430	22	101	D
WI07-32	0.84	6.25E-04	0.09801	0.00130	3.69700	0.08300	0.27420	0.00400	1570	18	1562	20	1586	25	98	D
WI07-33	1.05	2.00E-04	0.09291	0.00110	3.16600	0.06500	0.24830	0.00280	1449	16	1430	14	1486	22	96	D
WI07-34	0.64	1.11E-03	0.10690	0.00120	4.55600	0.09100	0.31070	0.00330	1741	17	1744	16	1747	21	100	D

			Isotopic ratios						Age estimates							
Spot name	Th/U	$^{204}Pb/^{206}Pb$	$^{207}Pb/^{206}Pb$	±1σ	$^{206}Pb/^{238}U$	±1σ	$^{207}Pb/^{235}U$	±1σ	$^{207}Pb/^{206}Pb$	±1σ	$^{206}Pb/^{238}U$	±1σ	$^{207}Pb/^{235}U$	±1σ	Conc. (%)	Zircon interpretation
WI07: Cameron Island (continued)																
WI07-35	0.01	5.00E-06	0.08413	0.00230	2.73500	0.06000	0.23760	0.00370	1337	16	1374	20	1295	48	106	M
WI07-36	1.32	2.08E-04	0.11093	0.00130	4.92000	0.14000	0.32350	0.00750	1803	23	1806	36	1814	21	100	D
WI07-37	0.02	1.11E-03	0.08518	0.00100	4.14000	0.19000	0.35500	0.01600	1655	39	1952	76	1319	23	148	D
WI07-39	0.02	7.81E-05	0.08419	0.00096	3.19100	0.06500	0.27660	0.00300	1455	16	1574	15	1297	22	121	D
WI07-40	0.62	1.35E-04	0.08744	0.00100	2.79900	0.05900	0.23340	0.00270	1355	16	1352	14	1370	22	99	D
WI07-41	1.24	8.93E-05	0.08793	0.00097	2.88200	0.05700	0.23880	0.00260	1377	15	1380	13	1381	21	100	D
WI07-42	1.00	1.18E-04	0.10940	0.00130	4.80400	0.10000	0.31970	0.00370	1785	17	1788	18	1789	21	100	D
WI07-43	0.03	1.49E-04	0.08496	0.00093	2.77100	0.05700	0.23750	0.00280	1348	15	1373	14	1315	21	104	M
WI07-44	0.77	0.00E+00	0.10884	0.00120	4.75400	0.09500	0.31790	0.00350	1777	17	1779	17	1780	20	100	D
WI07-45	0.01	5.00E-05	0.08320	0.00090	2.63300	0.05300	0.23020	0.00250	1310	15	1335	13	1274	21	105	M
WI07-46	0.79	4.76E-05	0.09139	0.00100	3.13000	0.06300	0.24900	0.00250	1440	16	1433	13	1455	21	99	D
WI07-47	0.54	1.89E-04	0.10998	0.00120	4.92100	0.09900	0.32520	0.00350	1805	17	1815	17	1799	20	101	D
WI07-48	0.70	0.00E+00	0.09836	0.00120	3.73500	0.08500	0.27620	0.00360	1578	18	1572	18	1593	22	99	D
WI07-49	0.69	0.00E+00	0.08772	0.00095	2.91600	0.06100	0.24200	0.00320	1386	16	1397	17	1376	21	102	D
WI07-50	1.24	1.75E-04	0.10934	0.00120	4.95000	0.11000	0.32840	0.00410	1810	18	1830	20	1788	20	102	D
WI07-51	0.27	4.35E-05	0.10755	0.00120	4.65800	0.09100	0.31400	0.00310	1760	16	1760	15	1758	20	100	D
WI07-52	0.17	7.30E-05	0.16980	0.00180	10.41000	0.24000	0.44590	0.00750	2474	24	2376	33	2556	18	93	D
WI07-53	0.10	1.69E-05	0.17513	0.00200	10.49000	0.23000	0.43380	0.00540	2478	20	2322	24	2607	19	89	D
WI07-54	0.80	3.33E-03	0.11056	0.00120	4.77800	0.09900	0.31270	0.00380	1781	17	1754	19	1808	20	97	D
WI07-55	1.57	5.00E-03	0.11124	0.00140	5.06500	0.11000	0.32950	0.00390	1829	19	1836	19	1819	23	101	D
WI07-56	0.22	0.00E+00	0.11052	0.00130	4.81500	0.10000	0.31530	0.00430	1787	18	1766	21	1808	21	98	D
WI07-57	1.51	0.00E+00	0.10896	0.00130	4.95900	0.11000	0.32870	0.00480	1812	19	1832	23	1782	22	103	D
WI07-59	0.32	2.50E-05	0.10804	0.00120	4.77200	0.09900	0.31850	0.00390	1780	17	1782	19	1766	21	101	D
WI07-61	0.01	2.63E-05	0.08528	0.00098	2.55500	0.05600	0.21580	0.00290	1287	16	1260	15	1322	22	95	M
WI07-62	0.85	1.16E-04	0.10570	0.00850	4.63000	0.39000	0.31530	0.00690	1752	58	1766	34	1726	110	102	D
WI07-65	0.66	5.56E-04	0.08708	0.00097	3.04700	0.06500	0.25210	0.00320	1419	16	1449	16	1362	21	106	D
WI07-68	0.52	1.30E-04	0.09865	0.00110	3.82900	0.08000	0.28010	0.00330	1599	17	1592	16	1599	21	100	D
WI07-69	0.43	4.76E-04	0.10185	0.00130	3.80100	0.13000	0.26970	0.00630	1592	24	1539	32	1658	23	93	D
WI07-70	0.51	9.01E-05	0.16882	0.00180	11.09000	0.27000	0.47450	0.00840	2529	23	2502	37	2546	18	98	D
WI07-71	0.38	1.43E-05	0.10980	0.00120	4.63800	0.10000	0.30530	0.00400	1755	18	1717	20	1796	20	96	D
WI07-72	0.25	5.88E-05	0.08540	0.00096	2.65500	0.05500	0.22490	0.00250	1316	15	1308	13	1325	22	99	M
WI07-73	0.43	6.33E-05	0.09903	0.00110	3.83200	0.07700	0.28050	0.00290	1599	16	1594	15	1606	20	99	D

			Isotopic ratios						Age estimates							
Spot name	Th/U	$^{204}Pb/^{206}Pb$	$^{207}Pb/^{206}Pb$	±1σ	$^{206}Pb/^{238}U$	±1σ	$^{207}Pb/^{235}U$	±1σ	$^{207}Pb/^{206}Pb$	±1σ	$^{206}Pb/^{238}U$	±1σ	$^{207}Pb/^{235}U$	±1σ	Conc. (%)	Zircon interpretation
WI07: Cameron Island (continued)																
WI07-74	0.66	1.96E-04	0.09807	0.00120	3.96800	0.09700	0.29330	0.00460	1626	20	1657	23	1588	22	104	D
WI07-75	0.31	1.12E-04	0.16675	0.00200	9.85000	0.21000	0.42770	0.00450	2387	19	2240	20	2525	19	89	D
WI07-77	0.67	4.55E-04	0.09869	0.00120	3.78500	0.07600	0.27820	0.00250	1589	16	1582	12	1599	23	99	D
WI07-78	0.10	3.23E-05	0.17784	0.00190	11.36000	0.22000	0.46360	0.00440	2553	18	2455	19	2633	18	93	D
WI07-79	0.48	7.14E-05	0.08885	0.00160	2.84200	0.06700	0.23220	0.00240	1366	17	1346	12	1401	32	96	D
WI07-80	0.03	0.00E+00	0.08468	0.00095	2.61700	0.05500	0.22420	0.00240	1302	15	1303	13	1308	22	100	M
WI07-81	0.02	7.43E-04	0.09007	0.00110	2.82900	0.05800	0.22790	0.00270	1363	15	1323	14	1427	23	93	D
WI07-82	0.38	1.54E-04	0.16729	0.00200	11.19000	0.24000	0.48450	0.00640	2538	20	2546	28	2530	20	101	D
WI07-83	1.20	3.03E-04	0.10501	0.00120	4.33000	0.08800	0.29830	0.00290	1699	17	1683	14	1714	21	98	D
WI07-86	1.17	0.00E+00	0.10779	0.00140	4.66500	0.10000	0.31280	0.00340	1760	18	1754	17	1762	23	100	D
WI07-87	0.45	7.35E-04	0.10847	0.00150	4.26800	0.09000	0.28440	0.00410	1687	17	1613	20	1773	25	91	D
WI07-89	0.76	1.56E-04	0.10903	0.00120	4.88500	0.09800	0.32330	0.00360	1799	17	1805	18	1783	20	101	D
WI07-90	0.53	2.63E-04	0.10747	0.00120	4.75100	0.10000	0.31860	0.00420	1776	18	1783	21	1757	20	101	D
WI07-91	0.40	1.43E-03	0.11235	0.00130	5.34200	0.11000	0.34300	0.00380	1875	18	1901	18	1838	21	103	D
WI07-92	1.41	1.52E-04	0.08665	0.00097	2.88100	0.05600	0.24000	0.00220	1377	15	1386	11	1353	22	103	D
WI07-93	2.04	2.33E-03	0.10920	0.00200	4.92000	0.16000	0.32500	0.00690	1802	27	1813	34	1783	34	102	D
WI07-94	0.54	1.04E-04	0.08716	0.00097	2.85200	0.05600	0.23690	0.00250	1371	15	1370	13	1364	23	100	D
WI07-95	0.04	2.50E-05	0.08314	0.00091	2.75900	0.05300	0.23990	0.00210	1344	14	1386	11	1272	21	109	M
WI40: Mitchell Peninsula																
WI40-1	0.15	1.79E-05	0.09269	0.00110	2.98500	0.10000	0.23380	0.00320	1404	26	1354	16	1482	22	91	D
WI40-2	1.06	8.33E-05	0.11108	0.00130	5.15000	0.17000	0.33560	0.00410	1844	28	1866	20	1817	21	103	D
WI40-3	0.17	1.72E-04	0.07933	0.00099	2.12500	0.07100	0.19456	0.00200	1157	23	1146	11	1180	25	97	M
WI40-4	0.04	4.76E-04	0.07979	0.00092	2.34800	0.07700	0.21383	0.00220	1227	23	1249	12	1192	23	105	M
WI40-5	0.05	6.25E-04	0.08138	0.00120	2.36000	0.08000	0.21113	0.00230	1231	24	1235	12	1230	28	100	M
WI40-7	0.05	7.19E-04	0.08495	0.00120	2.61300	0.09000	0.22500	0.00260	1306	25	1308	14	1313	28	100	M
WI40-8	0.06	9.09E-05	0.08903	0.00098	2.82800	0.09300	0.23240	0.00270	1363	25	1347	14	1405	21	96	D
WI40-10	0.03	7.69E-05	0.08684	0.00100	2.68500	0.09400	0.22600	0.00310	1324	26	1313	16	1357	23	97	M
WI40-11	0.04	1.11E-03	0.08266	0.00100	2.24700	0.07400	0.19873	0.00210	1196	23	1169	11	1261	24	93	M
WI40-12	0.05	0.00E+00	0.08037	0.00110	2.25500	0.07700	0.20514	0.00210	1198	24	1203	11	1209	26	99	M
WI40-15	1.13	5.88E-04	0.09181	0.00120	2.96700	0.11000	0.23620	0.00460	1398	28	1366	24	1463	24	93	D
WI40-16	0.31	0.00E+00	0.09124	0.00100	3.00500	0.10000	0.24070	0.00310	1409	26	1390	16	1452	22	96	D
WI40-17	0.17	5.26E-04	0.08102	0.00110	2.28000	0.08400	0.20500	0.00340	1199	25	1198	18	1222	27	98	M

			Isotopic ratios						Age estimates							
Spot name	Th/U	$^{204}Pb/^{206}Pb$	$^{207}Pb/^{206}Pb$	±1σ	$^{206}Pb/^{238}U$	±1σ	$^{207}Pb/^{235}U$	±1σ	$^{207}Pb/^{206}Pb$	±1σ	$^{206}Pb/^{238}U$	±1σ	$^{207}Pb/^{235}U$	±1σ	Conc. (%)	Zircon interpretation
WI40: Mitchell Peninsula (continued)																
WI40-18	0.04	9.62E-05	0.08089	0.00093	2.66700	0.09500	0.23990	0.00430	1319	26	1386	22	1219	23	114	M
WI40-19	0.01	4.17E-05	0.08283	0.00091	2.55300	0.08700	0.22400	0.00320	1287	25	1303	17	1265	22	103	M
WI40-20	0.57	0.00E+00	0.10909	0.00130	4.60300	0.16000	0.30690	0.00430	1749	29	1725	21	1784	21	97	D
WI40-21	0.25	2.27E-04	0.07921	0.00091	2.20800	0.07700	0.20240	0.00330	1183	24	1188	18	1177	23	101	M
WI40-22	0.45	1.18E-04	0.08671	0.00100	2.78200	0.09400	0.23280	0.00300	1351	25	1349	16	1354	22	100	D/ MD
WI40-23	0.10	4.35E-04	0.08053	0.00110	2.26200	0.07900	0.20370	0.00270	1200	24	1195	14	1209	26	99	M
WI40-24	0.06	2.22E-04	0.08070	0.00093	2.13100	0.07300	0.19160	0.00280	1158	24	1130	15	1214	23	93	M
WI40-25	0.92	1.25E-05	0.10046	0.00110	3.75500	0.13000	0.27080	0.00430	1583	28	1545	22	1633	20	95	D
WI40-26	0.06	7.14E-04	0.08106	0.00099	2.19400	0.07400	0.19670	0.00270	1179	24	1157	15	1222	24	95	M
WI40-29	0.20	2.38E-04	0.08230	0.00100	2.42100	0.08200	0.21360	0.00300	1249	24	1248	16	1252	25	100	M
WI40-30	0.01	5.88E-05	0.08468	0.00095	2.66700	0.08900	0.22810	0.00290	1319	25	1325	15	1308	22	101	M
WI40-31	0.04	4.35E-04	0.08415	0.00140	2.73100	0.09800	0.23440	0.00360	1336	26	1358	19	1296	31	105	M
WI40-32	0.45	1.67E-03	0.08217	0.00140	2.37900	0.09500	0.20930	0.00360	1235	28	1225	19	1249	31	98	M
WI40-33	0.05	1.11E-05	0.08019	0.00095	2.22000	0.07600	0.20060	0.00270	1187	24	1179	15	1201	23	98	M
WI40-34	0.36	1.43E-05	0.08389	0.00160	2.41400	0.09300	0.20820	0.00280	1246	27	1219	15	1289	36	95	M
WI40-35	0.77	5.35E-04	0.08200	0.00170	2.29900	0.09000	0.20290	0.00290	1211	27	1191	16	1244	38	96	M
WI40-36	0.08	3.85E-05	0.10893	0.00120	4.70400	0.16000	0.31320	0.00420	1768	29	1756	20	1782	20	99	D
WI40-18	0.04	9.62E-05	0.08089	0.00093	2.66700	0.09500	0.23990	0.00430	1319	26	1386	22	1219	23	114	M
WI40-37	0.63	7.41E-05	0.08771	0.00096	2.82300	0.10000	0.23340	0.00410	1361	27	1352	22	1376	21	98	D
WI40-38	0.64	1.85E-04	0.08343	0.00160	2.40800	0.09100	0.20900	0.00280	1245	26	1223	15	1279	35	96	M
WI40-39	0.04	1.25E-05	0.07984	0.00091	2.23100	0.07700	0.20270	0.00300	1190	24	1190	16	1193	22	100	M
WI40-40	0.07	1.04E-04	0.08066	0.00091	2.33700	0.07900	0.21010	0.00300	1223	24	1229	16	1213	22	101	M
WI40-41	0.01	4.35E-05	0.08488	0.00095	2.57400	0.08900	0.22030	0.00330	1293	25	1284	17	1313	22	98	M
WI40-42	1.69	1.25E-03	0.25148	0.00280	22.00000	0.76000	0.63790	0.01000	3186	37	3180	40	3194	17	100	D
WI40-44	1.04	6.67E-05	0.11039	0.00120	4.76100	0.16000	0.31370	0.00420	1778	28	1759	20	1806	20	97	D
WI40-45	0.11	4.76E-04	0.08575	0.00110	2.26300	0.08100	0.19230	0.00300	1200	25	1134	16	1332	25	85	M
WI40-46	0.06	0.00E+00	0.08035	0.00093	2.19900	0.07400	0.19940	0.00260	1181	24	1172	14	1205	23	97	M
WI40-47	0.05	1.25E-05	0.08008	0.00090	2.23200	0.07600	0.20280	0.00290	1191	24	1190	15	1199	22	99	M
WI40-49	0.03	3.45E-04	0.08076	0.00110	2.22000	0.07900	0.20050	0.00320	1187	25	1178	17	1215	26	97	M
WI40-51	0.36	8.40E-04	0.08350	0.00180	2.39200	0.09700	0.20770	0.00300	1239	28	1216	16	1279	39	95	M
WI40-52	0.05	2.22E-04	0.08157	0.00099	2.07800	0.08200	0.18550	0.00410	1141	27	1097	22	1235	23	89	M
WI40-53	0.72	6.67E-04	0.08238	0.00140	2.33200	0.08800	0.20620	0.00350	1221	26	1208	19	1253	32	96	M

			Isotopic ratios						Age estimates							
Spot name	Th/U	$^{204}Pb/^{206}Pb$	$^{207}Pb/^{206}Pb$	±1σ	$^{206}Pb/^{238}U$	±1σ	$^{207}Pb/^{235}U$	±1σ	$^{207}Pb/^{206}Pb$	±1σ	$^{206}Pb/^{238}U$	±1σ	$^{207}Pb/^{235}U$	±1σ	Conc. (%)	Zircon interpretation
WI40: Mitchell Peninsula (continued)																
WI40-54	0.92	4.35E-05	0.11018	0.00120	4.80000	0.16000	0.31720	0.00400	1785	28	1776	20	1802	20	99	D
WI40-55	1.53	6.67E-04	0.10682	0.00140	4.52600	0.16000	0.30860	0.00530	1735	30	1733	26	1745	23	99	D
WI40-56	0.12	0.00E+00	0.08037	0.00100	2.33200	0.08400	0.21100	0.00320	1221	25	1234	17	1206	24	102	M
WI40-57	0.36	1.49E-04	0.12907	0.00160	5.77000	0.23000	0.32530	0.00690	1940	34	1815	34	2085	21	87	D
WI40-58	1.03	3.23E-04	0.09186	0.00110	3.07200	0.11000	0.24330	0.00350	1425	26	1404	18	1464	22	96	D
WI40-59	0.01	6.21E-05	0.08338	0.00093	2.71300	0.09300	0.23630	0.00340	1332	25	1368	18	1278	22	107	M
WI40-60	0.68	4.76E-04	0.08706	0.00110	3.17700	0.11000	0.26540	0.00430	1451	27	1517	22	1362	23	111	D
WI40-61	0.02	1.35E-04	0.07951	0.00091	2.15700	0.07400	0.19730	0.00280	1167	24	1161	15	1185	23	98	M
WI40-63	0.14	5.88E-05	0.10688	0.00120	4.56600	0.15000	0.31050	0.00410	1743	28	1743	20	1747	21	100	D
WI40-65	0.99	1.25E-04	0.08912	0.00100	3.11700	0.11000	0.25440	0.00440	1436	27	1461	26	1407	22	104	D
WI40-67	0.88	0.00E+00	0.11549	0.00130	5.36600	0.19000	0.33810	0.00550	1879	30	1877	26	1887	21	99	D
WI40-68	0.07	8.26E-05	0.08153	0.00120	2.43500	0.09400	0.21680	0.00350	1252	27	1265	18	1234	28	103	M
WI40-70	0.06	1.27E-04	0.08157	0.00097	2.26300	0.08100	0.20140	0.00300	1197	25	1181	16	1235	23	96	M
WI40-71	0.51	3.11E-04	0.09115	0.00100	2.92500	0.11000	0.23320	0.00420	1388	27	1351	22	1450	22	93	D
WI40-72	0.17	1.79E-05	0.11054	0.00120	4.82000	0.18000	0.31710	0.00640	1788	31	1775	31	1808	20	98	D
WI40-73	0.06	3.57E-05	0.09014	0.00110	2.86700	0.11000	0.23180	0.00400	1373	28	1344	21	1429	22	94	D
WI40-74	0.07	5.26E-05	0.08265	0.00099	2.36200	0.08400	0.20760	0.00330	1230	25	1216	18	1261	23	96	M
WI40-75	0.01	1.02E-04	0.08118	0.00088	2.52400	0.08500	0.22570	0.00290	1279	25	1312	15	1226	21	107	M
WI40-76	0.26	6.45E-05	0.12225	0.00140	6.05300	0.21000	0.36020	0.00450	1983	30	1983	21	1989	20	100	D
WI40-77	0.11	2.13E-04	0.08261	0.00110	2.42400	0.08200	0.21290	0.00280	1250	24	1244	15	1260	25	99	M
WI40-78	0.05	7.14E-05	0.08753	0.00110	2.83400	0.11000	0.23500	0.00480	1363	30	1360	25	1372	24	99	D
WI40-79	0.37	9.09E-04	0.08380	0.00210	2.31300	0.09900	0.19990	0.00280	1216	31	1174	15	1285	46	91	M
WI40-80	0.19	1.67E-03	0.08249	0.00160	2.24000	0.13000	0.19740	0.00870	1192	42	1161	47	1256	37	92	M
WI40-81	0.06	6.94E-05	0.10216	0.00120	3.79800	0.13000	0.27080	0.00420	1592	28	1544	21	1664	22	93	D
WI40-82	0.98	5.26E-05	0.10686	0.00120	4.44700	0.16000	0.30240	0.00450	1721	29	1703	22	1746	21	98	D
WI40-83	0.01	2.50E-05	0.08240	0.00090	2.44100	0.08400	0.21530	0.00320	1254	25	1257	17	1255	21	100	M
WI40-86	0.35	8.33E-05	0.10977	0.00120	4.96600	0.18000	0.32920	0.00690	1813	32	1834	33	1796	20	102	D
WI40-87	0.05	2.00E-04	0.08148	0.00100	2.34700	0.08300	0.20950	0.00320	1226	25	1226	17	1232	24	100	M
WI40-88	0.06	4.00E-04	0.08135	0.00150	2.48500	0.09200	0.22200	0.00280	1267	28	1292	15	1229	33	105	M
WI40-89	0.51	6.67E-05	0.10942	0.00120	4.87400	0.18000	0.32420	0.00650	1796	31	1810	32	1790	20	101	D
WI40-90	0.02	1.00E-03	0.08101	0.00097	2.26200	0.08300	0.20330	0.00370	1200	26	1193	20	1221	23	98	M

			Isotopic ratios						Age estimates							
Spot name	Th/U	$^{204}Pb/^{206}Pb$	$^{207}Pb/^{206}Pb$	±1σ	$^{206}Pb/^{238}U$	±1σ	$^{207}Pb/^{235}U$	±1σ	$^{207}Pb/^{206}Pb$	±1σ	$^{206}Pb/^{238}U$	±1σ	$^{207}Pb/^{235}U$	±1σ	Conc. (%)	Zircon interpretation
WI89: Robinson Ridge (continued)																
WI89-1	0.51	5.26E-04	0.08380	0.00130	2.27600	0.04300	0.19650	0.00180	1205	13	1156	10	1287	31	90	M
WI89-2	0.30	1.35E-04	0.08790	0.00140	2.84000	0.15000	0.23180	0.00880	1359	40	1342	46	1377	30	97	D
WI89-3	0.28	1.08E-04	0.12860	0.00200	6.18000	0.25000	0.34430	0.00890	1995	36	1906	43	2077	27	92	D
WI89-4	0.16	9.09E-04	0.08349	0.00077	2.38300	0.03700	0.20500	0.00170	1237	11	1202	9	1280	18	94	M
WI89-5	0.22	1.00E-03	0.08420	0.00150	2.26200	0.05900	0.19280	0.00200	1200	18	1137	11	1296	34	88	M
WI89-6	0.16	3.91E-04	0.08396	0.00110	2.27300	0.04100	0.19450	0.00200	1204	13	1146	11	1291	25	89	M
WI89-7	0.79	1.96E-04	0.08867	0.00088	2.89500	0.04600	0.23460	0.00230	1380	12	1359	12	1397	21	97	D
WI89-10	0.35	3.85E-04	0.08320	0.00260	2.31500	0.09900	0.20120	0.00250	1217	30	1182	14	1272	52	93	M
WI89-9	0.07	4.76E-04	0.08024	0.00078	2.17800	0.03300	0.19600	0.00150	1174	11	1154	8	1202	19	96	M
WI89-11	0.51	1.67E-03	0.09280	0.00180	2.78400	0.07300	0.21730	0.00210	1351	19	1268	11	1483	34	85	D
WI89-12	0.22	1.00E-04	0.09769	0.00110	3.41200	0.05600	0.25350	0.00220	1507	13	1457	11	1580	21	92	D
WI89-14	0.05	3.33E-04	0.07993	0.00110	2.32700	0.04100	0.21177	0.00150	1221	13	1238	8	1195	25	104	M
WI89-15	0.63	2.27E-04	0.08967	0.00082	2.98500	0.04500	0.24290	0.00210	1405	12	1401	11	1418	17	99	D
WI89-16	0.55	1.00E-02	0.08106	0.00110	2.24000	0.04400	0.20140	0.00210	1193	14	1183	11	1221	27	97	M
WI89-17	0.13	3.33E-03	0.08094	0.00092	2.14000	0.03600	0.19330	0.00170	1162	12	1139	9	1219	22	93	M
WI89-18	0.44	0.00E+00	0.07961	0.00110	2.18300	0.03900	0.19980	0.00210	1175	13	1174	11	1186	27	99	M
WI89-19	0.63	1.25E-05	0.09865	0.00096	3.59300	0.05300	0.26520	0.00290	1549	12	1516	15	1599	18	95	D
WI89-20	0.06	0.00E+00	0.08072	0.00096	2.32800	0.04000	0.20970	0.00150	1221	12	1227	8	1214	23	101	M
WI89-21	0.33	1.45E-04	0.08946	0.00110	2.77200	0.04400	0.22520	0.00160	1348	12	1309	9	1413	23	93	D
WI89-22	0.23	4.44E-04	0.09497	0.00083	2.82400	0.04700	0.21590	0.00230	1362	12	1260	12	1527	16	83	D
WI89-23	0.81	0.00E+00	0.09217	0.00086	3.15100	0.04600	0.24850	0.00200	1445	11	1431	11	1470	18	97	D
WI89-24	0.53	3.13E-03	0.09120	0.00450	2.72500	0.17000	0.21630	0.00280	1335	39	1262	15	1450	75	87	D
WI89-25	0.10	0.00E+00	0.10776	0.00140	4.32400	0.07100	0.28980	0.00280	1698	13	1640	14	1762	23	93	D
WI89-26	0.03	1.75E-04	0.08127	0.00085	2.26700	0.05400	0.20190	0.00390	1201	17	1185	21	1227	20	97	M
WI89-27	0.62	4.35E-04	0.08591	0.00097	2.56000	0.06500	0.21580	0.00400	1288	18	1259	21	1335	22	94	D
WI89-28	0.34	3.33E-04	0.08406	0.00180	2.76400	0.09100	0.23790	0.00480	1345	23	1375	25	1293	42	106	M
WI89-29	0.90	0.00E+00	0.10052	0.00140	3.67300	0.07500	0.26440	0.00380	1565	16	1512	19	1634	25	93	D
WI89-30	0.64	6.67E-04	0.08824	0.00077	2.82200	0.06300	0.23180	0.00410	1360	17	1344	21	1387	17	97	D
WI89-31	0.47	1.75E-04	0.10438	0.00093	4.25100	0.09300	0.29490	0.00540	1683	18	1665	27	1703	16	98	D
WI89-32	0.79	4.35E-04	0.08888	0.00130	2.95000	0.12000	0.24020	0.00680	1394	29	1387	35	1401	27	99	D
WI89-33	0.45	2.38E-04	0.08607	0.00092	2.59400	0.06100	0.21880	0.00420	1302	17	1283	22	1340	20	96	D
WI89-34	0.40	5.56E-04	0.08270	0.00150	2.31000	0.06400	0.20290	0.00330	1215	19	1191	18	1261	35	94	M

			Isotopic ratios						Age estimates							
Spot name	Th/U	$^{204}Pb/^{206}Pb$	$^{207}Pb/^{206}Pb$	±1σ	$^{206}Pb/^{238}U$	±1σ	$^{207}Pb/^{235}U$	±1σ	$^{207}Pb/^{206}Pb$	±1σ	$^{206}Pb/^{238}U$	±1σ	$^{207}Pb/^{235}U$	±1σ	Conc. (%)	Zircon interpretation
WI89: Robinson Ridge																
WI89-35	0.38	5.00E-05	0.09387	0.00089	3.16000	0.06700	0.24490	0.00400	1447	16	1412	21	1505	18	94	D
WI89-36	0.91	1.52E-04	0.11593	0.00099	5.20000	0.14000	0.32610	0.00700	1850	22	1819	34	1894	15	96	D
WI89-38	0.17	1.43E-03	0.07956	0.00078	2.11400	0.04700	0.19380	0.00350	1153	15	1142	19	1186	19	96	M
WI89-39	0.09	9.09E-04	0.07907	0.00081	2.13500	0.04200	0.19700	0.00270	1160	13	1159	15	1173	20	99	M
WI89-40	0.18	3.70E-05	0.08484	0.00088	2.54900	0.06000	0.21880	0.00390	1285	17	1275	20	1311	20	97	M
WI89-42	0.10	2.94E-04	0.08104	0.00100	2.22500	0.05500	0.20010	0.00340	1188	17	1176	18	1222	24	96	M
WI89-43	0.07	1.00E-03	0.08081	0.00100	2.20200	0.05500	0.19840	0.00320	1181	17	1167	17	1216	25	96	M
WI89-44	0.04	3.57E-04	0.07926	0.00093	2.14800	0.04100	0.19720	0.00270	1164	15	1160	14	1178	22	98	M
WI89-45	0.08	0.00E+00	0.07970	0.00076	2.15900	0.04300	0.19710	0.00310	1167	14	1159	17	1189	19	97	M
WI89-47	0.30	0.00E+00	0.07933	0.00200	2.19000	0.06800	0.20090	0.00310	1177	20	1180	17	1179	45	100	M
WI89-48	0.94	9.17E-05	0.09637	0.00079	3.33400	0.08000	0.25110	0.00460	1488	19	1444	24	1555	15	93	D
WI89-49	0.72	1.11E-06	0.11099	0.00100	4.86100	0.12000	0.31790	0.00670	1794	21	1779	33	1816	16	98	D
WI89-50	0.85	1.09E-03	0.08700	0.00220	2.41300	0.07500	0.20120	0.00340	1246	21	1182	18	1359	45	87	M
WI89-51	0.43	1.16E-03	0.08550	0.00240	2.43700	0.10000	0.20680	0.00360	1253	27	1212	19	1327	48	91	M
WI89-52	0.57	1.82E-04	0.08931	0.00100	3.03300	0.06500	0.24660	0.00390	1416	16	1421	20	1411	21	101	D
WI89-53	0.81	1.89E-04	0.08880	0.00093	2.89500	0.06200	0.23700	0.00390	1380	16	1371	20	1399	20	98	D/MD
WI89-54	0.67	2.52E-04	0.10753	0.00095	5.26800	0.09100	0.35640	0.00460	1863	15	1965	22	1758	16	112	D
WI89-55	0.88	1.61E-03	0.08600	0.00310	2.37600	0.12000	0.20060	0.00400	1234	33	1178	21	1335	60	88	M
WI89-56	0.23	2.27E-04	0.08250	0.00100	2.29100	0.05800	0.20200	0.00350	1209	17	1186	19	1257	26	94	M
WI89-57	0.42	1.52E-04	0.10653	0.00090	4.35000	0.11000	0.29670	0.00640	1702	22	1674	32	1741	15	96	D
WI89-59	0.26	3.45E-04	0.09615	0.00110	3.43000	0.08100	0.25910	0.00440	1510	18	1485	23	1550	23	96	D
WI89-60	0.36	1.15E-04	0.10310	0.00120	3.90100	0.10000	0.27430	0.00490	1613	20	1562	25	1681	21	93	D
WI89-61	0.11	4.17E-04	0.08033	0.00120	2.29600	0.05300	0.20730	0.00240	1211	16	1214	13	1205	28	101	M
WI89-62	0.54	2.13E-03	0.08660	0.00590	2.44000	0.23000	0.20370	0.00480	1254	58	1195	25	1351	100	88	M
WI89-63	0.10	5.56E-04	0.08240	0.00100	2.20300	0.05000	0.19410	0.00300	1181	16	1143	16	1254	22	91	M
WI89-65	0.49	6.71E-04	0.08290	0.00250	2.34700	0.08900	0.20390	0.00320	1225	25	1196	17	1264	52	95	M
WI89-67	0.17	3.33E-04	0.08181	0.00150	2.43200	0.06200	0.21440	0.00320	1252	19	1252	17	1240	33	101	M
WI89-68	0.11	2.86E-04	0.08296	0.00089	2.25300	0.04700	0.19590	0.00310	1197	15	1153	17	1268	21	91	M
WI89-69	0.08	0.00E+00	0.08057	0.00110	2.31500	0.04900	0.20730	0.00330	1217	15	1214	17	1211	26	100	M
WI89-70	0.38	1.11E-03	0.08357	0.00260	2.53900	0.11000	0.21900	0.00300	1283	27	1276	16	1282	51	100	M
WI89-71	0.77	9.09E-05	0.09628	0.00084	3.47900	0.07200	0.26050	0.00420	1522	16	1492	21	1553	16	96	D
WI89-73	0.35	1.02E-03	0.08748	0.00220	2.42400	0.08800	0.19950	0.00430	1249	27	1172	23	1370	44	86	M

			Isotopic ratios						Age estimates							
Spot name	Th/U	$^{204}Pb/^{206}Pb$	$^{207}Pb/^{206}Pb$	±1σ	$^{206}Pb/^{238}U$	±1σ	$^{207}Pb/^{235}U$	±1σ	$^{207}Pb/^{206}Pb$	±1σ	$^{206}Pb/^{238}U$	±1σ	$^{207}Pb/^{235}U$	±1σ	Conc. (%)	Zircon interpretation
WI89: Robinson Ridge (continued)																
WI89-74	0.30	6.49E-04	0.08720	0.00110	2.41800	0.06600	0.19980	0.00450	1246	20	1174	24	1364	23	86	M
WI89-75	0.05	2.56E-04	0.08021	0.00099	2.26000	0.04900	0.20300	0.00320	1200	15	1191	17	1202	24	99	M
WI89-76	0.97	1.00E-03	0.08290	0.00320	2.39300	0.12000	0.20720	0.00310	1239	31	1214	17	1264	65	96	M
WI89-77	0.63	6.25E-04	0.10429	0.00097	4.10000	0.11000	0.28340	0.00630	1652	22	1608	32	1702	17	94	D
WI89-78	0.55	1.43E-03	0.10138	0.00100	4.14000	0.13000	0.29440	0.00810	1661	26	1663	40	1649	19	101	D
WI89-79	0.01	1.00E-04	0.07921	0.00086	2.39900	0.05200	0.21820	0.00320	1242	15	1272	17	1177	21	108	M
WI89-80	0.22	0.00E+00	0.08221	0.00160	2.34300	0.06500	0.20580	0.00350	1225	19	1206	18	1249	36	97	M
WI89-81	0.09	4.00E-04	0.08282	0.00110	2.62500	0.07400	0.22950	0.00580	1306	21	1331	30	1264	25	105	M
WI89-82	0.14	4.78E-04	0.08249	0.00150	2.27500	0.08300	0.19960	0.00500	1204	24	1173	27	1257	32	93	M
WI89-83	0.43	5.56E-05	0.08491	0.00084	2.54600	0.07000	0.21740	0.00570	1284	22	1268	30	1316	19	96	M
WI68: Herring Island																
WI68-1	0.70	3.33E-05	0.08651	0.00039	2.81300	0.04200	0.23600	0.00410	1359	11	1366	21	1349	9	101	D
WI68-2	0.49	5.00E-04	0.08731	0.00074	2.76000	0.05000	0.22940	0.00410	1344	13	1332	21	1366	16	97	D
WI68-3	1.06	4.55E-04	0.09560	0.00110	5.38000	0.45000	0.40700	0.03200	1868	72	2190	140	1539	22	142	D
WI68-4	0.03	6.06E-05	0.08051	0.00029	2.64700	0.04800	0.23840	0.00460	1314	13	1378	24	1209	7	114	M
WI68-5	0.58	2.63E-04	0.08776	0.00066	2.86500	0.04700	0.23690	0.00400	1373	12	1371	21	1377	14	100	D
WI68-6	0.72	1.67E-03	0.08638	0.00058	2.71000	0.04600	0.22770	0.00400	1331	13	1322	21	1346	13	98	D
WI68-7	0.38	0.00E+00	0.08530	0.00049	2.70200	0.06900	0.22980	0.00560	1328	19	1333	29	1322	11	101	D/MD
WI68-8	0.01	9.80E-05	0.07981	0.00033	2.38200	0.03500	0.21680	0.00370	1237	11	1265	20	1192	8	106	M
WI68-11	0.35	0.00E+00	0.08772	0.00033	2.84400	0.04300	0.23500	0.00400	1367	11	1361	21	1376	7	99	D
WI68-12	0.75	1.67E-04	0.08631	0.00043	2.70500	0.04500	0.22750	0.00430	1330	12	1321	23	1345	10	98	D
WI68-13	0.64	3.23E-04	0.08826	0.00056	2.89000	0.04500	0.23770	0.00410	1379	12	1374	22	1388	12	99	D
WI68-14	0.26	1.04E-04	0.08604	0.00043	2.70500	0.04400	0.22810	0.00400	1330	12	1324	21	1341	9	99	D
WI68-15	0.17	1.96E-04	0.08432	0.00044	2.63200	0.04000	0.22640	0.00390	1310	11	1316	21	1300	10	101	M
WI68-16	0.45	2.86E-04	0.08900	0.00065	2.92000	0.04700	0.23800	0.00410	1387	12	1377	22	1403	14	98	D
WI68-17	0.50	2.27E-04	0.08549	0.00042	2.61700	0.04600	0.22190	0.00400	1305	13	1292	21	1326	10	97	D
WI68-18	0.55	1.11E-04	0.08793	0.00048	2.90300	0.04400	0.23950	0.00440	1383	11	1384	23	1381	11	100	D
WI68-19	0.60	4.00E-04	0.09315	0.00043	3.14500	0.04800	0.24500	0.00410	1444	12	1413	21	1491	9	95	D
WI68-20	0.44	3.03E-04	0.08646	0.00061	2.79900	0.05400	0.23500	0.00450	1355	14	1360	23	1348	14	101	D
WI68-21	0.01	5.88E-05	0.08022	0.00028	2.30100	0.03400	0.20805	0.00350	1213	10	1218	18	1202	7	101	M
WI68-22	0.57	1.67E-04	0.08859	0.00040	3.24400	0.06600	0.26550	0.00590	1467	16	1518	30	1395	9	109	M
WI68-23	0.46	0.00E+00	0.08571	0.00068	2.67600	0.08700	0.22810	0.00680	1325	26	1324	35	1331	15	99	D/MD

			Isotopic ratios						Age estimates							
Spot name	Th/U	$^{204}Pb/^{206}Pb$	$^{207}Pb/^{206}Pb$	±1σ	$^{206}Pb/^{238}U$	±1σ	$^{207}Pb/^{235}U$	±1σ	$^{207}Pb/^{206}Pb$	±1σ	$^{206}Pb/^{238}U$	±1σ	$^{207}Pb/^{235}U$	±1σ	Conc. (%)	Zircon interpretation
WI68: Herring Island (continued)																
WI68-25	0.90	2.17E-04	0.08759	0.00047	3.38300	0.05900	0.28000	0.00520	1500	14	1591	26	1373	10	116	D
WI68-26	0.01	6.06E-05	0.08005	0.00031	2.48300	0.04100	0.22470	0.00410	1267	12	1307	22	1198	8	109	M
WI68-27	0.93	1.11E-05	0.08746	0.00029	2.80200	0.04200	0.23260	0.00390	1356	11	1348	21	1371	6	98	D
WI68-28	0.80	1.20E-04	0.08927	0.00041	3.04000	0.04500	0.24710	0.00420	1418	11	1423	22	1410	9	101	D
WI68-29	0.74	1.30E-04	0.08781	0.00040	2.85100	0.04200	0.23547	0.00390	1369	11	1363	21	1378	9	99	D
WI68-30	0.62	1.39E-04	0.08899	0.00051	2.81100	0.04700	0.22880	0.00400	1358	13	1328	21	1404	11	95	D
WI68-31	0.34	1.25E-05	0.08821	0.00028	3.11400	0.04500	0.25590	0.00430	1436	11	1469	22	1387	6	106	D
WI68-32	1.01	2.78E-04	0.08804	0.00050	2.87300	0.04500	0.23682	0.00400	1375	12	1370	21	1383	11	99	D
WI68-33	0.39	4.76E-04	0.08736	0.00068	2.90900	0.04900	0.24210	0.00430	1386	14	1397	22	1368	15	102	D
WI68-34	0.01	1.74E-04	0.08075	0.00031	2.32200	0.03500	0.20850	0.00350	1219	11	1221	19	1215	8	100	M
WI68-35	0.48	9.09E-05	0.08818	0.00067	2.93500	0.04900	0.24190	0.00510	1391	13	1397	26	1386	15	101	D
WI68-36	0.09	4.17E-05	0.08216	0.00021	2.40700	0.03900	0.21240	0.00380	1245	11	1242	20	1249	5	99	M
WI68-37	0.02	8.85E-05	0.08133	0.00024	2.39240	0.03500	0.21316	0.00350	1240	10	1246	19	1229	6	101	M
WI68-38	0.73	5.88E-04	0.08836	0.00055	2.85000	0.04300	0.23400	0.00400	1369	11	1355	21	1390	12	98	D
WI68-39	0.20	5.00E-05	0.08762	0.00026	2.80800	0.04600	0.23230	0.00430	1357	12	1347	22	1374	6	98	D
WI68-40	0.01	5.00E-05	0.08058	0.00025	2.37100	0.03600	0.21330	0.00360	1234	11	1246	19	1211	6	103	M
WI68-41	0.95	2.27E-04	0.08960	0.00041	2.93200	0.04600	0.23740	0.00420	1390	12	1373	22	1417	9	97	D
WI68-42	0.16	0.00E+00	0.10598	0.00035	4.42300	0.06500	0.30265	0.00500	1717	12	1704	25	1731	6	98	D
WI68-43	0.58	1.25E-05	0.08641	0.00041	2.72800	0.04200	0.22906	0.00390	1336	11	1330	20	1347	9	99	D
WI68-44	0.01	8.20E-05	0.07952	0.00028	2.50500	0.03800	0.22830	0.00400	1274	11	1326	21	1185	7	112	M
WI68-45	0.66	9.26E-05	0.08735	0.00041	3.17400	0.05400	0.26360	0.00470	1451	13	1508	24	1368	9	110	D
WI68-46	0.70	2.50E-04	0.08949	0.00064	3.03200	0.05300	0.24550	0.00440	1416	13	1415	23	1414	14	100	D
WI68-47	0.13	0.00E+00	0.08109	0.00048	2.43700	0.03700	0.21738	0.00360	1254	11	1268	19	1223	12	104	M
WI68-48	0.42	0.00E+00	0.08889	0.00034	2.91400	0.04500	0.23740	0.00400	1386	12	1373	21	1402	7	98	D
WI68-49	0.01	2.22E-04	0.07991	0.00043	2.46400	0.03900	0.22340	0.00400	1261	11	1300	21	1195	11	109	M
WI68-50	0.70	1.85E-04	0.08712	0.00040	2.78200	0.04200	0.23160	0.00390	1351	11	1343	20	1363	9	99	D
WI68-51	0.87	9.52E-05	0.08823	0.00030	2.86700	0.04300	0.23569	0.00400	1373	11	1364	21	1387	7	98	D
WI68-52	0.60	1.89E-04	0.08977	0.00056	2.95300	0.04800	0.23860	0.00420	1395	12	1380	22	1420	12	97	D
WI68-53	0.01	5.62E-05	0.07991	0.00030	2.47100	0.03900	0.22400	0.00420	1263	11	1303	22	1195	7	109	M
WI68-54	0.26	2.00E-05	0.08922	0.00032	2.90400	0.04900	0.23600	0.00460	1383	13	1366	24	1409	7	97	D
WI68-55	0.95	7.41E-05	0.08914	0.00025	2.92900	0.04400	0.23840	0.00410	1389	11	1378	21	1407	5	98	D
WI68-57	0.99	0.00E+00	0.08801	0.00035	2.85400	0.04300	0.23520	0.00400	1370	11	1361	21	1383	8	98	D

			Isotopic ratios						Age estimates							
Spot name	Th/U	$^{204}Pb/^{206}Pb$	$^{207}Pb/^{206}Pb$	±1σ	$^{206}Pb/^{238}U$	±1σ	$^{207}Pb/^{235}U$	±1σ	$^{207}Pb/^{206}Pb$	±1σ	$^{206}Pb/^{238}U$	±1σ	$^{207}Pb/^{235}U$	±1σ	Conc. (%)	Zircon interpretation
WI68: Herring Island (continued)																
WI68-58	0.05	1.06E-04	0.08197	0.00047	2.42100	0.03700	0.21416	0.00360	1249	11	1251	19	1244	11	101	M
WI68-59	0.17	4.85E-05	0.08674	0.00018	2.63600	0.03900	0.22057	0.00370	1311	11	1285	20	1355	4	95	D
WI68-60	1.09	3.57E-04	0.08838	0.00036	3.10800	0.04800	0.25470	0.00430	1435	12	1463	22	1391	8	105	D
WI68-61	0.84	0.00E+00	0.08890	0.00043	2.92800	0.04400	0.23870	0.00400	1389	11	1380	21	1402	9	98	D
WI68-62	0.01	8.33E-05	0.08014	0.00039	2.52100	0.04200	0.22800	0.00410	1278	12	1324	22	1200	10	110	M
WI68-64	1.20	9.43E-05	0.08854	0.00025	2.85700	0.04100	0.23352	0.00390	1371	11	1353	20	1394	6	97	D
WI68-65	0.30	8.40E-05	0.11607	0.00057	4.51900	0.07500	0.28200	0.00490	1734	14	1602	25	1896	9	84	D
WI68-66	0.01	1.06E-04	0.08074	0.00026	2.29370	0.03300	0.20621	0.00340	1210	10	1209	18	1215	6	99	M
WI68-67	1.08	5.00E-05	0.10257	0.00034	3.90700	0.05800	0.27610	0.00470	1615	12	1571	24	1671	6	94	D
WI68-68	0.90	1.37E-04	0.08978	0.00043	2.91400	0.04400	0.23539	0.00390	1386	11	1363	21	1421	9	96	D
WI68-70	0.86	0.00E+00	0.08760	0.00058	2.81400	0.04600	0.23290	0.00400	1359	12	1350	21	1373	13	98	D
WI68-71	0.70	7.41E-05	0.08899	0.00028	2.95200	0.04400	0.24020	0.00410	1395	11	1388	21	1404	6	99	D
WI68-73	0.88	1.01E-04	0.08895	0.00054	2.90400	0.04600	0.23640	0.00400	1383	12	1368	21	1403	12	97	D
WI68-74	0.42	1.25E-05	0.08825	0.00033	2.89700	0.04600	0.23810	0.00420	1381	12	1377	22	1388	7	99	D
WI68-75	0.81	1.59E-04	0.08833	0.00059	3.08300	0.06000	0.25290	0.00490	1428	15	1454	25	1389	13	105	D
WI68-76	1.23	4.00E-05	0.08864	0.00031	2.93500	0.04400	0.24000	0.00410	1391	11	1387	21	1396	7	99	D
WI68-77	0.93	7.69E-05	0.08958	0.00028	2.94200	0.04500	0.23790	0.00410	1393	12	1376	21	1417	6	97	D
WI68-78	0.61	3.03E-04	0.08825	0.00056	2.87600	0.04900	0.23630	0.00430	1375	13	1367	22	1387	12	99	D
WI68-79	0.99	1.47E-04	0.08907	0.00051	2.75600	0.04300	0.22412	0.00380	1344	12	1304	20	1405	11	93	D
WI68-80	0.80	3.85E-05	0.08859	0.00068	2.90500	0.06100	0.23750	0.00490	1383	16	1374	26	1395	15	98	D
WI68-81	0.01	5.85E-05	0.07912	0.00028	2.29100	0.03400	0.20980	0.00360	1210	11	1228	19	1175	7	104	M
WI68-82	0.01	0.00E+00	0.07952	0.00038	2.32200	0.03700	0.21130	0.00370	1219	11	1236	19	1185	10	104	M
WI68-83	0.76	2.63E-04	0.08880	0.00041	2.88800	0.04400	0.23620	0.00410	1379	11	1367	21	1400	9	98	D
WI68-84	0.76	1.67E-05	0.08726	0.00030	2.76500	0.04100	0.22969	0.00390	1346	11	1333	20	1366	7	98	D
WI68-85	0.28	5.26E-05	0.08600	0.00031	2.70400	0.04100	0.22750	0.00390	1330	11	1322	20	1338	7	99	D
WI68-86	0.53	7.69E-05	0.08792	0.00038	2.91200	0.04700	0.24010	0.00430	1385	12	1387	22	1380	8	100	D
WI68-87	0.69	7.14E-04	0.08829	0.00060	2.87700	0.04700	0.23620	0.00420	1376	12	1367	22	1388	13	98	D
WI68-88	0.69	3.33E-05	0.08632	0.00047	2.62500	0.04100	0.22050	0.00370	1308	11	1285	20	1345	10	96	D
WI68-90	0.81	1.89E-04	0.08693	0.00047	2.79300	0.04300	0.23300	0.00400	1353	11	1350	21	1359	10	99	D
WI68-91	0.60	9.62E-05	0.08839	0.00035	2.85500	0.05200	0.23400	0.00460	1370	14	1355	24	1391	8	97	D
WI68-92	0.83	0.00E+00	0.08790	0.00030	2.96400	0.04400	0.24430	0.00410	1398	11	1409	21	1380	7	102	D
WI68-93	1.02	4.35E-04	0.10303	0.00036	4.12800	0.06700	0.29050	0.00520	1660	13	1644	26	1679	7	98	D

			Isotopic ratios						Age estimates							
Spot name	Th/U	$^{204}Pb/^{206}Pb$	$^{207}Pb/^{206}Pb$	±1σ	$^{206}Pb/^{238}U$	±1σ	$^{207}Pb/^{235}U$	±1σ	$^{207}Pb/^{206}Pb$	±1σ	$^{206}Pb/^{238}U$	±1σ	$^{207}Pb/^{235}U$	±1σ	Conc. (%)	Zircon interpretation
WI68: Herring Island (continued)																
WI68-94	0.83	1.15E-04	0.08612	0.00027	3.17700	0.05700	0.26710	0.00500	1451	14	1526	26	1341	6	114	D
WI68-95	0.67	2.94E-04	0.08824	0.00056	2.94400	0.05300	0.24180	0.00460	1393	14	1396	24	1387	12	101	D
WI68-96	0.93	5.26E-05	0.08862	0.00029	2.88200	0.04600	0.23550	0.00410	1377	12	1363	22	1396	6	98	D
WI68-97	0.03	7.52E-05	0.08060	0.00027	2.40600	0.03500	0.21680	0.00380	1245	11	1265	20	1212	7	104	M
WI68-98	0.68	1.39E-04	0.08813	0.00037	2.88900	0.04500	0.23790	0.00420	1379	12	1376	22	1385	8	99	D
WI68-99	0.63	4.27E-04	0.09080	0.00100	2.97200	0.05800	0.23700	0.00440	1400	15	1371	23	1442	21	95	D
WI68-101	0.24	0.00E+00	0.08604	0.00042	2.68000	0.06900	0.22540	0.00590	1322	19	1310	31	1339	10	98	M
WI43: Syn-D_1 orthogneiss, Clark Peninsula																
WI43-1	0.11	5.88E-05	0.08645	0.00068	2.69300	0.05300	0.22590	0.00340	1326	14	1313	18	1348	15	97	
WI43-2	0.71	8.33E-05	0.08479	0.00084	2.58600	0.04700	0.22160	0.00260	1296	14	1290	14	1310	19	98	
WI43-3	0.22	4.26E-05	0.08851	0.00070	2.65300	0.04500	0.21810	0.00260	1315	13	1272	14	1393	15	91	
WI43-6	0.26	1.23E-05	0.08705	0.00068	2.77500	0.05000	0.23240	0.00300	1349	14	1347	16	1362	15	99	
WI43-7	0.81	1.25E-05	0.08802	0.00079	2.90800	0.05600	0.24110	0.00350	1384	14	1392	18	1383	17	101	
WI43-9	0.26	7.69E-05	0.08752	0.00072	2.74900	0.05100	0.22880	0.00310	1341	14	1328	16	1372	16	97	
WI43-10	0.73	0.00E+00	0.08852	0.00071	2.93000	0.05100	0.24100	0.00300	1389	13	1392	15	1394	15	100	
WI43-12	0.20	1.25E-04	0.08804	0.00076	2.76000	0.05400	0.22820	0.00370	1344	15	1325	19	1383	17	96	
WI43-13	0.88	0.00E+00	0.08902	0.00085	2.96700	0.07300	0.24250	0.00490	1398	19	1399	25	1404	18	100	
WI43-14	0.16	3.85E-05	0.08749	0.00070	2.85400	0.04700	0.23690	0.00270	1368	11	1370	14	1371	15	100	
WI43-16	0.15	2.50E-05	0.08767	0.00073	2.88200	0.05400	0.23870	0.00370	1377	14	1380	19	1375	16	100	
WI43-19	0.20	2.63E-05	0.08761	0.00081	2.73400	0.05700	0.22620	0.00330	1337	15	1314	17	1374	17	96	
WI43-20	0.81	2.86E-04	0.09152	0.00077	2.92000	0.05600	0.23140	0.00350	1387	15	1341	18	1457	16	92	
WI43-21	0.74	7.69E-04	0.08769	0.00080	2.81900	0.05500	0.23280	0.00310	1360	14	1349	16	1375	18	98	
WI43-22	0.23	5.26E-05	0.08723	0.00100	2.77500	0.05500	0.23020	0.00380	1348	15	1335	20	1365	22	98	
WI43-23	0.77	2.01E-04	0.08740	0.00072	2.77400	0.08000	0.22950	0.00590	1348	22	1332	31	1369	16	97	
WI43-24	0.76	2.17E-04	0.08857	0.00080	2.96600	0.06600	0.24250	0.00430	1398	17	1399	23	1395	17	100	
WI43-25	0.64	0.00E+00	0.08788	0.00079	2.91500	0.06600	0.24010	0.00440	1385	17	1387	23	1380	17	101	
WI43-26	0.79	2.56E-04	0.08439	0.00079	2.60000	0.06100	0.22300	0.00430	1299	17	1297	23	1301	18	100	
WI43-27	0.35	0.00E+00	0.08505	0.00081	2.62600	0.06800	0.22350	0.00450	1307	19	1300	24	1316	18	99	
WI43-29	0.81	2.86E-04	0.08500	0.00075	2.57000	0.05000	0.21870	0.00300	1292	14	1275	16	1316	17	97	
WI43-30	0.77	1.64E-04	0.08620	0.00078	2.69100	0.05400	0.22560	0.00340	1325	15	1311	18	1342	17	98	
WI43-31	0.23	0.00E+00	0.08600	0.00071	2.70100	0.05000	0.22680	0.00310	1328	14	1317	16	1338	16	98	
WI43-34	0.72	2.04E-04	0.08526	0.00077	2.61700	0.05200	0.22160	0.00340	1305	15	1290	18	1321	17	98	

			Isotopic ratios						Age estimates						
Spot name	Th/U	$^{204}Pb/^{206}Pb$	$^{207}Pb/^{206}Pb$	±1σ	$^{206}Pb/^{238}U$	±1σ	$^{207}Pb/^{235}U$	±1σ	$^{207}Pb/^{206}Pb$	±1σ	$^{206}Pb/^{238}U$	±1σ	$^{207}Pb/^{235}U$	±1σ	Conc. (%)
WI43: Syn-D_1 orthogneiss (continued)															
WI43-35	0.69	0.00E+00	0.08820	0.00086	2.83000	0.06700	0.23120	0.00400	1362	17	1340	21	1386	19	97
WI43-38	0.67	1.06E-04	0.08769	0.00080	2.92300	0.06300	0.24110	0.00400	1387	16	1392	21	1375	18	101
WI43-40	0.56	7.69E-05	0.08549	0.00075	2.69500	0.05200	0.22840	0.00340	1326	14	1326	18	1326	17	100
WI43-41	0.61	1.32E-04	0.08560	0.00076	2.79600	0.06100	0.23740	0.00400	1354	16	1373	21	1329	17	103
WI43-42	1.33	8.20E-05	0.08885	0.00081	3.00000	0.05300	0.24590	0.00310	1407	13	1417	16	1401	17	101
WI43-45	0.24	1.15E-04	0.08639	0.00095	2.57000	0.06400	0.21730	0.00430	1290	18	1267	23	1347	20	94
WI17: M_2 granite, Mitchell Peninsula															
WI17-3	3.09	0.00E+00	0.08108	0.00130	2.35800	0.05300	0.21110	0.00290	1230	16	1234	15	1223	31	100
WI17-4	4.02	5.88E-04	0.08123	0.00130	2.33500	0.05600	0.20860	0.00330	1222	17	1221	18	1227	32	100
WI17-5	0.87	2.00E-04	0.08070	0.00120	2.52200	0.05200	0.22640	0.00270	1278	15	1315	14	1214	30	103
WI17-9	0.10	5.46E-05	0.08065	0.00120	2.26800	0.05000	0.20390	0.00270	1202	16	1196	14	1213	30	99
WI17-10	5.49	9.35E-05	0.08168	0.00130	2.32700	0.06000	0.20670	0.00360	1223	17	1211	19	1237	30	99
WI17-12	2.46	5.00E-04	0.08182	0.00130	2.37100	0.05800	0.21040	0.00350	1233	17	1230	19	1241	31	100
WI17-13	0.08	9.62E-05	0.08274	0.00130	2.27600	0.05400	0.20030	0.00300	1207	17	1177	16	1263	31	98
WI17-14	0.02	5.26E-05	0.08430	0.00140	2.39400	0.05800	0.20550	0.00330	1240	17	1205	18	1299	32	97
WI17-16	2.99	0.00E+00	0.08151	0.00130	2.37200	0.06000	0.21100	0.00390	1233	18	1234	21	1233	31	100
WI17-17	2.95	1.35E-04	0.08258	0.00140	2.31100	0.06200	0.20430	0.00370	1215	19	1198	20	1259	33	99
WI17-18	3.58	0.00E+00	0.08071	0.00130	2.30500	0.05200	0.20730	0.00300	1213	16	1214	16	1214	31	100
WI17-19	4.95	5.88E-04	0.08191	0.00140	2.35300	0.05600	0.20770	0.00290	1228	17	1216	15	1243	32	99
WI17-20	3.13	3.45E-04	0.08136	0.00140	2.33200	0.09100	0.20730	0.00590	1221	27	1214	31	1230	34	99
WI17-21	1.22	0.00E+00	0.08113	0.00130	2.63800	0.05900	0.23570	0.00310	1311	16	1364	16	1224	32	104
WI17-23	2.38	2.44E-04	0.08158	0.00140	2.39800	0.06300	0.21290	0.00380	1241	19	1244	20	1235	34	100
WI17-24	3.97	3.85E-04	0.08222	0.00140	2.39200	0.06300	0.21090	0.00410	1239	19	1234	22	1250	33	100
WI17-25	0.05	0.00E+00	0.08138	0.00130	2.31100	0.05400	0.20600	0.00320	1215	16	1207	17	1230	30	99
WI17-26	3.70	1.82E-04	0.08085	0.00130	2.29800	0.05600	0.20610	0.00340	1211	17	1208	18	1217	31	100
WI17-28	3.09	9.09E-04	0.08185	0.00130	2.41600	0.05600	0.21340	0.00340	1247	17	1247	18	1241	31	100
WI17-31	3.05	0.00E+00	0.08197	0.00130	2.35600	0.05400	0.20850	0.00310	1229	16	1221	17	1244	32	99
WI17-32	3.35	3.57E-04	0.08309	0.00140	2.40900	0.06200	0.21000	0.00350	1245	18	1228	18	1275	35	99
WI17-33	3.63	9.09E-05	0.08173	0.00130	2.30100	0.05300	0.20440	0.00300	1212	16	1199	16	1239	31	99
WI17-36	3.78	1.92E-04	0.08097	0.00130	2.35100	0.05700	0.21060	0.00350	1227	17	1232	19	1220	32	100
WI17-37	4.03	3.33E-04	0.08234	0.00140	2.54000	0.05400	0.22370	0.00280	1283	16	1301	15	1253	32	101
WI17-39	3.86	5.00E-03	0.08156	0.00130	2.36000	0.06000	0.20980	0.00360	1230	18	1227	19	1234	32	100

			Isotopic ratios						Age estimates						
Spot name	Th/U	$^{204}Pb/^{206}Pb$	$^{207}Pb/^{206}Pb$	±1σ	$^{206}Pb/^{238}U$	±1σ	$^{207}Pb/^{235}U$	±1σ	$^{207}Pb/^{206}Pb$	±1σ	$^{206}Pb/^{238}U$	±1σ	$^{207}Pb/^{235}U$	±1σ	Conc. (%)
WI17: M_2 granite (continued)															
WI17-40	3.07	5.00E-03	0.08096	0.00130	2.35100	0.06000	0.21040	0.00390	1227	18	1231	21	1220	32	100
WI17-41	0.04	1.25E-05	0.08271	0.00140	2.26700	0.05300	0.19860	0.00350	1202	17	1168	19	1262	32	97
WI17-42	3.76	5.95E-04	0.08493	0.00140	2.46000	0.06200	0.21010	0.00320	1260	18	1229	17	1313	33	98
WI17-43	2.67	1.25E-04	0.08283	0.00130	2.36100	0.06200	0.20650	0.00390	1230	18	1210	21	1265	32	98
WI17-44	3.09	7.94E-04	0.08749	0.00150	2.53100	0.06400	0.21010	0.00350	1280	18	1229	19	1371	32	96
WI17-45	3.53	3.23E-04	0.08376	0.00150	2.38900	0.05800	0.20630	0.00330	1239	17	1209	18	1286	34	98
WI17-46	0.05	6.49E-05	0.08173	0.00130	2.48600	0.05200	0.21960	0.00280	1268	15	1280	15	1239	31	101
WI17-47	5.14	5.59E-04	0.08540	0.00150	2.52100	0.06000	0.21310	0.00270	1278	17	1245	14	1324	34	97
WI84: Ardery Charnockite, Robinson Ridge															
WI84-1	1.49	3.33E-03	0.07905	0.00120	2.18800	0.04600	0.20070	0.00240	1177	15	1179	13	1173	31	100
WI84-2	1.74	0.00E+00	0.07924	0.00130	2.14300	0.04700	0.19550	0.00210	1163	15	1151	11	1178	32	99
WI84-3	2.02	5.00E-03	0.08187	0.00150	2.30800	0.05500	0.20380	0.00280	1214	17	1195	15	1242	35	98
WI84-4	1.68	2.50E-03	0.07881	0.00130	2.16600	0.04900	0.19880	0.00240	1170	16	1169	13	1167	33	100
WI84-5	1.84	2.50E-03	0.07989	0.00140	2.18400	0.05200	0.19690	0.00240	1175	17	1159	13	1193	35	99
WI84-6	1.52	8.33E-04	0.07912	0.00120	2.17300	0.04700	0.19920	0.00240	1174	14	1171	13	1175	31	100
WI84-7	1.62	0.00E+00	0.07975	0.00130	2.18200	0.04900	0.19820	0.00280	1175	16	1166	15	1190	33	99
WI84-8	1.68	3.85E-04	0.07936	0.00130	2.17200	0.05200	0.19850	0.00280	1172	17	1167	15	1180	33	100
WI84-9	1.65	0.00E+00	0.07906	0.00140	2.16800	0.04900	0.19900	0.00230	1170	16	1170	13	1173	34	100
WI84-11	1.49	0.00E+00	0.07858	0.00130	2.14300	0.05100	0.19740	0.00250	1162	16	1161	13	1164	35	100
WI84-12	1.72	0.00E+00	0.07848	0.00130	2.15900	0.04700	0.19950	0.00250	1168	15	1173	13	1158	34	100
WI84-13	1.65	4.00E-04	0.07899	0.00130	2.17900	0.04900	0.20000	0.00260	1174	16	1175	14	1171	32	100
WI84-14	1.56	0.00E+00	0.07905	0.00130	2.18000	0.04800	0.19990	0.00250	1174	15	1175	14	1173	31	100
WI84-15	0.77	6.67E-04	0.07952	0.00120	2.19300	0.04700	0.20030	0.00230	1179	15	1177	12	1185	31	100
WI84-16	1.26	7.69E-04	0.07925	0.00150	2.21600	0.05800	0.20280	0.00330	1185	18	1190	18	1177	37	100
WI84-17	1.42	1.00E-02	0.07950	0.00130	2.19000	0.05100	0.19980	0.00270	1177	16	1174	15	1184	33	100
WI84-19	0.69	5.00E-04	0.07910	0.00130	2.17600	0.04700	0.20000	0.00240	1173	15	1175	13	1174	32	100
WI84-20	0.89	1.67E-03	0.07903	0.00140	2.17200	0.05200	0.19910	0.00310	1171	17	1170	17	1172	35	100
WI84-21	0.64	0.00E+00	0.07896	0.00130	2.18500	0.04600	0.20060	0.00230	1176	15	1179	12	1170	32	100
WI84-22	1.43	1.00E-02	0.07922	0.00130	2.20000	0.05100	0.20150	0.00310	1181	16	1183	17	1177	31	100
WI84-23	1.37	3.33E-04	0.07931	0.00120	2.20100	0.04900	0.20120	0.00270	1181	16	1182	15	1180	31	100
WI84-24	1.43	3.33E-03	0.07873	0.00130	2.19300	0.05400	0.20130	0.00280	1178	17	1182	15	1164	34	100
WI84-25	0.85	1.25E-03	0.07911	0.00140	2.17500	0.05000	0.19950	0.00290	1173	16	1173	16	1173	35	100

			Isotopic ratios						Age estimates						
Spot name	Th/U	$^{204}Pb/^{206}Pb$	$^{207}Pb/^{206}Pb$	±1σ	$^{206}Pb/^{238}U$	±1σ	$^{207}Pb/^{235}U$	±1σ	$^{207}Pb/^{206}Pb$	±1σ	$^{206}Pb/^{238}U$	±1σ	$^{207}Pb/^{235}U$	±1σ	Conc. (%)
WI85: Ardery Charnockite, Robinson Ridge															
WI85-1	1.43	2.50E-04	0.07888	0.00120	2.15700	0.04700	0.19800	0.00280	1167	15	1164	15	1169	31	100
WI85-2	1.57	3.45E-04	0.07976	0.00120	2.17500	0.04700	0.19720	0.00250	1173	15	1160	13	1191	31	99
WI85-3	1.59	4.76E-04	0.07895	0.00140	2.14200	0.05100	0.19680	0.00270	1162	16	1158	15	1170	36	100
WI85-4	0.81	2.00E-04	0.07953	0.00120	2.17200	0.04900	0.19800	0.00280	1172	16	1164	15	1185	31	99
WI85-5	1.15	2.50E-02	0.07888	0.00150	2.14300	0.05100	0.19700	0.00260	1162	17	1159	14	1173	38	100
WI85-6	1.55	0.00E+00	0.07911	0.00130	2.15200	0.04800	0.19730	0.00280	1167	16	1161	15	1174	32	99
WI85-7	0.86	2.00E-04	0.07942	0.00120	2.15300	0.04700	0.19620	0.00260	1166	15	1155	14	1182	31	99
WI85-8	0.63	3.45E-04	0.07966	0.00120	2.19000	0.04700	0.19930	0.00250	1178	15	1171	14	1188	30	99
WI85-9	1.47	5.00E-04	0.07942	0.00130	2.16000	0.04700	0.19730	0.00250	1168	15	1161	13	1182	31	99
WI85-10	1.58	0.00E+00	0.07947	0.00130	2.15100	0.04900	0.19610	0.00250	1165	16	1154	13	1183	33	99
WI85-11	0.07	2.70E-04	0.07932	0.00120	2.15400	0.04500	0.19670	0.00240	1166	15	1158	13	1180	31	99
WI85-12	1.59	3.03E-04	0.07935	0.00130	2.18100	0.05100	0.19950	0.00270	1175	16	1172	15	1180	34	100
WI85-13	1.59	0.00E+00	0.07940	0.00130	2.18000	0.05500	0.19960	0.00300	1174	18	1173	16	1181	33	100
WI85-14	1.56	1.25E-03	0.07909	0.00130	2.17300	0.04900	0.19910	0.00270	1172	16	1170	14	1174	32	100
WI85-15	1.10	2.22E-04	0.07957	0.00130	2.19400	0.04700	0.19990	0.00270	1179	15	1175	14	1186	31	100
WI85-16	1.40	3.23E-04	0.07909	0.00140	2.15800	0.05000	0.19780	0.00260	1167	16	1163	14	1173	36	100
WI85-17	1.06	8.33E-04	0.07904	0.00140	2.18600	0.05900	0.20110	0.00360	1176	19	1181	19	1172	35	100
WI85-18	1.09	0.00E+00	0.07919	0.00130	2.16900	0.06000	0.19860	0.00400	1171	19	1168	22	1176	32	100
WI85-19	1.61	1.00E-02	0.07939	0.00130	2.15900	0.05900	0.19680	0.00370	1167	19	1158	20	1181	32	99
WI85-20	1.73	1.30E-03	0.07869	0.00140	2.14400	0.05100	0.19740	0.00280	1163	17	1161	15	1163	35	100
WI85-21	0.87	2.86E-03	0.07980	0.00160	2.18000	0.05900	0.19780	0.00330	1174	19	1163	18	1189	40	99
WI85-22	0.43	6.67E-05	0.08092	0.00130	2.19400	0.05500	0.19670	0.00370	1179	17	1157	20	1219	31	98
WI85-23	1.18	5.26E-04	0.07909	0.00130	2.18400	0.05400	0.20000	0.00310	1175	17	1175	17	1174	33	100
WI85-24	1.54	4.76E-04	0.07902	0.00130	2.18900	0.05000	0.20090	0.00280	1177	16	1180	15	1172	34	100
WI85-25	0.73	0.00E+00	0.07933	0.00130	2.18600	0.04900	0.19970	0.00290	1176	16	1174	16	1180	32	100
WI85-26	1.56	7.14E-04	0.07876	0.00140	2.17500	0.05600	0.20020	0.00310	1172	18	1176	17	1165	34	100
WI85-27	0.78	3.33E-04	0.07938	0.00130	2.18900	0.05500	0.19910	0.00340	1177	17	1171	18	1181	33	99
WI85-28	0.65	9.09E-04	0.07935	0.00130	2.18500	0.04800	0.19960	0.00270	1176	15	1173	14	1181	31	100
WI85-29	0.66	1.06E-04	0.07903	0.00120	2.18400	0.05000	0.20050	0.00290	1176	16	1178	15	1172	31	100

Spot number	Interpretation	Zircon description
WI07: Cameron Island		
WI07-1	D	Bright oscillatory zoned core
WI07-2	D	Bright homogenous core
WI07-4	M	Dark homogenous rim
WI07-5	D	Dark homogenous core (surrounded by thin bright zone, likely resorption)
WI07-6	D	Bright unzoned core
WI07-7	D	Bright weakly zoned overgrowth on dark resorbed core
WI07-8	D	Dark resorbed core
WI07-9	D	Dark homogenous core (surrounded by thin bright zone, likely resorption)
WI07-10	D	Dark weakly zoned core
WI07-11	D	Dark inner rim on dark core (surrounded by thin second dark rim)
WI07-12	D	Dark homogenous core
WI07-13	D	Bright rim
WI07-14	D	Core with swirly zoning
WI07-15	M	Dark homogenous rim
WI07-16	D	Dark homogenous core (surrounded by bright weakly zoned inner rim)
WI07-17	M	Rim of homogenous dark grain
WI07-18	D/ MD	Oscillatory zoned core
WI07-19	D	Dark homogenous core (surrounded by thin bright zone, likely resorption)
WI07-20	D	Bright weakly oscillatory zoned core
WI07-21	D	Dark, weakly zoned core
WI07-22	D	Weakly oscillatory zoned core
WI07-24	D	Weakly sector zoned core
WI07-25	D	Bright, patchy zoned core
WI07-26	M	Dark homogenous rim
WI07-27	D	Oscillatory zoned core
WI07-28	D	Bright inner rim (surrounded by second thin dark homogenous rim)
WI07-29	D	Dark weakly zoned core
WI07-30	D	Dark unzoned core (surrounded by thin bright zone- likely resorption)
WI07-31	D	Weak, diffusively zoned core
WI07-32	D	Bright weakly zoned core
WI07-33	D	Weakly oscillatory zoned core
WI07-34	D	Dark diffusively zoned core
WI07-35	M	Dark homogenous zone (discontinous rim)
WI07-36	D	Weakly zoned core, zoning truncated by dark homogenous rim
WI07-37	D	Bright inner rim
WI07-39	D	Bright inner rim
WI07-40	D	Core with swirly zoning
WI07-41	D	Dark unzoned core (surrounded by thin bright zone- likely resorption)
WI07-42	D	Weakly oscillatory zoned core
WI07-43	M	Rim of dark homogenous grain
WI07-44	D	Dark weakly sector zoned core
WI07-45	M	Dark homogenous rim
WI07-46	D	Weakly oscillatory zoned core
WI07-47	D	Dark weakly oscillatory zoned core
WI07-48	D	Bright weakly zoned core
WI07-49	D	Dark unzoned core (surrounded by thin bright zone- likely resorption)
WI07-51	D	Bright weakly oscillatory zoned overgrowth on dark resorbed core
WI07-52	D	Dark unzoned core (surrounded by thin bright zone- likely resorption)
WI07-53	D	Dark unzoned core (surrounded by thin bright zone- likely resorption)
WI07-54	D	Bright, patchy zoned core

Spot number	Interpretation	Zircon description
WI07: Cameron Island (continued)		
WI07-55	D	Bright weakly zoned overgrowth on oscillatory zoned core
WI07-56	D	Oscillatory zoned core
WI07-57	D	Bright weakly zoned overgrowth on oscillatory zoned core
WI07-59	D	Oscillatory zoned core
WI07-61	M	Homogenous dark grain
WI07-62	D	Dark oscillatory zoned core
WI07-65	D	Dark weakly zoned core
WI07-68	D	Bright rim
WI07-69	D	Bright oscillatory zoned core
WI07-70	D	Patchy zoned core
WI07-71	D	Oscillatory zoned core
WI07-72	M	Homogenous dark rim
WI07-73	D	Dark inner rim on weakly zoned core (surrounded by thin bright zone- likely resorption)
WI07-74	D	Bright weakly zoned core
WI07-75	D	Bright inner rim, surrounded by second homogenous dark rim
WI07-77	D	Bright weakly zoned core
WI07-78	D	Dark unzoned core
WI07-79	D	Patchy zoned core
WI07-80	M	Dark homogenous rim
WI07-81	D	Bright inner rim on dark core
WI07-82	D	Bright zoned core
WI07-83	D	Weakly zoned core
WI07-86	D	Bright unzoned core
WI07-87	D	Oscillatory zoned core
WI07-89	D	Dark unzoned core
WI07-90	D	Oscillatory zoned core
WI07-91	D	Oscillatory zoned core
WI07-92	D	Dark weakly oscillatory zoned core
WI07-93	D	Bright unzoned core
WI07-94	D	Dark resorbed core
WI07-95	M	Dark homogenous rim
WI40: Mitchell Peninsula		
WI40-1	D	Dark weakly oscillatory zoned core
WI40-2	D	Dark oscillatory zoned core
WI40-3	M	Diffusively zoned grain
WI40-4	M	Dark homogenous outer rim
WI40-5	M	Diffusively zoned core
WI40-7	M	Bright rim
WI40-8	D	Dark core
WI40-10	M	Bright rim
WI40-11	M	Dark weakly zoned core (likely resorbed, zoning poorly preserved)
WI40-12	M	Diffusively zoned core
WI40-15	D	Bright, weakly oscillatory zoned core (thin zone of very bright CL response around core)
WI40-16	D	Dark weakly oscillatory zoned core
WI40-17	M	Bright rim
WI40-18	M	Bright rim
WI40-19	M	Dark homogenous inner rim (likely resorbed core)
WI40-20	D	Bright oscillatory zoned core
WI40-21	M	Diffusively zoned grain
WI40-22	D/ MD	Dark oscillatory zoned core

Spot number	Interpretation	Zircon description
WI40: Mitchell Peninsula (continued)		
WI40-23	M	Dark homogenous outer rim
WI40-24	M	Diffusively zoned grain
WI40-25	D	Dark weakly oscillatory zoned core
WI40-26	M	Diffusively zoned grain
WI40-29	M	Dark homogenous outer rim
WI40-30	M	Dark homogenous inner rim (likely resorbed core)
WI40-31	M	Bright rim
WI40-32	M	Bright rim
WI40-33	M	Dark diffusively zoned core
WI40-34	M	Bright rim
WI40-35	M	Bright rim
WI40-36	D	Dark weakly zoned core
WI40-37	D	Dark weakly zoned core
WI40-38	M	Bright rim
WI40-39	M	Diffuse resorbed core
WI40-40	M	Dark homogenous discontinuous rim
WI40-41	M	Dark homogenous inner rim (likely resorbed core)
WI40-42	D	Bright zoned core
WI40-44	D	Dark oscillatory zoned core
WI40-45	M	Diffusively zoned core
WI40-46	M	Diffusively zoned grain
WI40-47	M	Diffusively zoned grain
WI40-49	M	Diffusively zoned core
WI40-51	M	Bright rim
WI40-52	M	Diffuse resorbed core
WI40-53	M	Bright rim
WI40-54	D	Dark oscillatory zoned core
WI40-55	D	Bright oscillatory zoned core
WI40-56	M	Homogenous dark grain
WI40-57	D	Bright oscillatory zoned core
WI40-58	D	Bright oscillatory zoned core
WI40-59	M	Dark homogenous inner rim (likely resorbed core)
WI40-60	D	Bright oscillatory zoned core
WI40-61	M	Diffusively zoned grain
WI40-63	D	Dark weakly oscillatory zoned core
WI40-65	D	Dark oscillatory zoned core
WI40-67	D	Bright oscillatory zoned core
WI40-68	M	Bright rim
WI40-70	M	Dark homogenous resorbed rim
WI40-71	D	Bright oscillatory zoned core
WI40-72	D	Dark homogenous core
WI40-73	D	Dark weakly oscillatory zoned core
WI40-74	M	Dark homogenous core (likely resorbed)
WI40-75	M	Dark homogenous outer rim
WI40-76	D	Dark core
WI40-77	M	Bright rim
WI40-78	D	Dark weakly oscillatory zoned core
WI40-79	M	Bright inner rim
WI40-80	M	Bright inner rim
WI40-81	D	Dark homogenous core

Spot number	Interpretation	Zircon description
WI40: Mitchell Peninsula (continued)		
WI40-82	D	Dark oscillatory zoned core
WI40-83	M	Dark homogenous core, likely resorbed
WI40-86	D	Dark oscillatory zoned core
WI40-87	M	Homogenous dark outer rim
WI40-88	M	Bright rim
WI40-89	D	Bright weakly oscillatory zoned core
WI40-90	M	Diffusively zoned grain
WI89: Robinson Ridge		
WI89-1	M	Bright inner rim
WI89-2	D	Dark weakly zoned core (may be reset core)- spot may straddle zones
WI89-3	D	Dark oscillatory zoned core
WI89-4	M	Dark weakly zoned core (likely resorbed core)
WI89-5	M	Bright inner rim
WI89-6	M	Homogenous dark grain
WI89-7	D	Dark oscillatory zoned core
WI89-10	M	Bright unzoned core
WI89-9	M	Homogenous dark grain
WI89-11	D	Bright inner rim
WI89-12	D	Dark oscillatory zoned core
WI89-14	M	Dark rim
WI89-15	D	Dark oscillatory zoned core
WI89-16	M	Bright unzoned core
WI89-17	M	Bright unzoned core
WI89-18	M	Bright unzoned core
WI89-19	D	Dark unzoned core
WI89-20	M	Dark rim
WI89-21	D	Dark oscillatory zoned core
WI89-22	D	Diffusively zoned core (likely partially reset core with small detrital relic)- spot may straddle zones
WI89-23	D	Dark unzoned core
WI89-24	D	Bright inner rim
WI89-25	D	Dark unzoned core
WI89-26	M	Homogenous dark grain
WI89-27	D	Dark oscillatory zoned core
WI89-28	M	Bright inner rim
WI89-29	D	Dark unzoned core
WI89-30	D	Dark oscillatory zoned core
WI89-31	D	Oscillatory zoned core
WI89-32	D	Bright oscillatory zoned core
WI89-33	D	Dark weakly oscillatory zoned core
WI89-34	M	Bright inner rim
WI89-35	D	Dark unzoned core
WI89-36	D	Oscillatory zoned core
WI89-38	M	Bright unzoned core
WI89-39	M	Homogenous dark grain
WI89-40	M	Weakly zoned core (likely partially resorbed core with small detrital relic)- spot may straddle zones
WI89-42	M	Dark rim
WI89-43	M	Homogenous dark grain
WI89-44	M	Homogenous dark grain
WI89-45	M	Homogenous dark grain
WI89-47	M	Bright inner rim

Spot number	Interpretation	Zircon description
WI89: Robinson Ridge (continued)		
WI89-53	D/MD	Dark oscillatory zoned core
WI89-54	D	Oscillatory zoned core
WI89-55	M	Bright inner rim
WI89-56	M	Bright diffusively zoned core
WI89-57	D	Dark oscillatory zoned core
WI89-59	D	Bright oscillatory zoned core
WI89-60	D	Oscillatory zoned core (with resorbed edges)
WI89-61	M	Dark rim
WI89-62	M	Bright unzoned core
WI89-63	M	Dark unzoned core (likely resorbed core)
WI89-65	M	Bright inner rim
WI89-67	M	Dark rim
WI89-68	M	Dark unzoned core (likely resorbed core)
WI89-69	M	Dark rim
WI89-70	M	Bright inner rim
WI89-71	D	Dark weakly zoned core
WI89-73	M	Bright inner rim
WI89-74	M	Bright unzoned core
WI89-75	M	Dark rim
WI89-76	M	Bright unzoned core
WI89-77	D	Oscillatory zoned core
WI89-78	D	Oscillatory zoned core
WI89-79	M	Dark rim
WI89-80	M	Dark unzoned core (likely resorbed core)
WI89-81	M	Dark rim
WI89-82	M	Bright inner rim
WI89-83	M	Dark weakly zoned core (likely resorbed core)
WI68: Herring Island		
WI68-1	D	Dark, partially oscillatory zoned core
WI68-2	D	Bright oscillatory zoned core
WI68-3	D	Small very bright zone overgrown by dark rim (spot likely to straddle zones)
WI68-4	M	Dark homogenous rim
WI68-5	D	Bright oscillatory zoned grain
WI68-6	D	Oscillatory zoned grain
WI68-7	D/MD	Bright oscillatory zoned grain
WI68-8	M	Dark homogenous rim
WI68-11	D	Dark weakly zoned grain
WI68-12	D	Bright oscillatory zoned core
WI68-13	D	Bright oscillatory zoned core
WI68-14	D	Bright oscillatory zoned core
WI68-15	M	Dark homogenous rim
WI68-16	D	Bright oscillatory zoned core
WI68-17	D	Bright oscillatory zoned core
WI68-18	D	Bright oscillatory zoned core
WI68-19	D	Bright oscillatory zoned grain
WI68-20	D	Bright homogenous core
WI68-21	M	Dark homogenous rim
WI68-22	M	Dark homogenous zone (resorbed zone)
WI68-23	D/MD	Bright oscillatory zoned core (embayed)
WI68-25	D	Oscillatory zoned rim

Spot number	Interpretation	Zircon description
WI68: Herring Island (continued)		
WI68-26	M	Dark homogenous rim
WI68-27	D	Bright oscillatory zoned core
WI68-28	D	Oscillatory zoned grain
WI68-29	D	Dark oscillatory zoned rim
WI68-30	D	Bright oscillatory zoned core
WI68-31	D	Dark weakly zoned rim
WI68-32	D	Bright oscillatory zoned core
WI68-33	D	Bright oscillatory zoned inner rim
WI68-34	M	Dark homogenous rim
WI68-35	D	Bright oscillatory zoned core
WI68-36	M	Dark homogenous rim
WI68-37	M	Dark homogenous rim
WI68-38	D	Bright fir-tree zoning
WI68-39	D	Bright oscillatory zoned core
WI68-40	M	Dark homogenous rim
WI68-41	D	Bright oscillatory zoned core
WI68-42	D	Bright oscillatory zoned core
WI68-43	D	Oscillatory zoned core
WI68-44	M	Dark homogenous rim
WI68-45	D	Bright oscillatory zoned overgrowth on bright core
WI68-46	D	Bright core
WI68-47	M	Dark homogenous rim
WI68-48	D	Bright oscillatory zoned core
WI68-49	M	Dark homogenous rim
WI68-50	D	Bright oscillatory zoned core
WI68-51	D	Dark oscillatory zoned core
WI68-52	D	Bright oscillatory zoned core
WI68-53	M	Dark homogenous rim
WI68-54	D	Dark oscillatory zoned core
WI68-55	D	Bright oscillatory zoned grain
WI68-57	D	Bright oscillatory zoned core
WI68-58	M	Dark homogenous rim
WI68-59	D	Dark weakly zoned core
WI68-60	D	Dark oscillatory zoned core
WI68-61	D	Bright oscillatory zoned core
WI68-62	M	Dark homogenous rim
WI68-64	D	Bright oscillatory zoned core
WI68-65	D	Bright oscillatory zoned core
WI68-66	M	Dark homogenous rim
WI68-67	D	Dark oscillatory zoned core
WI68-68	D	Partially oscillatory zoned core (likely partially resorbed)
WI68-70	D	Bright oscillatory zoned core
WI68-71	D	Dark weakly oscillatory zoned core
WI68-73	D	Bright oscillatory zoned core
WI68-74	D	Large, bright oscillatory zoned core
WI68-75	D	Bright oscillatory zoned inner rim
WI68-76	D	Dark homogenous core
WI68-77	D	Dark weakly oscillatory zoned grain
WI68-78	D	Bright weakly oscillatory zoned core
WI68-79	D	Bright oscillatory zoned core

Spot number	Interpretation	Zircon description
WI68: Herring Island (continued)		
WI68-80	D	Bright homogenous core (small)
WI68-81	M	Dark homogenous rim
WI68-82	M	Dark homogenous rim
WI68-83	D	Bright oscillatory zoned core
WI68-84	D	Dark weakly zoned core
WI68-85	D	Dark diffusively zoned core
WI68-86	D	Bright oscillatory zoned core
WI68-87	D	Bright oscillatory zoned core
WI68-88	D	Bright oscillatory zoned core
WI68-90	D	Bright oscillatory zoned core
WI68-91	D	Sector zoned core
WI68-92	D	Dark oscillatory zoned rim
WI68-93	D	Bright homogenous core
WI68-94	D	Dark oscillatory zoned rim
WI68-95	D	Bright oscillatory zoned core
WI68-96	D	Dark homogenous grain
WI68-97	M	Dark homogenous rim
WI68-98	D	Oscillatory zoned grain
WI68-99	D	Bright homogenous core
WI68-101	M	Dark homogenous inner rim (likely resorbed core)

D = detrital core, MD = used for maximum depositional age (youngest concordant detrital grain), M = metamorphic rim

Spot	207/206 Age	176Hf/ 177Hf	2 S.E.	176Lu/ 177Hf	176Yb/ 177Hf	178Hf/ 177Hf	2 S.E.	176Hf/ 177Hf (i)	εHf	1s
WI07: Cameron Island, detrital analyses										
WI07-1	1379	0.282100	0.000120	0.001680	0.083400	1.467160	0.000120	0.282056	5.20	4.20
WI07-2	1358	0.282138	0.000086	0.002341	0.102960	1.467140	0.000110	0.282078	5.49	3.01
WI07-6	1389	0.281940	0.000075	0.001086	0.049700	1.467180	0.000093	0.281912	0.28	2.63
WI07-9	2484	0.281508	0.000081	0.001080	0.055000	1.467060	0.000100	0.281457	9.43	2.84
WI07-10	1821	0.281573	0.000055	0.001890	0.086500	1.467150	0.000078	0.281508	-4.13	1.93
WI07-12	1407	0.281909	0.000076	0.002090	0.085300	1.467170	0.000075	0.281853	-1.36	2.66
WI07-14	1746	0.281503	0.000067	0.000785	0.034680	1.467190	0.000079	0.281477	-6.95	2.35
WI07-16	1376	0.282214	0.000079	0.003313	0.152500	1.467160	0.000074	0.282128	7.67	2.77
WI07-18	1338	0.282102	0.000070	0.001075	0.049440	1.467140	0.000090	0.282075	4.92	2.45
WI07-20	1773	0.281569	0.000079	0.001132	0.050880	1.467150	0.000091	0.281531	-4.42	2.77
WI07-21	3025	0.280942	0.000081	0.001184	0.055440	1.467100	0.000110	0.280873	1.37	2.84
WI07-22	1777	0.281660	0.000100	0.001581	0.070860	1.467130	0.000110	0.281607	-1.64	3.50
WI07-25	1726	0.281632	0.000074	0.000907	0.041650	1.467090	0.000082	0.281602	-2.96	2.59
WI07-27	1403	0.282226	0.000093	0.001879	0.084200	1.467150	0.000100	0.282176	10.00	3.26
WI07-29	1587	0.281789	0.000079	0.000799	0.037900	1.467070	0.000087	0.281765	-0.38	2.77
WI07-30	1369	0.281994	0.000075	0.002119	0.099500	1.467100	0.000082	0.281939	0.81	2.63
WI07-31	1430	0.282044	0.000075	0.001383	0.069700	1.467080	0.000093	0.282007	4.61	2.63
WI07-32	1586	0.281746	0.000076	0.000657	0.031260	1.467090	0.000100	0.281726	-1.78	2.66
WI07-33	1486	0.282080	0.000077	0.001201	0.058600	1.467130	0.000085	0.282046	7.29	2.70
WI07-34	1747	0.281650	0.000072	0.001028	0.046090	1.467110	0.000084	0.281616	-2.00	2.52
WI07-36	1814	0.281606	0.000078	0.000831	0.034040	1.467110	0.000099	0.281577	-1.82	2.73
WI07-40	1370	0.281940	0.000088	0.001654	0.079000	1.467170	0.000093	0.281897	-0.65	3.08
WI07-41	1381	0.281953	0.000085	0.002270	0.100800	1.467060	0.000088	0.281894	-0.52	2.98
WI07-42	1789	0.281620	0.000057	0.001030	0.049650	1.467080	0.000077	0.281585	-2.12	2.00
WI07-44	1780	0.281497	0.000089	0.000685	0.030810	1.467160	0.000100	0.281474	-6.29	3.12
WI07-46	1455	0.282117	0.000094	0.003579	0.142300	1.467060	0.000096	0.282019	5.59	3.29
WI07-47	1799	0.281532	0.000060	0.001093	0.048200	1.467150	0.000082	0.281495	-5.11	2.10
WI07-48	1593	0.282037	0.000099	0.002188	0.107500	1.467030	0.000110	0.281971	7.07	3.47
WI07-49	1376	0.282160	0.000100	0.002876	0.150700	1.467080	0.000110	0.282085	6.17	3.50
WI07-50	1788	0.281487	0.000084	0.000801	0.036570	1.467100	0.000093	0.281460	-6.59	2.94
WI07-52	2556	0.281229	0.000071	0.000706	0.034430	1.467130	0.000086	0.281195	1.77	2.49
WI07-54	1808	0.281583	0.000065	0.000718	0.033280	1.467140	0.000085	0.281558	-2.63	2.28
WI07-56	1808	0.281524	0.000070	0.001216	0.053720	1.467140	0.000074	0.281482	-5.35	2.45
WI07-59	1766	0.281818	0.000075	0.001171	0.043810	1.467120	0.000081	0.281779	4.23	2.63
WI07-65	1362	0.281988	0.000081	0.001792	0.081800	1.467130	0.000079	0.281942	0.76	2.84
WI07-69	1658	0.281556	0.000079	0.001862	0.083800	1.467110	0.000095	0.281498	-8.24	2.77
WI07-70	2546	0.281236	0.000082	0.001361	0.061900	1.467060	0.000088	0.281170	0.66	2.87
WI07-71	1796	0.281560	0.000067	0.001444	0.068200	1.467090	0.000077	0.281511	-4.60	2.35
WI07-78	2633	0.281179	0.000099	0.003150	0.159500	1.467060	0.000100	0.281020	-2.62	3.47
WI07-79	1401	0.281911	0.000084	0.001766	0.076600	1.467150	0.000110	0.281864	-1.11	2.94
WI07-83	1714	0.281503	0.000080	0.000756	0.036980	1.467090	0.000092	0.281478	-7.63	2.80
WI07-86	1762	0.281360	0.000110	0.001934	0.089100	1.467170	0.000160	0.281295	-13.03	3.85
WI07-89	1783	0.281525	0.000086	0.001159	0.050180	1.467130	0.000094	0.281486	-5.79	3.01
WI07-91	1838	0.281834	0.000086	0.001540	0.063700	1.467110	0.000100	0.281780	5.92	3.01
WI07-92	1353	0.282053	0.000088	0.001952	0.089600	1.467010	0.000086	0.282003	2.71	3.08
WI07-93	1783	0.281462	0.000069	0.000301	0.013690	1.467120	0.000084	0.281452	-7.00	2.42
WI07-94	1364	0.282031	0.000082	0.002023	0.081800	1.467170	0.000088	0.281979	2.11	2.87
WI40: Mitchell Peninsula, detrital analyses										
WI40-1	1482	0.281890	0.000090	0.000486	0.022960	1.467010	0.000110	0.281876	1.16	3.15
WI40-16	1452	0.281826	0.000076	0.000673	0.028640	1.467020	0.000100	0.281808	-1.97	2.66

Spot	207/206 Age	176Hf/ 177Hf	2 S.E.	176Lu/ 177Hf	176Yb/ 177Hf	178Hf/ 177Hf	2 S.E.	176Hf/ 177Hf (i)	εHf	1s
WI40: Mitchell Peninsula, detrital analyses (continued)										
WI40-22	1354	0.281993	0.000085	0.000819	0.032000	1.466920	0.000110	0.281972	1.64	2.98
WI40-25	1633	0.281652	0.000074	0.001309	0.062600	1.466940	0.000090	0.281612	-4.78	2.59
WI40-36	1782	0.281539	0.000073	0.001567	0.068400	1.466980	0.000086	0.281486	-5.82	2.56
WI40-37	1376	0.281956	0.000069	0.001073	0.037270	1.467020	0.000082	0.281928	0.59	2.42
WI40-42	3194	0.280848	0.000071	0.001243	0.057670	1.466970	0.000096	0.280772	1.75	2.49
WI40-44	1806	0.281616	0.000081	0.001213	0.051400	1.467010	0.000092	0.281574	-2.12	2.84
WI40-63	1747	0.281641	0.000079	0.001190	0.047540	1.466950	0.000110	0.281602	-2.51	2.77
WI40-71	1450	0.282170	0.000100	0.002192	0.090100	1.466950	0.000098	0.282110	8.72	3.50
WI40-72	1808	0.281510	0.000098	0.000483	0.020600	1.467060	0.000120	0.281493	-4.94	3.43
WI40-73	1429	0.281741	0.000076	0.000560	0.024920	1.467000	0.000075	0.281726	-5.39	2.66
WI40-81	1664	0.281651	0.000098	0.003830	0.167400	1.467020	0.000093	0.281530	-6.95	3.43
WI40-82	1746	0.281598	0.000058	0.001418	0.057400	1.467020	0.000099	0.281551	-4.32	2.03
WI40-89	1790	0.281565	0.000070	0.000603	0.030670	1.467060	0.000076	0.281545	-3.55	2.45
WI89: Robinson Ridge, detrital analyses										
WI89-15	1418	0.282036	0.000082	0.001528	0.070700	1.467140	0.000098	0.281995	3.92	2.87
WI89-21	1413	0.282057	0.000062	0.002001	0.091290	1.467150	0.000076	0.282004	4.11	2.17
WI89-25	1762	0.281836	0.000083	0.001615	0.075700	1.467120	0.000085	0.281782	4.23	2.91
WI89-27	1335	0.282106	0.000072	0.002925	0.119710	1.467050	0.000080	0.282032	3.35	2.52
WI89-30	1387	0.282157	0.000070	0.001049	0.045000	1.467040	0.000110	0.282130	7.99	2.45
WI89-36	1894	0.281848	0.000079	0.001890	0.083600	1.467190	0.000081	0.281780	7.22	2.77
WI89-49	1816	0.281767	0.000078	0.001188	0.051800	1.467110	0.000087	0.281726	3.49	2.73
WI89-53	1399	0.281948	0.000069	0.001617	0.072700	1.467020	0.000092	0.281905	0.30	2.42
WI89-57	1741	0.281974	0.000066	0.002545	0.100800	1.467150	0.000086	0.281890	7.59	2.31
WI89-59	1550	0.282031	0.000083	0.002736	0.104500	1.467050	0.000088	0.281951	5.37	2.91
WI89-71	1553	0.281993	0.000067	0.001660	0.072400	1.467130	0.000092	0.281944	5.20	2.35
WI89-77	1702	0.281983	0.000066	0.001904	0.082870	1.467190	0.000083	0.281922	7.82	2.31
WI68: Herring Island, detrital analyses										
WI68-1	1349	0.282052	0.000084	0.001792	0.084200	1.467030	0.000086	0.282006	2.75	2.94
WI68-2	1366	0.281938	0.000086	0.001060	0.051300	1.467090	0.000094	0.281911	-0.26	3.01
WI68-6	1346	0.281931	0.000070	0.001210	0.053610	1.467090	0.000091	0.281900	-1.09	2.45
WI68-12	1345	0.282139	0.000099	0.001854	0.074100	1.466920	0.000110	0.282092	5.68	3.47
WI68-13	1388	0.281909	0.000090	0.001628	0.078700	1.467110	0.000099	0.281866	-1.33	3.15
WI68-14	1341	0.281907	0.000071	0.002100	0.094800	1.467050	0.000092	0.281854	-2.84	2.49
WI68-17	1326	0.281898	0.000087	0.001802	0.086200	1.467060	0.000091	0.281853	-3.21	3.05
WI68-19	1491	0.281840	0.000110	0.001654	0.067800	1.467140	0.000100	0.281793	-1.58	3.85
WI68-27	1371	0.282033	0.000080	0.001714	0.084230	1.467090	0.000110	0.281989	2.61	2.80
WI68-28	1410	0.281922	0.000091	0.001814	0.090300	1.467080	0.000090	0.281874	-0.57	3.19
WI68-29	1378	0.281926	0.000072	0.001256	0.060190	1.467110	0.000097	0.281893	-0.60	2.52
WI68-32	1383	0.281847	0.000075	0.001907	0.089100	1.467080	0.000078	0.281797	-3.90	2.63
WI68-35	1386	0.281754	0.000082	0.001969	0.096300	1.467030	0.000084	0.281702	-7.19	2.87
WI68-38	1390	0.281920	0.000120	0.001402	0.072300	1.467070	0.000130	0.281883	-0.69	4.20
WI68-39	1374	0.281950	0.000130	0.001910	0.099500	1.467110	0.000160	0.281900	-0.44	4.55
WI68-41	1417	0.281876	0.000086	0.001519	0.069400	1.466950	0.000110	0.281835	-1.77	3.01
WI68-42	1731	0.281722	0.000064	0.001607	0.075200	1.467050	0.000053	0.281669	-0.47	2.24
WI68-43	1347	0.281940	0.000079	0.001093	0.049400	1.467090	0.000090	0.281912	-0.64	2.77
WI68-48	1402	0.281814	0.000079	0.001115	0.051060	1.467080	0.000091	0.281784	-3.92	2.77
WI68-48	1402	0.281814	0.000079	0.001115	0.051060	1.467080	0.000091	0.281784	-3.92	2.77
WI68-50	1363	0.281919	0.000075	0.001299	0.057000	1.467020	0.000100	0.281886	-1.22	2.63
WI68-51	1387	0.281954	0.000090	0.001598	0.082500	1.467060	0.000087	0.281912	0.28	3.15
WI68-52	1420	0.281964	0.000086	0.001543	0.068400	1.467040	0.000090	0.281923	1.39	3.01

Spot	207/206 Age	176Hf/ 177Hf	2 S.E.	176Lu/ 177Hf	176Yb/ 177Hf	178Hf/ 177Hf	2 S.E.	176Hf/ 177Hf (i)	εHf	1s
WI68: Herring Island, detrital analyses (continued)										
WI68-54	1409	0.281947	0.000091	0.002786	0.132900	1.467010	0.000110	0.281873	-0.63	3.19
WI68-55	1407	0.281930	0.000100	0.002480	0.123300	1.467030	0.000100	0.281864	-0.98	3.50
WI68-57	1383	0.281942	0.000086	0.001687	0.080500	1.467140	0.000096	0.281898	-0.33	3.01
WI68-64	1394	0.281961	0.000093	0.003140	0.157000	1.467090	0.000085	0.281878	-0.77	3.26
WI68-68	1421	0.281983	0.000068	0.001886	0.081300	1.466980	0.000078	0.281932	1.75	2.38
WI68-70	1373	0.281883	0.000094	0.001305	0.058900	1.467100	0.000100	0.281849	-2.28	3.29
WI68-71	1404	0.281890	0.000100	0.001920	0.090000	1.467000	0.000130	0.281839	-1.94	3.50
WI68-73	1403	0.281956	0.000067	0.001837	0.089200	1.467020	0.000073	0.281907	0.46	2.35
WI68-76	1396	0.281920	0.000095	0.002110	0.108000	1.467130	0.000110	0.281864	-1.21	3.33
WI68-83	1400	0.281904	0.000084	0.001757	0.086700	1.467100	0.000110	0.281858	-1.38	2.94
WI68-84	1366	0.281961	0.000079	0.001642	0.076700	1.467030	0.000095	0.281919	0.02	2.77
WI68-85	1338	0.281877	0.000077	0.001458	0.065600	1.467120	0.000096	0.281840	-3.40	2.70
WI68-86	1380	0.282002	0.000087	0.001700	0.078500	1.466930	0.000094	0.281958	1.73	3.05
WI68-87	1388	0.281995	0.000080	0.001661	0.078900	1.467060	0.000100	0.281951	1.69	2.80
WI68-88	1345	0.281886	0.000087	0.001573	0.079300	1.467090	0.000100	0.281846	-3.03	3.05
WI68-90	1359	0.281863	0.000087	0.001570	0.078300	1.467100	0.000098	0.281823	-3.54	3.05
WI68-91	1391	0.281892	0.000088	0.002230	0.103100	1.467070	0.000096	0.281833	-2.44	3.08
WI68-95	1387	0.281874	0.000092	0.001410	0.067700	1.467020	0.000120	0.281837	-2.39	3.22
WI68-96	1396	0.281966	0.000081	0.001926	0.094570	1.467000	0.000100	0.281915	0.58	2.84
WI68-98	1385	0.281938	0.000076	0.001510	0.064580	1.466990	0.000080	0.281898	-0.26	2.66
WI43: syn-D_1 orthogneiss										
WI43-2	1310	0.281877	0.000080	0.000507	0.020770	1.467140	0.000110	0.281864	-3.18	2.80
WI43-6	1362	0.282124	0.000096	0.001700	0.065500	1.466940	0.000100	0.282080	5.66	3.36
WI43-7	1383	0.282053	0.000087	0.002256	0.104000	1.466960	0.000093	0.281994	3.08	3.05
WI43-10	1394	0.281936	0.000067	0.001958	0.095800	1.467120	0.000082	0.281884	-0.56	2.35
WI43-13	1404	0.281900	0.000072	0.001272	0.061900	1.467190	0.000085	0.281866	-0.97	2.52
WI43-14	1371	0.282128	0.000078	0.001559	0.061360	1.467040	0.000100	0.282088	6.13	2.73
WI43-16	1375	0.282097	0.000064	0.002415	0.101400	1.467080	0.000085	0.282034	4.33	2.24
WI43-21	1375	0.282096	0.000082	0.001196	0.057900	1.467100	0.000088	0.282065	5.42	2.87
WI43-22	1365	0.282064	0.000072	0.001505	0.070600	1.467110	0.000093	0.282025	3.78	2.52
WI43-23	1369	0.281992	0.000073	0.001102	0.050400	1.467190	0.000088	0.281963	1.69	2.56
WI43-24	1395	0.281940	0.000088	0.001568	0.074340	1.467130	0.000097	0.281899	-0.02	3.08
WI43-25	1380	0.282018	0.000084	0.001429	0.059100	1.467140	0.000091	0.281981	2.53	2.94
WI43-26	1301	0.282035	0.000087	0.000964	0.041400	1.467170	0.000093	0.282011	1.83	3.05
WI43-27	1316	0.282047	0.000073	0.001195	0.054400	1.467130	0.000110	0.282017	2.39	2.56
WI43-30	1342	0.282054	0.000086	0.001539	0.069300	1.467090	0.000110	0.282015	2.89	3.01
WI43-31	1338	0.282035	0.000064	0.002099	0.083550	1.467050	0.000076	0.281982	1.63	2.24
WI43-34	1321	0.281988	0.000057	0.001036	0.041800	1.467210	0.000078	0.281962	0.54	2.00
WI43-38	1375	0.282015	0.000062	0.000934	0.043140	1.467150	0.000082	0.281991	2.78	2.17
WI43-40	1326	0.282146	0.000098	0.002484	0.094800	1.467010	0.000099	0.282084	4.98	3.43
WI43-42	1401	0.282049	0.000092	0.002590	0.126700	1.467100	0.000077	0.281980	3.01	3.22
WI17: M_2 granite										
WI17-3	1234	0.282053	0.000073	0.000306	0.014990	1.467140	0.000096	0.282046	1.55	2.56
WI17-10	1211	0.282129	0.000074	0.000269	0.015430	1.467100	0.000092	0.282123	4.28	2.59
WI17-12	1230	0.282018	0.000061	0.000329	0.013580	1.467130	0.000067	0.282010	0.29	2.14
WI17-16	1234	0.282077	0.000076	0.000194	0.008960	1.467060	0.000074	0.282072	2.50	2.66
WI17-18	1214	0.282065	0.000068	0.000297	0.013670	1.467050	0.000092	0.282058	1.98	2.38
WI17-19	1216	0.282094	0.000087	0.000172	0.008950	1.467050	0.000097	0.282090	3.12	3.05
WI17-20	1214	0.282063	0.000069	0.000376	0.017010	1.467050	0.000092	0.282054	1.85	2.42
WI17-23	1244	0.282036	0.000072	0.000402	0.017600	1.467120	0.000067	0.282027	0.87	2.52

Spot	207/206 Age	176Hf/ 177Hf	2 S.E.	176Lu/ 177Hf	176Yb/ 177Hf	178Hf/ 177Hf	2 S.E.	176Hf/ 177Hf (i)	εHf	1s
WI17: M_2 granite (continued)										
WI17-24	1234	0.282044	0.000077	0.000182	0.009500	1.467120	0.000080	0.282040	1.33	2.70
WI17-26	1208	0.282087	0.000065	0.000210	0.010460	1.467060	0.000083	0.282082	2.84	2.28
WI17-31	1221	0.282081	0.000065	0.000346	0.016230	1.467140	0.000078	0.282073	2.51	2.28
WI17-32	1228	0.282056	0.000074	0.000438	0.018130	1.467070	0.000085	0.282046	1.55	2.59
WI17-33	1199	0.282092	0.000076	0.000270	0.013350	1.467060	0.000089	0.282086	2.96	2.66
WI17-36	1232	0.282071	0.000077	0.000213	0.010420	1.467090	0.000079	0.282066	2.27	2.70
WI17-37	1301	0.282050	0.000065	0.000249	0.010500	1.467090	0.000080	0.282044	1.49	2.28
WI17-39	1227	0.282083	0.000085	0.000177	0.008740	1.467060	0.000083	0.282079	2.72	2.98
WI17-40	1231	0.282075	0.000061	0.000312	0.014420	1.467100	0.000083	0.282068	2.33	2.14
WI84: Ardery Charnockite										
WI84-1	1173	0.282107	0.000077	0.001067	0.053400	1.467130	0.000095	0.282083	1.58	2.70
WI84-2	1178	0.282190	0.000090	0.001264	0.062920	1.467140	0.000098	0.282162	4.37	3.15
WI84-4	1167	0.282119	0.000079	0.001258	0.064200	1.467070	0.000092	0.282091	1.86	2.77
WI84-5	1193	0.282160	0.000100	0.000920	0.042000	1.467080	0.000110	0.282140	3.58	3.50
WI84-6	1175	0.282080	0.000078	0.000802	0.039600	1.467140	0.000098	0.282062	0.83	2.73
WI84-7	1190	0.282141	0.000087	0.000965	0.046800	1.467140	0.000093	0.282120	2.87	3.05
WI84-8	1180	0.282130	0.000087	0.001235	0.065100	1.467100	0.000110	0.282103	2.27	3.05
WI84-9	1173	0.282121	0.000080	0.001197	0.059390	1.467120	0.000088	0.282094	1.98	2.80
WI84-11	1164	0.282139	0.000094	0.000814	0.040100	1.467120	0.000100	0.282121	2.92	3.29
WI84-12	1158	0.282153	0.000096	0.001304	0.069900	1.467020	0.000110	0.282124	3.03	3.36
WI84-13	1171	0.282155	0.000072	0.001291	0.066820	1.467100	0.000100	0.282126	3.11	2.52
WI84-14	1173	0.282102	0.000088	0.001041	0.051600	1.467110	0.000100	0.282079	1.43	3.08
WI84-15	1185	0.282143	0.000084	0.000573	0.027460	1.467170	0.000084	0.282130	3.25	2.94
WI84-16	1177	0.282113	0.000078	0.000800	0.041300	1.467090	0.000090	0.282095	2.01	2.73
WI84-17	1184	0.282114	0.000086	0.000900	0.043700	1.467110	0.000090	0.282094	1.96	3.01
WI84-19	1174	0.282122	0.000075	0.000454	0.020700	1.467130	0.000087	0.282112	2.60	2.63
WI84-20	1172	0.282083	0.000091	0.000605	0.028030	1.467150	0.000110	0.282070	1.10	3.19
WI84-21	1170	0.282096	0.000087	0.000680	0.032000	1.467180	0.000110	0.282081	1.50	3.05
WI84-22	1177	0.282129	0.000091	0.001310	0.065600	1.467120	0.000090	0.282100	2.17	3.19
WI84-23	1180	0.282169	0.000080	0.000875	0.044100	1.467100	0.000094	0.282150	3.93	2.80
WI84-24	1164	0.282134	0.000091	0.001189	0.058600	1.467130	0.000085	0.282108	2.44	3.19
WI84-25	1173	0.282183	0.000085	0.000781	0.037400	1.467080	0.000100	0.282166	4.50	2.98
WI85: Ardery Charnockite										
WI85-1	1169	0.282081	0.000090	0.001199	0.058480	1.467130	0.000096	0.282054	0.56	3.15
WI85-2	1191	0.282080	0.000110	0.001178	0.057700	1.467140	0.000120	0.282054	0.54	3.85
WI85-3	1170	0.282135	0.000082	0.001111	0.054000	1.467150	0.000095	0.282110	2.54	2.87
WI85-4	1185	0.282152	0.000096	0.000812	0.037220	1.467080	0.000100	0.282134	3.38	3.36
WI85-5	1173	0.282162	0.000079	0.001196	0.060200	1.467100	0.000091	0.282135	3.43	2.77
WI85-6	1174	0.282105	0.000081	0.000877	0.042800	1.467170	0.000083	0.282086	1.66	2.84
WI85-7	1182	0.282130	0.000100	0.000639	0.028890	1.467130	0.000110	0.282116	2.74	3.50
WI85-8	1188	0.282168	0.000078	0.000555	0.025730	1.467090	0.000096	0.282156	4.15	2.73
WI85-9	1182	0.282185	0.000091	0.001224	0.060000	1.467070	0.000100	0.282158	4.23	3.19
WI85-10	1183	0.282136	0.000077	0.001229	0.060510	1.467030	0.000096	0.282109	2.48	2.70
WI85-11	1180	0.282092	0.000092	0.000405	0.017030	1.467170	0.000110	0.282083	1.57	3.22
WI85-12	1180	0.282142	0.000072	0.001223	0.060660	1.467080	0.000086	0.282115	2.70	2.52
WI85-13	1181	0.282161	0.000078	0.001320	0.067100	1.467050	0.000085	0.282132	3.30	2.73
WI85-14	1174	0.282120	0.000097	0.000982	0.049400	1.467140	0.000110	0.282098	2.11	3.40
WI85-15	1186	0.282208	0.000085	0.001095	0.054200	1.467100	0.000093	0.282184	5.14	2.98
WI85-16	1173	0.282186	0.000061	0.001139	0.057600	1.467020	0.000078	0.282161	4.33	2.14
WI85-17	1172	0.282125	0.000088	0.000798	0.037720	1.467110	0.000110	0.282107	2.43	3.08

Spot	207/206 Age	176Hf/ 177Hf	2 S.E.	176Lu/ 177Hf	176Yb/ 177Hf	178Hf/ 177Hf	2 S.E.	176Hf/ 177Hf (i)	εHf	1s
WI85: Ardery Charnockite (continued)										
WI85-21	1189	0.282124	0.000078	0.000607	0.027730	1.467100	0.000091	0.282111	2.55	2.73
WI85-23	1174	0.282151	0.000069	0.000833	0.040810	1.467120	0.000085	0.282132	3.33	2.42
WI85-24	1172	0.282150	0.000084	0.001073	0.051830	1.467100	0.000100	0.282126	3.10	2.94
WI85-25	1180	0.282127	0.000083	0.000814	0.037600	1.467180	0.000090	0.282109	2.49	2.91
WI85-26	1165	0.282064	0.000087	0.000790	0.040500	1.467180	0.000100	0.282046	0.28	3.05
WI85-27	1181	0.282108	0.000071	0.000616	0.028880	1.467170	0.000080	0.282094	1.97	2.49
WI85-28	1181	0.282160	0.000100	0.000516	0.023090	1.467070	0.000120	0.282149	3.90	3.50
WI85-29	1172	0.282049	0.000089	0.000567	0.025120	1.467140	0.000086	0.282036	-0.08	3.12

CHAPTER 3

This chapter is written for *Journal of Metamorphic Geology* as:

Morrissey, L.J., Hand, M., Kelsey, D.E. Assessing tectonic models for Stage I –Stage II metamorphism in the Antarctica segment of the Musgrave–Albany–Fraser Orogen using *P*–*T* constraints.

Statement of Authorship

Title of Paper	Assessing tectonic models for Stage I–Stage II metamorphism in the Antarctica segment of the Musgrave–Albany–Fraser Orogen using *P*–*T* constraints.
Publication status	☐Published ☐Accepted for publication ☐Submitted for publication ☒Unpublished and unsubmitted work written in manuscript style
Publication Details	

Principal Author

Name of Principal Author (Candidate)	Laura Morrissey		
Contribution to the Paper	Petrography, LA-ICP-MS data collection, processing, and interpretation, *P*–*T* pseudosection calculation and interpretation, manuscript design and composition, creation of figures.		
Overall percentage (%)	85		
Certification:	This paper reports on original research I conducted during the period of my Higher Degree by Research candidature and is not subject to any obligations or contractual agreements with a third party that would constrain its inclusion in this thesis. I am the primary author of this paper.		
Signature		Date	16/05/2016

Co-Author Contributions

By signing the Statement of Authorship, each author certifies that:

i. the candidate's stated contribution to the publication is accurate (as detailed above);
ii. permission is granted for the candidate in include the publication in the thesis; and
iii. the sum of all co-author contributions is equal to 100% less the candidate's stated contribution.

Name of Co-Author	Martin Hand		
Contribution to the Paper	Guidance with interpretation of petrography, geochronology and pseudosections, manuscript review.		
Signature		Date	17th May 2016

Name of Co-Author	David Kelsey		
Contribution to the Paper	Guidance with data interpretation, manuscript review.		
Signature		Date	18/05/2016

ABSTRACT

In situ U–Pb monazite geochronology and calculated metamorphic phase diagrams from the Windmill Islands in Wilkes Land, east Antarctica, show that the region experienced two phases of high thermal gradient metamorphism during the Mesoproterozoic. The first phase of metamorphism is recorded by monazite ages in two widely separated samples, and occurred at 1320–1300 Ma. This event was regional in extent and reached conditions of 3.5–4 kbar and 700–730 °C, corresponding to a very high thermal gradient. The elevated thermal regime is interpreted to reflect a period of accelerated extension in a back-arc setting that existed prior to c. 1330 Ma. The first metamorphic event was overprinted by granulite facies metamorphism that increases in intensity to the south. This event involved peak temperatures of >850 °C and pressures of ~4 kbar and was followed by isobaric cooling. Monazite age populations of c. 1180 Ma suggest that the second event was coeval with the intrusion of charnockite. A phase of granitic magmatism at c. 1250–1210 Ma, prior to the intrusion of the charnockite, is interpreted to reflect a phase of compression within an overall back-arc setting. The metamorphic evolution of the Wilkes Land region is very similar to that of the eastern Albany–Fraser Orogen and Musgrave Province in Australia and further demonstrate the remarkable consistency in the timing of metamorphism and the thermal gradients along the ~5000 km strike length of this system.

1. Introduction

Metamorphic rocks record pressure–temperature (*P–T*) signatures that reflect the specific thermal environment of metamorphism, and can therefore be used to characterise the likely tectonic setting (e.g. Brown, 2007, 2014; Stüwe, 2007). Terranes that record metamorphism at high thermal gradients that significantly exceed normal steady-state crustal conditions are of interest because they require a mechanism that allows the large-scale generation of high temperatures (e.g. Bohlen, 1991; Clark et al., 2011; De Yoreo et al., 1991; Harley, 2004; Kelsey and Hand, 2015; Morrissey et al., 2015; Schmitz and Bowring, 2003; Sizova et al., 2014). These terranes provide real geological examples of processes such as lithospheric extension or convergence that have long-term effects on the chemical and thermo-mechanical evolution of the crust (Brown, 2007, 2014; Fyfe, 1973; Vielzeuf et al., 1990).

The Musgrave–Albany–Fraser–Wilkes Orogen is an example of an extensive, high thermal gradient orogenic system that formed during the Mesoproterozoic. The footprint of Mesoproterozoic metamorphism extends for at least 5000 km from the Bunger Hills and Windmill Islands in east Antarctica to the Musgrave and Warumpi Provinces in central Australia (Fig. 1; e.g. Clark et al., 2014; Kirkland et al., 2011; Morrissey et al., 2011; Smits et al., 2014; Tucker et al., 2015; Walsh et al., 2015; Wong et al., 2015). Despite the vast strike distance of the orogen, each of the regions are characterised by a very similar two-stage metamorphic and magmatic history between 1340–1300 Ma and 1240–1140 Ma (e.g. Howard et al., 2015; Kirkland et al., 2011, 2013, 2015; Smithies et al., 2011; Zhang et al., 2012). Metamorphism in each region was long-lived and occurred at high to very high thermal gradients, with UHT rocks outcropping in much of the Musgrave Province (Clark et al., 2014; Morrissey et al., 2011; Smithies et al., 2011; Tucker et al., 2015; Walsh et al., 2015; Wong et al., 2015). However, despite the importance of this system as an example of long-lived, high thermal gradient metamorphism, the conditions and overall tectonic setting of metamorphism in each of the segments of this belt are not well defined, with models ranging from intracratonic (Gorczyk et al., 2015; Gorczyk and Vogt, 2015; Smithies et al., 2011) to accretionary (Smits et al., 2014) to a back-arc setting (Clark et al., 2014; Walsh et al., 2015; Wong et al., 2015).

The Windmill Islands are located along the Wilkes Land coast in east Antarctica and provide some of the only Antarctic outcrop of the system. Paleogeographic reconstructions based on geophysics suggest that the Wilkes Land geology was contiguous with the Nornalup Zone, on the eastern margin of the Albany–Fraser Orogen (Fig. 1; Aitken et al., 2014, 2016). Importantly, the Windmill Islands region also records the effects of both c. 1340–1300 Ma (M1) and c. 1240–1140 (M2) metamorphism within the Musgrave–Albany–Fraser system. This allows an assessment of the conditions of the two stages of metamorphism.

This study presents calculated metamorphic *P–T* pseudosections from four samples that each record a different part of the overall *P–T* history of the Windmill Islands. The pseudosections are combined with in situ LA-ICP-MS (laser ablation inductively coupled plasma mass spectrometry) monazite geochronology to constrain the timing of formation of the silicate mineral assemblages. The purpose of this study is to unravel the conditions of the two stages of metamorphism. This is then used to provide a metamorphic framework with which to assess

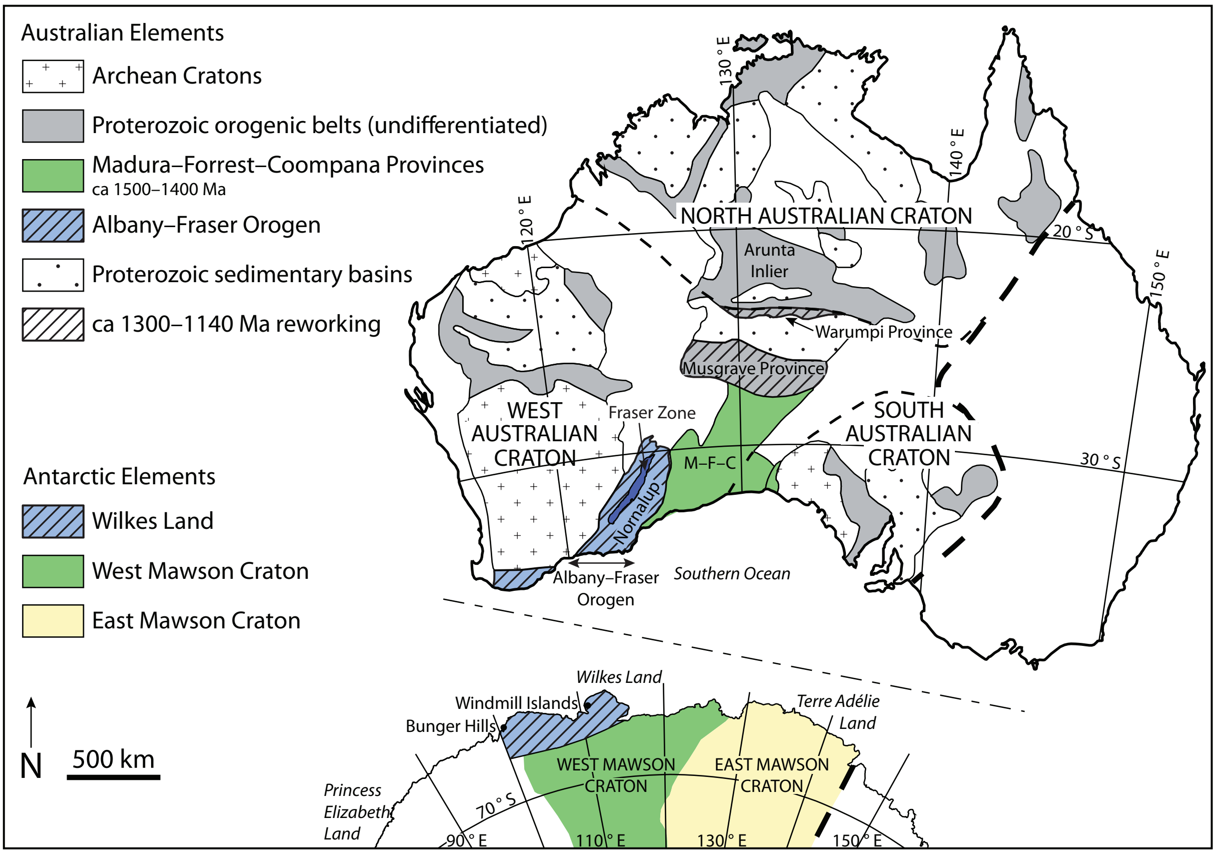

Figure 1: Simplified geological map of Australia and Antarctica showing relevant geological provinces and the extent of Mesoproterozoic reworking. Australian elements are modified from Kirkland et al. (2011). Tectonic interpretation of basement geology in Antarctica inferred from geophysics by Aitken et al. (2014).

tectonic models for Wilkes Land, and the Albany–Fraser system as a whole.

2. Geological setting

The Windmill Islands are located along the Wilkes Land coast near Australia's Antarctic Casey Station. They include approximately 400 km^2 of exposed outcrop on peninsulas and islands (Figs. 1, 2). The outcrops consist of high-grade deformed and migmatised pelitic to psammitic metasedimentary rocks, granitic to mafic orthogneisses, a voluminous charnockite suite and minor porphyritic granite and late-stage dolerite dykes (Blight and Oliver, 1977; Möller et al., 2002; Post, 2000; Zhang et al., 2012). Garnet-bearing orthogneiss and charnockite are the dominant rock types and make up ~70% of the outcrop (Fig. 2; Zhang et al., 2012). Detailed descriptions of each lithology and their distribution are given in Paul et al. (1995) and Post (2000).

The metasedimentary rocks are the oldest units in the Windmill Islands and were deposited in the interval 1350–1300 Ma (Morrissey et al., in review (Ch. 2); Post, 2000). The metasedimentary rocks were intruded by protoliths to the orthogneisses that formed during two periods of magmatic activity at c. 1315 Ma and c. 1250–1210 Ma (Post, 2000; Post et al., 1997; Zhang et al., 2012). These periods of magmatism were broadly coeval with two tectono-metamorphic events, M_1 and M_2, respectively. The structural and metamorphic history of the Windmill Islands has been described in detail by previous workers (Paul et al., 1995; Post, 2000) and is briefly summarised below.

The overall metamorphic grade in the Windmill Islands increases from upper amphibolite facies in the north to granulite facies in the south (Fig. 2; Blight and Oliver, 1977; Möller et al., 2002; Post, 2000). M_1/D_1 is interpreted to have occurred at 1320–1300 Ma and is only preserved in the northern part of the Windmill Islands (Fig. 2). D_1 involved the formation of a horizontal S_1 fabric parallel to compositional layering and F_1 isoclinal folds defined by folded leucosomes (Paul et al., 1995; Post, 2000). Metamorphic conditions associated with this event reached upper amphibolite to lower granulite facies conditions, with the formation of sillimanite–biotite–cordierite or sillimanite–biotite–garnet-bearing assemblages in pelitic rocks (Blight and Oliver, 1977; Paul et al., 1995) and the intrusion of granite at c. 1315 Ma (Fig. 2). Conventional thermobarometry and qualitative estimates based on mineral parageneses suggest peak conditions of ~750 °C and 4 kbar (Post, 2000).

The second phase of tectono-metamorphism, $M_2/D_{2a\text{-}2b}$, occurred at 1240–1140 Ma and involved two stages of deformation. The effects of the M_2 event increase progressively to the south, culminating in high grade granulite facies conditions in the southern islands (Fig. 2). In the south, garnet- and cordierite-bearing leucosomes formed early in M_2 and were then folded in tight isoclinal folds during D_{2a} (Blight and Oliver, 1977; Paul et al., 1995; Post, 2000). Map-scale F_{2a} folds occur in metasedimentary units on Clark, Bailey and Mitchell Peninsulas, trend E–W and are generally upright in the northern part of the region and more inclined in the southern part of the region (Post, 2000). Voluminous syn- to post-D_{2a} garnet-bearing granite intruded between 1250–1210 Ma (Fig. 2; Post, 2000; Zhang et al., 2012). These granites have variable ages, mineralology and Hf isotopic values, suggesting there are multiple, distinct intrusive sources (Morrissey et al., in review (Ch. 2); Post, 2000; Zhang et al., 2012). Deformation during D_{2b} involved open to tight southeast plunging folds, which

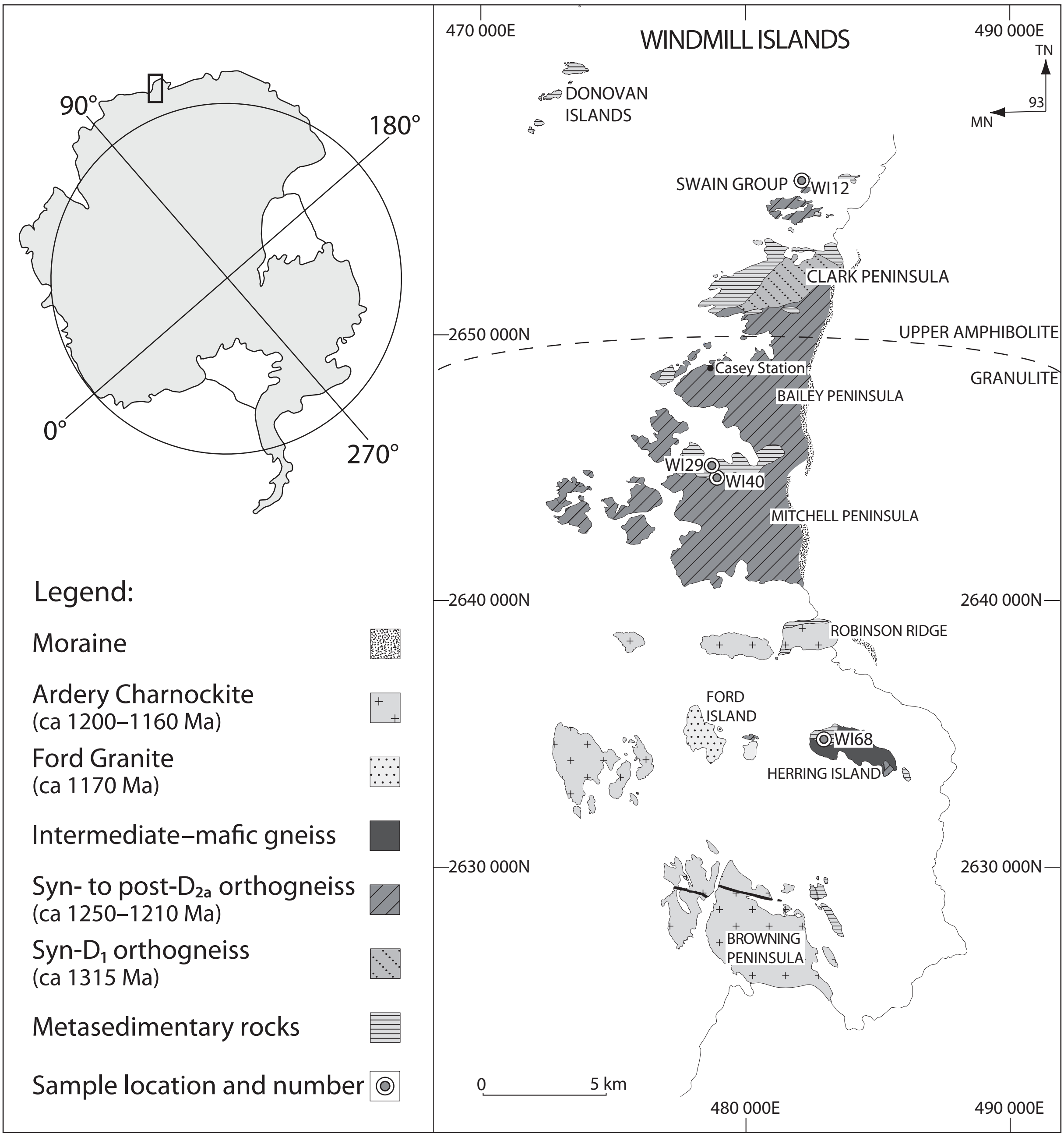

Figure 2: Sketch geological map of the Windmill Islands, from Post (2000). Ages of lithologies are from Post (2000) and Zhang et al. (2012).

resulted in complex fold interference patterns. Partial melting continued during D_{2b}, with garnet–orthopyroxene–cordierite-bearing leucosomes forming in the axial plane of D_{2b} folds. High temperatures are interpreted to have outlasted the deformation, suggested by structurally discordant orthopyroxene-bearing leucosomes on Bailey and Mitchell Peninsulas (Paul et al., 1995; Post, 2000). Conventional thermobarometry suggests that peak M_2 conditions in the southern Windmill Islands reached 5–7 kbar and 850–900 ºC. The final stages of M_2 involved the intrusion of the c. 1170 Ma Ford Granite and the voluminous c. 1200–1160 Ma Ardery Charnockite suite in the southern part of the terrane (Fig. 2; Post, 2000; Zhang et al., 2012). The Ardery Charnockite is interpreted to have crystallised at temperatures of 960–1100 °C and pressures of 3–4 kbar (Kilpatrick and Ellis, 1992). $\varepsilon_{Hf}(t)$ values show that it is the most juvenile rock type in the region and it is interpreted to be derived from the melting of mafic lower crust (Kilpatrick and Ellis, 1992; Morrissey et al., in review (Ch. 2); Zhang et al., 2012). Monazite ages of 1170–1140 Ma from samples of orthogneiss were interpreted to date the final stages of partial melting (Post, 2000). Garnet Sm–Nd ages from a variety of rock types range between 1153 and 1123 Ma, interpreted to date initial cooling (Möller et al., 2002; Post, 2000). The final stage of deformation involved the formation of cross-cutting, discrete retrograde D_3 shear zones that resulted in greenschist facies recrystallisation of the granulite facies rocks (Post, 2000).

3. Sample description and petrography

Four metapelitic samples were chosen to examine the change in metamorphic grade from upper amphibolite facies in the north to high-grade granulite facies in the south (Fig. 2). One sample was selected from the northern part of the Windmill Islands, interpreted to reflect M_1, two samples were selected to investigate the overprinting relationships between M_1 and M_2 and one sample was selected from the southern Windmill Islands, interpreted to record only M_2.The location of each sample is presented in Table 1. A summary of the petrography of

Table 1: Sample locations in UTM (WGS84).

Sample	Location		Zone	Easting	Northing
WI12	Cameron Island	(northern Windmill Islands)	49D	482480	2655956
WI40	Mitchell Peninsula	(central Windmill Islands)	49D	479134	2644765
WI29	Mitchell Peninsula	(central Windmill Islands)	49D	478651	2645187
WI68	Herring Island	(southern Windmill Islands)	49D	482772	2634855

Table 2: Summary of petrography.

Sample	M_1 assemblage	M_2 assemblage	Post-Peak M_2
WI12	g + pl + ksp + bi + cd + mt + ilm + sill + q	–	–
WI40	g + pl + ksp + bi + mt + ilm + sill + q	pl_2 + ksp + bi_2 + cd + sp + mt_2 + ilm_2 + (g_1)	–
WI29	–	g_1 + pl + ksp + mt + ilm + q + opx ± bi	bi + qz → cd + g_2
WI68	–	pl + ksp + opx + cd + mt + ilm + q	bi
	Minerals	**Modal proportion**	
WI12	g : pl : ksp : bi : cd: mt/ilm : sill : q	5 : 17 : 4 : 27 : 9 : 5 : 12 : 21	
WI40	g : pl : ksp : bi : cd : sp : mt/ilm : sill : q	18 : 20 : 15 : 17 : 20 : 2 : 3 : 1 : 4	
WI29	g : pl : ksp : opx : bi : cd : mt/ilm : q	9 : 18 : 18 : 1 : 27 : 0.5 : 6.5 : 20	
WI68	pl : ksp : opx : bi : cd : mt/ilm : q	20 : 22 : 11 : 12 : 17 : 3 : 15	

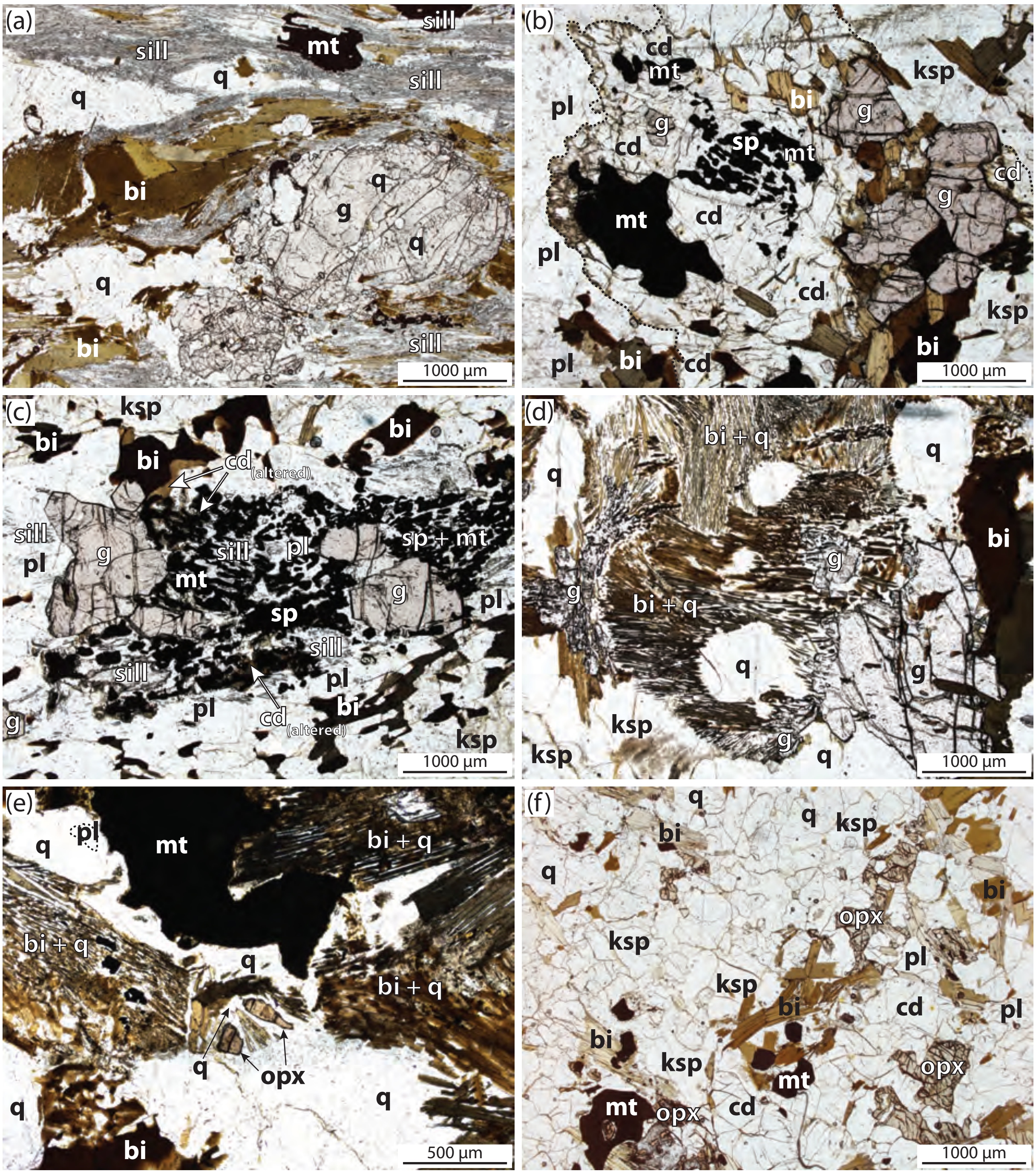

each sample is presented in Table 2. The modal proportion of minerals in each sample was visually estimated and is also summarised in Table 2.

3.1. WI12: Cameron Island (Swain Group)

Sample WI12 contains an S_1 fabric defined by alternating quartzofeldspathic leucosomes and layers containing biotite and sillimanite that define a strong foliation (Fig. 3a). The leucosomes are 3–5 mm in width and are dominantly composed of euhedral to subhedral plagioclase grains (up to 1 mm in diameter) that commonly contain aggregates of foliation-parallel acicular sillimanite. K-feldspar, quartz (~250–500 µm), minor cordierite (<1 mm) and rare biotite also occur in the leucosomes. In the biotite–sillimanite-rich domains,

Figure 3 (previous page): Photomicrographs illustrating important mineralogical relationships. (a) Sample WI12: garnet and aggregates of quartz are wrapped by a strong fabric defined by biotite and fine-grained sillimanite. (b) Sample WI40: garnet is partially replaced by cordierite–spinel–magnetite reaction microstructures. The cordierite is outlined with a dashed line. Fine-grained garnet occurs within the reaction microstructure. (c) Sample WI40: coarse-grained garnet and sillimanite are partially replaced by spinel–magnetite–plagioclase symplectites. In places plagioclase and spinel are separated by a thin corona of a mineral that is now altered (brown in colour) but is interpreted to have been cordierite. (d) Sample WI29: symplectites of bladed biotite and quartz form defined grain shapes and are interpreted to be pseudomorphing another mineral. Fine-grained garnet occurs intergrown with the biotite–quartz symplectites on the margins of coarse-grained garnet. (e) Fine-grained orthopyroxene occurs at the margins of the biotite–quartz symplectites and is interpreted to be relict. The biotite–quartz symplectites contain inclusions of magnetite. (f) Sample WI68: orthopyroxene occurs as ragged grains in the matrix and included in magnetite, where it is separated by a corona of plagioclase. Biotite is coarsest and most abundant in domains with orthopyroxene and magnetite.

sillimanite is predominantly acicular but may also occur as coarser-grained prismatic needles that are up to 2 mm in length (Fig. 3a). Biotite occurs intergrown with sillimanite and as coarser, tabular grains (>1 mm; Fig. 3a) that contain inclusions of sillimanite. Euhedral garnet porphyroblasts (1–3 mm) are commonly wrapped by the sillimanite-bearing foliation (Fig. 3a), though in places garnet also appears to overgrow coarse-grained sillimanite. The garnet grains contain rare inclusions of sillimanite, biotite and quartz. Cordierite occurs intergrown with sillimanite needles and may form poikiloblasts up to 1.5 mm. Elongate aggregates of quartz (500–1500 μm in length) are wrapped by the sillimanite-bearing fabric (Fig. 3a). Fine-grained plagioclase and Fe–Ti-oxides (up to 500 μm) also occur in these domains. Magnetite is the dominant oxide and ilmenite occurs as small, anhedral grains in direct contact with magnetite. Magnetite may contain inclusions of sillimanite, or be cross-cut by coarse-grained sillimanite (Fig. 3a). Minor amounts of apatite occur throughout the sample.

3.2. WI40: Mitchell Peninsula

Sample WI40 contains a gneissic fabric defined predominantly by leucosomes up to 5 mm in width and biotite-rich layers with varying abundances of plagioclase and cordierite. The leucosomes contain perthitic K-feldspar (up to 2 mm), plagioclase and antiperthite (250–2000 μm). Quartz is rare and occurs as inclusions within feldspar grains in the leucosomes. In the plagioclase–biotite-rich layers, abundant plagioclase and K-feldspar occur together with euhedral garnet (500–1000 μm) and biotite flakes of variable orientation and size (typically 750–1500 μm). These layers do not contain cordierite or sillimanite and Fe-oxides are rare. Other layers are dominantly composed of coarse-grained cordierite (up to 1.5 mm in diameter), together with coarse-grained magnetite (up to 2 mm), spinel and minor anhedral ilmenite. Sillimanite is relatively abundant in these layers as acicular, foliation-parallel inclusions in cordierite, but it does not occur as a matrix mineral. Angular, anhedral garnet is fine-grained (typically 150–200 μm) and occurs as inclusions in cordierite. Biotite occurs as small, anhedral flakes between 100–500 μm in length, and is less abundant and finer-grained in areas that contain sillimanite inclusions. This sample also contains biotite-rich layers that contain feldspar as well as cordierite, garnet and Fe–Ti-oxides. In these layers, garnet is up to 1.5 mm in diameter and commonly in contact with coarse-grained biotite flakes (up to 1.5 mm in length) that are randomly oriented. Fe-oxides (dominantly magnetite with rare ilmenite) occur as anhedral grains up to 2 mm in diameter and may contain rare inclusions of sillimanite, garnet or cordierite.

The sample contains two different mineral reaction microstructures involving spinel (together with lesser amounts of magnetite and ilmenite). The first mineral reaction microstructure involves symplectites of cordierite–spinel–magnetite that surround garnet (Fig. 3b). Cordierite in these reaction textures comprises an aggregate of small grains that have been variably altered to pinite (Fig. 3b). Spinel is typically fine-grained, anhedral and very dark in colour. Magnetite occurs as small, anhedral grains and also as coarser grains 1–2 mm in diameter (Fig. 3b). Ilmenite is much less common and occurs as small domains intergrown with magnetite. Small, anhedral garnets may be surrounded by cordierite (Fig. 3b). The first reaction microstructure is commonly surrounded by unoriented, coarse-grained biotite and plagioclase (Fig. 3b). The second reaction microstructure involves coarse-grained sillimanite and garnet which are partially replaced by symplectites of plagioclase, spinel, magnetite and ilmenite (Fig. 3c). Coarser-grained relics of anhedral sillimanite (up to 1 mm in length) occur within these reaction microstructures (Fig. 3c). These reaction microstructures also contain thin (<50 μm) coronas that separate magnetite and spinel from plagioclase (Fig. 3c). The mineral that makes up these coronas has now been replaced, but has a similar appearance to domains of highly altered (pinitised) cordierite elsewhere in the sample.

3.3. WI29: Mitchell Peninsula

Sample WI29 contains a gneissic fabric defined by alternating biotite-rich layers and quartzofeldspathic leucosomes. At outcrop scale, the leucosomes contain garnet and coarse-grained magnetite. Anhedral garnet porphyroblasts (up to 5 mm) typically occur in discrete layers together with coarse-grained biotite and the two minerals occur in direct contact. Garnet grains contain rare inclusions of acicular sillimanite that are parallel to the gneissic foliation as well as inclusions of magnetite, ilmenite, biotite and quartz. A second, fine-grained morphology of garnet also occurs on the margins of garnet porphyroblasts, intergrown with symplectites of bladed biotite and quartz (Fig. 3d). This finer-grained garnet contains inclusions of bladed quartz that are aligned with the symplectitc quartz, suggesting that the garnet overgrew the symplectite. The bladed biotite and quartz symplectites are abundant and commonly form euhedral grain shapes with well-defined edges and may be several millimetres in diameter (Fig. 3d). The symplectites contain inclusions of euhedral magnetite and ilmenite (250–500 μm) and quartz (500–1000 μm) (Fig. 3d and e). Orthopyroxene occurs in this sample as small grains (no larger than 50–100 μm) that are typically located on the edge of the biotite–quartz symplectites or near magnetite (Fig. 3e). Fine-grained biotite–quartz intergrowths also occur at the margins of coarse-grained biotite, and are in optical continuity. Magnetite and ilmenite aggregates are abundant and occur throughout the sample as anhedral grains that are up to 3 mm in length. They are coarsest at the margins between garnet and the biotite–quartz symplectites. Magnetite may contain inclusions of exolved spinel. In some parts of the sample, garnet and magnetite are separated by thin coronas of a mineral that has now been replaced. This mineral has a different alteration character to the feldspars observed elsewhere in the sample. Although it cannot be definitively proven, it is possible that this mineral was cordierite. The remainder of the sample comprises quartzofeldspathic leucosomes that are partially wrapped by the garnet–biotite-bearing layers. The quartzofeldspathic leucosomes contain coarse-grained perthitic K-feldspar (2.5–3 mm in diameter), finer-grained plagioclase (<1.5 mm in diameter) and quartz.

3.4. WI68: Herring Island
Sample WI68 is from Herring Island in the southern Windmill Islands. At outcrop scale, it contains cordierite and orthopyroxene-bearing leucosomes that are concordant with the gneissic fabric. The sample contains cordierite, orthopyroxene, K-feldspar, plagioclase, biotite, magnetite, ilmenite and quartz (Fig. 3g). Orthopyroxene occurs as anhedral, ragged grains (<500 μm across, commonly ~250 μm) in close proximity to biotite and cordierite (Fig. 3g). Cordierite grains are up to 1.5 mm and may contain inclusions of biotite. Biotite occurs throughout the matrix as small (150 μm) flakes, but it is more abundant and coarser-grained (up to 500 μm) in regions with cordierite, orthopyroxene and the Fe–Ti-oxides, where it may form coronas. Fe–Ti-oxides are most abundant in the relatively biotite-rich areas of the sample and are dominantly magnetite rather than ilmenite (Fig. 3g). The majority of the sample is comprised of K-feldspar, which occurs as grains up to 500 μm and may be perthitic (Fig. 3g). Plagioclase (up to 250 μm) and less common quartz make up the remainder of the sample.

4. Sampling and Methods

4.1. U–Pb monazite geochronology
U–Pb isotopic data was collected using LA-ICP-MS on in situ monazite grains in thin section. Prior to LA-ICP-MS analysis, monazite grains were imaged using a back-scattered electron detector on a Phillips XL30 SEM to determine their microstructural locations and any compositional variations.

LA-ICP-MS analyses were done at the University of Adelaide, following the method of Payne et al. (2008). U–Pb isotopic analyses were acquired using a New Wave 213 nm Nd–YAG laser coupled with an Agilent 7500cs ICP-MS. Ablation of monazites was performed in a He-ablation atmosphere with a frequency of 4 Hz. A spot size of 12 μm was used for all samples. The total acquisition time of each analysis was 100 s. This included 40 s of background measurement, 10 s of the laser firing with the shutter closed to allow for beam stabilisation, and 50 s of sample ablation. Isotopes measured were ^{204}Pb, ^{206}Pb, ^{207}Pb and ^{238}U for dwell times of 10, 15, 30 and 15 ms, respectively.

Monazite data were reduced using Glitter software (Griffin et al., 2004). Elemental fractionation and mass bias was corrected using the monazite standard MAdel (TIMS normalisation data: ^{207}Pb/^{206}Pb = 491.0 ± 2.7 Ma, ^{206}Pb/^{238}U = 518.37 ± 0.99 Ma and ^{207}Pb/^{235}U = 513.13 ± 0.19 Ma: updated from Payne et al. (2008) with additional TIMS analyses). Throughout the course of this study, MAdel yielded weighted mean ages of ^{207}Pb/^{206}Pb = 489 ± 8 Ma (MSWD = 0.33), ^{206}Pb/^{238}U = 518 ± 2 Ma (MSWD = 0.48), and ^{207}Pb/^{235}U = 513 ± 2 Ma (MSWD = 0.44) (n = 80). Data accuracy was monitored using monazite standard 94-222/Bruna-NW (c. 450 Ma: Payne et al., 2008). As a secondary standard, 94-222 yielded weighted mean ages of ^{207}Pb/^{206}Pb = 441 ± 12 Ma (MSWD = 0.75), ^{206}Pb/^{238}U = 452 ± 2 Ma (MSWD = 0.98), ^{207}Pb/^{235}U = 450 ± 2 Ma (MSWD = 1.10) (n = 30).

4.2. Mineral equilibria modelling
P–T pseudosections were calculated for four metapelitic samples using THERMOCALC

v3.40, using the internally consistent dataset, ds62, of Holland and Powell (2011) and the activity–composition (*a–x*) models re-parameterised for metapelitic rocks in the MnNCKFMASHTO system (Powell et al., 2014; White et al., 2014a, 2014b). Calculated phase diagrams were contoured for the abundance and composition of phases using TC Investigator (Pearce et al., 2015).

Whole-rock chemical compositions for the calculation of metamorphic phase equilibria were determined by crushing up a representative amount of each sample using a tungsten carbide mill. Analyses of bulk-rock chemical compositions were conducted by Franklin and Marshall College, Pennsylvania. Major elements were analysed by fusing a 0.4 g portion of the powdered sample with lithium tetraborate for analysis by XRF. Trace elements were analysed by mixing 7 g of crushed rock power with Copolywax powder and measurement by XRF. The whole rock chemistry for each sample used in the calculation of the mineral equilibria pseudosections is given in Supplementary Data S3.1.

The amount of H_2O and Fe_2O_3 in the bulk chemical composition that relates to the formation of the preserved metamorphic mineral assemblages can be difficult to determine, due to hydration and oxidation during low-*T* processes such as weathering and exposure of rock powders to air (e.g. Johnson and White, 2011; Kelsey and Hand, 2015; Lo Pò and Braga, 2014). The oxidation state can have a significant effect on the stability of Fe–Ti oxide minerals such as magnetite, ilmenite$_{(ss)}$ and rutile, as well as some silicate minerals (e.g. Boger et al., 2012; Diener and Powell, 2010; Morrissey et al., 2016b; White et al., 2002). The proportion of Fe_2O_3 to FeO for all samples was evaluated based on the modal abundance of Fe^{3+}-bearing minerals and an appraisal of the ferric iron content of those minerals as determined for measured mineral compositions using the stoichiometric method of Droop (1987). For the bulk compositions of these samples, the main effect of increasing the oxidation state is to increase magnetite stability to higher pressures and decrease garnet stability at lower pressures. However, the topology and *P–T* conditions of the main fields on the pseudosections are not significantly affected by small variations in oxidation state. The H_2O content for all samples was also estimated based on the modal proportion of H_2O-bearing minerals (biotite and cordierite) and a conservative estimate of the H_2O content of these minerals in granulites, based on electron microprobe totals (e.g. Bose et al., 2005; Cesare et al., 2008; Deer et al., 1992; Rigby and Droop, 2011). The main effect of decreasing the H_2O content of the bulk composition is to elevate the solidus, whereas increasing the amount of H_2O favours the stability of silicate melt at the expense of diminishing K-feldspar stability and to lower the temperature of the solidus. The interpreted peak conditions in these samples are not significantly affected by small variations in H_2O.

5. Results

5.1. U–Pb monazite geochronology

U–Pb isotopic data and information on microstructural location for all monazite analyses are presented in Supplementary Data S3.2. Representative BSE images of monazite grains are shown in Figure 4. Tera–Wasserburg plots for all samples are presented in Figure 5. Analyses that are shown as dashed grey ellipses are >5% discordant and have been excluded from the calculation of concordia ages and weighted average ages.

5.1.1. Sample WI12

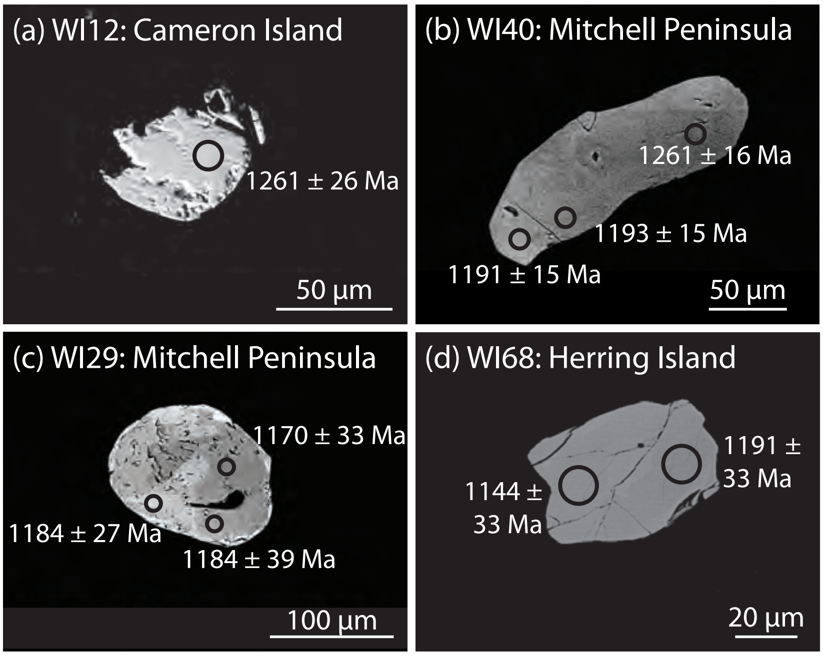

Figure 4: BSE images of representative monazite grains from each sample. The ages shown are the $^{207}Pb/^{206}Pb$ ages. (a) Sample WI12. (b) Sample WI40. (c) Sample WI29. (d) Sample WI68.

Twenty-two analyses were collected from twelve grains. Monazite grains are located throughout the biotite–sillimanite foliation and within the quartzofeldspathic leucosomes. They are typically 20–60 µm in diameter and appear unzoned in BSE images (Fig. 4a). The monazite analyses form a spread along concordia from 1300 Ma to 1150 Ma (Fig. 5a). There is no link between microstructural location and age. It is not possible to define two populations on the basis of $^{207}Pb/^{206}Pb$ ages. However, a probability density plot of the $^{206}Pb/^{238}U$ ages suggests that the analyses broadly define two peaks at c. 1200 Ma and c. 1260 Ma (Fig. 5a).

5.1.2. Sample WI40

Thirty-one analyses were collected from fourteen grains. Monazite grains are located throughout the sample, including as inclusions in garnet and coarse-grained feldspar as well as within the reaction microstructures. Monazite grains are typically 40–80 µm in diameter and some grains display weak, patchy zoning in BSE images (Fig. 4b). Four analyses that are >5% discordant are excluded from further interpretation. The remaining 27 analyses form a spread along concordia from c. 1320 to 1170 Ma (Fig. 5b). The dark, patchy zones commonly yield older ages but grains that appear unzoned in BSE also yield multiple ages (Fig. 5b). Monazite grains included in coarse-grained feldspar or garnet commonly yield older ages whereas those located within cordierite or along grain boundaries yield a range of ages (Fig. 5b). Multiple age populations cannot be clearly defined on the basis of the $^{207}Pb/^{206}Pb$ ages. However, a probability density plot of the $^{206}Pb/^{238}U$ ages suggests the analyses define two age peaks at c. 1290 Ma c. 1220 Ma, with a younger 'shoulder' at c. 1190 Ma (Fig. 5b).

5.1.3. Sample WI29

Thirty-one analyses were collected from fourteen grains located throughout the matrix of the sample and within the biotite–quartz symplectites. The grains are 50–200 µm in diameter and show patchy zoning in BSE images (Fig. 4c). All 31 analyses yield a concordia

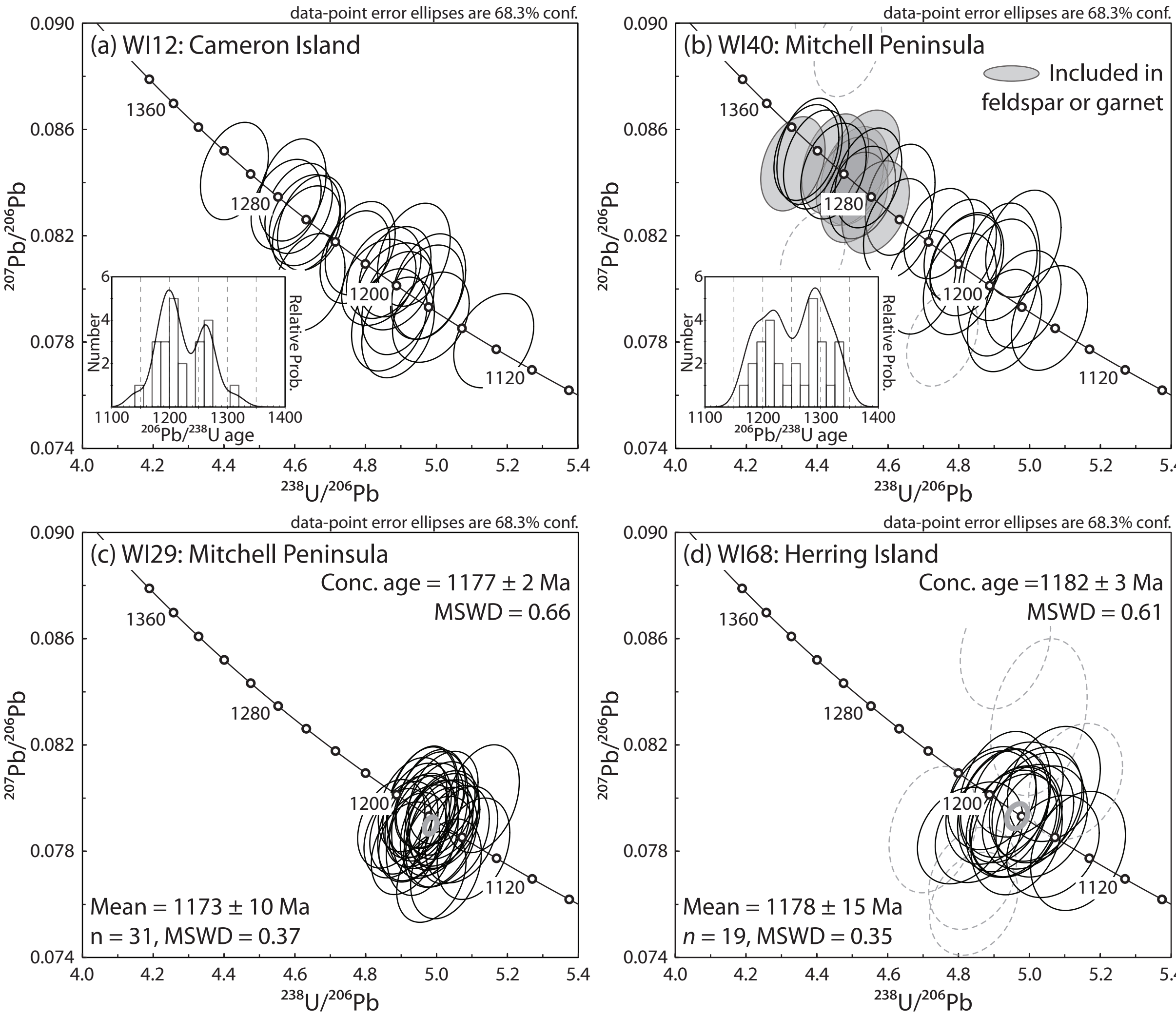

Figure 5: Tera–Wasserburg concordia plots for each of the samples in the study. Analyses denoted by dashed grey lines are excluded from the calculations based on discordance. Weighted mean ages are the $^{207}Pb/^{206}Pb$ ages. (a) Sample WI12. (b) Sample WI40. (c) Sample WI29. (d) Sample WI68.

age of 1177 ± 2 Ma (Fig. 5c; $MSWD_{(conc+equiv)}$ = 0.66, $probability_{(conc+equiv)}$ = 0.98) and a $^{207}Pb/^{206}Pb$ weighted average age of 1173 ± 10 Ma (MSWD = 0.37).

5.1.4. Sample WI68

Twenty-five analyses were collected from twenty grains located along grain boundaries or included within biotite. The grains are 20–80 μm in diameter and appear unzoned in BSE images (Fig. 4d). Six analyses that are >5% discordant are excluded from further interpretation. The remaining 19 analyses yield a concordia age of 1182 ± 3 Ma (Fig. 5d; $MSWD_{(conc+equiv)}$ = 0.61, $probability_{(conc+equiv)}$ = 0.97) and a $^{207}Pb/^{206}Pb$ weighted average age of 1178 ± 15 Ma (MSWD = 0.35).

5.2. Mineral chemistry

Representative electron microprobe analyses of the compositions of minerals in each sample are presented in Table 3. The compositional ranges for selected minerals are summarised in Table 4. The calculated end member proportions discussed below are defined in Table 4.

5.2.1. Garnet

Garnet occurs in samples WI12, WI29 and

WI40. Garnet cores in all three samples have similar X_{alm} of 0.54–0.59 and X_{grs} of 0.02–0.04. Garnet grains in sample WI12 have lower X_{py} of 0.12–0.14 and higher X_{sps} of 0.27–0.28 whereas garnet grains in sample WI29 have higher X_{py} of 0.29–0.34 and lower X_{sps} of 0.10. Garnet grains in sample WI40 have X_{py} of 0.21–0.24 and X_{sps} of 0.10–0.16.

Inclusions of magnetite and biotite in garnet cause a large spread in the core values for X_{alm} and X_{py}, particularly in sample WI29. Despite the range in core values, all samples do show minor zoning trends in some elements. Garnet grains in samples WI40 and WI29 show a minor increase in X_{alm} from core to rim, whereas all samples show a decrease in X_{py} from core to rim. None of the samples show significant zoning trends in X_{grs} and X_{sps}. Sample WI29 contains a second, fine-grained morphology of garnet that occurs at the margin between coarse-grained garnet and the biotite–quartz symplectites. The fine-grained garnet has a composition that is very similar to the rim analyses for the garnet porphyroblasts.

5.2.2. Biotite

Titanium content of biotite from all samples varies from 0.17 to 0.29 cations p.f.u. Biotite shows a decrease in X_{Fe} with increasing metamorphic grade, from 0.50–0.57 in sample WI12 to 0.37–0.42 in samples WI40 and WI29 and 0.24–0.29 in sample WI68. Conversely, F contents increase with increasing metamorphic grade from 0.05–0.07 anions p.f.u. in sample WI12 to 0.39–0.54 anions p.f.u. in sample WI68.

5.2.3. Orthopyroxene

Orthopyroxene occurs in sample WI29 and sample WI68. Sample WI29 has X_{Fe} in the range 0.36–0.39 and y(opx) of 0.07–0.12. Orthopyroxene in sample WI68 has X_{Fe} in the range 0.22–0.36 and y(opx) predominantly in the range 0.08–0.11.

5.2.4. Magnetite and ilmenite

Magnetite and ilmenite commonly occur in direct contact, with magnetite the dominant oxide. Ilmenite in all samples contains appreciable Mn, ranging from 0.07–0.32 cations p.f.u. Ilmenite in all samples is typically pure ilmenite, with i(ilm) values between 0.80–1.00.

5.2.5. Spinel

Spinel is abundant in sample WI40 and is dominantly hercynitic (X_{Fe} = 0.70–0.81) with 0.02–0.05 cations p.f.u Mn and 0.03 cations p.f.u Zn. In sample WI29 spinel is exolved from magnetite and contains 0.01 cations p.f.u Mn and 0.05–0.11 cations p.f.u Zn.

5.2.6. Feldspars

K-feldspar occurs in all samples and shows a general increase in X_{Na} with metamorphic grade from 0.07–0.13 in sample WI12 to 0.12–0.35 in sample WI68. X_{Na} of plagioclase in samples WI29 and WI68 varies from 0.26–0.31 and from 0.31–0.39 in samples WI12 and WI40.

5.2.7. Sillimanite

Sillimanite occurs in samples WI12 and WI40. Sillimanite in sample WI12 contains 0.91–1.64 wt% Fe_2O_3 (measured as FeO). In sample WI40, sillimanite within the plagioclase–magnetite–spinel reaction textures contains 0.99–1.27 wt% Fe_2O_3 whereas sillimanite included in garnet has a higher Fe_2O_3 content of 2.39 wt%.

5.3. Pressure temperature conditions

5.3.1. Interpretation of the mineral reaction microstructures

Samples WI40 and WI29 contain mineral reaction microstructures. One interpretation

Table 3: Representative electron microprobe analyses.

	WI12: Cameron Island									WI40: Mitchell Peninsula		
Mineral	g core	g rim	bi	cd	ksp	pl	mt	ilm	sill	g core	g rim	bi
SiO_2	36.77	36.84	34.75	47.66	63.47	58.35	0.00	0.08	35.94	37.03	36.97	35.66
TiO_2	0.02	0.00	3.68	0.01	0.02	0.00	0.02	51.64	0.00	0.03	0.02	4.29
Al_2O_3	20.69	20.79	19.25	33.47	19.10	25.94	0.28	0.06	62.60	21.20	21.37	16.60
Cr_2O_3	0.00	0.04	0.03	0.01	0.00	0.00	0.39	0.03	0.01	0.00	0.00	0.05
FeO	25.24	25.21	17.83	7.83	0.04	0.00	89.50	37.36	0.94	26.53	26.82	15.12
MnO	12.30	12.85	0.34	1.12	0.00	0.01	0.09	9.38	0.00	7.20	7.39	0.17
MgO	3.10	2.79	9.15	8.18	0.00	0.00	0.00	0.13	0.02	6.22	5.35	13.33
ZnO	0.01	0.00	0.05	0.10	0.00	0.03	0.12	0.03	0.00	0.01	0.01	0.01
CaO	1.26	1.10	0.00	0.00	0.00	7.03	0.00	0.00	0.00	1.00	1.05	0.01
Na_2O	0.04	0.02	0.16	0.27	1.03	7.70	0.00	0.04	0.01	0.00	0.00	0.13
K_2O	0.01	0.01	9.60	0.00	14.84	0.24	0.00	0.02	0.00	0.00	0.00	9.61
Cl	0.01	0.00	0.03	0.01	0.00	0.00	0.01	0.01	0.01	0.00	0.01	0.02
F	0.00	0.03	0.28	0.00	0.00	0.00	0.25	0.04	0.00	0.05	0.03	1.44
Total	**99.47**	**99.68**	**95.14**	**98.66**	**98.51**	**99.31**	**90.66**	**98.81**	**99.53**	**99.27**	**99.04**	**96.44**
No. Oxygens	12	12	11	18	8	8	4	3	5	12	12	11
Si	2.98	2.99	2.64	4.91	2.97	2.63	0.00	0.00	0.98	2.94	2.96	2.64
Ti	0.00	0.00	0.21	0.00	0.00	0.00	0.00	0.99	0.00	0.00	0.00	0.24
Al	1.98	1.99	1.72	4.07	1.05	1.38	0.01	0.00	2.00	1.99	2.02	1.45
Cr	0.00	0.00	0.00	0.00	0.00	0.00	0.01	0.00	0.00	0.00	0.00	0.00
Fe^{3+}	0.07	0.04	-	-	-	-	1.94	0.01	0.05	0.11	0.06	-
Fe^{2+}	1.64	1.67	1.13	0.68	0.00	0.00	1.03	0.78	0.00	1.65	1.74	0.94
Mn^{2+}	0.84	0.88	0.02	0.10	0.00	0.00	0.00	0.20	0.00	0.48	0.50	0.01
Mg	0.37	0.34	1.04	1.26	0.00	0.00	0.00	0.00	0.00	0.74	0.64	1.47
Zn	0.00	0.00	0.00	0.01	0.00	0.00	0.00	0.00	0.00	0.00	0.00	0.00
Ca	0.11	0.10	0.00	0.00	0.00	0.34	0.00	0.00	0.00	0.09	0.09	0.00
Na	0.01	0.00	0.02	0.05	0.09	0.67	0.00	0.00	0.00	0.00	0.00	0.02
K	0.00	0.00	0.93	0.00	0.88	0.01	0.00	0.00	0.00	0.00	0.00	0.91
Cl	0.00	0.00	0.00	0.00	0.00	0.00	0.00	0.00	0.00	0.00	0.00	0.00
F	0.00	0.01	0.07	0.00	0.00	0.00	0.03	0.00	0.00	0.01	0.01	0.34
Total Cations	**8.00**	**8.01**	**7.80**	**11.08**	**5.00**	**5.03**	**3.03**	2.00	3.00	8.01	**8.01**	**8.02**

Table 3 (continued).

	WI40 (continued)							WI29: Mitchell Peninsula				
Mineral	cd	ksp	pl	mt	ilm	sp	sill	g core	g rim	g sympl	bi	ksp
SiO_2	47.92	63.20	57.83	0.06	0.05	0.07	35.68	37.14	37.73	37.83	36.76	63.11
TiO_2	0.03	0.02	0.02	0.02	49.84	0.03	0.05	0.01	0.00	0.00	4.69	0.01
Al_2O_3	33.60	18.75	26.03	0.26	0.01	55.27	62.09	21.50	21.63	21.55	16.56	17.93
Cr_2O_3	0.00	0.04	0.02	0.09	0.04	0.18	0.00	0.00	0.03	0.00	0.05	0.00
FeO	5.44	0.03	0.13	89.62	43.12	35.66	1.15	25.60	27.31	27.71	14.75	0.01
MnO	0.57	0.02	0.00	0.05	4.41	1.14	0.06	4.60	4.69	5.03	0.11	0.00
MgO	10.25	0.00	0.00	0.00	0.25	4.47	0.01	8.59	7.64	6.72	14.00	0.00
ZnO	0.07	0.00	0.00	0.04	0.05	1.29	0.00	0.06	0.00	0.08	0.06	0.00
CaO	0.02	0.04	7.41	0.00	0.00	0.00	0.00	1.07	0.90	0.93	0.02	0.07
Na_2O	0.09	1.21	7.47	0.02	0.00	0.03	0.01	0.00	0.01	0.01	0.22	1.82
K_2O	0.01	14.80	0.14	0.01	0.00	0.00	0.01	0.00	0.01	0.00	9.46	13.83
Cl	0.00	0.00	0.01	0.01	0.02	0.00	0.00	0.00	0.00	0.00	0.03	0.00
F	0.00	0.00	0.00	0.29	0.13	0.02	0.00	0.06	0.02	0.06	1.29	0.00
Total	**98.01**	**98.11**	**99.07**	**90.48**	**97.92**	**98.15**	**99.05**	**98.64**	**99.98**	**99.93**	**98.01**	**96.78**
No. Oxygens	18	8	8	4	3	4	5	12	12	12	11	8
Si	4.91	2.97	2.61	0.00	0.00	0.00	0.97	2.92	2.95	2.97	2.67	2.99
Ti	0.00	0.00	0.00	0.00	0.96	0.00	0.00	0.00	0.00	0.00	0.26	0.00
Al	4.06	1.04	1.39	0.01	0.00	1.88	2.00	1.99	1.99	2.00	1.42	1.00
Cr	0.00	0.00	0.00	0.00	0.00	0.00	0.00	0.00	0.00	0.00	0.00	0.00
Fe^{3+}	-	-	-	1.94	0.06	0.11	0.05	0.15	0.11	0.04	-	-
Fe^{2+}	0.47	0.00	0.00	1.03	0.87	0.75	0.00	1.53	1.67	1.78	0.89	0.00
Mn^{2+}	0.05	0.00	0.00	0.00	0.10	0.03	0.00	0.31	0.31	0.33	0.01	0.00
Mg	1.57	0.00	0.00	0.00	0.01	0.19	0.00	1.01	0.89	0.79	1.51	0.00
Zn	0.01	0.00	0.00	0.00	0.00	0.03	0.00	0.00	0.00	0.00	0.00	0.00
Ca	0.00	0.00	0.36	0.00	0.00	0.00	0.00	0.09	0.08	0.08	0.00	0.00
Na	0.02	0.11	0.65	0.00	0.00	0.00	0.00	0.00	0.00	0.00	0.03	0.17
K	0.00	0.89	0.01	0.00	0.00	0.00	0.00	0.00	0.00	0.00	0.88	0.84
Cl	0.00	0.00	0.00	0.00	0.00	0.00	0.00	0.00	0.00	0.00	0.00	0.00
F	0.00	0.00	0.00	0.04	0.01	0.00	0.00	0.02	0.00	0.01	0.30	0.00
Total Cations	**11.07**	**5.01**	**5.03**	**3.04**	**2.01**	**3.00**	**3.00**	**8.00**	**8.00**	**8.00**	**7.97**	**5.01**

Table 3 (continued).

	WI29 (continued)				WI68: Herring Island						
Mineral	pl	opx	mt	ilm	bi	cd	ksp	pl	opx	mt	ilm
SiO_2	60.50	47.83	0.02	0.01	38.50	49.61	64.91	60.66	48.92	0.00	0.01
TiO_2	0.00	0.11	0.01	49.85	3.49	0.00	0.02	0.02	0.10	0.00	51.49
Al_2O_3	22.95	6.16	0.22	0.09	14.62	33.19	18.74	24.55	6.35	0.17	0.02
Cr_2O_3	0.02	0.02	0.16	0.00	0.00	0.00	0.00	0.02	0.03	0.02	0.00
FeO	0.05	24.02	90.55	44.66	11.15	4.55	0.02	0.00	22.36	92.45	40.17
MnO	0.00	1.17	0.03	3.43	0.16	0.27	0.00	0.01	1.22	0.05	6.61
MgO	0.00	19.54	0.00	0.29	18.01	11.27	0.01	0.01	20.88	0.02	0.44
ZnO	0.03	0.01	0.10	0.07	0.02	0.00	0.00	0.00	0.05	0.00	0.00
CaO	5.66	0.07	0.00	0.00	0.01	0.00	0.21	6.20	0.06	0.00	0.00
Na_2O	8.42	0.00	0.02	0.01	0.12	0.07	2.17	8.43	0.01	0.00	0.03
K_2O	0.47	0.00	0.02	0.00	9.88	0.01	13.73	0.17	0.01	0.00	0.00
Cl	0.00	0.00	0.00	0.01	0.01	0.00	0.00	0.01	0.00	0.00	0.00
F	0.00	0.00	0.46	0.22	2.22	0.00	0.00	0.00	0.07	0.32	0.08
Total	**98.10**	**98.95**	**91.57**	**98.65**	**98.19**	**98.97**	**99.81**	**100.08**	**100.05**	**93.02**	**98.87**
No. Oxygens	8	6	4	3	11	18	8	8	6	4	3
Si	2.75	1.81	0.00	0.00	2.74	4.99	2.98	2.70	1.82	0.00	0.00
Ti	0.00	0.00	0.00	0.96	0.19	0.00	0.00	0.00	0.00	0.00	0.98
Al	1.23	0.28	0.01	0.00	1.23	3.94	1.01	1.29	0.28	0.01	0.00
Cr	0.00	0.00	0.00	0.00	0.00	0.00	0.00	0.00	0.00	0.00	0.00
Fe^{3+}	-	0.09	1.93	0.07	-	-	-	-	0.07	1.95	0.02
Fe^{2+}	0.00	0.67	1.05	0.89	0.66	0.38	0.00	0.00	0.63	1.04	0.83
Mn^{2+}	0.00	0.04	0.00	0.07	0.01	0.02	0.00	0.00	0.04	0.00	0.14
Mg	0.00	1.10	0.00	0.01	1.91	1.69	0.00	0.00	1.16	0.00	0.02
Zn	0.00	0.00	0.00	0.00	0.00	0.00	0.00	0.00	0.00	0.00	0.00
Ca	0.28	0.00	0.00	0.00	0.00	0.00	0.01	0.30	0.00	0.00	0.00
Na	0.74	0.00	0.00	0.00	0.02	0.01	0.19	0.73	0.00	0.00	0.00
K	0.03	0.00	0.00	0.00	0.90	0.00	0.80	0.01	0.00	0.00	0.00
Cl	0.00	0.00	0.00	0.00	0.00	0.00	0.00	0.00	0.00	0.00	0.00
F	0.00	0.00	0.06	0.02	0.50	0.00	0.00	0.00	0.01	0.04	0.01
Total Cations	**5.02**	**4.00**	**3.06**	**2.02**	**8.16**	**11.04**	**5.01**	**5.02**	**4.01**	**3.04**	**2.01**

Table 4: Range of chemistry for selected minerals.

	WI12	**WI40**	**WI29**	**WI68**
Garnet (core)				
X_{alm}	0.55–0.58	0.56–0.59	0.54–0.58	–
X_{py}	0.12–0.14	0.21–0.24	0.29–0.34	–
X_{grs}	0.03–0.04	0.03	0.02–0.03	–
X_{sps}	0.27–0.28	0.16–0.18	0.10	–
Garnet (rim)				
X_{alm}	0.55–0.58	0.59–0.60	0.55–0.60	–
X_{py}	0.11–0.13	0.19–0.23	0.27–0.33	–
X_{grs}	0.03–0.04	0.03	0.02–0.03	–
X_{sps}	0.28–0.29	0.16–0.18	0.10	–
Garnet (symplectite)				
X_{alm}	–	–	0.58–0.62	–
X_{py}	–	–	0.25–0.30	–
X_{grs}	–	–	0.02–0.03	–
X_{sps}	–	–	0.10–0.11	–
Biotite				
X_{Fe}	0.50–0.57	0.37–0.42	0.37–0.39	0.24–0.29
Ti (cpfu)	0.17–0.23	0.21–0.25	0.25–0.29	0.19–0.25
F (apfu)	0.05–0.07	0.30–0.36	0.30–0.37	0.39–0.54
Cordierite				
X_{Fe}	0.32–0.35	0.23–0.25	–	0.18–0.19
Orthopyroxene				
X_{Fe}	–	–	0.36–0.39	0.22–0.36
y(opx)	–	–	0.07–0.12	0.08–0.11
Magnetite				
p(mt)	0.99–1.00	0.97–0.99	0.99–1.00	0.96–1.00
Ilmenite				
i(ilm)	0.96–0.99	0.93–0.99	0.92–0.96	0.80–1.00
Mn (cpfu)	0.14–0.20	0.09–0.10	0.07–0.08	0.11–0.32
Spinel				
Mn (cpfu)	–	0.02–0.05	0.01	–
Zn (cpfu)	–	0.03	0.05–0.11	–
Cr (cpfu)	–	0.003–0.005	0.004–0.006	–
K-feldspar				
X_{Na}	0.07–0.13	0.11–0.18	0.17–0.23	0.12–0.35
Plagioclase				
X_{Ca}	0.32–0.36	0.31–0.39	0.26–0.29	0.29–0.31

X_{alm} = Fe/(Fe + Mg + Ca + Mn)
X_{py} = Mg/(Fe + Mg + Ca + Mn)
X_{grs} = Ca/(Fe + Mg + Ca + Mn)
X_{sps} = Mn/(Fe + Mg + Ca + Mn)
X_{Fe} = Fe/(Fe^{2+} + Mg)
y(opx) = x_{AlM1}
X_{Na} = Na/(Na + Ca + K)
X_{Ca} = Na/(Na + Ca + K)

of reaction microstructures is that they reflect an arrested attempt to produce a new equilibrium assemblage, with the partially replaced minerals comprising disequilibrium relics (Kelsey and Hand, 2015). An alternative interpretation is that the newly formed minerals were in effective equilibrium with the relict minerals, producing a composite mineral assemblage in which the modal proportion of the reactants was simply reduced (Kelsey and Hand, 2015; Morrissey et al., 2016a; White et al., 2002).

In sample WI40, the mineral reaction microstructures are characterised by the partial replacement of garnet by a cordierite–spinel–magnetite-bearing assemblage and garnet and sillimanite by a plagioclase–cordierite–spinel–magnetite–ilmenite-bearing assemblage. Sillimanite only occurs as inclusions or relict grains within the mineral reaction microstructures (Fig. 3c) and is therefore not interpreted to form part of the M_2 equilibrium assemblage. The presence of a significant amount of MnO in spinel suggests that garnet was also partially replaced (Tables 3 and 4). However, garnet remains relatively abundant in the reaction microstructures (Fig. 3b and c) as well as in parts of the sample that do not have reaction microstructures, suggesting that it was part of the M_2 equilibrium assemblage (Table 2).

In sample WI29, biotite–quartz symplectites appear to have pseudomorphed another mineral. Small, rare grains of orthopyroxene occur near the biotite–quartz reaction microstructures (Fig. 3e). Similar biotite–quartz symplectites have been interpreted to represent replacement of a ferromagnesian mineral such as orthopyroxene or garnet in the presence of silicate melt (Sawyer, 2008). Isobaric *P–T* paths with limited melt escape allow back reaction (sensu lato), where reactions crossed along the prograde path are recrossed during the retrograde evolution (Brown, 2002; Kriegsman, 2001). Therefore, we interpret the biotite–quartz symplectites in sample WI29 to represent back reaction of a continuous fluid-absent melting reaction of the general form bi + q = melt ± opx ± g ± ksp (Vielzeuf and Holloway, 1988), whereby the modal abundance of biotite and quartz increases with cooling at the expense of melt and other phases on the right hand side of the reaction. Garnet is interpreted to have decreased in abundance, as the bi + q symplectites surround garnet grains, but is interpreted to form part of the peak assemblage (Table 2). Locally, fine-grained younger-generation garnet contains inclusions of bladed quartz, suggesting that garnet abundance may have increased slightly in some domains after the formation of the bi + q symplectites. Orthopyroxene is uncommon and therefore the remaining small grains of orthopyroxene are interpreted as disequilibrium relics of the peak assemblage (Table 2).

5.3.2. Assumptions and limitations of the P–T modelling

A number of limitations and assumptions in the *P–T* modelling must be acknowledged before interpreting the pseudosections. One limitation is that some of the components occurring in natural rocks, such as ZnO, Cr_2O_3 and P_2O_5, cannot be effectively modelled. Small amounts of apatite occur in some samples in this study. Apatite cannot be modelled in the MnNCKFMASHTO system (or any other system currently) but affects the calcium budget of the rock, resulting in models showing increased stability of Ca-bearing phases such as garnet and plagioclase. However, the bulk compositions of most samples contain very little P_2O_5 (Appendix

1), and all samples contain monazite, so the amount of apatite is interpreted to be minor (<<0.5%). Additionally, components such as ZnO, Cr_2O_3 and MnO are not incorporated into the *a–x* models for spinel, but are known to increase spinel stability to higher pressures and lower temperatures (Guiraud et al., 1997; Nichols et al., 1992; Tajcmanová et al., 2009; White et al., 2000, 2002). Spinel in this study contains minor amounts of these components (Tables 3 and 4) and therefore spinel-bearing fields cannot be used to provide absolute constraints on the *P–T* conditions.

Calculated *P–T* pseudosection models may result in large fields that provide very little quantitative *P–T* information. The range of *P–T* conditions can be further constrained using mineral proportion and compositional contours, particularly in cases where composition or mineral proportions change rapidly across a field (e.g. Powell and Holland, 2008). However, in high temperature terranes diffusive-related processes continue to operate during cooling, meaning that minerals in granulite facies rocks commonly do not record their original peak metamorphic chemical compositions (e.g. Fitzsimons and Harley, 1994; Frost and Chacko, 1989; Pattinson et al., 2003; Pattison and Bégin, 1994; Powell and Holland, 2008). Fe–Mg exchange thermometers may underestimate temperatures by >100 °C (Pattison and Bégin, 1994), limiting their utility as a further constraint on peak conditions. However, temperature-sensitive net transfer or coupled-exchange (Tshermaks) equilibria such as aluminium in orthopyroxene (*y*(opx)) are believed to be more robust at high temperatures (e.g. Fitzsimons and Harley, 1994; Pattison and Bégin, 1994).

Melt loss during prograde to peak metamorphism allows the preservation of anhydrous granulite-facies mineral assemblages that would otherwise be retrogressed during cooling (Brown, 2002; White and Powell, 2002). Therefore, at least in samples that do not contain significant development of retrograde symplectites or coronas, the modelled modal proportions should approximate the preserved mineral assemblage in the rock and may provide more robust constraints on the peak metamorphic conditions than the mineral compositions (Palin et al., in press; Powell and Holland, 2008). One limitation of this approach relates to natural petrographic variation at the sample and thin section scale (Palin et al., in press). Another is that determining the appropriate equilibration volume and therefore the effective bulk composition in high grade rocks is difficult, as it is likely to vary throughout the metamorphic evolution as a result of melt loss, changing temperature and different diffusion rates of elements (Guevara and Caddick, 2016; Kelsey and Hand, 2015). These factors may result in a mismatch between the mineral proportions observed in a 2D thin section and those present in the 3D, hand sample-sized volume used for XRF analysis. In addition, the modal proportions of minerals provided by THERMOCALC are mole proportions normalised to one oxide total basis and therefore are not a direct equivalent of the volumetric abundance of the mineral in the rock, but are approximately comparable.

We acknowledge that these uncertainties in the modelling place limitations on providing absolute constraints on the conditions of metamorphism (e.g. Palin et al., in press). However, we have selected samples with varying bulk compositions and mineral assemblages to minimise both systematic errors relating to *a–x* models and geological error. We have also provided *P–T* pseudosection models contoured for modal proportions and *y*(opx) values, to further constrain conditions and also as a way of assessing the correspondence between bulk composition and the observed petrographic relationships at thin section scale. The aim of the *P–T* modelling is therefore to provide general constraints on the conditions and thermal gradients of metamorphism.

5.3.3. Sample WI12: Cameron Island

The peak assemblage in sample WI12 is interpreted to be garnet + plagioclase + K-feldspar + biotite + cordierite + magnetite + ilmenite + sillimanite + quartz + silicate melt (Fig. 3a; Table 2). This assemblage occurs in a narrow field over a large range of conditions, from 690–800 °C and 2.9–5.9 kbar (Fig. 6a). This field is bounded by the elevated solidus and absence of cordierite at lower temperatures and pressures and by the absence of sillimanite at higher temperatures and pressures. The region of *P–T* space that bests matches the observed proportions of garnet, plagioclase, biotite, cordierite and sillimanite (Table 2) is between 3.7–4.2 kbar and 710–740 °C, in the region of the white star (Fig. 6a). This sample does not contain mineral reaction microstructures that could provide further information on the *P–T* evolution.

5.3.4. Sample WI40: Mitchell Peninsula

Sample WI40 contains well preserved reaction microstructures and textural evidence for two distinct mineral assemblages, an M_1 quartz–sillimanite-bearing assemblage and an M_2 cordierite–spinel-bearing assemblage (Table 2, Fig. 3b and c). However, likely melt loss during M_1 and M_2 metamorphism means that the current bulk composition is only appropriate for modelling the M_2 mineral assemblage, and no quantitative constraints can be placed on the conditions of M_1 metamorphism.

The interpreted M_2 assemblage in sample WI40 is cordierite + spinel + magnetite + ilmenite + plagioclase + K-feldspar + biotite + silicate melt. Garnet is also interpreted to form part of the peak assemblage, but in decreased abundance compared to M_1. This assemblage occurs over a wide range of conditions from 2.3 to 5.9 kbar and 830 to 900 °C (Fig. 6b). Garnet and cordierite proportions in thin section are approximately 18% and 20 % respectively, suggesting that peak pressures were likely to have been in the region of 3.5–4.5 kbar. The calculated proportions of plagioclase and K-feldspar in the interpreted peak field do not correspond to observations and so do not provide further constraints. This discrepancy may be due to the incorporation of different amounts of K-feldspar-rich leucosome in the rock volume analysed for the XRF whole rock composition compared to the thin section domain. Spinel in this sample contains significant MnO and minor amounts of Cr_2O_3 and ZnO, so the spinel stability field does not provide a robust temperature constraint. However, cordierite and plagioclase abundance decreases with increasing temperature, whereas the abundance of garnet increases (Fig. 6b). This is inconsistent with our interpretation of the petrographic observations, which is that the spatial arrangement of the minerals suggests

Figure 6 (facing pages): Calculated *P–T* pseudosection models for each sample. The bulk-rock composition in mol.% is given above each pseudosection. The bold dashed line in each pseudosection is the solidus. TC Investigator diagrams showing modal proportion contours for minerals of interest are presented for each sample. The white line on each diagram represents the value that corresponds with (or is closest to) the estimated proportion of the mineral in the sample as provided in Table 2. The white star represents the most likely *P–T* conditions for each sample within the peak field, based on the modal proportion contours. (a) Sample WI12. (b) Sample WI40. (c) Sample WI29. (d) Sample WI68.

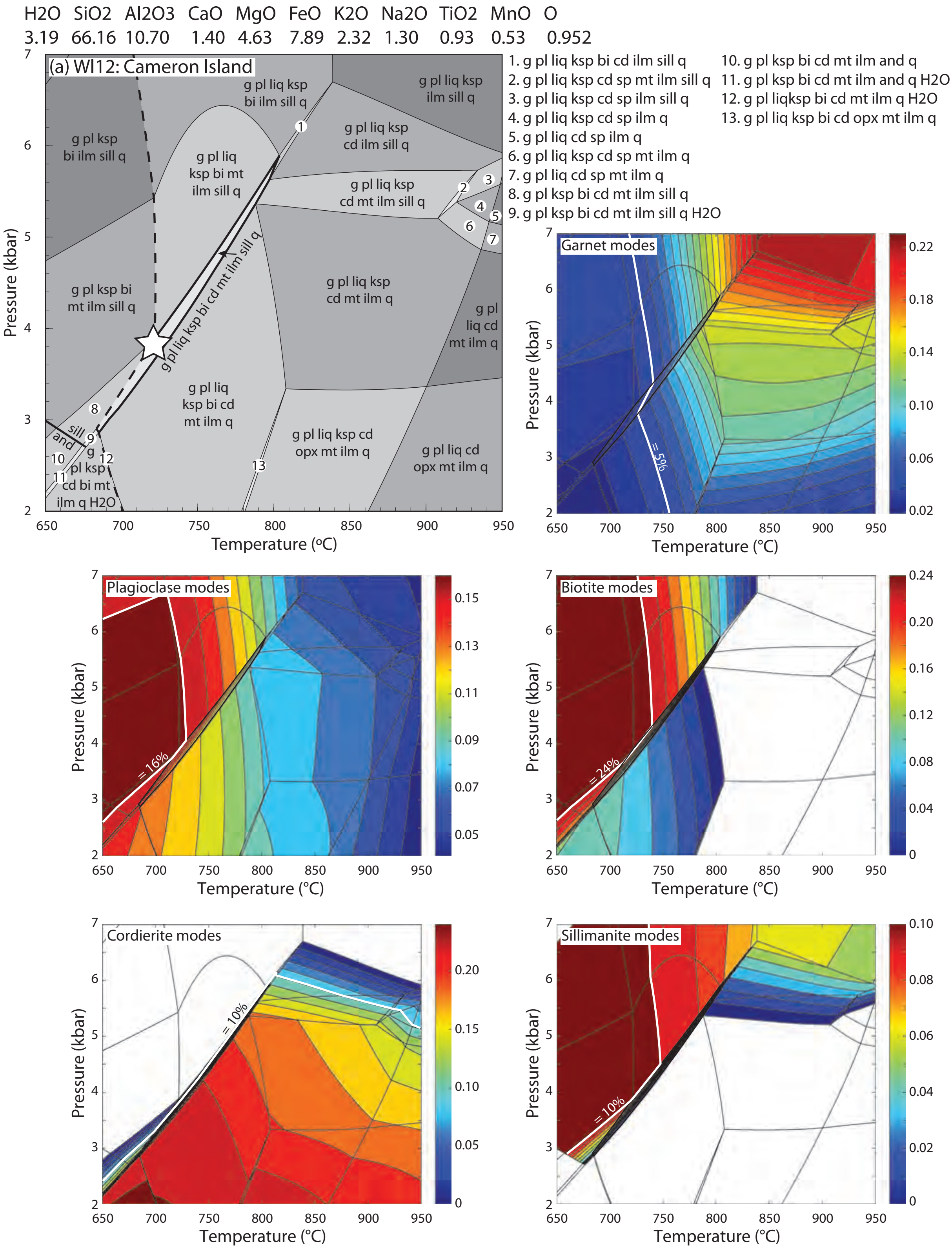

Figure 6: Calculated *P–T* pseudosection models for each sample.

H2O	SiO2	Al2O3	CaO	MgO	FeO	K2O	Na2O	TiO2	MnO	O
2.51	52.23	14.16	1.91	8.54	11.56	3.33	1.98	1.24	1.10	1.45

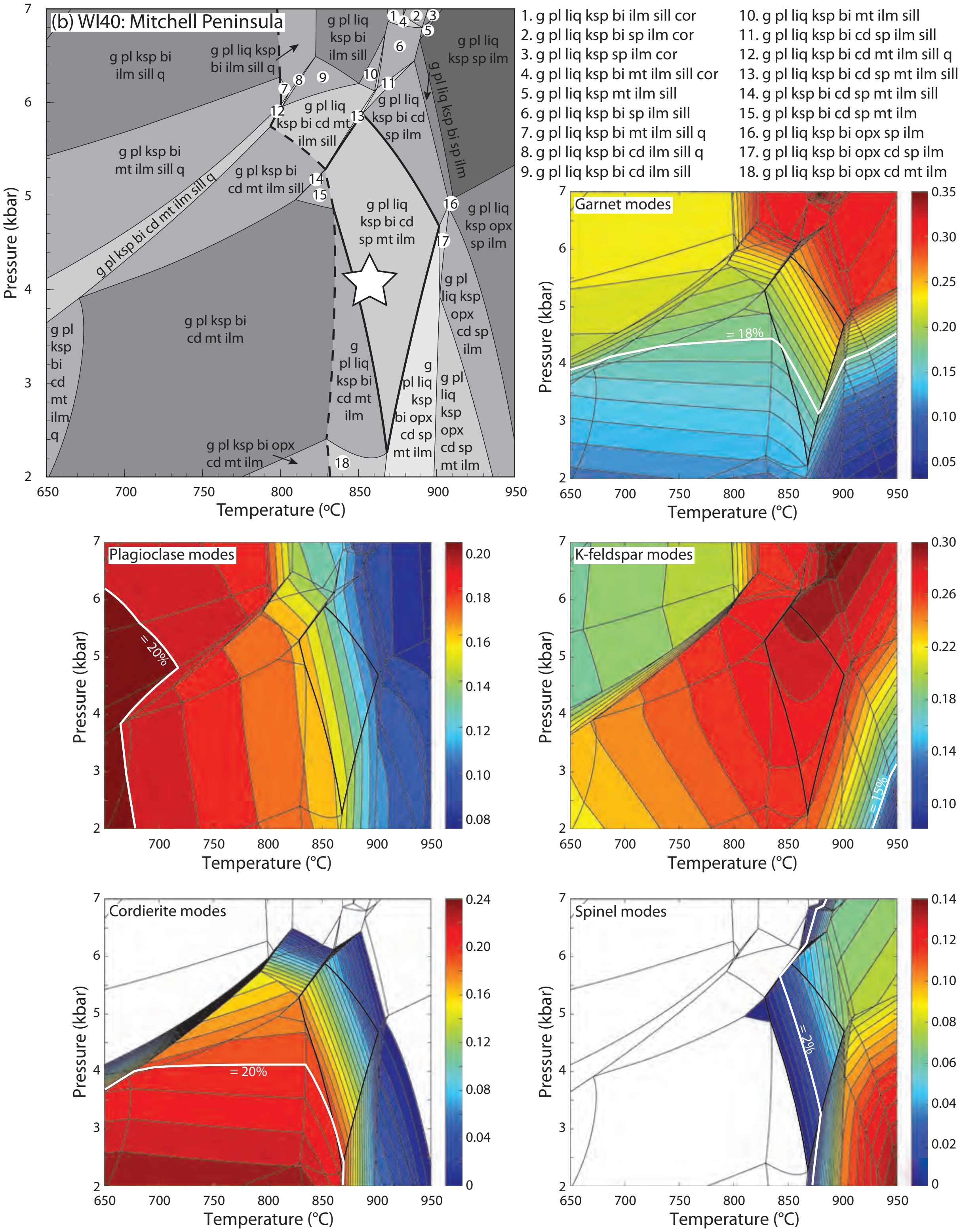

Figure 6 (continued).

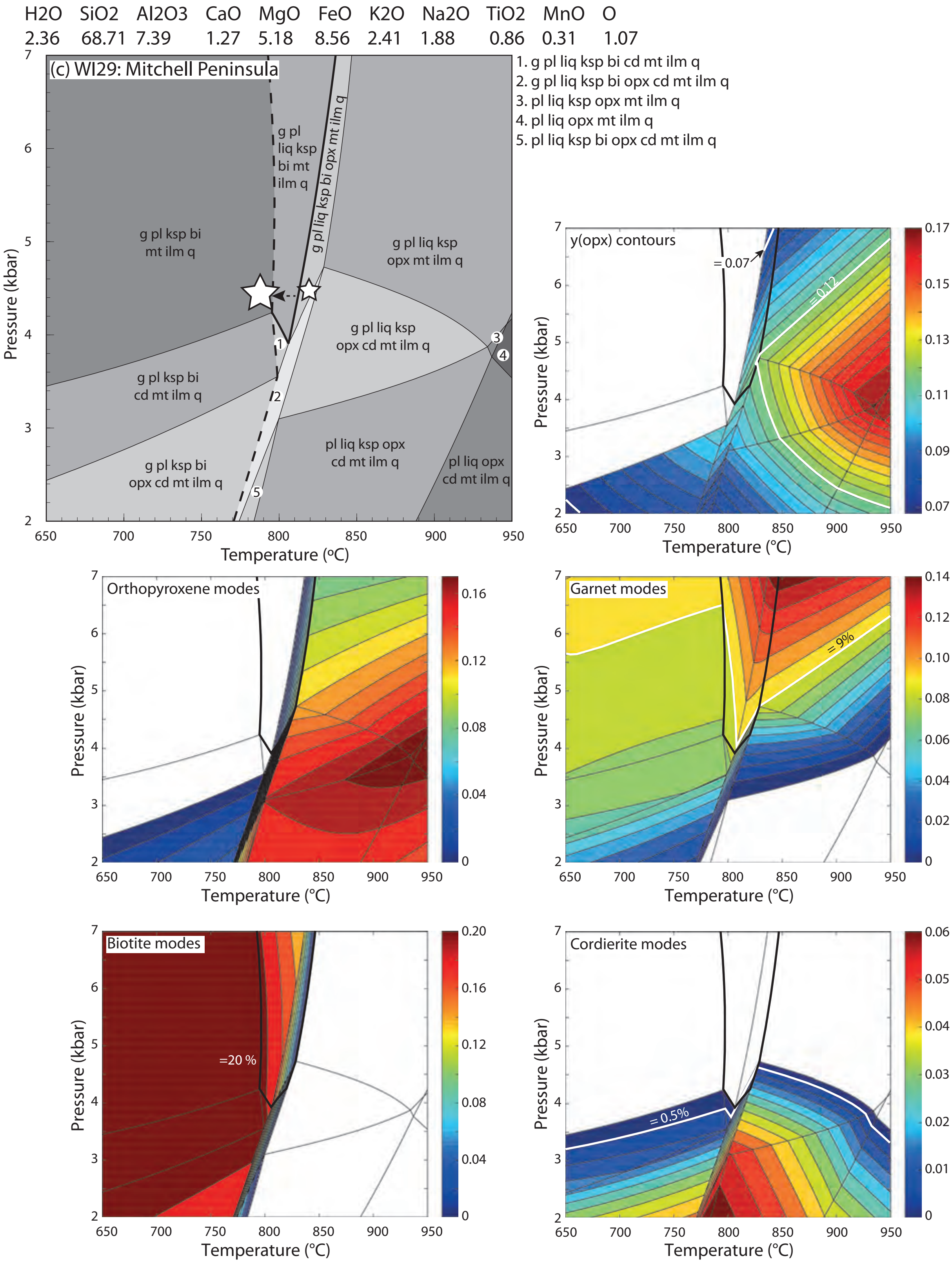

Figure 6 (continued).

H2O	SiO2	Al2O3	CaO	MgO	FeO	K2O	Na2O	TiO2	MnO	O
0.89	73.32	8.93	1.03	7.13	4.75	2.32	1.52	0.47	0.12	0.48

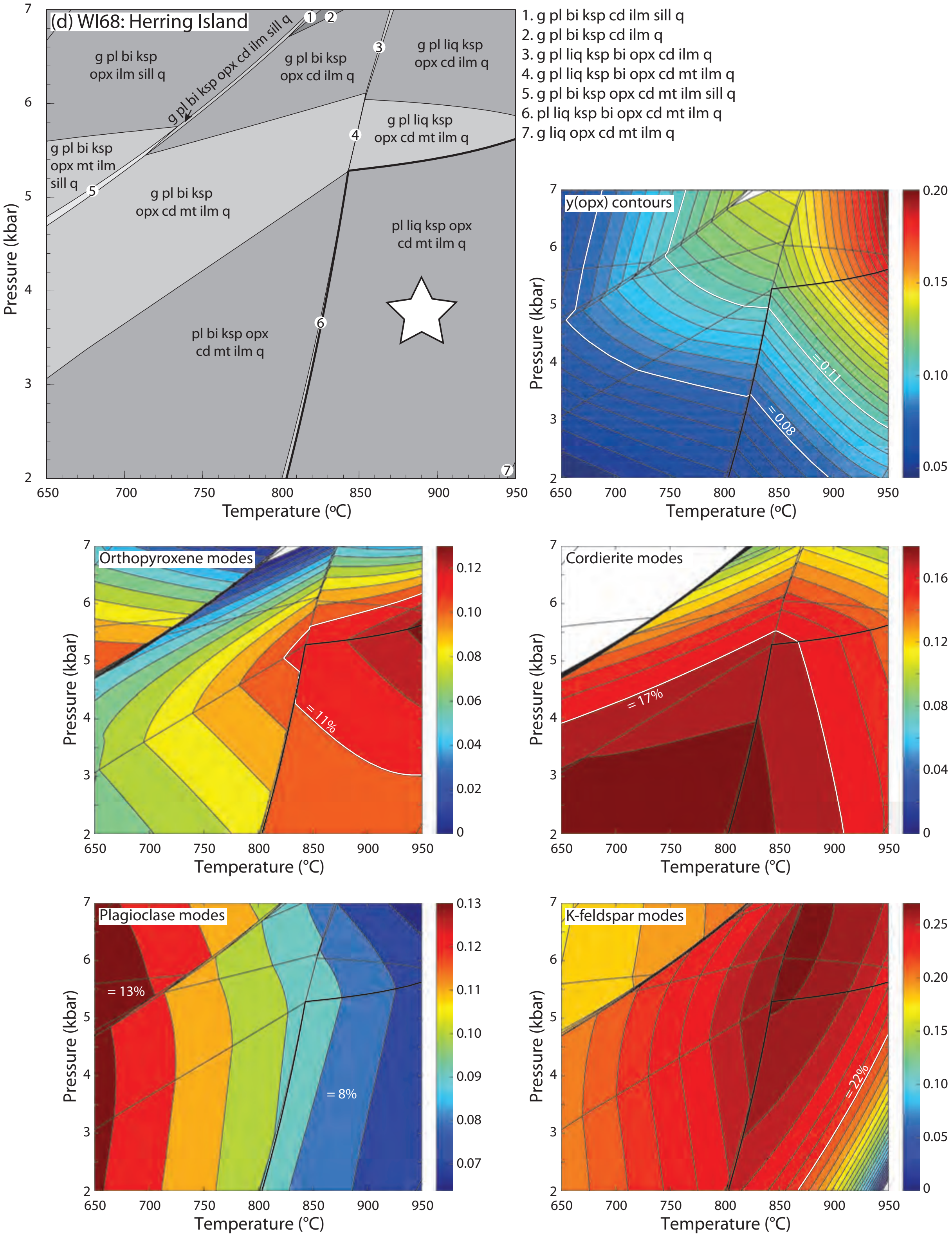

Figure 6 (continued).

that cordierite and plagioclase form at the expense of garnet. If this is correct, the lower-temperature part of this field corresponds better to the petrographic observations.

5.3.5. Sample WI29: Mitchell Peninsula

Sample WI29 contains the assemblage garnet + plagioclase + K-feldspar + magnetite + ilmenite + quartz. It also contains small grains of orthopyroxene and abundant reaction microstructures consisting of bladed biotite and quartz, interpreted to be retrograde replacement of peak orthopyroxene and garnet (Table 2, Fig. 3d and e). The peak assemblage with orthopyroxene occurs over a wide interval at pressures in excess of 3.9 kbar and temperatures in excess of 805 °C (Fig. 6c). The absence of peak cordierite provides a lower pressure constraint. Determining the likely proportion of orthopyroxene at peak conditions is difficult due to the extensive development of biotite–quartz symplectites and the likelihood that some of the symplectites have replaced garnet. However, biotite is abundant in this sample and can be coarse-grained, suggesting that both biotite and orthopyroxene were present at peak conditions and therefore temperatures were below ~ 850 °C. Orthopyroxene in this sample has a large range of y(opx) values between 0.07 to 0.12, which corresponds to the modelled orthopyroxene compositions in the peak field but does not further constrain conditions (Fig. 6c).

The currently preserved, effectually orthopyroxene-absent assemblage occurs in a large field that extends from 800–830 °C and pressures above 3.9 kbar (Fig. 6c). This sample also contains a second stage of retrograde mineral reaction microstructures. Fine-grained, younger-generation garnet appears to locally overgrow the biotite–quartz symplectites. In addition, garnet and magnetite may be separated by a thin corona of a mineral that has now been replaced, interpreted to be cordierite. Low modal proportions of cordierite can be produced at pressures below 4.2 kbar, which may suggest some decompression. However, the development of younger-generation garnet precludes significant decompression during the post-peak evolution. In addition, these second-stage reaction microstructures are likely to have developed in compositional micro-domains and so cannot be effectively modelled using the whole rock composition. A near-isobaric cooling evolution from the peak orthopyroxene-bearing field at pressures of ~4.5–5 kbar is the most consistent with the observed and interpreted petrography and the mineral modes (Fig. 6c).

5.3.6. Sample WI68: Herring Island

The peak assemblage in sample WI68 is plagioclase + K-feldspar + orthopyroxene + cordierite + magnetite + ilmenite + quartz + silicate melt. The absence of garnet provides an upper pressure constraint of 5.3–5.6 kbar (Fig. 6d). Biotite occurs as small flakes that are commonly in contact with magnetite, cordierite or orthopyroxene and is interpreted to be retrograde. The absence of peak biotite and the elevated solidus provide a lower temperature constraint of 800–840 °C. This assemblage occurs over a wide range of *P–T* space and therefore compositional contours of orthopyroxene were used to further constrain conditions. Orthopyroxene in this sample has y(opx) values between 0.08–0.11, which does not significantly constrain conditions but suggests pressures below 5 kbar and temperatures in excess of 830 °C (Fig. 6d). The calculated modal proportions of orthopyroxene and cordierite in the peak field correspond to observations (11% and 17% respectively), but do not significantly constrain conditions further

(Fig. 6d). The modal proportion of K-feldspar varies significantly across this field and suggests that at pressures of ~4 kbar, temperatures were less than 900 °C based on the observed abundance of K-feldspar (~22%; Table 2). The calculated abundance of plagioclase in the peak field does not correspond to observations. This sample does not contain mineral reaction microstructures that could provide further information on the *P–T* evolution.

6. Discussion

6.1. Monazite growth and the timing of metamorphism

Samples WI12 and WI40 contain concordant monazite U–Pb ages that range from c. 1320–1160 Ma (Fig. 5a and b). The oldest ages correspond to the timing of syn-D_1 magmatism at c. 1315 Ma (Post, 2000). The youngest ages in samples WI12 and WI40 correspond to the single c. 1180 Ma age populations in samples WI29 and WI68 (Fig. 5c and d) and the intrusion of the c. 1200–1160 Ma Ardery Charnockite in the southern Windmill Islands (Morrissey et al., in review (Ch. 2); Post, 2000; Post et al., 1997; Zhang et al., 2012).

It is well established that monazite is resistant to thermally induced Pb-loss to temperatures in excess of 900 °C (Cherniak, 2010; Cherniak et al., 2004; Sajeev et al., 2010; Schmitz and Bowring, 2003). However, it is far more reactive in the presence of fluid or melt (e.g. Harlov et al., 2011; Högdahl et al., 2012; Kelly et al., 2012; Kelsey et al., 2008; Kirkland et al., 2016; Rapp and Watson, 1986; Rubatto et al., 2013; Stepanov et al., 2012; Williams et al., 2011; Yakymchuk and Brown, 2014). This means that at high temperatures, monazite ages may record growth during melt crystallisation along the cooling path (e.g. Johnson et al., 2015; Kelsey et al., 2008; Korhonen et al., 2013; Stepanov et al., 2012; Yakymchuk and Brown, 2014). Alternatively, they may reflect partial to complete resetting of monazite during low-*T* fluid infiltration (e.g. Harlov et al., 2011; Kelly et al., 2012; Kirkland et al., 2016; Seydoux-Guillaume et al., 2002; Williams et al., 2011). In the Windmill Islands, syn to post-D_{2a} granites with emplacement ages between 1250 and 1210 Ma dominate the outcrop south of Clark Peninsula (Morrissey et al., in review (Ch. 2); Post, 2000; Zhang et al., 2012). It is possible that emplacement and crystallisation of these granites resulted in fluid flow events and that the young monazite ages, particularly in the northern Windmill Islands, reflect fluid-induced partial resetting of monazite rather than new growth during M_2. Therefore, to address the ambiguities in the interpretation of monazite geochronology, each of the samples must be considered in the context of the preserved silicate mineral assemblages, existing zircon geochronology and preserved structural relationships.

Detailed structural work shows that the northern Windmill Islands region (Cameron Island and northern Clark Peninsula) preserves S_1 foliations that are parallel to compositional layering and metamorphic evidence for M_1 (Paul et al., 1995; Post, 2000). South of Clark Peninsula, the M_1 assemblages are interpreted to have been progressively overprinted by the higher-grade M_2 event. The structural interpretation is supported by zircon geochronology. LA-ICP-MS zircon geochronology from a metasedimentary sample on Cameron Island yields discordant, c. 1300 Ma ages with no evidence for younger ages (Morrissey et al., in review (Ch. 2)). Similarly, LA-ICP-MS and SHRIMP U–Pb zircon geochronology from two samples of c. 1315 Ma D_1 orthogneiss and a sample of S_1 leucosome on Clark Peninsula (Fig. 2) shows no evidence for M_2 zircon growth, though the monazite geochronology for these samples is dominated by younger ages (Morrissey et al., in review (Ch. 2); Post, 2000). Therefore, despite the array of monazite ages in sample WI12, there is no structural evidence or zircon geochronology that suggests that the northern Windmill Islands record evidence for D_2/M_2, nor does sample WI12 contain any reaction microstructures to suggest that it records two phases of metamorphism. Instead, the spread of monazite ages in sample WI12 is interpreted to reflect fluid induced partial to complete resetting. In contrast, sample WI40 is from Mitchell Peninsula, within the zone that is structurally overprinted by M_2. This sample contains reaction microstructural evidence for two metamorphic events, with the formation of spinel–bearing reaction microstructures, as well as monazite and zircon evidence for M_1 and M_2 (Fig. 5b; Morrissey et al., in review (Ch. 2)). Samples WI29 and WI68 contain single monazite populations at c. 1180 Ma that are identical within error, and are interpreted to reflect the timing of M_2 (Fig. 5c and d).

The reasons why sample WI40 preserves older monazite whereas sample WI29 does not are not clear but may relate to the amount of melting during the upper-amphibolite facies M_1 event. The amount of melt produced is dominantly a function of the temperature attained and the amount and species of mica, particularly muscovite (e.g. Brown, 2010; Morrissey et al., 2016b; Patiño Douce and Harris, 1998; Vielzeuf and Holloway, 1988). Although it is difficult to reconstruct appropriate protolith compositions for samples WI40 and WI29, sample WI40 is significantly more aluminous than sample WI29, suggesting that it was probably more melt fertile during M_1. A significant amount of melt loss during M_1 would have meant that sample WI40 had a more refractory composition during M_2, limiting further melting and allowing for the preservation and partial resetting of older monazite and the formation of localised mineral reaction microstructures. In contrast, the monazite in sample WI29 may have been completely dissolved and recrystallised during cooling, consistent with the melt crystallisation microstructures developed in this sample.

6.2. Overall P–T–t evolution of the Windmill Islands

Each of the samples in this study preserves a different part of the overall *P–T* evolution of the Windmill Islands, as recorded by the silicate mineral assemblages and the monazite geochronology. Samples WI12 and WI68 are interpreted to record the peak conditions during M_1 and M_2, respectively. Samples WI40 and WI29 are from outcrops 650 m apart and are therefore likely to have experienced the same metamorphic conditions. These samples are interpreted together and are used to provide information on the interplay between M_1 and M_2.

The metasedimentary rocks in the Windmill Islands have maximum depositional ages of 1350–1340 Ma (Morrissey et al., in review (Ch. 2)). The timing of M_1 at c. 1320–1300 Ma provides a constraint on the minimum depositional age and suggests that deposition was closely or immediately followed by metamorphism. The occurrence of c. 1320–1300 Ma monazite (Fig. 5a and b) and zircon (Morrissey et al., in review (Ch. 2)) throughout the Windmill Islands region suggests that M_1 was a regional event that reached conditions of 710–740 °C and 3.7–4.2 kbar, corresponding to very high thermal gradients of >>150 °C/kbar (Fig. 6a). The event also involved the intrusion of the c. 1315 Ma syn-D_1 felsic orthogneiss on Clark Peninsula, which is interpreted to be derived from melting of the surrounding metasedimentary rocks (Morrissey et al., in review (Ch. 2); Post, 2000), and formation of a horizontal fabric and concordant antatectic leucosomes (Paul et al., 1995; Post, 2000). Following M_1, the Windmill Islands region was intruded by voluminous granitic rocks at c. 1250–1200 Ma (Morrissey et al., in review (Ch. 2); Post, 2000; Post et al., 1997; Zhang et al., 2012). These granitic rocks have a range of ages, Lu–Hf isotope values and mineralogy, suggesting that they have multiple, distinct intrusive sources. The granitic rocks contain some inherited zircon suggesting a crustal component, but they have radiogenic $\varepsilon_{Hf}(t)$ and $\varepsilon_{Nd}(t)$ values, suggesting that magmatism may have been associated with varying degrees of juvenile input (Möller et al., 2002; Morrissey et al., in review (Ch. 2); Zhang et al., 2012). Alternatively, the varying isotopic values of the granites could be consistent with derivation from a heterogeneous crustal source. The metasedimentary rocks of the Windmill Islands contain a significant proportion of c. 1400 Ma radiogenic zircons, providing a possible radiogenic crustal source for the relatively juvenile magmatism.

Sample WI40 contains a spread of monazite ages from c. 1320–1160 Ma and also contains mineral reaction microstructures, suggesting that it records both the M_1 and M_2 events. Likely melt loss during M_1 and M_2 means the current bulk composition cannot be used to provide quantitative *P–T* constraints on the M_1 quartz–garnet–sillimanite-bearing assemblage. The M_2 assemblage in sample WI40 was likely to have formed at temperatures of ~830–840 °C (Fig. 6b). Sample WI29 contains a single monazite population with a concordia age of 1177 ± 2 Ma, and microstructures consistent with melt crystallisation that suggest this sample did not lose significant amounts of melt during M_2, meaning it is difficult to determine a peak temperature for this sample. However, the crystallisation of melt to form biotite–quartz symplectites and growth of late garnet suggests that the retrograde evolution was likely to have involved near isobaric cooling at pressures above 4 kbar (Fig. 6c).

The peak conditions achieved during M_2 are poorly constrained by the most southerly located sample WI68 but the *y*(opx) contours suggest that maximum pressures were below 5 kbar and temperatures were approximately 840 °C, very close to the elevated solidus (Fig. 6d). The pressures recorded by sample WI68 and samples WI29 and WI40 are similar to within 1 kbar, suggesting that the southward increase in M_2 metamorphic grade is not due to differences

Figure 7 (facing page): Tectonic evolution of the eastern margin of the Albany–Fraser Orogen. Parts (a) and (b) represent two possible geodynamic settings for the region at c. 1410 Ma. (a) After Spaggiari et al. (2015), where the Arid Basin is a passive margin with east-dipping subduction that evolves into a foreland basin after accretion of the Loongana Arc. This model is likely to result in low thermal gradients. (b) After Morrissey et al. (in review (Ch. 2)), where west-dipping subduction places the Arid Basin is in a back-arc setting at c. 1410 Ma. This model is likely to result in high thermal gradients. Parts (c to e) represent a possible tectonic evolution using the data in this study. (c) Horizontal fabrics and high thermal gradients in the Windmill Islands suggest that M_1 was extensional. In this scenario, the Windmill Islands was located in the footwall. An extensional system is consistent with the orogen-wide mafic and felsic magmatism between c. 1330–1290 Ma (see text for details). This magmatism may have been focussed into the Fraser Zone, resulting in high temperature metamorphism and abundant mafic magmatism at c. 1290 Ma. (d) Upright folding and granitic magmatism between c. 1250–1210 Ma may represent a phase of compressional deformation (D_{2a}). The Fraser Zone was exhumed and thrust over the margin of the West Australian Craton by c. 1260 Ma. (e) Widespread charnockitic magmatism in the Wilkes Land–Albany–Fraser–Madura Province between 1220–1140 Ma suggests a period of extension (M_2).

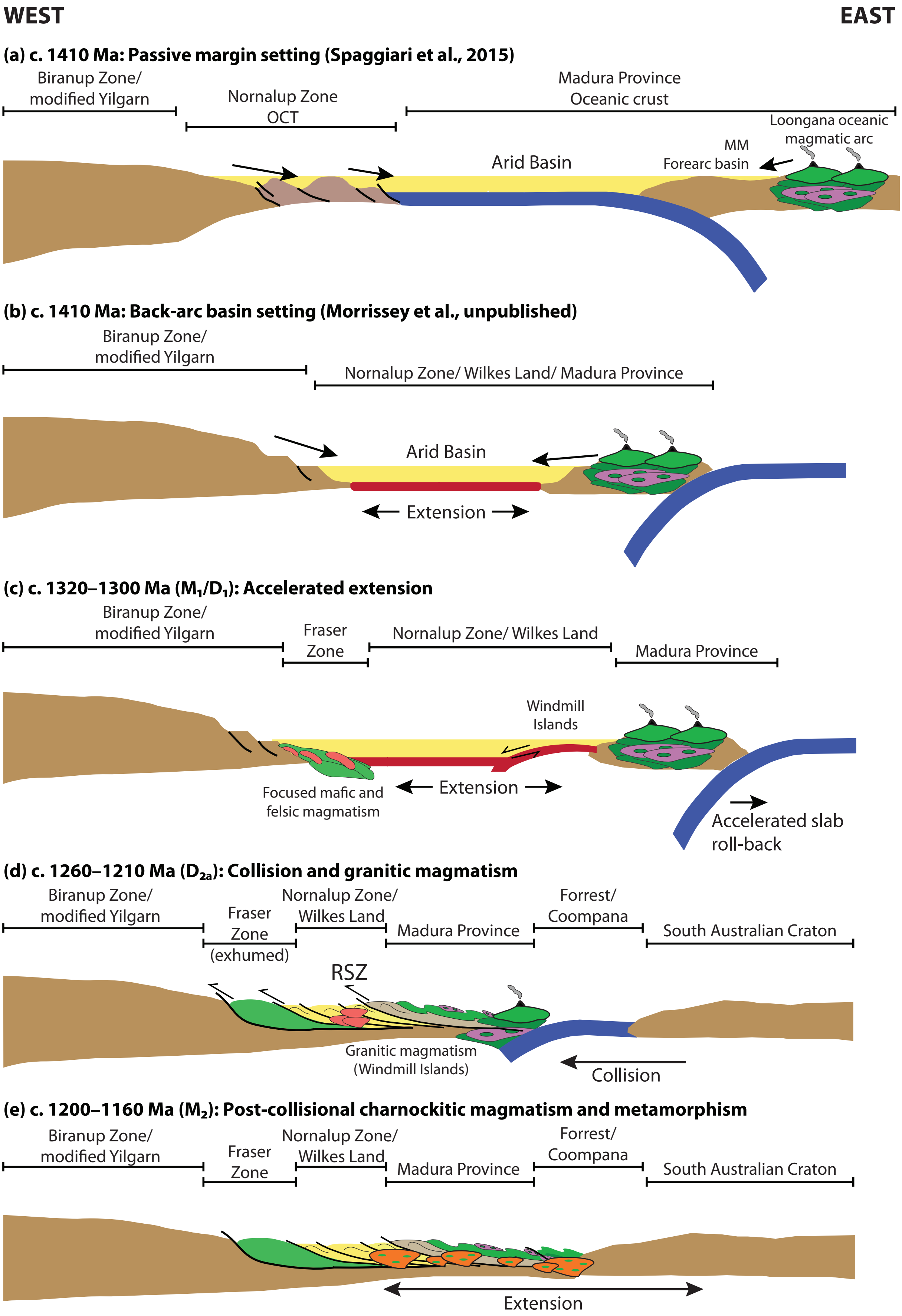
WEST
EAST
(a) c. 1410 Ma: Passive margin setting (Spaggiari et al., 2015)
Biranup Zone/ modified Yilgarn
Nornalup Zone OCT
Madura Province Oceanic crust
Loongana oceanic magmatic arc
MM
Forearc basin
Arid Basin
(b) c. 1410 Ma: Back-arc basin setting (Morrissey et al., unpublished)
Biranup Zone/ modified Yilgarn
Nornalup Zone/ Wilkes Land/ Madura Province
Arid Basin
Extension
(c) c. 1320–1300 Ma (M1/D1): Accelerated extension
Biranup Zone/ modified Yilgarn
Fraser Zone
Nornalup Zone/ Wilkes Land
Madura Province
Windmill Islands
Focused mafic and felsic magmatism
Extension
Accelerated slab roll-back
(d) c. 1260–1210 Ma (D2a): Collision and granitic magmatism
Biranup Zone/ modified Yilgarn
Fraser Zone (exhumed)
Nornalup Zone/ Wilkes Land
Madura Province
Forrest/ Coompana
South Australian Craton
RSZ
Granitic magmatism (Windmill Islands)
Collision
(e) c. 1200–1160 Ma (M2): Post-collisional charnockitic magmatism and metamorphism
Biranup Zone/ modified Yilgarn
Fraser Zone
Nornalup Zone/ Wilkes Land
Madura Province
Forrest/ Coompana
South Australian Craton
Extension

in exhumation. The c. 1180 Ma age for M_2 metamorphism (Fig. 5c and d) corresponds to the age of the high–*T* Ardery Charnockite, which dominates the outcrop in the southern Windmill Islands and is interpreted to have multiple intrusion phases between 1200 and 1160 Ma (Fig. 2; Morrissey et al., in review (Ch. 2); Post, 2000; Post et al., 1997; Zhang et al., 2012). The Ford Granite has a similar intrusion age of c. 1170 and is interpreted to be coeval with the Ardery Charnockite (Fig. 2; Post, 2000; Post et al., 1997). Episodic magmatic activity, particularly if each episode occurs within a short interval, is capable of generating relatively localised, high-*T* metamorphism (e.g. Robb et al., 1999; Rothstein and Hoisch, 1994; Tucker et al., 2015; Westphal et al., 2003). The increase in M_2 metamorphic grade to the south, the cooling dominated post-peak *P–T* evolution and observation that the M_2 thermal peak outlasted deformation (Paul et al., 1995; Post, 2000) are all consistent with a dominantly thermal overprint caused by the Ardery Charnockite.

6.3. Tectonic setting of metamorphism in the Wilkes Land–Albany–Fraser system

Geophysical interpretations have suggested that the Windmill Islands are representative of the ice covered outcrop elsewhere in Wilkes Land and that Wilkes Land basement geology correlates to the Nornalup Zone in the eastern Albany–Fraser Orogen (Fig. 1; Aitken et al., 2014, 2016). The metasedimentary rocks of the Windmill Islands have similar depositional ages to the youngest metasedimentary rocks of the c. 1600–1305 Ma Arid Basin in the Albany–Fraser Orogen (Morrissey et al., in review (Ch. 2); Spaggiari et al., 2014, 2015). M_1 metamorphism in the Windmill Islands corresponds to the Albany–Fraser Orogeny Stage I between c. 1345–1260 Ma and M_2 metamorphism corresponds to the Albany–Fraser Orogeny Stage II between c. 1225–1140 Ma (Clark et al., 2000, 2014; Kirkland et al., 2011, 2015; Spaggiari et al., 2015). Despite an extensive geochronological and isotopic dataset from the Albany–Fraser Orogen (e.g. Kirkland et al., 2011, 2015; Smithies et al., 2013, 2015; Spaggiari et al., 2015), there have been few modern metamorphic studies to provide a framework for the tectonic setting for the Albany–Fraser Orogen (e.g. Clark et al., 2014).

The currently proposed tectonic setting for the eastern Albany–Fraser Orogen (Arid Basin) involves the formation of a passive margin on the edge of the West Australian Craton, which evolves into a foreland basin at c. 1330 Ma after collision with the exotic c. 1410 Ma Loongana Arc (Fig. 7a; Spaggiari et al., 2014, 2015). However, recent detrital zircon geochronology from the Windmill Islands suggests that the metasedimentary rocks of the Windmill Islands contain detritus sourced from both the West Australian Craton and the Loongana Arc (Morrissey et al., in review (Ch. 2)). Therefore, an alternative interpretation is that the margin of the Albany–Fraser Orogen (represented by Wilkes Land and the Nornalup Zone) was in a wide back-arc setting at this time, and was bounded to the east by west-dipping subduction, represented by the c. 1410 Ma Loongana Arc (Fig. 7b; Morrissey et al., in review (Ch. 2)). The purpose of constraining the overall *P–T* conditions in the Windmill Islands is to provide a framework with which to assess tectonic models for Wilkes Land, and the Albany–Fraser system as a whole.

In the Albany–Fraser Orogen, Stage I was associated with voluminous mafic and granitic magmatism, represented by the c. 1330–1280 Ma Recherche Supersuite granites and the c. 1290 Ma Fraser Zone gabbros (Clark et al., 2000, 2014; Kirkland et al., 2011, 2015). There is a general increase in *P–T* conditions and decrease in age from east to west across the Albany–Fraser Orogen (Clark et al., 2000; Smithies et al., 2015). The eastern Nornalup Zone (Fig. 1) yields conventional thermobarometry estimates of 750 °C and 4 kbar and old (c. 1330–1310 Ma) ages for Recherche granites (Clark et al., 2000; Smithies et al., 2015), very similar to the timing and *P–T* estimates for M_1 in Wilkes Land. In the Fraser Zone to the west (Fig. 1), Stage I metamorphic conditions reached 850 °C and 7–9 kbar and were associated with mafic and felsic magmatism at c. 1290 Ma (Clark et al., 2014). The mafic magmas have isotopic signatures consistent with assimilation of older basement, likely to be the West Australian Craton (Smithies et al., 2013). The Fraser Zone has previously been interpreted as a back-arc or continental rift (Clark et al., 2014; Smithies et al., 2013). However, more recently the Fraser Zone mafic rocks have been proposed to be the result of mingling of mafic magmas with felsic partial melts in an orogen-wide lower-crustal hot zone (Smithies et al., 2015). The decrease in age from the Nornalup Zone in the southeast to the Fraser Zone in the northwest has been used to suggest that the magmatically active part of this hot zone migrated westwards during Stage I (Smithies et al., 2015). The higher proportion of mafic magmatism in the Fraser Zone compared to the Nornalup Zone has been interpreted to reflect increasing extension, though the higher metamorphic pressures recorded in the Fraser Zone may instead suggest that it is simply more deeply exhumed (Clark et al., 2000, 2014; Smithies et al., 2015). The hot zone is proposed to have initiated as a result of orogenic collapse following overthrusting of the Loongana Arc during collision with the West Australian Craton (Smithies et al., 2015). However, at present there is no metamorphic *P–T* path evidence to support the notion of orogenic collapse, nor is there any overt reason why orogenic collapse should lead to mantle melting. Alternatively, back-arcs are regions of thinned lithosphere and high heat flow that may remain hot and weak for upwards of 50 Myr and can accommodate deformation during collision or accretion at the adjacent margin (e.g. Collins, 2002; Currie and Hyndman, 2006; Hyndman et al., 2005). Notwithstanding the interpretation of Smithies et al. (2015), a back-arc setting for the eastern Albany–Fraser–Wilkes Land system is consistent with the short interval between deposition and high thermal gradient metamorphism, the orogen-wide mafic and felsic magmatism of the Recherche Supersuite and the observation that magmatism and deformation tend to be concentrated in the Nornalup and Fraser Zones (Kirkland et al., 2011; Smithies et al., 2015). The structural fabrics formed during M_1 in the Windmill Islands are horizontal and formed at high temperatures and shallow depths (~4 kbar) during M_1 metamorphism (Fig. 7c). Whereas this does not unequivocally point to an extensional regime, it is suggestive of one. In this scenario, the Fraser Zone was the focus for mafic magmatism and deformation and was therefore a thermo-mechanically weak zone whereas the Windmill Islands were located in the footwall of the extensional system (Fig. 7c).

Between M_1 and M_2, the Windmill Islands region was intruded by voluminous, isotopically juvenile granites at c. 1250–1210 Ma. The isotopically juvenile nature of the granites may reflect that the lower crust beneath the Windmill Islands contained little evolved material, consistent with a highly extended back-arc setting. These granites are interpreted to be syn- to post-D_{2a} deformation, which involved mesoscopic isoclinal folding and the formation of a composite S_1–S_{2a} foliation in the southern Windmill Islands. Map-scale F_{2a} folds are tight to isoclinal, upright in the north and inclined in the south and trend approximately E–W (Post, 2000). Granites with ages of c. 1250–1210 Ma have not been found in the Albany–Fraser Orogen, although much of the eastern Albany–Fraser Orogen is obscured by younger cover and therefore the basement geology in some parts is still unclear. However, the apparently localised spatial record of the c. 1250–1210 Ma granites means that their tectonic significance is difficult to determine. One alternative is that the magmatism at c. 1250–1210 Ma records a phase of compressional deformation (Fig. 7d), as suggested by the D_{2a} upright folding (Post, 2000). In the Albany–Fraser Orogen, the Fraser Zone does not record evidence for Stage II metamorphism and is interpreted to have been exhumed by c. 1260 Ma (Clark et al., 2014; Fletcher et al., 1991; Kirkland et al., 2011). If there was a phase of compressional deformation, the exhumation of the Fraser Zone could be a consequence of shortening strains partitioned into this comparatively low strength region. The direction of maximum stress recorded by the upright folding in the Windmill Islands is generally cratonwards and is consistent with the northwest-directed thrusting observed in the Fraser Zone (Bodorkos and Clark, 2004b; Kirkland et al., 2011).

Stage II in the Albany–Fraser Orogen (c. 1225–1140 Ma) is interpreted to record a major change in geodynamic setting with tectonism occurring within the newly assembled Australo–Antarctic system (Bodorkos and Clark, 2004a; Clark et al., 2000; Smithies et al., 2015). Tectonism is thought to be associated with extension, perhaps driven by delamination of the recently assembled lithospheric mantle. Evidence for Stage II high-temperature metamorphism occurs throughout the Biranup and Nornalup Zones but is not recorded in the Fraser Zone, suggesting the Fraser Zone was exhumed after Stage I, whereas the Biranup and Nornalup Zones were not (Bodorkos and Clark, 2004a; Clark et al., 2014; Kirkland et al., 2011). Stage II is also characterised by high temperature Esperance Supersuite magmatism between 1200–1140 Ma in the eastern Nornalup Zone. The Esperance Supersuite intrusions have distinctive compositional features similar to the Ardery Charnockite and have been interpreted to reflect extension and partial melting of an anhydrous, mafic lower crust (Kilpatrick and Ellis, 1992; Smithies et al., 2011, 2015; Zhang et al., 2012). The Ardery Charnockite appears to post-date the main phases of deformation in the Windmill Islands region, and may therefore reflect a phase of post-collisional extension (Fig. 7e). The M_2 thermal overprint in the Windmill Islands region is likely to reflect this event.

Although there remains debate as to whether the Albany–Fraser Orogen and the along-strike Musgrave Province are lithospheric equivalents (Smits et al., 2014), or are built on different basement (Kirkland et al., 2015), the Musgrave Province experienced a similar two-stage tectono-metamorphic history, with the 1345–1293 Ma Mount West Orogeny and the 1220–1150 Ma Musgrave Orogeny (Howard et al., 2015; Kirkland et al., 2013) corresponding in age and thermal style to the record in the Windmill Islands. The Musgrave Province has been the subject of several recent metamorphic and geodynamic studies and is therefore considered here for comparison (Gorczyk et al., 2015; Tucker et al., 2015; Walsh et al., 2015). At c. 1300 Ma, during the Mt West Orogeny, the Musgrave Province is interpreted to have been a back-arc, associated with the ongoing development of an overall convergent setting (Gorczyk et al., 2015; Smithies et al., in press). The Musgrave Orogeny involved regional, mantle-driven high thermal gradient metamorphism between c. 1220–1150 Ma that reached UHT conditions of >1000 ° C and 7–8 kbar (Smithies et al., 2011; Walsh et al., 2015). Voluminous, high-*T* magmatism of the Pitjantjatjara Supersuite intruded throughout this interval and caused short-lived, more localised UHT metamorphism (Smithies et al., 2011; Tucker et al., 2015). The Pitjantjatjara Supersuite shares compositional similarities with the Esperance Supersuite and Ardery Charnockite and is also interpreted to reflect extension (Kilpatrick and Ellis, 1992; Smithies et al., 2011, 2015; Zhang et al., 2012).

7. Conclusions

Calculated metamorphic phase diagrams combined with in situ geochronology from Wilkes Land, east Antarctica, suggest that the region experienced two phases of high thermal gradient metamorphism. M_1 was a regional, upper amphibolite facies event that occurred at c. 1320–1300 Ma and reached conditions of 710–740 °C and 3.7–4.2 kbar. The M_1 mineral assemblages are progressively overprinted by granulite facies M_2 assemblages related to the intrusion of the c. 1200–1160 Ma Ardery Charnockite. M_2 involved similar pressures to M_1 and reached peak conditions of ~850 °C. This metamorphic history is remarkably similar to that preserved in the eastern Albany–Fraser Orogen and the Musgrave Province. Each of these regions records a metamorphic and magmatic evolution that is consistent with a long-lived subduction setting, involving back-arc extension at c. 1300 Ma prior to M_1/ Stage I. The unique geochemistry of the high temperature magmas in each of these regions is consistent with melting of a mafic lower crust, which may have been generated as a result of the back-arc setting established prior to M_1. The attainment of high temperatures in all cases may be a result of advective heat transfer from charnockitic magmatism in an already elevated thermal regime.

Acknowledgements

This manuscript was funded by Australian Antarctic Science Project 4191. The Australian Antarctic Division and personnel at Casey Station during the summer of 2013–2014 are thanked for assistance with fieldwork and logistics.

References

Aitken, A.R.A., Betts, P.G., Young, D.A., Blankenship, D.D., Roberts, J.L., Siegert, M.J., 2016. The Australo-Antarctic Columbia to Gondwana transition. Gondwana Research 29, 136–152.

Aitken, A.R.A., Young, D.A., Ferraccioli, F., Betts, P.G., Greenbaum, J.S., Richter, T.G., Roberts, J.L., Blankenship, D.D., Siegert, M.J., 2014. The subglacial geology of Wilkes Land, East Antarctica. Geophysical Research Letters 41, 2390–2400.

Blight, D.F., Oliver, R.L., 1977. The metamorphic geology of the Windmill Islands, Antarctica: A preliminary account. Journal of the Geological Society of Australia 24, 239–262.

Bodorkos, S., Clark, D.J., 2004a. Evolution of a crustal-scale transpressive shear zone in the Albany–Fraser Orogen, SW Australia: 1. *P–T* conditions of Mesoproterozoic metamorphism in the Coramup Gneiss. Journal of Metamorphic Geology 22, 691–711.

Bodorkos, S., Clark, D.J., 2004b. Evolution of a crustal-scale transpressive shear zone in the Albany–Fraser Orogen, SW Australia: 2. Tectonic history of the Coramup Gneiss and a kinematic framework for Mesoproterozoic collision of the West Australian and Mawson cratons. Journal of Metamorphic Geology 22, 713–731.

Boger, S.D., White, R.W., Schulte, B., 2012. The importance of iron speciation (Fe^{+2}/Fe^{+3}) in determining mineral assemblages: an example from the high-grade aluminous metapelites of southeastern Madagascar. Journal of Metamorphic Geology 30, 997–1018.

Bohlen, S.R., 1991. On the formation of granulites. Journal of Metamorphic Geology 9, 223–229.

Bose, S., Das, K., Fukuoka, M., 2005. Fluorine content of biotite in granulite-grade metapelitic assemblages and its implications for the Eastern Ghats granulites. European Journal of Mineralogy 17, 665–674.

Brown, M., 2002. Retrograde processes in migmatites and granulites revisited. Journal of Metamorphic Geology 20, 25–40.

Brown, M., 2007. Metamorphic Conditions in Orogenic Belts: A Record of Secular Change. International Geology Review 49, 193–234.

Brown, M., 2010. The spatial and temporal patterning of the deep crust and implications for the process of melt extraction. Philosophical Transactions of the Royal Society A 368, 11–51.

Brown, M., 2014. The contribution of metamorphic petrology to understanding lithosphere evolution and geodynamics. Geoscience Frontiers 5, 553–569.

Cesare, B., Satish-Kumar, M., Cruciani, G., Pocker, S., Nodari, L., 2008. Mineral chemistry of Ti-rich biotite from pegmatite and metapelitic granulites of the Kerala Khondalite Belt (southeast India): Petrology and further insight into titanium substitutions. American Mineralogist 93, 327–338.

Cherniak, D.J., 2010. Diffusion in Accessory Minerals: Zircon, Titanite, Apatite, Monazite and Xenotime. Reviews in Mineralogy and Geochemistry 72, 827–869.

Cherniak, D.J., Watson, E.B., Grove, M., Harrison, T.M., 2004. Pb diffusion in monazite: a combined RBS/SIMS study. Geochimica et Cosmochimica Acta 68, 829–840.

Clark, C., Fitzsimons, I.C.W., Healy, D., Harley, S.L., 2011. How Does the Continental Crust Get Really Hot? Elements 7, 235–240.

Clark, C., Kirkland, C.L., Spaggiari, C.V., Oorschot, C., Wingate, M.T.D., Taylor, R.J., 2014. Proterozoic granulite formation driven by mafic magmatism: An example from the Fraser Range Metamorphics, Western Australia. Precambrian Research 240, 1–21.

Clark, D.J., Hensen, B.J., Kinny, P.D., 2000. Geochronological constraints for a two-stage history of the Albany–Fraser Orogen, Western Australia. Precambrian Research 102, 155-183.

Collins, W.J., 2002. Nature of extensional accretionary orogens. Tectonics 21, 1–12.

Currie, C.A., Hyndman, R.D., 2006. The thermal structure of subduction zone back arcs. Journal of Geophysical Research: Solid Earth 111, B08404.

De Yoreo, J.J., Lux, D.R., Guidotti, C.V., 1991. Thermal modelling in low-pressure/high-temperature metamorphic belts. Tectonophysics 188, 209–238.

Deer, W.A., Howie, R.A., Zussman, J., 1992. An introduction to the rock-forming minerals- 2nd edition. Longman, United Kingdom.

Diener, J.F.A., Powell, R., 2010. Influence of ferric iron on the stability of mineral assemblages. Journal of Metamorphic Geology 28, 599–613.

Droop, G.T.R., 1987. A general equation for estimating Fe^{3+} concentrations in ferromagnesian silicates and oxides from microprobe analyses, using stoichiometric criteria. Mineralogical Magazine 51, 431–435.

Fitzsimons, I.C.W., Harley, S.L., 1994. The Influence of Retrograde Cation Exchange on Granulite *P–T* Estimates and a Convergence Technique for the Recovery of Peak Metamorphic Conditions. Journal of Petrology 35, 543–576.

Fletcher, I.R., Myers, J.S., Ahmat, A.L., 1991. Isotopic evidence on the age and origin of the Fraser Complex, Western Australia: a sample of Mid-Proterozoic lower crust. Chemical Geology: Isotope Geoscience section 87, 197–216.

Frost, B.R., Chacko, T., 1989. The Granulite Uncertainty Principle: Limitations on Thermobarometry in Granulites. The Journal of Geology 97, 435–450.

Fyfe, W.S., 1973. The Granulite Facies, Partial Melting and the Archaean Crust. Philosophical Transactions of the Royal Society of London. Series A, Mathematical and Physical Sciences 273, 457–461.

Gorczyk, W., Smithies, H., Korhonen, F., Howard, H., Quentin De Gromard, R., 2015. Ultra-hot Mesoproterozoic evolution of intracontinental central Australia. Geoscience Frontiers 6, 23–37.

Gorczyk, W., Vogt, K., 2015. Tectonics and melting in intra-continental settings. Gondwana Research 27, 196–208.

Griffin, W.L., Belousova, E.A., Shee, S.R., Pearson, N.J., O'Reilly, S.Y., 2004. Archean crustal evolution in the northern Yilgarn Craton: U–Pb and Hf-isotope evidence from detrital zircons. Precambrian Research 131, 231–282.

Guevara, V.E., Caddick, M.J., 2016. Shooting at a moving target: phase equilibria modelling of high-temperature metamorphism. Journal of Metamorphic Geology, 34, 209–235.

Guiraud, M., Kienast, J., Rahmani, A., 1997. Petrological study of high-temperature granulites from In Ouzzal, Algeria: some implications on the phase relationships in the FMASTOCr system. European Journal of Mineralogy 8, 1375–1390.

Harley, S.L., 2004. Extending our understanding of Ultrahigh temperature crustal metamorphism. Journal of Mineralogical and Petrological Sciences 99, 140–158.

Harlov, D.E., Wirth, R., Hetherington, C.J., 2011. Fluid-mediated partial alteration in monazite: the role of coupled dissolution–reprecipitation in element redistribution and mass transfer. Contributions to Mineralogy and Petrology 162, 329–348.

Högdahl, K., Majka, J., Sjöström, H., Nilsson, K., Claesson, S., Konecný, P., 2012. Reactive monazite and robust zircon growth in diatexites and leucogranites from a hot, slowly cooled orogen: implications for the Palaeoproterozoic tectonic evolution of the central Fennoscandian Shield, Sweden. Contributions to Mineralogy and Petrology 163, 167–188.

Holland, T.J.B., Powell, R., 2011. An improved and extended internally consistent thermodynamic dataset for phases of petrological interest, involving a new equation of state for solids. Journal of Metamorphic Geology 29, 333–383.

Howard, H.M., Smithies, R.H., Kirkland, C.L., Kelsey, D.E., Aitken, A., Wingate, M.T.D., Quentin de Gromard, R., Spaggiari, C.V., Maier, W.D., 2015. The burning heart — The Proterozoic geology and geological evolution of the west Musgrave Region, central Australia. Gondwana Research 27, 64–94.

Hyndman, R.D., Currie, C.A., Mazzotti, S.P., 2005. Subduction zone backarcs, mobile belts, and orogenic heat. GSA Today 15, 4–10.

Johnson, T.E., Clark, C., Taylor, R.J.M., Santosh, M., Collins, A.S., 2015. Prograde and retrograde growth of monazite in migmatites: An example from the Nagercoil Block, southern India. Geoscience Frontiers 6, 373–387.

Johnson, T.E., White, R.W., 2011. Phase equilibrium constraints on conditions of granulite-facies metamorphism at Scourie, NW Scotland. Journal of the Geological Society 168, 147–158.

Kelly, N.M., Harley, S.L., Möller, A., 2012. Complexity in the behavior and recrystallization of monazite during high-*T* metamorphism and fluid infiltration. Chemical Geology 322–323, 192–208.

Kelsey, D.E., Clark, C., Hand, M., 2008. Thermobarometric modelling of zircon and monazite growth in melt-bearing systems: examples using model metapelitic and metapsammitic granulites. Journal of Metamorphic Geology 26, 199–212.

Kelsey, D.E., Hand, M., 2015. On ultrahigh temperature crustal metamorphism: phase equilibria, trace element thermometry, bulk composition, heat sources, timescales and tectonic settings. Geoscience Frontiers 6, 311–356.

Kilpatrick, J.A., Ellis, D.J., 1992. C-type magmas: igneous charnockites and their extrusive equivalents. Earth and Environmental Science Transactions of the Royal Society of Edinburgh 83, 155–164.

Kirkland, C.L., Erickson, T.M., Johnson, T.E., Danišík, M., Evans, N.J., Bourdet, J., McDonald, B.J., 2016. Discriminating prolonged, episodic or disturbed monazite age spectra: An example from the Kalak Nappe Complex, Arctic Norway. Chemical Geology 424, 96–110.

Kirkland, C.L., Smithies, R.H., Spaggiari, C.V., 2015. Foreign contemporaries – Unravelling disparate isotopic signatures from Mesoproterozoic Central and Western Australia. Precambrian Research 265, 218–231.

Kirkland, C.L., Smithies, R.H., Woodhouse, A.J., Howard, H.M., Wingate, M.T.D., Belousova, E.A., Cliff, J.B., Murphy, R.C., Spaggiari, C.V., 2013. Constraints and deception in the isotopic record; the crustal evolution of the west Musgrave Province, central Australia. Gondwana Research 23, 759–781.

Kirkland, C.L., Spaggiari, C.V., Pawley, M.J., Wingate, M.T.D., Smithies, R.H., Howard, H.M., Tyler, I.M., Belousova, E.A., Poujol, M., 2011. On the edge: U–Pb, Lu–Hf, and Sm–Nd data suggests reworking of the Yilgarn craton margin during formation of the Albany-Fraser Orogen. Precambrian Research 187, 223–247.

Korhonen, F.J., Clark, C., Brown, M., Bhattacharya, S., Taylor, R., 2013. How long-lived is ultrahigh temperature (UHT) metamorphism? Constraints from zircon and monazite geochronology in the Eastern Ghats orogenic belt, India. Precambrian Research 234, 322–350.

Kriegsman, L.M., 2001. Partial melting, partial melt extraction and partial back reaction in anatectic migmatites. Lithos 56, 75–96.

Lo Pò, D., Braga, R., 2014. Influence of ferric iron on phase equilibria in greenschist facies assemblages: the hematite-rich metasedimentary rocks from the Monti Pisani (Northern Apennines). Journal of Metamorphic Geology 32, 371–387.

Möller, A., Post, N., Hensen, B., 2002. Crustal residence history and garnet Sm–Nd ages of high-grade metamorphic rocks from the Windmill Islands area, East Antarctica. Int J Earth Sci (Geol Rundsch) 91, 993–1004.

Morrissey, L., Payne, J.L., Kelsey, D.E., Hand, M., 2011. Grenvillian-aged reworking in the North Australian Craton, central Australia: Constraints from geochronology and modelled phase equilibria. Precambrian Research 191, 141–165.

Morrissey, L.J., Hand, M., Kelsey, D.E., 2015. Multi-stage metamorphism in the Rayner–Eastern Ghats Terrane: *P–T–t* constraints from the northern Prince Charles Mountains, east Antarctica. Precambrian Research 267, 137–163.

Morrissey, L.J., Hand, M., Kelsey, D.E., Wade, B.P., 2016a. Cambrian high-temperature reworking of the Rayner–Eastern Ghats terrane, constraints from the northern Prince Charles Mountains region, east Antarctica. Journal of Petrology 57, 53–92.

Morrissey, L.J., Hand, M., Lane, K., Kelsey, D.E., Dutch, R.A., 2016b. Upgrading iron-ore deposits by melt loss during granulite facies metamorphism. Ore Geology Reviews 74, 101–121.

Morrissey, L.J., Payne, J.L., Hand, M., Clark, C., Taylor, R., Kirkland, C.L., Kylander-Clark, A.R.C., in review (Ch. 2). Linking the Windmill Islands, east Antarctica and the Albany–Fraser Orogen: insights from U–Pb zircon geochronology and Hf isotopes. Precambrian Research.

Nichols, G., Berry, R., Green, D., 1992. Internally consistent gahnitic spinel-cordierite-garnet equilibria in the FMASHZn system: geothermobarometry and applications. Contributions to Mineralogy and Petrology 111, 362–377.

Palin, R.M., Weller, O.M., Waters, D.J., Dyck, B., in press. Quantifying geological uncertainty in metamorphic phase equilibria modelling; a Monte Carlo assessment and implications for tectonic interpretations. Geoscience Frontiers.

Patiño Douce, A.E., Harris, N., 1998. Experimental Constraints on Himalayan Anatexis. Journal of Petrology 39, 689–710.

Pattinson, D.R.M., Chako,T., Farquhar, J., McFarlane, C.R.M., 2003. Temperatures of Granulite-facies Metamorphism: Constraints from Experimental Phase Equilibria and Thermobarometry Corrected for Retrograde Exchange. Journal of Petrology 44, 867–900.

Pattison, D.R.M., Bégin, N.J., 1994. Zoning patterns in orthopyroxene and garnet in granulites: implications for geothermometry. Journal of Metamorphic Geology 12, 387–410.

Paul, E., Stüwe, K., Teasdale, J., Worley, B., 1995. Structural and metamorphic geology of the Windmill Islands, east Antarctica: Field evidence for repeated tectonothermal activity. Australian Journal of Earth Sciences 42, 453–469.

Payne, J.L., Hand, M., Barovich, K.M., Wade, B.P., 2008. Temporal constraints on the timing of high-grade metamorphism in the northern Gawler Craton: implications for assembly of the Australian Proterozoic. Australian Journal of Earth Sciences 55, 623–640.

Pearce, M.A., White, A.J.R., Gazley, M.F., 2015. TCInvestigator: automated calculation of mineral mode and composition contours for thermocalc pseudosections. Journal of Metamorphic Geology 33, 413–425.

Post, N.J., 2000. Unravelling Gondwana fragments: An integrated structural, isotopic and petrographic investigation of the Windmill Islands, Antarctica. PhD Thesis, University of New South Wales, p. 213.

Post, N.J., Hensen, B.J., Kinny, P.D., 1997. Two Metamorphic Episodes during a 1340–1180

Convergent Tectonic Event in the Windmill Islands, East Antarctica, in: Ricci, C.A. (Ed.), The Antarctic Region: Geological Evolution and Processes. Terra Antartica Publication, Sienna, pp. 157–161.

Powell, R., Holland, T.J.B., 2008. On thermobarometry. Journal of Metamorphic Geology 26, 155–179.

Powell, R., White, R.W., Green, E.C.R., Holland, T.J.B., Diener, J.F.A., 2014. On parameterizing thermodynamic descriptions of minerals for petrological calculations. Journal of Metamorphic Geology 32, 245–260.

Rapp, R., Watson, E.B., 1986. Monazite solubility and dissolution kinetics: implications for the thorium and light rare earth chemistry of felsic magmas. Contributions to Mineralogy and Petrology 94, 304–316.

Rigby, M.J., Droop, G.T.R., 2011. Fluid-absent melting versus CO_2 streaming during the formation of pelitic granulites: A review of insights from the cordierite fluid monitor, in: van Reenen, D.D., Kramers, J.D., McCourt, S., Perchuck, L.L. (Eds.), Origin and Evolution of Precambrian High-Grade Gneiss Terranes, with Special Emphasis on the Limpopo Complex of Southern Africa. Geological Society of America Memoirs, pp. 39–60.

Robb, L.J., Armstrong, R.A., Waters, D.J., 1999. The History of Granulite-Facies Metamorphism and Crustal Growth from Single Zircon U–Pb Geochronology: Namaqualand, South Africa. Journal of Petrology 40, 1747–1770.

Rothstein, D.A., Hoisch, T.D., 1994. Multiple intrusions and low-pressure metamorphism in in the central Old Woman Mountains, south-eastern California: constraints from thermal modelling. Journal of Metamorphic Geology 12, 723–734.

Rubatto, D., Chakraborty, S., Dasgupta, S., 2013. Timescales of crustal melting in the Higher Himalayan Crystallines (Sikkim, Eastern Himalaya) inferred from trace element-constrained monazite and zircon chronology. Contributions to Mineralogy and Petrology 165, 349–372.

Sajeev, K., Williams, I.S., Osanai, Y., 2010. Sensitive high-resolution ion microprobe U–Pb dating of prograde and retrograde ultrahigh-temperature metamorphism as exemplified by Sri Lankan granulites. Geology 38, 971–974.

Sawyer, E.W., 2008. Atlas of migmatites. NRC Research Press, Ottawa, Ontario.

Schmitz, M.D., Bowring, S.A., 2003. Ultrahigh-temperature metamorphism in the lower crust during Neoarchean Ventersdorp rifting and magmatism, Kaapvaal Craton, southern Africa. Geological Society of America Bulletin 115, 533–548.

Seydoux-Guillaume, A.-M., Paquette, J.-L., Wiedenbeck, M., Montel, J.-M., Heinrich, W., 2002. Experimental resetting of the U–Th–Pb systems in monazite. Chemical Geology 191, 165–181.

Sizova, E., Gerya, T., Brown, M., 2014. Contrasting styles of Phanerozoic and Precambrian continental collision. Gondwana Research 25, 522–545.

Smithies, H.R., Spaggiari, C.V., Kirkland, C., 2015. Building the crust of the Albany–Fraser Orogen: constraints from granite geochemistry. Geological Survey of Western Australia, Report 150, p. 49.

Smithies, H.R., Spaggiari, C.V., Kirkland, C., Howard, H., Maier, W.D., 2013. Petrogenesis of gabbros of the Mesoproterozoic Fraser Zone: constraints on the tectonic evolution of the Albany–Fraser Orogen. Geological Survey of Western Australia, Record 2013/5, p. 29.

Smithies, R.H., Howard, H.M., Evins, P.M., Kirkland, C.L., Kelsey, D.E., Hand, M., Wingate, M.T.D., Collins, A.S., Belousova, E., 2011. High-temperature granite magmatism, crust–mantle interaction and the Mesoproterozoic intracontinental evolution of the Musgrave Province, Central Australia. Journal of Petrology 52, 931–958.

Smithies, R.H., Kirkland, C.L., Korhonen, F.J., Aitken, A.R.A., Howard, H.M., Maier, W.D., Wingate, M.T.D., Quentin de Gromard, R., Gessner, K., in press. The Mesoproterozoic thermal evolution of the Musgrave Province in central Australia — Plume vs. the geological record. Gondwana Research.

Smits, R.G., Collins, W.J., Hand, M., Dutch, R., Payne, J.L., 2014. A Proterozoic Wilson cycle identified by Hf isotopes in central Australia: Implications for the assembly of Proterozoic Australia and Rodinia. Geology, 42, 231–234.

Spaggiari, C.V., Kirkland, C., Smith, J., Wingate, M.T.D., 2014. Tectonic links between Proterozoic sedimentary cycles, basin formation and magmatism in the Albany–Fraser Orogen, Western Australia, Record 2014/6. Geological Survey of Western Australia, p. 165.

Spaggiari, C.V., Kirkland, C.L., Smithies, R.H., Wingate, M.T.D., Belousova, E.A., 2015. Transformation of an Archean craton margin during Proterozoic basin formation and magmatism: The Albany–Fraser Orogen, Western Australia. Precambrian Research 266, 440–466.

Stepanov, A.S., Hermann, J., Rubatto, D., Rapp, R.P., 2012. Experimental study of monazite/melt partitioning with implications for the REE, Th and U geochemistry of crustal rocks. Chemical Geology 300–301, 200–220.

Stüwe, K., 2007. Geodynamics of the Lithosphere: An Introduction. Springer Berlin Heidelberg.

Tajcmanová, L., Konopásek, J., Košler, J., 2009. Distribution of zinc and its role in the stabilization of spinel in high-grade felsic rocks of the Moldanubian domain (Bohemian Massif). European Journal of Mineralogy 21, 407–418.

Tucker, N.M., Hand, M., Kelsey, D.E., Dutch, R.A., 2015. A duality of timescales: Short-lived ultrahigh temperature metamorphism preserving a long-lived monazite growth history in the Grenvillian Musgrave–Albany–Fraser Orogen. Precambrian Research 264, 204–234.

Vielzeuf, D., Clemens, J.D., Pin, C., Moinet, E., 1990. Granites, Granulites, and Crustal Differentiation, in: Vielzeuf, D., Vidal, P. (Eds.), Granulites and Crustal Evolution. Springer Netherlands, pp. 59–85.

Vielzeuf, D., Holloway, J.R., 1988. Experimental determination of the fluid-absent melting relations in the pelitic system. Contributions to Mineralogy and Petrology 98, 257–276.

Walsh, A.K., Kelsey, D.E., Kirkland, C.L., Hand, M., Smithies, R.H., Clark, C., Howard, H.M., 2015. *P–T–t* evolution of a large, long-lived, ultrahigh-temperature Grenvillian belt in central Australia. Gondwana Research 28, 531–564.

Westphal, M., Schumacher, J.C., Boschert, S., 2003. High-Temperature Metamorphism and the Role of Magmatic Heat Sources at the Rogaland Anorthosite Complex in Southwestern Norway. Journal of Petrology 44, 1145–1162.

White, R.W., Powell, R., 2002. Melt loss and the preservation of granulite facies mineral assemblages. Journal of Metamorphic Geology 20, 621–632.

White, R.W., Powell, R., Clarke, G.L., 2002. The interpretation of reaction textures in Fe-rich metapelitic granulites of the Musgrave Block, central Australia: constraints from mineral equilibria calculations in the system K_2O–FeO–MgO–Al_2O_3–SiO_2–H_2O–TiO_2–Fe_2O_3. Journal of Metamorphic Geology 20, 41–55.

White, R.W., Powell, R., Holland, T.J.B., Johnson, T.E., Green, E.C.R., 2014a. New mineral activity–composition relations for thermodynamic calculations in metapelitic systems. Journal of Metamorphic Geology 32, 261–286.

White, R.W., Powell, R., Holland, T.J.B., Worley, B.A., 2000. The effect of TiO_2 and Fe_2O_3 on metapelitic assemblages at greenschist and amphibolite facies conditions: mineral equilibria calculations in the system K_2O–FeO–MgO–Al_2O_3–SiO_2–H_2O–TiO_2–Fe_2O_3. Journal of Metamorphic Geology 18, 497–511.

White, R.W., Powell, R., Johnson, T.E., 2014b. The effect of Mn on mineral stability in metapelites revisited: new *a–x* relations for manganese-bearing minerals. Journal of Metamorphic Geology 32, 809–828.

Williams, M.L., Jercinovic, M.J., Harlov, D.E., Budzyn, B., Hetherington, C.J., 2011. Resetting monazite ages during fluid-related alteration. Chemical Geology 283, 218–225.

Wong, B.L., Morrissey, L.J., Hand, M., Fields, C.E., Kelsey, D.E., 2015. Grenvillian-aged reworking of late Paleoproterozoic crust of the southern North Australian Craton, central Australia: Implications for the assembly of Mesoproterozoic Australia. Precambrian Research 270, 100–123.

Yakymchuk, C., Brown, M., 2014. Behaviour of zircon and monazite during crustal melting. Journal of the Geological Society 171, 465–479.

Zhang, S.-H., Zhao, Y., Liu, X.-C., Liu, Y.-S., Hou, K.-J., Li, C.-F., Ye, H., 2012. U–Pb geochronology and geochemistry of the bedrocks and moraine sediments from the Windmill Islands: Implications for Proterozoic evolution of East Antarctica. Precambrian Research 206–207, 52–71.

	WI12	WI40	WI29	WI68
Major elements (wt%)				
SiO_2	62.19	47.26	65.50	68.4
TiO_2	1.17	1.50	1.08	0.58
Al_2O_3	17.08	21.74	11.96	14.14
$Fe_2O_{3(TOTAL)}$	9.86	13.90	10.85	5.89
MnO	0.59	1.17	0.35	0.13
MgO	2.92	5.18	3.31	4.46
CaO	1.23	1.62	1.13	0.9
Na_2O	1.26	1.85	1.85	1.46
K_2O	3.41	4.73	3.61	3.39
P_2O_5	0.16	0.26	0.06	0.07
LOI	3.45	1.55	1.42	0.96
Total	99.87	100.76	101.12	100.38
Trace elements (ppm)				
Rb	225.8	333.6	183.7	228.4
Sr	158	212	102	60
Y	29.1	40.8	26.6	18.4
Zr	136	79	188	193
V	187	201	171	98
Ni	79	113	69	17
Cr	160	309	97	15
Nb	19.9	22.6	32.3	12.1
Ga	18.9	27.8	24.8	17.5
Cu	56	13	14	22
Zn	103	135	175	74
Co	33	70	35	15
Ba	1220	943	754	758
La	15	21	27	26
Ce	30	70	65	62
U	<0.5	<0.5	<0.5	0.5
Th	10.5	33.5	35.3	20.3
Sc	34	26	16	11
Pb	30	14	20	14

	Isotopic Ratios						Age Estimates							Morphology and location
Spot name	$^{207}Pb/^{206}Pb$	±1σ	$^{206}Pb/^{238}U$	±1σ	$^{207}Pb/^{235}U$	±1σ	$^{207}Pb/^{206}Pb$	±1σ	$^{206}Pb/^{238}U$	±1σ	$^{207}Pb/^{235}U$	±1σ	Conc. (%)	Textural location
Sample WI12: Cameron Island														
2A1	0.08029	0.00107	0.20672	0.00296	2.28731	0.03686	1204	26	1211	16	1208	11	101	Margin of qz and mt
2A2	0.08323	0.00112	0.21855	0.00312	2.50654	0.04063	1274	26	1274	16	1274	12	100	Margin of qz and mt
2A3	0.08014	0.00108	0.20484	0.00293	2.26219	0.03676	1201	26	1201	16	1201	11	100	Margin of qz and mt
10A1	0.07898	0.00112	0.20062	0.00288	2.18353	0.03669	1172	28	1179	15	1176	12	101	Within bi-sill fabric
11A1	0.07809	0.00117	0.19372	0.00280	2.08487	0.03618	1149	29	1142	15	1144	12	99	Within bi-sill fabric
53B1	0.08263	0.00113	0.21607	0.00309	2.46042	0.04040	1261	26	1261	16	1261	12	100	Within bi-sill fabric
53A1	0.08066	0.00114	0.20612	0.00295	2.29114	0.03821	1213	27	1208	16	1210	12	100	Within bi-sill fabric
53A2	0.08447	0.00121	0.22576	0.00323	2.62831	0.04426	1303	28	1312	17	1309	12	101	Within bi-sill fabric
57A1	0.08028	0.00121	0.21548	0.00310	2.38423	0.04148	1204	29	1258	16	1238	12	104	Edge of crack
57A2	0.07887	0.00127	0.20546	0.00297	2.23336	0.04067	1169	32	1205	16	1192	13	103	Edge of crack
64A1	0.08230	0.00107	0.21585	0.00294	2.44808	0.03760	1253	25	1260	16	1257	11	101	Margin of pl grain in leucosome
65A1	0.08069	0.00112	0.20478	0.00281	2.27709	0.03645	1214	27	1201	15	1205	11	99	Within bi-sill fabric
65A2	0.08307	0.00112	0.21687	0.00296	2.48280	0.03899	1271	26	1265	16	1267	11	100	Within bi-sill fabric
74A1	0.08125	0.00115	0.20964	0.00286	2.34707	0.03799	1228	28	1227	15	1227	12	100	Grain boundary in leucosome
74A2	0.08254	0.00118	0.21519	0.00293	2.44730	0.03990	1258	28	1256	16	1257	12	100	Grain boundary in leucosome
74A3	0.08158	0.00116	0.20899	0.00285	2.34945	0.03805	1236	28	1224	15	1227	12	99	Grain boundary in leucosome
75A1	0.07993	0.00117	0.20107	0.00274	2.21460	0.03667	1195	29	1181	15	1186	12	99	Within bi-sill fabric
81A1	0.07860	0.00125	0.20442	0.00283	2.21405	0.03887	1162	31	1199	15	1186	12	103	Within coarse-grained bi
81B1	0.08133	0.00128	0.20257	0.00278	2.27037	0.03927	1230	31	1189	15	1203	12	97	Margin of coarse-grained bi
75A2	0.08015	0.00131	0.20086	0.00278	2.21812	0.03956	1201	32	1180	15	1187	12	98	Within bi-sill fabric
81B2	0.07953	0.00128	0.20443	0.00282	2.23996	0.03950	1185	32	1199	15	1194	12	101	Margin of coarse-grained bi
65A3	0.08379	0.00127	0.21771	0.00298	2.51325	0.04260	1288	29	1270	16	1276	12	99	Within bi-sill fabric
Sample WI40: Mitchell Peninsula														
29A1	0.08506	0.00110	0.22041	0.00307	2.58499	0.04012	1317	25	1284	16	1296	11	98	Within pl
29A2	0.08405	0.00110	0.22263	0.00311	2.57995	0.04056	1294	25	1296	16	1295	12	100	Within pl
31A1	0.09099	0.00155	0.22551	0.00322	2.82913	0.05275	1446	32	1311	17	1363	14	91	Margin of g
31A2	0.08905	0.00121	0.22280	0.00312	2.73540	0.04388	1405	26	1297	16	1338	12	92	Margin of g
39A1	0.08345	0.00112	0.22197	0.00309	2.55392	0.04076	1280	26	1292	16	1288	12	101	Included in antiperthite
39A2	0.08471	0.00124	0.22467	0.00315	2.62401	0.04399	1309	28	1307	17	1307	12	100	Included in antiperthite
39A3	0.08426	0.00122	0.22198	0.00311	2.57875	0.04311	1298	28	1292	16	1295	12	100	Included in antiperthite
49A1	0.07961	0.00121	0.20072	0.00284	2.20336	0.03804	1187	30	1179	15	1182	12	99	Grain boundary between sp and cd
50A1	0.08093	0.00128	0.20735	0.00295	2.31379	0.04112	1220	31	1215	16	1217	13	100	Grain boundary between sp and cd

	Isotopic Ratios						Age Estimates							Morphology and location
Spot name	$^{207}Pb/^{206}Pb$	±1σ	$^{206}Pb/^{238}U$	±1σ	$^{207}Pb/^{235}U$	±1σ	$^{207}Pb/^{206}Pb$	±1σ	$^{206}Pb/^{238}U$	±1σ	$^{207}Pb/^{235}U$	±1σ	Conc. (%)	Textural location
Sample WI40 (continued)														
50A2	0.08019	0.00126	0.20821	0.00295	2.30214	0.04072	1202	31	1219	16	1213	13	101	Grain boundary between sp and cd
51A1	0.08476	0.00117	0.23087	0.00320	2.69646	0.04343	1310	27	1339	17	1328	12	102	Included in g
52A1	0.08519	0.00119	0.22886	0.00317	2.68640	0.04361	1320	27	1329	17	1325	12	101	In reaction texture, boundary between mt and cd
52A2	0.07816	0.00118	0.21032	0.00294	2.26503	0.03874	1151	30	1231	16	1202	12	107	In reaction texture, boundary between mt and cd
52B1	0.08493	0.00123	0.22741	0.00316	2.66110	0.04417	1314	28	1321	17	1318	12	101	Grain boundary of ksp and pl
52B2	0.08041	0.00190	0.20354	0.00318	2.25507	0.05450	1207	46	1194	17	1198	17	99	Grain boundary of ksp and pl
83A1	0.08153	0.00126	0.20816	0.00292	2.33808	0.04066	1234	30	1219	16	1224	12	99	Included in cd
83A2	0.08525	0.00132	0.22839	0.00318	2.68230	0.04652	1321	30	1326	17	1324	13	100	Included in cd
83A3	0.08177	0.00133	0.20070	0.00283	2.26088	0.04070	1240	32	1179	15	1200	13	95	Included in cd
83A4	0.07897	0.00130	0.19777	0.00278	2.15165	0.03896	1171	32	1163	15	1166	13	99	Included in cd
81C1	0.08343	0.00138	0.21578	0.00303	2.47999	0.04495	1279	32	1260	16	1266	13	98	Margin of apatite and pl
17A1	0.08113	0.00112	0.20750	0.00286	2.32025	0.03708	1225	27	1216	15	1219	11	99	Grain boundary of pl
17A2	0.08212	0.00112	0.21078	0.00290	2.38552	0.03794	1248	26	1233	15	1238	11	99	Grain boundary of pl
29A3	0.08311	0.00115	0.21906	0.00302	2.50920	0.04019	1272	27	1277	16	1275	12	100	Within pl
29A4	0.08123	0.00112	0.22785	0.00313	2.55092	0.04079	1227	27	1323	16	1287	12	108	Within pl
35A1	0.08366	0.00115	0.22090	0.00303	2.54712	0.04069	1285	27	1287	16	1286	12	100	Included in coarse-grained cd
35A2	0.08447	0.00119	0.22492	0.00309	2.61844	0.04238	1303	27	1308	16	1306	12	100	Included in coarse-grained cd
65A1	0.08231	0.00124	0.21607	0.00300	2.45105	0.04144	1253	29	1261	16	1258	12	101	Included in coarse-grained cd
65A2	0.07885	0.00127	0.20286	0.00285	2.20442	0.03915	1168	32	1191	15	1182	12	102	Included in coarse-grained cd
65A3	0.08075	0.00126	0.20335	0.00283	2.26325	0.03927	1216	30	1193	15	1201	12	98	Included in coarse-grained cd
81B1	0.08422	0.00124	0.22005	0.00302	2.55399	0.04242	1297	28	1282	16	1288	12	99	In reaction texture, in coarse-grained cd
81B2	0.08029	0.00129	0.21309	0.00297	2.35798	0.04167	1204	31	1245	16	1230	13	103	In reaction texture, in coarse-grained cd
Sample WI29: Mitchell Peninsula														
28A1	0.07898	0.00104	0.20145	0.00262	2.19209	0.03290	1172	26	1183	14	1179	10	101	Within bi-q symplectite
28A2	0.07924	0.00115	0.19927	0.00264	2.17551	0.03499	1178	29	1171	14	1173	11	99	Within bi-q symplectite
30A1	0.07943	0.00110	0.19918	0.00261	2.17956	0.03391	1183	27	1171	14	1175	11	99	Included in q
30A2	0.07891	0.00131	0.20262	0.00275	2.20351	0.03917	1170	33	1189	15	1182	12	102	Included in q
30A3	0.07946	0.00160	0.20077	0.00286	2.19808	0.04549	1184	39	1180	15	1180	14	100	Included in q
39A1	0.07907	0.00110	0.19909	0.00260	2.16924	0.03378	1174	27	1170	14	1171	11	100	Within bi-q symplectite, adjacent to g
39A2	0.07868	0.00120	0.19722	0.00262	2.13809	0.03554	1164	30	1160	14	1161	12	100	Within bi-q symplectite, adjacent to g
48A1	0.07922	0.00116	0.20189	0.00266	2.20402	0.03555	1178	29	1185	14	1182	11	101	Margin of g
48A2	0.07857	0.00124	0.19946	0.00264	2.15969	0.03675	1161	31	1172	14	1168	12	101	Margin of g

Spot name	Isotopic Ratios $^{207}Pb/^{206}Pb$	±1σ	$^{206}Pb/^{238}U$	±1σ	$^{207}Pb/^{235}U$	±1σ	Age Estimates $^{207}Pb/^{206}Pb$	±1σ	$^{206}Pb/^{238}U$	±1σ	$^{207}Pb/^{235}U$	±1σ	Conc. (%)	Morphology and location: Textural location
Sample WI29 (continued)														
48A3	0.07813	0.00126	0.19592	0.00260	2.10959	0.03658	1150	32	1153	14	1152	12	100	Margin of g
49B1	0.07908	0.00110	0.20525	0.00264	2.23662	0.03458	1174	27	1204	14	1193	11	102	Margin of mt
49A1	0.07894	0.00115	0.20376	0.00264	2.21616	0.03523	1171	28	1196	14	1186	11	102	Included in bi
49A2	0.07708	0.00113	0.20059	0.00260	2.13061	0.03420	1123	29	1179	14	1159	11	105	Included in bi
61A1	0.07816	0.00115	0.20359	0.00263	2.19267	0.03514	1151	29	1195	14	1179	11	104	Included in fine-grained pl
61A2	0.07958	0.00118	0.20224	0.00262	2.21754	0.03580	1187	29	1187	14	1187	11	100	Included in fine-grained pl
62A1	0.07868	0.00122	0.19805	0.00258	2.14702	0.03592	1164	31	1165	14	1164	12	100	Included in g
62A2	0.07893	0.00119	0.20018	0.00259	2.17700	0.03549	1171	29	1176	14	1174	11	100	Included in g
62B1	0.07986	0.00143	0.20156	0.00270	2.21762	0.04129	1194	35	1184	14	1187	13	99	Within bi-q symplectite, in contact with mt
62D1	0.07740	0.00124	0.19894	0.00261	2.12129	0.03633	1131	32	1170	14	1156	12	103	Within bi-q symplectite, in contact with mt
62D2	0.07992	0.00137	0.20168	0.00266	2.22050	0.03987	1195	33	1184	14	1188	13	99	Within bi-q symplectite, in contact with mt
62D3	0.07867	0.00149	0.20162	0.00273	2.18482	0.04290	1164	37	1184	15	1176	14	102	Within bi-q symplectite, in contact with mt
62C1	0.07976	0.00105	0.20082	0.00257	2.20746	0.03292	1191	26	1180	14	1183	10	99	Included in coarse-grained mt
62C2	0.08001	0.00134	0.19495	0.00261	2.14975	0.03828	1197	33	1148	14	1165	12	96	Included in coarse-grained mt
62C3	0.07857	0.00111	0.20271	0.00261	2.19468	0.03422	1161	28	1190	14	1179	11	102	Included in coarse-grained mt
62C4	0.07902	0.00112	0.19977	0.00257	2.17553	0.03412	1173	28	1174	14	1173	11	100	Included in coarse-grained mt
68A1	0.07872	0.00111	0.20447	0.00264	2.21815	0.03461	1165	28	1199	14	1187	11	103	Margin of coarse-grained bi
75A1	0.08006	0.00115	0.19924	0.00257	2.19822	0.03475	1198	28	1171	14	1181	11	98	Within coarse-grained q
83A1	0.07839	0.00113	0.19980	0.00258	2.15858	0.03422	1157	28	1174	14	1168	11	102	Included in g within bi-q symplectite
83A2	0.07965	0.00116	0.19958	0.00258	2.19075	0.03493	1188	28	1173	14	1178	11	99	Included in g within bi-q symplectite
83A3	0.07979	0.00117	0.20275	0.00263	2.22951	0.03577	1192	29	1190	14	1190	11	100	Included in g within bi-q symplectite
83A4	0.07996	0.00120	0.20066	0.00260	2.21128	0.03609	1196	29	1179	14	1185	11	99	Included in g within bi-q symplectite
Sample WI68: Herring Island														
5A1	0.07802	0.00147	0.19569	0.00339	2.10417	0.04604	1147	37	1152	18	1150	15	100	Margin of bi and q
5B1	0.07690	0.00127	0.20720	0.00351	2.19586	0.04428	1119	32	1214	19	1180	14	109	Included in cd
11A1	0.08286	0.00173	0.20120	0.00357	2.29744	0.05393	1266	40	1182	19	1212	17	93	Grain boundary of q
11B1	0.07925	0.00136	0.19992	0.00341	2.18342	0.04525	1178	34	1175	18	1176	14	100	Grain boundary of ksp
17A1	0.07864	0.00125	0.20646	0.00348	2.23762	0.04442	1163	31	1210	19	1193	14	104	Included in ksp
19A1	0.07975	0.00137	0.19958	0.00340	2.19357	0.04553	1191	34	1173	18	1179	14	99	Grain boundary of bi and pl
24A1	0.08530	0.00144	0.20413	0.00347	2.39976	0.04936	1322	32	1198	19	1243	15	91	Included in q
35A1	0.08065	0.00143	0.19771	0.00339	2.19756	0.04664	1213	35	1163	18	1180	15	96	Margin of bi and mt
35B1	0.08006	0.00128	0.20506	0.00345	2.26256	0.04509	1198	31	1202	18	1201	14	100	Margin of bi and cd

Spot name	Isotopic Ratios						Age Estimates							Morphology and location
	$^{207}Pb/^{206}Pb$	±1σ	$^{206}Pb/^{238}U$	±1σ	$^{207}Pb/^{235}U$	±1σ	$^{207}Pb/^{206}Pb$	±1σ	$^{206}Pb/^{238}U$	±1σ	$^{207}Pb/^{235}U$	±1σ	Conc. (%)	Textural location
Sample WI68 (continued)														
34A1	0.08002	0.00134	0.20327	0.00344	2.24178	0.04608	1197	33	1193	18	1194	14	100	Included in bi
34A2	0.07646	0.00129	0.20672	0.00351	2.17848	0.04512	1107	33	1211	19	1174	14	109	Included in bi
31B1	0.07906	0.00134	0.20229	0.00346	2.20402	0.04547	1174	33	1188	19	1182	14	101	Margin of bi and q
31B2	0.07929	0.00130	0.20033	0.00341	2.18907	0.04431	1179	32	1177	18	1178	14	100	Margin of bi and q
33A1	0.07855	0.00119	0.20792	0.00351	2.25086	0.04372	1161	30	1218	19	1197	14	105	Grain boundary of ksp
36A1	0.08021	0.00117	0.20189	0.00339	2.23175	0.04238	1202	28	1186	18	1191	13	99	Included in cd
36B1	0.07961	0.00141	0.20020	0.00345	2.19647	0.04662	1187	35	1176	19	1180	15	99	Included in bi
36C1	0.07855	0.00125	0.20412	0.00347	2.20968	0.04413	1161	31	1197	19	1184	14	103	Included in pl
36C2	0.07827	0.00144	0.21389	0.00371	2.30713	0.05012	1154	36	1250	20	1215	15	108	Included in pl
44A1	0.07933	0.00139	0.20150	0.00347	2.20286	0.04647	1180	34	1183	19	1182	15	100	Margin of bi and cd
44B1	0.07909	0.00143	0.20499	0.00355	2.23428	0.04810	1174	35	1202	19	1192	15	102	Margin of bi and cd
44B2	0.07816	0.00127	0.19747	0.00336	2.12702	0.04307	1151	32	1162	18	1158	14	101	Margin of bi and cd
57A1	0.07974	0.00139	0.20544	0.00354	2.25753	0.04766	1191	34	1205	19	1199	15	101	Margin of ksp and q
19A1	0.07790	0.00130	0.20468	0.00350	2.19728	0.04523	1144	33	1200	19	1180	14	105	Margin of bi and pl
31A1	0.07966	0.00139	0.20393	0.00351	2.23865	0.04735	1189	34	1196	19	1193	15	101	Included in bi

CHAPTER 4

This chapter is published as:

Morrissey, L.J., Hand, M., Raimondo, T., Kelsey, D.E., 2014. Long-lived high-temperature, low-pressure granulite facies metamorphism in the Arunta Region, central Australia. *Journal of Metamorphic Geology*, **32**, 25–47.

Statement of Authorship

Title of Paper	Long-lived high-temperature, low-pressure granulite facies metamorphism in the Arunta Region, central Australia.
Publication status	☒Published ☐Accepted for publication ☐Submitted for publication ☐Unpublished and unsubmitted work written in manuscript style
Publication Details	Morrissey, L.J., Hand, M., Raimondo, T., Kelsey, D.E., 2014. Long-lived high-temperature, low-pressure granulite facies metamorphism in the Arunta Region, central Australia. *Journal of Metamorphic Geology*, **32**, 25–47.

Principal Author

Name of Principal Author (Candidate)	Laura Morrissey		
Contribution to the Paper	Fieldwork and sample preparation, LA-ICPMS data collection, processing, and interpretation, *P–T* pseudosection calculation and interpretation, manuscript composition, creation of figures.		
Overall percentage (%)	80		
Certification:	This paper reports on original research I conducted during the period of my Higher Degree by Research candidature and is not subject to any obligations or contractual agreements with a third party that would constrain its inclusion in this thesis. I am the primary author of this paper.		
Signature		Date	16/05/2016

Co-Author Contributions

By signing the Statement of Authorship, each author certifies that:

i. the candidate's stated contribution to the publication is accurate (as detailed above);
ii. permission is granted for the candidate in include the publication in the thesis; and
iii. the sum of all co-author contributions is equal to 100% less the candidate's stated contribution.

Name of Co-Author	Martin Hand		
Contribution to the Paper	Project design, fieldwork, guidance with data interpretation, manuscript review.		
Signature		Date	17th May 2016

Name of Co-Author	Tom Raimondo		
Contribution to the Paper	Fieldwork, partial collection of LA-ICP-MS data, assisted with creation of figures, manuscript review.		
Signature		Date	18/05/2016

Name of Co-Author	David Kelsey		
Contribution to the Paper	Fieldwork, guidance with *P–T* modelling, assistance with data interpretation, manuscript review.		
Signature		Date	18/5/2016

ABSTRACT

In situ LA–ICP–MS U–Pb monazite geochronology from the Boothby Hills in the Aileron Province, central Australia, indicates that the region records more than 80 Ma of high-temperature, low-pressure (HTLP) anatectic conditions during the Early Mesoproterozoic. Monazite ages from granulite facies rocks and leucosomes span the interval 1576–1542 Ma. Pegmatites that overprint the regional gneissic fabric and are interpreted to record the last vestiges of melt crystallisation give ages between 1523–1513 Ma. Calculated *P–T* pseudosections suggest peak metamorphic conditions in excess of 850 °C at 0.65–0.75 GPa. The retrograde evolution was characterised by a *P–T* path that involved minor decompression and then cooling, culminating with the development of andalusite. Integration of the geochronological dataset with the inferred *P–T* path trajectory suggests that suprasolidus cooling must have been slow, in the order of 2.5 to 4 °C Ma^{-1}. In addition, the retrograde *P–T* path trajectory suggests that HTLP conditions were generated within crust of relatively normal thickness. Despite the long duration over which anatectic conditions occurred, there is no evidence for external magmatic inputs or evidence that HTLP conditions were associated with long-lived extension. Instead, it seems probable that the long-lived HTLP metamorphism was driven to a significant extent by long-lived conductive heating provided by high crustal heat production in voluminous pre-metamorphic granitic rocks.

1. Introduction

Regional-scale high temperature metamorphism involving high thermal gradients (>1300 °C GPa^{-1}) represents a significant departure from normal crustal thermal conditions (Fig. 1). The most dramatic manifestation of such thermally extreme conditions is the development of low to medium-pressure, ultrahigh-temperature (UHT; >900 °C) metamorphic terranes (e.g. Brown, 2006; Harley, 2004; Kelsey, 2008). The evolution and thermal drivers of these terranes have been the subject of significant attention (e.g. Clark et al., 2011; Currie and Hyndman, 2006; Harley, 2004; Hyndman et al., 2005; Kelsey, 2008; Kelsey et al., 2007; Sizova et al., 2014). However, there are also a large number of lower temperature terranes that preserve mineralogical evidence for anomalously high thermal gradients (Fig. 1). Such terranes may simply represent the upper crustal levels of currently unroofed high thermal gradient UHT terranes.

In some cases the high-temperature, low-pressure (HTLP) metamorphism was caused by heat transfer from magmatic processes (e.g. De Yoreo et al., 1991; Westphal et al., 2003). Orogenic-scale examples of magmatically driven HTLP metamorphism include the Namaqualand Metamorphic Complex, South Africa, and the Grenvillian-aged Musgrave Province, Australia (e.g. Robb et al., 1999; Smithies et al., 2011). In other instances, petrological and structural evidence suggests that HTLP conditions were attained during either exhumation within thickened crust, or within crust that was undergoing extension (e.g. Cubley et al., 2013; Goscombe and Hand, 2000; Rey et al., 2009; Rubatto et al., 2013; Sandiford and Powell, 1986).

The duration of metamorphism provides an important constraint for determining the causative mechanism of HTLP metamorphism. Short-lived (<10 Ma) HTLP metamorphism typically involves coeval magmatism in mid- to upper-crustal levels, or rapid exhumation that is documented by distinctive petrological

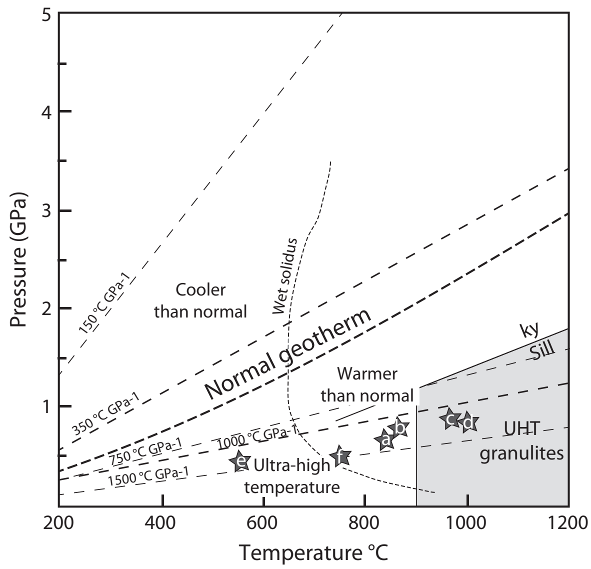

Figure 1: Figure of thermal gradients found in the crust, after Brown, (2006). High thermal gradient metamorphic conditions plotted on are: (a) Reynolds Range (this study); (b) Mawson Coast, Rayner Complex, east Antarctica (Halpin et al., 2007); (c) Eastern Ghats Province (Korhonen et al., in press); (d) Musgrave Province (Smithies et al., 2011); (e) Warumpi Province (Morrissey et al., 2011); (f) Broken Hill, Curnamona Province (White et al., 2004).

evidence such as decompressional reaction microstructures. Longer lived (>10 Ma) HTLP metamorphism is more suggestive of limited exhumation and crust that is in approximate isostatic equilibrium. However, longer-lived metamorphism is also usually associated with coeval, voluminous magmatism. Ancient examples of regionally extensive, long-lived HTLP metamorphism include the ultrahigh-temperature terranes of the Napier Complex, Antarctica (Hokada et al., 2004; Kelly and Harley, 2005; Suzuki et al., 2006), the Eastern Ghats Province−Rayner Complex (Boger et al., 2000; Boger and White, 2003; Halpin et al., 2007; Korhonen et al., 2013) and the Musgrave Province, Australia (Smithies et al., 2010, 2011). The cause of HTLP metamorphism in examples where there is little or no coeval magmatism or evidence for extension is less obvious. A long-lived, non-magmatic heat source is required to sustain the elevated temperatures and thermal gradient.

The Reynolds Range in the Aileron Province, central Australia, is an exceptional example of apparently long-lived HTLP granulite facies metamorphism where evidence for coeval magmatism or extension is absent (Fig. 2). Existing zircon and monazite U–Pb isotopic age data from the Reynolds Range suggest that anatectic conditions were sustained for up to 30 Ma during the Early Mesoproterozoic (Rubatto et al., 2001; Williams et al., 1996), and were followed by approximately 100 Ma of slow cooling (Buick et al., 1999; Vry and Baker, 2006). Metamorphism resulted in the development of a spectacular regional HTLP metamorphic field gradient (Fig. 2), from greenschist facies assemblages in the NW, through andalusite-cordierite-bearing amphibolite facies mineral assemblages, and culminating in fluid-absent anatectic granulite facies assemblages in the SE (Dirks et al., 1991; Hand and Buick, 2001). The HTLP metamorphism preserved in the Reynolds Range is intriguing as it appears to be amagmatic and associated with contractional deformation (Buick et al., 1998; Dirks et al., 1991; Hand and Buick, 2001).

The purpose of this paper is to use in situ U–Pb monazite geochronology and metamorphic phase equilibria modelling to establish the duration and thermal conditions of metamorphism in the Boothby Hills region in the SE Reynolds Range (Fig. 3). The results of this work, coupled with existing age data, suggest that regional suprasolidus HTLP metamorphic conditions were maintained for at least 80 Ma. Such a long-lived, amagmatic thermal structure challenges conventional notions concerning the generation of high temperature, high thermal gradient conditions

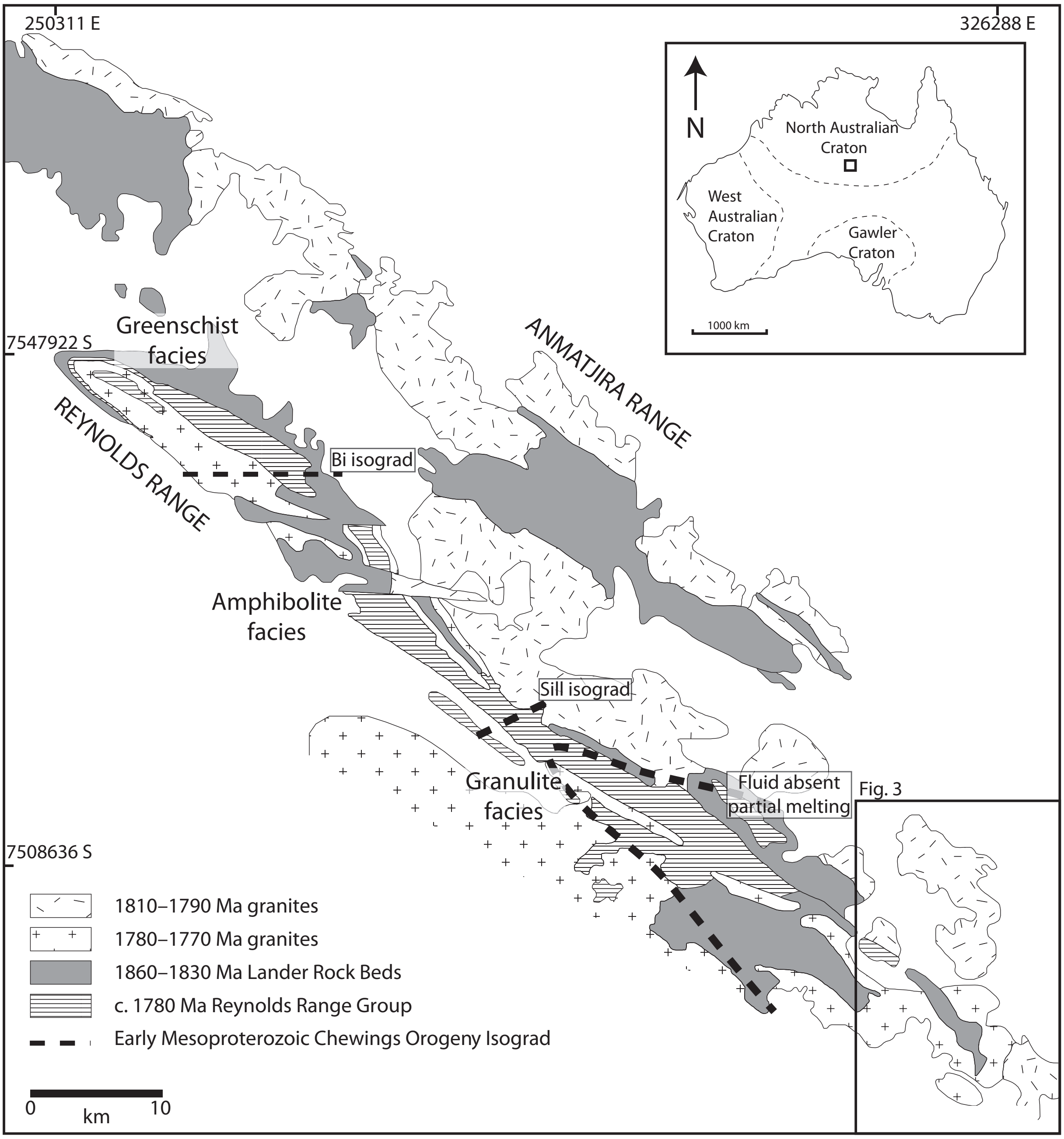

Figure 2: Simplified geological map of the Reynolds and Anmatjira Ranges adapted from Williams et al. (1996). References for the age of each unit are provided in the geological setting.

in the crust. We propose that the suprasolidus HTLP conditions in the central Aileron Province were sustained for such a lengthy period due to slow exhumation of high-heat producing crust.

2. Geological setting

The Reynolds-Anmatjira Ranges (Fig. 2) are a NW-trending structural domain in the Aileron Province of the Arunta Region, central Australia (Clarke and Powell, 1991; Collins and Vernon, 1991; Collins and Williams, 1995; Dirks and Wilson, 1990; Hand et al., 1992). Rocks of the Reynolds-Anmatjira Ranges record a series of deformational, metamorphic and magmatic events ranging in age from Proterozoic to Palaeozoic (Cartwright et al., 1999, 2001; Hand and Buick, 2001; Raimondo et al., 2011, 2012; Vry et al., 1996). The oldest rocks in the Reynolds Range are pelitic and psammitic metasediments of the Lander Rock Formation, which have depositional ages between 1860 and 1840 Ma (Fig. 2, 3; Claoué-Long et al., 2008a; Dirks et al., 1991; Dirks and Wilson, 1990; Donnellan, 2008; Hand and Buick, 2001; Vry et al., 1996). These were deformed and metamorphosed under high thermal gradient conditions associated with voluminous granitic magmatism at 1810–1790 Ma (Buick et al., 1999; Cartwright et al., 1999; Collins and Vernon, 1991; Collins and Williams, 1995; Rubatto et al., 2001, 2006; Worden et al., 2008).

The Lander Rock Formation and c. 1810 Ma granitic rocks are unconformably overlain by shallow marine (meta)sediments of the c. 1780 Ma Reynolds Range Group (Fig. 2, 3; Claoué-Long et al., 2008a; Dirks et al., 1991; Dirks and Wilson, 1990; Hand and Buick, 2001; Vry et al., 1996). Voluminous magmatism at c. 1780–1770 Ma intruded the Lander Rock Formation as well as the Reynolds Range Group, causing minor deformation and localised amphibolite facies contact metamorphism (Buick et al., 1999; Collins and Williams, 1995; Hand and Buick, 2001; Smith, 2001). Together, the two generations of magmatism make up 60% of the exposed area of the region (Fig. 2; Hand and Buick, 2001).

The Reynolds-Anmatjira region underwent another period of high thermal gradient metamorphism during the c. 1590−1560 Ma Chewings Orogeny (Hand and Buick, 2001; Rubatto et al., 2001; Scrimgeour, 2003, 2004; Vry et al., 1996; Williams et al., 1996). This event involved NE–SW shortening to form upright, NW–SE-trending, tight to isoclinal upright folds and a steep NW–SE-trending foliation (Buick et al., 1999; Hand and Buick, 2001). Estimates of metamorphic conditions based on conventional thermobarometry and rudimentary qualitative phase equilibria for granulite facies rocks in the south east Reynolds Range suggest medium to low pressures (0.4–0.6 GPa) at maximum temperatures of 700–800 °C (Buick et al., 1998; Dirks et al., 1991; Vry and Cartwright, 1994).

The Chewings Orogeny in the Reynolds Range region has been recognised as a moderately long-lived (c. 30−50 Ma) event based on differences between U–Pb metamorphic ages from zircon and monazite from different rocks (Rubatto et al., 2001; Williams et al., 1996). U–Pb zircon ages range from 1594 ± 6 Ma in granulite facies metapelites to 1564 ± 4 Ma in discordant leucosomes (Rubatto et al., 2001; Williams et al., 1996). U–Pb monazite geochronology yields ages from 1585 ± 5 Ma to 1557 ± 2 Ma, with the oldest ages coming from the peak fabric and concordant leucosomes, and the younger ages from discordant leucosomes (Rubatto et al., 2001; Vry et al., 1996; Williams et al., 1996). Coupled with an additional U–Pb rutile age of 1544 ± 8 Ma (Vry and Baker, 2006) and a Pb–Pb garnet age of 1576 ± 6 Ma (Buick et al., 1999), this large temporal spread has been interpreted as evidence of slow cooling from peak metamorphic conditions (Buick et al., 1999; Kelsey et al., 2008; Vry and Baker, 2006; Williams et al., 1996). However, despite the body of existing geochronological data, there has been no modern metamorphic work, nor studies that integrate in situ geochronology with the evolving metamorphic conditions in the region, suggesting that the total duration of melt-bearing conditions is uncertain.

The final event affecting the Reynolds-Anmatjira Ranges was the Mid-Palaeozoic Alice Springs Orogeny at 450–300 Ma (Collins and Shaw, 1995; Dunlap and Teyssier, 1995; Haines et al., 2001; Shaw et al., 1992).This event produced discrete northwest-trending, hydrous shear zones up to several hundred metres wide (Cartwright et al., 1999; Collins and Teyssier, 1989; Raimondo et al., 2011, 2012) and resulted in differential exhumation of the terrane (Buick et al., 1998; Cartwright and Buick, 1999; Dirks et al., 1991; Hand and Buick, 2001). The consequence of this differential exhumation was to create a regional metamorphic gradient expressed by the early Mesoproterozoic assemblages, which ranges from greenschist facies in the northwest Reynolds Range to granulite facies towards the southeast (Fig. 2).

3. Sample selection and petrography

The samples chosen for petrographic analysis, phase equilibria modelling and geochronology are located in the Boothby Hills in the SE Reynolds Range (Fig. 3, Table 1). Three locations were selected from within the Aileron Metamorphics (Fig. 3). The selected samples represent different stages of the evolving metamorphic and thermal system during the Early Mesoproterozoic Chewings Orogeny. Samples displaying the regional gneissic fabric were taken from locations north and south of Mount Boothby. Pegmatites that cross-cut the regional gneissic fabric were sampled to constrain the timing of crystallisation of the last melt, and thus place a lower age limit on

Table 1: Summary of sample locations and geochronology.

Sample	Easting	Northing	Textural location	Age (Ma)
Boothby-09-1	325078	7505909	Gt-cd gneissic fabric	1576 ± 10
Boothby-09-2A	325078	7505909	Gt-cd gneissic fabric	1572 ± 10
RR-01	322372	7497549	Whole rock: matrix and segregations	–
RR-03	322372	7497549	Gt-cd-bi matrix	1563 ± 11
RR-04	322372	7497549	Opx-gt-cd melt segregation	1560 ± 10
RR-05	322372	7497549	Bi-cd-pl retrogressed assemblage	1542 ± 12
BPG-01	325039	7503826	Qz-bi-ksp pegmatite	1522 ± 9
BPG-03	325039	7503826	Qz-bi-ksp pegmatite	1510 ± 12

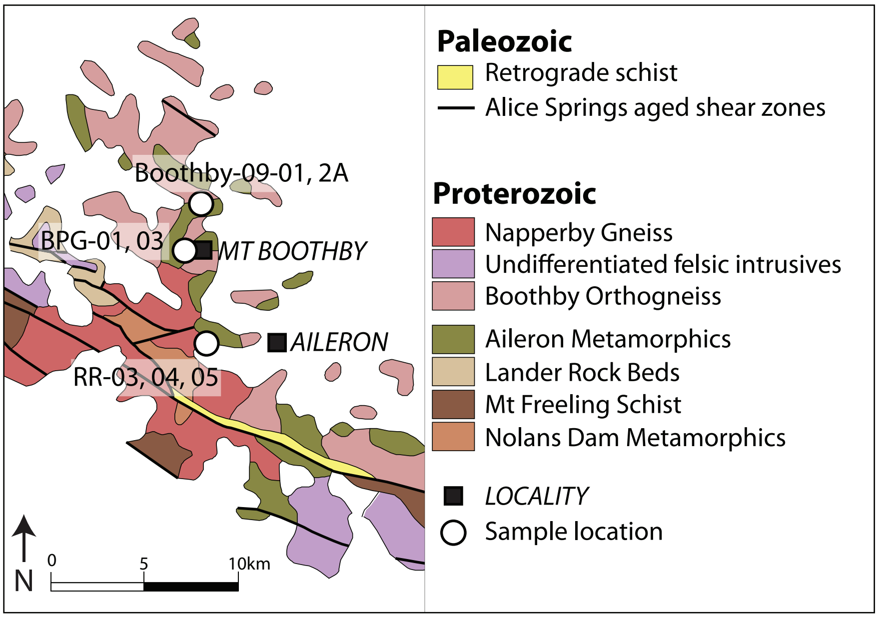

Figure 3: Detailed map of sample area showing key lithologies, after Raimondo et al. (2011).

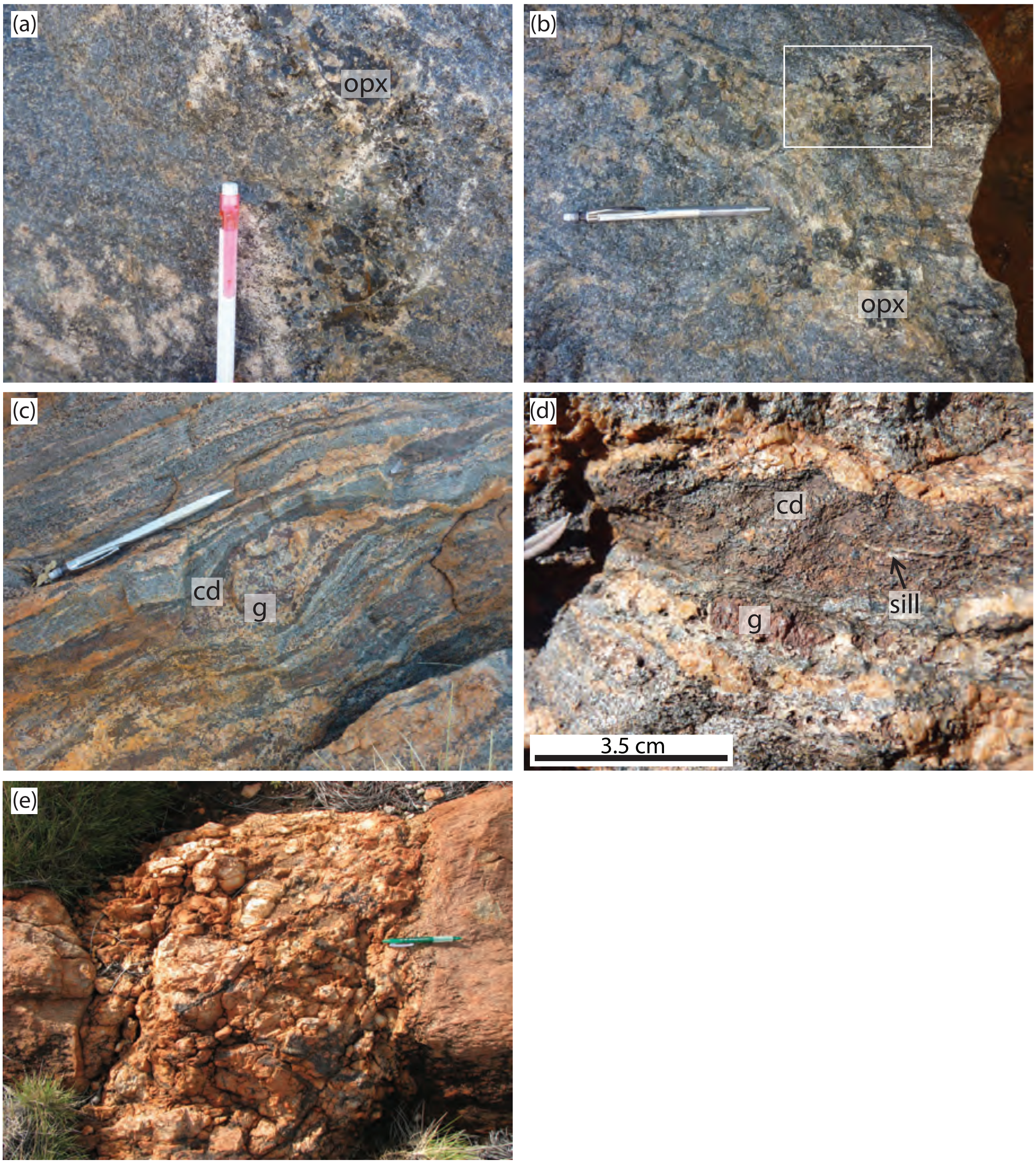

Figure 4: Field photographs. (a) Samples RR-03, RR-04: Coarse-grained orthopyroxene-K-feldspar bearing segregation within cordierite-garnet-biotite bearing metapelites. (b) Samples RR-04, RR-05: Partial replacement (outlined) of orthopyroxene-K-feldspar bearing segregation by biotite, cordierite and plagioclase. (c) Sample Boothby-09-2A: Early formed garnet-bearing migmatitic segregation in layered metapelites enclosed within a foliation defined by biotite and cordierite. (d) Sample Boothby-09-2A: Early sillimanite is armoured within cordierite and is not part of the foliation defining assemblage. (e) Pegmatite from west of Mt Boothby cross-cutting the regional gneissic foliation at a high angle.

suprasolidus conditions.

3.1. South of Mount Boothby

At this location (WGS84, 53K 322372 mE, 7497549 mS), the granulite-facies outcrop is dominated by cordierite-rich gneiss, cross-cut by volumetrically minor (5–10% of outcrop) orthopyroxene ± garnet bearing segregations that are up to 50 cm long and 20 cm wide (Fig. 4a). The segregations are variably retrogressed to biotite-rich mineral assemblages (Fig. 4b). In some instances, the development of biotite has proceeded to the extent that orthopyroxene-garnet has been completely replaced.

To allow links to be drawn between the petrology and the calculated phase diagrams and geochronology, descriptions are given in terms of three separate rock domains. The overall rock is represented by sample RR-01, which contains all three domains. Following the development of the orthopyroxene-garnet bearing segregations, the matrix and segregations are interpreted to have been chemically discrete domains, on the basis that they develop contrasting mineral assemblages (see below). These domains have been treated as separate samples for the purposes of phase diagram calculations and geochronology.

3.1.1. Sample RR-03

Sample RR-03 represents the cordierite-rich, gneissic host rock and comprises medium- to coarse-grained cordierite, garnet, quartz, plagioclase, biotite, K-feldspar and fine- to very-fine grained magnetite, ilmenite, sillimanite, fibrolitic sillimanite and rare andalusite. The mineralogy of the gneiss is dominantly cordierite, quartz and biotite. Alternating biotite-rich and biotite-poor layers define the gneissic fabric (Fig. 4a); however, biotite grains themselves do not have a preferred orientation at thin section scale. Cordierite porphyroblasts (>1 mm) contain rare inclusions of unoriented patches of sillimanite (Fig. 5a). Cordierite grain boundaries are commonly decorated with very fine-grained, unoriented, fibrolitic sillimanite (Fig. 5a). Garnet grains are anhedral, commonly <3 mm and usually occur in contact with cordierite and quartz (Fig. 5a). They are occasionally partially surrounded by large, optically continuous cordierite grains. Magnetite most commonly occurs either as inclusions within biotite or along biotite grain boundaries. However, magnetite also occurs with quartz and in contact with garnet. Ilmenite occurs intergrown with magnetite. Andalusite is fine-grained (<0.1 mm), anhedral and occurs in partial replacement of biotite (Fig. 5b).

3.1.2. Sample RR-04

Sample RR-04 represents the discordant and undeformed segregations that overprint the gneissic fabric. They contain coarse- to very coarse-grained orthopyroxene (≤5 cm diameter), plagioclase, garnet (≤1.5 cm), cordierite and biotite, and less abundant, finer-grained magnetite, ilmenite and K-feldspar (Fig. 5c). Orthopyroxene commonly either mantles garnet or contains inclusions of garnet (Fig. 5c); these observations can be seen both at outcrop and thin section scale. Garnet also occurs as inclusions within large grains of cordierite and plagioclase. At the outcrop scale, biotite occurs in patchy 'clumps' in the segregation. The presence of biotite in sample RR-04 is interpreted to represent partial retrogression of the (essentially) anhydrous leucosome assemblage (Fig. 5c). Anhedral, fine-grained andalusite occurs in the biotite-rich areas of the segregation (Fig. 5c). Secondary garnet occurs on the rims of relict garnet grains, and is associated with the replacement of orthopyroxene.

3.1.3. Sample RR-05

Sample RR-05 represents segregations that are extremely biotite-rich. In this sample, orthopyroxene and garnet have been entirely replaced, and the mineralogy is biotite, cordierite, plagioclase, magnetite and ilmenite ± andalusite. These biotite-rich parts are interpreted to be retrogressed segregations, and may represent crystallised melt pockets

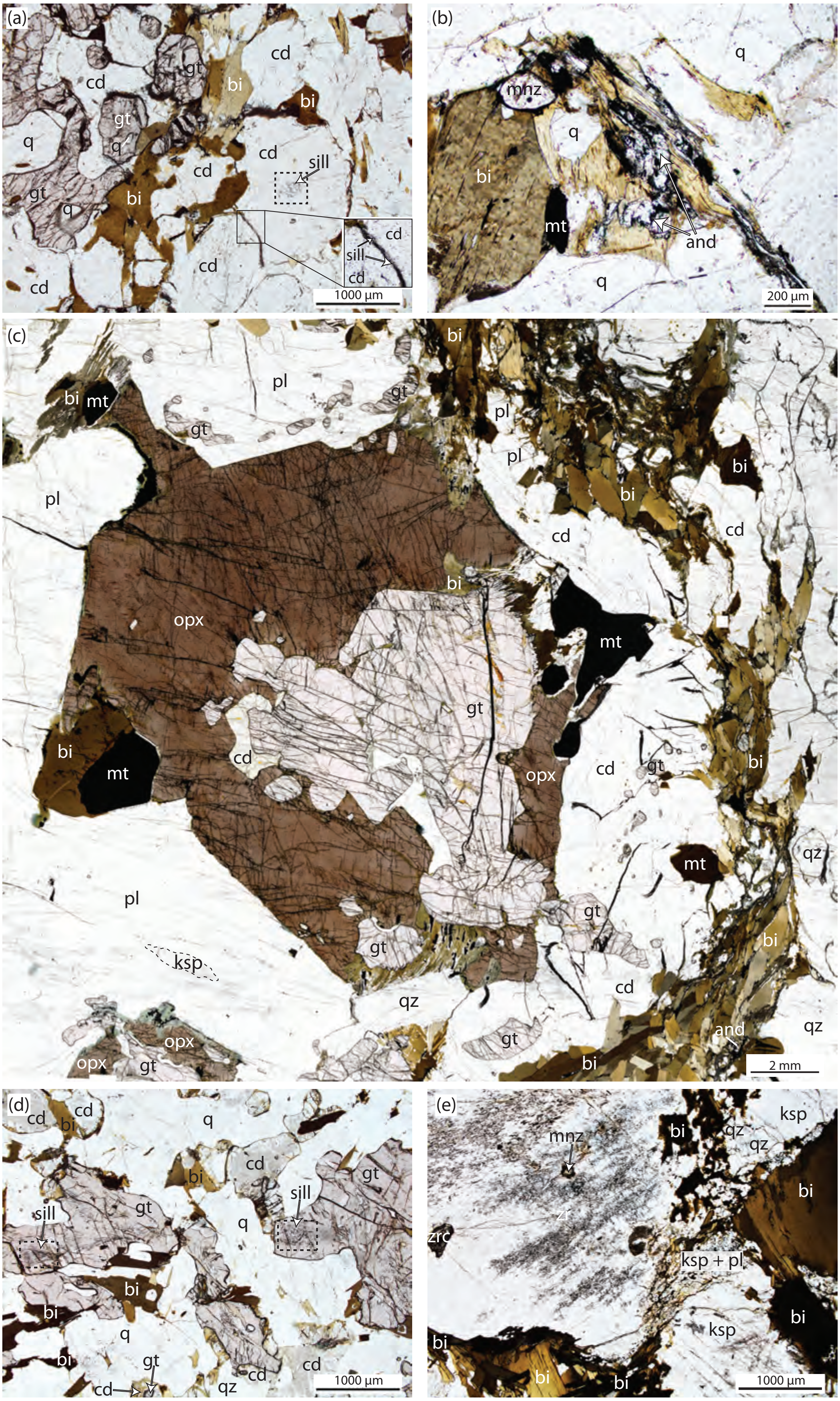
(a)
cd
gt
bi
bi
q
cd
sill
1000 µm
(b)
mnz
q
bi
mt
and
200 µm
(c)
bi
mt
pl
gt
opx
cd
ksp
qz
and
2 mm
(d)
sill
1000 µm
(e)
mnz
zrc
ksp
ksp + pl
1000 µm

Figure 5 (previous page): Photomicrographs of key petrological relationships. (a) Sample RR-03: anhedral garnet occurs in contact with biotite, cordierite and quartz. The cordierite contains patches of fine-grained sillimanite (shown inside the dashed box). Fibrolite occurs at the boundaries of cordierite grains (shown in the inset box on the right hand side of the image). (b) Sample RR-03: Fine-grained, retrograde andalusite grows in association with biotite and magnetite. (c) Sample RR-04: Garnet-orthopyroxene bearing leucosome. Coarse garnet is rimmed by coarse orthopyroxene, which is in turn rimmed by porphyroblasts of cordierite and plagioclase. Magnetite is separated from orthopyroxene by rims of cordierite. Smaller garnet grains are also included within large cordierite grains. The edges of the segregation have been partially retrogressed by a biotite-rich assemblage. Anhedral, fine-grained andalusite occurs in association with the biotite. (d) Sample Boothby-09-2A: anhedral garnet contains patches of fine-grained sillimanite (shown inside the dashed boxes). Garnet is enclosed by a quartz-cordierite-biotite-rich matrix. At the bottom of the image, a small garnet grain is completely enclosed by cordierite. (e) Sample BPG-01: The pegmatites are dominantly made up of coarse-grained K-feldspar and biotite. Fine-grained plagioclase and quartz also occur in direct contact with finer-grained K-feldspar. Coarse-grained monazite and zircon are also common.

(e.g. Spear et al., 1999; White and Powell, 2002). In both the hydrous and anhydrous segregations, cordierite grain boundaries are decorated with very fine-grained, unoriented, fibrolitic sillimanite.

3.1.4. Overall outcrop

For the overall outcrop, the peak mineral assemblage is interpreted as cordierite + garnet + orthopyroxene + plagioclase + biotite + magnetite + ilmenite + silicate melt + K-feldspar. Within the segregations that are comparatively biotite poor, the abundance of garnet is interpreted to have decreased through time, commensurate with the formation of orthopyroxene, cordierite and plagioclase. In the segregations that contain abundant biotite (especially in RR-05), andalusite and fibrolitic sillimanite are additionally interpreted to be retrograde (post-peak) in origin.

3.2. North of Mount Boothby

North of Mount Boothby (WGS84, 53K 325078 mE, 7505909 mS), metapelitic gneisses contain garnet-bearing felsic segregations that are wrapped by a cordierite + biotite bearing foliation (Fig. 4c and d). At outcrop scale, layers rich in cordierite contain folia of sillimanite. However, sillimanite is always armoured by cordierite, and is not in contact with the biotite grains defining the mineral foliation in the outcrop (Fig. 4d).

3.2.1. Sample Boothby-09-1

Sample Boothby-09-1 comprises garnet, cordierite, biotite, quartz and minor K-feldspar and plagioclase. Garnet grains are porphyroblastic, commonly ~4 mm, but can be up to 8 mm in diameter, and contain unoriented inclusions of biotite and ovoid quartz. Biotite makes up a large proportion (~30%) of the sample. There appears to be two generations of biotite. One generation has well defined grain shapes and forms part of a foliation that wraps garnet. The second generation is green-brown and has a less well defined grain shape, but has a similar orientation to the brown biotite and forms part of the foliation. Magnetite occurs most commonly along biotite grain boundaries. Quartz is the second-most abundant mineral and occurs throughout the matrix. Cordierite (0.5–1 mm) occurs with quartz and biotite and its grain boundaries are pronounced by the presence of fine-grained fibrolitic sillimanite intergrown with fine-grained biotite. Fibrolitic sillimanite also occurs occasionally along grain boundaries of garnet.

3.2.2. Sample Boothby-09-2A

Sample Boothby-09-2A comprises garnet,

K-feldspar, biotite, cordierite, quartz, plagioclase and magnetite. Garnet occurs in K-feldspar-bearing felsic segregations wrapped by a cordierite-rich foliation. Garnet is anhedral and medium grained (~5 mm diameter), and occasionally contains randomly-oriented inclusions of sillimanite (Fig. 5d). The matrix assemblage comprises coarse-grained K-feldspar, cordierite and quartz, along with two generations of biotite. Brown biotite is more common and is probably part of the prograde-peak assemblage, whereas green biotite is finer grained and possibly part of the retrograde assemblage. Magnetite grains (up to 0.2 mm diameter) usually occur in contact with biotite. Cordierite is of variable size, but can be up to 1 mm in diameter. Extremely fine-grained fibrolitic sillimanite occurs along cordierite grain boundaries. Andalusite is fine grained with a poorly developed grain shape and occurs intergrown with green biotite.

3.2.3. Overall outcrop

For the overall outcrop, the peak mineral assemblage is interpreted to be garnet + cordierite + plagioclase + K-feldspar + magnetite + quartz ± biotite. The prograde evolution is interpreted to have involved the formation of garnet and cordierite at the expense of sillimanite and biotite (Fig. 4c and d). Post-peak, the retrograde evolution involved the increasing abundance of biotite and cordierite. Andalusite and fibrolite are also interpreted to be retrograde in origin and post-date cordierite.

3.3. Mount Boothby region pegmatites

3.3.1. Samples BPG-01 and BPG-03

Samples BPG-01 and BPG-03 (WGS84, 53K 325039 mE, 7503826 mS) are coarse-grained pegmatites immediately east of Mount Boothby. These pegmatites are metre scale in width and trend for several tens of metres. They cross-cut the regional gneissic foliation at a high angle (Fig. 4e). They comprise K-feldspar, biotite, quartz and minor plagioclase (Fig. 5e). K-feldspar is coarse-grained (1–5 cm) and occurs as both microcline and mesoperthite. Biotite is of varying size. Coarse biotite (up to 2 mm) occurs as platy grains which do not show a preferred orientation. Finer-grained biotite (<0.5 mm) occurs as more elongate grains which appear to wrap K-feldspar porphyroblasts. Monazite occurs as large grains, up to 1 mm in diameter (Fig. 5e). Other accessory minerals include apatite, rutile, zircon, xenotime and allanite.

4. Methods

4.1. Monazite Geochronology

In situ Laser Ablation–Inductively Coupled Plasma–Mass Spectrometry (LA−ICP−MS) U–Pb monazite geochronology was performed on all samples described above except the 'whole rock/outcrop' sample RR-01. Monazite grains were imaged using a back-scattered electron detector on a Phillips XL30 SEM to determine their microstructural location and any internal compositional variation. Representative BSE images are shown in Figure 6.

LA−ICP−MS analyses were performed at the University of Adelaide, following the method of Payne et al. (2008). U–Pb isotopic analyses were acquired using a New Wave 213 nm Nd–YAG laser coupled with an Agilent 7500cs ICP-MS. Ablation of monazites was done in a He-ablation atmosphere with a frequency of 4 Hz for the metapelitic samples and a frequency of 5 Hz for the pegmatite samples. A spot size of 12 μm was used for all samples except RR-05, where larger monazite grains allowed for a spot size of 15 μm. The total acquisition time of each analysis was 80 s. This included 30 s of background measurement, 10 s of the laser firing with the shutter closed to allow for beam stabilisation, and 40 s of sample ablation.

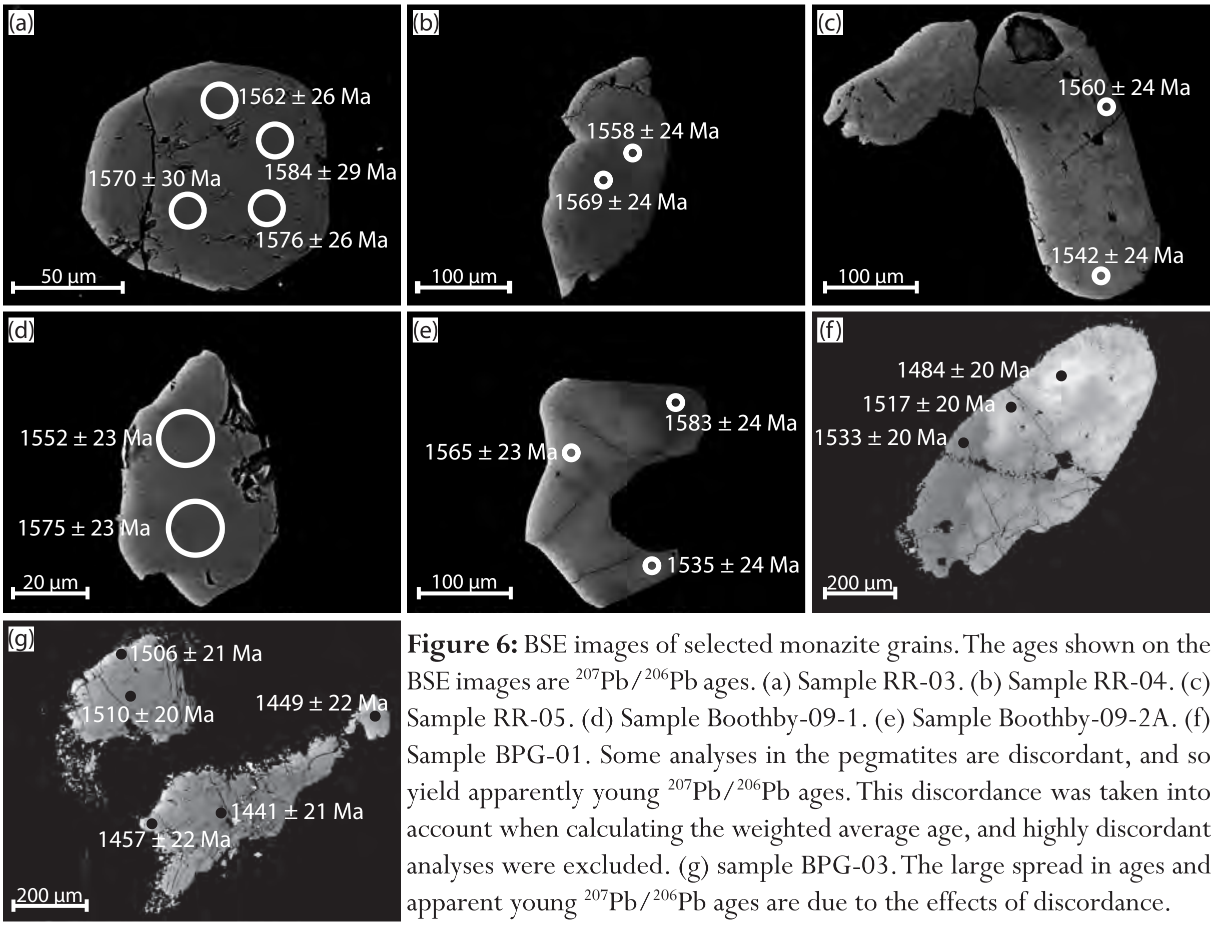

Figure 6: BSE images of selected monazite grains. The ages shown on the BSE images are $^{207}Pb/^{206}Pb$ ages. (a) Sample RR-03. (b) Sample RR-04. (c) Sample RR-05. (d) Sample Boothby-09-1. (e) Sample Boothby-09-2A. (f) Sample BPG-01. Some analyses in the pegmatites are discordant, and so yield apparently young $^{207}Pb/^{206}Pb$ ages. This discordance was taken into account when calculating the weighted average age, and highly discordant analyses were excluded. (g) sample BPG-03. The large spread in ages and apparent young $^{207}Pb/^{206}Pb$ ages are due to the effects of discordance.

Isotopes measured were ^{204}Pb, ^{206}Pb, ^{207}Pb and ^{238}U for dwell times of 10, 15, 30 and 15 ms, respectively.

Monazite data were reduced using Glitter software (Griffin et al., 2004). Elemental fractionation and mass bias was corrected using the monazite standard 44069 for the metapelitic samples [TIMS normalisation data: $^{207}Pb/^{206}Pb$ = 425.3 ± 1.1 Ma, $^{206}Pb/^{238}U$ = 424.86 ± 0.36 Ma and $^{207}Pb/^{235}U$ = 424.89 ± 0.35 Ma: Aleinikoff et al. (2006)] and the monazite standard MAdel for the pegmatite samples (TIMS normalisation data: $^{207}Pb/^{206}Pb$ = 490.7 Ma, $^{206}Pb/^{238}U$ = 514.8 Ma and $^{207}Pb/^{235}U$ = 510.4 Ma: Payne et al. (2008) with an overestimated uncertainty of 1% attached to each normalisation age). Throughout the course of this study, 44069 as a primary standard yielded weighted mean ages of $^{207}Pb/^{206}Pb$ = 425.9 ± 7.4 Ma, $^{206}Pb/^{238}U$ = 424.6 ± 1.5 Ma and $^{207}Pb/^{235}U$ = 424.8 ± 1.5 (n = 86). MAdel yielded weighted mean ages of $^{207}Pb/^{206}Pb$ = 501 ± 13 Ma, $^{206}Pb/^{238}U$ = 513 ± 2.8 Ma, and $^{207}Pb/^{235}U$ = 510.8 ± 2.6 Ma (n = 32).

Data accuracy was monitored using monazite standard MAdel as an internal standard for the metapelitic samples, while 94-222/Bruna-NW (c. 450 Ma: Payne et al. 2008) was used for the pegmatites and as an additional standard for RR-03. As a secondary standard, MAdel yielded weighted mean ages of $^{207}Pb/^{206}Pb$ = 502 ± 10 Ma, $^{206}Pb/^{238}U$ = 516.6 ± 2.5 Ma, $^{207}Pb/^{235}U$ = 513.5 ± 2.4 Ma (n = 42), while 94-222 yielded weighted mean ages of ^{207}Pb/206Pb = 441 ± 18 Ma, $^{206}Pb/^{238}U$ = 449.4 ± 3.7 Ma, $^{207}Pb/^{235}U$ = 448.3 ± 3.6 Ma (n = 12).

Isotopic age data for all samples were anchored to a lower intercept of 360 ± 25 Ma. This age corresponds to the timing of Alice Springs Orogeny shear zone activity in the Reynolds-Anmatjira Ranges, as established by several previous studies (Cartwright et al., 1999, 2001; Raimondo et al., 2011, 2012). It was considered that the use of this value as a lower anchor would provide consistency between samples as some of the samples display poorly defined discordance. The upper intercept ages calculated using free regression and anchored regression are similar, so the use of a lower anchor is not considered to have a significant effect on the age. All monazite U–Pb age data from this study are tabulated in Supplementary Data S4.1.

4.2. Bulk rock and mineral chemistry

Bulk-rock chemical compositions for use in the calculation of metamorphic phase diagrams were obtained from Amdel Laboratories, Adelaide (Supplementary Data S4.2). For RR-01, approximately 20 kg of fresh rock was crushed. This encompassed the matrix, orthopyroxene-bearing segregations and some retrogressed (biotite-rich) segregations. For samples RR-03, RR-04 and RR-05, bulk-rock chemistry was obtained by crushing small amounts of these domains (several centimetres in size). For Boothby-09-2A, a representative amount of rock was crushed. The crushed rock was then homogenized using a tungsten carbide mill. Major elements were analysed by fusing a 0.1 g portion of the powdered sample with lithium metaborate before dissolution and analysis using Inductively Coupled Plasma-Optical Emission Spectroscopy (ICP–OES). Rare Earth elements were analysed by digestion of the analytical pulp in HF acid before analysis using ICP–MS. Wet chemistry methods were used to determine the amount of FeO and Fe_2O_3.

Chemical analyses of minerals were obtained using a Cameca SX51 electron microprobe at the University of Adelaide. A beam current of 20 nA and accelerating voltage of 15 kV was used for all point analyses. Representative analyses for each mineral are given in Table 2.

4.3. Mineral equilibria modelling

Mineral equilibria relevant to the bulk chemical compositions of samples RR-01, RR-03, RR-04, RR-05 and Boothby-09-2A were calculated using THERMOCALC v3.33, employing the internally-consistent data set of Holland and Powell (1998a; dataset tcds55 November 2003 update) for the geologically realistic system NCKFMASHTO (Na_2O–CaO–K2O–FeO–MgO–Al_2O_3–SiO_2–H_2O–TiO_2–Fe_2O_3). The following activity-composition relationships were used: silicate melt, garnet and biotite (White et al., 2007); cordierite (Holland and Powell, 1998b); orthopyroxene and magnetite (White et al., 2002); ilmenite (White et al., 2000); muscovite (Coggon and Holland, 2002) and plagioclase and K-feldspar (Holland and Powell, 2003). The principal uncertainties on bulk composition for calculating mineral equilibria relate to H_2O and Fe_2O_3 (Johnson and White, 2011). LOI was used as an upper estimate for H_2O for the hydrous assemblage of sample RR-05. However, samples RR-01, RR-03, RR-04 and Boothby-09-2A preserve residual mineral assemblages, suggesting they have experienced melt loss (Fyfe, 1973; Powell and Downes, 1990; White and Powell, 2002). The H_2O content was estimated based on the abundance and chemical compositions of the observed mineral assemblages, and to ensure that the calculations involved a dry solidus at peak pressures (~0.7 GPa). The main effect of decreasing the H_2O content is to elevate the solidus to higher temperatures and increase the stability of biotite and K-feldspar (e.g. Gallien et al., 2010; White and Powell, 2002), but

Table 2: Representative electron microprobe data

	RR-03								RR-04							
Mineral	gt rim	gt core	bi	cd	pl	ksp	mt	ilm	gt rim	gt core	opx rim	opx core	pl	cd	ksp	bi
SiO_2	36.43	37.47	34.48	48.05	59.87	66.11	0.02	0.03	37.10	37.08	46.57	46.53	58.92	49.65	63.82	40.92
TiO_2	0.02	0.03	4.14	0.00	0.02	-	0.01	52.46	0.03	0.06	0.14	1.82	0.02	0.00	0.02	1.85
Al_2O_3	21.33	21.37	15.71	32.78	25.60	18.45	0.18	0.01	21.56	21.68	7.63	5.25	24.97	32.46	17.89	17.40
Cr_2O_3	0.02	0.00	0.01	0.00	-	0.05	0.31	0.03	0.01	0.00	0.04	0.00	0.02	0.01	0.00	0.01
FeO	31.58	31.68	14.52	4.65	0.04	-	88.58	46.60	30.21	31.02	26.44	25.24	0.01	5.77	0.00	11.94
MnO	0.35	0.38	0.00	0.03	-	-	0.01	0.19	0.45	0.46	0.13	0.09	0.01	0.04	0.00	0.01
MgO	7.28	7.03	14.13	11.23	0.00	0.01	0.00	0.23	8.47	8.27	18.83	20.74	0.00	10.29	0.02	12.79
ZnO	0.05	0.00	0.07	0.07	0.02	-	0.11	-	0.06	0.00	0.17	0.12	0.00	0.06	0.00	0.44
CaO	1.23	1.01	0.00	0.04	8.10	0.01	0.02	0.01	1.23	0.98	0.13	0.05	7.25	0.01	0.08	0.08
Na_2O	0.01	0.03	0.16	0.00	7.01	1.31	0.01	0.01	0.03	0.01	0.06	0.03	7.53	0.05	1.20	0.17
K_2O	0.01	0.00	9.69	0.00	0.12	14.49	0.00	0.02	0.00	0.00	0.02	0.00	0.15	0.01	14.57	7.58
Total	**98.31**	**99.00**	**92.89**	**96.85**	**100.77**	**100.43**	**89.25**	**99.58**	**99.15**	**99.57**	**100.16**	**99.88**	**98.87**	**98.36**	**97.60**	**93.20**
No. Oxygens	12	12	11	18	8	8	4	3	12	12	6	6	8	18	8	11
Si	2.92	2.97	2.66	4.95	2.65	3.01	0.00	0.00	2.93	2.92	1.74	1.75	2.66	5.05	3.01	3.00
Ti	0.00	0.00	0.24	0.00	0.00	0.00	0.00	1.00	0.00	0.00	0.01	0.05	0.00	0.00	0.00	0.10
Al	2.02	2.00	1.43	3.98	1.34	0.99	0.01	0.00	2.00	2.01	0.32	0.23	1.33	3.89	0.99	1.51
Cr	0.00	0.00	0.00	0.00	0.00	0.00	0.01	0.00	0.00	0.00	0.00	0.00	0.00	0.00	0.00	0.00
Fe^{3+}	- -	-	-	-	-	-	1.98		-	-	0.18	0.17	-	-	-	-
Fe^{2+}	2.12	2.10	0.94	0.40	0.00	0.00	1.00	0.99	1.99	2.04	0.64	0.62	0.00	0.49	0.00	0.73
Mn^{2+}	0.02	0.03	0.00	0.00	0.00	0.00	0.00	0.00	0.03	0.03	0.00	0.00	0.00	0.00	0.00	0.00
Mg	0.87	0.83	1.62	1.72	0.00	0.00	0.00	0.01	1.00	0.97	1.09	1.16	0.00	1.56	0.00	1.40
Zn	0.00	0.00	0.00	0.01	0.00	0.00	0.00	0.00	0.00	0.00	0.00	0.00	0.00	0.00	0.00	0.02
Ca	0.11	0.09	0.00	0.00	0.38	0.00	0.00	0.00	0.10	0.08	0.00	0.00	0.35	0.00	0.00	0.01
Na	0.00	0.01	0.02	0.00	0.60	0.12	0.00	0.00	0.00	0.00	0.00	0.00	0.66	0.01	0.11	0.02
K	0.00	0.00	0.95	0.00	0.01	0.84	0.00	0.00	0.00	0.00	0.00	0.00	0.01	0.00	0.88	0.71
Total Cations	**8.07**	**8.03**	**7.87**	**11.06**	**4.98**	**4.97**	**3.00**	**2.00**	**8.06**	**8.06**	**4.00**	**4.00**	**5.01**	**11.01**	**4.99**	**7.51**

Table 2 (continued).

	RR-04			**RR-05**					**Boothby-09-2A**						
Mineral	ilm	mt	and	pl	bi	mt	ilm	cd	gt rim	gt core	bi	pl	ksp	mt	and
SiO_2	0.13	0.05	35.37	58.04	35.75	0.19	0.01	49.54	37.35	36.20	35.16	58.80	66.25	0.07	36.84
TiO_2	50.75	0.18	0.08	0.05	4.33	0.16	51.26	0.01	0.00	0.00	3.18	0.02	0.02	0.11	0.02
Al_2O_3	0.11	0.91	57.33	25.50	15.56	0.23	0.00	32.55	20.89	20.43	16.27	26.28	18.37	0.38	58.84
Cr_2O_3	0.08	2.25	0.06	0.34	0.19	2.62	0.52	-	0.03	0.00	0.01	0.01	0.02	0.84	0.07
FeO	45.97	85.55	4.00	0.02	15.62	84.74	44.12	5.79	34.29	36.22	19.66	0.08	0.03	86.87	2.13
MnO	0.34	-	0.01	0.03	0.01	0.00	0.23	0.07	0.71	0.96	0.03	0.01	-	0.00	0.05
MgO	0.48	0.08	0.16	0.00	12.86	0.04	0.43	10.29	4.72	3.39	10.65	-	0.01	0.01	0.61
ZnO	-	0.13	0.06	0.00	0.00	0.09	0.05	0.03	0.04	0.05	0.11	0.07	0.02	0.00	0.03
CaO	0.01	0.01	0.05	8.08	0.00	0.02	0.00	0.01	1.47	1.41	0.05	8.96	0.09	0.03	0.05
Na_2O	0.00	-	0.00	7.01	0.08	0.00	0.00	0.07	0.00	0.01	0.21	6.65	2.22	0.00	0.07
K_2O	0.00	0.02	0.02	0.22	9.57	0.00	0.01	0.00	0.00	0.00	9.31	0.10	13.38	0.02	0.09
Total	**97.88**	**89.17**	**97.13**	**99.30**	**93.98**	**88.09**	**96.61**	**98.36**	**99.49**	**98.67**	**94.62**	**100.99**	**100.39**	**88.34**	**98.81**
No. Oxygens	3	4	5	8	11	4	3	18	12	12	11	8	8	4	5
Si	0.00	0.00	0.99	2.62	2.73	0.01	0.00	5.04	2.99	2.96	2.39	2.61	3.01	0.00	1.01
Ti	0.98	0.01	0.00	0.00	0.25	0.00	1.00	0.00	0.00	0.00	0.16	0.00	0.00	0.00	0.00
Al	0.00	0.04	1.90	1.36	1.40	0.01	0.00	3.90	1.97	1.97	1.30	1.37	0.99	0.02	1.90
Cr	0.00	0.07	0.00	0.01	0.01	0.08	0.01	0.00	0.00	0.00	0.00	0.00	0.00	0.03	0.00
Fe^{3+}		1.87	0.11			1.88	0.00							1.94	0.00
Fe^{2+}	0.99	1.00	0.00	0.00	1.00	1.01	0.96	0.49	2.25	2.35	1.12	0.00	0.00	1.00	0.05
Mn^{2+}	0.01	0.00	0.00	0.00	0.00	0.00	0.01	0.01	0.05	0.07	0.00	0.00	0.00	0.00	0.00
Mg	0.02	0.00	0.01	0.00	1.46	0.00	0.02	1.56	0.56	0.41	1.08	0.00	0.00	0.00	0.03
Zn	0.00	0.00	0.00	0.00	0.00	0.00	0.00	0.00	0.00	0.00	0.01	0.00	0.00	0.00	0.00
Ca	0.00	0.00	0.00	0.39	0.00	0.00	0.00	0.00	0.13	0.12	0.00	0.43	0.00	0.00	0.00
Na	0.00	0.00	0.00	0.61	0.01	0.00	0.00	0.01	0.00	0.00	0.03	0.57	0.20	0.00	0.00
K	0.00	0.00	0.00	0.01	0.93	0.00	0.00	0.00	0.00	0.00	0.81	0.01	0.78	0.00	0.00
Total Cations	**2.01**	**3.00**	**3.02**	**5.01**	**7.79**	**3.00**	**2.00**	**11.02**	**7.95**	**7.88**	**6.90**	**4.99**	**4.98**	**3.00**	**3.00**

it is not considered to significantly affect the topology of the ferromagnesian part of mineral assemblages in the pseudosections (Johnson and White, 2011). FeO vs Fe_2O_3 was measured using wet chemistry methods at Amdel Laboratories (see section 4.2 above).

5. Results

5.1. Monazite geochronology

5.1.1. RR-03

Thirty-four analyses were collected from 18 grains located throughout the foliated cordierite-biotite bearing matrix. Monazite grains are 20–100 µm in diameter. Most grains are euhedral or rounded and some display zoning, particularly near the rims (Fig. 6a). Four discordant analyses which appear to be outliers and may have been partially reset were excluded from the calculations (grey ellipses). The weighted average $^{207}Pb/^{206}Pb$ age for the remaining 30 concordant analyses is 1561 ± 10 Ma (MSWD = 0.51). A concordia plot anchored to 360 ± 25 Ma yields an upper intercept age of 1562 ± 8 Ma (MSWD = 1.7; Fig. 7a).

5.1.2. RR-04

Twenty-two analyses were collected from 13 grains throughout the garnet-orthopyroxene-bearing segregation. Monazite is coarse (up to 200 µm in diameter) and abundant. Most of the grains are unzoned; however, rare grains display patchy zoning (Fig. 6b). There is no difference in age between monazite included in orthopyroxene and that included in garnet, plagioclase or cordierite. The weighted average $^{207}Pb/^{206}Pb$ age of 22 analyses is 1560 ± 10 Ma (MSWD = 0.45). A concordia plot anchored to 360 ± 25 Ma yields an upper intercept of 1563 ± 6 Ma (MSWD = 1.5; Fig. 7b).

5.1.3. RR-05

Twenty analyses were collected from 11 grains from the retrograde biotite-plagioclase-cordierite assemblage that replaced the orthopyroxene-garnet segregation. Monazite in the segregation is very abundant and coarse grained (up to 500 µm in diameter). Some grains display patchy zoning (Fig. 6c). One discordant analysis which was considered to be an outlier from the main population was excluded from the calculations (shown as a grey ellipse). The weighted average $^{207}Pb/^{206}Pb$ age from the remaining 19 concordant analyses is 1542 ± 12 Ma (MSWD = 0.38). A concordia plot anchored to 360 ± 25 Ma yields an upper intercept of 1540 ± 8 Ma (MSWD = 1.5, Fig. 7c).

5.1.4. Boothby-09-1

Thirty-one analyses were collected from 24 grains located throughout the cordierite-biotite bearing foliated matrix. Monazite grains are 40–100 µm in diameter and are commonly unzoned (Fig. 6d). One discordant analysis which appears to be an outlier and may have been partially reset was excluded from the calculations (grey ellipse). The weighted average $^{207}Pb/^{206}Pb$ age from the remaining 30 concordant analyses is 1576 ± 10 (MSWD = 0.67). A concordia plot anchored to 360 ± 25 Ma yields an upper intercept of 1575 ± 9 Ma (MSWD =1.9; Fig. 7d).

5.1.5. Boothby-09-2A

Twenty-four analyses were collected from 14 grains located throughout the foliated matrix. Monazite grains are commonly located at grain boundaries and are occasionally included in cordierite or quartz. Monazite grains are commonly 40–50 µm in diameter but some grains are up to 100 µm in diameter. Some grains display patchy zoning (Fig. 6e). The weighted average $^{207}Pb/^{206}Pb$ age from 24 analyses is 1572 ± 10 Ma (MSWD 0.52). A concordia plot anchored to 360 ± 25 Ma yields

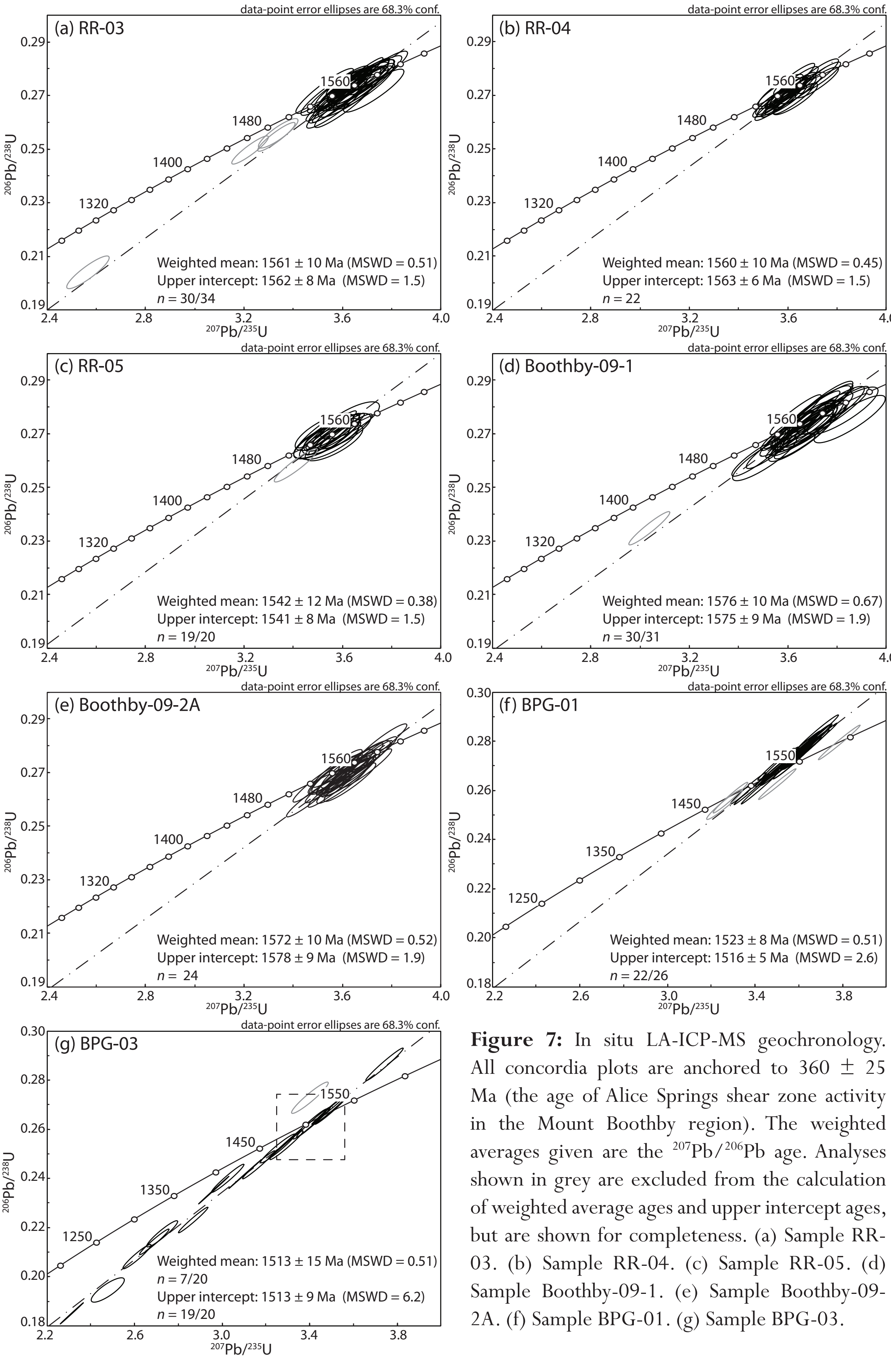

Figure 7: In situ LA-ICP-MS geochronology. All concordia plots are anchored to 360 ± 25 Ma (the age of Alice Springs shear zone activity in the Mount Boothby region). The weighted averages given are the $^{207}Pb/^{206}Pb$ age. Analyses shown in grey are excluded from the calculation of weighted average ages and upper intercept ages, but are shown for completeness. (a) Sample RR-03. (b) Sample RR-04. (c) Sample RR-05. (d) Sample Boothby-09-1. (e) Sample Boothby-09-2A. (f) Sample BPG-01. (g) Sample BPG-03.

an upper intercept age of 1578 ± 9 Ma (MSWD = 1.9; Fig. 7e).

5.1.6. Pegmatite BPG-01

Twenty-six analyses were obtained from 8 grains that were located within coarse K-feldspar and along grain boundaries. Monazite is coarse-grained (up to 1 mm in diameter). Monazite commonly occurs with other accessory minerals allanite and huttonite. Some grains show complex zoning patterns (Fig. 6f). Four analyses that were considered to be outliers (inherited and/or partially reset grains, shown as grey ellipses) were excluded from the calculations to provide a tighter age constraint. The weighted average $^{207}Pb/^{206}Pb$ age from the remaining 22 analyses is 1523 ± 8 Ma (MSWD = 0.26). A concordia plot anchored to 360 ± 25 Ma yields an upper intercept of 1516 ± 5 Ma (MSWD = 2.6; Fig. 7f).

5.1.7. Pegmatite BPG-03

Twenty analyses were obtained from nine grains that were located within coarse K-feldspar and along grain boundaries. Monazite is coarse-grained (up to 1 mm in diameter). Monazite grains commonly have irregular, ragged boundaries (Fig. 6g). Some grains display patchy zoning. One reversely discordant analysis that fell outside the general trend was excluded (shown as a grey ellipse). The remaining 19 analyses define a discord that yields an upper intercept age of 1513 ± 9 Ma (MSWD = 6.2; Fig. 7g). As the data are strongly discordant, a weighted average $^{207}Pb/^{206}Pb$ age was calculated using only data that fell within ± 3% concordance. The weighted average age of these seven analyses is 1513 ± 15 Ma (MSWD = 0.51).

5.2. Pressure–temperature conditions

5.2.1. RR-01: prograde and peak P–T conditions

We have assumed that the large bulk sample RR-01, which contains the cordierite-rich (host) gneiss, the garnet-orthopyroxene-bearing segregations and partially retrogressed segregations, represents a valid compositional system in which the peak metamorphic assemblages developed. The peak mineral assemblage of cordierite + garnet + orthopyroxene (in segregations) + quartz + plagioclase + biotite + silicate melt (as represented by the segregations) + minor K-feldspar, magnetite and ilmenite defines a narrow divariant field (field 14) with *P–T* conditions ranging from 0.6–0.77 GPa and 860–890 °C (Fig. 8a). However, it is petrologically difficult to determine whether biotite forms part of the peak assemblage or whether the majority of biotite formed along the retrograde path. Therefore, it is possible that the neighbouring biotite-absent trivariant field (to higher temperature) best represents the peak assemblage. This would mean that peak conditions occurred at temperatures in excess of ~870 °C. The presence of garnet in the gneissic host rock (see sample RR-03) as well as in some segregations constrains the pressure to be above 0.65 GPa, whereas the presence of magnetite and absence of sillimanite in the matrix suggests pressures below ~0.75 GPa (Fig. 8a).

The absolute prograde *P–T* history is difficult to constrain for granulite facies rocks from which melt loss has occurred (e.g. Kelsey, 2008; White et al., 2004). However, qualitatively, the volumetrically most dominant cordierite-rich (host) gneiss is interpreted to comprise an early (prograde) garnet-sillimanite-cordierite-bearing assemblage in which sillimanite has been almost completely consumed by cordierite prior to reaching peak metamorphic conditions. Evidence for prograde sillimanite is restricted to its presence in the core of cordierite grains. Therefore, although the prograde history

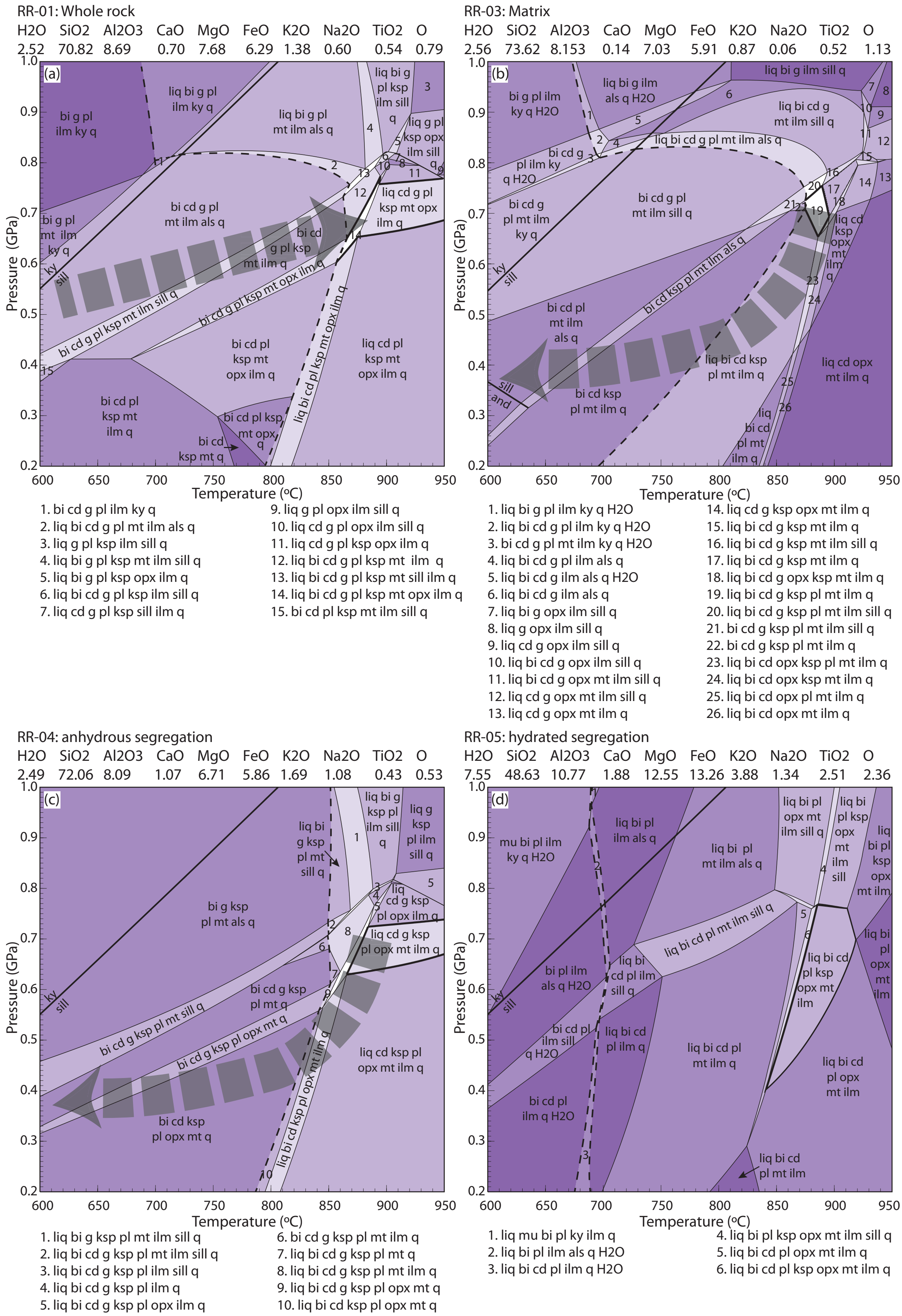

Figure 8: Calculated *P–T* pseudosections.

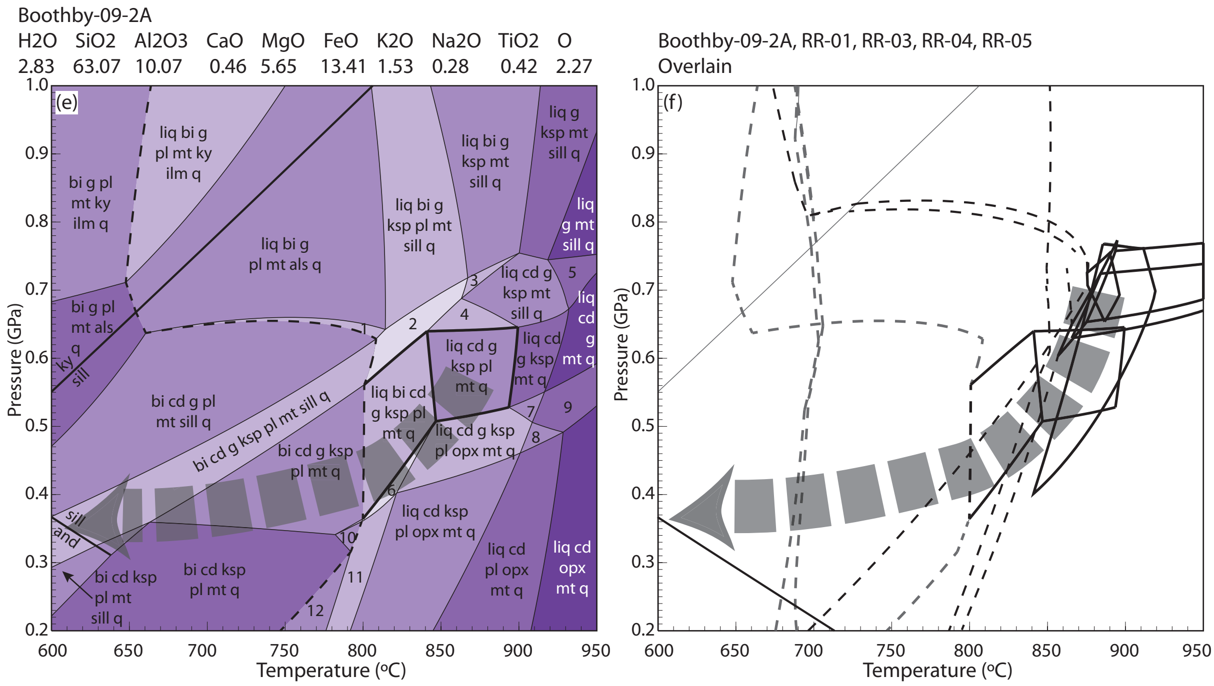

1. liq bi cd g pl mt sill q
2. liq bi cd g ksp pl mt sill q
3. liq bi cd g ksp mt sill q
4. liq cd g ksp pl mt sill q
5. liq cd g mt sill q
6. liq bi cd g ksp pl opx mt q
7. liq cd g ksp opx mt q
8. liq cd g pl opx mt q
9. liq cd g opx mt q
10. bi cd ksp pl opx mt q
11. liq bi cd ksp pl opx mt q
12. liq bi cd ksp pl mt q

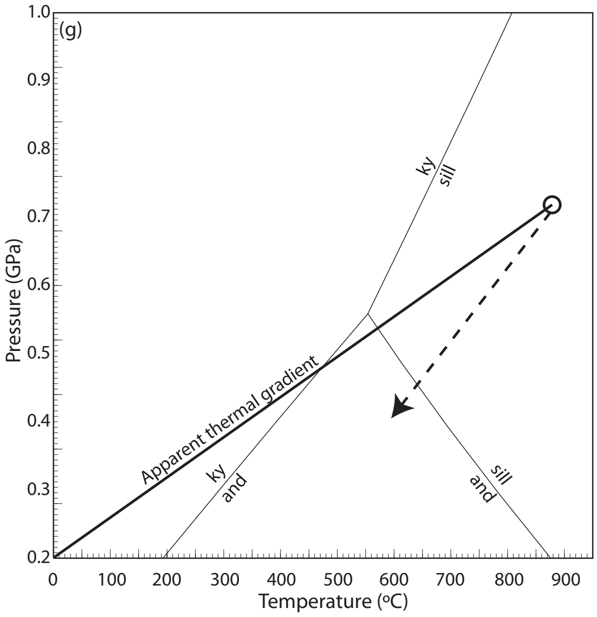

Figure 8 (continued).

Figure 8 (previous pages): Calculated *P–T* pseudosections. The bold dashed line is the solidus. Fields are shaded according to the variance of the assemblage, with a white field denoting a variance of two. (a) Sample RR-01. The fields outlined in bold are the interpreted peak (see text for discussion of each field). The grey arrow is the inferred prograde *P–T* path. Although there is limited information on the prograde evolution, it must have involved sillimanite. (b) Sample RR-03. The peak assemblage is outlined in bold. The bold dashed line is the inferred retrograde *P–T* path, which involved increasing cordierite and decreasing garnet, culminating in the development of late andalusite. (c) Sample RR-04. The peak assemblage is outlined in bold. The interpretation of biotite is problematic, so the outlined fields include a biotite present and biotite absent field. The early post-peak evolution involved decompression and increasing abundance of orthopyroxene at the expense of garnet. The formation of late garnet suggests the *P–T* path then became cooling dominated. (d) Sample RR-05. The high temperature field outlined in bold corresponds to the 'peak' assemblage recorded by the orthopyroxene leucosomes. The lower temperature field corresponding to the retrograde assemblage is outlined in bold. The field representing the formation of the retrograde assemblage is large, as there are few minerals to constrain the conditions. The possible retrograde conditions occur between 690–870 °C and below 0.75 GPa. (e) Sample Boothby-09-2A. The interpreted peak fields are outlined in bold (see text for discussion of each field). The grey line is the inferred *P–T* path. (f) All five pseudosections overlain, with interpreted peak fields shown in bold. The solidi of each sample are shown as dashed lines for comparison. (g) Inferred retrograde *P–T* path plotted against the apparent thermal gradient.

cannot be definitively determined, it must have involved the stability of sillimanite (Fig. 8a).

5.2.2. RR-03, RR-04, RR-05: retrograde P–T evolution

Given the scale of the orthopyroxene-garnet segregations in the outcrop (RR-04), we assume that it is also valid to treat the cordierite-rich (host) gneiss between segregations (RR-03) as a separate compositional system with regard to the retrograde evolution. The cordierite-rich (host) gneiss was not able to develop orthopyroxene at the peak of metamorphism (orthopyroxene is only present in the segregations, RR-04), perhaps due to slight compositional changes related to melt and segregation formation. Therefore, the conditions of the respective peak assemblages calculated for the host gneiss (RR-03) and segregation (RR-04) compositions should overlap. They should also correspond to the peak conditions calculated using the bulk composition of sample RR-01.

The peak assemblage in sample RR-03 is interpreted to be garnet + cordierite + biotite + K-feldspar + quartz + plagioclase + magnetite + ilmenite + melt (Fig. 5a). This assemblage is calculated to occur at ~870 °C and 0.7 GPa and overlaps well with the peak mineral assemblage field for RR-01 (Fig. 8b). The partial replacement of garnet by cordierite suggests a *P–T* evolution that involved decompression. However, the presence of K-feldspar and the absence of secondary growth of sillimanite (except for the minor development of fibrolite, which occurred at a scale much smaller than the equilibration volume considered here) suggest that the *P–T* path involved decompression and cooling along a high thermal gradient. Retrograde andalusite lends further support to the inference that the retrograde *P–T* path followed a high thermal gradient towards lower temperatures (Fig. 5b).

Sample RR-04 contains the assemblage orthopyroxene + cordierite + plagioclase + garnet + K-feldspar + magnetite + ilmenite + quartz + biotite (Fig. 5c). It is difficult to interpret whether biotite forms part of the peak mineral assemblage in these segregations. However, the absence of biotite inclusions in garnet or orthopyroxene in the segregations suggests biotite may not have been part of the peak assemblage. The interpreted peak assemblage orthopyroxene + cordierite + plagioclase + garnet + K-feldspar + magnetite + ilmenite without biotite occurs at 0.6–0.75 GPa and temperatures in excess of 860 °C (Fig. 8c). However, if biotite is interpreted to form part of the peak assemblage, the peak conditions occur at 840–890 °C and 0.56–0.76 GPa (Fig. 8c). These conditions overlap with the peak conditions calculated for samples RR-01 and RR-03. The mantling of garnet by orthopyroxene and inclusions of garnet in cordierite support the interpretation that cordierite and orthopyroxene abundance increased at the expense of garnet along the retrograde path (Fig. 5c). Therefore, some of the segregations that are garnet-absent may have lost all their original garnet. However, in the case of sample RR-04, the growth of orthopyroxene + cordierite at the expense of garnet implies a decompressive path that probably tracked into the orthopyroxene + cordierite + biotite + K-feldspar + plagioclase field. However, the growth of late garnet at the margins of relict garnet, and the replacement of orthopyroxene by biotite, suggests that the rocks may have tracked back into a garnet bearing field. This could suggest that after initial decompression, the retrograde path became cooling dominated (Fig. 8c).

The retrogressed segregation, sample RR-05, does not contain orthopyroxene or garnet, and instead comprises biotite and plagioclase, with lesser amounts of K-feldspar, quartz, cordierite, magnetite and ilmenite (Fig. 5c). However, based on partially retrogressed segregations (e.g. sample RR-04), it is assumed that the peak assemblage would have been orthopyroxene-bearing prior to retrogression. The inferred peak assemblage occurs above 850 °C, which is consistent with the *P–T* conditions inferred for the bulk composition of sample RR-01, and the bulk compositions represented by samples RR-03 and RR-04. As K-feldspar is predicted to only occurs at peak temperatures in the pseudosection (Fig. 8d), K-feldspar observed in sample RR-05 is interpreted to be relict. The mineral assemblage in RR-05 (without K-feldspar) is interpreted to represent complete retrogression of the peak assemblage and crystallisation of trapped melt in the segregation. Retrograde *P–T* conditions are not particularly tightly constrained by the biotite + cordierite + plagioclase + quartz + magnetite + ilmenite + melt assemblage (Fig. 8d). However, anhedral andalusite occurs in the sample, located along grain boundaries of biotite. This implies that the rock reached low pressure, amphibolite facies conditions along its retrograde *P–T* trajectory.

5.2.3. Boothby-09-2A

The peak assemblage in Boothby-09-2A is interpreted as garnet + cordierite + quartz + K-feldspar + plagioclase + magnetite (Fig. 5d and e). The interpretation of biotite is problematic. The grains are anhedral, but in some cases contain a cleavage, and they are comparatively abundant in the sample. Therefore, it is difficult to determine with certainty whether it forms part of the peak assemblage. If biotite is a peak mineral then the peak mineral assemblage occurs between 800–850 °C and 0.35–0.6 GPa (Fig. 8e). If biotite is not a peak mineral and instead formed on the retrograde path then the assemblage occurs at higher temperatures and pressures of 850–900 °C and 0.5–0.64 GPa (Fig. 8e). Silicate melt is also interpreted to have formed part of the peak assemblage, based on the presence of felsic segregations in outcrop. The presence of melt requires temperatures to have been above 800 °C (Fig. 8e). Sillimanite is not interpreted to form part of the peak assemblage, and only occurs as fine grained inclusions within garnet (Fig. 5d) and armoured in cordierite (Fig. 4d). The lack of sillimanite in the peak mineral assemblage provides an upper pressure limit of 0.65 GPa, while the lack of orthopyroxene constrains pressures to above 0.35 GPa (Fig. 8e). Fine-grained andalusite is also present along grain boundaries in association with late biotite, suggesting the retrograde *P–T* path cooled through the andalusite field.

6. Discussion

The aim of this study is to provide a greater understanding of the conditions and duration of Early Mesoproterozoic high thermal gradient metamorphism in the Arunta Region. We have investigated the timing and conditions of metamorphism by integrating in situ geochronology with calculated pseudosections from samples that represent the progression of suprasolidus *P–T* conditions from prograde/peak through to retrograde.

6.1. Duration of the high-T conditions

U–Pb monazite ages obtained in this study show a spread from 1576–1513 Ma (Fig. 7; Table 1). The oldest ages were obtained from granulite facies metapelites north of Mount Boothby, which yielded $^{207}Pb/^{206}Pb$ weighted average ages of 1576 ± 10 Ma and 1572 ± 10 Ma (Fig. 7d and e). Further south, monazite from the peak gneissic foliation (sample RR-03) and overprinting orthopyroxene-bearing segregations (sample RR-04) gave $^{207}Pb/^{206}Pb$ weighted average ages of 1563 ± 11 and 1560 ± 10 Ma, respectively (Fig. 7c and d). The hydrous assemblage (sample RR-05) is interpreted to record hydration of a peak metamorphic orthopyroxene-bearing assemblage and gave a younger age of 1542 ± 12 Ma (Fig. 7c), albeit still within error of the peak assemblages. Monazite ages obtained from two cross-cutting pegmatites near Mount Boothby (samples BPG-01 and BPG-03) yield weighted averages of 1523 ± 8 Ma and 1513 ± 15 Ma, respectively (Fig. 7f and g).

Monazite age data from each sample in this study does not display a range of ages, as is commonly observed in high-temperature rocks (e.g. Ashwal et al., 1999; Claoué-Long et al., 2008b; Halpin et al., 2012; Korhonen et al., 2013). However, there is a spread of ages between samples. Monazite ages from high-grade, partially melted rocks have historically been interpreted as the age of cooling below isotopic (Pb) closure (e.g. Copeland et al., 1988; Kelsey et al., 2003; Parrish, 1990; Smith and Giletti, 1997). However, it has been demonstrated experimentally that monazite may be resistant to Pb diffusion at temperatures up to or even in excess of 900 ºC (Cherniak, 2010; Cherniak et al., 2004), such that monazite may preserve growth ages, rather than cooling ages, at elevated temperatures. Natural studies on high-temperature and ultrahigh-temperature granulite facies rocks seem to lend support to the preservation of growth ages even at very high temperatures (e.g. Clark et al., 2011; Goncalves et al., 2004; Kelsey et al., 2003, 2007; Schmitz and Bowring, 2003).

Kelsey et al. (2008) proposed that monazite stability in high-grade, melt-bearing rocks is related to the melting history of the rock as well as the impact that melting has on the whole-rock Light Rare Earth Element (LREE) content. For *average* pelitic compositions and LREE rock contents, monazite *growth* is postulated to occur at temperatures approximating the effective solidus for a melted rock (Kelsey et al., 2008). This interpretation of high monazite solubility has been questioned by Stepanov et al. (2012), who claim that monazite solubility is not as high—and conversely, its growth is not as restricted to near-solidus conditions on a down-temperature evolution path—as that predicted by Kelsey et al. (2008). Regardless, in the present case, our monazite age data may be interpreted as recording growth rather than cooling ages. This implies that in high-temperature rocks, the majority of monazite growth may occur after peak metamorphism, as the rocks cool and melt crystallises. Therefore, in slowly cooled terranes the majority of monazite growth may post-date peak metamorphism, and thus give an indication of the approximate age at which the solidus was crossed in a particular rock (or local composition).

The samples chosen for this study show a general correlation between the stage of metamorphic evolution and the age recorded. The oldest ages (1576–1560 Ma) are found in rocks that record the peak mineral assemblages (samples RR-03, RR-04, Boothby-09-1, Boothby-09-2A; Fig. 7a, b, d and e). The monazite age obtained from the retrogressed segregation (sample RR-05, Fig. 7c) gives a younger age (c. 1542 Ma); especially when compared to the age data from samples Boothby-09-1 and Boothby-09-2A (1576–1572 Ma). Sample RR-05 is interpreted to represent monazite growth during crystallisation of the hydrous melt phase (to form biotite as the most obvious manifestation). This suggests that the general premise of Kelsey et al. (2008) is correct.

The regional gneissic foliation is overprinted by numerous pegmatites (Fig. 4e), which are commonly considered to represent the last vestiges of melt crystallisation (Simmons and Webber, 2008). The temperature of pegmatite crystallisation is variable, depending on the presence of volatiles; however, it is generally interpreted to approximate the wet granitic solidus of 650–700 °C (London, 2005; Nabelek et al., 2010; Simmons and Webber, 2008; Sirbescu et al., 2008). Therefore, the pegmatites in this study are crucial for underpinning arguments about the duration of high-temperature, suprasolidus conditions during Early Mesoproterozoic metamorphism. U–Pb monazite data indicate that they record the youngest ages of 1523–1513 Ma (Fig. 7f and g). The monazite grains in the pegmatites are large (up to 1 mm) and analyses from both cores and rims yield younger ages. Therefore, these data are interpreted to be growth ages and represent the timing of the crystallisation of the pegmatites. It is possible that these pegmatites represent a separate thermal event at c. 1520 Ma. However, the terrane experienced slow cooling (Anderson et al., 2013; Buick et al., 1998; Kelsey et al., 2008; Rubatto et al., 2001; Vry and Baker, 2006), and there is no other evidence for a separate thermal event. Therefore, we prefer the interpretation that monazite growth over >60 Ma represents the maintenance of an elevated thermal regime over a prolonged period.

An analogous correlation between the age and metamorphic progression of each sample documented in this study is reflected by existing geochronology from adjacent areas of the Reynolds Range (Fig. 9, Table 3). Monazite and zircon hosted in the regional gneissic foliation in granulite-facies metapelites give the oldest ages (c. 1594 Ma), whereas discordant leucosomes yield younger ages of c. 1560 Ma (Rubatto et al., 2001; Vry et al., 1996; Williams et al., 1996). Rutile geochronology from the Lander Rock Formation gives a mean isochron age of 1544 ± 8 Ma (Vry and Baker, 2006). This sample was taken to the north west of the samples from this study. As the terrane is obliquely exposed, the location of the rutile sample represents a higher structural level, corresponding to lower temperature conditions. Therefore, the c. 1544

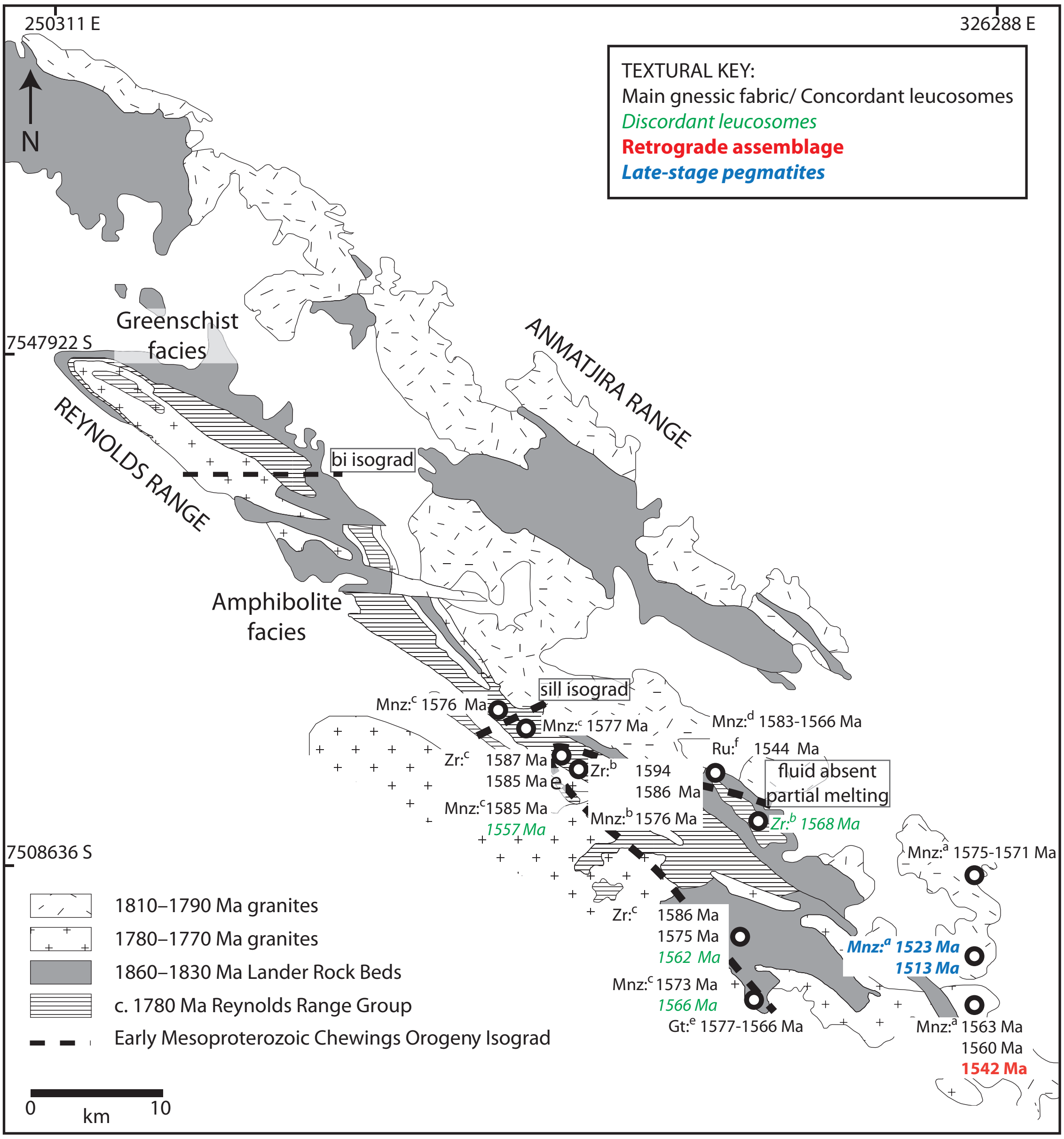

Figure 9: Existing geochronology from the Reynolds Range, showing the minerals used and their reported ages. The style and colour of text indicates the textural position of the geochronological samples (see key). Further detail is provided in Table 3. Numbers refer to references: (a) This study; (b) Williams, et al., (1996); (c) Rubatto, et al., (2001); (d) Vry, et al., (1996); (e) Buick, et al., (1999); (f) Vry & Baker (2006).

Ma rutile age is not inconsistent with the young (c. 1520 Ma) pegmatite ages from this study and supports the inference of a long-lived, elevated thermal regime. When this previously published geochronology is combined with age estimates obtained in this study, the age range associated with Early Mesoproterozoic metamorphism expands to more than 80 Ma from 1594 to 1513 Ma.

6.2. Thermal character of Early Mesoproterozoic metamorphism in the Aileron Province

Figure 8 shows the modelled *P*–*T* conditions for the interpreted peak metamorphic assemblages. While there is some ambiguity regarding the interpretation of peak assemblages in some samples, particularly relating to biotite, there is good consistency amongst samples for the estimated peak conditions. The peak conditions

Table 3: Summary of previously published geochronology from the Reynolds Range.

Author	Method	Zr age (Ma)	Mnz age (Ma)	Ru age (Ma)	Gt age (Ma)	Texture
Williams et al., (1996)	SHRIMP U–Pb	1594 ± 6	1576 ± 8			Semi-pelitic granulite (all RRG)
		1582 ± 8	1576 ± 12			Semi-concordant segregation
		1568 ± 4				Discordant segregation
Rubatto et al., (2001)	SHRIMP U–Pb		1576–1573			Amphibolite facies pelites (all RRG)
		1585 ± 5	1585 ± 3			Amphibolite-granulite facies metapelite
		1587 ± 4	1587 ± 4			Concordant leucosome
			1557 ± 2			Granitic pod within metapelite
		1575 ± 3	1573 ± 2			Migmatitc granulites (RRG)
		1586 ± 3				Concordant leucosome
		1562 ± 4	1566 ± 3			Discordant leucosome
Vry et al., (1996)	SHRIMP U–Pb		1583–1566			Deformed Yaningidjara Orthogneiss
			1583 ± 2			High grade metapelite (LRF)
Vry & Baker (2006)	Pb–Pb Rutile			1544 ± 8		High grade metapelite (LRF)
Buick et al., 1999	Pb–Pb Garnet				1577–1566	Hydrothermal quartz vein (RRG)

The texture of the samples and the unit from which they were collected is given for comparison with the age. RRG, Reynolds Range Group; LRF, Lander Rock Formation.

are inferred to be in excess of 850 °C at pressures of 0.65–0.75 GPa (Fig. 8f and g). This corresponds to a high apparent thermal gradient of >1300–1400 °C/GPa.

On the basis of the geochronological data, which suggests anatectic conditions were sustained for >60–80 Ma, the cooling from peak conditions (~850 °C) to the temperature of the wet solidus (~650 °C) must have been slow, in the order of 2.5–4 °C Ma^{-1}. These estimates are consistent with earlier estimates for cooling rates in the Reynolds-Anmatjira Range region (Buick et al., 1999; Kelsey et al., 2008; Vry and Baker, 2006). Constraints from petrographic observations, including the increasing abundance of cordierite and biotite at the expense of garnet and orthopyroxene and the retrograde growth of andalusite, suggest that the retrograde *P–T* evolution involved decompression and cooling along a path that intersected the andalusite field (Fig. 8g).

High-*T*, low-*P* metamorphism is commonly transient and involves distinctive characteristics that allow the identification of its thermal driver. The duration of high thermal gradients caused by the advection of magma is usually <10 Ma (e.g. De Yoreo et al., 1991; Rothstein and Hoisch, 1994; Sandiford and Powell, 1986), though successive periods of voluminous magma emplacement can give the impression of a long-lived event (e.g. Robb et al., 1999). However, there is no evidence for substantial coeval magmatism associated with Early Mesoproterozoic metamorphism in the Reynolds-Anmatjira Range (e.g. Hand and Buick, 2001; Rubatto et al., 2006; Vry et al., 1996). Lithospheric extension is an alternative mechanism that can create long-lived high thermal gradients, as evidenced by contemporary terranes such as the Basin and Range Province (Dickinson, 2002; Hyndman and Currie, 2011; Scarberry et al., 2010; Snow and Wernicke, 2000; Sullivan and Snoke, 2007). However, the structures formed in the

Reynolds Range are compressional rather than extensional (Dirks and Wilson, 1990; Hand and Buick, 2001).

The lack of evidence for magmatism coeval with metamorphism in the Reynolds Range implies that the lower crust did not experience large-scale melting during the Early Mesoproterozoic. Melt loss from the lower crust during earlier Palaeoproterozoic events is a possible mechanism for limiting significant granitic magmatism during future reworking events (Brown, 2001; Clark et al., 2011). Partial melting of the lower crust results in migration of the melt to the upper crust, leaving the lower crust with a more restitic composition (e.g. Hawkesworth and Kemp, 2006; Pollack, 1986; Rudnick, 1995). Modelling of the effect of melt loss shows that it has the capacity to significantly elevate the solidus of the residual rock (e.g. Korhonen et al., 2010; White and Powell, 2002). Dehydration and melting reactions consume heat and therefore act as a barrier to the mid- to deep-crust reaching higher temperatures (Brown and Korhonen, 2009; Stüwe and Powell, 1995). By contrast, the loss of melt and consequent elevation of the solidus allows the residual system to reach higher temperatures without inducing further substantial melting (Hand et al., 1999). In the Reynolds Range, voluminous felsic magmatism occurred during the interval 1810–1770 Ma (Fig. 2; Collins and Williams, 1995; Hand and Buick, 2001; Vry et al., 1996). These granitic rocks were emplaced in the upper and middle crust and comprise more than 60% of outcrop exposure in the Reynolds-Anmatjira Ranges (Fig. 2; Hand and Buick, 2001). It is probable that the melting events that produced the felsic magmatism caused the lower crust to become dehydrated and more restitic in composition. This could explain the low volume of melting that occurred during Early Mesoproterozoic metamorphism, despite the attainment of high temperatures.

Previous studies have suggested that burial of high heat-producing crust may provide a mechanism for long-lived, conductively-induced high-temperature–low-pressure metamorphism (eg. Chamberlain and Sonder, 1990; Hand et al., 1999; McLaren et al., 1999; Sandiford and Hand, 1998). Consistent with this possibility, Australian Proterozoic terranes are characterised by surface heat flows that are significantly higher than the global Proterozoic average of 49–54 mW m^{-2} (Cull, 1982; McLaren et al., 2003; Morgan, 1984; Sass and Lachenbruch, 1979). Surface heat flow in Australian Proterozoic terranes involves a significant contribution from felsic igneous rocks in the upper crust (McLaren et al., 2003, 2005; Sandiford and Hand, 1998). In the Reynolds Range, the voluminous felsic magmatic rocks emplaced between 1810 Ma and 1770 Ma contain elevated Th and U concentrations, resulting in modern day surface heat flow of 85 mWm^{-2} (McLaren et al., 1999, 2005; Sandiford and Hand, 1998). These granitic rocks have dramatically enriched the mid- to upper-crust in high-heat-producing elements (Hand and Buick, 2001; Hand et al., 1999; McLaren et al., 2005). Their emplacement location within the mid- to upper crust at the onset of early Mesoproterozoic metamorphism may have provided the long-term incubative thermal mechanism for long-lived, high-temperature metamorphism in the mid-crust during this event (Hand and Buick, 2001; Hand et al., 1999; Sandiford and Hand, 1998).

Slow cooling rates over a 60–80 Ma period suggest the Reynolds Range region experienced only minor exhumation at this time. The lack of exhumation implies that metamorphism and compressional deformation was not associated with the establishment of significant topography, as rapid erosion rates are not supported by the geochronological data or the inferred high thermal gradient of the retrograde *P–T* path. Instead, it appears that after some decompression, the *P–T* path was cooling dominated. Crust enriched in heat-producing elements would also be unlikely to support significant thickening, so it is probable that exhumation potential would be reduced (McLaren et al., 2005). This means that the region could have remained at mid-crustal depths for a prolonged period. Therefore, the Reynolds Range may have been approximately topographically neutral for approximately 80 Ma. This is consistent with the suggestion that peak temperatures outlasted the strain history (Hand and Buick, 2001), and supports the observation that the undeformed orthopyroxene bearing segregations of the peak assemblage overprint the regional gneissic fabric.

7. Conclusions

This study combines in situ U–Pb geochronology with calculated metamorphic phase equilibria from samples that record different stages in the thermal evolution of the Reynolds Range during HTLP Early Mesoproterozoic metamorphism. This approach has been used to establish the duration and conditions of suprasolidus temperatures, thus placing important constraints on the driving mechanism for metamorphism. We demonstrate that the Reynolds Range experienced suprasolidus, high apparent thermal gradient conditions for >60–80 Ma. The geochronology in this study crucially includes U–Pb monazite data from late, cross-cutting pegmatites. High heat-producing granitic rocks emplaced >180 Ma earlier may have been the mechanism responsible for the long duration of suprasolidus metamorphic conditions. Slow cooling along a retrograde *P–T* path that follows a high thermal gradient implies that exhumation potential was limited, suggesting that metamorphism occurred in crust of relatively normal thickness. Therefore, the Reynolds Range region may have remained relatively topographically neutral for approximately 80 Ma. This study demonstrates the importance of a systematic approach that combines field observations with quantitative phase equilibria calculations and geochronology from carefully selected samples in order to tackle fundamental questions about rate, duration and mechanisms of thermal processes in the crust.

Acknowledgements

Angus Netting and Ben Wade at Adelaide Microscopy are thanked for their assistance with analytical equipment. Liz McBride is thanked for her assistance with data collection. Kathryn Cutts and an anonymous reviewer are thanked for thorough and constructive reviews, which improved the manuscript. This work was supported by ARC LP100200127 (DEK), ARC DP1095456 (MH) and ARC DP0879330 (CC). LJM is supported by an Australian Postgraduate Award. This manuscript forms TRaX no. 280.

References

Aleinikoff, J.N., Schenck, W.S., Plank, M.O., Srogi, L.A., Fanning, C.M., Kamo, S.L., Bosbyshell, H., 2006. Deciphering igneous and metamorphic events in high-grade rocks of the Wilmington complex, Delaware: Morphology, cathodoluminescence and backscattered electron zoning, and SHRIMP U–Pb geochronology of zircon and monazite. Bulletin of the Geological Society of America 118, 39–64.

Anderson, J.R., Kelsey, D.E., Hand, M., Collins, W.J., 2013. Conductively driven, high-thermal gradient metamorphism in the Anmatjira Range, Arunta region, central Australia. Journal of Metamorphic Geology 31, 1003–1026.

Ashwal, L.D., Tucket, R.D., Zinner, E.K., 1999.

Slow cooling of deep crustal granulites and Pb-loss in zircon. Geochimica et Cosmochimica Acta 63, 2839–2851.

Boger, S.D., Carson, C.J., Wilson, C.J.L., Fanning, C.M., 2000. Neoproterozoic deformation in the Radok Lake region of the northern Prince Charles Mountains, east Antarctica; evidence for a single protracted orogenic event. Precambrian Research 104, 1–24.

Boger, S.D., White, R.W., 2003. The metamorphic evolution of metapelitic granulites from Radok Lake, northern Prince Charles Mountains, east Antarctica; evidence for an anticlockwise *P–T* path. Journal of Metamorphic Geology 21, 285–298.

Brown, M., 2001. Orogeny, migmatites and leucogranites; a review. Proceedings of the Indian Academy of Science (Earth and Planetary Sciences) 110, 313–336.

Brown, M., 2006. Duality of thermal regimes is the distinctive characteristic of plate tectonics since the Neoarchean. Geology 34, 961–964.

Brown, M., Korhonen, F.J., 2009. Some Remarks on Melting and Extreme Metamorphism of Crustal Rocks Physics and Chemistry of the Earth's Interior, in: Gupta, A.K., Dasgupta, S. (Eds.). Springer New York, pp. 67–87.

Buick, I.S., Cartwright, I., Harley, S.L., 1998. The retrograde *P–T–t* path for low-pressure granulites from the Reynolds Range, central Australia: petrological constraints and implications for low-*P*/high-*T* metamorphism. Journal of Metamorphic Geology 16, 511–529.

Buick, I.S., Frei, R., Cartwright, I., 1999. The timing of high-temperature retrogression in the Reynolds Range, central Australia: constraints from garnet and epidote Pb–Pb dating. Contributions to Mineralogy and Petrology 135, 244–254.

Cartwright, Buick, 1999. The flow of surface-derived fluids through Alice Springs age middle-crustal ductile shear zones, Reynolds Range, central Australia. Journal of Metamorphic Geology 17, 397–414.

Cartwright, I., Buick, I.S., Foster, D.A., Lambert, D.D., 1999. Alice Springs age shear zones from the southeastern Reynolds Range, central Australia. Australian Journal of Earth Sciences 46, 355–363.

Cartwright, I., Buick, I.S., Vry, J.K., 2001. Fluid-rock interaction in the Reynolds Range, central Australia: superimposed, episodic, and channelled fluid flow systems. Geological Society, London, Special Publications 184, 357–379.

Chamberlain, C.P., Sonder, L.J., 1990. Heat-Producing Elements and the Thermal and Baric Patterns of Metamorphic Belts. Science 250, 763–769.

Cherniak, D.J., 2010. Diffusion in Accessory Minerals: Zircon, Titanite, Apatite, Monazite and Xenotime. Reviews in Mineralogy and Geochemistry 72, 827–869.

Cherniak, D.J., Watson, E.B., Grove, M., Harrison, T.M., 2004. Pb diffusion in monazite: a combined RBS/SIMS study. Geochimica et Cosmochimica Acta 68, 829–840.

Claoué-Long, J., Edgoose, C.J., Worden, K., 2008a. A correlation of Aileron Province stratigraphy in central Australia. Precambrian Research 166, 230–245.

Claoué-Long, J., Maidment, D., Hussey, K., Huston, D., 2008b. The duration of the Strangways Event in central Australia: Evidence for prolonged deep crust processes. Precambrian Research 166, 246–262.

Clark, C., Fitzsimons, I.C.W., Healy, D., Harley, S.L., 2011. How Does the Continental Crust Get Really Hot? Elements 7, 235–240.

Clarke, G.L., Powell, R., 1991. Proterozoic granulite facies metamorphism in the southeastern Reynolds Range, central Australia: geological context, *P–T* path and overprinting relationships. Journal of Metamorphic Geology 9, 267–281.

Coggon, R., Holland, T.J.B., 2002. Mixing properties of phengitic micas and revised garnet-phengite thermobarometers. Journal of Metamorphic Geology 20, 683–696.

Collins, W.J., Shaw, R.D., 1995. Geochronological constraints on orogenic events in the Arunta Inlier: a review. Precambrian Research 71, 315–346.

Collins, W.J., Teyssier, C., 1989. Crustal scale ductile fault systems in the Arunta Inlier, central Australia. Tectonophysics 158, 49–66.

Collins, W.J., Vernon, R.H., 1991. Orogeny associated with anticlockwise *P–T–t* paths: Evidence from low-*P*, high-*T* metamorphic terranes in the Arunta inlier, central Australia.

Geology 19, 835–838.
Collins, W.J., Williams, I., 1995. SHRIMP ionprobe dating of short-lived Proterozoic tectonic cycles in the northern Arunta Inlier, central Australia. Precambrian Research 71, 69–89.
Copeland, P., Parrish, R.R., Harrison, T.M., 1988. Identification of inherited radiogenic Pb in monazite and its implications for U–Pb systematics. Nature 333, 760–763.
Cubley, J.F., Pattison, D.R.M., Tinkham, D.K., Fanning, C.M., 2013. U–Pb geochronological constraints on the timing of episodic regional metamorphism and rapid high-T exhumation of the Grand Forks complex, British Columbia. Lithos 156–159, 241–267.
Cull, J., 1982. An appraisal of Australian heat-flow data. BMR Journal of Australian Geology and Geophysics 7, 11–21.
Currie, C.A., Hyndman, R.D., 2006. The thermal structure of subduction zone back arcs. Journal of Geophysical Research: Solid Earth 111, B08404.
De Yoreo, J.J., Lux, D.R., Guidotti, C.V., 1991. Thermal modelling in low-pressure/high-temperature metamorphic belts. Tectonophysics 188, 209–238.
Dickinson, W.R., 2002. The Basin and Range Province as a Composite Extensional Domain. International Geology Review 44, 1–38.
Dirks, P.H.G.M., Hand, M., Powell, R., 1991. The *P–T*–deformation path for a mid-Proterozoic, low-pressure terrane: the Reynolds Range, central Australia. Journal of Metamorphic Geology 9, 641–661.
Dirks, P.H.G.M., Wilson, C.J.L., 1990. The geological evolution of the Reynolds Range, central Australia: evidence for three distinct structural–metamorphic cycles. Journal of Structural Geology 12, 651–665.
Donnellan, N., 2008. Mount Peake and Lander River, Northern Territory. 1:250 000 geological map series explanatory notes, SF 53 05, 53 01. Northern Territory Geological Survey, Darwin.
Dunlap, W.J., Teyssier, C., 1995. Paleozoic deformation and isotopic disturbance in the southeastern Arunta Block, central Australia. Precambrian Research 71, 229–250.
Fyfe, W.S., 1973. The Granulite Facies, Partial Melting and the Archaean Crust. Philosophical Transactions of the Royal Society of London. Series A, Mathematical and Physical Sciences 273, 457–461.
Gallien, F., Mogessie, A., Bjerg, E., Delpino, S., Castro de Machuca, B., Thöni, M., Klötzli, U., 2010. Timing and rate of granulite facies metamorphism and cooling from multi-mineral chronology on migmatitic gneisses, Sierras de La Huerta and Valle Fértil, NW Argentina. Lithos 114, 229–252.
Goncalves, P., Nicollet, C., Montel, J.-M., 2004. Petrology and in situ U–Th–Pb Monazite Geochronology of Ultrahigh-Temperature Metamorphism from the Andriamena Mafic Unit, North–Central Madagascar. Significance of a Petrographical *P–T* Path in a Polymetamorphic Context. Journal of Petrology 45, 1923–1957.
Goscombe, B., Hand, M., 2000. Contrasting *P–T* Paths in the Eastern Himalaya, Nepal: Inverted Isograds in a Paired Metamorphic Mountain Belt. Journal of Petrology 41, 1673–1719.
Griffin, W.L., Belousova, E.A., Shee, S.R., Pearson, N.J., O'Reilly, S.Y., 2004. Archean crustal evolution in the northern Yilgarn Craton: U–Pb and Hf-isotope evidence from detrital zircons. Precambrian Research 131, 231–282.
Haines, P.W., Hand, M., Sandiford, M., 2001. Palaeozoic synorogenic sedimentation in central and northern Australia: a review of disribution and timing with implications for the evolution of intracontinental orogens. Australian Journal of Earth Sciences 48, 911–928.
Halpin, J.A., Clarke, G.L., White, R.W., Kelsey, D.E., 2007. Contrasting *P–T–t* paths for Neoproterozoic metamorphism in MacRobertson and Kemp Lands, east Antarctica. Journal of Metamorphic Geology 25, 683–701.
Halpin, J.A., Daczko, N.R., Milan, L.A., Clarke, G.L., 2012. Decoding near-concordant U–Pb zircon ages spanning several hundred million years: recrystallisation, metamictisation or diffusion? Contributions to Mineralogy and Petrology 163, 67–85.
Hand, M., Buick, I.S., 2001. Tectonic evolution of the Reynolds-Anmatjira Ranges: a case study in terrain reworking from the Arunta Inlier, central Australia. Geological Society of London, Special Publications 184, 237–260.

Hand, M., Dirks, P., Powell, R., Buick, I.S., 1992. How well established is isobaric cooling in Proterozoic orogenic belts? An example from the Arunta Inlier, central Australia. Geology 20, 649–652.

Hand, M., Sandiford, M., Wyborn, L., 1999. Some thermal consequences of high heat production in the Australian Proterozoic. AGSO Research Newsletter 30, 20–23.

Harley, S.L., 2004. Extending our understanding of Ultrahigh temperature crustal metamorphism. Journal of Mineralogical and Petrological Sciences 99, 140–158.

Hawkesworth, C.J., Kemp, A.I.S., 2006. Evolution of the continental crust. Nature 443, 811–817.

Hokada, T., Misawa, K., Yokoyama, K., Shiraishi, K., Yamaguchi, A., 2004. SHRIMP and electron microprobe chronology of UHT metamorphism in the Napier Complex, East Antarctica: implications for zircon growth at >1,000 °C. Contributions to Mineralogy and Petrology 147, 1–20.

Holland, T.J.B., Powell, R., 1998a. An internally consistent thermodynamic dataset for phases of petrological interest. Journal of Metamorphic Geology 16, 309–343.

Holland, T.J.B., Powell, R., 1998b. An internally consistent thermodynamic dataset for phases of petrological interest. Journal of Metamorphic Geology 16, 309–343.

Holland, T.J.B., Powell, R., 2003. Activity-composition relations for phases in petrological calculations: an asymmetric multicomponent formulation. Contributions to Mineralogy and Petrography 145, 492–501.

Hyndman, R.D., Currie, C.A., 2011. Why is the North America Cordillera high? Hot backarcs, thermal isostasy, and mountain belts. Geology 39, 783–786.

Hyndman, R.D., Currie, C.A., Mazzotti, S.P., 2005. Subduction zone backarcs, mobile belts, and orogenic heat. GSA Today 15, 4–10.

Johnson, T.E., White, R.W., 2011. Phase equilibrium constraints on conditions of granulite-facies metamorphism at Scourie, NW Scotland. Journal of the Geological Society 168, 147–158.

Kelly, N., Harley, S., 2005. An integrated microtextural and chemical approach to zircon geochronology: refining the Archaean history of the Napier Complex, east Antarctica. Contributions to Mineralogy and Petrology 149, 57–84.

Kelsey, D.E., 2008. On ultrahigh-temperature crustal metamorphism. Gondwana Research 13, 1–29.

Kelsey, D.E., Clark, C., Hand, M., 2008. Thermobarometric modelling of zircon and monazite growth in melt-bearing systems: examples using model metapelitic and metapsammitic granulites. Journal of Metamorphic Geology 26, 199–212.

Kelsey, D.E., Hand, M., Clark, C., Wilson, C.J.L., 2007. On the application of in situ monazite chemical geochronology to constraining *P–T–t* histories in high-temperature (>850 °C) polymetamorphic granulites from Prydz Bay, East Antarctica. Journal of Geological Society, London 164, 667–683.

Kelsey, D.E., Powell, R., Wilson, C.J.L., Steel, D.A., 2003. (Th+U)–Pb monazite ages from Al–Mg-rich metapelites, Rauer Group, east Antarctica. Contributions to Mineralogy and Petrography 146, 326–340.

Korhonen, F.J., Clark, C., Brown, M., Bhattacharya, S., Taylor, R., 2013. How long-lived is ultrahigh temperature (UHT) metamorphism? Constraints from zircon and monazite geochronology in the Eastern Ghats orogenic belt, India. Precambrian Research 234, 322–350.

Korhonen, F.J., Saito, S., Brown, M., Siddoway, C.S., 2010. Modeling multiple melt loss events in the evolution of an active continental margin. Lithos 116, 230–248.

London, D., 2005. Granitic pegmatites: an assessment of current concepts and directions for the future. Lithos 80, 281–303.

McLaren, S., Sandiford, M., Hand, M., 1999. High radiogenic heat-producing granites and metamorphism - an example from the western Mount Isa inlier, Australia. Geology 27, 679–682.

McLaren, S., Sandiford, M., Hand, M., Neumann, N., Wyborn, L., Bastrakova, I., 2003. The hot southern continent: heat flow and heat production in Australian Proterozoic terranes. Geological Society of America Special Papers 372, 157–167.

McLaren, S., Sandiford, M., Powell, R., 2005. Contrasting styles of Proterozoic crustal evolution: A hot-plate tectonic model for Australian terranes. Geology 33, 673–676.

Morgan, P., 1984. The thermal structure and thermal evolution of the continental lithosphere. Physics and Chemistry of the Earth 15, 107–193.

Morrissey, L., Payne, J.L., Kelsey, D.E., Hand, M., 2011. Grenvillian-aged reworking in the North Australian Craton, central Australia: Constraints from geochronology and modelled phase equilibria. Precambrian Research 191, 141–165.

Nabelek, P., Whittington, A., Sirbescu, M.-L., 2010. The role of H_2O in rapid emplacement and crystallization of granite pegmatites: resolving the paradox of large crystals in highly undercooled melts. Contributions to Mineralogy and Petrology 160, 313–325.

Parrish, R.R., 1990. U–Pb dating of monazite and its application to geological problems. Canadian Journal of Earth Sciences 27, 1431–1450.

Payne, J.L., Hand, M., Barovich, K.M., Wade, B.P., 2008. Temporal constraints on the timing of high-grade metamorphism in the northern Gawler Craton: implications for assembly of the Australian Proterozoic. Australian Journal of Earth Sciences 55, 623–640.

Pollack, H.N., 1986. Cratonization and thermal evolution of the mantle. Earth and Planetary Science Letters 80, 175–182.

Powell, R., Downes, J., 1990. Garnet porphyroblast-bearing leucosomes in metapelites: mechanisms, phase diagrams, and an example from Broken Hill, Australia, in: Ashworth, J.R., Brown, M. (Eds.), High-temperature Metamorphism and Crustal Anatexis. Springer Netherlands, pp. 105–123.

Raimondo, T., Clark, C., Hand, M., Cliff, J., Harris, C., 2012. High-resolution geochemical record of fluid–rock interaction in a mid-crustal shear zone: a comparative study of major element and oxygen isotope transport in garnet. Journal of Metamorphic Geology 30, 255–280.

Raimondo, T., Clark, C., Hand, M., Faure, K., 2011. Assessing the geochemical and tectonic impacts of fluid–rock interaction in mid-crustal shear zones: A case study from the intracontinental Alice Springs Orogen, central Australia. Journal of Metamorphic Geology 29, 821–850.

Rey, P.F., Teyssier, C., Whitney, D.L., 2009. Extension rates, crustal melting, and core complex dynamics. Geology 37, 391–394.

Robb, L.J., Armstrong, R.A., Waters, D.J., 1999. The History of Granulite-Facies Metamorphism and Crustal Growth from Single Zircon U–Pb Geochronology: Namaqualand, South Africa. Journal of Petrology 40, 1747–1770.

Rothstein, D.A., Hoisch, T.D., 1994. Multiple intrusions and low-pressure metamorphism in in the central Old Woman Mountains, south-eastern California: constraints from thermal modelling. Journal of Metamorphic Geology 12, 723–734.

Rubatto, D., Chakraborty, S., Dasgupta, S., 2013. Timescales of crustal melting in the Higher Himalayan Crystallines (Sikkim, Eastern Himalaya) inferred from trace element-constrained monazite and zircon chronology. Contributions to Mineralogy and Petrology 165, 349–372.

Rubatto, D., Hermann, J., Buick, I.S., 2006. Temperature and Bulk Composition Control on the Growth of Monazite and Zircon During Low-pressure Anatexis (Mount Stafford, Central Australia). Journal of Petrology 47, 1973–1996.

Rubatto, D., Williams, I.S., Buick, I.S., 2001. Zircon and monazite response to prograde metamorphism in the Reynolds Range, central Australia. Contributions to Mineralogy and Petrology 140, 458–468.

Rudnick, R.L., 1995. Making continental crust. Nature 378, 571–578.

Sandiford, M., Hand, M., 1998. Australian Proterozoic high-temperature, low-pressure metamorphism in the conductive limit. Geological Society, London, Special Publications 138, 109–120.

Sandiford, M., Powell, R., 1986. Deep crustal metamorphism during continental extension: modern and ancient examples. Earth and Planetary Science Letters 79, 151–158.

Sass, J.H., Lachenbruch, A.H., 1979. Thermal regime of the Australian continental crust, in: McElhinny, M.W. (Ed.), The Earth: Its Origin, Structure and Evolution. Academic Press, London, pp. 301–351.

Scarberry, K.C., Meigs, A.J., Grunder, A.L., 2010. Faulting in a propagating continental rift: Insight from the late Miocene structural development of the Abert Rim fault, southern Oregon, USA. Tectonophysics 488, 71–86.

Schmitz, M.D., Bowring, S.A., 2003. Ultrahigh-temperature metamorphism in the lower crust during Neoarchean Ventersdorp rifting and magmatism, Kaapvaal Craton, southern Africa. Geological Society of America Bulletin 115, 533–548.

Scrimgeour, I.R., 2003. Developing a revised framework for the Arunta Region, Annual Geoscience Exploration Seminar (AGES) 2003. Record of Abstracts. Northern Territory Geological Survey Record 2003–001.

Scrimgeour, I.R., 2004. A revised province definition and Palaeoproterozoic framework for the Arunta Region, central Australia. Geological Society of Australia Abstracts 73, 185.

Shaw, R.D., Zeitler, P.K., Mcdougall, I., Tingate, P.R., 1992. The Paleozoic history of an unusual intracratonic thrust belt in central Australia based on ^{40}Ar–^{39}Ar, K–Ar and fission-track dating. Journal of the Geological Society 149, 937–954.

Simmons, W.B.S., Webber, K.L., 2008. Pegmatite genesis: state of the art. European Journal of Mineralogy 20, 421–438.

Sirbescu, M.-L., Hartwick, E., Student, J., 2008. Rapid crystallization of the Animikie Red Ace Pegmatite, Florence county, northeastern Wisconsin: inclusion microthermometry and conductive-cooling modeling. Contributions to Mineralogy and Petrology 156, 289–305.

Sizova, E., Gerya, T., Brown, M., 2014. Contrasting styles of Phanerozoic and Precambrian continental collision. Gondwana Research 25, 522–545.

Smith, H.A., Giletti, B.J., 1997. Lead diffusion in monazite. Geochimica et Cosmochimica Acta 61, 1047–1055.

Smith, J., 2001. Summary of Results: Joint NTGS – AGSO Age Determination Program 1999 - 2001. Northern Territory Geological Survey.

Smithies, H., Howard, H.M., Evins, P., Kirkland, C., Kelsey, D.E., Hand, M., Wingate, M.T.D., Collins, A.S., Belousova, E.A., Allchurch, S., 2010. Geochemistry, geochronology, and petrogenesis of Mesoproterozoic felsic rocks in the west Musgrave Province, central Australia, and implications for the Mesoproterozoic tectonic evolution of the region. Geological Society of Western Australia, Perth, 82 p.

Smithies, R.H., Howard, H.M., Evins, P.M., Kirkland, C.L., Kelsey, D.E., Hand, M., Wingate, M.T.D., Collins, A.S., Belousova, E., 2011. High-temperature granite magmatism, crust-mantle interaction and the Mesoproterozoic intracontinental evolution of the Musgrave Province, Central Australia. Journal of Petrology 52, 931–958.

Snow, J.K., Wernicke, B., 2000. Cenozoic tectonism in the central Basin and Range; magnitude, rate, and distribution of upper crustal strain. American Journal of Science 300, 659–719.

Spear, F.S., Kohn, M.J., Cheney, J.T., 1999. *P–T* paths from anatectic pelites. Contributions to Mineralogy and Petrology 134, 17–32.

Stepanov, A.S., Hermann, J., Rubatto, D., Rapp, R.P., 2012. Experimental study of monazite/melt partitioning with implications for the REE, Th and U geochemistry of crustal rocks. Chemical Geology 300–301, 200–220.

Stüwe, K., Powell, R., 1995. *P–T* Paths from modal proportions: application to the Koralm Complex, Eastern Alps. Contributions to Mineralogy and Petrology 119, 83–93.

Sullivan, W.A., Snoke, A.W., 2007. Comparative anatomy of core-complex development in the northeastern Great Basin, U.S.A. Rocky Mountain Geology 42, 1–29.

Suzuki, S., Arima, M., Williams, I., Shiraishi, K., Kagami, H., 2006. Thermal History of UHT Metamorphism in the Napier Complex, East Antarctica: Insights from Zircon, Monazite, and Garnet Ages. The Journal of Geology 114, 65–84.

Vry, J., Compston, W., Cartwright, I., 1996. SHRIMP II dating of zircons and monazites: reassessing the timing of high-grade metamorphism and fluid flow in the Reynolds Range, northern Arunta Block, Australia. Journal of Metamorphic Geology 14, 335–350.

Vry, J.K., Baker, J.A., 2006. LA-MC-ICPMS Pb–Pb dating of rutile from slowly cooled granulites: Confirmation of the high closure temperature for Pb diffusion in rutile. Geochimica et Cosmochimica Acta 70, 1807–1820.

Vry, J.K., Cartwright, I., 1994. Sapphirine-kornerupine rocks from the Reynolds Range, central Australia: constraints on the uplift history of a Proterozoic low pressure terrain. Contributions to Mineralogy and Petrology 116, 78–91.

Westphal, M., Schumacher, J.C., Boschert, S., 2003. High-Temperature Metamorphism and the Role of Magmatic Heat Sources at the Rogaland Anorthosite Complex in Southwestern Norway. Journal of Petrology 44, 1145–1162.

White, R.W., Powell, C.M., Halpin, J.A., 2004. Spatially-focussed melt formation in aluminous metapelites from Broken Hill, Australia. Journal of Metamorphic Geology 22, 825–845.

White, R.W., Powell, R., 2002. Melt loss and the preservation of granulite facies mineral assemblages. Journal of Metamorphic Geology 20, 621–632.

White, R.W., Powell, R., Clarke, G.L., 2002. The interpretation of reaction textures in Fe-rich metapelitic granulites of the Musgrave Block, central Australia: constraints from mineral equilibria calculations in the system K_2O–FeO–MgO–Al_2O_3–SiO_2–H_2O–TiO_2–Fe_2O_3. Journal of Metamorphic Geology 20, 41–55.

White, R.W., Powell, R., Holland, T.J.B., 2007. Progress relating to calculation of partial melting equilibria for metapelites. Journal of Metamorphic Geology 25, 511–527.

White, R.W., Powell, R., Holland, T.J.B., Worley, B.A., 2000. The effect of TiO_2 and Fe_2O_3 on metapelitic assemblages at greenschist and amphibolite facies conditions: mineral equilibria calculations in the system K_2O–FeO–MgO–Al_2O_3–SiO_2–H_2O–TiO_2–Fe_2O_3. Journal of Metamorphic Geology 18, 497–511.

Williams, I.S., Buick, I.S., Cartwright, I., 1996. An extended episode of early Mesoproterozoic metamorphic fluid flow in the Reynolds Range, central Australia. Journal of Metamorphic Geology 14, 29–47.

Worden, K.E., Carson, C.J., Close, D.F., Donnellan, N., Scrimgeour, I., 2008. Summary of results. Joint NTGS-GA geochronology project: Tanami Region, Arunt11.5

	Isotopic ratios						Age estimates						
Spot name	$^{207}Pb/^{206}Pb$	±1σ	$^{206}Pb/^{238}U$	±1σ	$^{207}Pb/^{235}U$	±1σ	$^{207}Pb/^{206}Pb$	±1σ	$^{206}Pb/^{238}U$	±1σ	$^{207}Pb/^{235}U$	±1σ	Conc. (%)
RR-03													
4A1	0.09938	0.00158	0.27189	0.00528	3.72590	0.08111	1613	29	1550	27	1577	17	96
4A2	0.09749	0.00146	0.27847	0.00539	3.74344	0.07952	1577	28	1584	27	1581	17	100
9A1	0.09770	0.00144	0.27409	0.00530	3.69283	0.07798	1581	27	1562	27	1570	17	99
9B1	0.09743	0.00138	0.26561	0.00510	3.56852	0.07441	1576	26	1519	26	1543	17	96
9B2	0.09701	0.00137	0.26746	0.00516	3.57798	0.07457	1568	26	1528	26	1545	17	97
10A1*	0.09122	0.00144	0.20402	0.00399	2.56635	0.05627	1451	30	1197	21	1291	16	82
20A1	0.09638	0.00186	0.27256	0.00551	3.62211	0.08902	1555	36	1554	28	1554	20	100
27A1	0.09748	0.00147	0.27270	0.00533	3.66592	0.07894	1577	28	1555	27	1564	17	99
27A2	0.09690	0.00145	0.27431	0.00537	3.66565	0.07891	1565	28	1563	27	1564	17	100
27A3	0.09741	0.00166	0.26992	0.00536	3.62578	0.08278	1575	32	1540	27	1555	18	98
28A1	0.09787	0.00151	0.27299	0.00537	3.68423	0.08062	1584	28	1556	27	1568	17	98
28A2	0.09715	0.00152	0.27511	0.00543	3.68540	0.08141	1570	29	1567	27	1568	18	100
35A1	0.09814	0.00144	0.26622	0.00532	3.60315	0.07731	1589	27	1522	27	1550	17	96
35B1	0.09708	0.00129	0.26810	0.00531	3.58928	0.07396	1569	25	1531	27	1547	16	98
3A1	0.09628	0.00126	0.27051	0.00536	3.59165	0.07379	1553	24	1543	27	1548	16	99
2A1	0.09596	0.00125	0.27596	0.00547	3.65202	0.07503	1547	24	1571	28	1561	16	102
40A1	0.09629	0.00135	0.26864	0.00536	3.56723	0.07521	1553	26	1534	27	1542	17	99
40A2	0.09604	0.00134	0.27208	0.00543	3.60333	0.07590	1549	26	1551	28	1550	17	100
47A1	0.09605	0.00140	0.27297	0.00547	3.61565	0.07748	1549	27	1556	28	1553	17	100
47A2	0.09715	0.00142	0.27267	0.00547	3.65284	0.07844	1570	27	1554	28	1561	17	99
57A1	0.09662	0.00134	0.27565	0.00550	3.67275	0.07753	1560	26	1569	28	1566	17	101
63A1	0.09510	0.00145	0.27076	0.00544	3.55061	0.07811	1530	29	1545	28	1539	17	101
71A1	0.09418	0.00143	0.27167	0.00548	3.52836	0.07725	1512	28	1549	28	1534	17	102
71A2	0.09540	0.00148	0.27186	0.00550	3.57647	0.07913	1536	29	1550	28	1544	18	101
9A1*	0.09371	0.00116	0.24959	0.00347	3.22487	0.04898	1502	23	1436	18	1463	12	96
9A4*	0.09493	0.00116	0.25458	0.00355	3.33186	0.05059	1527	23	1462	18	1489	12	96
9A5	0.09612	0.0012	0.27313	0.0038	3.61984	0.05536	1550	23	1557	19	1554	12	100
10A1*	0.09464	0.00129	0.25587	0.00358	3.33892	0.05356	1521	25	1469	18	1490	13	97
20A2	0.09599	0.0013	0.27141	0.0038	3.59236	0.05748	1548	25	1548	19	1548	13	100
20A3	0.09543	0.00131	0.27529	0.00385	3.62224	0.05837	1537	26	1568	19	1554	13	102
27A4	0.09729	0.00132	0.27749	0.00388	3.72235	0.05971	1573	25	1579	20	1576	13	100
27A5	0.09628	0.00133	0.27371	0.00385	3.63332	0.05898	1553	26	1560	19	1557	13	100
28A3	0.09747	0.00133	0.27897	0.00391	3.74894	0.06035	1576	25	1586	20	1582	13	101
28A4	0.09672	0.00132	0.27731	0.00388	3.69803	0.05974	1562	25	1578	20	1571	13	101
RR-04													
2a1	0.09612	0.00114	0.27148	0.00375	3.59799	0.05315	1550	22	1548	19	1549	12	100
2a2	0.09636	0.00122	0.27166	0.00378	3.60957	0.05526	1555	24	1549	19	1552	12	100
3a1	0.09785	0.00119	0.26863	0.00371	3.62422	0.05427	1584	23	1534	19	1555	12	97
3a2	0.09671	0.00118	0.26608	0.00367	3.54802	0.05321	1562	23	1521	19	1538	12	97
31a1	0.09709	0.00125	0.26838	0.00373	3.59305	0.05549	1569	24	1533	19	1548	12	98
31a2	0.09652	0.00122	0.27277	0.00379	3.63008	0.05571	1558	24	1555	19	1556	12	100
34a1	0.09603	0.00123	0.26831	0.00372	3.55263	0.05483	1548	24	1532	19	1539	12	99
34a2	0.09605	0.00123	0.26738	0.00371	3.54120	0.05470	1549	24	1528	19	1537	12	99
29d1	0.09716	0.00125	0.27767	0.00384	3.71974	0.05766	1570	24	1580	19	1576	12	101
29b1	0.09709	0.00127	0.27110	0.00375	3.62933	0.05666	1569	24	1546	19	1556	12	99
29c1	0.09816	0.00127	0.27478	0.00381	3.71899	0.05791	1590	24	1565	19	1576	12	98
18a1	0.09686	0.00118	0.26759	0.00374	3.57366	0.05398	1565	23	1529	19	1544	12	98

	Isotopic ratios						Age estimates						
Spot name	$^{207}Pb/^{206}Pb$	±1σ	$^{206}Pb/^{238}U$	±1σ	$^{207}Pb/^{235}U$	±1σ	$^{207}Pb/^{206}Pb$	±1σ	$^{206}Pb/^{238}U$	±1σ	$^{207}Pb/^{235}U$	±1σ	Conc. (%)
RR-04 (continued)													
18a2	0.09619	0.00121	0.27109	0.00382	3.59545	0.05536	1552	23	1546	19	1549	12	100
9a1	0.09530	0.00118	0.27600	0.00387	3.62637	0.05541	1534	23	1571	20	1555	12	102
9a2	0.09779	0.00123	0.27649	0.00389	3.72780	0.05767	1582	23	1574	20	1577	12	99
9a3	0.09603	0.00124	0.27484	0.00387	3.63914	0.05690	1548	24	1565	20	1558	12	101
34b	0.09624	0.00123	0.27077	0.00382	3.59299	0.05614	1553	24	1545	19	1548	12	99
34b2	0.09648	0.00126	0.26775	0.00377	3.56184	0.05628	1557	24	1529	19	1541	13	98
40a1	0.09721	0.00128	0.27262	0.00385	3.65383	0.05811	1571	25	1554	20	1561	13	99
42a1	0.09801	0.00136	0.26864	0.00382	3.63015	0.05960	1587	26	1534	19	1556	13	97
42a2	0.09531	0.00135	0.27186	0.00388	3.57247	0.05934	1534	26	1550	20	1543	13	101
43a1	0.09542	0.00133	0.27076	0.00385	3.56195	0.05864	1536	26	1545	20	1541	13	101
RR-05													
13a	0.09383	0.00113	0.27121	0.00425	3.50851	0.05780	1505	23	1547	22	1529	13	103
13b	0.09622	0.00114	0.27124	0.00424	3.59859	0.05887	1552	22	1547	21	1549	13	100
12a1	0.09590	0.00115	0.26856	0.00420	3.55116	0.05858	1546	22	1534	21	1539	13	99
12b1	0.09583	0.00120	0.27102	0.00427	3.58086	0.06036	1545	23	1546	22	1545	13	100
12c1	0.09511	0.00116	0.27199	0.00427	3.56677	0.05939	1530	23	1551	22	1542	13	101
11a*	0.09579	0.00121	0.25827	0.00407	3.41091	0.05777	1544	24	1481	21	1507	13	96
7a	0.09663	0.00122	0.26867	0.00424	3.57952	0.06066	1560	23	1534	22	1545	13	98
7b	0.09568	0.00120	0.26844	0.00423	3.54129	0.05987	1542	23	1533	22	1537	13	99
4a	0.09492	0.00119	0.27068	0.00427	3.54230	0.06010	1526	24	1544	22	1537	13	101
3a	0.09709	0.00125	0.27096	0.00430	3.62690	0.06241	1569	24	1546	22	1556	14	99
1a	0.09545	0.00172	0.27033	0.00445	3.55774	0.07481	1537	34	1543	23	1540	17	100
2a	0.09699	0.00182	0.26662	0.00440	3.56557	0.07697	1567	35	1524	22	1542	17	97
4b	0.09586	0.00184	0.27407	0.00454	3.62250	0.07924	1545	36	1561	23	1555	17	101
5a	0.09547	0.00177	0.26719	0.00440	3.51729	0.07530	1538	34	1527	22	1531	17	99
10a1	0.09573	0.00181	0.27503	0.00455	3.63010	0.07868	1542	35	1566	23	1556	17	102
10b1	0.09631	0.00182	0.27088	0.00447	3.59701	0.07801	1554	35	1545	23	1549	17	99
9a	0.09530	0.00181	0.26765	0.00442	3.51697	0.07647	1534	35	1529	22	1531	17	100
9b	0.09628	0.00191	0.26704	0.00445	3.54518	0.07956	1553	37	1526	23	1537	18	98
8a	0.09588	0.00186	0.26902	0.00445	3.55644	0.07839	1546	36	1536	23	1540	17	99
8b	0.09450	0.00187	0.27067	0.00450	3.52664	0.07877	1518	37	1544	23	1533	18	102
Boothby-09-1													
102a1	0.09892	0.00144	0.26905	0.00556	3.66943	0.08221	1604	27	1536	28	1565	18	96
102a2	0.09817	0.00144	0.27036	0.00559	3.65938	0.08237	1590	27	1543	28	1563	18	97
115a1	0.09951	0.00182	0.27863	0.00584	3.82303	0.09444	1615	34	1585	29	1598	20	98
116a1	0.09810	0.00153	0.27150	0.00565	3.67217	0.08492	1588	29	1548	29	1565	18	97
117a1	0.09834	0.00157	0.27372	0.00572	3.71113	0.08685	1593	30	1560	29	1574	19	98
123a1	0.09873	0.00159	0.26817	0.00560	3.65067	0.08565	1600	30	1532	28	1561	19	96
123a2	0.09747	0.00154	0.27274	0.00571	3.66527	0.08586	1576	29	1555	29	1564	19	99
131a1	0.09778	0.00167	0.27375	0.00579	3.69044	0.08947	1582	32	1560	29	1569	19	99
131a2	0.10140	0.00179	0.27548	0.00584	3.85162	0.09481	1650	32	1569	30	1604	20	95
135a1	0.09745	0.00165	0.26091	0.00553	3.50587	0.08544	1576	31	1495	28	1529	19	95
152a1	0.09879	0.00151	0.27868	0.00591	3.79597	0.08756	1601	28	1585	30	1592	19	99
18a1	0.09687	0.00144	0.27977	0.00591	3.73688	0.08523	1565	28	1590	30	1579	18	102
18b1	0.09857	0.00155	0.27267	0.00579	3.70599	0.08628	1597	29	1554	29	1573	19	97
18b2	0.09807	0.00146	0.27181	0.00575	3.67560	0.08397	1588	28	1550	29	1566	18	98
59c1	0.09697	0.00146	0.27023	0.00572	3.61335	0.08281	1567	28	1542	29	1553	18	98

	Isotopic ratios						Age estimates						
Spot name	$^{207}Pb/^{206}Pb$	±1σ	$^{206}Pb/^{238}U$	±1σ	$^{207}Pb/^{235}U$	±1σ	$^{207}Pb/^{206}Pb$	±1σ	$^{206}Pb/^{238}U$	±1σ	$^{207}Pb/^{235}U$	±1σ	Conc. (%)
Boothby-09-1(continued)													
62a1	0.09703	0.00153	0.27359	0.00581	3.66042	0.08536	1568	29	1559	29	1563	19	99
66a1	0.09783	0.00162	0.27654	0.00590	3.73045	0.08864	1583	31	1574	30	1578	19	99
90a1	0.09825	0.00163	0.27868	0.00594	3.77542	0.08979	1591	31	1585	30	1588	19	100
99a1	0.09677	0.00158	0.27896	0.00594	3.72229	0.08787	1563	30	1586	30	1576	19	101
8a1	0.09751	0.00115	0.26827	0.00465	3.60733	0.06452	1577	22	1532	24	1551	14	97
9a1*	0.09386	0.00117	0.23472	0.00409	3.03767	0.05577	1505	23	1359	21	1417	14	90
10a1	0.09738	0.00119	0.27347	0.00477	3.67234	0.06688	1575	23	1558	24	1565	15	99
10a2	0.09622	0.00118	0.27157	0.00474	3.60340	0.06564	1552	23	1549	24	1550	14	100
10b1	0.09716	0.00126	0.27540	0.00484	3.68967	0.06937	1570	24	1568	24	1569	15	100
18a1	0.09643	0.00127	0.27862	0.00493	3.70477	0.07027	1556	25	1584	25	1572	15	102
18b1	0.09680	0.00122	0.27346	0.00481	3.65031	0.06775	1563	24	1558	24	1561	15	100
20c1	0.09613	0.00127	0.27110	0.00479	3.59335	0.06817	1550	25	1546	24	1548	15	100
20c2	0.09504	0.00123	0.27705	0.00490	3.63107	0.06828	1529	24	1577	25	1556	15	103
21a1	0.09655	0.00136	0.26107	0.00462	3.47524	0.06793	1559	26	1495	24	1522	15	96
42a1	0.09659	0.00138	0.28183	0.00505	3.75349	0.07410	1559	27	1601	25	1583	16	103
9a2	0.09703	0.00135	0.26422	0.00471	3.53512	0.06912	1568	26	1511	24	1535	15	96
Boothby-09-2a													
43a1	0.09779	0.00122	0.26376	0.00447	3.55591	0.06348	1583	23	1509	23	1540	14	95
43a2	0.09687	0.00118	0.26549	0.00450	3.54567	0.06296	1565	23	1518	23	1538	14	97
43a3	0.09535	0.00119	0.26584	0.00453	3.49439	0.06290	1535	23	1520	23	1526	14	99
36a1	0.09672	0.00118	0.26009	0.00442	3.46797	0.06190	1562	23	1490	23	1520	14	95
26b1	0.09759	0.00122	0.27631	0.00472	3.71750	0.06723	1579	23	1573	24	1575	14	100
26a1	0.09706	0.00125	0.28076	0.00483	3.75694	0.06895	1568	24	1595	24	1584	15	102
17a1	0.09560	0.00125	0.27150	0.00469	3.57825	0.06637	1540	24	1548	24	1545	15	101
17a2	0.09600	0.00127	0.26917	0.00466	3.56227	0.06671	1548	25	1537	24	1541	15	99
10a1	0.09772	0.00131	0.27090	0.00471	3.64932	0.06896	1581	25	1545	24	1560	15	98
10a2	0.09624	0.00133	0.26980	0.00472	3.57978	0.06868	1553	26	1540	24	1545	15	99
4a1	0.09673	0.00134	0.27131	0.00476	3.61803	0.06989	1562	26	1547	24	1554	15	99
26b2	0.09708	0.00132	0.26871	0.00472	3.59652	0.06916	1569	25	1534	24	1549	15	98
44b1	0.09780	0.00120	0.27451	0.00485	3.70088	0.06842	1583	23	1564	25	1572	15	99
44a1	0.09756	0.00121	0.26832	0.00475	3.60871	0.06710	1578	23	1532	24	1552	15	97
44c1	0.09705	0.00122	0.27358	0.00486	3.65989	0.06851	1568	23	1559	25	1563	15	99
46a1	0.09743	0.00124	0.27101	0.00481	3.63969	0.06862	1575	24	1546	24	1558	15	98
46a2	0.09804	0.00126	0.26865	0.00477	3.63049	0.06888	1587	24	1534	24	1556	15	97
46b1	0.09889	0.00129	0.26629	0.00474	3.62973	0.06929	1603	24	1522	24	1556	15	95
46b2	0.09830	0.00128	0.26559	0.00473	3.59889	0.06878	1592	24	1518	24	1549	15	95
77a1	0.09798	0.00132	0.26814	0.00479	3.62102	0.07015	1586	25	1531	24	1554	15	97
78a1	0.09636	0.00136	0.26910	0.00482	3.57358	0.07066	1555	26	1536	24	1544	16	99
78a2	0.09736	0.00138	0.27449	0.00491	3.68320	0.07309	1574	26	1564	25	1568	16	99
78a3	0.09728	0.00135	0.26878	0.00483	3.60389	0.07107	1573	26	1535	25	1550	16	98
BPG-01													
BPG1_01	0.09465	0.00094	0.27555	0.00441	3.59622	0.05582	1521	19	1569	22	1549	12	103
BPG1_02	0.09402	0.00095	0.27124	0.00430	3.51671	0.05458	1509	19	1547	22	1531	12	103
BPG1_03	0.09441	0.00102	0.26846	0.00426	3.49669	0.05535	1516	20	1533	22	1527	13	101
BPG1_04	0.09483	0.00098	0.26855	0.00431	3.51139	0.05540	1525	19	1533	22	1530	12	101
BPG1_05	0.09540	0.00099	0.27125	0.00433	3.56826	0.05606	1536	19	1547	22	1543	12	101
BPG1_06	0.09506	0.00107	0.26079	0.00415	3.41935	0.05481	1529	21	1494	21	1509	13	98

	Isotopic ratios						Age estimates						
Spot name	$^{207}Pb/^{206}Pb$	±1σ	$^{206}Pb/^{238}U$	±1σ	$^{207}Pb/^{235}U$	±1σ	$^{207}Pb/^{206}Pb$	±1σ	$^{206}Pb/^{238}U$	±1σ	$^{207}Pb/^{235}U$	±1σ	Conc. (%)
BPG-01 (continued)													
BPG1_07*	0.09679	0.00109	0.26252	0.00417	3.50300	0.05629	1563	21	1503	21	1528	13	96
BPG1_08*	0.09280	0.00094	0.25697	0.00411	3.28821	0.05154	1484	19	1474	21	1478	12	99
BPG1_09	0.09526	0.00098	0.27807	0.00442	3.65246	0.05719	1533	19	1582	22	1561	12	103
BPG1_10	0.09444	0.00096	0.26787	0.00427	3.48770	0.05473	1517	19	1530	22	1524	12	101
BPG1_11	0.09432	0.00101	0.26043	0.00415	3.38675	0.05362	1515	20	1492	21	1501	12	99
BPG1_12	0.09375	0.00094	0.27059	0.00431	3.49762	0.05489	1503	19	1544	22	1527	12	103
BPG1_13*	0.09293	0.00118	0.25426	0.00410	3.26085	0.05470	1486	24	1460	21	1472	13	98
BPG1_14*	0.09822	0.00108	0.27948	0.00463	3.78527	0.06335	1591	20	1589	23	1590	13	100
BPG1_15	0.09539	0.00097	0.27132	0.00430	3.56854	0.05570	1536	19	1548	22	1543	12	101
BPG1_16	0.09374	0.00107	0.26072	0.00421	3.37033	0.05525	1503	21	1494	22	1498	13	99
BPG1_17	0.09487	0.00096	0.28015	0.00455	3.66385	0.05830	1526	19	1592	23	1564	13	104
BPG1_18	0.09495	0.00098	0.27433	0.00440	3.58962	0.05651	1527	19	1563	22	1547	13	102
BPG1_19	0.09471	0.00100	0.27561	0.00442	3.59698	0.05701	1522	20	1569	22	1549	13	103
BPG1_20	0.09466	0.00102	0.27814	0.00449	3.62836	0.05856	1521	20	1582	23	1556	13	104
BPG1_21	0.09537	0.00103	0.28055	0.00450	3.68721	0.05880	1535	20	1594	23	1569	13	104
BPG1_22	0.09476	0.00098	0.27993	0.00454	3.65613	0.05848	1523	19	1591	23	1562	13	104
BPG1_23	0.09533	0.00100	0.27525	0.00442	3.61533	0.05715	1535	20	1567	22	1553	13	102
BPG1_24	0.09437	0.00104	0.27735	0.00454	3.60796	0.05958	1516	21	1578	23	1551	13	104
BPG1_25	0.09433	0.00105	0.28364	0.00467	3.68738	0.06159	1515	21	1610	23	1569	13	106
BPG1_26	0.09509	0.00097	0.27512	0.00444	3.60425	0.05718	1530	19	1567	22	1551	13	102
BPG1_23	0.09533	0.00100	0.27525	0.00442	3.61533	0.05715	1535	20	1567	22	1553	13	102
BPG1_24	0.09437	0.00104	0.27735	0.00454	3.60796	0.05958	1516	21	1578	23	1551	13	104
BPG-03													
BPG3_01*	0.09035	0.00120	0.27276	0.00423	3.40136	0.05579	1433	25	1555	21	1505	13	109
BPG3_02	0.09427	0.00096	0.25358	0.00389	3.29457	0.04930	1514	19	1457	20	1480	12	96
BPG3_03	0.09463	0.00097	0.26816	0.00407	3.50043	0.05197	1521	19	1531	21	1527	12	101
BPG3_04	0.09358	0.00112	0.25209	0.00388	3.25380	0.05191	1500	22	1449	20	1470	12	97
BPG3_05	0.09102	0.00114	0.20826	0.00325	2.61137	0.04291	1447	24	1220	17	1304	12	84
BPG3_06	0.09319	0.00101	0.24173	0.00383	3.10512	0.04921	1492	20	1396	20	1434	12	94
BPG3_07	0.09442	0.00098	0.26286	0.00404	3.41785	0.05163	1517	19	1505	21	1509	12	99
BPG3_08	0.09389	0.00103	0.25416	0.00391	3.28792	0.05064	1506	21	1460	20	1478	12	97
BPG3_09	0.09410	0.00096	0.26213	0.00397	3.40121	0.05030	1510	19	1501	20	1505	12	99
BPG3_10	0.09110	0.00105	0.21424	0.00342	2.69082	0.04410	1449	22	1251	18	1326	12	86
BPG3_11	0.09149	0.00105	0.23998	0.00381	3.02614	0.04944	1457	22	1387	20	1414	12	95
BPG3_12	0.09075	0.00098	0.18497	0.00284	2.31286	0.03548	1441	20	1094	15	1216	11	76
BPG3_13	0.09132	0.00099	0.23531	0.00369	2.96215	0.04643	1453	20	1362	19	1398	12	94
BPG3_14	0.09362	0.00095	0.24550	0.00381	3.16791	0.04825	1500	19	1415	20	1449	12	94
BPG3_15	0.09094	0.00115	0.21740	0.00349	2.72659	0.04665	1445	24	1268	19	1336	13	88
BPG3_16	0.09237	0.00165	0.19465	0.00328	2.47775	0.05077	1475	34	1147	18	1266	15	78
BPG3_17	0.09330	0.00094	0.22298	0.00346	2.86799	0.04364	1494	19	1298	18	1374	11	87
BPG3_18	0.09478	0.00095	0.28636	0.00441	3.74126	0.05638	1524	19	1623	22	1580	12	107
BPG3_19	0.09458	0.00097	0.26817	0.00412	3.49648	0.05281	1520	19	1532	21	1526	12	101
BPG3_20	0.09438	0.00102	0.26834	0.00413	3.49164	0.05394	1516	20	1532	21	1525	12	101

* Analysis excluded from calculation of weighted average ages and concordia ages (shown in grey in Fig. 6)

Sample	RR-01	RR-03	RR-04	RR-05	Boothby-09-2a
SiO_2	67.70	71.30	69.30	44.70	59.80
TiO_2	0.69	0.69	0.54	3.07	0.53
Al_2O_3	14.10	13.40	13.20	16.80	16.20
Fe_2O_3 (TOTAL)	7.99	7.61	7.49	16.20	16.90
FeO	5.40	4.20	5.53	9.39	10.00
MnO	0.04	0.03	0.04	0.04	0.23
MgO	4.93	4.57	4.33	7.74	3.59
CaO	0.62	0.13	0.96	1.61	0.41
Na_2O	0.59	0.06	1.07	1.27	0.27
K_2O	2.07	1.33	2.56	5.59	2.27
LOI	1.43	0.53	0.80	1.03	1.08

CHAPTER 5

This chapter is published as:

Morrissey, L.J., Hand, M., Kelsey, D.E., 2015. Multi-stage metamorphism in the Rayner–Eastern Ghats Terrane: *P–T–t* constraints from the northern Prince Charles Mountains, east Antarctica. *Precambrian Research*, **267**, 137–163.

Statement of Authorship

Title of Paper	Multi-stage metamorphism in the Rayner–Eastern Ghats Terrane: *P–T–t* constraints from the northern Prince Charles Mountains, east Antarctica.
Publication status	☒Published ☐Accepted for publication ☐Submitted for publication ☐Unpublished and unsubmitted work written in manuscript style
Publication Details	Morrissey, L.J., Hand, M., Kelsey, D.E., 2015. Multi-stage metamorphism in the Rayner–Eastern Ghats Terrane: *P–T–t* constraints from the northern Prince Charles Mountains, east Antarctica. *Precambrian Research*, **267**, 137–163.

Principal Author

Name of Principal Author (Candidate)	Laura Morrissey		
Contribution to the Paper	Petrography, LA-ICP-MS data collection, processing, and interpretation, *P–T* pseudosection calculation and interpretation, manuscript design and composition, creation of figures.		
Overall percentage (%)	85		
Certification:	This paper reports on original research I conducted during the period of my Higher Degree by Research candidature and is not subject to any obligations or contractual agreements with a third party that would constrain its inclusion in this thesis. I am the primary author of this paper.		
Signature		Date	16/05/2016

Co-Author Contributions

By signing the Statement of Authorship, each author certifies that:

i. the candidate's stated contribution to the publication is accurate (as detailed above);
ii. permission is granted for the candidate in include the publication in the thesis; and
iii. the sum of all co-author contributions is equal to 100% less the candidate's stated contribution.

Name of Co-Author	Martin Hand		
Contribution to the Paper	Project design, fieldwork, guidance with data interpretation, manuscript review.		
Signature		Date	17th May 2016

Name of Co-Author	David Kelsey		
Contribution to the Paper	Guidance with *P–T* modelling and data interpretation, manuscript review.		
Signature		Date	18/05/2016

ABSTRACT

Metapelitic rocks from the northern Prince Charles Mountains in the Rayner Complex in east Antarctica record evidence for a protracted metamorphic history during the late Mesoproterozoic to early Neoproterozoic. In situ LA-ICP-MS U–Pb monazite geochronology yields ages in the interval 1030–880 Ma. There is a spread in U–Pb ages both between and within individual samples. Two samples record monazite populations at c. 1020 Ma, which have been variably reset. The remaining samples contain single monazite populations with $^{206}Pb/^{238}U$ weighted mean ages of 940–900 Ma. Calculated metamorphic phase diagrams for a sample preserving a defined late Mesoproterozoic monazite population suggest this early part of the metamorphic history may reflect a higher-pressure phase of metamorphism. This stage was overprinted by a cordierite-bearing assemblage, texturally accompanied by monazite growth at 950–900 Ma. The conditions of the second event are consistent between samples, and suggest that it involved lower pressures of 6–7 kbar and temperatures of 850–880 °C. The geochronology and metamorphic conditions for the Neoproterozoic metamorphism obtained in this study are consistent with the evolution proposed for elsewhere in the Rayner Complex and also the contemporaneous and formerly contiguous UHT metamorphism in the Eastern Ghats Province in India. This is the first study to integrate metamorphic constraints from the now separate terranes, and it suggests that that Rayner–Eastern Ghats terrane as a whole records prolonged high temperatures over a spatially large (> 500,000 km^2) area. This has implications for the timescales and footprint of geodynamic processes involving the mid-to-deep crust.

1. Introduction

Metamorphism along high thermal gradients (> 100 °C/kbar), particularly if it reaches ultrahigh temperature (UHT) conditions, has been the focus of much attention as it has implications for lithospheric rheology, crust–mantle interaction and the geodynamic settings in which high thermal gradients can be developed and maintained (e.g. Brown, 2007; Clark et al., 2011; Harley, 2004; Kelsey, 2008; Kelsey and Hand, 2015; Sizova et al., 2014). It is increasingly appreciated that many regional greenschist and amphibolite-facies high thermal gradient terranes may simply be the upper crustal levels of granulite to ultrahigh-*T* (G–UHT) terranes, and therefore G–UHT metamorphism may be relatively common in the crust (e.g. Brown, 2007, 2014; Clark et al., 2011; Kelsey and Hand, 2015; Morrissey et al., 2014; Sandiford and Powell, 1986; Stüwe, 2007). However, the requirements and mechanisms for the regional generation of these high temperatures remain uncertain (e.g. Brown, 2007; Brown and Korhonen, 2009; Clark et al., 2011; Gorczyk et al., 2015; Jamieson and Beaumont, 2013; Kelsey and Hand, 2015; Santosh and Kusky, 2010; Sizova et al., 2010, 2014; Vielzeuf et al., 1990). Large terranes that preserve long-lived (many tens of millions of years), high thermal gradients are of particular interest, as they provide direct evidence that the crust is capable of sustaining extreme thermal conditions for very long timescales. An investigation of the timescale of metamorphism and the *P*–*T* evolution of these terranes provide a guide to the possible geodynamic setting of G–UHT terranes (e.g. Brown, 2007; Kelsey and Hand, 2015). Moreover, detailed geological and metamorphic constraints from terranes recording high thermal gradients are required to underpin geodynamic forward models that are used to propose geodynamic settings for the formation of G–UHT conditions.

The once contiguous Rayner–Eastern Ghats (R–EG) terrane formed a vast Meso–Neoproterozoic (c. 1140–900 Ma) orogenic belt, the fragments of which now reside in eastern India and east Antarctica (Fig. 1a and b). The R–EG terrane records voluminous charnockitic and granitic magmatism and high thermal gradient metamorphism, with the exposure of UHT rocks in the Eastern Ghats Province (Dharma Rao et al., 2012; Korhonen et al., 2013a, 2013b, 2014; Mezger and Cosca, 1999; Simmat and Raith, 2008). *P–T* evolutions in both regions appear to be anticlockwise, dominated by isobaric cooling and associated with magmatism (Boger and White, 2003; Clarke et al., 1989; Dasgupta et al., 1995; Halpin et al., 2007a; Kamineni and Rao, 1988; Korhonen et al., 2013a; Mukhopadhyay and Bhattachrya, 1997; Sengupta et al., 1990). Geochronology from both the Rayner Complex and Eastern Ghats Province suggests that high temperatures may have persisted for > 100 Ma (Boger et al., 2000; Bose et al., 2011; Halpin et al., 2012; Korhonen et al., 2013b; Simmat and Raith, 2008).

Detailed *P–T–t* studies have been undertaken on rocks from the Eastern Ghats Province, providing important information for geodynamic forward models (e.g. Korhonen et al., 2011, 2013a, 2013b, 2014; Sizova et al., 2014). In contrast, studies from the Rayner Complex that have combined in situ geochronology with modern metamorphic phase equilibria have been largely limited to the MacRobertson and Kemp Land coasts (Fig. 1; Halpin et al., 2007a, 2007b). Therefore, detailed *P–T–t* constraints required as critical input for geodynamic forward models are limited for much of the Rayner Complex.

The northern Prince Charles Mountains (nPCM) are a large region of inland outcrop in the Rayner Complex (Fig. 1), and therefore provide an opportunity to further investigate the thermobarometric architecture of the orogen. Previous attempts to temporally constrain the deformation and metamorphism have relied on geochronology from structurally controlled samples and predominantly conventional thermobarometry (e.g. Boger et al., 2000; Boger and White, 2003; Fitzsimons and Harley, 1992; Nichols, 1995; Stephenson and Cook, 1997; Thost and Hensen, 1992). There have been no studies that combine in situ U–Pb geochronology with modern metamorphic analysis to constrain the temporal evolution of the major silicate mineral assemblages in the region.

This study uses samples of metapelite from across the nPCM to better constrain the metamorphic and temporal evolution of Grenvillian-aged metamorphism. The results from this study will then be discussed in the context of previous work elsewhere in the Rayner Complex and the Eastern Ghats. This provides a clear metamorphic framework with which to evaluate the geodynamic models for the R–EG terrane.

2. Geological setting

The Prince Charles Mountains (PCM) outcrop as a series of steep sided massifs and nunataks that stretch for 600 km inland from the Mawson Coast in MacRobertson Land, east Antarctica (Fig. 1c). They have been divided into four distinct geological terranes (e.g. Boger et al., 2008; Mikhalsky et al., 2001, 2006a; Phillips et al., 2006; Tingey, 1991). The southern Prince Charles Mountains (sPCM) are composed of the Ruker Terrane, which has an Archean history, and the Lambert Terrane, which has an Archean–Paleoproterozoic history and makes up much of the Mawson Escarpment (Fig. 1c; Boger et al., 2008; Corvino et al., 2008;

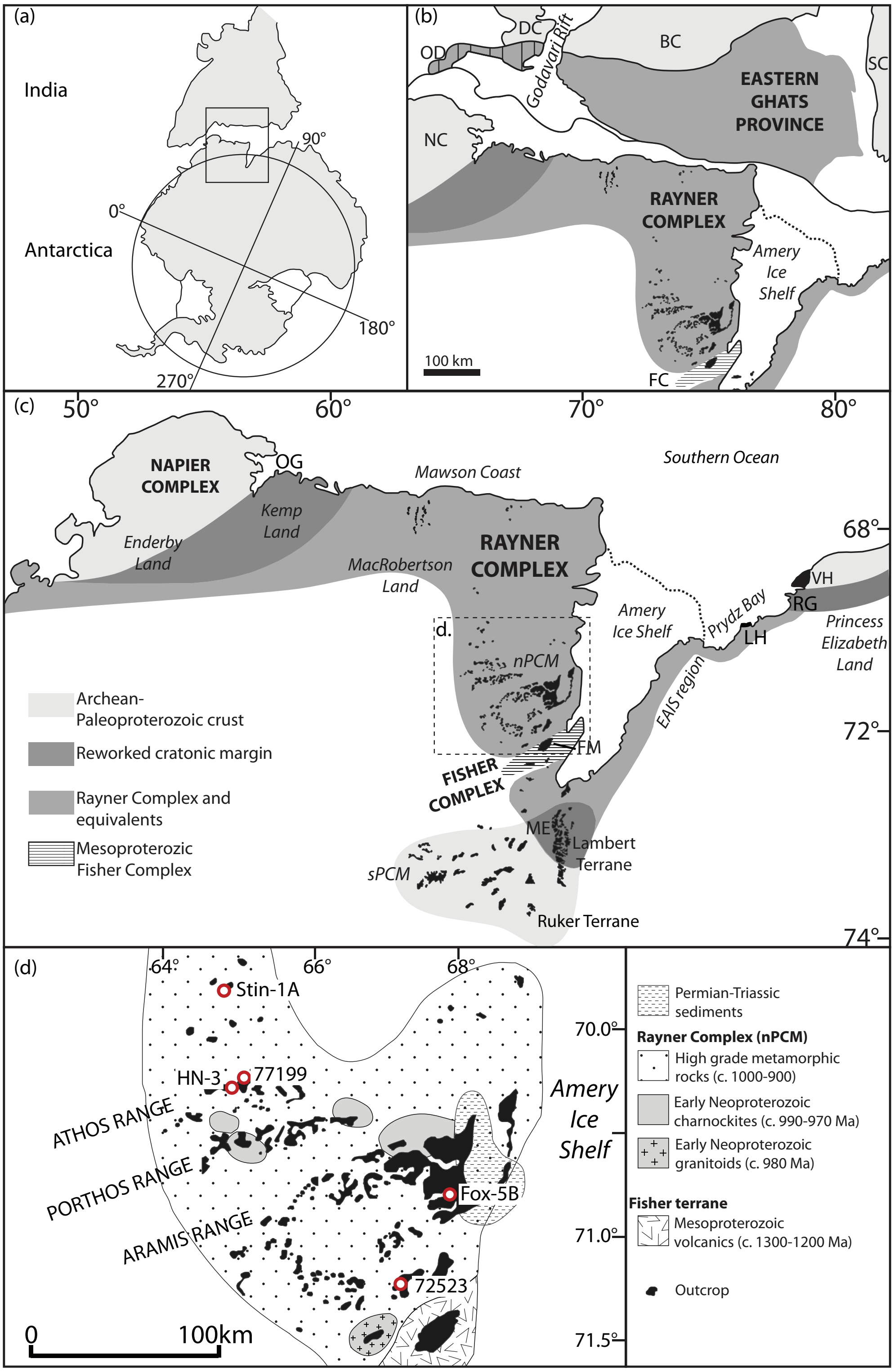

Figure 1: 1(a and b) Reconstruction of India and Antarctica, showing the Rayner Complex and Eastern Ghats Province in context of the present day continents. OD: Ongole Domain; DC: Dharwar Craton; BC: Bastar Craton; SC: Singhbhum Craton; NC: Napier Complex; FC: Fisher Complex. (c) Simplified geological map showing the Rayner Complex and Prince Charles Mountains in the context of the surrounding terranes, after Corvino et al. (2011). OG: Oygarden Group; FM: Fisher Massif; ME: Mawson Escarpment; LH: Larsemann Hills; RG: Rauer Group. (d) Outcrop map of the northern Prince Charles Mountains showing sample locations and main ranges, after Mikhalsky et al. (2001).

Mikhalsky et al., 2001, 2006b; Phillips et al., 2006). The Fisher Complex is located between the sPCM and nPCM and is composed of 1300–1200 Ma calc-alkaline volcanics that have been metamorphosed to amphibolite facies, with late granitoids emplacedat 1050–1020 Ma (Fig. 1c; Beliatsky et al., 1994; Kinny et al., 1997; Mikhalsky et al., 1996, 2001). The nPCM form part of the Proterozoic Rayner Complex. The Rayner Complex is interpreted to extend west from Enderby Land to Princess Elizabeth Land in the east, and south from the coastline of Kemp and MacRobertson Lands to the Fisher Terrane and sPCM (Fig. 1c; e.g. Boger, 2011; Kamenev, 1972; Kelly et al., 2002; Liu et al., 2009a; Phillips et al., 2009; Tingey, 1991). Outcrop in the Rayner Complex is sparse and occurs mainly along the MacRobertson and Kemp Land coasts and within the nPCM (Fig. 1c).

The Rayner Complex is dominantly composed of granulite facies felsic and mafic gneisses, with comparatively minor interleaved metasedimentary units (e.g. Boger et al., 2000; Fitzsimons and Thost, 1992; Hand et al., 1994b; Thost and Hensen, 1992; Tingey, 1991). The emplacement of orthogneiss protoliths in the nPCM has been dated at 1070–1020 Ma (Boger et al., 2000; Mikhalsky and Sheraton, 2011).

The Rayner Complex was deformed and metamorphosed during the Grenvillian-aged Rayner Orogeny at c. 1000–900 Ma (e.g. Boger et al., 2000; Carson et al., 2000; Halpin et al., 2007a, 2012, 2013; Hensen et al., 1997; Kelly et al., 2002; Kinny et al., 1997). This event was accompanied by voluminous charnockitic and granitic magmatism (e.g. Carson et al., 2000; Kinny et al., 1997; Manton et al., 1992; Munksgaard et al., 1992; Tingey, 1991; Zhao et al., 1997). However, detailed geochronology along the Mawson Coast appears to record evidence of discrete charnockite ‘events’ at 1145–1140 Ma, 1080–1050 Ma and 985–960 Ma (Halpin et al., 2012). This suggests that the high temperature evolution in the Rayner Complex may have begun as early as 1145 Ma, and proceeded either continuously or as a punctuated thermal system for c. 250 Myr.

The structural evolution of the Rayner Orogeny appears to be consistent throughout the nPCM, although the events have been assigned different nomenclature by various workers (e.g. Boger et al., 2000; Fitzsimons and Thost, 1992; Hand et al., 1994b; McKelvey and Stephenson, 1990; Nichols, 1995; Scrimgeour and Hand, 1997; Thost and Hensen, 1992). The structural studies have been summarised by Boger et al. (2000). D_1 involved the formation of a layer-parallel foliation, which forms the dominant fabric throughout the nPCM. This foliation was folded into recumbent, isoclinal, layer-parallel folds during D_2. The evolution from D_1 to D_2 has been interpreted to have been progressive, and to have occurred at c. 990 Ma (Boger et al., 2000; Fitzsimons and Thost, 1992; Hand et al., 1994b; Thost and Hensen, 1992). The layer-parallel foliation and isoclinal folds were reoriented about upright E–W trending folds during D_3 at c. 940 Ma. Intensification of strain on the limbs of these folds led to the development of E–W trending, steeply dipping shear zones late in D_3 (Boger et al., 2000; Fitzsimons and Thost, 1992; Hand et al., 1994b; Nichols, 1995; Thost and Hensen, 1992). Discrete mylonites and pseudotachylites are the final stage of deformation (D_4), and have been dated at c. 500–475 Ma (Boger et al., 2000, 2002; Nichols, 1995).

The Rayner Orogeny is typically considered to have involved an anticlockwise *P–T* evolution, dominated by isobaric cooling

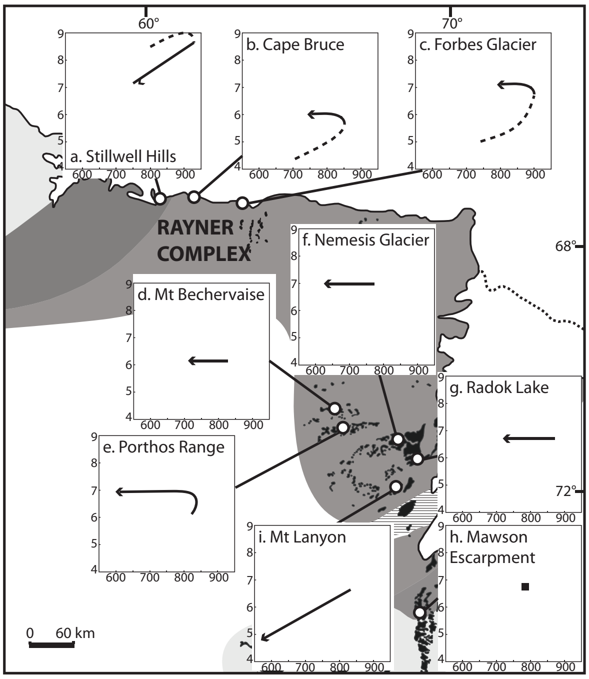

Figure 2: Summary of previously inferred *P–T* evolutions for the Neoproterozoic Rayner Orogeny, after Boger and White (2003) and Phillips et al. (2009). (a) Kemp Land: Halpin et al. (2007b). (b and c) Mawson Coast, MacRobertson Land: Halpin et al. (2007a). (d) Mt Bechervaise: Nichols (1995). (e) Porthos Range: Thost and Hensen (1992). (f) Nemesis Glacier: Fitzsimons and Harley (1992). (g) Radok Lake: Stephenson and Cook (1997); Boger and White (2003). (h) Mawson Escarpment: Phillips et al. (2009); Corvino et al., (2011). (i) Mt Lanyon: Nichols (1995).

(Fig. 2; e.g. Boger and White, 2003; Clarke et al., 1989; Fitzsimons and Harley, 1992; Halpin et al., 2007a; Stephenson and Cook, 1997; Thost and Hensen, 1992). Along the Mawson Coast, metamorphism occurred at 990–970 Ma and involved high thermal gradients (~140–175 °C/kbar), with peak temperatures of 850 °C and pressures of 5.6–6.2 kbar at Cape Bruce, and 900 °C and 5.4–6.2 kbar at Forbes Glacier (Fig. 2). The rocks record an anticlockwise *P–T* evolution, with peak temperatures followed by crustal thickening to 6–7 kbar, synchronous with repeated pluton emplacement (Fig. 2; Halpin et al., 2007a). However, further west in Kemp Land, metamorphism occurred later at c. 940–900 Ma (Kelly et al., 2002), and involved a clockwise *P–T* evolution from peak pressures of 7.4–10 kbar and peak temperatures of 870–990 °C. Peak pressures have been interpreted to increase westwards, towards the margin of the Napier Craton (Halpin et al., 2007b). The terrane then experienced decompression to 5 kbar (Fig. 2; Halpin et al., 2007b; Kelly and Harley, 2004). The differences in the timing of metamorphism and *P–T* path along the Mawson Coast have been attributed to differences in crustal strength between the younger, more melt prone Rayner Complex and the residual Kemp Land rocks, and displacement of the Kemp Land cratonic margin from the main magma flux during orogenesis (Halpin et al., 2007a).

In the nPCM, early work using conventional thermobarometry was used to interpret isobaric cooling from peak temperatures of 800–850 °C at 7 kbar to 650 °C (Fig. 2; e.g. Fitzsimons and Harley, 1992; Nichols, 1995; Thost and Hensen, 1992). Samples from the Aramis Range (Fig. 1d) also provide evidence for an anticlockwise metamorphic evolution, involving increasing temperatures, followed by crustal thickening (Boger and White, 2003). Peak conditions are estimated to have reached temperatures of ~880 °C and pressures of 6.0–6.5 kbar (Fig. 2; Boger and White, 2003). In contrast, some locations in the nPCM appear to have experienced post-peak, down-pressure histories (Hand et al., 1994a; Nichols, 1995; Stüwe and Hand, 1992). However, more recently, in situ monazite U–Pb geochronology has been used to suggest that these decompressive style *P–T* paths are probably the result of high-*T* overprinting during the Cambrian and do not reflect a continuous metamorphic evolution (Morrissey et al., 2016).

Table 1: Sample locations in the nPCM.

Sample	Location	UTM zone	Easting	Northing
Stin-1A	Stinear Nunataks	41D	573171	2266528
77199	Mt Dovers	41D	575096	2214645
HN-3	Hunt Nunataks	41D	570684	2212172
Fox-5B	Fox Ridge	42D	458986	2146913
72523	Mt Lanyon	42D	433985	2095840

Metamorphism between 960 and 905 Ma is also recorded in the northern Mawson Escarpment (Fig. 1c). This reached peak conditions of 6.5–7.1 kbar and 790–810 ºC (Fig. 2; Corvino et al., 2008, 2011; Phillips et al., 2009). However, the interpretation of the *P*–*T* evolution of this region is complicated by reworking during the Cambrian (Boger and Wilson, 2005; Corvino et al., 2011; Phillips et al., 2009).

The Rayner Complex has been variably affected by Cambrian tectonism (e.g. Boger et al., 2002; Kelsey et al., 2008b; Liu et al., 2007, 2009b). This overprint is strongest in the Prydz Bay region, where it reached UHT conditions in the Rauer Group (Carson et al., 1997; Fitzsimons, 1996; Harley, 1998; Kelsey et al., 2003b, 2007). However, the overprint has also been recognised in the Ruker and Lambert Terranes in the sPCM (Boger et al., 2001, 2008; Boger and Wilson, 2005; Corvino et al., 2008; Phillips et al., 2007, 2009) and the nPCM (Boger et al., 2002; Morrissey et al., 2016). In the nPCM, the Cambrian event appears to have reached temperatures of 800–850 °C and was associated with localised deformation and minor emplacement of pegmatite and granite (Boger et al., 2002; Carson et al., 2000; Hensen et al., 1997; Manton et al., 1992; Morrissey et al., 2016). However, the record of Cambrian reworking in the nPCM is patchy, and many areas appear to record little or no evidence of Cambrian metamorphism. The patchy nature of Cambrian recrystallisation may have been controlled by the distribution of late Grenvillian-aged retrogression, with areas affected by retrogression being metamorphically reactive during the Cambrian whereas those that escaped retrogression remaining metamorphically inert (Morrissey et al., 2016). This study uses samples with in situ monazite geochronology that provide no evidence for disturbance during the Cambrian.

3. Sample selection and petrography

Samples were selected from metapelitic rocks located throughout the nPCM (Fig. 1d, Table 1). Samples used in this study were obtained during field seasons in the late 1980s and early 1990s and are from collections archived at the University of Tasmania and the University of Adelaide. Numbered samples are from the rock library at the University of Tasmania; the samples beginning with letters are from the University of Adelaide.

3.1. Sample Stin-1A: Stinear Nunataks

Stinear Nunataks are an isolated group of rock outcrops located north of the main ranges of the nPCM (Fig. 1d). Sample Stin-1A contains garnet, sillimanite, cordierite, K-feldspar, quartz, plagioclase, ilmenite and minor biotite. The sample has a weak foliation defined by sillimanite and quartzofeldspathic segregations. Garnet grains (2–3 mm in diameter) are anhedral with lobate edges and contain inclusions of rounded quartz grains and rare elongate grains of sillimanite, ilmenite and biotite (Fig. 3a). Some garnet grains are rimmed by fine-grained sillimanite. Cordierite may form porphyroblasts (up to 1.5 mm) and some grains contain patches of fine-grained sillimanite (Fig. 3a). Sillimanite can be coarse-grained (up to 2 mm) and in rare cases contains inclusions of ilmenite (Fig. 3a). Biotite is uncommon (<2 % of the sample) and forms anhedral grains that are 200–500 μm in length (Fig. 3a). Biotite occurs most commonly near garnet or cordierite grains. K-feldspar is commonly perthitic and forms grains up to 1 mm in diameter. The remainder of the sample is composed of rounded quartz (up to 1 mm) and less common plagioclase (~200 μm). The sample does not contain obvious reaction microstructures.

The peak assemblage is interpreted to be garnet + cordierite + sillimanite + K-feldspar + plagioclase + quartz + ilmenite. The post-peak evolution is interpreted to have involved the formation of biotite.

3.2. Sample 77199: Mt Dovers

Mount Dovers is located in the northern Athos Range (Fig. 1d). Sample 77199 contains garnet, sillimanite, cordierite, K-feldspar, quartz, plagioclase, ilmenite, biotite and rare spinel. The sample contains a foliation defined by biotite-rich layers, aligned sillimanite and quartzofeldspathic segregations. Porphyroblastic garnet (up to 5 mm) contains inclusions of quartz, ilmenite, biotite and abundant fine-grained sillimanite (Fig. 3b). Garnet also contains rare inclusions of pinitised cordierite, which may themselves contain fine-grained sillimanite (Fig. 3b). Garnet grains are wrapped by the foliation. Several garnet grains are also mantled by much smaller garnet grains at their edges (25–50 μm; Fig. 3b). Sillimanite is abundant and occurs as blocky grains up to 1 mm in length which define the foliation, and also as fine-grained inclusions in cordierite and garnet (Fig. 3b and c). Coarse-grained sillimanite encloses cordierite porphyroblasts (Fig. 3c). The matrix is made up of coarse K-feldspar, quartz and cordierite. Cordierite forms coarse-grained porphyroblasts (up to 3 mm) throughout the matrix. These porphyroblasts may have abundant sillimanite inclusions (Fig. 3c). K-feldspar occurs throughout the matrix as grains up to 500 μm and may contain well-developed perthitic textures. At sample scale, biotite roughly parallels the gneissic foliation, but at the microscopic scale, biotite is anhedral and usually fine-grained (Fig. 3b and c). It typically occurs on the boundaries of garnet and cordierite porphyroblasts (Fig. 3b) and less commonly fills fractures within garnet or occurs intergrown with fine-grained cordierite. Spinel is very uncommon but two small (<100 μm) grains do occur near garnet.

The peak mineral assemblage is interpreted to be cordierite + garnet + sillimanite + K-feldspar + plagioclase + ilmenite + quartz. The post-peak evolution is interpreted to involve the formation of new generation garnet and fine-grained biotite.

3.3. Sample HN-3: Hunt Nunataks

Hunt Nunataks are located in the northern Athos Range (Fig. 1d). Sample HN-3 contains garnet, biotite, sillimanite, spinel, K-feldspar, ilmenite and apatite. Abundant (30 %), coarse-grained, euhedral garnet porphyroblasts (up to 7 mm in diameter) are wrapped by a fabric dominantly composed of biotite, with minor sillimanite, K-feldspar, ilmenite and spinel. Garnet porphyroblasts contain inclusions of biotite (up to 500 μm), which do not have a preferred orientation, K-feldspar and rare apatite (up to 750 μm). Garnet also occurs as less common, anhedral, finer-grained (<1 mm) grains. K-feldspar occurs as coarser grains (up to 1 mm) throughout the biotite matrix (Fig.

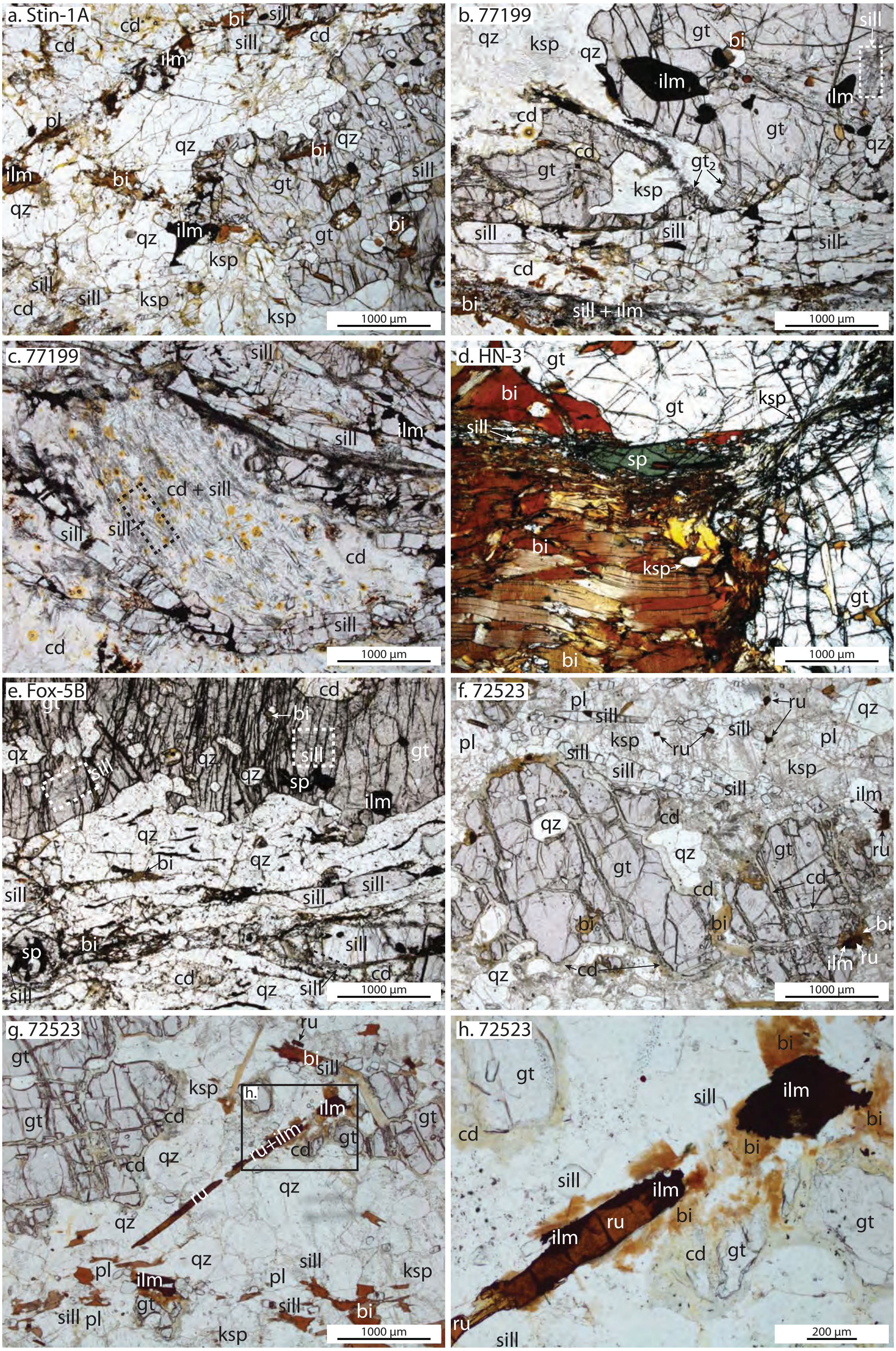
a. Stin-1A
cd
bi
sill
cd
ilm
pl
qz
ilm
bi
qz
gt
qz
ilm
ksp
gt
sill
cd
ksp
1000 µm
b. 77199
qz
ksp
qz
gt
bi
sill
ilm
ilm
cd
cd
gt
gt$_2$
ksp
sill
cd
sill + ilm
1000 µm
c. 77199
sill
ilm
cd + sill
sill
cd
1000 µm
d. HN-3
gt
bi
ksp
sill
sp
bi
ksp
gt
1000 µm
e. Fox-5B
gt
cd
bi
qz
sill
sp
ilm
1000 µm
f. 72523
pl
sill
ksp
ru
qz
ilm
cd
gt
bi
1000 µm
g. 72523
gt
ksp
h.
ru
bi
ilm
ru+ilm
cd
qz
pl
1000 µm
h. 72523
gt
cd
sill
ilm
bi
ru
200 µm

Figure 3 (previous page): Representative photomicrographs for each sample. (a) sample Stin-1A: Stinear Nunataks. Garnet grains in a matrix of quartz, K-feldspar, cordierite and sillimanite, with minor anhedral biotite. (b) sample 77199: Mt Dovers. Garnet porphyroblast with biotite, ilmenite, cordierite, sillimanite and quartz inclusions. The dashed box outlines fine-grained sillimanite in garnet. A further generation of garnet occurs on the margins of coarse garnet. (c) sample 77199: Mt Dovers. Cordierite porphyroblast wrapped by coarse-grained sillimanite. The dashed box outlines fine-grained sillimanite in cordierite. (d) sample HN-3: Hunt Nunataks. Garnet porphyroblasts are wrapped by a fabric of biotite, spinel, sillimanite and K-feldspar. In the top right corner, sillimanite and K-feldspar wrap garnet grains. (e) sample Fox-5B: Fox Ridge. Garnet porphyroblast containing inclusions of fine-grained sillimanite, spinel, quartz, cordierite and ilmenite. Coarse-grained sillimanite contains spinel and defines the foliation along with fine-grained biotite. The dashed boxes outline fine-grained sillimanite in garnet and fine-grained sillimanite on the edge of coarse sillimanite in the bottom right of the image. (f) sample 72523: Mt Lanyon. Garnet porphyroblast with thin cordierite corona. Euhedral rutile occurs in the top of the image near blocky sillimanite. In the right of the image, rutile partially replaced by ilmenite is surrounded by a corona of biotite. (g) sample 72523: Mt Lanyon. Elongate, coarse-grained rutile occurs in the matrix and is partially replaced by ilmenite. Garnet grains are surrounded by thin cordierite coronas. The box gives the location of Fig. 3h. (h) Rutile and ilmenite in direct contact, with ilmenite partially mimicking the grain shape of rutile. Anhedral biotite coronas occur on rutile/ilmenite.

3d) and as finer grains intergrown with biotite surrounding anhedral, small garnet grains. The matrix also contains sillimanite grains. These are up to 500 μm in length and are foliation-parallel. Spinel (up to 1 mm, 1–2% of the sample) occurs in the matrix, commonly along the margins of garnet, but it is never included in garnet (Fig. 3d). Apatite grains (~500 μm) occur throughout the matrix and comprise ~0.5 % of the sample. Ilmenite occurs as inclusions within biotite and along biotite cleavages, but also as anhedral grains in the matrix. There are two morphologies of biotite. The first is coarse-grained biotite (up to 2 mm in length), which defines the foliation (Fig. 3d). The second is finer-grained biotite that occurs in association with fine-grained K-feldspar, near small, anhedral garnet grains that are interpreted to be relict.

The peak mineral assemblage is interpreted to be coarse-grained garnet + biotite + sillimanite + K-feldspar + spinel + ilmenite + apatite. Post-peak, garnet is interpreted to decrease in abundance, as suggested by small, anhedral relict garnet grains, and the formation of fine-grained biotite.

3.4. Sample Fox-5B: Fox Ridge

Fox Ridge, in the Aramis Range (Fig. 1d), is transected by an E–W trending high strain zone, interpreted to be equivalent to the D3 high strain zones of Boger et al. (2000). Sample Fox-5B contains garnet, sillimanite, biotite, cordierite, spinel, quartz, K-feldspar and plagioclase. Garnet, sillimanite and cordierite form porphyroblasts in a matrix dominantly composed of fine-grained quartz, plagioclase, K-feldspar and minor biotite. The fine-grained quartz forms aggregates with K-feldspar and less common plagioclase and these quartzofeldspathic segregations define a foliation together with coarse-grained sillimanite (up to 2 mm in length). Garnet porphyroblasts (up to 5 mm in diameter) contain inclusions of rounded cordierite, spinel, ilmenite, quartz, fine-grained sillimanite and rare biotite (Fig. 3e). The coarse-grained sillimanite may contain inclusions of spinel and ilmenite (Fig. 3e). Cordierite porphyroblasts (up to 1.5 mm) occur throughout the sample and contain inclusions of fine-grained sillimanite. Spinel does not occur in the matrix, and the inclusions in garnet and sillimanite make up <1% of the sample. Garnet, cordierite and sillimanite porphyroblasts are commonly rimmed by fine-grained sillimanite (fibrolite). Aggregates of secondary, fine-grained sillimanite and fine-grained, anhedral biotite (up to 50 μm) define a mylonitic foliation which wraps the porphyroblasts. The sample contains little biotite (~2 % of the sample).

The peak mineral assemblage in this sample is present in the matrix and involved garnet + sillimanite + cordierite + K-feldspar + plagioclase + ilmenite + quartz. The formation of fine-grained biotite and sillimanite is interpreted to have occurred near the end of the *P–T* evolution.

3.5. Sample 72523: Mt Lanyon

Mt Lanyon is located in the southern Aramis Range, near the boundary with the Fisher Terrane (Fig. 1d). At hand sample scale, sillimanite- and biotite-rich layers define a gneissic foliation together with quartzofeldspathic segregations. Garnet porphyroblasts contain inclusions of fine-grained sillimanite, biotite, rounded quartz and less common rutile. Garnets are surrounded by narrow, partially pinitised coronas of cordierite (up to 100 μm wide; Fig. 3f and g). The matrix is mainly comprised of coarse-grained quartz and K-feldspar, with less common and finer-grained plagioclase (500 μm) and sillimanite (Fig. 3f and g). K-feldspar occurs as perthite and occasionally microcline. Aggregates of sillimanite (up to 750 μm) define the foliation. Euhedral rutile (up to 300 μm) occurs throughout the matrix, but occurs most commonly in contact with or located near sillimanite. It also occurs included in K-feldspar and less commonly occurs included in garnet. Rutile may occur in direct contact with ilmenite; in places ilmenite closely mimics the grain shape of ilmenite, giving the impression that ilmenite has partially replaced rutile in some instances (Fig. 3h). Biotite occurs throughout the matrix but in low abundance (<5 %) and occurs in two morphological forms. Well-shaped crystals tend to have a preferred orientation and form a weak foliation; whereas anhedral, crystals do not have a preferred orientation. Anhedral biotite grains may occur as coronas on ilmenite or ilmenite/rutile grains (Fig. 3f and h).

The sample is interpreted to preserve two mineral assemblages. The early mineral assemblage is interpreted to involve garnet + sillimanite + K-feldspar + plagioclase + quartz + rutile + ilmenite + biotite. The second mineral assemblage is localised and is interpreted to involve the formation of cordierite at the expense of garnet and sillimanite and the partial replacement of rutile with ilmenite.

4. Methods

4.1. Monazite U–Pb LA-ICP-MS geochronology

U–Pb isotopic data was collected using Laser Ablation–Inductively Coupled Plasma–Mass Spectrometry (LA-ICP-MS) on in situ monazite grains in thin section. Prior to LA-CP-MS analysis, monazite grains were imaged using a back-scattered electron detector on a Phillips XL30 scanning electron microscope to determine their microstructural locations and any compositional variations.

LA-ICP-MS analyses were performed at the University of Adelaide, following the method of Payne et al. (2008). U–Pb isotopic analyses were acquired using a New Wave 213 nm Nd–YAG laser coupled with an Agilent 7500cs ICP-MS. Ablation of monazites was performed in a He-ablation atmosphere with a frequency of 4 Hz. A spot size of 12 μm was used for all samples. The total acquisition time of each analysis was 100 s. This included 40 s of background measurement, 10 s of the laser firing with the shutter closed to allow for beam stabilisation, and 50 s of sample ablation. Isotopes measured were ^{204}Pb, ^{206}Pb, ^{207}Pb and ^{238}U for dwell times of 10, 15, 30 and 15 ms, respectively.

Monazite data were reduced using Glitter software (Griffin et al., 2004). Elemental fractionation and mass bias were corrected using the monazite standard MAdel (TIMS normalisation data: $^{207}Pb/^{206}Pb$ = 491.0 ± 2.7 Ma, $^{206}Pb/^{238}U$ = 518.37 ± 0.99 Ma and $^{207}Pb/^{235}U$ = 513.13 ± 0.19 Ma: updated from Payne et al. (2008) with additional TIMS analyses). Throughout the course of this study, MAdel yielded weighted mean ages of $^{207}Pb/^{206}Pb$ = 491 ± 5 Ma, $^{206}Pb/^{238}U$ = 518 ± 1 Ma, and $^{207}Pb/^{235}U$ = 513 ± 1 Ma (n = 142). Data accuracy was monitored using monazite standard 94-222/Bruna-NW (c. 450 Ma: Payne et al., 2008). As a secondary standard, 94-222 yielded weighted mean ages of $^{207}Pb/^{206P}b$ = 459 ± 9 Ma, $^{206}Pb/^{238}U$ = 450 ± 2 Ma, $^{207}Pb/^{235}U$ = 452 ± 2 Ma (n = 56).

4.2. Mineral chemistry

Chemical analyses of minerals were obtained using a Cameca SXFive electron microprobe at the University of Adelaide. Beam conditions of 20 nA and accelerating voltage of 15 kV were used for all point analyses. Calibration was performed on certified synthetic and natural mineral standards from Astimex Pty Ltd. and P & H Associates. Data calibration and reduction was carried out in Probe for EPMA, distributed by Probe Software Inc.

4.3. Phase equilibria modelling

Phase equilibria for the samples were calculated using THERMOCALC v3.33, using the internally consistent data set of Holland and Powell (1998; dataset tcds55 November 2003 update), for the geologically realistic system NCKFMASHTO (Na_2O–CaO–K_2O–FeO–MgO–Al_2O_3–SiO_2–H_2O–TiO_2–Fe_2O_3). The following activity–composition (*a–x*) relationships were used: silicate melt, garnet and biotite (White et al., 2007); cordierite (Holland and Powell, 1998); spinel, orthopyroxene and magnetite (White et al., 2002); ilmenite (White et al., 2000); and plagioclase and K-feldspar (Holland and Powell, 2003). Rutile, the aluminosilicates and H_2O are pure end-member phases.

As the samples show no evidence for mineral reaction microstructure development (except the development of cordierite coronas in sample 72523), and are homogeneous at the thin section scale, whole-rock chemical compositions for the calculation of metamorphic phase equilibria were determined by crushing up a representative amount of the rock (approximately 100–200 g) and homogenising the sample using a tungsten carbide mill. Bulk-rock chemical compositions were obtained from Franklin and Marshall College, Pennsylvania. Major elements were analysed by fusing a 0.4 g portion of the powdered sample with lithium tetraborate for analysis by XRF. Trace elements were analysed by mixing 7 g of crushed rock power with Copolywax powder and measurement by XRF. The whole rock chemistry for each sample used in the calculation of the mineral equilibria psuedosections is given in Table 2.

Despite the simple procedure to determine a bulk composition in a contemporary sample, the principle uncertainty in pseudosection modelling relates to the determination of the effective bulk composition at the time of metamorphism (particularly Fe_2O_3, H_2O and the effect of melt loss; Kelsey and Hand, 2015), as well as limitations relating to components that may affect mineral stability but are not modelled, such as ZnO, and Cr_2O_3. Cr_2O_3 contents of spinel in the modelled samples vary from 0.51–1.71 wt%, whereas ZnO contents of spinel in these samples vary from 2.95–10.44 wt% (Tables 3 and 4). However, spinel *a–x* models used for the calculation of phase diagrams do not include Zn or Cr, which are known to expand spinel stability to higher pressures and lower temperatures (Nichols et al., 1992; Tajcmanová et al., 2009). Therefore, the spinel-bearing fields cannot be used to provide absolute constraints on pressure and temperature conditions for samples Fox-5B and HN-3. In sample HN-3, apatite forms ~0.5% of the mineral assemblage. The large amount of CaO in apatite (~50–55 wt%; Deer et al., 1992) creates an overly calcic bulk composition with respect to the minerals that can be modelled in THERMOCALC. Using such a composition would result in the calculated stability of Ca-bearing minerals such as plagioclase and grossular-enriched garnet, which do not occur in the sample. This sample contains abundant monazite, and therefore the P_2O_5 content of the rock cannot be used as an approximation of the amount of apatite. Therefore, for the calculation of the pseudosection in Figure 7c, the amount of CaO in the bulk composition was based on the modal proportion of CaO-bearing phases (garnet) and its average composition as determined by electron microprobe data.

The oxidation state can have a significant effect on the stability of Fe–Ti oxide minerals such as magnetite, ilmenite$_{(ss)}$ and rutile, as well as some silicate minerals (e.g. Boger et al., 2012; Diener and Powell, 2010; Korhonen et al., 2012; Morrissey et al., 2013; White et al., 2000). For the purposes of exploring the effect that Fe_2O_3 may have on the mineral assemblage and determining an appropriate amount of Fe_2O_3, T–M_O and P–M_O sections were calculated for sample Stin-1A (Fig 4a and b; taken as representative for all samples except sample HN-3). As HN-3 contains a different mineral assemblage and bulk composition to the other metapelitic samples, T–M_O and P–M_O sections were also calculated for this sample (Fig. 4c and d). The pressures and temperatures for these sections were selected after a first pass estimate of metamorphic conditions. The effect of Fe_2O_3 in these samples is to stabilise rutile to lower pressures in the least oxidised compositions (Fig. 4b) and to stabilise magnetite at Fe_2O_3 values of >5 mol% (Fig. 4). In highly oxidised compositions, garnet is no longer stable (Fig. 4). However, the T–M_O and P–M_O sections illustrate that small

Table 2: Whole rock geochemistry in wt%.

	Stin-1A	77199	HN-3	Fox-5B	72523
SiO_2	61.97	60.02	39.05	59.02	57.47
TiO_2	1.01	1.13	2.69	0.95	0.73
Al_2O_3	18.37	18.56	19.28	20.62	20.01
Fe_2O_3	10.30	11.19	22.16	13.13	8.70
MnO	0.14	0.25	0.19	0.24	0.09
MgO	3.54	2.73	7.98	4.03	3.40
CaO	0.50	0.71	1.07	0.36	2.75
Na_2O	0.73	1.52	0.21	0.20	2.91
K_2O	3.13	4.26	6.00	0.90	3.21
P_2O_5	0.05	0.09	0.61	0.05	0.07
LOI	1.05	0.79	2.26	1.84	1.43
Total	**100.10**	**100.30**	**101.50**	**100.33**	**99.98**

variations in Fe_2O_3 do not significantly affect the topology or *P–T* conditions of fields on the pseudosections (Fig. 4). For the samples in this study, 3–5% of total Fe was estimated to be Fe_2O_3 (Fig. 4), based on the absence of magnetite in all samples, the $P–T–M_O$ section results and the low modal abundance of Fe^{3+} bearing minerals such as ilmenite and biotite and an appraisal of the ferric iron content of those minerals as determined from measured mineral compositions using the stoichiometric method of Droop (1987).

As some of the samples show evidence of low-*T* retrogression of cordierite, LOI was not considered to be an appropriate estimation of the H_2O content of these samples at the time the peak mineral assemblages developed. In addition, in granulite-facies terranes, it is likely that some of the volatile content of minerals such as cordierite and biotite is not H_2O, but rather CO_2 or Cl and F (e.g. Bose et al., 2005; Deer et al., 1992; Peterson et al., 1991; Rigby and Droop, 2011; Santosh et al., 1993; Thompson et al., 2001). The rocks in this study preserve high-grade assemblages with little biotite, consistent with melt loss (e.g. Diener et al., 2008; Kelsey et al., 2003b; Korhonen et al., 2010; White and Powell, 2002). Therefore, the H_2O content for each sample was adjusted so that the interpreted peak assemblages occur just above the elevated solidus, to reflect the conditions where the assemblage would have been in equilibrium with the last vestiges of melt (e.g. Diener et al., 2008; Korhonen et al., 2013a; White et al., 2004). As there is evidence for older (c. 1145–970 Ma) charnockitic and granitic magmatism (Boger et al., 2000; Halpin et al., 2012; Kinny et al., 1997; Mikhalsky and Sheraton, 2011), it is possible that the metapelitic rocks had already undergone melt loss prior to metamorphism during the Rayner Orogeny. Due to the uncertainties in the amount and timing of melt-loss events, the aim of metamorphic modelling was to constrain the general conditions of peak metamorphism, rather than utilise melt reintegration modelling to determine a quantitative prograde path for these samples (Diener et al., 2008; Korhonen et al., 2013a).

5. Results

5.1. Monazite U–Pb LA–ICP–MS geochronology

U–Pb isotopic data and information on microstructural location for all monazite analyses are presented as Supplementary Data S5.1. All samples are plotted on a Tera–Wasserburg plot to better depict common lead in some samples. Analyses that are shown as grey, dashed ellipses have been excluded from the calculation of weighted average ages but are shown on the concordia diagram for completeness.

5.1.1. Sample Stin-1A

Thirty analyses were collected from 17 grains. Analysed grains are located along grain boundaries in the cordierite-bearing matrix. One grain hosted within garnet was analysed; however, it was not isolated from microfractures. Grains are commonly rounded, 40–80 μm in diameter and rarely display patchy zoning under BSE (Fig. 5a). The 30 analyses form a clustered population (Fig. 6a), with a $^{207}Pb/^{206}Pb$ weighted average age of 916 ± 9 Ma (MSWD = 0.74) and a $^{206}Pb/^{238}U$ weighted average age of 920 ± 7 Ma (MSWD = 1.6).

5.1.2. Sample 77199 (Mt Dovers)

Thirty-one analyses were collected from 15 grains. The majority of grains were located along grain boundaries in matrix, though in rare cases grains were located within quartz, cordierite or garnet porphyroblasts. Some monazite grains display concentric zoning under BSE,

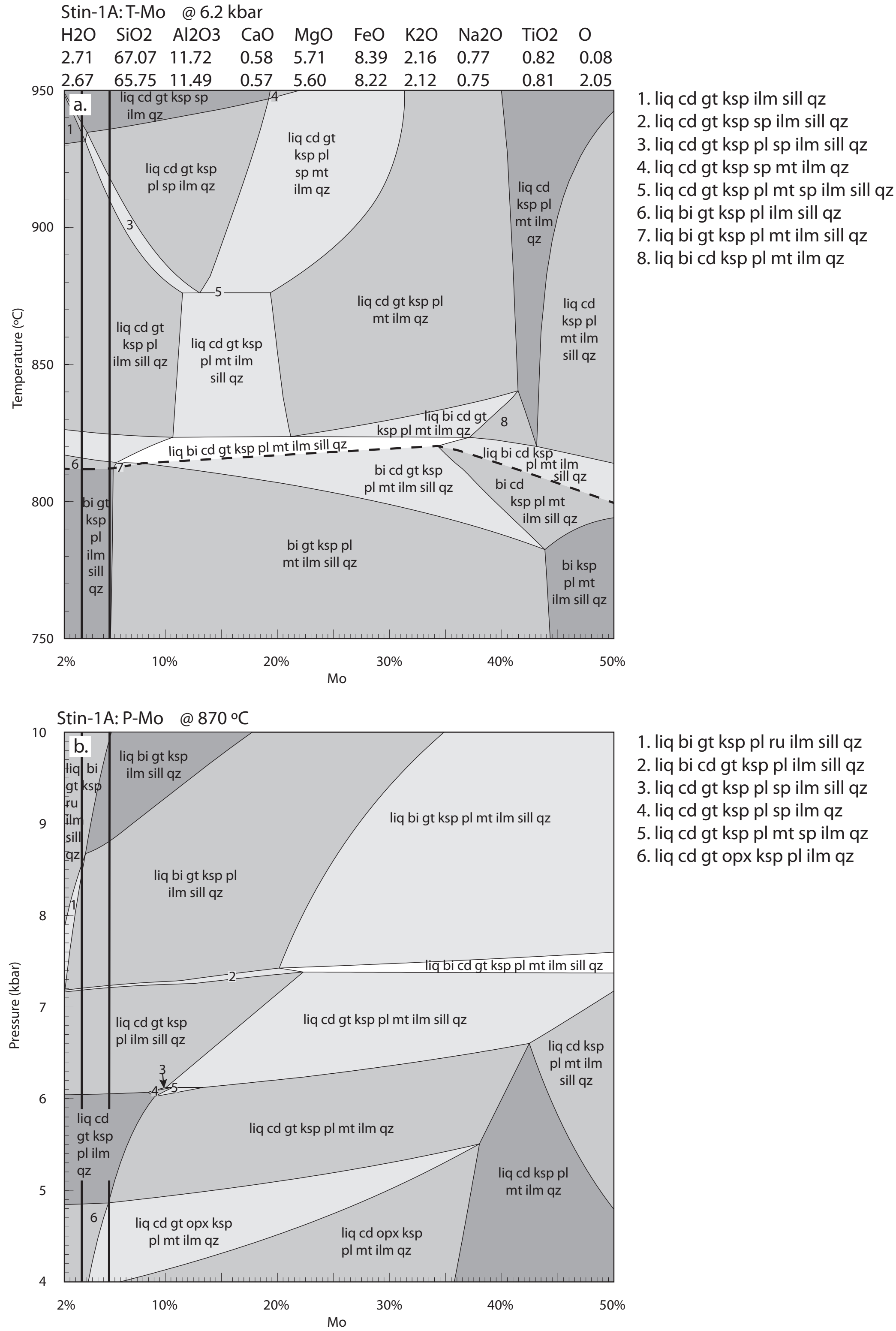

Figure 4: T–M_O and P–M_O sections. The composition is given in mole %. (a and b) T–M_O and P–M_O sections calculated for the composition of Stin-1A, which was considered representative of all samples except HN-3. The bold vertical lines represent the range of Fe_2O_3 values (~3–5 %) used for P–T pseudosection modelling for samples Stin-1A, 77199, Fox-5B and 72523 in Figure 7. (c and d) T–M_O and P–M_O sections calculated for the composition of sample HN-3. The bold vertical line represents the Fe_2O_3 value used for pseudosection modelling.

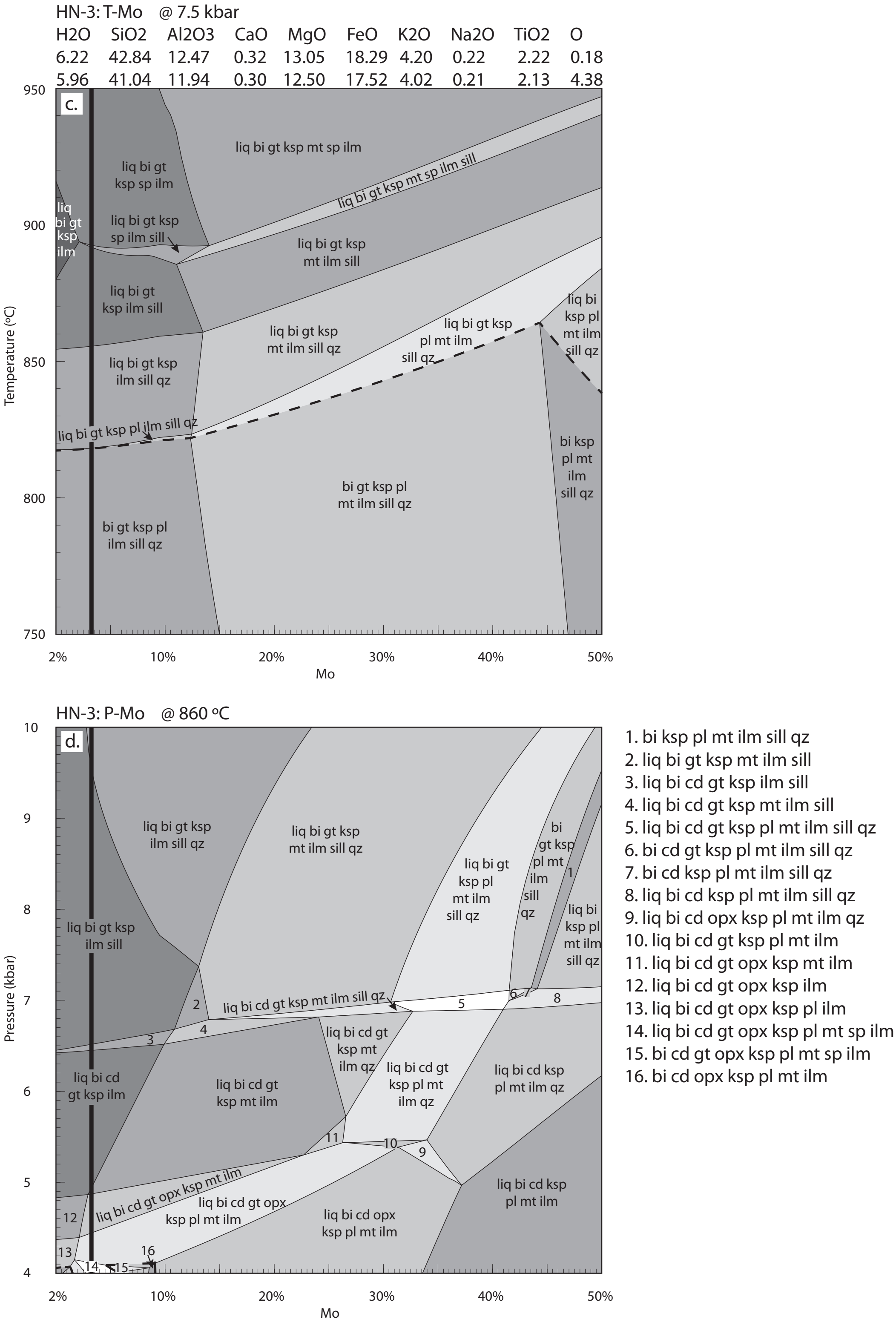

Figure 4 (continued).

with patchy darker cores (Fig. 5b). However, there is no clear relationship between the age of the analyses and either microstructural location or monazite compositional zoning. Grains are commonly rounded and 30–50 µm in diameter. Twelve analyses that appear to be outliers from the main population were excluded. The remaining 19 analyses yield a $^{207}Pb/^{206}Pb$ weighted average age of 950 ± 10 Ma (MSWD = 0.42) and a $^{206}Pb/^{238}U$ weighted average age of 944 ± 8 Ma (MSWD = 1.5; Fig. 6b). A number of these outliers form a weak discordia trending towards c. 500 Ma, which may reflect minor disturbance during the Cambrian (Morrissey et al., 2016).

5.1.3. Sample HN-3 (Hunt Nuntaks)

Forty-two analyses were collected from 13 grains. Analysed grains are hosted both within garnet and in the biotite-rich matrix. Monazite is abundant and varies in size from finer grains (20–30 µm in diameter) to coarser grains up to 200 µm in diameter. Most grains are rounded, though some are anhedral. Some large grains display compositional zoning under BSE, but the majority of grains are unzoned (Fig. 5c). Three analyses were excluded from the calculation of weighted average ages. The analyses form an array of concordant analyses from 1050 to 800 Ma, but broadly define three populations (Fig. 6c). The older population of 24 analyses yields a $^{207}Pb/^{206}Pb$ weighted average age of 1020 ± 10 Ma (MWSD = 0.74) and a $^{206}Pb/^{238}U$ weighted average age of 1018 ± 8 Ma (MSWD = 1.8). A second, younger population yields a $^{207}Pb/^{206}Pb$ weighted average age of 928 ± 16 Ma (MSWD = 0.29) and a $^{206}Pb/^{238}U$ weighted average age of 934 ± 8 Ma (n = 10, MSWD = 0.58). The third population is smaller and defined by only 5 analyses, but yields a $^{207}Pb/^{206}Pb$ weighted average age of 890 ± 22 (MSWD = 0.21) and a $^{206}Pb/^{238}U$ weighted average age of 885 ± 10 Ma (MSWD = 0.7). Although some grains yield both older and younger ages (Fig. 5c), in general, older ages are obtained from grains hosted in garnet.

5.1.4. Sample Fox-5B (Fox Ridge)

Twenty-eight analyses were collected from 11 grains. The majority of grains are located within the matrix, though some are included in garnet but occur along microfractures. Analysed monazite grains are rounded and 20–150 µm in diameter (Fig. 5d). Three analyses were excluded from the calculation of the weighted average age. The $^{207}Pb/^{206}Pb$ weighted average age of the remaining 25 analyses is 916 ± 19 Ma (MSWD = 1.4) and the $^{206}Pb/^{238}U$ weighted average age is 902 ± 7 Ma (MSWD = 1.8; Fig. 6d).

5.1.5. Sample 72523 (Mt Lanyon)

Twenty-five analyses were collected from 11 grains. Monazite grains are 30–100 µm in diameter. Grains are located in the quartzo-feldspathic matrix, as inclusions in garnet and adjacent to unoriented biotite. Analysed grains were also located in the cordierite coronas and cordierite-bearing fractures within garnet. Some grains display clear compositional zoning under BSE, with darker cores and brighter rims (Fig. 5e). A concordia plot of all analyses displays a clustered population at c. 1020 Ma and an array of younger analyses of variable concordance to c. 850 Ma (Fig. 6e). There is a link between microstructural location of monazite and age. Monazite grains located within garnet generally yield older ages, unless located in the large cordierite-bearing fractures. In the grains that display BSE zoning, the older ages come from the darker cores, with the brighter rims yielding younger ages (Fig. 5e). The $^{207}Pb/^{206}Pb$ weighted average age of the older, concordant population (outlined in the dashed box) is 1034 ± 13 Ma (MSWD = 0.38) and the $^{206}Pb/^{238}U$ age is 1016 ± 8 Ma (n = 15;

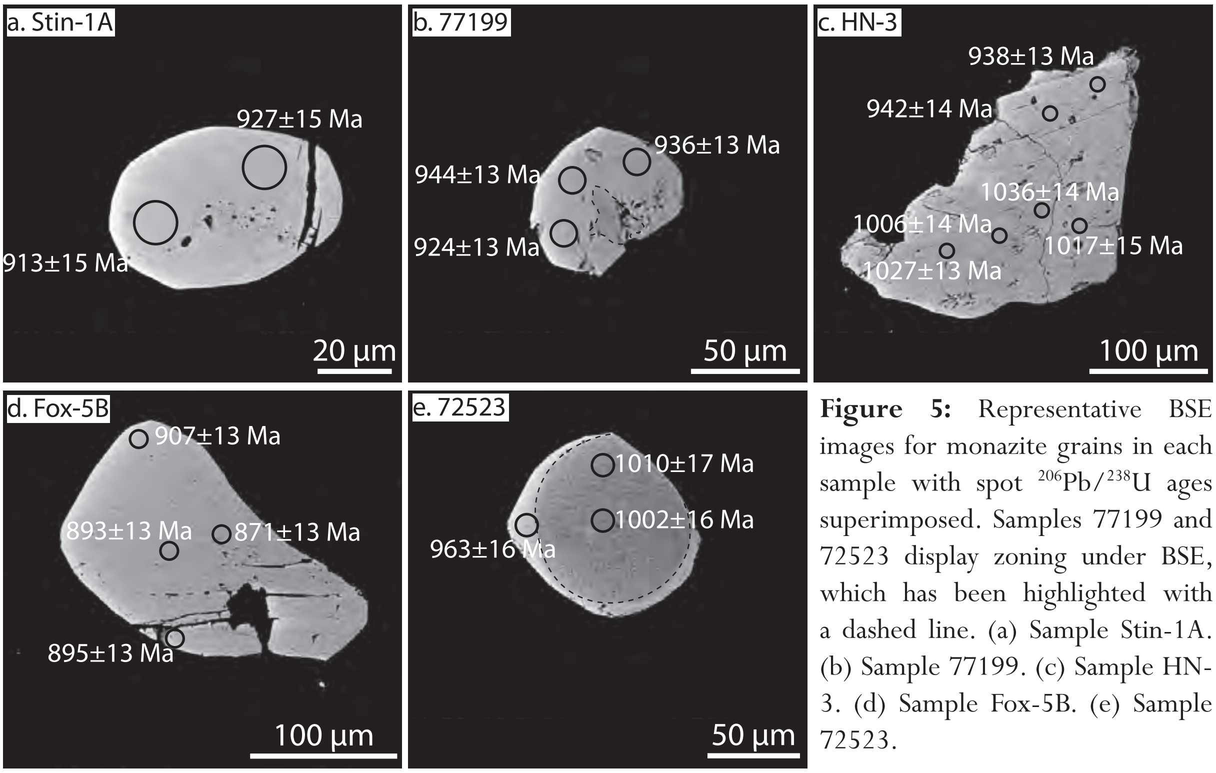

Figure 5: Representative BSE images for monazite grains in each sample with spot $^{206}Pb/^{238}U$ ages superimposed. Samples 77199 and 72523 display zoning under BSE, which has been highlighted with a dashed line. (a) Sample Stin-1A. (b) Sample 77199. (c) Sample HN-3. (d) Sample Fox-5B. (e) Sample 72523.

MSWD = 1.08). Analyses from monazite grains hosted in the cordierite coronas or cordierite-bearing fractures in garnet are shown as dark grey, bold ellipses and range in age from 930 to 850 Ma (Fig. 6e). Similarly, analyses from matrix monazite or the brighter rims yield an array of ages from c. 960 to 880 Ma.

5.2. Mineral chemistry

Representative electron microprobe mineral analyses are given in Table 3. The range of values for elements in each mineral are given in Table 4. The chemistry of selected minerals is discussed below. The calculated end member proportions discussed in the text are defined in Table 4.

5.2.1. Garnet

Garnets in all samples are predominantly almandine–pyrope mixtures, with core X_{alm} values of 0.608–0.746 and core X_{py} values of 0.196–0.354. In the three samples which display zoning in X_{alm} and X_{py} (samples 77199, HN-3 and 72523), the rims show an enrichment in X_{alm} to values of 0.72–0.83 and depletion in X_{py} values to 0.14–0.24 (Table 4). Sample HN-3 is the only sample to show garnet zoning in X_{grs}, with a decrease from core to rim from 0.026–0.030 to 0.015–0.020. Samples HN-3 and 72523 both show compositional evidence of garnet resorption (e.g. Kohn and Spear, 2000), with a minor increase in X_{sps} from 0.008–0.011 at the core, to 0.012–0.013 at the rim.

5.2.2. Biotite

Biotite in all samples is titanium-rich, with TiO_2 values of 2.75–5.79 wt%. Fluorine contents are variable between samples, ranging from 0.75–2.75 wt%. Biotite analyses from samples Stin-1A and HN-3 tend to be higher in both titanium and fluorine than other samples, while biotite analyses from sample Fox-5B contain relatively little fluorine when compared to the other samples (Table 4).

5.2.3. Spinel

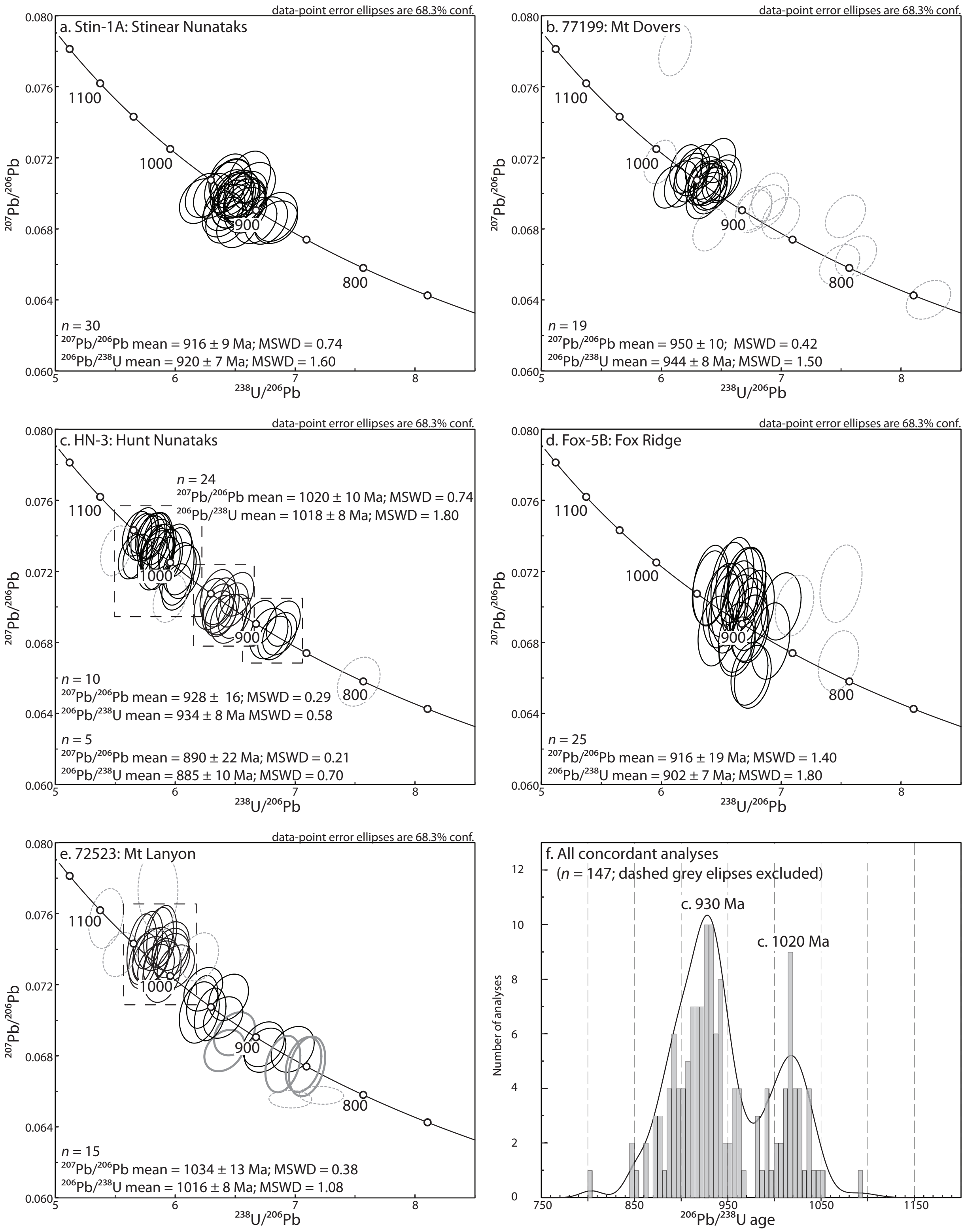

Figure 6: Tera–Wasserburg concordia plots. The $^{207}Pb/^{206}Pb$ and $^{206}Pb/^{238}U$ weighted average ages are given. (a) Sample Stin-1A. (b) Sample 77199. (c) Sample HN-3. (d) Sample Fox-5B. (e) Sample 72523. (f) Histogram of all concordant analyses (grey, dashed ellipses excluded) from all samples in this study highlights two age groupings.

Spinel occurs in samples 77199, HN-3 and Fox-5B. In sample 77199, spinel is uncommon (only two grains) and contains ZnO contents of 7.13–7.59 wt% and Cr_2O_3 contents of 0.62–0.81 wt%. In HN-3, spinel contains high amounts of ZnO (9.72–10.44 wt%) and Cr_2O_3 (1.18–1.71 wt%). In Fox-5B, spinel in garnet generally has lower ZnO and Cr_2O_3 contents (2.85–4.64 wt% and 0.51–0.99 wt% respectively) than spinel included in sillimanite, which has ZnO values of 4.85–8.57 wt% and Cr_2O_3 contents of 1.95–2.09 wt% (Table 4).

5.2.4. Cordierite

Matrix cordierite in all samples has X_{Fe} of 0.2–0.29. In sample Fox-5B, cordierite included in garnet has a higher X_{Fe} of 0.35–0.36 when compared to cordierite in the matrix, which has X_{Fe} of 0.29. In sample 77199, cordierite included in garnet has a lower X_{Fe} of 0.24 when compared to the cordierite in the matrix, which has X_{Fe} of 0.25–0.28. Samples Stin-1A and 72523 only contain matrix cordierite and have X_{Fe} of 0.20–0.23.

5.2.5. Feldspar

K-feldspar in all samples has X_{Or} of 0.83–0.90. Plagioclase has variable X_{Ab} between samples. In Fox-5B, plagioclase is rare and more calcic, with X_{Ab} of 0.55, whereas in samples Stin-1A and 72523 plagioclase is more abundant and less calcic, with X_{Ab} of 0.71–0.72 and 0.65–0.66 respectively.

5.2.6. Ilmenite

Ilmenite occurs in all samples. Samples Stin-1A, Fox-5B and 72523 have MnO contents between 0.12–0.16 wt%, whereas HN-3 has MnO contents between 0.15–0.19 wt%. Ilmenite in sample 77199 has a large spread and higher MnO contents of 0.15–0.32 wt%. Samples Stin-1A, 77199 and 72523 have similar TiO_2 contents ranging between 52.84 and 54.93 wt%, whereas sample HN-3 has TiO_2 contents of 50.25–51.31 wt% and sample Fox-5B has the lowest TiO_2 contents, ranging between 47.86 and 48.79 wt%.

5.3. Calculated P–T pseudosections

As the aim of the *P–T* modelling is to constrain the general conditions of peak metamorphism, in this study we have not engaged in melt reintegration modelling (e.g. Anderson et al., 2013; Korhonen et al., 2013a), and therefore do not attempt to make inferences about the prograde path. The interpreted peak fields have been contoured for mg(g) (= Mg/(Fe^{2+} + Mg + Ca)), and these values have been compared to the values of garnet cores obtained from electron microprobe data, as the closest approximation to peak metamorphic conditions (Table 4).

5.3.1. Sample Stin-1A

From the petrography, the peak assemblage in sample Stin-1A is interpreted to be garnet + cordierite + sillimanite + K-feldspar + plagioclase + ilmenite + quartz + silicate melt. The presence of sillimanite provides a lower pressure constraint of 6 kbar, whereas the presence of cordierite provides an upper pressure constraint of 7.3 kbar (Fig. 7a). Biotite is uncommon and texturally late and so is not interpreted to form part of the peak assemblage. This suggests that peak temperatures are above 830 ºC. Therefore, the peak assemblage is modelled to have formed at conditions of 830 ºC to temperatures in excess of 950 ºC and 6–7.3 kbar (Fig. 7a). Compositional contours for values of mg(g) corresponding to the composition of the garnet cores determined by electron microprobe data (mg(g) = 0.33–0.36) are modelled to plot in the peak assemblage field.

Sample Stin-1A does not contain obvious mineral reaction microstructures that could

Table 3: Representative electron microprobe analyses.

	Stin-1A: Stinear Nunataks								77199: Mt Dovers							
Mineral	gt	bi	cd	pl	ksp	qz	sill	ilm	gt core	gt rim	bi	cd	ksp	qz	sp	sill
SiO_2	39.47	38.37	50.23	61.65	65.59	101.29	37.13	0.04	37.47	37.52	35.80	48.65	62.25	98.18	0.03	36.25
TiO_2	0.00	5.79	0.00	0.01	0.01	0.02	0.00	53.54	0.00	0.02	4.85	0.00	0.02	0.03	0.14	0.00
Al_2O_3	21.81	14.07	33.03	23.76	17.96	0.05	62.09	0.00	21.36	21.48	16.05	32.41	17.69	0.04	58.27	61.80
Cr_2O_3	0.05	0.11	0.03	0.00	0.02	0.01	0.26	0.01	0.02	0.08	0.11	0.00	0.02	0.02	0.61	0.01
FeO	28.76	11.59	5.11	0.06	0.01	0.03	0.12	41.97	31.47	31.43	13.37	6.67	0.03	0.17	24.84	0.32
MnO	0.53	0.01	0.00	0.01	0.00	0.00	0.00	0.12	0.89	1.05	0.00	0.06	0.00	0.04	0.03	0.00
MgO	9.11	15.57	10.81	0.00	0.00	0.00	0.00	1.30	7.17	6.98	14.30	9.75	0.01	0.01	5.80	0.00
ZnO	0.05	0.04	0.00	0.03	0.00	0.01	0.04	0.00	0.01	0.11	0.03	0.03	0.16	0.06	7.59	0.03
CaO	0.91	0.00	0.00	5.94	0.06	0.01	0.02	0.02	0.49	0.49	0.00	0.02	0.03	0.01	0.00	0.02
Na_2O	0.02	0.09	0.06	8.34	1.52	0.00	0.01	0.00	0.00	0.00	0.09	0.07	1.26	0.00	0.00	0.00
K_2O	0.00	9.93	0.01	0.12	14.57	0.02	0.01	0.00	0.00	0.00	9.45	0.00	14.54	0.01	0.00	0.01
F	0.11	1.92	0.00	0.00	0.00	0.00	0.00	0.10	0.00	0.00	1.09	0.00	0.00	0.00	0.00	0.00
Cl	0.00	0.04	0.00	0.00	0.00	0.00	0.00	0.00	0.00	0.02	0.02	0.03	0.00	0.00	0.00	0.01
Total	**100.82**	**97.53**	**99.30**	**99.91**	**99.75**	**101.43**	**99.66**	**97.09**	**98.87**	**99.18**	**95.17**	**97.69**	**96.02**	**98.58**	**97.32**	**98.46**
No. Oxygens	12	11	18	8	8	2	5	3	12	12	11	18	8	2	4	5
Si	3.02	2.78	5.04	2.74	3.02	1.00	1.01	0.00	2.98	2.97	2.67	5.01	2.99	1.00	0.00	0.99
Ti	0.00	0.32	0.00	0.00	0.00	0.00	0.00	1.04	0.00	0.00	0.27	0.00	0.00	0.00	0.00	0.00
Al	1.97	1.20	3.91	1.24	0.97	0.00	1.98	0.00	2.00	2.01	1.41	3.93	1.00	0.00	1.97	2.00
Cr	0.00	0.01	0.00	0.00	0.00	0.00	0.01	0.00	0.00	0.00	0.01	0.00	0.00	0.00	0.01	0.00
Fe^{3+}	-	-	-	-	-	-	0.00	0.00	-	-	-	-	-	0.01	0.00	0.01
Fe^{2+}	1.84	0.70	0.43	0.00	0.00	0.00	0.00	0.91	2.09	2.08	0.84	0.57	0.00	0.00	0.59	0.00
Mn^{2+}	0.03	0.00	0.00	0.00	0.00	0.00	0.00	0.00	0.06	0.07	0.00	0.01	0.00	0.00	0.00	0.00
Mg	1.04	1.68	1.62	0.00	0.00	0.00	0.00	0.05	0.85	0.83	1.59	1.50	0.00	0.00	0.25	0.00
Zn	0.00	0.00	0.00	0.00	0.00	0.00	0.00	0.00	0.00	0.01	0.00	0.00	0.01	0.00	0.16	0.00
Ca	0.07	0.00	0.00	0.28	0.00	0.00	0.00	0.00	0.04	0.04	0.00	0.00	0.00	0.00	0.00	0.00
Na	0.00	0.01	0.01	0.72	0.14	0.00	0.00	0.00	0.00	0.00	0.01	0.01	0.12	0.00	0.00	0.00
K	0.00	0.92	0.00	0.01	0.86	0.00	0.00	0.00	0.00	0.00	0.90	0.00	0.89	0.00	0.00	0.00
F	0.02	0.31	0.00	0.00	0.00	0.00	0.00	0.01	0.00	0.00	0.18	0.00	0.00	0.00	0.00	0.00
Cl	0.00	0.00	0.00	0.00	0.00	0.00	0.00	0.00	0.00	0.00	0.00	0.00	0.00	0.00	0.00	0.00
Total Cations	**8.00**	**7.93**	**11.01**	**5.00**	**4.99**	**1.00**	**3.00**	**2.01**	**8.02**	**8.02**	**7.89**	**11.03**	**5.01**	**1.00**	**3.00**	**3.00**

Table 3 (continued).

	77199	HN-3: Hunt Nunataks							Fox-5B: Fox Ridge							
Mineral	ilm	gt core	gt rim	bi (gt)	bi (m)	ksp	sp	sill	ilm	gt	bi	cd	pl	ksp	qz	sp (gt)
SiO_2	0.01	36.85	36.77	35.28	35.88	64.90	0.06	36.90	0.05	37.71	35.87	48.89	56.89	64.61	101.13	0.00
TiO_2	54.82	0.01	0.11	4.86	4.78	0.02	0.01	0.16	51.31	0.01	3.30	0.01	0.02	0.01	0.01	0.01
Al_2O_3	0.02	21.07	21.14	15.76	16.45	18.06	54.02	62.07	0.03	21.03	16.61	31.06	27.06	18.64	0.03	55.37
Cr_2O_3	0.00	0.03	0.01	0.08	0.08	0.00	1.65	0.09	0.07	0.00	0.05	0.00	0.00	0.00	0.00	0.54
FeO	44.21	33.47	36.44	13.75	15.82	0.06	27.01	0.35	44.10	32.96	18.45	8.14	0.13	0.01	0.01	30.89
MnO	0.15	0.49	0.69	0.00	0.00	0.01	0.03	0.03	0.15	0.94	0.03	0.10	0.00	0.00	0.00	0.09
MgO	0.66	5.55	3.38	13.52	12.95	0.00	4.06	0.01	0.15	5.37	9.91	8.24	0.00	0.01	0.00	5.69
ZnO	0.01	0.05	0.02	0.05	0.05	0.06	10.44	0.01	0.32	0.00	0.05	0.00	0.04	0.01	0.00	3.06
CaO	0.00	1.02	0.53	0.00	0.00	0.00	0.00	0.00	0.00	1.29	0.00	0.01	9.41	0.00	0.00	0.00
Na_2O	0.01	0.02	0.00	0.24	0.15	1.33	0.02	0.00	0.02	0.00	0.07	0.09	6.22	1.42	0.01	0.03
K_2O	0.00	0.00	0.05	9.41	10.27	14.87	0.02	0.01	0.00	0.00	9.56	0.01	0.11	15.64	0.01	0.00
F	0.00	0.00	0.14	2.59	2.00	0.00	0.00	0.00	0.03	0.08	0.59	0.00	0.00	0.00	0.00	0.00
Cl	0.00	0.01	0.00	0.06	0.06	0.01	0.01	0.00	0.00	0.00	0.05	0.00	0.00	0.01	0.00	0.00
Total	**99.90**	**98.58**	**99.28**	**95.61**	**98.49**	**99.32**	**97.33**	**99.64**	**96.24**	**99.38**	**94.55**	**96.54**	**99.89**	**100.35**	**101.21**	**95.69**
No. Oxygens	3	12	12	11	11	8	4	5	3	12	11	18	8	8	2	4
Si	0.00	2.97	2.98	2.65	2.64	3.01	0.00	1.00	0.00	3.01	2.75	5.12	2.56	2.98	1.00	0.00
Ti	1.04	0.00	0.01	0.27	0.26	0.00	0.00	0.00	1.01	0.00	0.19	0.00	0.00	0.00	0.00	0.00
Al	0.00	2.00	2.02	1.39	1.42	0.99	1.88	1.98	0.00	1.98	1.50	3.83	1.43	1.01	0.00	1.91
Cr	0.00	0.00	0.00	0.00	0.00	0.00	0.04	0.00	0.00	0.00	0.00	0.00	0.00	0.00	0.00	0.01
Fe^{3+}	0.00	-	-	-	-	-	0.08	0.01	0.00	-	-	-	-	-	-	0.08
Fe^{2+}	0.93	2.26	2.47	0.86	0.97	0.00	0.59	0.00	0.97	2.20	1.18	0.71	0.00	0.00	0.00	0.68
Mn^{2+}	0.00	0.03	0.05	0.00	0.00	0.00	0.00	0.00	0.00	0.06	0.00	0.01	0.00	0.00	0.00	0.00
Mg	0.02	0.67	0.41	1.51	1.42	0.00	0.18	0.00	0.01	0.64	1.13	1.29	0.00	0.00	0.00	0.25
Zn	0.00	0.00	0.00	0.00	0.00	0.00	0.23	0.00	0.01	0.00	0.00	0.00	0.00	0.00	0.00	0.07
Ca	0.00	0.09	0.05	0.00	0.00	0.00	0.00	0.00	0.00	0.11	0.00	0.00	0.45	0.00	0.00	0.00
Na	0.00	0.00	0.00	0.03	0.02	0.12	0.00	0.00	0.00	0.00	0.01	0.02	0.54	0.13	0.00	0.00
K	0.00	0.00	0.00	0.90	0.96	0.88	0.00	0.00	0.00	0.00	0.94	0.00	0.01	0.92	0.00	0.00
F	0.00	0.00	0.03	0.43	0.33	0.00	0.00	0.00	0.00	0.01	0.10	0.00	0.00	0.00	0.00	0.00
Cl	0.00	0.00	0.00	0.01	0.01	0.00	0.00	0.00	0.00	0.00	0.01	0.00	0.00	0.00	0.00	0.00
Total Cations	**2.00**	**8.03**	**8.02**	**8.07**	**8.04**	**5.00**	**3.00**	**3.00**	**2.00**	**8.00**	**7.83**	**10.98**	**5.00**	**5.04**	**1.00**	**3.00**

Table 3 (continued).

	Fox-5B			72523: Mt Lanyon									
Mineral	sp (sill)	sill	ilm	gt core	gt rim	bi	cd	pl	ksp	qz	ru	sill	ilm
SiO_2	0.00	36.84	0.01	38.86	38.22	37.73	49.64	58.12	65.35	101.39	0.00	35.54	0.00
TiO_2	0.00	0.01	48.78	0.05	0.03	3.56	0.00	0.01	0.03	0.01	96.98	0.01	52.93
Al_2O_3	52.07	61.37	0.01	20.43	20.57	15.47	31.44	24.00	17.86	0.01	0.00	57.49	0.00
Cr_2O_3	2.08	0.03	0.10	0.04	0.03	0.04	0.01	0.01	0.00	0.01	0.14	0.09	0.01
FeO	28.89	0.53	46.82	29.45	33.84	13.65	5.57	0.01	0.01	0.03	0.08	0.17	44.48
MnO	0.05	0.00	0.16	0.32	0.58	0.03	0.02	0.00	0.00	0.00	0.00	0.00	0.14
MgO	3.76	0.01	0.15	8.16	5.01	14.58	10.45	0.01	0.02	0.00	0.00	0.00	0.91
ZnO	8.57	0.04	0.05	0.04	0.02	0.11	0.00	0.02	0.00	0.04	0.00	0.02	0.13
CaO	0.02	0.00	0.01	1.08	1.06	0.00	0.02	6.89	0.06	0.00	0.00	0.01	0.00
Na_2O	0.04	0.01	0.00	0.02	0.02	0.10	0.07	7.36	1.57	0.00	0.01	0.00	0.02
K_2O	0.00	0.00	0.01	0.01	0.01	9.93	0.01	0.15	14.90	0.02	0.00	0.01	0.00
F	0.00	0.00	0.15	0.06	0.13	1.38	0.00	0.00	0.00	0.00	0.00	0.00	0.16
Cl	0.02	0.00	0.00	0.01	0.00	0.16	0.00	0.00	0.00	0.00	0.00	0.00	0.00
Total	**95.49**	**98.86**	**96.24**	**98.53**	**99.52**	**96.74**	**97.22**	**96.56**	**99.81**	**101.52**	**97.23**	**93.34**	**98.78**
No. Oxygens	4	5	3	12	12	11	18	8	8	2	2	5	3
Si	0.00	1.01	0.00	3.06	3.05	2.78	5.10	2.68	3.01	1.00	0.00	1.03	0.00
Ti	0.00	0.00	0.96	0.00	0.00	0.20	0.00	0.00	0.00	0.00	1.00	0.00	1.01
Al	1.86	1.98	0.00	1.90	1.93	1.34	3.81	1.31	0.97	0.00	0.00	1.96	0.00
Cr	0.05	0.00	0.00	0.00	0.00	0.00	0.00	0.00	0.00	0.00	0.00	0.00	0.00
Fe^{3+}	0.10	0.01	0.07	-	-	-	-	-	-	-	-	0.00	0.00
Fe^{2+}	0.63	0.00	0.96	1.94	2.26	0.84	0.48	0.00	0.00	0.00	0.00	0.00	0.94
Mn^{2+}	0.00	0.00	0.00	0.02	0.04	0.00	0.00	0.00	0.00	0.00	0.00	0.00	0.00
Mg	0.17	0.00	0.01	0.96	0.60	1.60	1.60	0.00	0.00	0.00	0.00	0.00	0.03
Zn	0.19	0.00	0.00	0.00	0.00	0.01	0.00	0.00	0.00	0.00	0.00	0.00	0.00
Ca	0.00	0.00	0.00	0.09	0.09	0.00	0.00	0.34	0.00	0.00	0.00	0.00	0.00
Na	0.00	0.00	0.00	0.00	0.00	0.01	0.01	0.66	0.14	0.00	0.00	0.00	0.00
K	0.00	0.00	0.00	0.00	0.00	0.93	0.00	0.01	0.88	0.00	0.00	0.00	0.00
F	0.00	0.00	0.01	0.01	0.02	0.23	0.00	0.00	0.00	0.00	0.00	0.00	0.01
Cl	0.00	0.00	0.00	0.00	0.00	0.02	0.00	0.00	0.00	0.00	0.00	0.00	0.00
Total Cations	**3.00**	**3.00**	**2.01**	**7.99**	**8.00**	**7.95**	**11.01**	**5.00**	**5.01**	**1.00**	**1.00**	**3.00**	**2.00**

Table 4: Range of chemistry for selected minerals.

	Stin-1A	77199	HN-3	Fox-5B	72523
Garnet core					
X_{alm}	0.608–0.633	0.679–0.670	0.736–0.746	0.703–0.740	0.644–0.682
X_{py}	0.329–0.354	0.264–0.285	0.215–0.225	0.196–0.235	0.282–0.319
X_{grs}	0.025–0.028	0.013–0.017	0.026–0.030	0.038–0.040	0.030–0.033
X_{sps}	0.010–0.013	0.019–0.024	0.010–0.011	0.021–0.024	0.007–0.008
mg(g)	0.33–0.36	0.27–0.29	0.22–0.23	0.20–0.23	0.29–0.33
Garnet rim					
X_{alm}	0.608–0.633 (u)	0.720–0.747	0.786–0.831	0.703–0.740 (u)	0.745–0.760
X_{py}	0.329–0.354 (u)	0.212–0.243	0.137–0.178	0.196–0.235 (u)	0.197–0.231
X_{grs}	0.025–0.028 (u)	0.013–0.017 (u)	0.015–0.020	0.038–0.040 (u)	0.007–0.008 (u)
X_{sps}	0.010–0.013 (u)	0.019–0.024 (u)	0.013–0.016	0.021–0.024 (u)	0.012–0.013
Biotite					
F (wt%)	1.67–2.08	0.75–1.78	1.81–2.75	0.55–0.59	1.00–1.62
TiO_2 (wt%)	4.97–5.79	3.39–5.15	4.51–4.86	3.27–3.37	2.75–3.75
X_{Fe}	0.27–0.29	0.25–0.38	0.36–0.41	0.51–0.54	0.30–0.37
Cordierite					
X_{Fe}	0.20–0.21	0.24–0.28	-	0.29–0.36	0.22–0.23
K-feldspar					
X_{Or}	0.86–0.88	0.83–0.89	0.86–0.87	0.88–0.90	0.85–0.86
Plagioclase					
X_{Ab}	0.71–0.72	-	-	0.54	0.65–0.66
Spinel					
ZnO (wt%)	-	7.13–7.59	9.72–10.44	2.95–8.57	-
Cr_2O_3 (wt%)	-	0.62–0.81	1.18–1.71	0.51–2.09	-
Ilmenite					
MnO (wt%)	0.12–0.17	0.15–0.32	0.15–0.19	0.12–0.16	0.12–0.14
TiO_2 (wt%)	52.84–53.71	54.03–54.93	50.25–51.31	47.86–49.79	52.93–53.04

$X_{alm} = Fe^{2+}/(Fe^{2+}+Mg+Ca+Mn)$
$X_{py} = Mg/(Fe^{2+}+Mg+Ca+Mn)$
$X_{grs} = Ca/(Fe^{2+}+Mg+Ca+Mn)$
$X_{sps} = Mn/(Fe^{2+}+Mg+Ca+Mn)$
$mg(g) = Mg/(Fe^{2+}+Mg+Ca)$
$X_{Fe} = Fe/(Fe^{2+}+Mg)$
$X_{Or} = K/(K+Na+Ca)$
$X_{Ab} = Na/(Na+Ca)$
(u) denotes unzoned garnet

be used to define a post-peak *P–T* evolution. However, the post-peak evolution is interpreted to have included the formation of minor biotite.

5.3.2. Sample 77199 (Mt Dovers)

The peak assemblage in sample 77199 is cordierite + garnet + sillimanite + K-feldspar + ilmenite + quartz + silicate melt. Spinel is not interpreted to be part of the modelled peak mineral assemblage as it is very uncommon, and contains appreciable amounts of Zn (Table 4). Plagioclase occurs throughout the pseudosection, but is not present in the rock. However, in the peak assemblage field, plagioclase is modelled to occur in modally small amounts (3–5 mol%) and to decrease with increasing temperature, and is possibly not represented in the thin sections prepared from

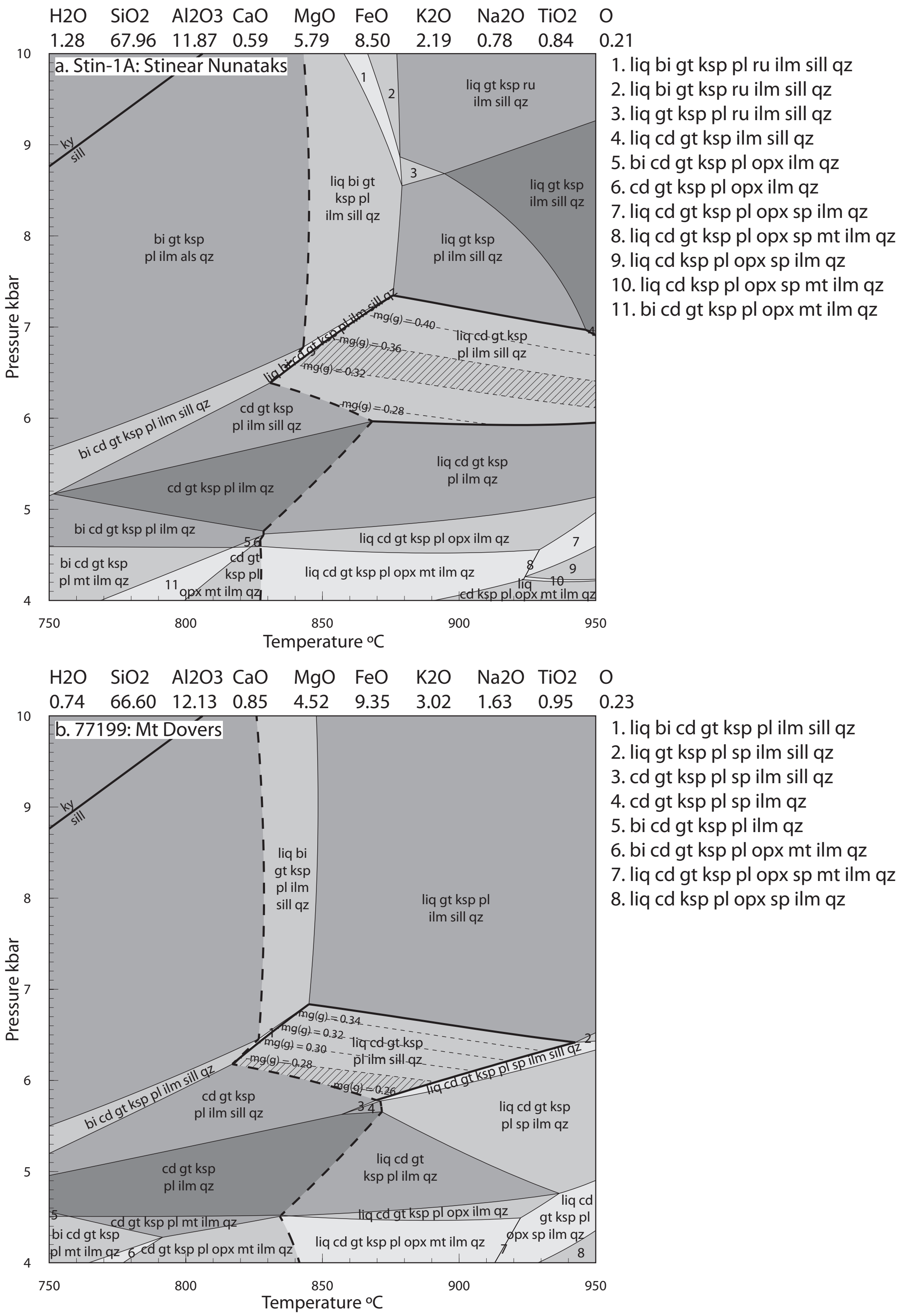

Figure 7: Calculated NCKFMASHTO *P–T* pseudosections, using ds55 (Holland and Powell, 1998). The bold dashed line is the solidus. The peak field for each sample is outlined in bold. The composition for the pseudosection in mole % is given above each pseudosection. The pseudosections have been contoured for *mg*(g) but due to probable equilibration in some samples, actual garnet compositions are generally more Fe-rich than the calculated garnet compositions in the peak assemblage fields. (a) Sample Stin-1A. (b) Sample 77199. (c) Sample HN-3. (d) Sample Fox-5B. (e) Sample 72523. (f) Peak fields for all samples overlain.

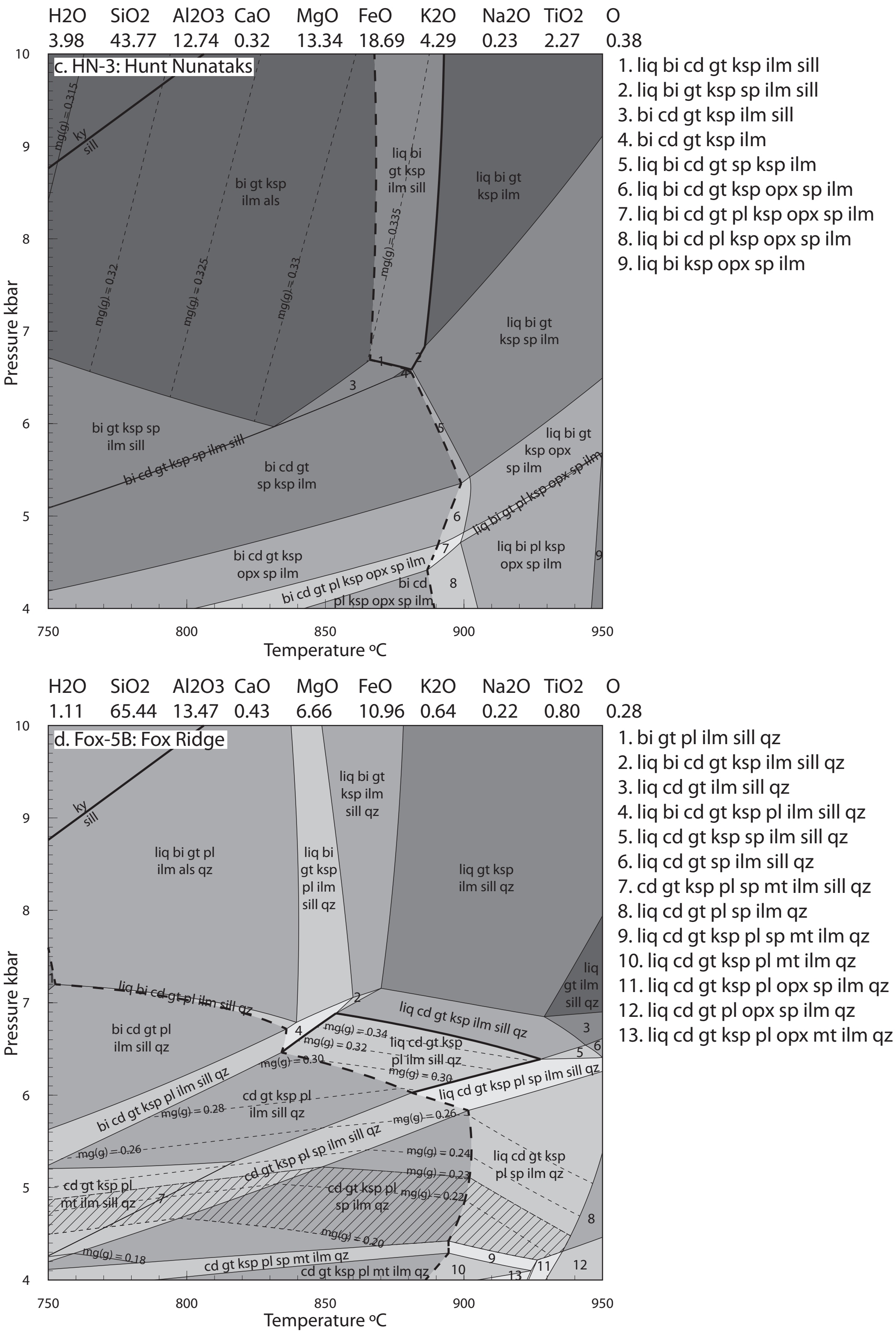

Figure 7 (continued).

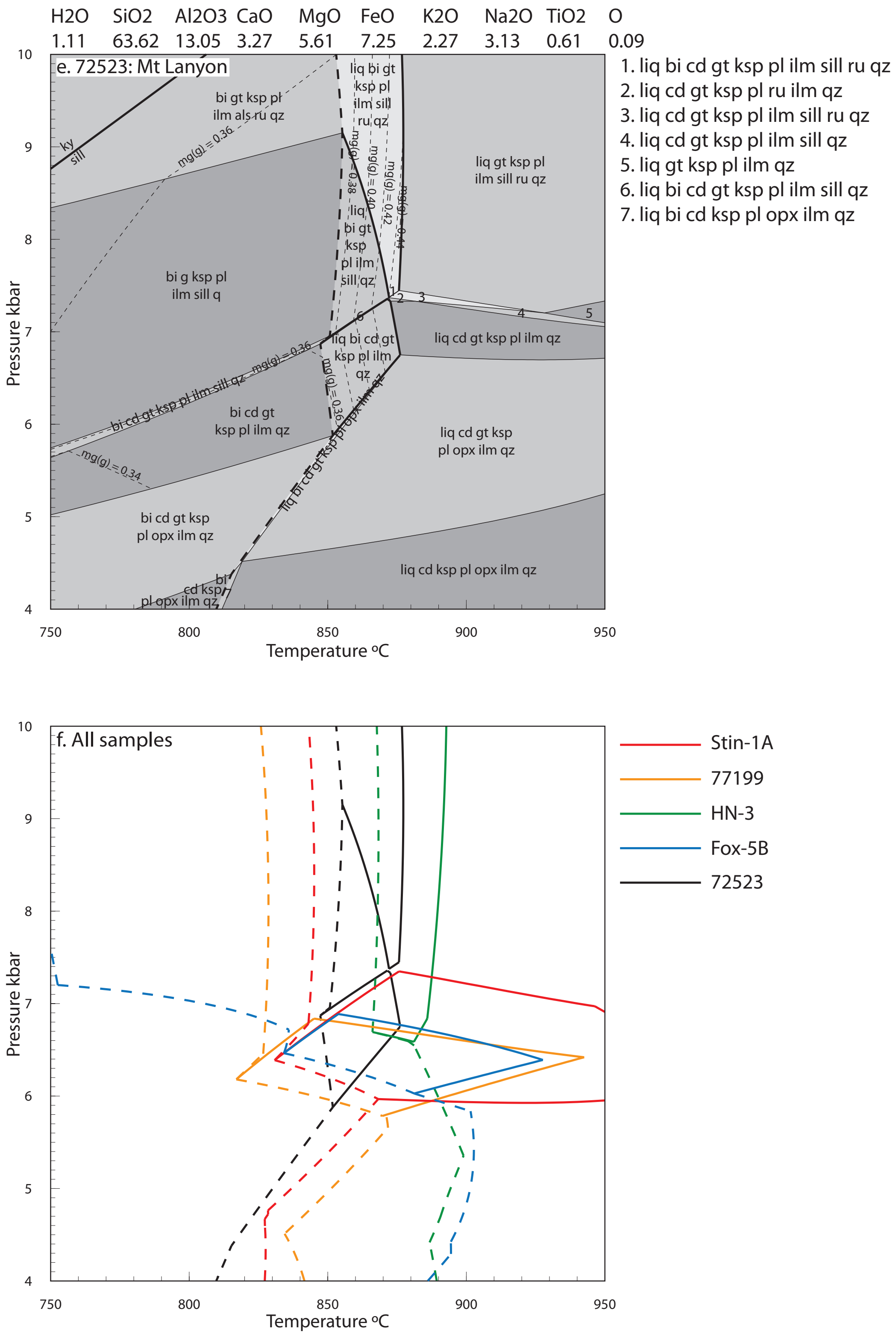

Figure 7 (continued).

the sample. Biotite is not abundant and most commonly occurs as inclusions within garnet as well as anhedral grains which occur on the rims of garnet and cordierite. Therefore, as it does not form a coarse-grained matrix phase, it is not interpreted to form part of the peak assemblage. The peak assemblage constrains peak conditions to 5.8–6.8 kbar and 820–940 °C (Fig. 7b). Modelled compositional contours of *mg*(g) corresponding to the garnet core (0.26–0.28) plot in this field. The post-peak evolution of the sample involved the formation of minor biotite. The formation of small, new generation garnet on the rims of some garnet porphyroblasts is very localised and likely to have occurred at a smaller equilibration volume than that considered here, but may suggest a post-peak evolution dominated by cooling rather than decompression.

5.3.3. Sample HN-3 (Hunt Nunataks)

The peak assemblage in sample HN-3 is interpreted to be coarse-grained garnet + biotite + sillimanite + spinel + K-feldspar + ilmenite ± silicate melt. However, although there is 1–2% of spinel in the matrix, it contains appreciable Zn (Table 4), so cannot be adequately modelled as part of the stable assemblage. The elevated solidus occurs at ~870 °C. However, the sample does not contain quartzofeldspathic leucosomes or clear evidence of melting structures, and therefore it is possible that the stable mineral assemblage is sub-solidus. Biotite contains 1.81–2.75 wt% fluorine (Table 4), suggesting that despite the large volume of biotite, the H_2O content of the rock is low. The presence of sillimanite suggests temperatures did not exceed 890 °C. The absence of cordierite provides a lower pressure constraint of 6.7 kbar (Fig. 7c). Therefore, the interpreted peak assemblage occurs over a large range of conditions, from temperatures up to 890 °C and pressures in excess of 6.5 kbar. Modelled compositional contours for *mg*(g) do not correspond to the electron microprobe data for the core of the garnet porphyroblasts from this sample and so therefore do not provide a tighter constraint on conditions. There are no clear mineral reaction microstructures that could be used to define a post-peak *P–T* evolution.

5.3.4. Sample Fox-5B (Fox Ridge)

In sample Fox-5B, garnet contains inclusions of sillimanite, spinel, ilmenite, cordierite and rare biotite. This assemblage suggests that the prograde evolution of the rock may have involved low pressures, but as the prograde path cannot be quantitatively modelled, this assemblage does not provide robust constraints on the *P–T* conditions. The matrix assemblage involves cordierite + sillimanite + garnet + K-feldspar + plagioclase + ilmenite + quartz + silicate melt. This assemblage suggests that peak pressures were below 6.9 kbar and temperatures were ~835–925 °C (Fig. 7d). Modelled contours for *mg*(g) corresponding of the composition of the garnet cores (0.20–0.23) plot in the spinel-bearing field at pressures below 5.3 kbar (Fig. 7d). Fine-grained biotite and sillimanite are present on the margins of cordierite porphyroblasts, suggesting a cooling-dominated post-peak evolution.

5.3.5. Sample 72523 (Mt Lanyon)

In sample 72523, garnet contains inclusions of sillimanite, biotite, quartz and rare rutile (Fig. 3f). Rutile also occurs in the matrix. Therefore, the early assemblage is interpreted to be garnet + K-feldspar + plagioclase + ilmenite + rutile + quartz + silicate melt. The rutile–biotite-bearing field occurs at 850–880 °C and pressures above 7.4 kbar (Fig. 7e). Modelled contours corresponding to *mg*(g) values obtained from electron microprobe data (0.29–0.32) do not plot within the *P–T* window modelled in the pseudosection (Fig. 7e).

Cordierite, sillimanite and rutile only occur together in a very small field (field 1, Fig. 7e), suggesting that it is likely these phases may not have formed an equilibrium assemblage. Instead, it is possible that the formation of cordierite occurred later, which is suggested by cordierite coronas on garnet (Fig. 3f and g). Garnet in this sample shows a minor increase in Mn at the rims (Table 4), indicating that it probably decreased in abundance. There is some evidence for rutile being replaced by ilmenite (Fig. 3h), and biotite coronas on rutile/ilmenite crystals (Fig. f–h). However, as the formation of cordierite is localised and in low abundance, and sillimanite and rutile are present in the matrix, the formation of the cordierite-bearing assemblage during the second event is not interpreted to have involved significant, if any, amounts of further melting. Although caution must be exercised when using a single bulk composition for different stages of a high-grade metamorphic history (e.g. Kelsey and Hand, 2015), the formation of cordierite together with biotite suggests that subsequent to the formation of the rutile-bearing assemblage, the rock experienced a decrease in pressure. Conceivably, the rutile could be detrital in origin. However, the presence of coarse-grained, detrital rutile in aluminous metapelitic granulite would be unusual, and likely to be accompanied by substantial amounts of detrital zircon and ilmenite, which are not observed in this sample. Therefore, we suggest that the rutile is metamorphic in origin.

6. Discussion

6.1. Monazite U–Pb geochronology

The monazite ages obtained in this study range between 1091 and 804 Ma (Fig. 6f). Samples from both the northern and southern areas of the nPCM (Hunt Nunataks and Mt Lanyon- samples HN-3 and 72523) yield older analyses in the range 1040–1010 Ma (Fig. 6c, e and f). These analyses form concordant age populations and suggest that the samples preserve some evidence for an early event. All samples contain younger-aged analyses corresponding to the generally inferred timing of the Rayner Orogeny (e.g. Boger et al., 2000; Halpin et al., 2007a). Samples Stin-1A, 77199 and Fox-5B preserve single monazite populations, with $^{206}Pb/^{238}U$ weighted average ages ranging between 945 ± 9 Ma and 902 ± 7 Ma (Fig. 6). Smaller c. 950–930 Ma populations in samples HN-3 and 72523 are consistent with these ages. In addition, all samples yield small, younger monazite populations at c. 880 Ma, although in some cases these analyses are within error of the main monazite population, or are discordant and may reflect Cambrian disturbance (Fig. 6; Morrissey et al., 2016). Therefore, the samples in this study provide evidence for discrete periods of monazite growth or recrystallisation in the nPCM at c. 1040–1010 Ma, c. 950–900 Ma and c. 880 Ma (Fig. 6f).

The range of ages in this study is similar to the spread of ages from elsewhere in the Rayner Complex. LA-ICP-MS zircon geochronology from the >3000 km2 Mawson Charnockite on the Mawson Coast (Fig. 1c) suggests that it was emplaced episodically, at c. 1145–1140 Ma, c. 1080–1050 Ma and c. 985–960 Ma (Halpin et al., 2012). Further south, biotite granite at Fisher Massif (Fig. 1c) has an age of 1020 ± 48 Ma (Kinny et al., 1997), and inherited zircon populations from a leucosome in the Aramis Range and pegmatite in the Porthos Range have ages of 1017 ± 31 Ma and 1013 ± 31, respectively (Fig. 1d; Boger et al., 2000; Carson et al., 2000). East of the Amery Ice Shelf (Fig. 1c), SHRIMP zircon ages of c.

1060–1020 Ma have been found in several samples of orthogneiss (Liu et al., 2009b, 2014). These ages are consistent with the older c. 1040–1010 Ma monazite ages found in the nPCM metapelites in this study (Fig. 6c, e and f). The significance of this event in the nPCM is unclear, but may indicate that the magmatism was accompanied by metamorphism.

In the nPCM, SHRIMP U–Pb zircon geochronology from felsic intrusive rocks yield ages of 990–970 Ma (Boger et al., 2000; Carson et al., 2000; Kinny et al., 1997), interpreted to date the timing of voluminous magmatism. Widespread partial melting along the Mawson Coast and Kemp Land coast has been dated at 990–940 Ma using anatectic zircon (Halpin et al., 2013), and EPMA monazite ages of c. 970 Ma from grains hosted in garnet are interpreted to date peak metamorphism on the Mawson Coast (Halpin et al., 2007a). However, that study also yielded a smear of spot ages from 1076 to 818 Ma, similar to the range seen in this study, and the majority of monazite grains hosted by matrix minerals yielded ages in the range 940–910 Ma (Halpin et al., 2007a). Granitic dykes and leucosomes in the nPCM also yield zircon ages of 940–900 Ma (Boger et al., 2000; Carson et al., 2000). In Kemp Land (Fig. 1c), EPMA monazite ages of c. 940–900 Ma have been interpreted to date peak metamorphism in this region (Halpin et al., 2007a; Kelly et al., 2002, 2012; Kelly and Harley, 2004). Therefore, the majority of monazite ages obtained in the Rayner Complex fall in the range 940–900 Ma (this study; Halpin et al., 2007a).

Ages similar to the youngest c. 880 Ma populations in this study (Fig. 6) have also been noted in monazite studies from Kemp Land, and were attributed to in situ recrystallisation at the end of the Rayner Orogeny (Kelly et al., 2012). They are broadly similar to zircon ages from the Oygarden Group further west in Kemp Land (Kelly et al., 2002). EPMA spot monazite ages of 900–814 Ma, younger than inferred peak metamorphism, have also been noted along the Mawson Coast (Halpin et al., 2007a). Therefore, there appear to be periods of monazite and zircon growth that are consistently observed throughout the Rayner Complex. These include the c. 1145–1120, c. 1060–1020, c. 990–970, c. 940–900 and c. 880 Ma age intervals.

The closure temperature of monazite in a dry system may exceed 900 ºC (Cherniak, 2010; Cherniak et al., 2004), with natural studies on high temperature and ultrahigh temperature granulite facies rocks suggesting that growth ages or inheritance may be preserved at very high temperatures (e.g. Clark et al., 2011; Cutts et al., 2013; Goncalves et al., 2004; Kelsey et al., 2003a, 2007; Sajeev et al., 2010; Schmitz and Bowring, 2003; Walsh et al., in press). However, it is understood that monazite growth and stability is related to the presence of fluid and melt (e.g. Harlov et al., 2011; Högdahl et al., 2012; Kelly et al., 2012; Kelsey et al., 2008a; Rapp and Watson, 1986; Stepanov et al., 2012; Williams et al., 2011; Yakymchuk and Brown, 2014). Therefore, grains within minerals such as garnet that are thus armoured from fluid or melt may yield older ages (e.g. Montel et al., 2000). Such a shielding effect may be an explanation for the older ages in this study (Fig. 6), as these ages are predominantly from monazite hosted in garnet, as well as the population of c. 970 Ma analyses on the Mawson Coast (Halpin et al., 2007a). However, in general, the c. 940–900 Ma ages most commonly determined from monazite geochronology throughout the Rayner Complex (e.g. this study; Halpin et al., 2007a; Kelly et al., 2002) are younger than the 990–

970 Ma U–Pb zircon ages interpreted to date the emplacement of granitic and charnockitic bodies (Boger et al., 2000; Carson et al., 2000; Halpin et al., 2012; Kinny et al., 1997). Researchers have suggested that monazite ages in high-*T* rocks may reflect growth of monazite after peak conditions, as rocks begin to cool and melt begins to crystallise (Brown and Korhonen, 2009; Kelsey et al., 2008a; Korhonen et al., 2013b; Reno et al., 2012; Weinberg et al., 2013; Yakymchuk and Brown, 2014). Granitic dykes and leucosomes in the nPCM yield U–Pb zircon ages of 940–900 Ma (Boger et al., 2000; Carson et al., 2000), suggesting that the similar monazite ages throughout the Rayner Complex may represent growth during melt crystallisation rather than representing the timing of peak metamorphism. The variation in weighted average ages between samples (945–900 Ma; Fig. 6) may reflect slow cooling, consistent with the lack of compositional zoning in garnet in several samples (discussed below; Table 4). However, in the case of sample Fox-5B (Fox Ridge), the c. 900 Ma monazite age may reflect the formation of the D_3 high strain fabric that hosts the monazite and therefore date the latter stages of the Rayner Orogeny.

6.2. P–T conditions and constraints on P–T path

Petrography, combined with geochronology, suggests that at least the southern nPCM may preserve evidence for a polymetamorphic history. Sample 72523 appears to preserve two mineral assemblages, and two distinct monazite age populations, with an older, concordant monazite population at c. 1020 Ma (Fig. 6e). One assemblage is modelled to have formed at pressures in excess of 7.2 kbar, based on the presence of rutile, and a second is interpreted to have formed at lower-*P*, based on the presence of cordierite (Fig. 7e). Inclusions of sillimanite, rutile and biotite within garnet may have formed part of a mineral assemblage that is stable at temperatures of 840–880 °C and pressures in excess of 7.4 kbar. Although caution must be exercised when modelling the conditions of multiple events using a single bulk composition, the localised nature of the cordierite coronas around garnet suggest that sample 72523 was mostly unreactive during the formation of the second recorded assemblage and did not experience significant melting. This may be an explanation for the preservation of large numbers of older monazite grains, including grains in the matrix. Therefore, the mineral assemblage and bulk composition in sample 72523 is interpreted to predominantly reflect the composition during the earlier c. 1020 Ma event. Sample HN-3 also contains a c. 1020 Ma-aged monazite population (Fig. 6c). However, sample HN-3 does not provide robust *P–T* constraints or mineral reaction microstructures that could be used to support the inference of an earlier, high-*P* event and a later, low-*P* event. Nonetheless, the assemblage in HN-3 is stable to high pressures (Fig. 7), similar to the *P–T* conditions of the early assemblage in sample 72523, and as such, an earlier, higher-*P* history for this sample cannot be ruled out. As this sample does not contain clear evidence for melting, it is possible that it was similarly unreactive, allowing for the preservation of older monazite.

By contrast, samples Stin-1A, 77199 and Fox-5B contain simple monazite age populations at c. 940–900 Ma and no evidence of mineral reaction microstructures that could be used to infer a complex, multi-stage history. The cordierite-bearing assemblages in these samples formed at temperatures of 820–930 °C and pressures of 6–7 kbar (Fig. 7). Sample 72523 also contains evidence for monazite growth at c. 930 Ma, and new mineral development in the form of local cordierite coronas on garnet, though the conditions of cordierite formation cannot be robustly modelled using the whole rock composition. In general though, the *P–T* conditions of the cordierite-bearing assemblages in all samples is consistent, and correspond to high thermal gradients of 120–150 °C/kbar during the c. 930 Ma event (Fig. 7f). Although none of the samples provide information on the retrograde path post-900 Ma, all samples contain the formation of late, post-peak biotite, suggesting that after peak metamorphism during the Rayner Orogeny, the rocks followed a *P–T* evolution dominated by cooling to an elevated solidus at 730–840 °C. (Fig. 7). Garnets in several samples in this study are unzoned, particularly in calcium and manganese (Table 4). This may provide support for a slow cooling rate post-900 Ma.

If sample 72523 is interpreted to preserve two mineral assemblages, and the rutile-bearing assemblage records a higher-*P* metamorphic event at c. 1020 Ma, then it appears that the nPCM records evidence for polymetamorphism. However, as only sample HN-3 and 72523 contain older monazite, the significance of this event is uncertain and may represent early monazite growth as a result of magmatism. There is no evidence for the c. 1020 Ma high-*P* event in samples from the Mawson Coast (Fig. 2; Halpin et al., 2007a, 2007b; Kelly et al., 2002). Although metapelitic rocks from the Kemp Land coast record a higher-*P* evolution, this event has been related to c. 965–900 Ma monazite and anatectic zircon ages (Halpin et al., 2007b, 2013; Kelly et al., 2002). A c. 1020 Ma monazite population from the Oygarden Group was previously interpreted to be either relict detrital ages or artefacts caused by recrystallisation (Kelly et al., 2012).

The significance of differences in preservation of the two metamorphic events between samples in the nPCM is unclear. The large distances between the sample locations mean that it is difficult to draw structural links between samples (Fitzsimons and Thost, 1992), and where locations are nearby, such as in the case of samples HN-3 and 77199, the ice cover and paucity of exposed outcrop mean that it is difficult to determine the relationship between them. One alternative is that the samples with single monazite populations are a younger cover sequence, deposited after c. 1020 Ma. Traditional detrital geochronology is difficult in the Rayner Complex, due to widespread zircon dissolution during the Rayner Orogeny (Halpin et al., 2013), and is beyond the scope of this study. There are no detrital zircon constraints on metasedimentary sequences in the nPCM. However, a Mesoproterozoic metasedimentary succession deposited after c. 1100–1080 Ma has been recognised along the Mawson Coast using Lu–Hf and U–Pb isotopic signatures from zircon (Halpin et al., 2013), and is thought to be consistent with a maximum deposition age of c. 1023 Ma from metasediments in the Larsemann Hills in Prydz Bay (Fig. 1c; Grew et al., 2012; Wang et al., 2008). Therefore, it is conceivable that the samples that show contrasting age populations are from different aged metasedimentary successions. A second alternative relates to monazite reactivity. As discussed above, monazite appears to be more reactive in the presence of fluid or melt (e.g. Harlov et al., 2011; Högdahl et al., 2012; Kelly et al., 2012; Kelsey et al., 2008a; Rapp and Watson, 1986; Stepanov et al., 2012; Williams et al., 2011; Yakymchuk and Brown, 2014). If the late Mesoproterozoic metamorphism was followed by a period of cooling, melt crystallisation may have created biotite-rich, reactive rocks that remelted during early Neoproterozoic melting, destroying the Mesoproterozoic monazite. As the interpreted peak temperatures are similar for both the earlier and later phases of metamorphism, the rocks are likely to preserve similar petrological relationships.

6.3. Correlations with Eastern Ghats

Paleogeographic reconstructions interpret the now separate Eastern Ghats Province (EGP) and Rayner Complex to have once been part of a large, contiguous terrane (Boger, 2011; Fitzsimons, 2000; Li et al., 1995, 2008; Mezger and Cosca, 1999). The geochronology of the EGP is similar to that observed in the Rayner Complex. Concordant SHRIMP analyses from monazite and zircon span the range 1130–930 Ma (Korhonen et al., 2013b). Monazite hosted within orthopyroxene yields ages of c. 1040–1000 Ma (Bose et al., 2011; Korhonen et al., 2011), whereas the majority of weighted mean zircon and monazite ages in the Eastern Ghats Province fall in the range between 980–930 Ma (Bose et al., 2011; Das et al., 2011; Korhonen et al., 2011, 2013b; Mezger and Cosca, 1999; Shaw et al., 1997; Simmat and Raith, 2008). Extensive charnockitic and granitic magmatism occurred in the EGP at 1000–950 Ma (Dobmeier and Raith, 2003; Korhonen et al., 2013b). As in the Rayner Complex, enigmatic, concordant monazite U–Pb ages post-dating the main phase of metamorphism (e.g. younger than c. 930 Ma) also occur, and are interpreted to relate to the release of fluids during the final stages of melt crystallisation (Korhonen et al., 2013b).

The range in ages from 1130 to 970 Ma in the EGP is interpreted to date the prograde, peak and initial isobaric cooling of a single, long-lived metamorphic event, and the large number of monazite and zircon weighted average ages at 970–930 Ma have been interpreted to represent melt crystallisation near an elevated solidus (Korhonen et al., 2013b). Calculated metamorphic phase diagrams for rocks of the EGP constrain peak conditions to be 950–1020 °C at ~7–8 kbar (Fig. 8; Korhonen et al., 2013a, 2014). The rocks are interpreted to have experienced a counter-clockwise *P–T* path, with the post-peak evolution involving an increase in pressure to 8 kbar and isobaric cooling to 900 °C (Korhonen et al., 2013a, 2014). These conditions correspond to a high thermal gradient in the EGP of >120 °C/kbar.

Although temperatures in the EGP are higher than those obtained for the Rayner Complex for the c. 940–900 Ma metamorphism, they correspond to a similarly high thermal gradient, and the UHT conditions in the EGP may simply represent a more deeply exhumed section of the orogenic system than that exposed in the Rayner Complex. However, although some older thermobarometric studies seem to suggest a decompressive *P–T* evolution for the EGP (see summary in Mukhopadhyay and Basak, 2009), modern metamorphic studies do not provide evidence for an earlier, higher-*P* event at c. 1020 Ma. The combined geochronology and calculated metamorphic conditions suggest slow cooling of the EGP in the order of 1 °C/Ma (Korhonen et al., 2013a). Although cooling rates in the Rayner Complex post-900 Ma are not well constrained, the Rayner Complex and EGP appear to have experienced a similar evolution at 980–900 Ma, with high thermal gradient metamorphism and *P–T* evolutions dominated by cooling rather than decompression (this study; Halpin et al., 2007a, 2012; Korhonen et al., 2013a, 2013b). Together, the R–EG terrane is over 500 km wide (Liu et al., 2014), suggesting that these conditions were maintained over a spatially large area for at least 80 Myr, and the elevated thermal regime may have begun as early as 1130 Ma and persisted for >150 Myr (Halpin et al., 2012; Korhonen et al., 2013b). Despite

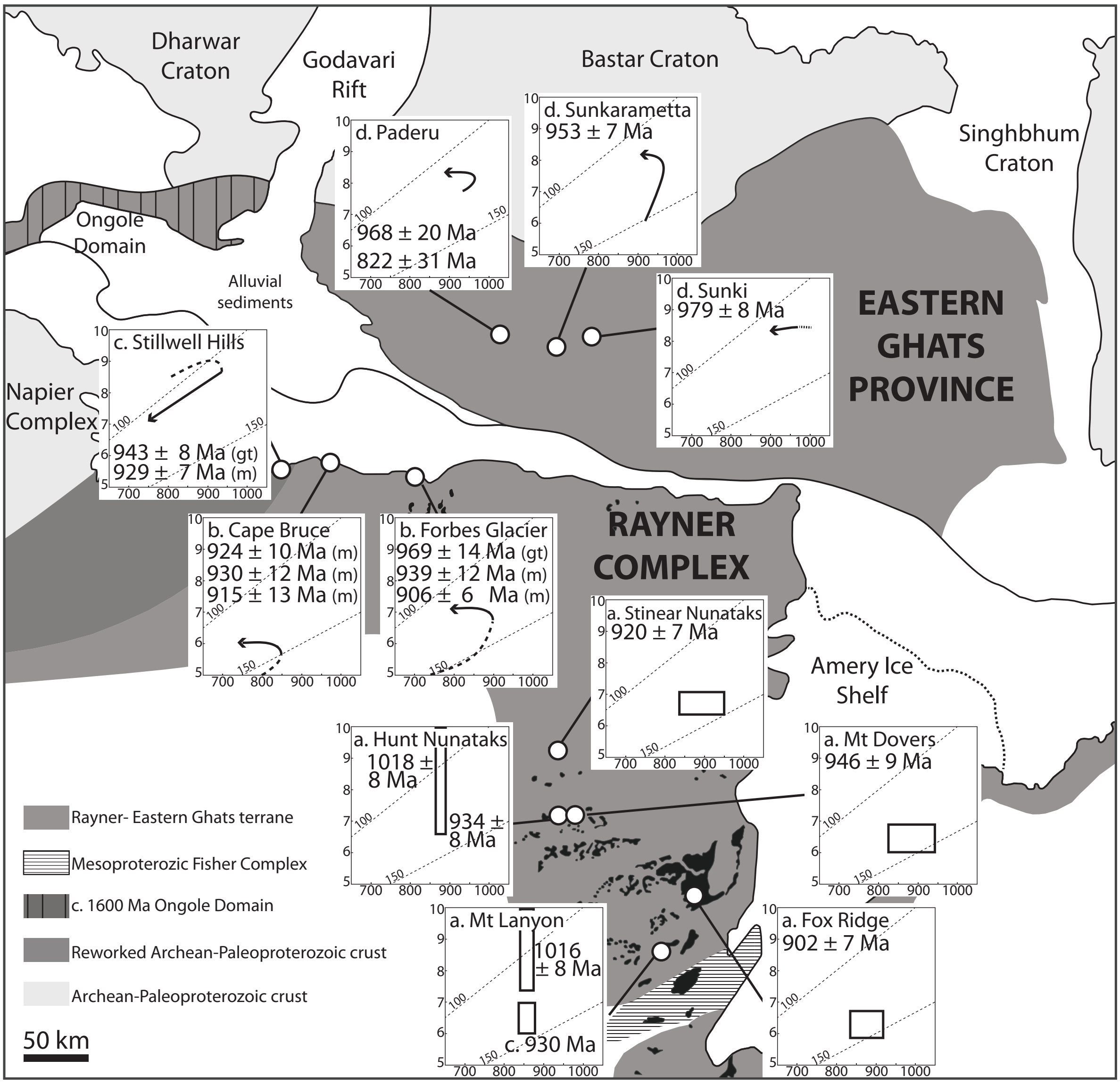

Figure 8: Compilation of *P–T* paths throughout the Rayner–Eastern Ghats terrane, derived from calculated *P–T* pseudosections in samples with associated in situ monazite geochronology. Pseudosections are calculated using ds55 (Holland and Powell, 1998). Ages given are in situ monazite weighted average ages for each sample. The dashed lines represent the 100 °C/kbar and 150 °C/kbar thermal gradients, where thermal gradients > 75 ºC/kbar correspond to high *T/P* 'Barrovian' regimes, and gradients > 150 ºC/kbar correspond to ultra-high *T/P* '*HT–LP*' (Brown, 2006; Kelsey and Hand, 2015). (a) This study. (b) Halpin et al. (2007a). Ages are interpreted populations from Halpin et al. (2007a), where (gt) is monazite in garnet and (m) is the matrix. (c) Halpin et al. (2007b). (d) Korhonen et al. (2013a; 2013b).

these similarities, if the interpretation of the Mesoproterozoic to early Neoproterozoic evolution in the southern Rayner Complex is correct, then the early stage of the evolution appears to have occurred at higher pressures than that in the EGP, and the more shallowly exhumed Rayner Complex may record punctuated stages of metamorphism rather than the single, long-lived event recorded in the deeply exhumed EGP.

6.4. Mechanisms for the high-T metamorphism in the Rayner–Eastern Ghats context

Regional UHT conditions and long-lived, hot thermal regimes are commonly proposed to reflect inverted extensional systems, with slow post-peak cooling and isobaric or modest post-peak pressure changes, reflecting limited thickening of the extensional system (e.g. Brown, 2007; Brown and Korhonen, 2009; Collins, 2002; Currie and Hyndman, 2006; Cutts et al., 2013; Gupta, 2012; Sizova et al., 2014; Walsh et al., in press), and therefore the setting is intrinsically related to subduction (e.g. Brown, 2006; Collins, 2002; Kelsey and Hand, 2015; Sizova et al., 2014). The attainment and maintenance of long-lived, regional-scale high thermal gradients and G–UHT conditions in inverted extensional systems requires slow exhumation and elevated crustal heat production in crust that has been preconditioned (dehydrated) to reduce the effect of thermal buffering from melt production, either as a result of previous metamorphism or during prolonged prograde metamorphism (Brown and Korhonen, 2009; Clark et al., 2011; Kelsey and Hand, 2015; Morrissey et al., 2014; Stüwe, 1995; Vielzeuf et al., 1990).

The R–EG terrane has been interpreted to be a continental arc that evolved from the margin of the Indian craton (e.g. Corvino et al., 2011; Grew et al., 2012; Liu et al., 2014; Mikhalsky et al., 2001; Stephenson, 2000). Arc-related rocks from southern Prydz Bay and the East Amery Ice Shelf region (Fig. 1c) yield protolith ages between 1380–1020 Ma, suggesting long-lived magmatic accretion for c. 360 Myr (Fig. 1c; Grew et al., 2012; Liu et al., 2009b, 2014). The R–EG continental arc has been interpreted to have been separated from the Indian craton by a back-arc basin, in which protoliths to metasedimentary rocks now exposed in Prydz Bay are interpreted to have been deposited at c. 1000 Ma (Grew et al., 2012, 2013). These rocks have been tentatively correlated with a metasedimentary succession deposited after 1100–1080 Ma along the Mawson Coast and in the Framnes Mountains, and have been interpreted to form part of a large Mesoproterozoic basin (Halpin et al., 2013).

Recent geochemical work has suggested the presence of three arcs (from north to south the Rayner, Fisher and Clemence arcs) between the Indian and east Antarctic cratons (the Lambert and/or Ruker terranes) (Liu et al., 2014). The proposition is that a two-stage collision occurred, where the east Antarctic cratons collided successively with the three arcs at c. 1000–970 Ma, followed by final closure of the back-arc basin separating the Rayner arc and the Indian craton at c. 930–900 Ma (Liu et al., 2014). However, if the older c. 1020 Ma populations and the apparent higher-*P* assemblage preserved at Mt Lanyon (sample 72523) reflect an earlier phase of metamorphism, this may suggest that at least one phase of arc accretion occurred earlier. The lack of evidence of the higher-*P* phase along the Mawson Coast and in the EGP may conceivably reflect the increasing distance from the southern margin of the Rayner arc.

Two-dimensional geodynamic forward modelling of Proterozoic systems such as that of the R–EG terrane provides a scenario where tectonic switching from convergence to extension occurs as a consequence of shallow slab breakoff. Shallow slab breakoff results in rollback and consequent extension, basin formation and hybrid (i.e. crustally-contaminated) magmatism (Sizova et al., 2014). Sizova et al. (2014) show that if renewed convergence is minor, such subduction-related extensional systems result in the development of plateau-like orogens, with limited topography, limiting erosionallydriven exhumation. Such an orogenic structure would promote maintenance of high-*T* conditions by slow cooling unless there was a dramatic change in the boundary conditions. In relation to the results presented here from the Rayner Complex, convergence during the Rayner Orogeny may have resulted in limited topography, therefore allowing the maintenance of high thermal gradient conditions over a long period. The episodic emplacement of granitic and charnockitic magmatism, possibly in response to tectonic switching, would also have facilitated the maintenance of high temperatures (Boger et al., 2000; Carson et al., 2000; Halpin et al., 2012; Howard et al., 2015; Kinny et al., 1997). These charnockites have isotopic signatures consistent with derivation from pre-existing crustal sources (Munksgaard et al., 1992; Zhao et al., 1997), suggesting that the terrane remained hot between the two 'events' and rocks deeper in the crustal pile are the probable source for the magmatic rocks.

7. Conclusions

Calculated metamorphic phase diagrams combined with in situ monazite geochronology from the nPCM in the Rayner Complex, east Antarctica, show that the rocks preserve evidence for elevated thermal gradients and temperatures at c. 1030–900 Ma corresponding to discrete periods of monazite growth. Metamorphic conditions at c. 1020 Ma involved higher pressures (>7.4 kbar) and temperatures of 840–880 ºC, based on the presence of rutile in one sample preserving an older monazite population. This was overprinted by a cordierite-bearing assemblage that formed at temperatures of 850–880 ºC and pressures of 6–7 kbar. The formation of late biotite in all samples suggests that the post-peak evolution was dominated by cooling. All samples preserve evidence for monazite growth c. 940–900 Ma, coeval with leucosomes and the emplacement of granitic dykes and interpreted to date the timing of melt crystallisation in the nPCM. The emplacement of charnockite along the Mawson Coast began at or before c. 1140 Ma, and suggests the elevated temperatures may have persisted for >150 Myr, either continuously or as a punctuated system. The monazite ages in this study are similar to ages observed in the Eastern Ghats Province in India. It seems likely that these terranes inherited their elevated thermal structure from an extensional basin or back-arc setting inboard of a long-lived continental arc which was then overprinted by shortening, resulting in the formation of counter-clockwise *P–T* paths at c. 970–900 Ma. The multiple phases of metamorphism presented here are important to provide further constraints on geodynamic forward models investigating the physical and thermal characteristics of long-lived, high-*T* systems. The high thermal gradients were facilitated by melt loss during the prolonged prograde evolution, which dehydrated the terrane and prevented the buffering of temperatures by melting.

Acknowledgements

The staff at Adelaide Microscopy are thanked for their help with analytical work. Isabella von Lichtan at the rock library at the University of Tasmania is thanked for providing some of the samples for this study. Stan Mertzman at Franklin and Marshall College is thanked for geochemical analysis. Jacqueline Halpin and Johann Diener are thanked for thorough and constructive reviews. LJM is supported by an Australian Postgraduate Award. This forms a part of Australian Antarctic Science Project 4191.

References

Anderson, J.R., Kelsey, D.E., Hand, M., Collins, W.J., 2013. Conductively driven, high-thermal gradient metamorphism in the Anmatjira Range, Arunta region, central Australia. Journal of Metamorphic Geology 31, 1003–1026.

Beliatsky, B.V., Laiba, A.A., Mikhalsky, E.V., 1994. U-Pb zircon age of the metavolcanic rocks of Fisher Massif (Prince Charles Mountains, East Antarctica). Antarctic Science 6, 355–358.

Boger, S.D., 2011. Antarctica — Before and after Gondwana. Gondwana Research 19, 335–371.

Boger, S.D., Carson, C.J., Fanning, C.M., Hergt, J.M., Wilson, C.J.L., Woodhead, J.D., 2002. Pan-African intraplate deformation in the northern Prince Charles Mountains, east Antarctica. Earth and Planetary Science Letters 195, 195–210.

Boger, S.D., Carson, C.J., Wilson, C.J.L., Fanning, C.M., 2000. Neoproterozoic deformation in the Radok Lake region of the northern Prince Charles Mountains, east Antarctica; evidence for a single protracted orogenic event. Precambrian Research 104, 1–24.

Boger, S.D., Maas, R., Fanning, C.M., 2008. Isotopic and geochemical constraints on the age and origin of granitoids from the central Mawson Escarpment, southern Prince Charles Mountains, East Antarctica. Contributions to Mineralogy and Petrology 155, 379–400.

Boger, S.D., White, R.W., 2003. The metamorphic evolution of metapelitic granulites from Radok Lake, northern Prince Charles Mountains, east Antarctica; evidence for an anticlockwise *P–T* path. Journal of Metamorphic Geology 21, 285–298.

Boger, S.D., White, R.W., Schulte, B., 2012. The importance of iron speciation (Fe^{+2}/Fe^{+3}) in determining mineral assemblages: an example from the high-grade aluminous metapelites of southeastern Madagascar. Journal of Metamorphic Geology 30, 997–1018.

Boger, S.D., Wilson, C.J.L., 2005. Early Cambrian crustal shortening and a clockwise *P–T–t* path from the southern Prince Charles Mountains, East Antarctica: implications for the formation of Gondwana. Journal of Metamorphic Geology 23, 603–623.

Boger, S.D., Wilson, C.J.L., Fanning, C.M., 2001. Early Paleozoic tectonism within the East Antarctic craton: The final suture between east and west Gondwana? Geology 29, 463–466.

Bose, S., Das, K., Fukuoka, M., 2005. Fluorine content of biotite in granulite-grade metapelitic assemblages and its implications for the Eastern Ghats granulites. European Journal of Mineralogy 17, 665–674.

Bose, S., Dunkley, D.J., Dasgupta, S., Das, K., Arima, M., 2011. India-Antarctica-Australia-Laurentia connection in the Paleoproterozoic–Mesoproterozoic revisited: Evidence from new zircon U–Pb and monazite chemical age data from the Eastern Ghats Belt, India. Geological Society of America Bulletin 123, 2031–2049.

Brown, M., 2006. Duality of thermal regimes is the distinctive characteristic of plate tectonics since the Neoarchean. Geology 34, 961–964.

Brown, M., 2007. Metamorphic Conditions in Orogenic Belts: A Record of Secular Change. International Geology Review 49, 193–234.

Brown, M., 2014. The contribution of metamorphic petrology to understanding lithosphere evolution and geodynamics. Geoscience Frontiers 5, 553–569.

Brown, M., Korhonen, F.J., 2009. Some Remarks on Melting and Extreme Metamorphism of Crustal Rocks Physics and Chemistry of the Earth's Interior, in: Gupta, A.K., Dasgupta, S. (Eds.). Springer New York, pp. 67–87.

Carson, C.J., Boger, S.D., Fanning, C.M., Wilson, C.J.L., Thost, D.E., 2000. SHRIMP U–Pb geochronology from Mount Kirkby, northern Prince Charles Mountains, East Antarctica. Antarctic Science 12, 429–442.

Carson, C.J., Powell, R., Wilson, C.J.L., Dirks, P.H.G.M., 1997. Partial melting during tectonic exhumation of a granulite terrane: an example from the Larsemann Hills, East Antarctica. Journal of Metamorphic Geology 15, 105–126.

Cherniak, D.J., 2010. Diffusion in Accessory Minerals: Zircon, Titanite, Apatite, Monazite and Xenotime. Reviews in Mineralogy and Geochemistry 72, 827–869.

Cherniak, D.J., Watson, E.B., Grove, M., Harrison, T.M., 2004. Pb diffusion in monazite: a combined RBS/SIMS study. Geochimica et Cosmochimica Acta 68, 829–840.

Clark, C., Fitzsimons, I.C.W., Healy, D., Harley, S.L., 2011. How Does the Continental Crust Get Really Hot? Elements 7, 235–240.

Clarke, G.L., Powell, R., Guiraud, M., 1989. Low-pressure granulite facies metapelitic assemblages and corona textures from MacRobertson Land, east Antarctica: the importance of Fe_2O_3 and TiO_2 in accounting for spinel-bearing assemblages. Journal of Metamorphic Geology 7, 323–335.

Collins, W.J., 2002. Nature of extensional accretionary orogens. Tectonics 21, 1024.

Corvino, A.F., Boger, S.D., Henjes-Kunst, F., Wilson, C.J.L., Fitzsimons, I.C.W., 2008. Superimposed tectonic events at 2450 Ma, 2100 Ma, 900 Ma and 500 Ma in the North Mawson Escarpment, Antarctic Prince Charles Mountains. Precambrian Research 167, 281–302.

Corvino, A.F., Wilson, C.J.L., Boger, S.D., 2011. The structural and tectonic evolution of a Rodinian continental fragment in the Mawson Escarpment, Prince Charles Mountains, Antarctica. Precambrian Research 184, 70–92.

Currie, C.A., Hyndman, R.D., 2006. The thermal structure of subduction zone back arcs. Journal of Geophysical Research: Solid Earth 111, B08404.

Cutts, K.A., Kelsey, D.E., Hand, M., 2013. Evidence for late Paleoproterozoic (ca 1690–1665 Ma) high- to ultrahigh-temperature metamorphism in southern Australia: Implications for Proterozoic supercontinent models. Gondwana Research 23, 617–640.

Das, K., Bose, S., Karmakar, S., Dunkley, D.J., Dasgupta, S., 2011. Multiple tectonometamorphic imprints in the lower crust: first evidence of ca. 950 Ma (zircon U–Pb SHRIMP) compressional reworking of UHT aluminous granulites from the Eastern Ghats Belt, India. Geological Journal 46, 217–239.

Dasgupta, S., Sengupta, P., Ehl, J., Raith, M., Bardhan, S., 1995. Reaction Textures in a Suite of Spinel Granulites from the Eastern Ghats Belt, India: Evidence for Polymetamorphism, a Partial Petrogenetic Grid in the System KFMASH and the Roles of ZnO and Fe_2O_3. Journal of Petrology 36, 435–461.

Deer, W.A., Howie, R.A., Zussman, J., 1992. An introduction to the rock-forming minerals- 2nd edition. Longman, United Kingdom.

Dharma Rao, C.V., Santosh, M., Chmielowski, R.M., 2012. Sapphirine granulites from Panasapattu, Eastern Ghats belt, India: Ultrahigh-temperature metamorphism in a Proterozoic convergent plate margin. Geoscience Frontiers 3, 9–31.

Diener, J.F.A., Powell, R., 2010. Influence of ferric iron on the stability of mineral assemblages. Journal of Metamorphic Geology 28, 599–613.

Diener, J.F.A., White, R.W., Powell, R., 2008. Granulite facies metamorphism and subsolidus fluid-absent reworking, Strangways Range, Arunta Block, central Australia. Journal of Metamorphic Geology 26, 603–622.

Dobmeier, C.J., Raith, M.M., 2003. Crustal architecture and evolution of the Eastern Ghats Belt and adjacent regions of India, in: Yoshida, M., Windley, B.F., Dasgupta, S. (Eds.), Proterozoic East Gondwana: Supercontinent Assembly and Breakup. Geological Society of London Special Publications, pp. 145–168.

Droop, G.T.R., 1987. A general equation for estimating Fe^{3+} concentrations in ferromagnesian silicates and oxides from microprobe analyses, using stoichiometric criteria. Mineralogical Magazine 51, 431–435.

Fitzsimons, I.C.W., 1996. Metapelitic Migmatites from Brattstrand Bluffs, East Antarctica—Metamorphism, Melting and Exhumation of the Mid Crust. Journal of Petrology 37, 395–414.

Fitzsimons, I.C.W., 2000. A review of tectonic events in the East Antarctic Shield and their implications for Gondwana and earlier supercontinents. Journal of African Earth Sciences 31, 3–23.

Fitzsimons, I.C.W., Harley, S.L., 1992. Mineral reaction textures in high-grade gneisses: evidence for contrasting pressure-temperature paths in the Proterozoic Complex of East Antarctica. Recent Progress in Antarctic Earth Science, 103–111.

Fitzsimons, I.C.W., Thost, D.E., 1992. Geological relationships in high-grade basement gneiss of the northern Prince Charles Mountains, East Antarctica. Australian Journal of Earth Sciences 39, 173–193.

Goncalves, P., Nicollet, C., Montel, J.-M., 2004. Petrology and in situ U–Th–Pb Monazite Geochronology of Ultrahigh-Temperature Metamorphism from the Andriamena Mafic Unit, North–Central Madagascar. Significance of a Petrographical P–T Path in a Polymetamorphic Context. Journal of Petrology 45, 1923–1957.

Gorczyk, W., Smithies, H., Korhonen, F., Howard, H., Quentin De Gromard, R., 2015. Ultra-hot Mesoproterozoic evolution of intracontinental central Australia. Geoscience Frontiers 6, 23–37.

Grew, E.S., Carson, C.J., Christy, A.G., Boger, S.D., 2013. Boron- and phosphate-rich rocks in the Larsemann Hills, Prydz Bay, East Antarctica: tectonic implications. Geological Society, London, Special Publications 383, 73–94.

Grew, E.S., Carson, C.J., Christy, A.G., Maas, R., Yaxley, G.M., Boger, S.D., Fanning, C.M., 2012. New constraints from U–Pb, Lu–Hf and Sm–Nd isotopic data on the timing of sedimentation and felsic magmatism in the Larsemann Hills, Prydz Bay, East Antarctica. Precambrian Research 206–207, 87–108.

Griffin, W.L., Belousova, E.A., Shee, S.R., Pearson, N.J., O'Reilly, S.Y., 2004. Archean crustal evolution in the northern Yilgarn Craton: U–Pb and Hf-isotope evidence from detrital zircons. Precambrian Research 131, 231–282.

Gupta, S., 2012. Strain localization, granulite formation and geodynamic setting of 'hot orogens': a case study from the Eastern Ghats Province, India. Geological Journal 47, 334–351.

Halpin, J.A., Clarke, G.L., White, R.W., Kelsey, D.E., 2007a. Contrasting *P–T–t* paths for Neoproterozoic metamorphism in MacRobertson and Kemp Lands, east Antarctica. Journal of Metamorphic Geology 25, 683–701.

Halpin, J.A., Daczko, N.R., Clarke, G.L., Murray, K.R., 2013. Basin analysis in polymetamorphic terranes: An example from east Antarctica. Precambrian Research 231, 78–97.

Halpin, J.A., Daczko, N.R., Milan, L.A., Clarke, G.L., 2012. Decoding near-concordant U–Pb zircon ages spanning several hundred million years: recrystallisation, metamictisation or diffusion? Contributions to Mineralogy and Petrology 163, 67–85.

Halpin, J.A., White, R.W., Clarke, G.L., Kelsey, D.E., 2007b. The Proterozoic *P–T–t* Evolution of the Kemp Land Coast, East Antarctica; Constraints from Si-saturated and Si-undersaturated Metapelites. Journal of Petrology 48, 1321–1349.

Hand, M., Scrimgeour, I., Powell, R., Stüwe, K., Wilson, C.J.L., 1994a. Metapelitic granulites from Jetty Peninsula, east Antarctica: formation during a single event or by polymetamorphism? Journal of Metamorphic Geology 12, 557–573.

Hand, M., Scrimgeour, I., Stuwe, K., Arne, D., Wilson, C.J.L., 1994b. Geological observations in high-grade mid-Proterozoic rocks from Else Platform, northern Prince Charles Mountains region, east Antarctica. Australian Journal of Earth Sciences 41, 311–329.

Harley, S.L., 1998. Ultrahigh temperature granulite metamorphism (1050 °C, 12 kbar) and decompression in garnet (Mg70)–orthopyroxene–sillimanite gneisses from the Rauer Group, East Antarctica. Journal of Metamorphic Geology 16, 541–562.

Harley, S.L., 2004. Extending our understanding of Ultrahigh temperature crustal metamorphism. Journal of Mineralogical and Petrological Sciences 99, 140–158.

Harlov, D.E., Wirth, R., Hetherington, C.J., 2011. Fluid-mediated partial alteration in monazite: the role of coupled dissolution–reprecipitation in element redistribution and mass transfer. Contributions to Mineralogy and Petrology 162, 329–348.

Hensen, B.J., Zhou, B., Thost, D.E., 1997. Recognition of Multiple High Grade Metamorphic Events with Garnet Sm–Nd Chronology in the Northern Prince Charles Mountains, Antarctica, in: Ricci, C.A. (Ed.), The Antarctic Region: Geological Evolution and Processes. Terra Antarctica Publication, Sienna, pp. 97–104.

Högdahl, K., Majka, J., Sjöström, H., Nilsson, K., Claesson, S., Konecný, P., 2012. Reactive monazite and robust zircon growth in diatexites and leucogranites from a hot, slowly cooled orogen: implications for the Palaeoproterozoic tectonic evolution of the central Fennoscandian Shield, Sweden. Contributions to Mineralogy and Petrology 163, 167–188.

Holland, T.J.B., Powell, R., 1998. An internally consistent thermodynamic data set for phases of petrological interest. Journal of Metamorphic Geology 16, 309–343.

Holland, T.J.B., Powell, R., 2003. Activity-composition relations for phases in petrological calculations: an asymmetric multicomponent formulation. Contributions to Mineralogy and Petrography 145, 492–501.

Howard, H.M., Smithies, R.H., Kirkland, C.L., Kelsey, D.E., Aitken, A., Wingate, M.T.D., Quentin de Gromard, R., Spaggiari, C.V., Maier, W.D., 2015. The burning heart — The Proterozoic geology and geological evolution of the west Musgrave Region, central Australia. Gondwana Research 27, 64–94.

Jamieson, R.A., Beaumont, C., 2013. On the origin of orogens. Geological Society of America Bulletin.

Kamenev, E.N., 1972. Geological structure of Enderby Land, in: Adie, R.J. (Ed.), Antarctic Geology and Geophysics. Oslo: International Union of Geologial Sciences (IUGS), pp. 579–583.

Kamineni, D.C., Rao, A.T., 1988. Sapphirine-Bearing Quartzite from the Eastern Ghats Granulite Terrain, Vizianagaram, India. The Journal of Geology 96, 209–220.

Kelly, N.M., Clarke, G.L., Fanning, C.M., 2002. A two-stage evolution of the Neoproterozoic Rayner Structural Episode: new U–Pb sensitive high resolution ion microprobe constraints from the Oygarden Group, Kemp Land, East Antarctica. Precambrian Research 116, 307–330.

Kelly, N.M., Harley, S.L., 2004. Orthopyroxene-corundum in Mg–Al-rich granulites from the Oygarden Islands, east Antarctica. Journal of Petrology 45, 1481–1512.

Kelly, N.M., Harley, S.L., Möller, A., 2012. Complexity in the behavior and recrystallization of monazite during high-*T* metamorphism and fluid infiltration. Chemical Geology 322–323, 192–208.

Kelsey, D.E., 2008. On ultrahigh-temperature crustal metamorphism. Gondwana Research 13, 1–29.

Kelsey, D.E., Clark, C., Hand, M., 2008a. Thermobarometric modelling of zircon and monazite growth in melt-bearing systems: examples using model metapelitic and metapsammitic granulites. Journal of Metamorphic Geology 26, 199–212.

Kelsey, D.E., Hand, M., 2015. On ultrahigh temperature crustal metamorphism: phase equilibria, trace element thermometry, bulk composition, heat sources, timescales and tectonic settings. Geoscience Frontiers 6, 311–356.

Kelsey, D.E., Hand, M., Clark, C., Wilson, C.J.L., 2007. On the application of in situ monazite chemical geochronology to constraining *P–T–t* histories in high-temperature (>850 °C) polymetamorphic granulites from Prydz Bay, East Antarctica. Journal of Geological Society, London 164, 667–683.

Kelsey, D.E., Powell, R., Wilson, C.J.L., Steel, D.A., 2003a. (Th+U)–Pb monazite ages from Al–Mg-rich metapelites, Rauer Group, east Antarctica. Contributions to Mineralogy and Petrography 146, 326–340.

Kelsey, D.E., Wade, B.P., Collins, A.S., Hand, M., Sealing, C.R., Netting, A., 2008b. Discovery of a Neoproterozoic basin the in Prydz Belt in East Antarctica and its implications for Gondwana assembly and ultrahigh temperature metamorphism. Precambrian Research 161, 355–388.

Kelsey, D.E., White, R.W., Powell, R., Wilson, C.J.L., Quinn, C.D., 2003b. New constraints on metamorphism in the Rauer Group, Prydz Bay, east Antarctica. Journal of Metamorphic Geology 21, 739–759.

Kinny, P.D., Black, L.P., Sheraton, J.W., 1997. Zircon U-Pb ages and geochemistry of igneous and metamorphic rocks in the northern Prince Charles Mountains, Antarctica. AGSO Journal of Australian Geology and Geophysics 16, 637–654.

Kohn, M.J., Spear, F., 2000. Retrograde net transfer reaction insurance for pressure-temperature estimates. Geology 28, 1127–1130.

Korhonen, F.J., Brown, M., Clark, C., Bhattacharya, S., 2013a. Osumilite–melt interactions in ultrahigh temperature granulites: phase equilibria modelling and implications for the *P–T–t* evolution of the Eastern Ghats Province, India. Journal of Metamorphic Geology 31, 881–907.

Korhonen, F.J., Clark, C., Brown, M., Bhattacharya, S., Taylor, R., 2013b. How long-lived is ultrahigh temperature (UHT) metamorphism? Constraints from zircon and monazite geochronology in the Eastern Ghats orogenic belt, India. Precambrian Research 234, 322–350.

Korhonen, F.J., Clark, C., Brown, M., Taylor, R.J.M., 2014. Taking the temperature of Earth's hottest crust. Earth and Planetary Science Letters 408, 341–354.

Korhonen, F.J., Powell, R., Stout, J.H., 2012. Stability of sapphirine + quartz in the oxidized rocks of the Wilson Lake terrane, Labrador: calculated equilibria in NCKFMASHTO. Journal of Metamorphic Geology 30, 21–36.

Korhonen, F.J., Saito, S., Brown, M., Siddoway, C.S., 2010. Modeling multiple melt loss events in the evolution of an active continental margin. Lithos 116, 230–248.

Korhonen, F.J., Saw, A.K., Clark, C., Brown, M., Bhattacharya, S., 2011. New constraints on UHT metamorphism in the Eastern Ghats Province through the application of phase equilibria modelling and in situ geochronology. Gondwana Research 20, 764–781.

Li, Z.-X., Zhang, L., Powell, C.M., 1995. South China in Rodinia: Part of the missing link between Australia–East Antarctica and Laurentia? Geology 23, 407–410.

Li, Z.X., Bogdanova, S.V., Collins, A.S., Davidson, A., De Waele, B., Ernst, R.E., Fitzsimons, I.C.W., Fuck, R.A., Gladkochub, D.P., Jacobs, J., Karlstrom, K.E., Lu, S., Natapov, L.M., Pease, V., Pisarevsky, S.A., Thrane, K., Vernikovsky, V., 2008. Assembly, configuration, and break-up history of Rodinia: A synthesis. Precambrian Research 160, 179–210.

Liu, X., Hu, J., Zhao, Y., Lou, Y., Wei, C., Liu, X., 2009a. Late Neoproterozoic/Cambrian high-pressure mafic granulites from the Grove Mountains, East Antarctica: *P–T–t* path, collisional orogeny and implications for assembly of East Gondwana. Precambrian Research 174, 181–199.

Liu, X., Jahn, B.-m., Zhao, Y., Liu, J., Ren, L., 2014. Geochemistry and geochronology of Mesoproterozoic basement rocks from the Eastern Amery Ice Shelf and southwestern Prydz Bay, East Antarctica: Implications for a long-lived magmatic accretion in a continental arc. American Journal of Science 314, 508–547.

Liu, X., Zhao, Y., Song, B., Liu, J., Cui, J., 2009b. SHRIMP U–Pb zircon geochronology of high-grade rocks and charnockites from the eastern Amery Ice Shelf and southwestern Prydz Bay, East Antarctica: Constraints on Late Mesoproterozoic to Cambrian tectonothermal events related to supercontinent assembly. Gondwana Research 16, 342–361.

Liu, X., Zhao, Y., Zhao, G., Jian, P., Xu, G., 2007. Petrology and Geochronology of Granulites from the McKaskle Hills, Eastern Amery Ice Shelf, Antarctica, and Implications for the Evolution of the Prydz Belt. Journal of Petrology 48, 1443–1470.

Manton, W.I., Grew, E.S., Hofmann, J., Sheraton, J.W., 1992. Granitic rocks of the Jetty Peninsula, Amery Ice Shelf area, East Antarctica, in: Yoshida, Y., Kaminuma, K., Shiraishi, K. (Eds.), Recent Progress in Antarctic Earth Science. Terra Scientific Publishing Company, Tokyo, pp. 179–189.

McKelvey, B.C., Stephenson, N.C.N., 1990. A geological reconnaissance of the Radok Lake area, Amery Oasis, Prince Charles Mountains. Antarctic Science 2, 53–66.

Mezger, K., Cosca, M.A., 1999. The thermal history of the Eastern Ghats Belt (India) as revealed by U–Pb and $^{40}Ar/^{39}Ar$ dating of metamorphic and magmatic minerals: implications for the SWEAT correlation. Precambrian Research 94, 251–271.

Mikhalsky, E., Laiba, A., Beliatsky, B., 2006a. Tectonic Subdivision of the Prince Charles Mountains: A Review of Geologic and Isotopic Data, in: Fütterer, D., Damaske, D., Kleinschmidt, G., Miller, H., Tessensohn, F. (Eds.), Antarctica. Springer Berlin Heidelberg, pp. 69–81.

Mikhalsky, E.V., Beliatsky, B.V., Sheraton, J.W., Roland, N.W., 2006b. Two distinct Precambrian terranes in the Southern Prince Charles Mountains, East Antarctica: SHRIMP dating and geochemical constraints. Gondwana Research 9, 291–309.

Mikhalsky, E.V., Sheraton, J.W., 2011. The Rayner tectonic Province of East Antarctica: Compositional features and geodynamic setting. Geotectonics 45, 496–512.

Mikhalsky, E.V., Sheraton, J.W., Laiba, A.A., Beliatsky, B.V., 1996. Geochemistry and origin of Mesoproterozoic metavolcanic rocks from Fisher Massif, Prince Charles Mountains, East Antarctica. Antarctic Science 8, 85–104.

Mikhalsky, E.V., Sheraton, J.W., Laiba, A.A., Tingey, R.J., Thost, D.E., Kamenev, I.A., Fedorov, L.V., 2001. Geology of the Prince Charles Mountains, Antarctica. AGSO- Geoscience Australia Bulletin 247.

Montel, J.M., Kornprobst, J., Vielzeuf, D., 2000.

Preservation of old U–Th–Pb ages in shielded monazite: example from the Beni Bousera Hercynian kinzigites (Morocco). Journal of Metamorphic Geology 18, 335–342.

Morrissey, L.J., Hand, M., Kelsey, D.E., in prep. Cambrian high-temperature reworking of the Rayner-Eastern Ghats terrane, constraints from the northern Prince Charles Mountains region, east Antarctica. Journal of Petrology.

Morrissey, L.J., Hand, M., Raimondo, T., Kelsey, D.E., 2014. Long-lived high-temperature, low-pressure granulite facies metamorphism in the Arunta Region, central Australia. Journal of Metamorphic Geology 32, 25–47.

Morrissey, L.J., Hand, M., Wade, B.P., Szpunar, M., 2013. Early Mesoproterozoic metamorphism in the Barossa Complex, South Australia: links with the eastern margin of Proterozoic Australia. Australian Journal of Earth Sciences 60, 769–795.

Mukhopadhyay, A.K., Bhattachrya, A., 1997. Tectonothermal evolution of the gneiss complex at Salur in the Eastern Ghats Grnaulite Belt of India. Journal of Metamorphic Geology 15, 719–734.

Mukhopadhyay, D., Basak, K., 2009. The Eastern Ghats Belt …A polycyclic granulite terrain. Journal of the Geological Society of India 73, 489–518.

Munksgaard, N.C., Thost, D.E., Hensen, B.J., 1992. Geochemistry of Proterozoic granulites from northern Prince Charles Mountains, East Antarctica. Antarctic Science 4, 59–69.

Nichols, G., Berry, R., Green, D., 1992. Internally consistent gahnitic spinel-cordierite-garnet equilibria in the FMASHZn system: geothermobarometry and applications. Contributions to Mineralogy and Petrology 111, 362–377.

Nichols, G.T., 1995. The role of mylonites in the uplift of an oblique lower crustal section, East Antarctica. Journal of Metamorphic Geology 13, 223–238.

Payne, J.L., Hand, M., Barovich, K.M., Wade, B.P., 2008. Temporal constraints on the timing of high-grade metamorphism in the northern Gawler Craton: implications for assembly of the Australian Proterozoic. Australian Journal of Earth Sciences 55, 623–640.

Peterson, J.W., Chacko, T., Kuehner, S.M., 1991. The effects of fluorine on the vapor-absent melting of phlogopite + quartz; implications for deep-crustal processes. American Mineralogist 76, 470–476.

Phillips, G., Kelsey, D.E., Corvino, A.F., Dutch, R.A., 2009. Continental Reworking during Overprinting Orogenic Events, Southern Prince Charles Mountains, East Antarctica. Journal of Petrology 50, 2017–2041.

Phillips, G., White, R.W., Wilson, C.J.L., 2007. On the roles of deformation and fluid during rejuvenation of a polymetamorphic terrane: inferences on the geodynamic evolution of the Ruker Province, East Antarctica. Journal of Metamorphic Geology 25, 855–871.

Phillips, G., Wilson, C.J.L., Campbell, I.H., Allen, C.M., 2006. U–Th–Pb detrital zircon geochronology from the southern Prince Charles Mountains, East Antarctica—Defining the Archaean to Neoproterozoic Ruker Province. Precambrian Research 148, 292–306.

Rapp, R., Watson, E.B., 1986. Monazite solubility and dissolution kinetics: implications for the thorium and light rare earth chemistry of felsic magmas. Contributions to Mineralogy and Petrology 94, 304–316.

Reno, B.L., Piccoli, P.M., Brown, M., Trouw, R.A.J., 2012. In situ monazite (U–Th)–Pb ages from the Southern Brasília Belt, Brazil: constraints on the high-temperature retrograde evolution of HP granulites. Journal of Metamorphic Geology 30, 81–112.

Rigby, M.J., Droop, G.T.R., 2011. Fluid-absent melting versus CO_2 streaming during the formation of pelitic granulites: A review of insights from the cordierite fluid monitor. Geological Society of America Memoirs 207, 39–60.

Sajeev, K., Williams, I.S., Osanai, Y., 2010. Sensitive high-resolution ion microprobe U–Pb dating of prograde and retrograde ultrahigh-temperature metamorphism as exemplified by Sri Lankan granulites. Geology 38, 971–974.

Sandiford, M., Powell, R., 1986. Deep crustal metamorphism during continental extension: modern and ancient examples. Earth and Planetary Science Letters 79, 151–158.

Santosh, M., Jackson, D.H., Harris, N.B.W., 1993. The Significance of Channel and Fluid-Inclusion

CO_2 in Cordierite: Evidence from Carbon Isotopes. Journal of Petrology 34, 233–258.

Santosh, M., Kusky, T., 2010. Origin of paired high pressure–ultrahigh-temperature orogens: a ridge subduction and slab window model. Terra Nova 22, 35–42.

Schmitz, M.D., Bowring, S.A., 2003. Ultrahigh-temperature metamorphism in the lower crust during Neoarchean Ventersdorp rifting and magmatism, Kaapvaal Craton, southern Africa. Geological Society of America Bulletin 115, 533–548.

Scrimgeour, I., Hand, M., 1997. A metamorphic perspective on the Pan African overprint in the Amery area of Mac. Robertson Land, East Antarctica. Antarctic Science 9, 313–335.

Sengupta, P., Dasgupta, S., Bhattacharya, P.K., Fukuoka, M., Chakraborti, S., Bhowmick, S., 1990. Petro-tectonic Imprints in the Sapphirine Granulites from Anantagiri, Eastern Ghats Mobile Belt, India. Journal of Petrology 31, 971–996.

Shaw, R.K., Arima, M., Kagami, H., Fanning, C.M., Shiraishi, K., Motoyoshi, Y., 1997. Proterozoic Events in the Eastern Ghats Granulite Belt, India: Evidence from Rb–Sr, Sm–Nd Systematics, and SHRIMP Dating. The Journal of Geology 105, 645–656.

Simmat, R., Raith, M.M., 2008. U–Th–Pb monazite geochronometry of the Eastern Ghats Belt, India: Timing and spatial disposition of poly-metamorphism. Precambrian Research 162, 16–39.

Sizova, E., Gerya, T., Brown, M., 2014. Contrasting styles of Phanerozoic and Precambrian continental collision. Gondwana Research 25, 522–545.

Sizova, E., Gerya, T., Brown, M., Perchuck, L.L., 2010. Subduction styles in the Precambrian: Insight from numerical experiments. Lithos 116, 209–229.

Stepanov, A.S., Hermann, J., Rubatto, D., Rapp, R.P., 2012. Experimental study of monazite/melt partitioning with implications for the REE, Th and U geochemistry of crustal rocks. Chemical Geology 300–301, 200–220.

Stephenson, N.C.N., 2000. Geochemistry of granulite-facies granitic rocks from Battye Glacier, northern Prince Charles Mountains, East Antarctica. Australian Journal of Earth Sciences 47, 83–94.

Stephenson, N.C.N., Cook, N., 1997. Metamorphic evolution of calcsilicate granulites near Battye Glacier, northern Prince Charles Mountains, East Antarctica. Journal of Metamorphic Geology 15, 361–378.

Stüwe, K., 1995. Thermal buffering effects at the solidus. Implications for the equilibration of partially melted metamorphic rocks. Tectonophysics 248, 39–51.

Stüwe, K., 2007. Geodynamics of the Lithosphere: An Introduction. Springer Berlin Heidelberg.

Stüwe, K., Hand, M., 1992. Geology and structure of Depot Peak, MacRobertson Land. More evidence for the continous extent of the 1000 Ma event of East Antarctica. Australian Journal of Earth Sciences 39, 211–222.

Tajcmanová, L., Konopásek, J., Košler, J., 2009. Distribution of zinc and its role in the stabilization of spinel in high-grade felsic rocks of the Moldanubian domain (Bohemian Massif). European Journal of Mineralogy 21, 407–418.

Thompson, P., Harley, S., Carrington, D., 2001. The distribution of H_2O–CO_2 between cordierite and granitic melt under fluid-saturated conditions at 5 kbar and 900 °C. Contributions to Mineralogy and Petrology 142, 107–118.

Thost, D.E., Hensen, B.J., 1992. Gneisses of the Porthos and Athos Ranges, northern Prince Charles Mountains, East Antarctica: Constraints on the prograde and retrograde *P–T* path, in: Yoshida, Y., Kaminuma, K., Shiraishi, K. (Eds.), Recent Progress in Antarctic Earth Science. Terra Scientific Publishing Company, Tokyo, pp. 93–102.

Tingey, R.J., 1991. The regional geology of Archaean and Proterozoic rocks in Antarctica, in: Tingey, R.J. (Ed.), The Geology of Antarctica. Oxford University Press, U.S.A.

Vielzeuf, D., Clemens, J.D., Pin, C., Moinet, E., 1990. Granites, Granulites, and Crustal Differentiation, in: Vielzeuf, D., Vidal, P. (Eds.), Granulites and Crustal Evolution. Springer Netherlands, pp. 59–85.

Walsh, A.K., Kelsey, D.E., Kirkland, C.L., Hand, M., Smithies, R.H., Clark, C., Howard, H.M., in press. *P–T–t* evolution of a large, long-lived, ultrahigh-temperature Grenvillian belt in central

Australia. Gondwana Research.

Wang, Y., Liu, D., Chung, S.-L., Tong, L., Ren, L., 2008. SHRIMP zircon age constraints from the Larsemann Hills region, Prydz Bay, for a late Mesoproterozoic to early Neoproterozoic tectono-thermal event in East Antarctica. American Journal of Science 308, 573–617.

Weinberg, R.F., Hasalová, P., Ward, L., Fanning, C.M., 2013. Interaction between deformation and magma extraction in migmatites: Examples from Kangaroo Island, South Australia. Geological Society of America Bulletin 125, 1282–1300.

White, R.W., Powell, C.M., Halpin, J.A., 2004. Spatially-focussed melt formation in aluminous metapelites from Broken Hill, Australia. Journal of Metamorphic Geology 22, 825–845.

White, R.W., Powell, R., 2002. Melt loss and the preservation of granulite facies mineral assemblages. Journal of Metamorphic Geology 20, 621–632.

White, R.W., Powell, R., Clarke, G.L., 2002. The interpretation of reaction textures in Fe-rich metapelitic granulites of the Musgrave Block, central Australia: constraints from mineral equilibria calculations in the system K_2O–FeO–MgO–Al_2O_3–SiO_2–H_2O–TiO_2–Fe_2O_3. Journal of Metamorphic Geology 20, 41–55.

White, R.W., Powell, R., Holland, T.J.B., 2007. Progress relating to calculation of partial melting equilibria for metapelites. Journal of Metamorphic Geology 25, 511–527.

White, R.W., Powell, R., Holland, T.J.B., Worley, B.A., 2000. The effect of TiO_2 and Fe_2O_3 on metapelitic assemblages at greenschist and amphibolite facies conditions: mineral equilibria calculations in the system K_2O–FeO–MgO–Al_2O_3–SiO_2–H_2O–TiO_2–Fe_2O_3. Journal of Metamorphic Geology 18, 497–511.

Williams, M.L., Jercinovic, M.J., Harlov, D.E., Budzyn, B., Hetherington, C.J., 2011. Resetting monazite ages during fluid-related alteration. Chemical Geology 283, 218–225.

Yakymchuk, C., Brown, M., 2014. Behaviour of zircon and monazite during crustal melting. Journal of the Geological Society.

Zhao, J.-x., Ellis, D.J., Kilpatrick, J.A., McCulloch, M.T., 1997. Geochemical and Sr–Nd isotopic study of charnockites and related rocks in the northern Prince Charles Mountains, East Antarctica: implications for charnockite petrogenesis and proterozoic crustal evolution. Precambrian Research 81, 37–66.

Spot name	Isotopic ratios $^{207}Pb/^{206}Pb$	±1σ	$^{206}Pb/^{238}U$	±1σ	$^{207}Pb/^{235}U$	±1σ	Age estimates $^{207}Pb/^{206}Pb$	±1σ	$^{206}Pb/^{238}U$	±1σ	$^{207}Pb/^{235}U$	±1σ	Conc. (%)	Morphology Textural setting	Zoning (BSE)	Spot location
Stin-1A: Stinear Nunataks																
19A1	0.07007	0.00085	0.15467	0.00274	1.49376	0.02739	931	25	927	15	928	11	100	Matrix	Core-rim	Core
19B1	0.06998	0.00085	0.15176	0.00269	1.46369	0.02684	928	25	911	15	916	11	99	Matrix	Weak core-rim	Core
19B2	0.06939	0.00082	0.15190	0.00267	1.45272	0.02621	910	24	912	15	911	11	100	Matrix	Weak core-rim	Core
19D1	0.06908	0.00085	0.15180	0.00267	1.44535	0.02652	901	25	911	15	908	11	100	Matrix	None	-
19D2	0.06924	0.00086	0.15601	0.00275	1.48864	0.02735	906	25	935	15	926	11	101	Matrix	None	-
31A1	0.06826	0.00084	0.15338	0.00269	1.44277	0.02643	876	25	920	15	907	11	101	Matrix	None	-
31A2	0.07043	0.00089	0.15019	0.00264	1.45773	0.02693	941	26	902	15	913	11	99	Matrix	None	-
31A3	0.06851	0.00086	0.14991	0.00263	1.41546	0.02607	884	26	901	15	896	11	101	Matrix	None	-
44B1	0.07086	0.00092	0.15496	0.00272	1.51328	0.02815	953	26	929	15	936	11	99	In gt, near rim	Discontinuous rim	Core
44A1	0.07061	0.00091	0.15469	0.00271	1.50528	0.02796	946	26	927	15	933	11	99	Matrix	None	-
44A2	0.06989	0.00083	0.15825	0.00275	1.52436	0.02728	925	24	947	15	940	11	101	Matrix	None	-
47A1	0.06992	0.00082	0.16002	0.00279	1.54197	0.02749	926	24	957	15	947	11	101	In cd	Patchy	Core
49A1	0.06997	0.00083	0.15302	0.00267	1.47545	0.02647	927	24	918	15	920	11	100	Matrix	None	-
49A2	0.06972	0.00085	0.15303	0.00267	1.47048	0.02669	920	25	918	15	918	11	100	Matrix	None	-
49A3	0.06885	0.00084	0.15640	0.00273	1.48408	0.02698	894	25	937	15	924	11	101	Matrix	None	-
49B1	0.06959	0.00083	0.16131	0.00281	1.54716	0.02783	916	24	964	16	949	11	102	Matrix	Weak core-rim	Overlapping
56A1	0.06852	0.00085	0.15563	0.00272	1.46963	0.02689	884	25	932	15	918	11	102	Matrix	None	-
71A1	0.06999	0.00089	0.15331	0.00268	1.47881	0.02725	928	26	920	15	922	11	100	Matrix	None	-
71B1	0.07094	0.00097	0.15107	0.00265	1.47704	0.02810	956	28	907	15	921	12	98	Matrix	None	-
71B2	0.07036	0.00094	0.15586	0.00273	1.51131	0.02848	939	27	934	15	935	12	100	Matrix	None	-
79B1	0.06841	0.00079	0.14619	0.00253	1.37830	0.02445	881	24	880	14	880	10	100	Matrix	Patchy	-
79B2	0.06929	0.00081	0.15442	0.00267	1.47470	0.02628	907	24	926	15	920	11	101	Matrix	Patchy	-
79A1	0.07057	0.00090	0.15467	0.00270	1.50438	0.02777	945	26	927	15	932	11	99	Matrix	None	-
79A2	0.06960	0.00082	0.15208	0.00264	1.45882	0.02610	917	24	913	15	914	11	100	Matrix	None	-
94A1	0.06979	0.00090	0.15390	0.00268	1.48023	0.02743	922	26	923	15	922	11	100	Matrix	Weak core-rim	Core
71C1	0.06943	0.00089	0.15441	0.00270	1.47753	0.02744	912	26	926	15	921	11	100	In ksp	Patchy	Rim
71C2	0.06992	0.00086	0.15425	0.00268	1.48651	0.02705	926	25	925	15	925	11	100	In ksp	Patchy	Core
67C1	0.06870	0.00091	0.14625	0.00256	1.38484	0.02602	890	27	880	14	883	11	100	Matrix	None	-
67C2	0.06957	0.00089	0.15193	0.00265	1.45674	0.02691	916	26	912	15	913	11	100	Matrix	None	-
67C3	0.06850	0.00088	0.14795	0.00257	1.39675	0.02581	884	26	889	14	888	11	100	Matrix	None	-

Spot name	Isotopic ratios						Age estimates							Morphology		
	$^{207}Pb/^{206}Pb$	±1σ	$^{206}Pb/^{238}U$	±1σ	$^{207}Pb/^{235}U$	±1σ	$^{207}Pb/^{206}Pb$	±1 σ	$^{206}Pb/^{238}U$	±1 σ	$^{207}Pb/^{235}U$	±1 σ	Conc. (%)	Textural setting	Zoning (BSE)	Spot location
77199: Mt Dovers																
11A1	0.07039	0.00078	0.16462	0.00245	1.59685	0.02445	940	23	982	14	969	10	101	Matrix	Patchy	Rim
11A2	0.07110	0.00079	0.15996	0.00237	1.56733	0.02396	960	23	957	13	957	9	100	Matrix	Patchy	Rim
11B1*	0.07809	0.00095	0.16352	0.00240	1.75973	0.02776	1149	24	976	13	1031	10	95	Matrix	Core-rim	Core
19A1	0.07134	0.00081	0.15963	0.00236	1.56938	0.02407	967	23	955	13	958	10	100	Matrix	None	-
19A2	0.07181	0.00081	0.16693	0.00248	1.65185	0.02548	981	23	995	14	990	10	100	Matrix	None	-
19A3	0.06980	0.00079	0.15746	0.00234	1.51461	0.02332	923	23	943	13	936	9	101	Matrix	None	-
22B1*	0.06919	0.00081	0.14768	0.00218	1.40812	0.02187	904	24	888	12	892	9	99	Matrix	Patchy	Dark zone at rim
22B2*	0.06903	0.00079	0.14770	0.00218	1.40507	0.02174	900	24	888	12	891	9	100	Matrix	Patchy	Overlapping
22B3*	0.06932	0.00079	0.14523	0.00215	1.38740	0.02148	908	23	874	12	884	9	99	Matrix	Patchy	Dark zone at rim
22A1	0.07141	0.00090	0.16108	0.00236	1.58523	0.02554	969	26	963	13	964	10	100	In gt, on crack	Core-rim	Rim
10A1	0.07005	0.00077	0.15625	0.00231	1.50840	0.02278	930	22	936	13	934	9	100	Matrix	Patchy	Rim
10A2	0.07056	0.00078	0.15768	0.00233	1.53317	0.02326	945	22	944	13	944	9	100	Matrix	Patchy	Rim
10A3	0.07072	0.00079	0.15417	0.00228	1.50255	0.02292	949	23	924	13	931	9	99	Matrix	Patchy	Rim
10B1	0.07073	0.00079	0.15596	0.00231	1.52020	0.02323	950	23	934	13	939	9	100	Matrix	None	-
10B2	0.07052	0.00078	0.15653	0.00232	1.52127	0.02322	944	23	938	13	939	9	100	Matrix	None	-
22D1	0.07029	0.00079	0.15604	0.00229	1.51144	0.02304	937	23	935	13	935	9	100	In gt, on crack	None	-
22D2	0.07090	0.00079	0.15701	0.00232	1.53413	0.02343	955	23	940	13	944	9	100	In gt, on crack	None	-
23A1	0.07155	0.00082	0.15765	0.00234	1.55458	0.02403	973	23	944	13	952	10	99	Matrix	Core-rim	Rim
23A2	0.07079	0.00082	0.16014	0.00237	1.56233	0.02428	951	23	958	13	955	10	100	Matrix	Core-rim	Rim
35B1	0.07189	0.00082	0.15445	0.00229	1.53009	0.02372	983	23	926	13	943	10	98	Matrix	Weak	Core
35B2*	0.06984	0.00089	0.14474	0.00213	1.39300	0.02259	924	26	871	12	886	10	98	Matrix	Weak	Overlapping
38B1*	0.06797	0.00078	0.15610	0.00229	1.46226	0.02247	868	24	935	13	915	9	102	Matrix	None	-
46B1*	0.06404	0.00072	0.12153	0.00181	1.07259	0.01655	743	24	739	10	740	8	100	Matrix	Patchy	Core
46B2*	0.06603	0.00074	0.13356	0.00198	1.21526	0.01874	807	23	808	11	808	9	100	Matrix	Patchy	Overlapping
46A1*	0.06865	0.00077	0.14290	0.00212	1.35190	0.02076	888	23	861	12	868	9	99	Matrix	None	-
46A2*	0.06875	0.00079	0.13270	0.00195	1.25713	0.01941	891	24	803	11	827	9	97	Matrix	None	-
46A3*	0.06647	0.00077	0.13116	0.00195	1.20150	0.01869	821	24	795	11	801	9	99	Matrix	None	-
54A1	0.07063	0.00081	0.15710	0.00234	1.52904	0.02377	947	23	941	13	942	10	100	Matrix	Discontinuous rim	Core
10B3	0.07037	0.00081	0.15527	0.00231	1.50563	0.02347	939	23	931	13	933	10	100	Matrix	None	-
17C1	0.07092	0.00085	0.15336	0.00226	1.49885	0.02357	955	24	920	13	930	10	99	Matrix	None	-

	Isotopic ratios						Age estimates							Morphology		
Spot name	$^{207}Pb/^{206}Pb$	±1σ	$^{206}Pb/^{238}U$	±1σ	$^{207}Pb/^{235}U$	±1σ	$^{207}Pb/^{206}Pb$	±1 σ	$^{206}Pb/^{238}U$	±1 σ	$^{207}Pb/^{235}U$	±1 σ	Conc. (%)	Textural setting	Zoning (BSE)	Spot location
77199: Mt Dovers																
17C2	0.07057	0.00086	0.16221	0.00241	1.57745	0.02519	945	25	969	13	961	10	101	Matrix	None	-
HN-3: Hunt Nunataks																
MNZ1A	0.07304	0.00093	0.17095	0.00259	1.72069	0.02858	1015	26	1017	14	1016	11	100	In gt	None	-
MNZ1B	0.07247	0.00098	0.17184	0.00261	1.71627	0.02935	999	27	1022	14	1015	11	101	In gt	None	-
MNZ1C	0.07387	0.00097	0.17159	0.00262	1.74684	0.02959	1038	26	1021	14	1026	11	100	In gt	None	-
MNZ2A	0.07320	0.00099	0.16673	0.00255	1.68199	0.02893	1020	27	994	14	1002	11	99	In gt	Very weak	Core
MNZ2B	0.07218	0.00097	0.16568	0.00253	1.64808	0.02826	991	27	988	14	989	11	100	In gt	Very weak	Rim
MNZ2C	0.07308	0.00106	0.17055	0.00258	1.71752	0.03045	1016	29	1015	14	1015	11	100	In gt	Very weak	Core
MNZ3A	0.07318	0.00143	0.17095	0.00269	1.72388	0.03721	1019	39	1017	15	1018	14	100	In gt (on crack)	None	-
MNZ3B	0.07286	0.00103	0.16880	0.00258	1.69475	0.02973	1010	28	1006	14	1007	11	100	In gt (on crack)	None	-
MNZ3C	0.07059	0.00102	0.15733	0.00243	1.53055	0.02742	946	29	942	14	943	11	100	In gt (on crack)	None	-
MNZ3D	0.07006	0.00106	0.15661	0.00240	1.51213	0.02759	930	31	938	13	935	11	100	In gt (on crack)	None	-
MNZ4A*	0.07320	0.00093	0.18163	0.00279	1.83198	0.03058	1020	25	1076	15	1057	11	102	In gt	None	-
MNZ5A	0.07294	0.00092	0.17082	0.00264	1.71687	0.02875	1012	25	1017	15	1015	11	100	Matrix	Very weak	Core
MNZ5B*	0.07052	0.00089	0.16793	0.00259	1.63184	0.02731	944	26	1001	14	983	11	102	Matrix	Very weak	Rim
MNZ5C	0.06937	0.00091	0.15518	0.00240	1.48343	0.02535	910	27	930	13	924	10	101	Matrix	Very weak	Rim
MNZ5D	0.07335	0.00108	0.17100	0.00266	1.72818	0.03124	1024	29	1018	15	1019	12	100	Matrix	Very weak	Core
MNZ5E	0.07201	0.00099	0.16488	0.00257	1.63618	0.02873	986	28	984	14	984	11	100	Matrix	Very weak	Core
MNZ6A	0.07021	0.00095	0.15856	0.00246	1.53393	0.02666	934	28	949	14	944	11	100	Matrix	None	-
MNZ6B	0.06854	0.00094	0.14749	0.00230	1.39300	0.02456	885	28	887	13	886	10	100	Matrix	None	-
MNZ6C*	0.06583	0.00091	0.13279	0.00207	1.20454	0.02137	801	29	804	12	803	10	100	Matrix	None	-
MNZ10A	0.07232	0.00144	0.16641	0.00271	1.65841	0.03727	995	40	992	15	993	14	100	Matrix	Weak core-rim	Core
MNZ2D	0.07286	0.00083	0.17708	0.00251	1.77823	0.02634	1010	23	1051	14	1038	10	101	In gt	Very weak	Core
MNZ3E	0.07395	0.00080	0.17267	0.00244	1.75980	0.02547	1040	22	1027	13	1031	9	100	In gt	None	-
MNZ3F	0.07433	0.00085	0.17438	0.00247	1.78637	0.02651	1050	23	1036	14	1041	10	100	In gt	None	-
MNZ5F	0.07402	0.00086	0.17224	0.00244	1.75708	0.02623	1042	23	1024	13	1030	10	99	Matrix	Large grain (core)	Core
MNZ5G	0.07074	0.00081	0.15348	0.00216	1.49637	0.02210	950	23	921	12	929	9	99	Matrix	Large grain (rim)	Rim
MNZ16A	0.07289	0.00082	0.17587	0.00248	1.76658	0.02595	1011	23	1044	14	1033	10	101	Matrix	Weak core-rim	Core
MNZ11A	0.07415	0.00083	0.17600	0.00248	1.79861	0.02635	1046	23	1045	14	1045	10	100	In gt	None	-
MNZ11B	0.07333	0.00084	0.17210	0.00241	1.73923	0.02558	1023	23	1024	13	1023	9	100	In gt	None	-

	Isotopic ratios						Age estimates							Morphology		
Spot name	$^{207}Pb/^{206}Pb$	±1σ	$^{206}Pb/^{238}U$	±1σ	$^{207}Pb/^{235}U$	±1σ	$^{207}Pb/^{206}Pb$	±1 σ	$^{206}Pb/^{238}U$	±1 σ	$^{207}Pb/^{235}U$	±1 σ	Conc. (%)	Textural setting	Zoning (BSE)	Spot location
HN-3: Hunt Nunataks																
MNZ11C	0.07397	0.00087	0.17482	0.00247	1.78215	0.02683	1041	24	1039	14	1039	10	100	In gt	None	-
MNZ11D	0.07343	0.00084	0.16998	0.00239	1.72015	0.02536	1026	23	1012	13	1016	9	100	In gt	None	-
MNZ13A	0.06952	0.00077	0.15673	0.00212	1.50168	0.02123	914	23	939	12	931	9	101	Matrix	None	-
MNZ13B	0.07010	0.00080	0.15721	0.00213	1.51906	0.02170	931	23	941	12	938	9	100	Matrix	None	-
MNZ13C	0.06974	0.00079	0.15731	0.00213	1.51204	0.02158	921	23	942	12	935	9	101	Matrix	None	-
MNZ12A	0.07269	0.00083	0.16891	0.00229	1.69211	0.02428	1005	23	1006	13	1006	9	100	In gt (on crack)	None	-
MNZ14A	0.07014	0.00082	0.15439	0.00208	1.49243	0.02157	933	24	926	12	927	9	100	Matrix	Very weak, patchy	-
MNZ14B	0.06908	0.00084	0.14490	0.00196	1.37972	0.02042	901	25	872	11	880	9	99	Matrix	Very weak, patchy	-
MNZ14C	0.06851	0.00079	0.14553	0.00198	1.37418	0.01980	884	24	876	11	878	8	100	Matrix	Very weak, patchy	-
MNZ15A	0.07392	0.00088	0.17394	0.00236	1.77220	0.02595	1039	24	1034	13	1035	10	100	In gt (on crack)	None	-
MNZ15B	0.07116	0.00086	0.16632	0.00226	1.63098	0.02419	962	25	992	12	982	9	101	In gt (on crack)	None	-
MNZ14D	0.06913	0.00083	0.14917	0.00203	1.42129	0.02103	903	25	896	11	898	9	100	Matrix	Very weak, patchy	-
MNZ14E	0.06828	0.00081	0.14642	0.00199	1.37786	0.02027	877	24	881	11	880	9	100	Matrix	Very weak, patchy	-
MNZ13D	0.06951	0.00082	0.15400	0.00210	1.47519	0.02167	914	24	923	12	920	9	100	Matrix	None	-
Fox-5B: Fox Ridge																
MNZ2A	0.07005	0.00125	0.14287	0.00225	1.37949	0.02809	930	36	861	13	880	12	98	In gt	None	-
MNZ3A	0.07127	0.00136	0.14906	0.00236	1.46447	0.03120	965	38	896	13	916	13	98	Matrix	Patchy	Core
MNZ3B	0.07127	0.00137	0.14962	0.00237	1.47000	0.03156	965	39	899	13	918	13	98	Matrix	Patchy	Rim
MNZ3C	0.07008	0.00139	0.14928	0.00236	1.44252	0.03154	931	40	897	13	907	13	99	Matrix	Patchy	Core
MNZ4A	0.06781	0.00110	0.15077	0.00226	1.40876	0.02650	863	33	905	13	893	11	101	Matrix	Weak core-rim	Overlapping
MNZ4B*	0.06611	0.00117	0.14785	0.00222	1.34679	0.02678	810	37	889	12	866	12	103	Matrix	Weak core-rim	Rim
MNZ4C	0.06628	0.00117	0.14846	0.00224	1.35586	0.02710	815	37	892	13	870	12	103	Matrix	Weak core-rim	Rim
MNZ6A	0.06833	0.00130	0.15081	0.00231	1.42001	0.03004	879	39	906	13	897	13	101	Matrix	None	-
MNZ6B	0.06962	0.00134	0.14870	0.00228	1.42651	0.03020	917	39	894	13	900	13	99	Matrix	None	-
MNZ6C	0.07003	0.00119	0.15026	0.00226	1.45039	0.02813	929	35	902	13	910	12	99	Matrix	None	-
MNZ6D	0.07009	0.00113	0.14062	0.00210	1.35861	0.02543	931	33	848	12	871	11	97	Matrix	None	-
MNZ7A	0.06904	0.00137	0.14856	0.00230	1.41367	0.03075	900	40	893	13	895	13	100	Matrix	Thin discontinuous rim	Core
MNZ7B	0.07117	0.00145	0.14890	0.00231	1.46077	0.03247	962	41	895	13	914	13	98	Matrix	Thin discontinuous rim	Core
MNZ7C	0.06810	0.00142	0.14471	0.00225	1.35836	0.03080	872	43	871	13	871	13	100	Matrix	Thin discontinuous rim	Core
MNZ5A	0.06878	0.00126	0.14829	0.00226	1.40588	0.02892	892	38	891	13	891	12	100	Matrix	None	-

Spot name	Isotopic ratios $^{207}Pb/^{206}Pb$	±1σ	$^{206}Pb/^{238}U$	±1σ	$^{207}Pb/^{235}U$	±1σ	Age estimates $^{207}Pb/^{206}Pb$	±1 σ	$^{206}Pb/^{238}U$	±1 σ	$^{207}Pb/^{235}U$	±1 σ	Conc. (%)	Morphology Textural setting	Zoning (BSE)	Spot location
Fox-5B: Fox Ridge																
MNZ3D	0.07001	0.00152	0.15383	0.00241	1.48462	0.03472	929	44	922	13	924	14	100	Matrix	Patchy	Core
MNZ3E	0.07016	0.00154	0.15214	0.00239	1.47119	0.03475	933	45	913	13	919	14	99	Matrix	Patchy	Core
MNZ7D	0.07152	0.00159	0.15119	0.00239	1.49049	0.03548	972	45	908	13	927	14	98	Matrix	Thin discontinuous rim	Rim
MNZ9A	0.07111	0.00138	0.15604	0.00240	1.52895	0.03255	961	39	935	13	942	13	99	Matrix	None	-
MNZ9B	0.07042	0.00136	0.15313	0.00236	1.48607	0.03162	941	39	919	13	925	13	99	Matrix	None	-
MNZ8A	0.07005	0.00135	0.14738	0.00226	1.42267	0.03013	930	39	886	13	899	13	99	Matrix	None	-
MNZ8B	0.06869	0.00130	0.15489	0.00236	1.46595	0.03074	890	39	928	13	917	13	101	Matrix	None	-
MNZ8C	0.07061	0.00134	0.15038	0.00229	1.46311	0.03071	946	39	903	13	915	13	99	Matrix	None	-
MNZ11A	0.07125	0.00150	0.15591	0.00241	1.53056	0.03465	965	42	934	13	943	14	99	Matrix	None	-
MNZ11B	0.06969	0.00147	0.15272	0.00235	1.46615	0.03326	919	43	916	13	917	14	100	Matrix	None	-
MNZ13A*	0.07136	0.00144	0.13335	0.00206	1.31106	0.02872	968	41	807	12	851	13	95	In gt	Patchy	Core
MNZ13B*	0.06701	0.00112	0.13374	0.00199	1.23475	0.02354	838	34	809	11	817	11	99	In gt	Patchy	Rim
MNZ12A	0.07136	0.00154	0.15221	0.00237	1.49647	0.03452	968	43	913	13	929	14	98	Matrix	Weak core-rim	Rim
72523: Mt Lanyon																
68B1	0.07408	0.00080	0.17118	0.00292	1.74695	0.02985	1044	22	1019	16	1026	11	99	In gt (on crack)	Thin discontinuous rim	Core
68B2	0.07309	0.00081	0.16652	0.00285	1.67649	0.02901	1016	22	993	16	1000	11	99	In gt (on crack)	Thin discontinuous rim	Core
66A1*	0.07376	0.00082	0.18046	0.00308	1.83379	0.03170	1035	22	1070	17	1058	11	101	Matrix	Core-rim	Core
66A2	0.07181	0.00081	0.16040	0.00275	1.58676	0.02765	980	23	959	15	965	11	99	Matrix	Core-rim	Rim
54B1	0.07384	0.00092	0.16781	0.00287	1.70729	0.03099	1037	25	1000	16	1011	12	99	In gt (on crack)	Thin discontinuous rim	Core
54A1	0.06835	0.00077	0.15600	0.00268	1.46902	0.02577	879	23	935	15	918	11	102	Cd-bearing fracture	None	-
54A2	0.06929	0.00080	0.15397	0.00266	1.46994	0.02601	908	24	923	15	918	11	101	Cd-bearing fracture	None	-
43A1	0.07323	0.00085	0.16984	0.00293	1.71367	0.03046	1020	23	1011	16	1014	11	100	In gt	Discontinuous rim	Core
43A2	0.07304	0.00085	0.17122	0.00296	1.72312	0.03076	1015	23	1019	16	1017	11	100	In gt	Discontinuous rim	Core
34A1	0.07343	0.00088	0.17251	0.00299	1.74544	0.03151	1026	24	1026	16	1026	12	100	In gt (on crack)	Patchy	Core
14A1	0.07019	0.00077	0.15624	0.00264	1.51135	0.02589	934	22	936	15	935	10	100	Matrix	Core-rim	Core
17A1	0.06904	0.00083	0.15156	0.00257	1.44188	0.02564	900	25	910	14	907	11	100	Matrix	None	-
17A2	0.06835	0.00082	0.14815	0.00251	1.39551	0.02480	879	25	891	14	887	11	100	Matrix	None	-
17A3	0.06834	0.00085	0.14322	0.00243	1.34890	0.02435	879	26	863	14	867	11	100	Matrix	None	-
17B1*	0.06575	0.00082	0.14425	0.00244	1.30702	0.02355	799	26	869	14	849	10	102	Matrix	Patchy	-
17B2*	0.06582	0.00082	0.13851	0.00235	1.25621	0.02276	801	26	836	13	826	10	101	Matrix	Patchy	-

	Isotopic ratios						Age estimates							Morphology		
Spot name	$^{207}Pb/^{206}Pb$	±1σ	$^{206}Pb/^{238}U$	±1σ	$^{207}Pb/^{235}U$	±1σ	$^{207}Pb/^{206}Pb$	±1 σ	$^{206}Pb/^{238}U$	±1 σ	$^{207}Pb/^{235}U$	±1 σ	Conc. (%)	Textural setting	Zoning (BSE)	Spot location
72523: Mt Lanyon																
28A1	0.07128	0.00086	0.15532	0.00263	1.52551	0.02715	965	24	931	15	941	11	99	Matrix	Core-rim	Rim
28A2*	0.07324	0.00088	0.15803	0.00268	1.59489	0.02837	1021	24	946	15	968	11	98	Matrix	Core-rim	Core
28A3	0.07328	0.00089	0.16507	0.00280	1.66664	0.02993	1022	25	985	15	996	11	99	Matrix	Core-rim	Core
29A1	0.07436	0.00091	0.16814	0.00285	1.72291	0.03101	1051	25	1002	16	1017	12	98	Matrix	Core-rim	Core
34A2	0.07366	0.00102	0.17245	0.00301	1.75075	0.03348	1032	28	1026	17	1027	12	100	In gt (on crack)	Patchy	Rim
34A3	0.07577	0.00111	0.18437	0.00324	1.92522	0.03801	1089	29	1091	18	1090	13	100	In gt (on crack)	Patchy	Overlapping
34A4*	0.07736	0.00189	0.17075	0.00320	1.82020	0.04984	1131	48	1016	18	1053	18	97	In gt (on crack)	Patchy	Core
29A2	0.07047	0.00114	0.16126	0.00286	1.56621	0.03261	942	33	964	16	957	13	101	Matrix	Core-rim	Rim
29A3	0.07284	0.00119	0.16977	0.00303	1.70434	0.03589	1010	33	1011	17	1010	13	100	Matrix	Core-rim	Core
1A1	0.07339	0.00102	0.17441	0.00242	1.76372	0.02850	1025	28	1036	13	1032	10	100	Matrix	None	-
28A4	0.07037	0.00098	0.15894	0.00220	1.54127	0.02503	939	28	951	12	947	10	100	Matrix	Core-rim	Rim
28A5	0.07108	0.00098	0.16062	0.00222	1.57320	0.02536	960	28	960	12	960	10	100	Matrix	Core-rim	Rim
34A6	0.07406	0.00131	0.17475	0.00251	1.78328	0.03419	1043	35	1038	14	1039	12	100	In gt (on crack)	Patchy	Core
34A7	0.07474	0.00109	0.17061	0.00237	1.75727	0.02941	1062	29	1016	13	1030	11	99	In gt (on crack)	Patchy	Rim
57A1	0.07455	0.00107	0.17317	0.00240	1.77912	0.02950	1056	29	1030	13	1038	11	99	In gt	None	-
60A1	0.06743	0.00111	0.14085	0.00198	1.30897	0.02380	851	34	850	11	850	10	100	In cd corona	None	-
60A2	0.06757	0.00105	0.14497	0.00202	1.34995	0.02358	855	32	873	11	868	10	101	In cd corona	None	-
60A3	0.06754	0.00102	0.14144	0.00197	1.31658	0.02253	854	31	853	11	853	10	100	In cd corona	None	-
61A1	0.07474	0.00116	0.16984	0.00237	1.74957	0.03038	1061	31	1011	13	1027	11	98	In gt	None	-

CHAPTER 6

This chapter is published as:

Morrissey, L.J., Hand, M., Lane, K., Kelsey, D.E., Dutch, R.A., 2016. Upgrading iron-ore deposits by melt loss during granulite facies metamorphism. *Ore Geology Reviews*, **74**, 101–121.

Statement of Authorship

Title of Paper	Upgrading iron-rich sequences to economic grade iron-ore deposits by melt loss during granulite-facies metamorphism.
Publication status	☒Published ☐Accepted for publication ☐Submitted for publication ☐Unpublished and unsubmitted work written in manuscript style
Publication Details	Morrissey, L.J., Hand, M., Lane, K., Kelsey, D.E., Dutch, R., 2016. Upgrading iron-rich sequences to economic grade iron-ore deposits by melt loss during granulite-facies metamorphism. *Ore Geology Reviews*, **74**, 101–121.

Principal Author

Name of Principal Author (Candidate)	Laura Morrissey		
Contribution to the Paper	Project design, sample selection, *P–T* pseudosection calculation and interpretation, manuscript design and composition, creation of figures.		
Overall percentage (%)	90		
Certification:	This paper reports on original research I conducted during the period of my Higher Degree by Research candidature and is not subject to any obligations or contractual agreements with a third party that would constrain its inclusion in this thesis. I am the primary author of this paper.		
Signature		Date	16/05/2016

Co-Author Contributions

By signing the Statement of Authorship, each author certifies that:

i. the candidate's stated contribution to the publication is accurate (as detailed above);
ii. permission is granted for the candidate in include the publication in the thesis; and
iii. the sum of all co-author contributions is equal to 100% less the candidate's stated contribution.

Name of Co-Author	Martin Hand		
Contribution to the Paper	Project design, *P–T* pseudosection interpretation, manuscript review.		
Signature		Date	17th May 2016

Name of Co-Author	Kathleen Lane		
Contribution to the Paper	Sample collection and preparation, manuscript review.		
Signature		Date	19/05/2016

Name of Co-Author	David Kelsey		
Contribution to the Paper	Guidance with *P–T* modelling, manuscript review.		
Signature		Date	18/05/2016

Name of Co-Author	Rian Dutch		
Contribution to the Paper	Manuscript review.		
Signature		Date	20/05/2016

ABSTRACT

Forward modelling of Fe-rich phyllite is used to evaluate the effects of partial melting and melt loss on the concentration of iron in the residual rock package, leading to enrichment in Fe-oxide minerals (magnetite and hematite). The effect of melt loss during prograde metamorphism to peak conditions of ~850 °C was modelled using a series of calculated pressure–temperature (*P–T*) phase diagrams (pseudosections). The results show that metapelitic rocks with lower iron content are more fertile, produce more melt and therefore show a more significant increase (up to 35%) in the Fe-oxide content in the residual (melt depleted) rock package. Rocks with primary Fe-rich compositions are less fertile, lose less melt and therefore do not experience the same relative increase in the amount of Fe-oxides in the residuum. The results of the modelling have implications for the formation of economic-grade iron ore deposits in metamorphic terranes. Fe-rich compositions that represent primary ore horizons prior to metamorphism may not experience significant enrichment. However, those horizons with lower primary iron contents may be significantly upgraded as a result of melt loss, thereby improving the overall grade of the ore system. The application of the modelling to the highly metamorphosed Palaeoproterozoic Warramboo magnetite–hematite deposit in the southern Gawler Craton suggests that melt loss during granulite facies metamorphism led to upgrading of sub-economic units within the low-grade Price Metasediments to form the economically viable granulite facies Warramboo ore system. The results of this study suggest that high-temperature metamorphic terranes offer attractive exploration targets for magnetite-dominated iron ore deposits.

1. Introduction

Hematite ore has traditionally been considered to be of greater economic importance than magnetite ore, as high-grade hematite ore contains fewer impurities and therefore has lower processing costs (McKay et al., 2014). Australia is one of the largest global producers of iron ore, and the dominant ore exported by Australia is hematite ore (McKay et al., 2014). However, there has been a gradual decrease over time in the discovery of large hematite ore bodies, as well as a decline in the quality of hematite ore exported from large-scale producers such as Australia (McKay et al., 2014; Mudd, 2010). As a result, magnetite deposits are increasingly generating economic interest, as simpler procedures for concentrating the ore allow for the formation of a high quality beneficiation product that attracts high prices (IronRoad, 2014; McKay et al., 2014). Magnetite deposits hosted in granulite facies rocks are additionally of economic interest, as the coarse-grained nature of the rock allows for easier concentration of the iron ore (e.g. IronRoad, 2014).

In the southern Gawler Craton, the Warramboo deposit is an example of an economic-grade, granulite facies, magnetite-dominant iron ore deposit (Figs. 1 and 2). Recent work has correlated the magnetite gneisses at Warramboo to the Price Metasediments, a sequence of magnetite and hematite-bearing phyllites in the southern Gawler Craton (Fig. 1; Lane et al., 2015). The stratigraphic links between the greenschist facies Price Metasediments and the granulite facies magnetite gneisses that comprise the Warramboo deposit provide an opportunity to model the effect of high-grade metamorphism and partial melting on the iron concentration of a primary magnetite and hematite-bearing sedimentary package.

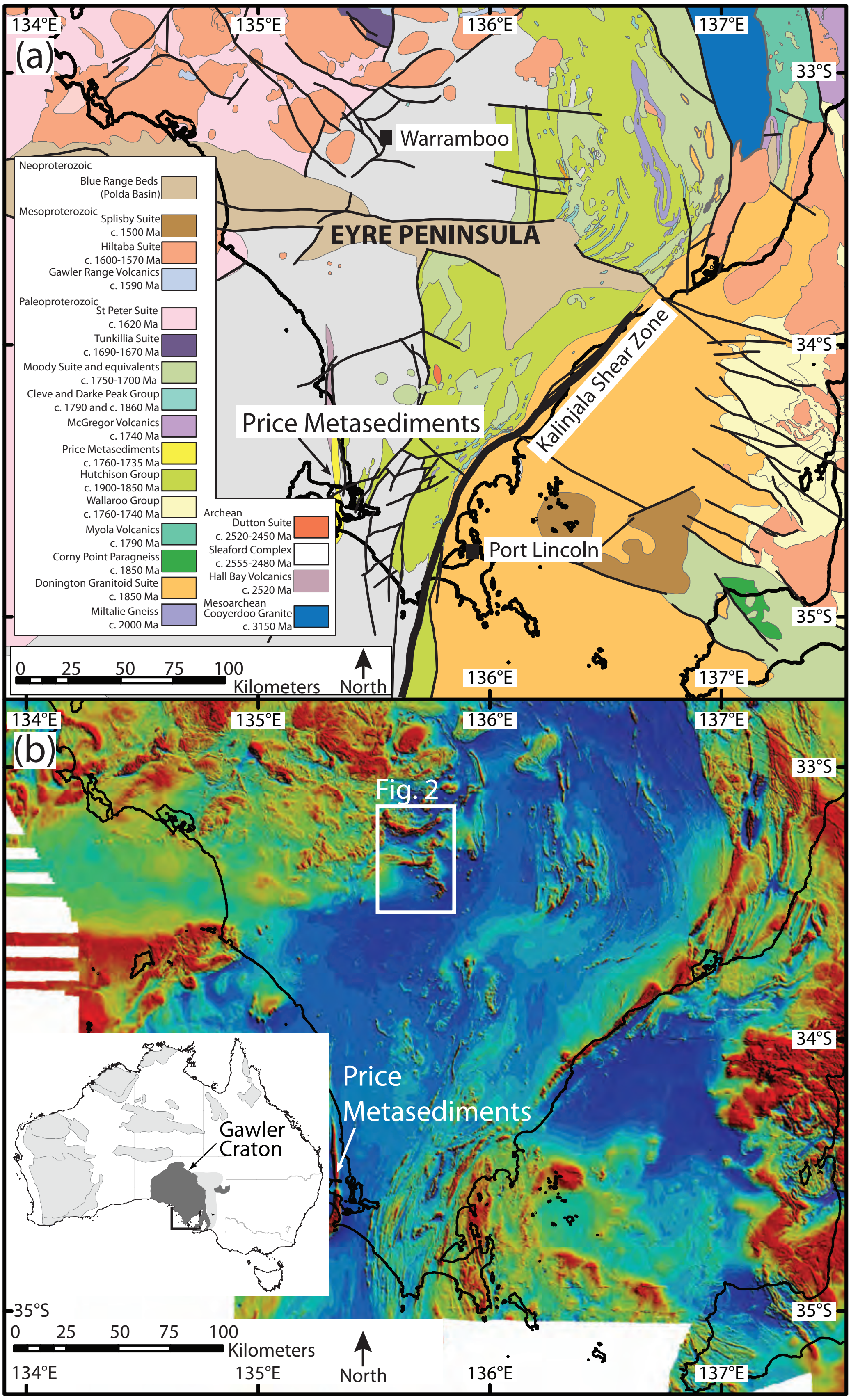

Figure 1: Interpreted geology of the southern Gawler Craton, after Lane et al. (2015). (b) TMI magnetic image of the southern Gawler Craton (from SARIG <https://sarig.pir.sa.gov.au/Map>).

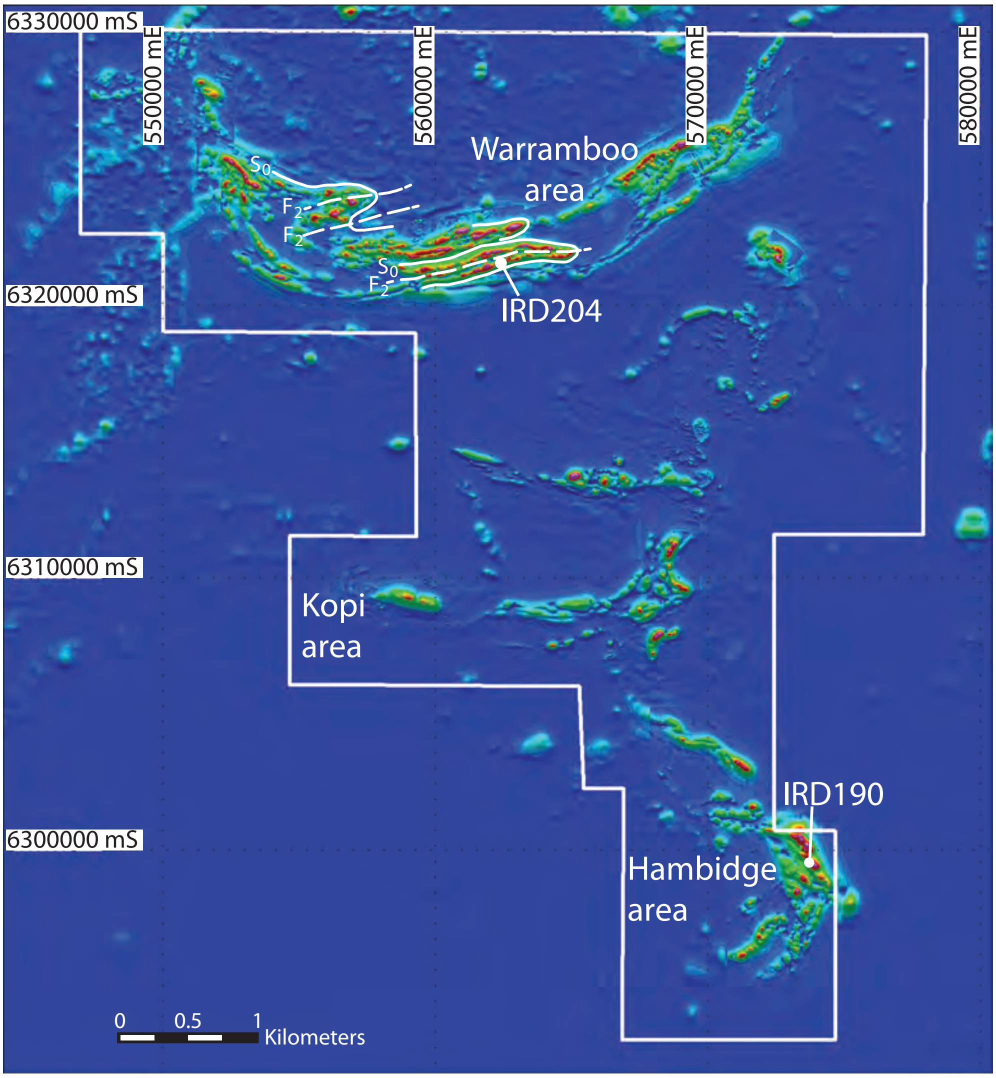

Figure 2: Aeromagnetic image of Warramboo deposit, showing the Warramboo, Kopi and Hambidge deposits. Interpreted structural features of the Warramboo deposit are also shown, after Lane et al. (2015).

An average pelite may produce up to 50–60 vol.% total melt at conditions attainable during orogenesis (Clemens, 2006; Clemens and Vielzeuf, 1987). As melts are mobile, and many granites contain appreciable volumes of crustal material, volume reduction in the source region associated with melt loss is a mechanism to concentrate elements such as iron in the residual rock package (e.g. Brown, 2013; Droop et al., 2003; Redler et al., 2013; Sawyer, 1994; Vielzeuf and Holloway, 1988; White and Powell, 2002; Yakymchuk and Brown, 2014). For a layered sequence that contains variable amounts of magnetite and hematite, up to and including ore-grade concentrations, the concentration of iron as a result of melt loss may be an important process in improving iron ore grades.

In this paper we investigate the effect of melt loss on bulk rock iron content ($Fe_2O_{3(TOTAL)}$) and the proportion of magnetite and hematite using samples from the Price Metasediments. The computed metamorphic phase diagrams from the greenschist facies Price Metasediments are compared with those using compositions from the residual (melt depleted) granulite facies Warramboo deposit to show that melt loss from the Price Metasediments is a plausible mechanism to upgrade sub-economic Fe-bearing sequences. We also model the effect of varying oxidation state of the bulk rock and its impact on the proportion of magnetite to hematite.

2. Geological Setting

2.1. Gawler Craton

The Gawler Craton preserves a protracted geological history from c. 3150 Ma to c. 1450 Ma (Fig. 1; Daly et al., 1998; Fraser et al., 2010; Hand et al., 2007; Payne et al., 2009; Reid and Hand, 2012). The oldest rocks in the Gawler Craton are c. 3250–3150 Ma granitic gneisses that outcrop within a discrete shear-zone bounded tectonostratigraphic domain in the south-eastern Gawler Craton (Fraser et al., 2010). Seismic data suggests that these rocks may form the basement to a large part of the Gawler Craton (Fraser et al., 2010; Reid and Hand, 2012). The Neoarchean to earliest Paleoproterozoic Mulgathing Complex in the central-western Gawler Craton, and the Sleaford Complex in the southern Gawler Craton, dominantly comprise c. 2560–2480 Ma volcanic and sedimentary successions, as well as 2520–2420 Ma intrusive rocks, and are interpreted to represent portions of a single late Archean belt (Reid and Hand, 2012; Reid et al., 2014; Swain et al., 2005). Both these complexes were deformed and metamorphosed during the 2470–2410 Ma Sleafordian Orogeny (Daly et al., 1998; Dutch et al., 2010; McFarlane, 2006; Reid et al., 2014).

Following the Sleafordian Orogeny, the Gawler Craton experienced c. 400 Myr of tectonic quiescence. From c. 2000–1730 Ma, the tectonic setting of the western, northern and eastern Gawler Craton has been interpreted to have been dominantly extensional, with a series of rifting events resulting in basin development and widespread deposition of a number of volcanoclastic sedimentary sequences (Fig. 1; Fanning et al., 2007; Hand et al., 2007; Howard et al., 2011a; Howard et al., 2011b; Payne et al., 2009; Reid and Hand, 2012). In central and western Eyre Peninsula, these include the c. 1760 Ma Price Metasediments (Fig. 1; Lane et al., 2015; Oliver and Fanning, 1997). In the northern Gawler Craton, magnetite-bearing metasediments with deposition ages of 1750–1730 Ma have been intersected in drill holes (Cutts et al., 2013; Payne et al., 2006; Payne et al., 2008); metasedimentary successions with depositional ages of 1760–1700 Ma are also found in the western Gawler Craton (Howard et al., 2011a).

Widespread basin development and sedimentation was terminated by the Kimban Orogeny at c. 1730–1690 Ma. The Kimban Orogeny was a craton-wide event that involved the development of crustal-scale shear zones, granitic magmatism and widespread metamorphism (e.g. Dutch et al., 2008; Dutch et al., 2010; Fanning et al., 2007; Hand et al., 2007; Howard et al., 2011b; Payne et al., 2008; Vassallo and Wilson, 2002). Preserved metamorphic conditions during the Kimban Orogeny vary widely, reflecting large exhumation gradients in the terrane (Dutch et al., 2008).

Following the Kimban Orogeny, the Gawler Craton was dominated by magmatic processes, with the formation of the c. 1690–1670 Ma Tunkillia Suite (Hand et al., 2007), the c. 1620 Ma St Peter Suite (Swain et al., 2008) and at c. 1580 Ma the voluminous Gawler Range Volcanics and the Hiltaba Suite Granites (Daly et al., 1998; Fanning et al., 1988; Hand et al., 2007). Magmatism at c. 1580 Ma was accompanied by widespread, high-grade metamorphism in the northern and southeastern Gawler Craton (Cutts et al., 2011; Forbes et al., 2012; Morrissey et al., 2013; Payne et al., 2008).

2.2. Price Metasediments–Warramboo system

The Warramboo deposit consists of significant iron concentrations at Warramboo, Hambidge and Kopi in the central Eyre Peninsula (Figs. 1 and 2). The deposits are entirely buried beneath Tertiary to Recent cover sequences, with mineralisation projected to occur at depths between 200 and 600 m (IronRoad, 2014). All samples used in this study come from exploration and resource-defining drilling. The iron deposits consist of granulite facies, magnetite-rich metapelitic gneisses interlayered with magnetite-poor felsic gneisses. The Warramboo deposit is the largest known magnetite deposit in Australia, with a resource of 3.7 billion tonnes at 16 wt% Fe (IronRoad, 2014; Lane et al., 2015). The granulite facies host rock is coarse-grained and therefore the Fe-oxides are easier to concentrate. After concentration, it is estimated that the Warramboo deposit will produce a beneficiation product of 67% Fe (IronRoad, 2014).

The Warramboo deposit appears on regional aeromagnetic imagery as a series of east–west trending domains that outline an isoclinal fold system (Fig. 2; Lane et al., 2015). Although detailed geochronology and structural interpretation has focussed on the Warramboo area, the Hambidge area to the south preserves similar relationships and lithologies, and is therefore interpreted to correlate with the units in the Warramboo area.

The lithologies at Warramboo are described in more detail in Lane et al. (2015) and have been divided into magnetite-poor lithologies, magnetite-bearing horizons, and the magnetite-rich ore zones. The magnetite-poor lithologies include metasedimentary felsic gneiss, interpreted to have been deposited between 2470 and 2445 Ma, and two felsic, metaigneous units with magmatic ages of 2474–2466 Ma. The magnetite-poor lithologies were interpreted to be part of the Sleaford Complex of the southern Gawler Craton, and were deformed and metamorphosed at c. 2445 Ma during the Sleaford Orogeny (Lane et al., 2015). In contrast, the magnetite-bearing gneisses were interpreted to be a younger cover sequence, deposited between 1760 and 1735 Ma (Lane et al., 2015). The magnetite-bearing units are compositionally and mineralogically heterogeneous and contain horizons enriched in manganese that can be correlated across the deposit, interpreted to represent primary compositional layering inherited from a heterogeneous sedimentary package (Lane et al., 2015). Overall, the average grade of the magnetite gneisses of the Warramboo deposit is ~16 wt% Fe (IronRoad, 2014).

The presence of detrital zircons within the Fe-rich units indicates they are clastic in origin. The detrital zircon age spectra are dominated by 1790–1750 Ma grains, similar to the greenschist facies, Fe-rich Price Metasediments in southern Eyre Peninsula (Fig. 1; Lane et al., 2015; Oliver and Fanning, 1997). In addition, the Price Metasediments and Warramboo magnetite-bearing gneisses have similar Sm–Nd isotopic compositions and both contain abundant spessartine-rich (i.e. Mn-rich) garnet, suggesting a common sedimentary source (Lane et al., 2015; Oliver and Fanning, 1997). Structurally, both the Price Metasediments and the Warramboo magnetite-gneisses are isoclinally folded and bounded by gneisses of the Sleaford Complex (Dutch et al., 2008; Lane et al., 2015). Therefore, the Warramboo gneisses are interpreted to be a high-grade

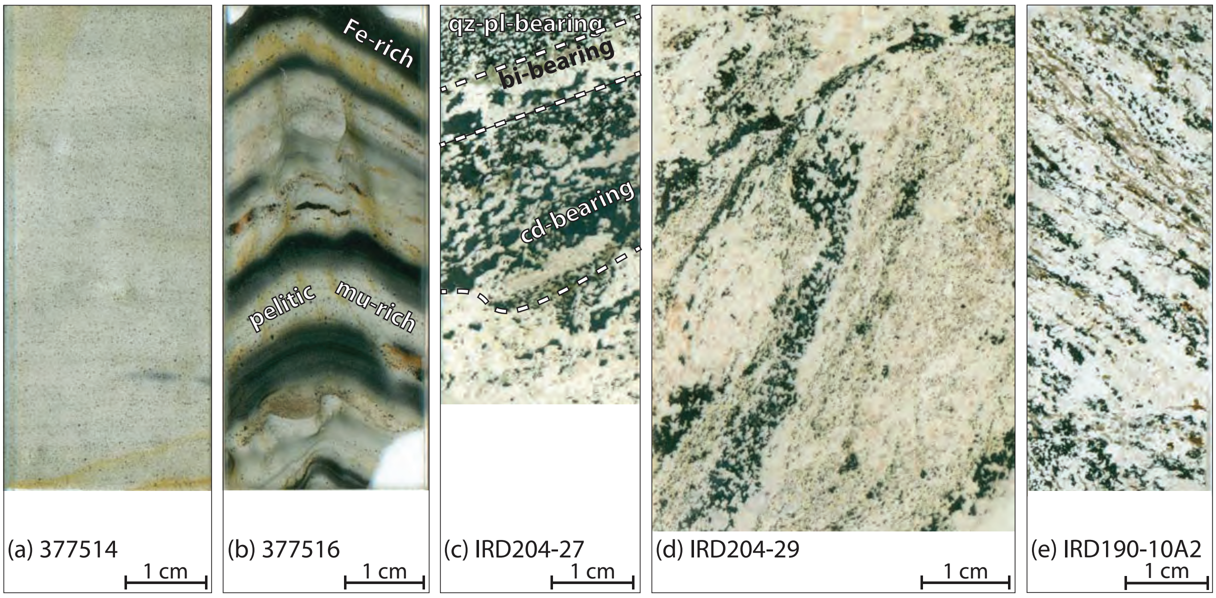

Figure 3: Thin section images. (a) Sample 377514. (b) Sample 377516. (c) Sample IRD204-27. (d) Sample IRD204-29. (e) Sample IRD190-10A2.

correlative of the Price Metasediments.

Metamorphic zircon from the Warramboo deposit suggests it was deformed and metamorphosed at c. 1735 Ma during the Kimban Orogeny (Lane et al., 2015). However, there are no quantitative constraints on the pressure–temperature (*P*–*T*) conditions of the Warramboo deposit. Similarly, regional structural relationships indicate that the Price Metasediments were also deformed and metamorphosed during the Kimban Orogeny (Dutch et al., 2010). However, in contrast to the Warramboo deposit, the Price Metasediments are sub-to un-economic for iron ore. The purpose of this paper is to examine the impact of Kimban Orogeny metamorphism on the iron contents of the Price Metasediments, and the implications for concentrations of magnetite and hematite. This paper also provides the first quantitative constraints on the *P*–*T* conditions of the Warramboo deposit.

3. Sample Descriptions

3.1. Price Metasediments

The Price Metasediments are characterised by fine-grained, grey-green, magnetite-bearing phyllite with a well-developed spaced cleavage (Oliver and Fanning, 1997). They are finely bedded and compositionally layered on a 1–10 mm scale. These compositional layers include aluminous pelite, psammite and layers that are very rich in Fe-oxide minerals. The Price Metasediments occur on aeromagnetic images as a prominent, north–south trending magnetic high in the southern Eyre Peninsula (Fig. 1). The chosen samples have been selected as representatives of comparatively magnetite-poor (sample 377514) and magnetite-rich layers (sample 377516) within the package. The abundances of magnetite and hematite were determined using point counting; abundances of the remaining minerals were determined using visual estimates.

3.1.1. Sample RS 377514: Magnetite-poor

Sample 377514 (53H 525844E 6159150S) is fine-grained with mineralogical layering defined by muscovite-rich and quartz-rich layers (Fig. 3a). Muscovite is abundant (~50 vol.% of the sample), and occurs as small flakes (commonly <10 μm) that define a weak foliation in some layers. Quartz is also abundant (~30 vol.% of the sample) and occurs as anhedral grains ~50 μm size. Magnetite comprises 6–8 vol.% of the sample and occurs as small euhedral crystals, ranging in size from 10–200 μm, distributed throughout the thin section. Small, ragged grains of hematite are much less common than magnetite (<0.5 vol.% of the sample). Garnet occurs throughout the rock as equant euhedral crystals ~10–50 μm in size and may contain fine-grained inclusions of magnetite. Biotite occurs in minor amounts as small flakes up to 100 μm in size that are commonly unoriented. Chlorite occurs as flakes that are aligned with the foliation, or adjacent to garnet and magnetite and along biotite cleavage planes. Plagioclase occurs in both the muscovite- and quartz-rich domains.

3.1.2. Sample RS 377516: Magnetite-rich

Sample 377516 (53H 529725E 6159716S) is compositionally layered, with layers 1–10 mm in width (Fig. 3b). The sample is dominantly comprised of inter-bedded pelitic and Fe-oxide-rich layers. The compositional layering is discordant to a weak foliation that is present in some layers. The pelitic layers have similar mineralogy to sample 377514 and are dominated by quartz and muscovite, with euhedral magnetite (100–200 μm) and less common hematite distributed throughout the layers. Biotite flakes (up to 100 μm), and subordinate chlorite, occur in contact with magnetite porphyroblasts. Small euhedral garnet grains (up to 100 μm) occur throughout the sample, but are more common in the pelitic horizons. The Fe-oxide-rich layers contain abundant magnetite and hematite (up to ~40 vol.% of the layer), small anhedral quartz grains and biotite flakes that occur in contact with magnetite. Magnetite is the dominant oxide in these layers and occurs as porphyroblasts (100–200 μm), whereas hematite occurs as smaller, elongate grains. The sample also contains an apatite-rich layer, as well as layers dominantly comprised of quartz and plagioclase. These layers also contain magnetite and small biotite flakes (50 μm) that define a weak foliation. Although the sample has lithological, and hence mineralogical, domains, on a thin section scale it contains ~15–16 vol.% Fe-oxides (approximately 70% magnetite to 30% hematite).

3.2. Warramboo gneisses

The magnetite-bearing units from the Warramboo deposit range from sparsely magnetite-bearing to magnetite-rich ore, but at the metre-scale all lithologies contain deformed K-feldspar–quartz ± plagioclase leucosomes and variable abundances of hematite and spessartine-rich garnets (Lane et al., 2015). Two samples from the Warramboo area (samples IRD204-27 and IRD204-29) and one sample from the Hambidge area (sample IRD190-10A2) were selected for modelling. The magnetite-bearing gneisses in the Hambidge area contain similar mineral assemblages to the gneisses from the Warramboo area but are variably retrogressed, with alteration of cordierite to pinite and replacement of feldspars in some samples. The abundances of magnetite and hematite were determined using point counting.

3.2.1. Sample IRD204-27

Sample IRD204-27 (53H 562340E 6321437S) was collected from exploration drill hole IRD204, depth interval 237.8–237.9 m. The sample contains interlayered Fe-oxide-rich pelitic and psammitic horizons and Fe-oxide poor quartzofeldspathic leucosomes on a scale from a few millimetres to 2 cm in thickness. The sample is very rich in magnetite and hematite, which together comprise ~30 vol.% of the sample (Fig. 3c).

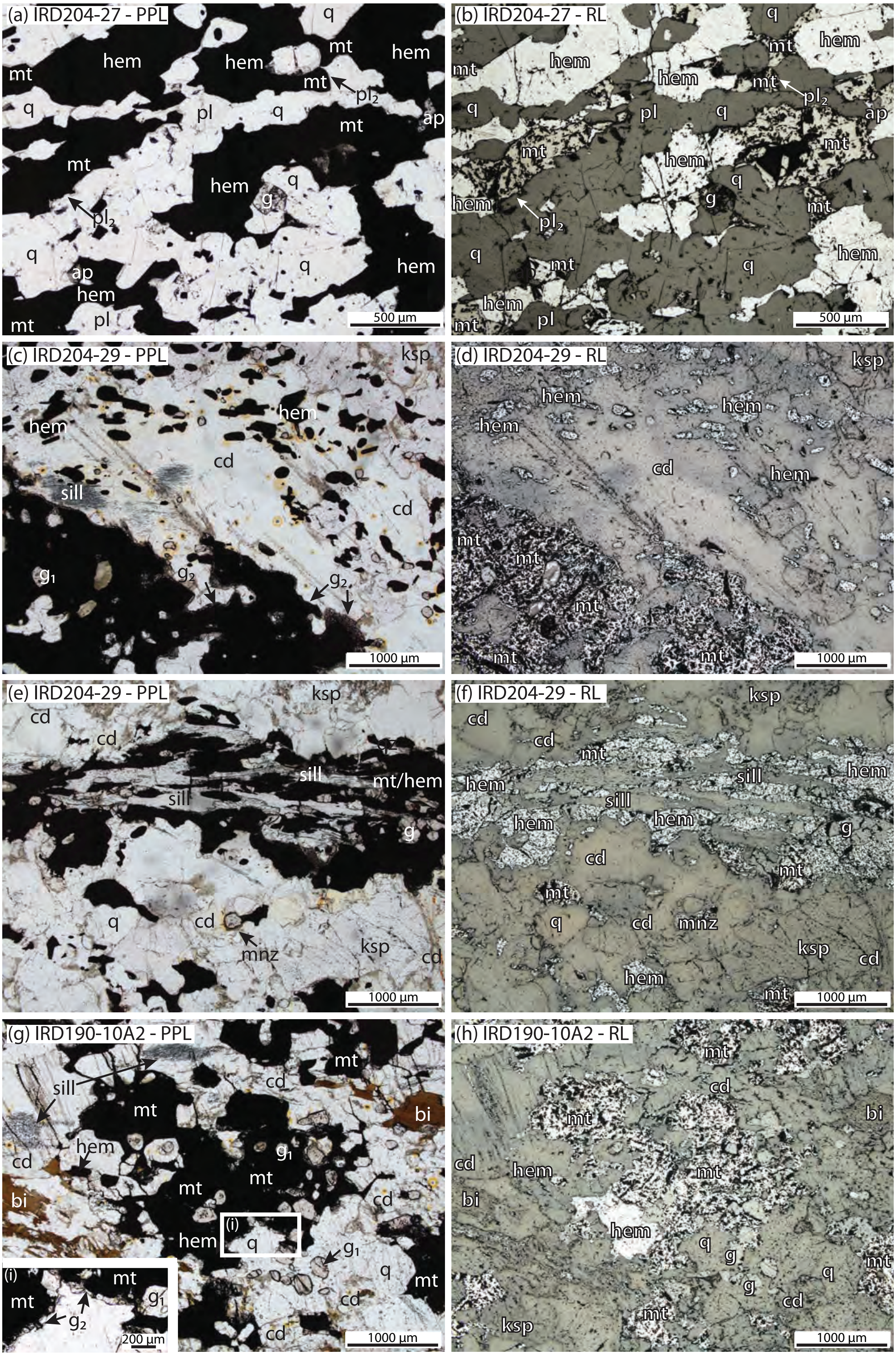
(a) IRD204-27 - PPL
(b) IRD204-27 - RL
(c) IRD204-29 - PPL
(d) IRD204-29 - RL
(e) IRD204-29 - PPL
(f) IRD204-29 - RL
(g) IRD190-10A2 - PPL
(h) IRD190-10A2 - RL
(i)
q
mt
hem
pl
pl2
ap
g
cd
sill
ksp
g1
g2
mt/hem
mnz
bi
500 µm
1000 µm
200 µm

Figure 4 (previous page): Photomicrographs showing representative mineral relationships. Each photomicrograph is shown in plain polarised light and reflected light. (a and b) sample IRD204-27: Fe-oxide-rich psamitic horizon, dominantly comprised of quartz, magnetite, hematite and minor plagioclase and garnet. Plagioclase coronas (pl_2) separate magnetite and quartz. (c and d) sample IRD204-29: fine-grained patches of sillimanite are included in cordierite and are common near magnetite/hematite. Euhedral garnet and cordierite are included in magnetite/hematite, and a second generation of garnet forms coronas on magnetite/hematite porphyroblasts. (e and f) sample IRD204-29: sillimanite associated with magnetite/hematite aggregates aligned with the gneissic foliation, euhedral garnet is also included in magnetite/hematite. Cordierite is abundant and partially envelops magnetite/hematite. (g and h) sample IRD190-10A2: euhedral garnet inclusions in magnetite/hematite. A second generation of garnet occurs as coronas on magnetite/hematite. Cordierite includes patches of aligned sillimanite and partially envelops magnetite/hematite. (i) Inset image in the bottom left corner of Fig. 4g, showing the secondary garnet coronas in more detail.

In the Fe-oxide-rich psammitic horizons, hematite and magnetite grains (<1 mm in diameter) occur in approximately equal proportions, together with abundant quartz, plagioclase, minor euhedral garnet (<100 μm) and rare apatite (Fig. 4a and b). Magnetite may be separated from quartz by thin coronae of plagioclase (Fig. 4a and b). The Fe-oxide-rich pelitic horizons are predominantly composed of cordierite, magnetite and hematite. Hematite is the dominant Fe-oxide and forms coarse grains up to 5 mm (Fig. 4a). Cordierite occurs as coarse-grained (up to 5 mm) porphyroblasts that contain inclusions of magnetite, elongate, euhedral hematite, patches of sillimanite and quartz. Fine-grained cordierite also occurs as inclusions in hematite. Small euhedral garnet grains occur throughout the pelitic layers in contact with magnetite and hematite. The sample contains biotite (<7 vol.% of the sample), that occurs at the interface between the pelitic and psammitic horizons as coarse-grained flakes up to 2 mm (Fig. 3c) and as anhedral grains associated with magnetite and hematite in the pelitic layers. The Fe-oxide-poor quartzofeldspathic leucosomes in this sample are ~3 mm in width and dominantly composed of K-feldspar and quartz with minor cordierite and rare plagioclase.

3.2.2. Sample IRD204-29

Sample IRD204-29 (53H 562340E, 6321437S) was collected from exploration drill hole IRD204, depth interval 284.9–285 m and contains magnetite, hematite, cordierite, garnet, K-feldspar, plagioclase, minor biotite and sillimanite (Fig. 3d). Magnetite and hematite occur in approximately equal proportions and together comprise 15–18 vol.% of the sample. Coarse-grained magnetite and hematite are commonly intergrown with quartz and sometimes finer-grained plagioclase (up to 500 μm), and may be enveloped by cordierite. Garnet is abundant and occurs throughout the sample as euhedral grains ~250 μm in diameter and also as coronae on coarse-grained magnetite and hematite. Cordierite is abundant and occurs as porphyroblasts (up to 1 cm) that include small, foliation-parallel hematite grains, patches of foliation-parallel sillimanite and horizons of euhedral garnet (Fig. 4c and d). The sample contains quartzofeldspathic leucosomes that are composed of coarse-grained microcline and perthitic K-feldspar (up to 3.5 mm in diameter), quartz (up to 1.5 mm) and variable amounts of plagioclase. Sillimanite is abundant and occurs as patches in cordierite (Fig. 4c and d) or as aligned aggregates with hematite and magnetite (up to 3 mm in length; Fig. 4e and f). Less commonly, it occurs as inclusions in quartz or K-feldspar or along grain boundaries of cordierite and quartz.

3.2.3. Sample IRD190-10A2

Sample IRD190-10A2 (53H 573640E, 6299430S) was collected from exploration drill hole IRD190, depth interval 237.6–241.76 m. This sample contains a gneissic foliation defined by magnetite–hematite-rich layers and quartzofeldspathic leucosomes (Fig. 3e). Small, euhedral garnet grains (250 μm, rarely up to 500 μm) occur in discrete layers commonly associated with magnetite and hematite (Fig. 4g and h). They may occur included in magnetite and hematite, cordierite and K-feldspar. Cordierite is abundant and contains patches of fine-grained sillimanite, which are commonly parallel to the gneissic fabric. The patches of fine-grained sillimanite included in cordierite are more abundant in the magnetite and hematite-rich layers, and in these layers cordierite commonly envelops magnetite and hematite. Cordierite also occurs within the quartzofeldspathic leucosomes, together with abundant perthite (up to 3 mm in diameter), quartz (up to 2 mm) and less common antiperthite and plagioclase (up to 750 μm). Magnetite and hematite are abundant (~13 vol.%, with magnetite the dominant oxide) and occur as euhedral grains that are parallel to the foliation (300–800 μm) and coarse anhedral porphyroblasts (up to 3 mm). Coarse-grained magnetite and hematite contain inclusions of garnet, quartz (~100 μm) and rare euhedral biotite and cordierite. A second generation of garnet occurs as thin (<50 μm) coronae on magnetite and hematite grains (shown in the inset image in Fig. 4g) and in places magnetite and hematite are separated from coarse-grained euhedral garnet by a corona of cordierite and garnet (Fig. 4g and h). Biotite forms anhedral flakes commonly associated with magnetite, hematite and garnet. It also occurs in domains as elongate grains (up to 1.5 mm in length and 250 μm in width), associated with elongate magnetite and hematite (Fig. 3e).

4. Metamorphic Modelling

Although it cannot be definitively proven that the magnetite-rich gneisses that form the Warramboo deposit and the sub-economic Price Metasediments are the same Fe-rich sequence, the similarity in depositional age, detrital zircon populations, enclosing basement and Nd isotopic composition between the two argues that they are part of the same sequence (Lane et al., 2015). The Warramboo gneisses contain quartzo-feldspathic leucosomes, suggesting they have melted. They also preserve

Table 1: Bulk rock compositions in weight % for pseudosection modelling.

	773514: Price Metasediments				773516: Price Metasediments				IRD: mt gneisses		
wt%	Protolith	ML1	ML2	ML3	Protolith	ML1	ML2	ML3	204-27	204-29	190-10A2
SiO_2	58.51	58.04	56.33	54.87	57.74	57.32	56.69	55.98	41.97	50.27	53.11
TiO_2	0.55	0.57	0.67	0.74	0.46	0.48	0.50	0.54	0.77	0.93	0.42
Al_2O_3	15.58	15.72	16.07	16.24	11.00	10.93	10.76	10.57	7.83	13.56	12.24
Fe_2O_3	7.75	8.16	9.49	10.50	14.55	15.19	16.09	16.91	39.70	19.91	15.50
FeO	6.05	6.36	7.42	8.18	7.13	7.43	7.86	8.27	4.20	6.29	8.63
MnO	0.81	0.86	1.00	1.11	0.83	0.86	0.91	0.96	0.38	2.08	1.04
MgO	2.30	2.42	2.82	3.11	1.61	1.68	1.78	1.87	2.82	2.89	2.30
CaO	0.68	0.69	0.70	0.67	1.25	1.29	1.34	1.38	0.56	0.75	1.07
Na_2O	0.84	0.69	0.41	0.32	1.47	1.38	1.26	1.18	0.33	0.78	1.13
K_2O	4.62	4.62	4.34	3.99	2.68	2.57	2.39	2.20	0.94	2.19	3.85
H_2O	2.31	1.87	0.76	0.30	1.28	0.88	0.41	0.14	0.50	0.35	0.70
$Fe_2O_{3(TOTAL)}$	14.48	15.23	17.74	19.59	22.47	23.45	24.83	26.10	44.36	26.90	25.09
Melt lost (mol%)	-	6.40	17.40	11.30	-	5.50	7.20	6.20	-	-	-

granulite facies mineral assemblages typical of aluminous metasedimentary rocks (i.e. garnet–cordierite–sillimanite-bearing; White et al., 2001) with little (<10 vol.%) biotite, and in general have compositions that are depleted in elements such as K_2O when compared to the Price Metasediments (Table 1; Oliver and Fanning, 1997). These features are consistent with melt loss from a sedimentary protolith during high-temperature metamorphism (e.g. Diener et al., 2008; Powell and Downes, 1990; White and Powell, 2002). The purpose of this study is to use the sub-economic Price Metasediments and their economic granulite facies equivalents as a case study to investigate the general process of Fe-oxide enrichment as a result of melt loss during high-grade metamorphism.

For the purposes of the phase equilibria modelling, mol.% and vol.% are approximately equivalent. The following abbreviations are used: g = garnet; pl = plagioclase; liq = silicate melt; ep = epidote; ksp = K-feldspar; bi = biotite; opx = orthopyroxene; cd = cordierite; mu = muscovite; chl = chlorite; mt = magnetite; ilm = ilmenite; hem = hematite; pa = paragonite; ab = albite; sill = sillimanite; and = andalusite; ky = kyanite; q = quartz.

4.1. Determining the conditions of metamorphism of the Price Metasediments–Warramboo system

Pressure–temperature pseudosections were calculated for samples 377514 and 377516 (Price Metasediments) and IRD204-27, IRD204-29 and IRD190-10A2 (Warramboo gneisses). *P–T* pseudosections for the samples were calculated using THERMOCALC v3.40, using the internally consistent dataset, ds62, of Holland and Powell (2011) and the activity–composition (*a–x*) models re-parameterised for metapelitic rocks in the MnNCKFMASHTO system (Powell et al., 2014; White et al., 2014a; White et al., 2014b), where 'O' is a proxy for Fe_2O_3. Whole-rock chemical compositions for the calculation of metamorphic phase equilibria were determined by crushing up a representative amount of each sample (100–200 g) and using a tungsten carbide mill. Bulk-rock chemical compositions were conducted by Franklin and Marshall College, Pennsylvania. Major elements were analysed by fusing a 0.4 g portion of the powdered sample with lithium tetraborate for analysis by XRF. Trace elements were analysed by mixing 7 g of crushed rock power with Copolywax powder and measurement by XRF. The whole rock chemistry for each sample used in the calculation of the mineral equilibria pseudosections is given as Supplementary Data S6.1.

The amount of H_2O and Fe_2O_3 in the bulk chemical composition that relates to the formation of the peak (i.e. maximum temperature) metamorphic mineral assemblages can be difficult to determine, due to hydration and oxidation during low-*T* processes such as weathering (e.g. Johnson and White 2011). The proportion of Fe_2O_3 to FeO for all samples was evaluated using T–M_O sections (see below) and was determined based on the proportion of magnetite to hematite. Subsolidus metamorphism is interpreted to involve aqueous fluid-present mineral assemblages, therefore the modelling of the Price Metasediments was done with water set in excess (i.e. always present across the subsolidus part of *P–T* space). Determining the appropriate amount of H_2O at peak conditions for granulite facies rocks is more problematic, as low-*T* retrogression and the presence of other volatiles such as CO_2, F and Cl means that the measured LOI may be an overestimation. Therefore, the H_2O content of the Warramboo gneisses during peak metamorphism was estimated based on the modal proportion of H_2O-bearing minerals (biotite and cordierite) and a conservative estimate of the H_2O content of these minerals (Deer et al., 1992; Rigby and Droop, 2011).

4.2. Modelling the effects of melt loss

The amount and composition of melt within a given rock is dependent on the *P–T* conditions and the initial bulk rock composition of the protolith, and may be modelled using a closed system (e.g. Johnson et al., 2008; Korhonen et al., 2010; White and Powell, 2002; Yakymchuk and Brown, 2014). However, the continental crust is an open system with respect to melt, whereby melt accumulates until it reaches a critical threshold and is then lost episodically from the source rock (Brown, 2010, 2013; Handy et al., 2001; Sawyer, 1994; Yakymchuk and Brown, 2014; Yakymchuk et al., 2013). A rock may experience a series of melt loss events throughout a single orogenic cycle, each of which modify the chemical composition and therefore fertility of the source rock (Brown, 2013; Korhonen et al., 2010; Vielzeuf et al., 1990; White et al., 2002; Yakymchuk and Brown, 2014). We investigate the effect of these melt loss events on the composition of the Price Metasediments using a series of *P–T* pseudosections and the interpreted peak conditions of the Warramboo deposit (as determined below). The amount of H_2O in the starting bulk composition is based on LOI, the amount of starting Fe_2O_3 was determined based on the proportion of magnetite to hematite (as above).

5. Results of Metamorphic Modelling

5.1. The effect of oxidation state

Before determining the likely *P–T* conditions of the Price Metasediments and the Warramboo deposit, it is necessary to explore the effect of variable oxidation state of the bulk rock composition on the mineralogy. The oxidation state of the rock composition can have a significant effect on the stability of mineral assemblages (e.g. Boger et al., 2012; Diener and Powell, 2010; Johnson and White, 2011; Johnson et al., 2008; Lo Pò and Braga, 2014; Morrissey et al., 2015). This is because highly oxidised rocks contain elevated levels of Fe_2O_3, which favours the stability of minerals like magnetite and hematite that sequester Fe, resulting in the growth of comparatively Mg–Al enriched minerals such as cordierite in the silicate-dominated part of the assemblage. Determination of Fe_2O_3 by titration may overestimate the amount of Fe_2O_3 in the bulk rock due to low-*T* oxidation during weathering, or oxidation during sample preparation for geochemical analysis (e.g. Johnson and White, 2011; Lo Pò and Braga, 2014). Therefore, the effect of varying the Fe_2O_3 amount was investigated using T–M_O sections for both samples of the Price Metasediments (samples 377514 and 377516), where $x = 0$ is equivalent to 1% of total iron being Fe_2O_3 and 99% being FeO; and $x = 1$ equivalent to 99% of total iron being Fe_2O_3 and 1% being FeO (Fig. 5). The T–M_O sections were calculated at pressures of 3 kbar to investigate the effect of oxidation state on the original greenschist facies assemblages, and at 6 kbar using the original protolith compositions above the solidus prior to melt loss.

For sample 377514, the magnetite–hematite-bearing fields occur between $M_O = 0.49$–0.80; similarly sample 377516 requires $M_O = 0.59$–0.90 (Fig. 5a and c). Varying the oxidation state within this interval does not significantly affect the total amount of these oxides, but does affect the proportion of magnetite to hematite. In highly oxidised compositions hematite is the dominant oxide, whereas magnetite is more abundant in less oxidised compositions.

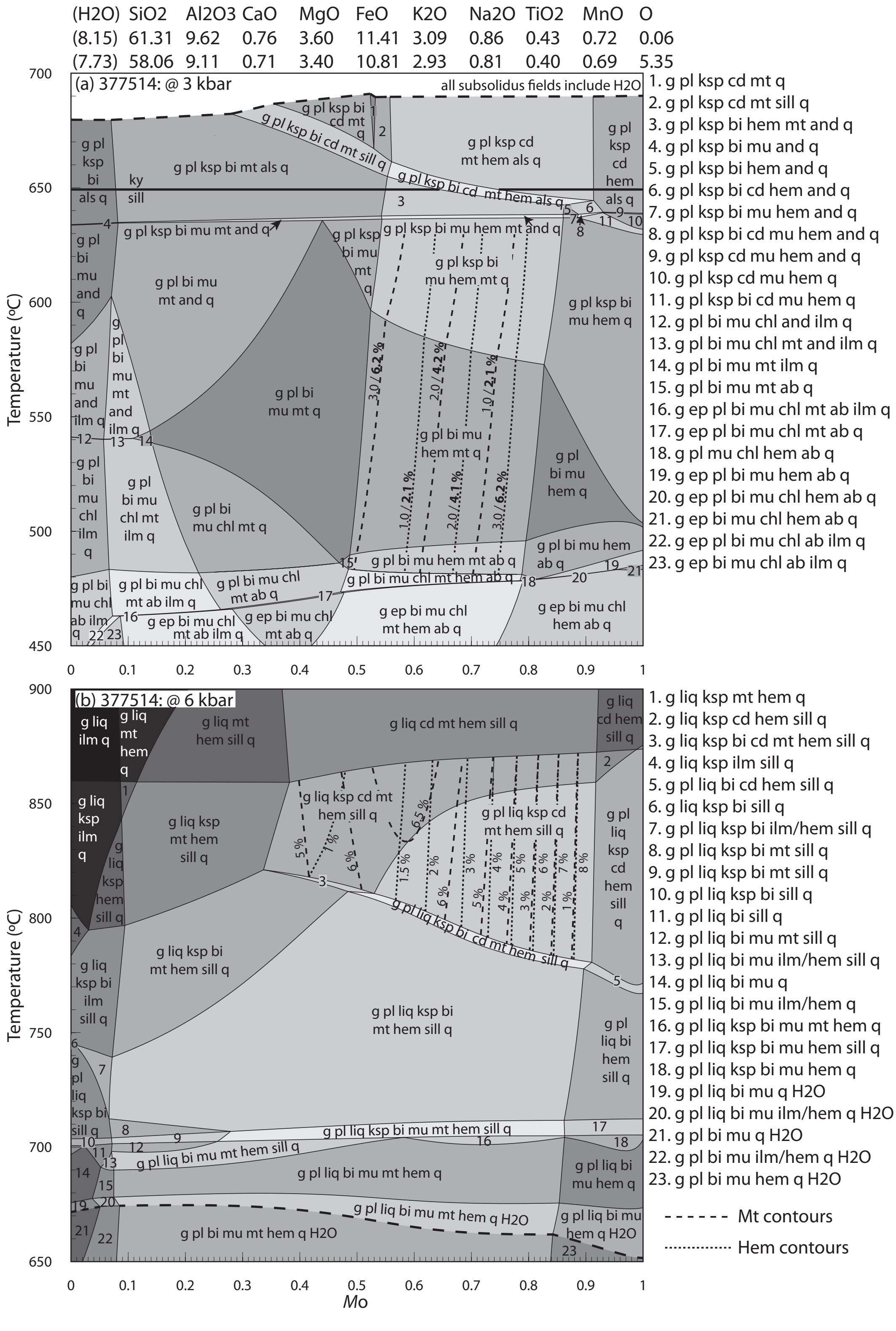

Figure 5: T–M_O sections for samples 377514 and 377516. The compositions are given above each pseudosection. At $x = 0$, 1% of total Fe is modelled to be Fe^{3+}, whereas at $x = 1$, 99% of total Fe modelled to be Fe^{3+}. The sections have been contoured for the proportion of magnetite to hematite. For the subsolidus sections with H_2O in excess, the amounts of magnetite and hematite are given including free water (regular text) and the absolute proportion not including free water (bold text). (a) Sample 377514, at 3 kbar, with H_2O in excess. (b) Sample 377514, at 6 kbar. (c) Sample 377516, at 3 kbar, with H2O in excess. (d) Sample 377516, at 6 kbar.

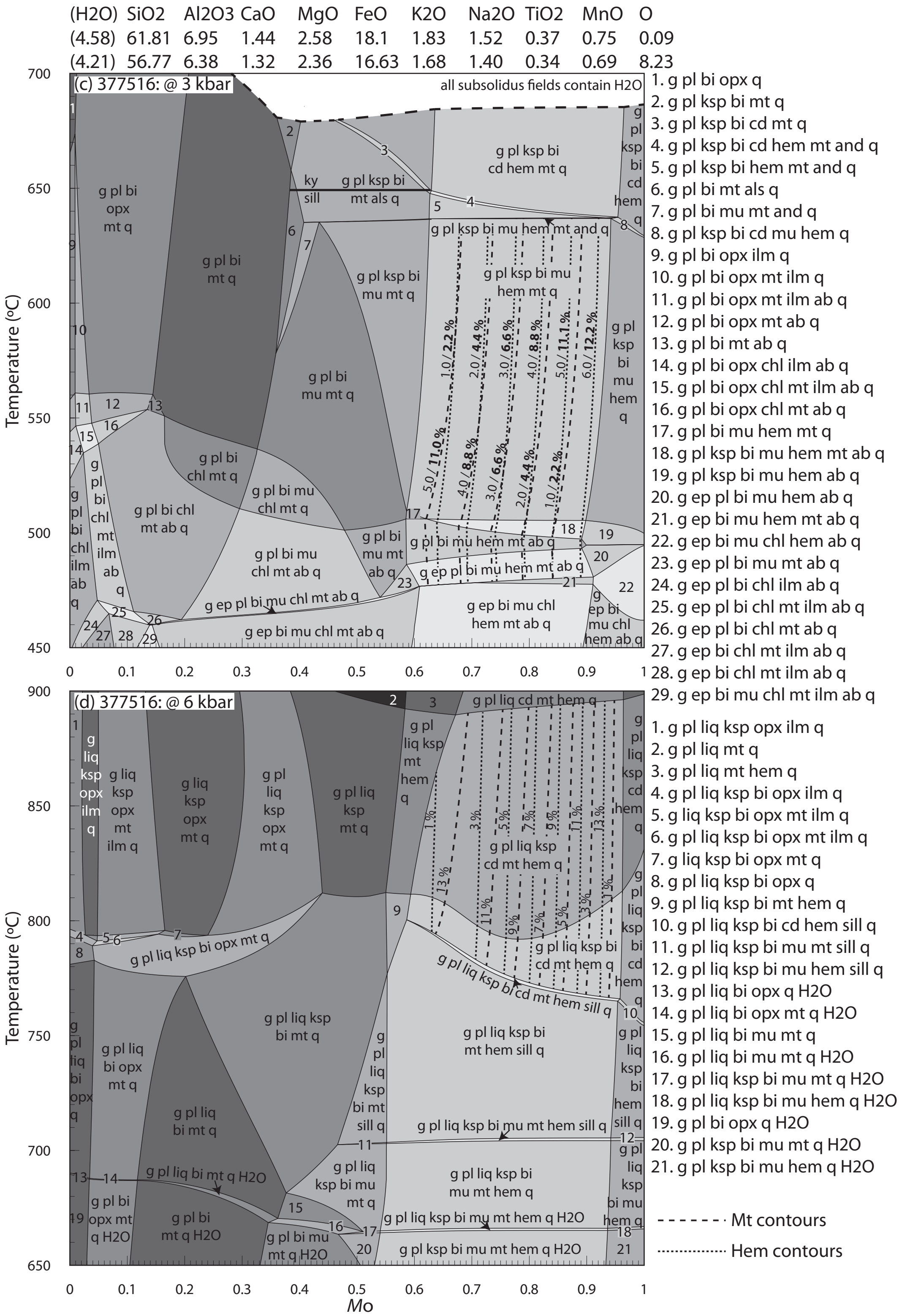

Figure 5 (continued).

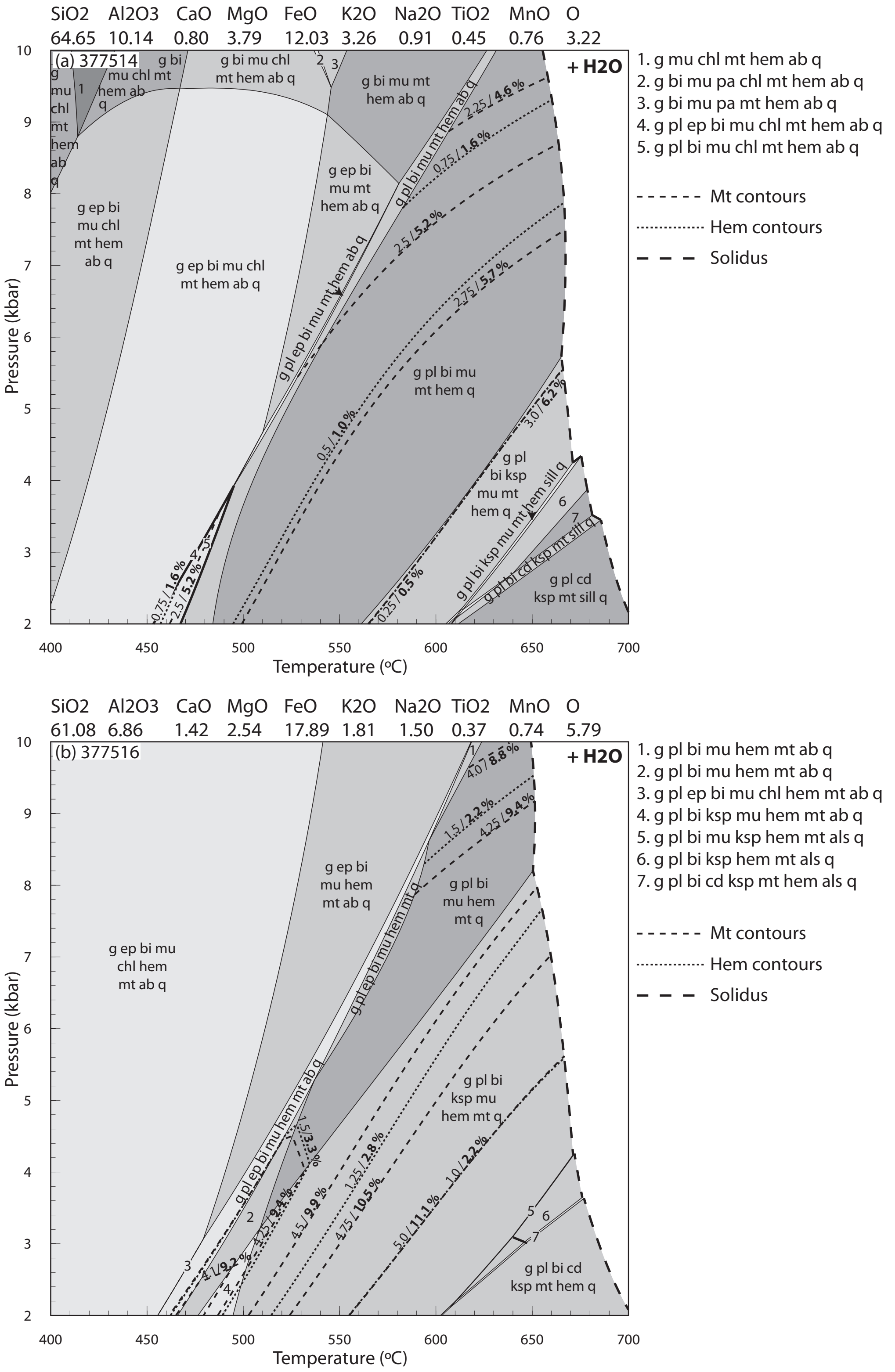

Figure 6: *P–T* pseudosections for the Price Metasediments. The composition in mol.% is given above each pseudosection. The pseudosections have been calculated with H_2O in excess. The bold dashed line is the solidus. The interpreted peak fields have been contoured for modal proportion of magnetite and hematite (in mol.%). The higher number (bold text) is the absolute proportion of magnetite and hematite, excluding free water as a phase. The second number (regular text) is the proportion of magnetite and hematite calculated with free water as a phase. (a) Sample 377514. (b) Sample 377516.

Within the magnetite–hematite field, varying the amount of Fe_2O_3 slightly affects the pressures and temperatures of the main silicate boundaries, but does not affect the stable phase assemblages.

5.2. Metamorphic conditions of the Price Metasediments

It is necessary to determine the pressure–temperature (*P*–*T*) evolution and conditions of metamorphism of the Price Metasediments and the Warramboo deposit to provide a framework for modelling the effects of melt loss.

5.2.1. Sample 377514

The peak metamorphic assemblage is interpreted as garnet, quartz, muscovite, hematite, magnetite, plagioclase, chlorite and minor biotite. This assemblage occurs in a narrow triangular field from ~450–470 °C and pressures less than 4 kbar (Fig. 6a). This assemblage is predicted to contain 5.2 mol.% magnetite and 1.6 mol.% hematite, excluding excess H_2O as a free fluid phase. With increasing temperature, the total amount of Fe-oxide minerals remains approximately constant at ~6.7 mol.%, but the proportion of magnetite to hematite increases with temperature (Fig. 7a). The total amount of Fe-oxides modelled (~6.8 mol.%) is consistent with observations (~6–8 vol.%; Fig. 3a).

5.2.2. Sample 377516

The peak metamorphic assemblage is interpreted as garnet, muscovite, magnetite, hematite, quartz, plagioclase and minor biotite. The absence of epidote and K-feldspar suggest that the mineral assemblage formed at 465–535 °C and 2–5 kbar (a narrow, triangular field in Fig. 6b, consistent with the conditions inferred for sample 377514). The mineral assemblage in this field is predicted to contain ~9.2–9.4 mol.% magnetite and ~3.3 mol.% hematite, excluding excess H_2O as a free fluid phase. The total amount of Fe-oxides modelled (12.5–13 mol.%) is broadly consistent with that observed (15–16 vol.%; Fig. 3b).

5.3. Metamorphic conditions of Warramboo deposit

5.3.1. Sample IRD204-27

The peak metamorphic assemblage is interpreted as garnet, plagioclase, K-feldspar, cordierite, magnetite, hematite, quartz and silicate melt. The presence of cordierite and absence of sillimanite constrains pressures to below 7.8 kbar (Fig. 7a). In this sample, the biotite-out boundary occurs at 840–850 °C. Biotite in this sample is typically anhedral and intergrown with magnetite–hematite or occurs at the interface between compositional domains, and therefore the majority of biotite is interpreted to be retrograde. At temperatures near the biotite-out boundary, the absence of orthopyroxene provides a lower pressure constraint of 5–5.5 kbar (Fig. 7a). The sample is modelled to contain 33–34 mol.% magnetite and hematite, consistent with the high proportion of Fe-oxide minerals observed in this sample (~30 vol.%; Fig. 3c).

5.3.2. Sample IRD204-29

The peak metamorphic assemblage is interpreted as garnet, plagioclase, K-feldspar, cordierite, magnetite, hematite, sillimanite (occurring as inclusions in cordierite, along grain boundaries with cordierite and as sillimanite–magnetite–hematite aggregates), quartz and silicate melt. This assemblage occurs over a wide range of conditions, from pressures of ~2.6–6.8 kbar and temperatures in excess of 770 °C (Fig. 7b). Biotite in this sample is not interpreted to be part of the peak assemblage. The peak field for this sample is modelled to contain 18–19 mol.% magnetite and hematite, in approximately equal proportions (Fig. 7b), consistent with the quantity of magnetite and

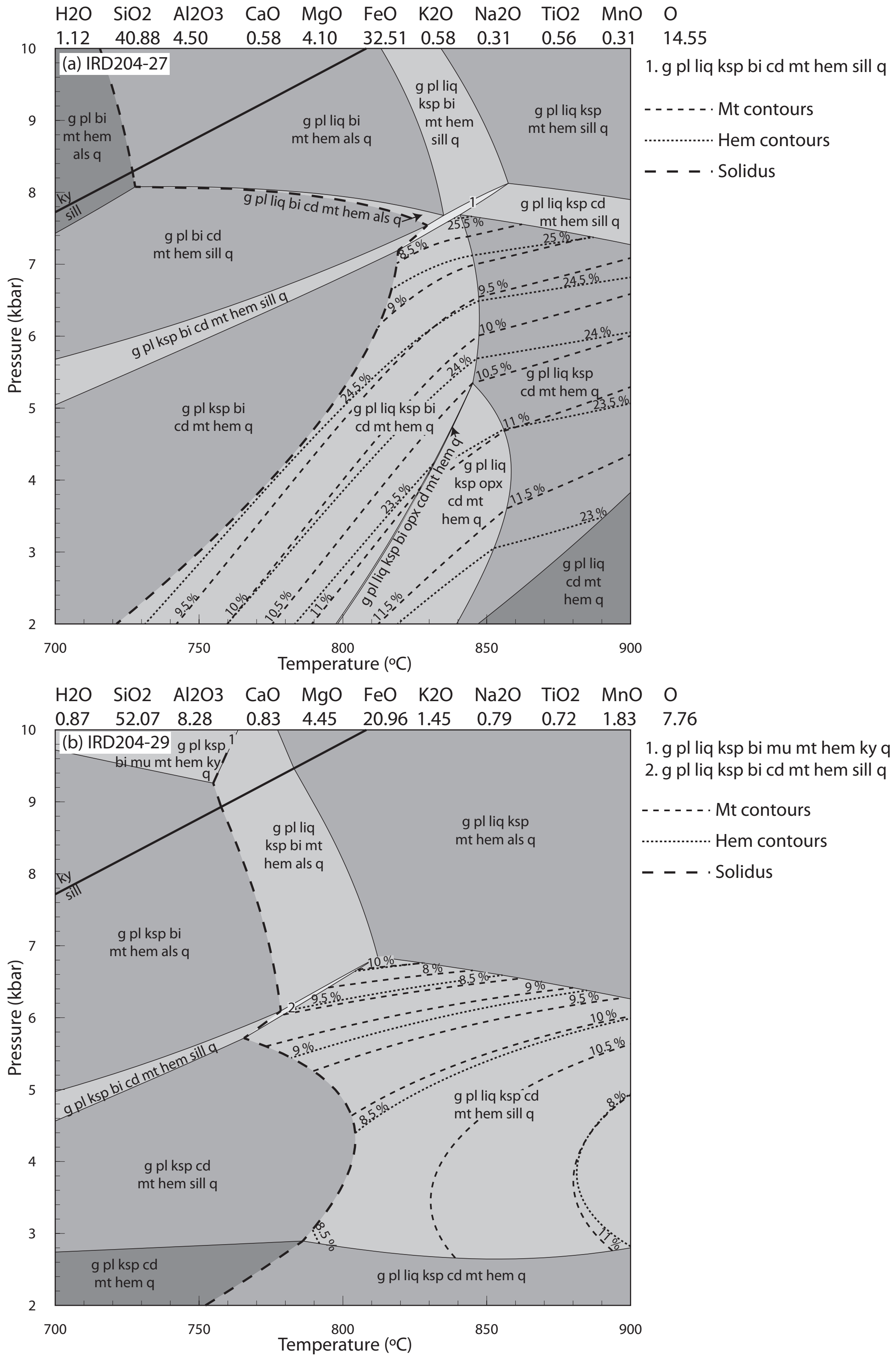

Figure 7: *P–T* pseudosections of the Warramboo gneisses. The composition in mol.% is given above each pseudosection. The solidus is denoted by a bold, dashed line. The interpreted peak fields are contoured for the proportion of magnetite and hematite (in mol.%). (a) Sample IRD190-10A2. (b) Sample IRD204-27. (c) Sample IRD204-29.

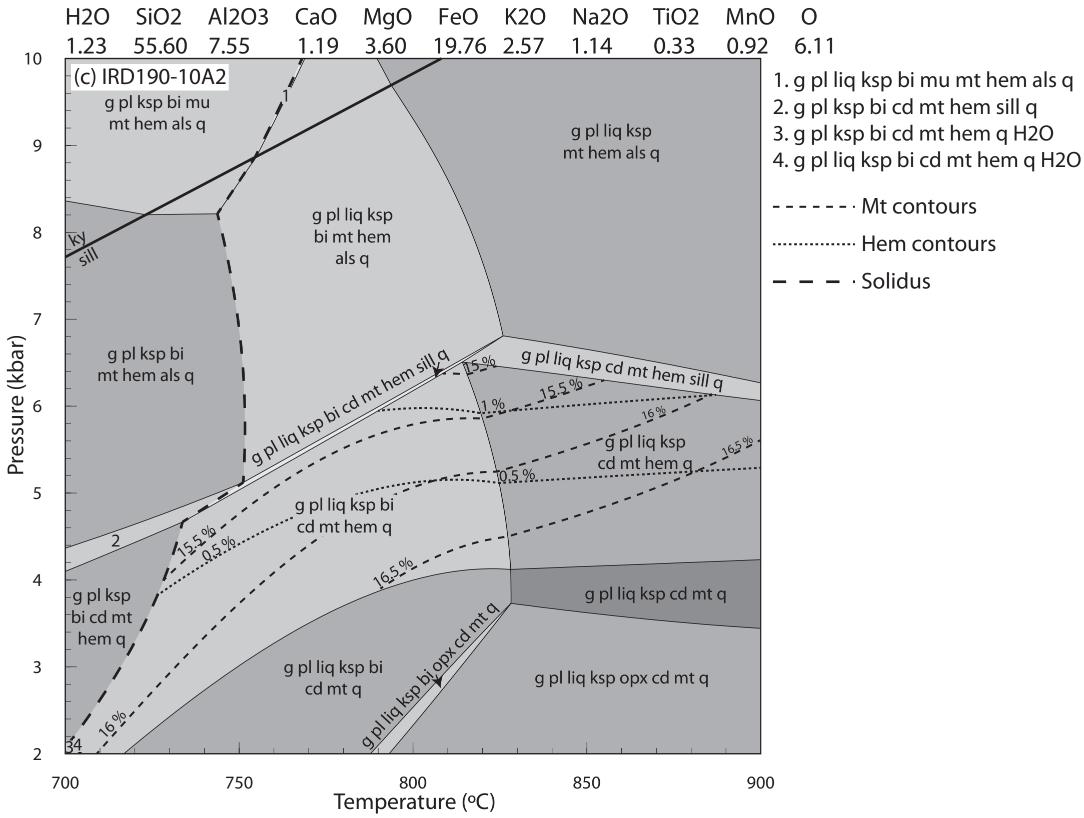

Figure 7 (continued).

hematite in observed in the rock (15–18 vol.%; Fig. 3d).

5.3.3. Sample IRD190-10A2

The peak metamorphic assemblage is interpreted as garnet, plagioclase, K-feldspar, cordierite, magnetite, hematite, quartz and silicate melt. The presence of cordierite and absence of sillimanite, except as inclusions in cordierite, suggests pressures were below 6.8 kbar (Fig. 7c). Biotite occurs as randomly oriented, anhedral flakes associated with magnetite–hematite as well as elongate grains that define the foliation in some parts of the sample, together with elongate magnetite–hematite. The ambiguity in the textural interpretation of biotite means that temperatures for the peak assemblage are poorly constrained. However, the general paucity of biotite in this sample (Fig. 3e) suggests that peak temperatures were near the biotite-out boundary, at 815–830 °C (Fig. 7c). The amount of magnetite modelled in the peak field in this sample (either with or without biotite) is 15–16.5 mol.%, whereas the amount of hematite is < 1 mol.%. The sample contains 13 vol.% Fe-oxides (Fig. 3e) with magnetite the dominant oxide, consistent with the modelling.

5.4. Overall P–T evolution and conditions of the Price Metasediments–Warramboo system

The modelling of the Price Metasediments suggests metamorphism reached temperatures of ~460–470 °C. Peak pressures are poorly constrained but were less than 4 kbar (Fig. 6). This corresponds to an overall thermal gradient in excess of 115 °C/kbar. The mineral assemblages in the Warramboo gneisses occur over a large range of *P–T* conditions, but peak conditions are interpreted to be 830–850 °C and 5–6.8 kbar (Fig. 7), corresponding to a similar thermal gradient in excess of

120 °C/kbar. The prograde *P–T* path of the Warramboo gneisses is not well defined. The presence of aligned sillimanite inclusions in cordierite in several samples, together with the observation that cordierite contains inclusions of magnetite, hematite and garnet, suggests that the earlier evolution may have occurred outside the cordierite stability field and therefore involved higher pressures and/or lower temperatures (Fig. 7). The similar thermal gradient throughout the Warramboo–Price Metasediment system suggests a prograde evolution that necessarily involved increasing temperatures with increasing crustal depth. However, any quantitative inferences about the prograde history are necessarily poorly constrained because the current residual bulk composition of the rock is not appropriate for modelling the prograde history (e.g. Johnson and White, 2011; Kelsey and Hand, 2015; Korhonen et al., 2013; White and Powell, 2002). The difficulty in constraining the prograde history, combined with the high thermal gradient that involves large changes in temperature relative to pressure, means that for the purposes of modelling melt loss we have assumed a (simplified) isobaric heating path. A pressure of 6 kbar is used for the isobaric heating path, so that it intersected the interpreted peak conditions of the Warramboo deposit (Fig. 7).

5.5. Modelling the effects of prograde metamorphism and melt loss using the Price Metasediments

Forward modelling in a closed (i.e. isochemical) system using the compositions of the samples of Price Metasediments suggests that they are capable of producing the magnetite–cordierite–K-feldspar-bearing assemblages observed in the Warramboo gneisses at conditions similar to those inferred for the Warramboo deposit (Figs. 8a and 9a). However, the amount of melt modelled to be present in these assemblage fields in the closed system situation is ~50 mol.% (Figs. 8a and 9a), which is rheologically impossible. Instead, melt was likely to have been lost via a series of melt loss events during prograde metamorphism. Three melt loss events were modelled to occur; the first is just up-temperature of the wet solidus, and the second and third are just up-temperature of the terminal muscovite and biotite breakdown-reactions where large volumes of melt are produced over a small temperature interval (shown as stars in Figures 8 and 9; Clemens, 2006; Redler et al., 2013; White and Powell, 2002). Melt loss events were modelled by removing all but 1 mol.% of melt (interpreted to be the amount of melt retained on grain boundaries; Holness and Sawyer, 2008). After the removal of melt, another *P–T* pseudosection was calculated using the new composition (Table 1; Figs. 8b–d and 9b–d). This procedure was repeated after each melt loss event.

There are minor mismatches between the positions of some reaction boundaries in the subsolidus versus suprasolidus forward models, due to differences in the subsolidus and suprasolidus magnetite *a–x* models (White et al., 2002; White et al., 2000; White et al., 2014b). These differences prevent a direct comparison of the modal proportions of magnetite and hematite between the subsolidus and suprasolidus modelling. Importantly however, the effect of episodic melt loss on the modal proportions of these minerals at the interpreted peak conditions can be directly compared (Figs. 8 and 9). The bulk compositions and proportion of melt removed after each melt loss event are summarised in Table 1.

5.5.1. Sample 377514

At the peak conditions inferred for the Warramboo deposit, the total amount of melt

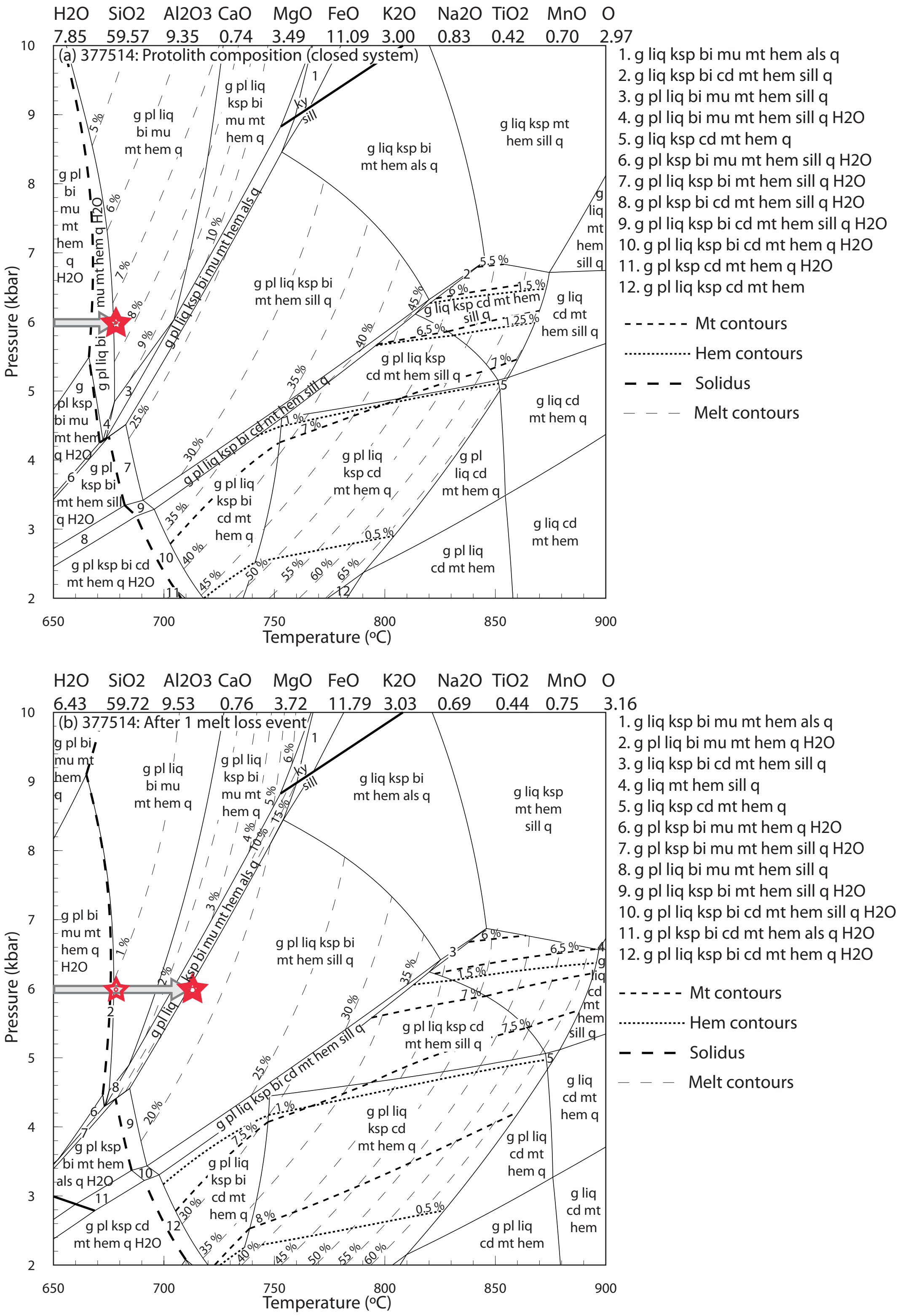

Figure 8: *P–T* pseudosections modelling melt loss events for sample 377514. The composition in mol.% is given above each pseudosection. The bold dashed line is the solidus, whereas the fine dashed lines represent contours of modal proportion of melt. The interpreted peak fields are contoured for the modal proportion of magnetite and hematite (in mol.%). The grey arrow is the inferred isobaric heating path at 6 kbar and the stars mark the *P–T* conditions of each melt loss event. (a) Closed system situation (no melt loss) using the original composition. (b) After one melt loss event. (c) After two melt loss events. (d) After three melt loss events.

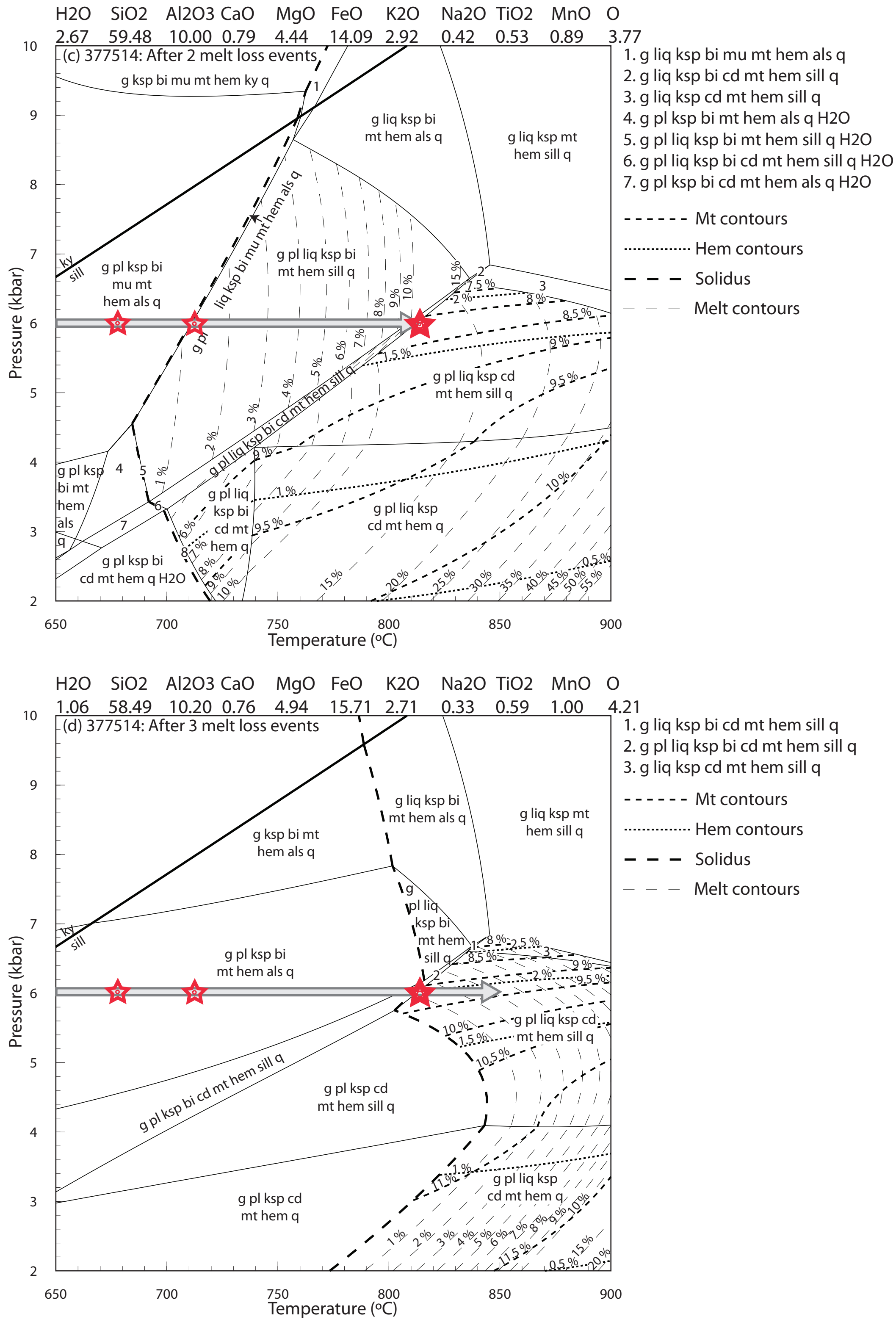

Figure 8 (continued).

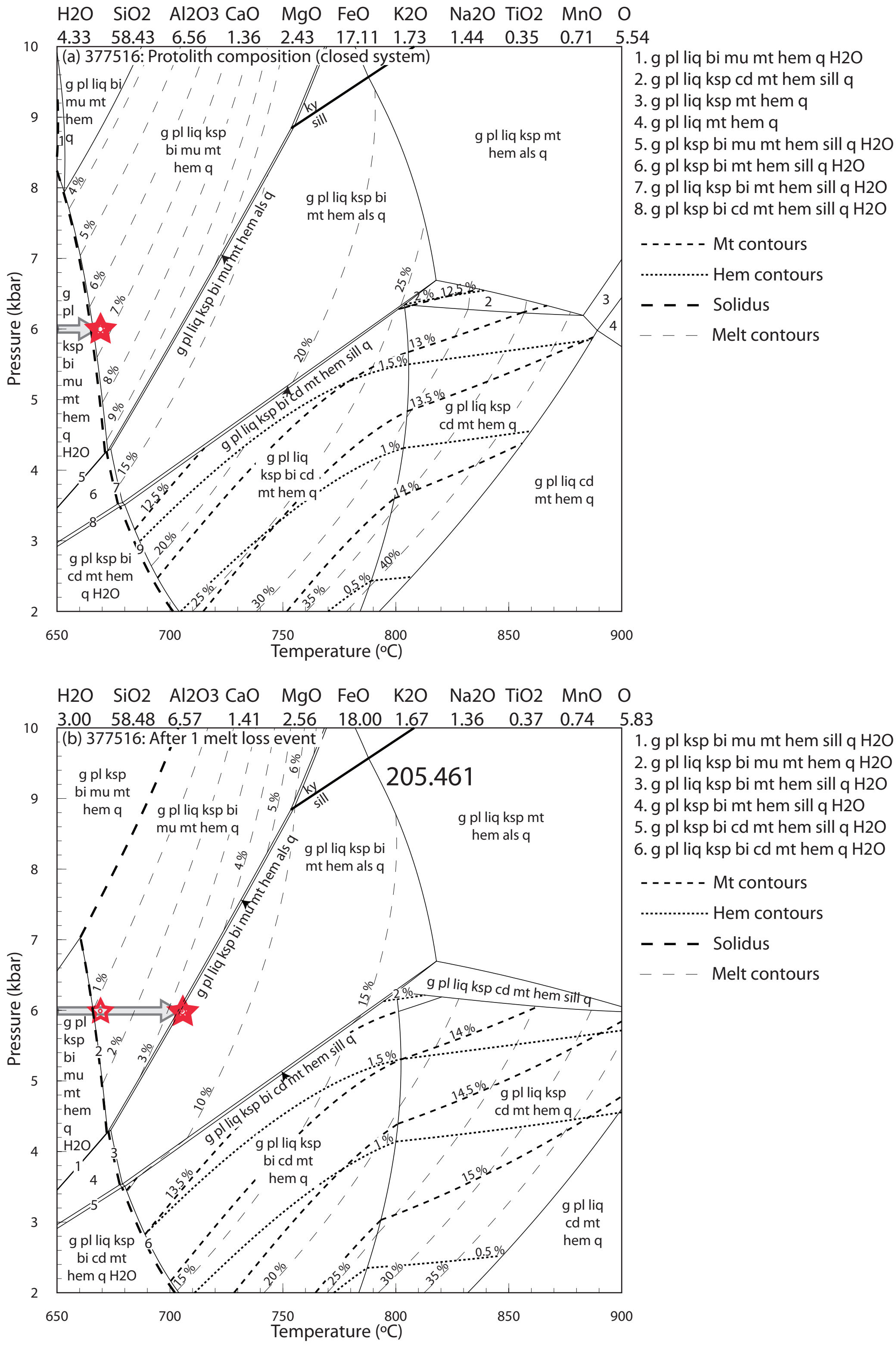

Figure 9: *P–T* pseudosections modelling melt loss events for sample 377516. The composition in mol.% is given above each pseudosection. The bold dashed line is the solidus, whereas the fine dashed lines represent contours of modal proportion of melt. The interpreted peak fields are contoured for the modal proportion of magnetite and hematite (in mol.%). The grey arrow is the inferred isobaric heating path at 6 kbar and the stars mark the *P–T* conditions of each melt loss event. (a) Closed system situation (no melt loss) using the original composition. (b) After one melt loss event. (c) After two melt loss events. (d) After three melt loss events.

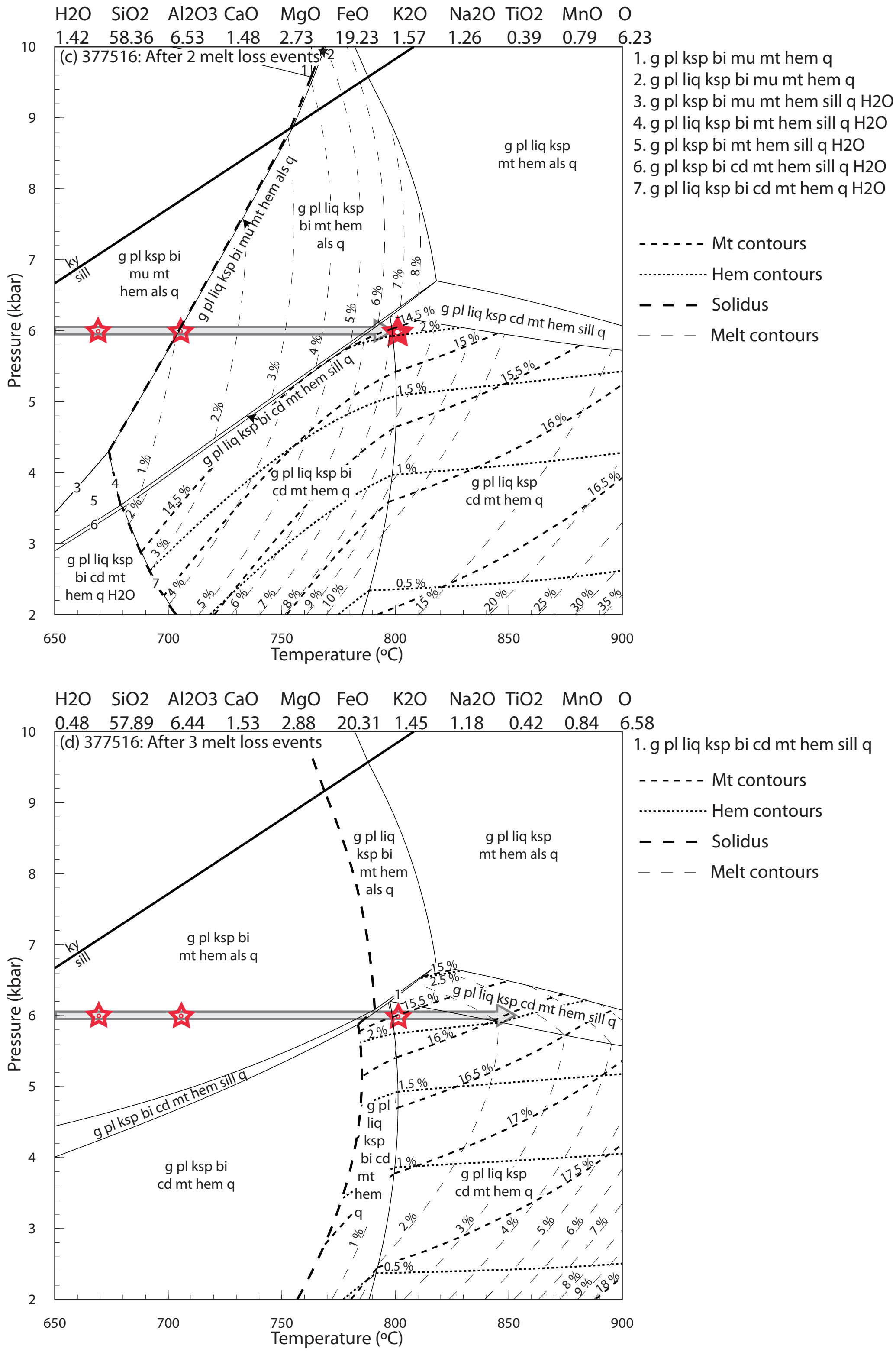

Figure 9 (continued).

that can be produced using the composition of 377514 in a closed system is ~50–65 mol.% (Fig. 8a). However, if melt is removed episodically along the prograde evolution when the rock crosses the terminal H_2O, muscovite and biotite boundaries, the total cumulative amount of melt that can be produced by the time the rock reaches the interpreted peak conditions is 35–40 mol.% (Table 1; Fig. 8d). At the interpreted peak conditions, the original 'closed system' composition of sample 377514 produces 6–7 mol.% magnetite and 1–1.5 mol.% hematite (Fig. 8a). After three melt loss events, approximately 35 mol.% melt is modelled to have been removed from the composition (Table 1). The resulting amount of magnetite modelled to be present at the peak conditions increases to 8.5–10.5% and the amount of hematite increases to 1.5–2.5 mol.% (Fig. 8d). Therefore, at the peak metamorphic conditions for the Warramboo deposit, sample 377514 shows a relative increase in total Fe-oxides from 7.5–8 mol.% to 11.5–12 mol.% as a result of three melt loss events, equivalent to a relative increase of ~35%. The relative amount of $Fe_2O_{3(TOTAL)}$ in the bulk composition increases by 35%, from 14.48 to 19.59 wt% (Table 1).

5.5.2. Sample 377516

At the interpreted peak conditions of the Warramboo deposit, the amount of melt that can be produced in a closed system using the original composition of sample 377516 is ~30–40 mol.% (Fig. 9a). The original 'closed system' composition is modelled to produce 12.5–13.5 mol.% magnetite and ~1.25–2 mol.% hematite at peak conditions (Fig. 9a). After three melt loss events, approximately 19 mol.% melt has been removed from the composition and the amount of magnetite and hematite modelled to be present at the peak conditions increases to 15.5–16.5 mol.% and 1.5–2.5 mol.% respectively (Fig. 9d). Therefore, sample 377516 is modelled to show an increase in the total amount of Fe-oxides at peak conditions from ~14–14.5 mol.% to ~18 mol.% as a result of melt loss, equivalent to an increase of ~25%. The relative amount of $Fe_2O_{3(TOTAL)}$ in the bulk composition increases 16%, from 22.47 to 26.10 wt.% (Table 1).

6. Discussion

6.1. Implications for the generation of magnetite ore during metamorphism

Both the Price Metasediments and Warramboo magnetite-bearing gneisses display compositional heterogeneity on the metre to millimetre scale (Fig. 3). Therefore, the variation in iron oxide amounts in the Warramboo and Hambidge samples is likely to relate to differences in composition inherited from the original protoliths. The modelling suggests that the amount of $Fe_2O_{3(TOTAL)}$ in the bulk composition of the relatively iron-rich, muscovite-poor sample of Price Metasediments (sample 377516) can be increased by melt loss to values similar to samples IRD190-10A2 and IRD204-29 (in the range 25–27 wt.% $Fe_2O_{3(TOTAL)}$; Table 1). This provides support for the inference that the magnetite gneisses at Warramboo are correlatives of the Price Metasediments (Lane et al., 2015), and suggest that granulite facies metamorphism is a plausible mechanism to significantly upgrade sub-economic iron occurrences.

Metasedimentary rocks such as the Price Metasediments–Warramboo system are likely to contain interbedded pelitic and iron-rich psammitic layers, which together comprise the overall resource. Price Metasediments sample 377514 is modelled to cumulatively produce more melt during metamorphism to ~850 °C than sample 377516 (35 mol.% compared to 19 mol.%; Table 1). The larger volume of melt

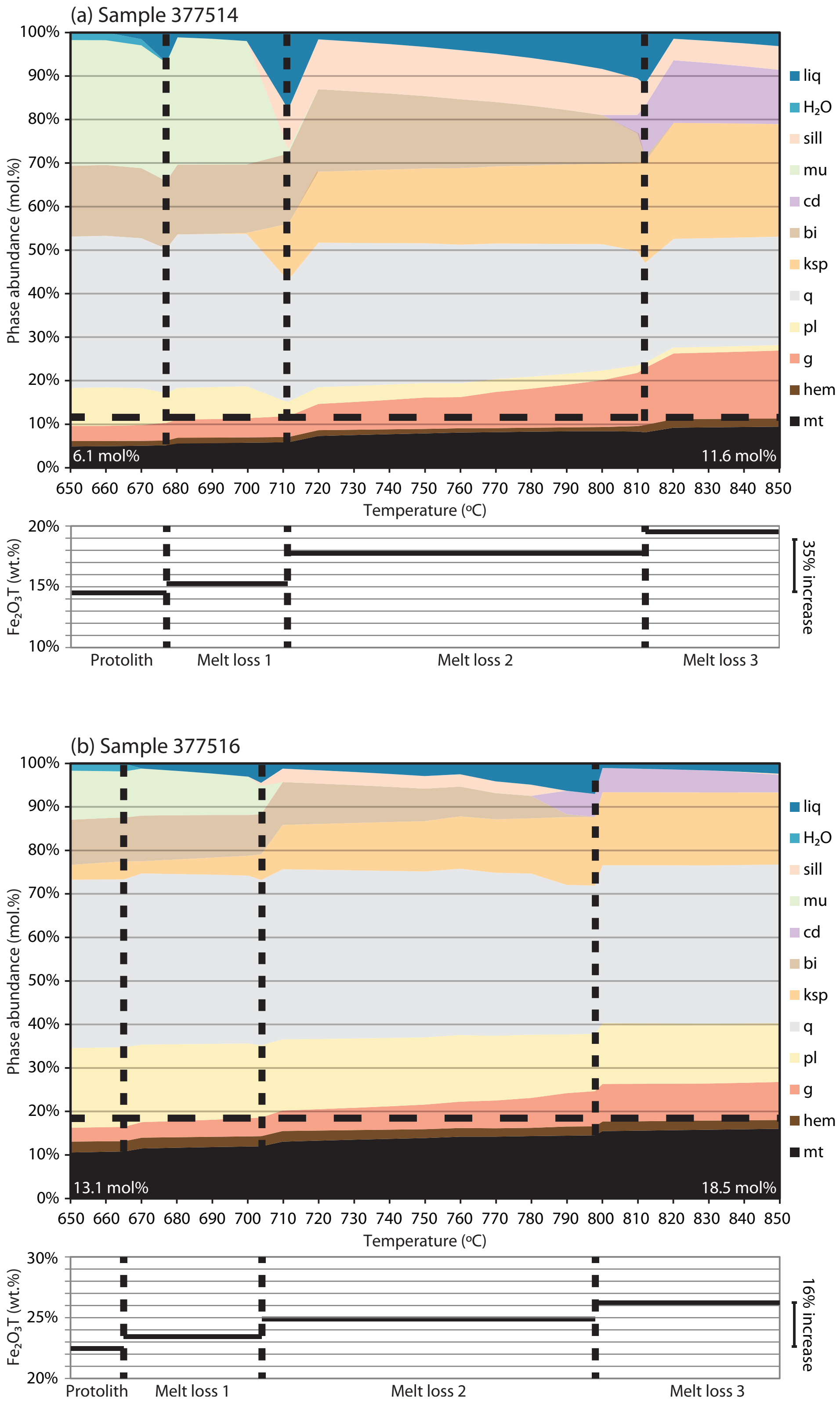

Figure 10: Change in mole proportion of phases as a function of temperature and melt loss along a prograde isobaric heating path from 650 to 850 °C. The vertical bold dashed lines represent melt loss events. The white numbers give the total abundance of magnetite and hematite in mol.%, and the horizontal dashed line illustrates the increased abundance along the isobaric heating path. The amount of $Fe_2O_{3(TOTAL)}$ in the bulk composition along the prograde path for each sample is shown below. (a) Sample 377514. (b) Sample 377516.

in sample 377514 reflects its higher proportion of muscovite (e.g. Brown, 2010; Patiño Douce and Harris, 1998; Vielzeuf and Holloway, 1988; White and Powell, 2002) compared to sample 377516. Sample 377514 also shows a more significant increase in the amount of $Fe_2O_{3(TOTAL)}$ in the bulk composition, with melt loss able to increase the amount of $Fe_2O_{3(TOTAL)}$ in the melt-depleted residuum by ~35%, as opposed to ~16% for the less melt-fertile sample 377516 (Fig. 10; Table 1). Packages that are originally rich in iron and more psammitic such as sample 377516 produce less melt than more pelitic compositions at any fixed temperature, and therefore experience a less significant increase in $Fe_2O_{3(TOTAL)}$ in the melt-depleted residuum. Therefore, the modelling suggests that whereas melt loss may not significantly enrich the horizons that were already enriched in iron but comparatively deficient in mica, melt loss from the more pelitic layers serves to improve iron contents in what would otherwise (at low metamorphic grades) have been very low value parts of the deposit system, thereby improving the overall size of the resource.

Metamorphism is also a mechanism to increase the abundance of Fe-oxide minerals by increasing temperatures. Figures 8 and 9 illustrate the increasing proportion of magnetite and hematite at peak conditions, as a function of changing composition. Figure 10 illustrates the combined effect of prograde heating from 650–850 °C and melt loss on the proportion of the phases and the amount of total iron ($Fe_2O_{3(TOTAL)}$) in the melt-depleted rock. It suggests that increasing temperature as well as compositional changes as a result of melt loss both play a role in increasing the proportion of iron oxides. The effect of both isobaric heating and melt loss in sample 377514 is to significantly increase the sum amount of magnetite and hematite from 6.1 to 11.6 mol.% (Fig. 10a), whereas the sum amount of magnetite and hematite in sample 377516 increases from 13.1 to 18.5 mol.% (Fig. 10b). In addition, high-grade metamorphism will typically increase grain size, improving crushing and concentration processes.

6.2. Limitations of the modelling

One of the main limitations of the *P–T* modelling discussed above is that some of the components commonly occurring in natural rocks, such as ZnO, Cr_2O_3 and P_2O_5, cannot be effectively modelled in the currently available thermodynamic system. The whole rock chemistry shows that the samples in this study are also rich in MnO (0.37–2.06 wt.%; Table 1). The current Mn-bearing activity–composition (*a–x*) models have been developed for metapelitic rocks containing typical amounts of MnO (<0.3 wt.%), and therefore they may not be reliable for the MnO-rich rocks in this study (White et al., 2014b). The *a–x* models for hematite, garnet, cordierite, and biotite (and chlorite, subsolidus) incorporate Mn, and in particular, Mn exerts an important influence on the stability of garnet (e.g. Boger and Hansen, 2004; Johnson et al., 2003; Mahar et al., 1997; Tinkham and Ghent, 2005; Tinkham et al., 2001; White et al., 2014b). However, the *a–x* model for magnetite does not incorporate Mn (White et al., 2002; White et al., 2000), and therefore modelling using the current *a–x* models may underestimate the amount of magnetite by artificially stabilising minerals such as garnet, which sequester Fe, in the calculations. In addition, both the Price Metasediments samples and sample IRD204-27 contain small amounts of apatite, which affects the calcium budget of the rock, but cannot be modelled in the MnNCKFMASHTO system (or any other system currently). The presence of abundant monazite in some samples means that the effect of apatite cannot be easily accounted for using the amount of P_2O_5 in the bulk composition. Therefore, this limitation may artificially stabilise Ca-bearing phases such as garnet and plagioclase in the calculations.

In applying the results specifically to the Price Metasediment–Warramboo system, there is some uncertainty in modelling melt loss as the prograde *P–T* path is poorly constrained, and therefore determining the number of likely melt loss 'events' is difficult. An isobaric heating path at 6 kbar was selected as a proxy for the 'flat' apparent thermal gradient recorded by the low- and high-temperature samples, as it intersected cordierite-bearing fields at the interpreted peak conditions. A different pressure evolution would produce slightly less melt at higher pressure and slightly more melt at lower pressure. The crossing of the wet solidus and the main hydrate breakdown reactions have been used as a proxy for melt loss events. In the case of the muscovite-breakdown reaction, this means that up to 19 mol.% melt was modelled to be present in the rock prior to melt loss (Figs. 8 and 9). However, in a static system, melt loss has been interpreted to occur when the melt connectivity threshold is exceeded, at ~7% melt (Rosenberg and Handy, 2005). In a system that is undergoing deformation, this threshold is likely to be much lower, and melt loss may even be continuous (e.g. Brown, 2010; Handy et al., 2001; Johnson et al., 2011). Therefore, due to the uncertainties in constraining the *P–T* path and the threshold of melt loss applicable to the Price Metasediment–Warramboo system, the modelling in this study is likely to underestimate the number of melt loss events. An increased number of melt loss events is likely to produce slightly less cumulative melt overall, as each melt loss event makes the remaining rock more residual and more difficult to melt (e.g. Brown, 2013; Vielzeuf et al., 1990; White and Powell, 2002). However, these uncertainties are not interpreted to significantly affect the relationship between melting and the proportion of iron in the residual rock.

6.3. Implications for exploration for magnetite-rich iron ore deposits

Most large magnetite deposits are interpreted to form as a result of primary igneous processes (e.g. Naslund et al., 2002; Nystroem and Henriquez, 1994), deposition of iron oxides as a result of secondary hydrothermal processes (e.g. Dare et al., 2015; Kalczynski and Gates, 2014; Puffer and Gorring, 2005; Sillitoe and Burrows, 2002), or a combination of the two (Knipping et al., 2015). There are comparatively few examples of magnetite deposits analogous to the Warramboo deposit, where mineralisation is hosted in a Fe-rich, clastic sediment (e.g. Lupulescu et al., 2014; Mücke, 2005; Palmer, 1970; Tyler et al., 2014). However, recognition of this deposit type may have important implications for iron ore exploration in high temperature (>650–700 °C) metamorphic terranes that have undergone partial melting. Similar magnetite deposits that are hosted in granulite facies metasedimentary rocks include the Benson Mine in the Grenville Orogen (Lupulescu et al., 2014; Palmer, 1970) and the Southdown magnetite deposit in the Albany–Fraser Orogen in Western Australia (Tyler et al., 2014). The Benson Mine was proposed to have formed by metamorphism of pelitic sediment (Lupulescu et al., 2014; Palmer, 1970). Although there are no modern metamorphic *P–T* constraints, the surrounding rocks have been migmatised (Palmer, 1970) suggesting that combined metamorphism and melt loss may have been the mechanism for creating and upgrading this deposit. Similarly, the Southdown magnetite deposit is hosted in granulite facies gneisses and has been interpreted to have been an Fe-rich sediment that experienced two phases of high temperature metamorphism (Tyler et al., 2014).

Therefore, the combination of increased grain size and increased Fe-oxide contents linked to melt loss makes high-temperature metamorphic terranes attractive targets for magnetite-dominated iron ore deposits. The modelling suggests that the proportion of magnetite to hematite increases towards higher temperatures and lower pressures (Figs. 7–9). Therefore, low pressure, high temperature terranes may be more prospective for magnetite-dominated rather than hematite-dominated iron ore deposits. Combining regional geophysical techniques such as aeromagnetic imagery with an understanding of the metamorphic conditions of a terrane (particularly with respect to the melting and melt loss history) may be a powerful tool for exploration.

7. Conclusions

Phase equilibria forward modelling suggests that melt loss associated with progressive metamorphism, culminating in granulite facies conditions is a mechanism to enrich the Fe-oxide content of metasedimentary rocks. The specific extent of enrichment is controlled by the melt fertility of the rock. For the Price Metasediments, the combined effect of metamorphism and melt loss from muscovite-rich horizons with more melt-fertile compositions increases the total amount of Fe-oxides from ~6 mol.% to 11.5 mol.%, equivalent to a relative increase of ~90%. The relative amount of $Fe_2O_{3(TOTAL)}$ in the bulk composition increases by ~35% as a result of melt loss. More Fe-rich, muscovite-poor horizons produce less melt and therefore do not show the same increase, with the total amount of Fe-oxides increasing ~40%, from 13 mol.% to ~18.5 mol.%, and the relative amount of $Fe_2O_{3(TOTAL)}$ in the bulk composition increases 16%. Varying the oxidation state of a rock does not significantly affect the amount of Fe-oxides at granulite facies, but it does affect the proportion of magnetite to hematite. The results of this work suggest that melt loss is a realistic mechanism to improve the overall ore grade within metamorphic iron ore deposits.

Acknowledgements

Stan Mertzman is thanked for the geochemical analyses. Chris Yakymchuck and Tim Johnson are thanked for their constructive reviews. Iron Road is thanked for providing the samples for this study. IronRoad and the Geological Survey of South Australia are thanked for providing funding. This manuscript forms TRaX record # 337. RAD publishes with the permission of the Director, Geological Survey of South Australia.

References

Boger, S.D., Hansen, D., 2004. Metamorphic evolution of the Georgetown Inlier, northeast Queensland, Australia; evidence for an accreted Palaeoproterozoic terrane? Journal of Metamorphic Geology 22, 511–527.

Boger, S.D., White, R.W., Schulte, B., 2012. The importance of iron speciation (Fe^{+2}/Fe^{+3}) in determining mineral assemblages: an example from the high-grade aluminous metapelites of southeastern Madagascar. Journal of Metamorphic Geology 30, 997–1018.

Brown, M., 2010. The spatial and temporal patterning of the deep crust and implications for the process of melt extraction. Philosophical Transactions of the Royal Society A 368, 11–51.

Brown, M., 2013. Granite: From genesis to emplacement. Geological Society of America Bulletin 125, 1079–1113.

Clemens, J.D., 2006. Melting of the continental crust: fluid regimes, melting reactions, and source-rock fertility, in: Brown, M., Rushmer, T. (Eds.), Evolution and Differentiation of the Continental Crust. Cambridge University Press, Cambridge, pp. 297–331.

Clemens, J.D., Vielzeuf, D., 1987. Constraints on melting and magma production in the crust. Earth and Planetary Science Letters 86, 287–306.

Cutts, K., Hand, M., Kelsey, D.E., 2011. Evidence for early Mesoproterozoic (ca. 1590Ma) ultrahigh-temperature metamorphism in southern Australia. Lithos 124, 1–16.

Cutts, K.A., Kelsey, D.E., Hand, M., 2013. Evidence for late Paleoproterozoic (ca 1690–1665 Ma) high- to ultrahigh-temperature metamorphism in southern Australia: Implications for Proterozoic supercontinent models. Gondwana Research 23, 617–640.

Daly, S.J., Fanning, C.M., Fairclough, M.C., 1998. Tectonic evolution and exploration potential of the Gawler Craton, South Australia. AGSO Journal of Australia Geology and Geophysics 17, 145–168.

Dare, S.S., Barnes, S.-J., Beaudoin, G., 2015. Did the massive magnetite "lava flows" of El Laco (Chile) form by magmatic or hydrothermal processes? New constraints from magnetite composition by LA-ICP-MS. Miner Deposita 50, 607–617.

Deer, W.A., Howie, R.A., Zussman, J., 1992. An introduction to the rock-forming minerals- 2nd edition. Longman, United Kingdom.

Diener, J.F.A., Powell, R., 2010. Influence of ferric iron on the stability of mineral assemblages. Journal of Metamorphic Geology 28, 599–613.

Diener, J.F.A., White, R.W., Powell, R., 2008. Granulite facies metamorphism and subsolidus fluid-absent reworking, Strangways Range, Arunta Block, central Australia. Journal of Metamorphic Geology 26, 603–622.

Droop, G.T.R., Clemens, J.D., Dalrymple, D.J., 2003. Processes and Conditions During Contact Anatexis, Melt Escape and Restite Formation: the Huntly Gabbro Complex, NE Scotland. Journal of Petrology 44, 995–1029.

Dutch, R., Hand, M., Kinny, P.D., 2008. High-grade Paleoproterozoic reworking in the southeastern Gawler Craton, South Australia. Australian Journal of Earth Sciences 55, 1063–1081.

Dutch, R.A., Hand, M., Kelsey, D.E., 2010. Unravelling the tectonothermal evolution of reworked Archean granulite facies metapelites using in situ geochronology: an example from the Gawler Craton, Australia. Journal of Metamorphic Geology 28, 293–316.

Fanning, C.M., Flint, R.B., Parker, A.J., Ludwig, K.R., Blissett, A.H., 1988. Refined Proterozoic evolution of the Gawler Craton, South Australia, through U–Pb zircon geochronology. Precambrian Research 40–41, 363–386.

Fanning, C.M., Reid, A.J., Teale, G.S., 2007. A geochronological framework for the Gawler Craton, South Australia, South Australia. Geological Survey. Bulletin 55.

Forbes, C.J., Giles, D., Jourdan, F., Sato, K., Omori, S., Bunch, M., 2012. Cooling and exhumation history of the northeastern Gawler Craton, South Australia. Precambrian Research 200–203, 209–238.

Fraser, G., McAvaney, S., Neumann, N., Szpunar, M., Reid, A., 2010. Discovery of early Mesoarchean crust in the eastern Gawler Craton, South Australia. Precambrian Research 179, 1–21.

Hand, M., Reid, A.J., Jagodzinski, E., 2007. Tectonic Framework and Evolution of the Gawler Craton, Southern Australia. Economic Geology 102, 1377–1395.

Handy, M.R., Mulch, A., Rosenau, M., Rosenberg, C.L., 2001. The role of fault zones and melts as agents of weakening, hardening and differentiation of the continental crust: a synthesis. Geological Society, London, Special Publications 186, 305–332.

Holland, T.J.B., Powell, R., 2011. An improved and extended internally consistent thermodynamic dataset for phases of petrological interest, involving a new equation of state for solids. Journal of Metamorphic Geology 29, 333–383.

Holness, M.B., Sawyer, E.W., 2008. On the Pseudomorphing of Melt-filled Pores During the Crystallization of Migmatites. Journal of Petrology 49, 1343–1363.

Howard, K.E., Hand, M., Barovich, K.M., Payne, J.L., Belousova, E.A., 2011a. U–Pb, Lu–Hf and Sm–Nd isotopic constraints on provenance and depositional timing of metasedimentary rocks in the western Gawler Craton: Implications for Proterozoic reconstruction models. Precambrian Research 184, 43–62.

Howard, K.E., Hand, M., Barovich, K.M., Payne, J.L., Cutts, K.A., Belousova, E.A., 2011b. U–Pb zircon, zircon Hf and whole-rock Sm–Nd isotopic constraints on the evolution of Paleoproterozoic rocks in the northern Gawler Craton. Australian Journal of Earth Sciences 58, 615–638.

IronRoad, 2014. Presentation: Central Eyre Iron Project- Our Technical Journey, http://www.ironroadlimited.com.au/images/files/presentations/20141029%20IRD%20CEIP%20Our%20Journey%20.pdf.

Johnson, T.E., Brown, M., Solar, G.S., 2003. Low–pressure subsolidus and suprasolidus phase equilibria in the MnNCKFMASH system: Constraints on conditions of regional metamorphism in western Maine, northern Appalachians. American Mineralogist 88, 624–638.

Johnson, T.E., White, R.W., 2011. Phase equilibrium constraints on conditions of granulite-facies metamorphism at Scourie, NW Scotland. Journal of the Geological Society 168, 147–158.

Johnson, T.E., White, R.W., Brown, M., 2011. A year in the life of an aluminous metapelite xenolith—The role of heating rates, reaction overstep, H_2O retention and melt loss. Lithos 124, 132–143.

Johnson, T.E., White, R.W., Powell, R., 2008. Partial melting of metagreywacke: a calculated mineral equilibria study. Journal of Metamorphic Geology 26, 837–853.

Kalczynski, M.J., Gates, A.E., 2014. Hydrothermal alteration, mass transfer and magnetite mineralization in dextral shear zones, western Hudson Highlands, New York, United States. Ore Geology Reviews 61, 226–247.

Kelsey, D.E., Hand, M., 2015. On ultrahigh temperature crustal metamorphism: phase equilibria, trace element thermometry, bulk composition, heat sources, timescales and tectonic settings. Geoscience Frontiers 6, 311–356.

Knipping, J.L., Bilenker, L.D., Simon, A.C., Reich, M., Barra, F., Deditius, A.P., Lundstrom, C., Bindeman, I., Munizaga, R., 2015. Giant Kiruna-type deposits form by efficient flotation of magmatic magnetite suspensions. Geology 43, 591–594.

Korhonen, F.J., Brown, M., Clark, C., Bhattacharya, S., 2013. Osumilite–melt interactions in ultrahigh temperature granulites: phase equilibria modelling and implications for the *P–T–t* evolution of the Eastern Ghats Province, India. Journal of Metamorphic Geology 31, 881–907.

Korhonen, F.J., Saito, S., Brown, M., Siddoway, C.S., 2010. Modeling multiple melt loss events in the evolution of an active continental margin. Lithos 116, 230–248.

Lane, K., Jagodzinski, E.A., Dutch, R., Reid, A.J., Hand, M., 2015. Age constraints on the timing of iron ore mineralisation in the southeastern Gawler Craton. Australian Journal of Earth Sciences 62, 55–75.

Lo Pò, D., Braga, R., 2014. Influence of ferric iron on phase equilibria in greenschist facies assemblages: the hematite-rich metasedimentary rocks from the Monti Pisani (Northern Apennines). Journal of Metamorphic Geology 32, 371–387.

Lupulescu, M.V., Bailey, D.G., Hawkins, M., Carl, J.D., Chiarenzelli, J.R., 2014. The Benson Mines, St. Lawrence County, New York: History of the Discovery, Mining, and Mineralogy of the Deposit. Rocks & Minerals 89, 118–131.

Mahar, E.M., Baker, J.M., Powell, R., Holland, T.J.B., Howell, N., 1997. The effect of Mn on mineral stability in metapelites. Journal of Metamorphic Geology 15, 223–238.

McFarlane, C.R.M., 2006. Palaeoproterozoic evolution of the Challenger Au deposit, South Australia, from monazite geochronology. Journal of Metamorphic Geology 24, 75–87.

McKay, A.D., Miezitis, Y., Porritt, K., Britt, A.F., Champion, D.C., Cadman, S., Towner, R., Summerfield, D., Whitaker, A., Huston, D., Jaireth, S., Sexton, M., Schofield, A., Hoatson, D., Senior, A.B., Carson, L., 2014. Australia's Identified Mineral Resources 2013. Geoscience Australia, Canberra, Australia.

Morrissey, L.J., Hand, M., Kelsey, D.E., 2015. Multi-stage metamorphism in the Rayner–Eastern Ghats Terrane: *P–T–t* constraints from the northern Prince Charles Mountains, east Antarctica. Precambrian Research 267, 137–163.

Morrissey, L.J., Hand, M., Wade, B.P., Szpunar, M., 2013. Early Mesoproterozoic metamorphism in the Barossa Complex, South Australia: links with the eastern margin of Proterozoic Australia. Australian Journal of Earth Sciences 60, 769–795.

Mudd, G.M., 2010. The Environmental sustainability of mining in Australia: key mega-trends and looming constraints. Resources Policy 35, 98–

115.

Mücke, A., 2005. The Nigerian manganese-rich iron-formations and their host rocks—from sedimentation to metamorphism. Journal of African Earth Sciences 41, 407–436.

Naslund, H., Henríquez, F., Nyström, J., Vivallo, W., Dobbs, F., 2002. Magmatic iron ores and associated mineralization: Examples from the Chilean High Andes and Coastal Cordillera, in: Porter, T.M. (Ed.), Hydrothermal iron oxide copper-gold and related deposits: A global perspective. PCG Publishing, Adelaide, Australia, pp. 207–226.

Nystroem, J.O., Henriquez, F., 1994. Magmatic features of iron ores of the Kiruna type in Chile and Sweden; ore textures and magnetite geochemistry. Economic Geology 89, 820–839.

Oliver, R.L., Fanning, C.M., 1997. Australia and Antarctica: Precise Correlation of Palaeoproterozoic Terrains, in: Ricci, C.A. (Ed.), The Antarctic Region: Geological Evolution and Processes. Terra Antartica Publication, Sienna, pp. 163–172.

Palmer, D.F., 1970. Geology and ore deposits near Benson mines, New York. Economic Geology 65, 31–39.

Patiño Douce, A.E., Harris, N., 1998. Experimental Constraints on Himalayan Anatexis. Journal of Petrology 39, 689–710.

Payne, J.L., Barovich, K., Hand, M., 2006. Provenance of metasedimentary rocks in the northern Gawler Craton, Australia: Implications for Palaeoproterozoic reconstructions. Precambrian Research 148, 275–291.

Payne, J.L., Hand, M., Barovich, K.M., Reid, A., Evans, D.A.D., 2009. Correlations and reconstruction models for the 2500–1500 Ma evolution of the Mawson Continent. Geological Society, London, Special Publications 323, 319–355.

Payne, J.L., Hand, M., Barovich, K.M., Wade, B.P., 2008. Temporal constraints on the timing of high-grade metamorphism in the northern Gawler Craton: implications for assembly of the Australian Proterozoic. Australian Journal of Earth Sciences 55, 623–640.

Powell, R., Downes, J., 1990. Garnet porphyroblast-bearing leucosomes in metapelites: mechanisms, phase diagrams, and an example from Broken Hill, Australia, in: Ashworth, J.R., Brown, M. (Eds.), High-temperature Metamorphism and Crustal Anatexis. Springer Netherlands, pp. 105–123.

Powell, R., White, R.W., Green, E.C.R., Holland, T.J.B., Diener, J.F.A., 2014. On parameterizing thermodynamic descriptions of minerals for petrological calculations. Journal of Metamorphic Geology 32, 245–260.

Puffer, J.H., Gorring, M.L., 2005. The Edison magnetite deposits in the context of pre-, syn-, and post-orogenic metallogenesis in the Grenville Highlands of New Jersey. Canadian Journal of Earth Sciences 42, 1735–1748.

Redler, C., White, R.W., Johnson, T.E., 2013. Migmatites in the Ivrea Zone (NW Italy): Constraints on partial melting and melt loss in metasedimentary rocks from Val Strona di Omegna. Lithos 175–176, 40-53.

Reid, A.J., Hand, M., 2012. Mesoarchean to Mesoproterozoic evolution of the southern Gawler Craton, South Australia. Episodes 35, 216–225.

Reid, A.J., Jagodzinski, E.A., Fraser, G.L., Pawley, M.J., 2014. SHRIMP U–Pb zircon age constraints on the tectonics of the Neoarchean to early Paleoproterozoic transition within the Mulgathing Complex, Gawler Craton, South Australia. Precambrian Research 250, 27–49.

Rigby, M.J., Droop, G.T.R., 2011. Fluid-absent melting versus CO_2 streaming during the formation of pelitic granulites: A review of insights from the cordierite fluid monitor, in: van Reenen, D.D., Kramers, J.D., McCourt, S., Perchuck, L.L. (Eds.), Origin and Evolution of Precambrian High-Grade Gneiss Terranes, with Special Emphasis on the Limpopo Complex of Southern Africa. Geological Society of America Memoirs, pp. 39–60.

Rosenberg, C.L., Handy, M.R., 2005. Experimental deformation of partially melted granite revisited: implications for the continental crust. Journal of Metamorphic Geology 23, 19–28.

Sawyer, E.W., 1994. Melt segregation in the continental crust. Geology 22, 1019–1022.

Sillitoe, R.H., Burrows, D.R., 2002. New field evidence bearing on the origin of the El Laco magnetite deposit, Northern Chile. Economic

Geology 97, 1101–1109.

Swain, G., Barovich, K., Hand, M., Ferris, G., Schwarz, M., 2008. Petrogenesis of the St Peter Suite, southern Australia: Arc magmatism and Proterozoic crustal growth of the South Australian Craton. Precambrian Research 166, 283–296.

Swain, G., Woodhouse, A., Hand, M., Barovich, K., Schwarz, M., Fanning, C.M., 2005. Provenance and tectonic development of the late Archaean Gawler Craton, Australia; U–Pb zircon, geochemical and Sm–Nd isotopic implications. Precambrian Research 141, 106–136.

Tinkham, D.K., Ghent, E.D., 2005. Estimating garnet growth *P*–*T* conditions with pseudosections and the problem of effective bulk composition. The Canadian Mineralogist 43, 35–50.

Tinkham, D.K., Zuluaga, C.A., Stowell, H.H., 2001. Metapelite phase equilibria modeling in MnNCKFMASH: The effect of variable Al_2O_3 and MgO/(MgO + FeO) on mineral stability. Geological Materials Research 3, 1–42.

Tyler, I.M., Spaggiari, C.V., Occhipinti, S.A., Kirkland, C.L., Smithies, H.R., 2014. The Albany–Fraser deep reflection seismic and MT survey: Implications for mineral systems, in: Spaggiari, C.V., Tyler, I.M. (Eds.), Albany–Fraser Orogen seismic and magnetotelluric (MT) workshop 2014: extended abstracts. Geological Survey of Western Australia, pp. 174–182.

Vassallo, J.J., Wilson, C.J.L., 2002. Palaeoproterozoic regional-scale non-coaxial deformation: an example from eastern Eyre Peninsula, South Australia. Journal of Structural Geology 24, 1–24.

Vielzeuf, D., Clemens, J.D., Pin, C., Moinet, E., 1990. Granites, Granulites, and Crustal Differentiation, in: Vielzeuf, D., Vidal, P. (Eds.), Granulites and Crustal Evolution. Springer Netherlands, pp. 59–85.

Vielzeuf, D., Holloway, J., 1988. Experimental determination of the fluid-absent melting relations in the pelitic system. Contributions to Mineralogy and Petrology 98, 257–276.

White, R.W., Powell, R., 2002. Melt loss and the preservation of granulite facies mineral assemblages. Journal of Metamorphic Geology 20, 621–632.

White, R.W., Powell, R., Clarke, G.L., 2002. The interpretation of reaction textures in Fe-rich metapelitic granulites of the Musgrave Block, central Australia: constraints from mineral equilibria calculations in the system K_2O–FeO–MgO–Al_2O3–SiO_2–H_2O–TiO_2–Fe_2O_3. Journal of Metamorphic Geology 20, 41–55.

White, R.W., Powell, R., Holland, T.J.B., 2001. Calculation of partial melting equilibria in the system Na_2O–CaO–K_2O–FeO–MgO–Al_2O_3–SiO_2–H_2O (NCKFMASH). Journal of Metamorphic Geology 19, 139–153.

White, R.W., Powell, R., Holland, T.J.B., Johnson, T.E., Green, E.C.R., 2014a. New mineral activity–composition relations for thermodynamic calculations in metapelitic systems. Journal of Metamorphic Geology 32, 261–286.

White, R.W., Powell, R., Holland, T.J.B., Worley, B.A., 2000. The effect of TiO_2 and Fe_2O_3 on metapelitic assemblages at greenschist and amphibolite facies conditions: mineral equilibria calculations in the system K_2O–FeO–MgO–Al_2O_3–SiO_2–H_2O–TiO_2–Fe_2O_3. Journal of Metamorphic Geology 18, 497–511.

White, R.W., Powell, R., Johnson, T.E., 2014b. The effect of Mn on mineral stability in metapelites revisited: new *a*–*x* relations for manganese-bearing minerals. Journal of Metamorphic Geology 32, 809–828.

Yakymchuk, C., Brown, M., 2014. Consequences of open-system melting in tectonics. Journal of the Geological Society 171, 21–40.

Yakymchuk, C., Brown, M., Ivanic, T.J., Korhonen, F.J., 2013. Leucosome distribution in migmatitic paragneisses and orthogneisses: A record of self-organized melt migration and entrapment in a heterogeneous partially-molten crust. Tectonophysics 603, 136–154.

Sample	773514	773516	IRD204-27	IRD204-29	190-10A2
SiO_2	58.19	57.54	41.51	49.71	52.75
TiO_2	0.54	0.46	0.76	0.91	0.41
Al_2O_3	15.49	10.97	7.74	13.42	12.15
Fe_2O_3	10.88	19.45	39.27	19.69	15.40
FeO	3.16	2.65	4.15	6.22	8.56
MnO	0.81	0.82	0.37	2.06	1.03
MgO	2.29	1.61	2.79	2.85	2.29
CaO	0.67	1.25	0.55	0.74	1.06
Na_2O	0.84	1.46	0.33	0.77	1.12
K_2O	4.60	2.67	0.92	2.17	3.82
P_2O_5	0.18	0.33	0.34	0.19	0.22
LOI	2.32	1.28	0.85	1.18	0.86
Total	**99.97**	**100.49**	**99.58**	**99.90**	**99.67**

CHAPTER 7

This chapter is published as:

Morrissey, L.J., Hand, M., Kelsey, D.E., Wade, B.P., 2016. Cambrian high-temperature reworking of the Rayner–Eastern Ghats terrane: constraints from the Northern Prince Charles Mountains region, East Antarctica. *Journal of Petrology*, **57**, 53–92.

Statement of Authorship

Title of Paper	Cambrian high-temperature reworking of the Rayner-Eastern Ghats terrane: constraints from the northern Prince Charles Mountains region, east Antarctica.
Publication status	☒Published ☐Accepted for publication ☐Submitted for publication ☐Unpublished and unsubmitted work written in manuscript style
Publication Details	Morrissey, L.J., Hand, Kelsey, D.E., Wade, B., 2016. Cambrian high-temperature reworking of the Rayner-Eastern Ghats terrane: constraints from the northern Prince Charles Mountains region, east Antarctica. *Journal of Petrology*, **57**, 53–92.

Principal Author

Name of Principal Author (Candidate)	Laura Morrissey		
Contribution to the Paper	Project design, petrography, *P–T* pseudosection calculation and interpretation, manuscript design and composition, creation of figures.		
Overall percentage (%)	80		
Certification:	This paper reports on original research I conducted during the period of my Higher Degree by Research candidature and is not subject to any obligations or contractual agreements with a third party that would constrain its inclusion in this thesis. I am the primary author of this paper.		
Signature		Date	16/05/2016

Co-Author Contributions

By signing the Statement of Authorship, each author certifies that:

i. the candidate's stated contribution to the publication is accurate (as detailed above);
ii. permission is granted for the candidate in include the publication in the thesis; and
iii. the sum of all co-author contributions is equal to 100% less the candidate's stated contribution.

Name of Co-Author	Martin Hand		
Contribution to the Paper	Guidance with geochronology and pseudosection interpretation, manuscript review.		
Signature		Date	17th May 2016

Name of Co-Author	David Kelsey		
Contribution to the Paper	Guidance with geochronology and pseudosection interpretation, manuscript review.		
Signature		Date	18/05/2016

Name of Co-Author	Ben Wade		
Contribution to the Paper	Assistance with LA-ICP-MS data collection, manuscript review.		
Signature		Date	20/5/2016

ABSTRACT

Metapelitic rocks from the northern Prince Charles Mountains–East Amery Ice Shelf region of the Rayner Complex, east Antarctica, record high-temperature reworking during the Cambrian. Calculated metamorphic phase diagrams from rocks with varying chemical compositions and mineral assemblages suggest peak temperatures were 800–870 °C with pressures of 5.5–6.5 kbar. However, Cambrian-aged, high-*T* reworking is patchy and only recorded in some locations, with other areas recording pristine early Mesoproterozoic–Neoproterozoic assemblages formed during the c. 1000–900 Ma Rayner Orogeny. The spatial distribution of reworking may reflect that the comparatively anhydrous residual rock compositions inherited from the Rayner Orogeny were relatively inert to reworking during the Cambrian. Domains which record Cambrian reworking conceivably underwent hydrous retrogression at the end of the Rayner Orogeny and were therefore comparatively reactive during reheating in the Cambrian. High-*T* reworking during the Cambrian has previously been recognised in the Prydz Bay region at the margin of the Rayner Complex, but not in the northern Prince Charles Mountains. The Eastern Ghats Province in India, which was formerly contiguous with the Rayner Complex, preserves a similarly enigmatic record of Cambrian geochronology, suggesting that the Rayner–Eastern Ghats terrane as a whole may have experienced selective reworking during the Cambrian. The geodynamic setting for the formation of this thermal regime is not well understood, but the attainment of high crustal temperatures may have been facilitated by a reduced capacity for thermal buffering, arising from limited partial melting within a previously dehydrated crustal column.

1. Introduction

Inferring tectono-metamorphic histories for a terrane relies on a detailed combined geochronological and metamorphic approach to decipher the pressure–temperature (*P–T*) evolution of an area. However, the interpretation of the geological history of a terrane may be complicated by polymetamorphism. The application of efficient geochronological tools, and the increasing use of in situ geochronology, has allowed for a better understanding of the development of reaction textures, including recognising when rocks record the effects of multiple, temporally unrelated events (e.g. Dutch et al., 2005; Goncalves et al., 2004; Hand et al., 1992; Hensen and Zhou, 1995b; Kelsey et al., 2007; Korhonen et al., 2012; Yakymchuk et al., 2015). However, deciphering metamorphic events can be difficult in terranes which have undergone extensive metamorphism and melt loss. These terranes have reduced potential for further melting during subsequent metamorphic events, and as a result, subsequent events may occur at subsolidus conditions, even if they involve high temperatures (e.g. Clark et al., 2011; Diener et al., 2008; Korhonen et al., 2012; Vielzeuf et al., 1990; White and Powell, 2002). The paucity or lack of a fluid phase creates unreactive rock compositions that are less likely to record evidence of further events, either by the formation of new mineral assemblages or by the resetting of geochronometers (e.g. Korhonen et al., 2012; Phillips et al., 2007a, 2009; Tenczer et al., 2006; White and Powell, 2002). Additionally, terranes that have previously undergone partial melting are susceptible to high-*T* thermal reworking because they largely avoid the energetic requirements for melting (e.g. Brown and Korhonen, 2009; Clark et al., 2011; Morrissey et al., 2014; Stüwe, 1995; Vielzeuf et al., 1990; Walsh et al., 2015).

One way of recognising polymetamorphism in residual terranes is to carefully investigate the preserved petrographic relationships throughout a region. For example, terranes which appear to preserve substantially different *P–T* paths for spatially adjacent areas are candidates for cryptically preserved polymetamorphism.

The Rayner Complex in east Antarctica forms part of a vast terrane that includes the Eastern Ghats Province in India (Fig. 1). It underwent high temperature metamorphism and extensive melting during the c. 1000–900 Ma Rayner Orogeny (e.g. Boger et al., 2000; Boger and White, 2003; Carson et al., 2000; Halpin et al., 2007a; Kinny et al., 1997; Morrissey et al., 2015; Zhao et al., 1997). This event has previously been characterised as recording anticlockwise *P–T* paths that are dominated by cooling (Boger and White, 2003; Fitzsimons and Harley, 1992; Halpin et al., 2007a; Thost and Hensen, 1992). However, some locations preserve mineral reaction microstructures that are more commonly interpreted to reflect clockwise-style *P–T* paths, particularly at locations that are characterised by the formation of secondary cordierite-bearing mineral assemblages (Corvino et al., 2011; Halpin et al., 2007b; Hand et al., 1994a; Nichols, 1995; Nichols and Berry, 1991; Stüwe and Hand, 1992). The clockwise *P–T* evolution in Kemp Land on the margin of the Rayner Complex (Fig. 1) has been interpreted to reflect differences in strain partitioning and magma flux between the older Archean Napier Complex and more juvenile Proterozoic Rayner Complex (Halpin et al., 2007b). However, in the central Rayner Complex, the significance of these apparent clockwise *P–T* paths remains unclear.

This study investigates seven locations from the ostensibly early Neoproterozoic northern Prince Charles Mountains (nPCM)–East Amery Ice Shelf (EAIS) region of the Rayner Complex in east Antarctica (Table 1; Fig. 1d). Samples from these locations contain secondary cordierite-bearing assemblages that appear inconsistent with the inferred isobaric cooling paths inferred elsewhere in the Rayner Complex (e.g. Boger and White, 2003; Fitzsimons and Harley, 1992; Fitzsimons and Thost, 1992; Halpin et al., 2007a). Calculated metamorphic phase diagrams are combined with in situ geochronology to constrain the timing of the cordierite-bearing mineral assemblages.

We find that secondary cordierite-bearing mineral assemblages are Cambrian in age, and that the textural metamorphic response of the Rayner Complex during the Cambrian is patchy. We suggest that high-*T* Cambrian mineral assemblages only formed in regions that were retrogressed at the end of the Rayner Orogeny. The bulk of the Rayner Complex does not record high-*T* Cambrian reworking due to relatively anhydrous and thus inert rock compositions.

2. Geological Framework

Much of Antarctica is poorly outcropping; however, the Prince Charles Mountains (PCM) in east Antarctica provide a 600 km cross section extending inland from the Mawson Coast in MacRobertson Land, east Antarctica (Fig. 1c). The PCM have been divided into four distinct geological terranes (e.g. Boger et al., 2008; Mikhalsky et al., 2001b, 2006a; Phillips et al., 2006; Tingey, 1991). The southern Prince Charles Mountains (sPCM) are composed of the Ruker Complex, which has an Archean history, and the Lambert Complex, which has an Archean–Paeloproterozoic history and makes up much of the Mawson Escarpment (Fig. 1c; Boger et al., 2008; Corvino et al.,

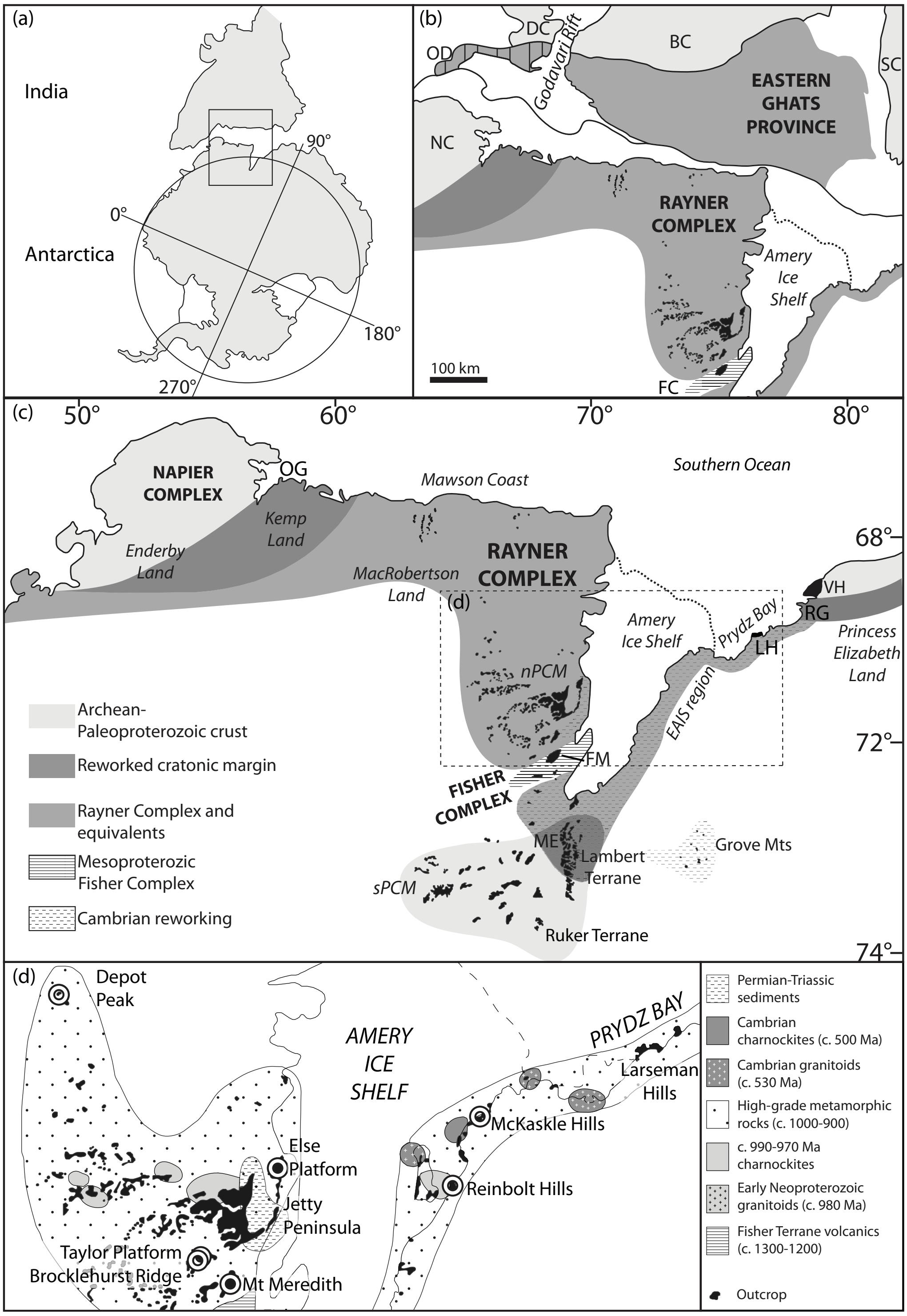

Figure 1: (a and b) Schematic reconstruction of India and Antarctica, showing the Rayner Complex and Eastern Ghats Province in context of the present day continents. OD: Ongole Domain; DC: Dharwar Craton; BC: Bastar Craton; SC: Singhbhum Craton; NC: Napier Complex; FC: Fisher Complex. (c) Simplified geological map showing the Rayner Complex and Prince Charles Mountains in the context of the surrounding terranes, after Phillips et al. (2009). The Rayner Complex extends west from Enderby Land to Princess Elizabeth Land, and south from the Mawson and Kemp Land coasts. OG: Oygarden Group; FM: Fisher Massif; ME: Mawson Escarpment; LH: Larsemann Hills, RG: Rauer Group, VH: Vestfold Hills, EAIS: East Amery Ice Shelf. (d) Outcrop map of the northern Prince Charles Mountains showing sample locations, after Mikhalsky et al. (2001b) and Liu et al. (2009b).

Table 1: Sample location and sample summary.

Sample	Location		Easting	Northing	Description	Age
Northern Prince Charles Mountains (nPCM)						
DP-1	Depot Peak	41D	563934	2340118	Pegmatite within shear zone	Cambrian
DP-11	Depot Peak	41D	563934	2340118	Late pegmatite	Cambrian
DP-7	Depot Peak	41D	563934	2340118	Gt-sill gneiss with cd-sp-ilm coronas	Bimodal: c. 930 and Cambrian
PCM-83	Else Platform	42D	491213	2188537	Gt-sill gneiss with cd-sp-ilm coronas	Bimodal: c. 930 and Cambrian
77090	Taylor Platform	42D	433206	2120313	Gt-cd gneiss	Dominantly Cambrian
77102B	Brocklehurst Ridge	42D	431390	2118426	Gt-cd-sill-bi gneiss	Dominantly Cambrian
77079	Mt Meredith	42D	455042	2099832	Gt-bi-qz granofels	Cambrian
East Amery Ice Shelf (EAIS)						
72046A	Reinbolt Hills	43D	406808	2178312	Gt-sill gneiss with cd-sp-ilm coronas	Bimodal: c. 930 and Cambrian
77223	McKaskle Hills	43D	423647	2232948	Gt gneiss with cd-qz and pl-qz coronas	Dominantly Cambrian

2008; Mikhalsky et al., 2001b, 2006b; Phillips et al., 2006). The Fisher Complex is located between the sPCM and nPCM and is composed of 1300–1200 Ma calc-alkaline volcanics that have been metamorphosed to amphibolite facies, with late granitoids emplaced at 1050–1020 Ma (Fig. 1c; Beliatsky et al., 1994; Kinny et al., 1997; Mikhalsky et al., 1996, 2001b). The nPCM form part of the Proterozoic Rayner Complex and are the focus of this study. The Rayner Complex was defined to separate crust with a Proterozoic tectonic history from blocks that record an Archean history (Kamenev, 1972), and is interpreted to extend inland from the coastline of Kemp and MacRobertson Lands to the Fisher Complex and southern Prince Charles Mountains (sPCM) and from Enderby Land in the west to Princess Elizabeth Land, east of the Amery Ice Shelf (Fig. 1; e.g. Boger, 2011; Tingey, 1991). The rocks in the EAIS and Prydz Bay regions are now interpreted to have a similar history to those in the nPCM, but preserve evidence for pervasive high-grade reworking during the Cambrian (Fig. 1; Grew et al., 2012; Hensen and Zhou, 1995a, 1995b; Kelsey et al., 2007; Liu et al., 2009b, 2014; Wang et al., 2008). The Rayner Complex is generally considered to have been contiguous with rocks from the Eastern Ghats Province in India (Fig. 1; e.g. Boger, 2011; Fitzsimons, 2000; Mezger and Cosca, 1999), and therefore their tectonic evolution should logically be considered in the same context.

The Rayner Complex was deformed and metamorphosed during the Rayner Orogeny (Table 2; e.g. Boger et al., 2000; Halpin et al., 2007a, 2007b, 2013; Kelly et al., 2002; Kelly and Harley, 2004; Kinny et al., 1997; Morrissey et al., 2015). The effects of the

Table 2: Summary of the metamorphic conditions in the nPCM–EAIS region.

Location	Age	Peak conditions	*P-T* path	References
Mawson Coast: MacRobertson Land	Rayner Event 990–970 Ma	850–900 °C; 5.5–6 kbar	Anticlockwise- isobaric cooling	Halpin et al., 2007a
Mawson Coast: Kemp Land	Rayner Event c. 930 Ma	850–990 °C; 9–10 kbar	Decompression	Halpin et al., 2007b
nPCM: Radok Lake	Rayner Event 940–910 Ma	880 °C; 6.0–6.5 kbar	Anticlockwise- isobaric cooling	Boger and White, 2003; Morrissey et al., 2015
nPCM: Else Platform	Rayner Event 2 events?	800°C; 6.5-7 kbar	Cooling, then decompression and reheating to 700 °C	Hand et al., 1994a, b
nPCM: Depot Peak	Rayner Event 2 events?	700 °C; 5.6 kbar	Minor decompression and cooling	Stüwe and Hand, 1992
Mawson Escarpment	Rayner Event 2 events?	790–810 °C; 6.5–7.1 kbar	Possible decompression?	Corvino et al., 2011; Phillips et al., 2009
EAIS: McKaskle Hills	Cambrian	880–950 °C; 9–9.5 kbar	Decompression and cooling	Liu et al., 2007b
Prydz Bay: Rauer Group	Cambrian	950–975 °C; 10–10.6 kbar	Decompression	Kelsey et al., 2003c
Prydz Bay: Brattstrand Bluffs	Cambrian	860 °C; 6 kbar	Decompression	Fitzsimons, 1996
Prydz Bay: Larsemann Hills	Cambrian	800 °C, 7 kbar	Decompression	Carson et al., 1997

Rayner Orogeny are widespread and involved reworking of the cratonic margin of the Napier Complex (Halpin et al., 2007b), as well as the Rayner Complex in the northern Prince Charles Mountains (nPCM), Mawson Coast and EAIS regions (Fig. 1; e.g. Boger et al., 2000; Grew et al., 2012; Halpin et al., 2007a; Liu et al., 2014; Morrissey et al., 2015). This event was accompanied by voluminous charnockitic and granitic magmatism between 990 and 900 Ma that dominates much of the outcropping Rayner Complex (e.g. Carson et al., 2000; Kinny et al., 1997; Manton et al., 1992; Munksgaard et al., 1992; Tingey, 1991; Zhao et al., 1997). However, an earlier, higher-*P* phase of metamorphism at c. 1020 Ma has also been recognised in the nPCM (Morrissey et al., 2015), and was accompanied by magmatism in the southern EAIS and Fisher Complex (Kinny et al., 1997; Liu et al., 2009b, 2014). Detailed geochronology from the Mawson Charnockite along the Mawson Coast suggests that episodic magmatism occurred from c. 1150–950 Ma, suggesting that thermal regime related to the Rayner Orogeny may have commenced as early as c. 1150 Ma and proceeded either continuously or as a punctuated thermal system for c. 250 Myr (Halpin et al., 2012).

Contrasting *P–T* paths have been proposed for the Rayner Complex during the Rayner Orogeny (Table 2). Metamorphism at 990–970 Ma recorded in rocks along the Mawson Coast appears to be high thermal gradient in character, with an anticlockwise *P–T* evolution reaching peak temperatures of 850–900 °C at 5.5–6 kbar, followed by crustal thickening to pressures of 6–7 kbar, synchronous with repeated pluton emplacement (Halpin et al., 2007a). Conversely, further west in Kemp Land (Fig. 1), younger c. 930 Ma metamorphism occurred at similar temperatures of 850–990 °C, but at higher pressures of 9–10 kbar, and involved a clockwise *P–T* evolution (Halpin et al., 2007b; Kelly and Harley, 2004), interpreted to reflect reworking of a stronger cratonic margin. In the nPCM, the Rayner Orogeny has been interpreted to have involved an anticlockwise *P–T* evolution with peak conditions related to the emplacement of granitic and charnockitic magmas and reaching 800–850 °C and 6–7 kbar, followed by isobaric cooling (Boger and White, 2003; Fitzsimons and Harley, 1992; Fitzsimons and Thost, 1992; Morrissey et al., 2015; Nichols, 1995; Stephenson and Cook, 1997). However, it has also been suggested that some locations in the nPCM and EAIS region experienced clockwise *P–T* histories. A sample from Mt Lanyon, located in the southern nPCM, was interpreted to record decompression from a rutile-bearing assemblage to a cordierite-bearing assemblage (Nichols, 1995). However, recent in situ geochronology suggests that this apparent clockwise *P–T* path may be the result of the superposition of an earlier, higher-*P* event at c. 1020 Ma and a younger, lower-*P* event at c. 930 Ma (Morrissey et al., 2015). Similarly, samples from Depot Peak, Else Platform and the Reinbolt Hills show garnet–sillimanite assemblages that have been partially replaced by cordierite–spinel symplectites, interpreted to reflect decompression (Hand et al., 1994b; Nichols and Berry, 1991; Scrimgeour and Hand, 1997; Stüwe and Hand, 1992). However, none of these studies were combined with geochronology, and therefore the possibility that the apparent decompressional *P–T* paths also reflect two unrelated events cannot be excluded (e.g. Hand et al., 1994a). Metamorphism associated with shortening at 960–905 Ma is also recorded in the northern Mawson Escarpment (Fig. 1c), and reached peak conditions of 6.5–7.1 kbar and 790–810 °C (Corvino et al., 2011; Phillips et al., 2009). Therefore, the Rayner Orogeny involved high-grade metamorphism with temperatures in excess of 850 °C. It resulted in voluminous melting and magmatism, creating a dehydrated, residual granulite-facies terrane.

2.1. Cambrian reworking in the Rayner Complex

The architecture of the East Antarctic shield is now considered to have been the result of juxtaposition of different crustal blocks during Cambrian orogenesis, associated with the formation of Gondwana (e.g. Boger, 2011; Fitzsimons, 2000; Meert, 2003). Parts of the Rayner Complex were reworked during the Cambrian (Table 2; e.g. Boger et al., 2002; Carson et al., 1997; Fitzsimons, 1996, 1997; Hensen and Zhou, 1995a; Kelsey et al., 2003a, 2007, 2008b; Liu et al., 2009a, 2009b; Wang et al., 2008; Zhao et al., 2003). The effects of this event are most evident in the Prydz Bay region (Fig. 1c). In the Rauer Group, rocks reached UHT conditions of 950–975 °C and 10–10.6 kbar, followed by decompression (Fig. 1c; Table 2; Harley, 1998; Kelsey et al., 2003c, 2007; Tong and Wilson, 2006). Peak conditions of 800–860 °C and 6–7 kbar, followed by decompression, are recorded in the Brattstrand Bluffs and Larsemann Hills (Table 2; Carson et al., 1995, 1997; Fitzsimons, 1996; Fitzsimons and Harley, 1991, 1992). The event was accompanied by extensive anatexis (Carson et al., 1996; Fitzsimons et al., 1997; Zhao et al., 2003) and deformation (Dirks and Hand, 1995; Dirks and Wilson, 1995; Wilson et al., 2007).

In the EAIS (Fig. 1c), peak metamorphism is interpreted to have occurred at c. 535 Ma (Liu et al., 2009b). Conventional thermobarometry from mafic granulites in the McKaskle Hills (Fig. 1d) indicate peak conditions of 880–950 °C at 9–9.5 kbar, followed by decompression and cooling to conditions of 700–750 °C and 6.6–7.2 kbar (Liu et al., 2007b). Intrusion of the Jennings Charnockite also occurred at c. 500 Ma (Liu et al., 2009b). However, evidence for Cambrian reworking in the EAIS is variable and seems to be restricted to discrete locations. Zircon geochronology from the Reinbolt Hills (Fig. 1d) appears to indicate metamorphism at c. 930 Ma, with very little evidence of a Cambrian overprint (Liu et al., 2009b). However, U–Th–Pb monazite geochronology from a sillimanite-bearing pegmatite from the Reinbolt Hills gives a mean age of 534 ± 17 Ma, interpreted to represent new growth of monazite at granulite facies conditions, or anatexis of metasedimentary protoliths (Ziemann et al., 2005).

Further south, the Grove Mountains (Fig. 1c) record an extensive and pervasive Cambrian history (Liu et al., 2007a, 2009a). Peak pressures from erratic boulders of mafic granulites have been constrained to 11.8–14.0 kbar and 770–840 °C at c. 545 Ma, before near-isothermal decompression to ~6 kbar at c. 530 Ma (Liu et al., 2009a). Charnockitic and granitic magmatism occurred at 550–500 Ma (Liu et al., 2006; Mikhalsky et al., 2001a; Zhao et al., 2003). It is unclear whether the Grove Mountains form part of the Rayner Complex or a separate terrane (Liu et al., 2009a; Mikhalsky et al., 2001a), but the high pressure metamorphism has been interpreted as evidence for a collisional setting during the formation of Gondwana (Liu et al., 2009a).

In the sPCM, both the Ruker and Lambert Complexes (Fig. 1c) preserve evidence of Cambrian reworking at c. 530–490 Ma (Boger and Wilson, 2005; Boger et al., 2001; Corvino et al., 2008, 2011; Phillips et al., 2009). In the southern Lambert Complex, Cambrian deformation is pervasive and metamorphism involved a clockwise *P–T* path from peak conditions of 650–700 °C and 6–7 kbar, followed by 3 kbar of isothermal decompression (Boger and Wilson, 2005). In the northern Lambert Complex, granitic and pegmatite intrusives are recorded at c. 510–490 Ma, and replacement of sillimanite by a lower-*P* cordierite-bearing assemblage has also been interpreted to relate to Cambrian reworking (Corvino et al., 2008, 2011; Phillips et al., 2009). However, unlike the southern Lambert Complex, deformation is restricted to discrete shear zones, and some samples contain Cambrian monazite but no evidence of Cambrian zircon (Corvino et al., 2008, 2011; Phillips et al., 2009). In the Ruker Complex, Cambrian deformation occurred along high-strain zones and involved metamorphic conditions of 565–640 °C and 4–5.2 kbar (Phillips et al., 2007a).

In the nPCM, Cambrian reworking has been thought to be of minor importance. Isotopic systems such as Rb–Sr were reset at c. 500 Ma (Manton et al., 1992; Tingey, 1991), and garnet Sm–Nd geochronology gives a range of ages from 825–555 Ma, suggesting thermal reworking post-900 Ma (Hensen et al., 1997; Zhou and Hensen, 1995). However, in many cases zircon geochronology from intrusive rocks is dominated by older ages (c. 1000–900 Ma), with most samples containing only minor resetting and no c. 500 Ma zircon growth (Kinny et al., 1997; Manton et al., 1992). Emplacement of biotite granite and pegmatite occurred at c. 550–500 Ma on Jetty Peninsula, Mt Kirkby and Else Platform (Boger et al., 2002; Carson et al., 2000; Manton et al., 1992), and at Else Platform c. 500 Ma felsic dykes have been migmatised (Hand et al., 1994b; Scrimgeour and Hand, 1997). Together, these indicate some amount of melting and high-temperature reworking in the Cambrian (Hand et al., 1994b; Manton et al., 1992; Scrimgeour and Hand, 1997). However, overall, Cambrian-aged reworking in the nPCM has been interpreted to be restricted to discrete northeast trending mylonitic zones that commonly occur on the margins of c. 550–520 Ma pegmatites (Boger et al., 2002; Carson et al., 2000). These mylonites have not been directly dated, but have been interpreted to post-date c. 550–520 Ma pegmatites and predate Rb–Sr biotite ages of c. 475 Ma (Boger et al., 2002). They record contractional kinematics, with southeast over northwest thrust movement (Boger et al., 2002), and have been interpreted to have formed at *P*–*T* conditions of 524 ± 20 ºC and 7.6 ± 4 kbar (Boger et al., 2002). They are thought to be similar to undated mylonites in the Reinbolt Hills in the EAIS and from the Mawson Coast (Clarke, 1988; Nichols, 1995).

3. Petrography and sample descriptions

The samples used in this study are a combination of legacy samples collected over several field seasons in the late 1980s and early 1990s. Numbered samples are from the rock library at the University of Tasmania, the samples beginning with letters are from collections at the University of Adelaide. The samples chosen for this study are from locations throughout the nPCM–EAIS region (Fig. 1d). The often large gaps between outcrop in the nPCM means that it is difficult to draw structural links between samples (e.g. Fitzsimons and Thost, 1992). Most samples in this study preserve interpreted growth of post-peak cordierite or are biotite-rich metapelites, which appear to metamorphically contrast with the assemblages that preserve evidence for Early Neoproterozoic isobaric cooling observed elsewhere in the nPCM (e.g. Boger and White, 2003; Fitzsimons and Harley, 1992; Fitzsimons and Thost, 1992; Nichols, 1995). Pegmatite from within granulite facies shear zones at Depot Peak (Figs. 1d and 2) was selected to

Table 3: Petrography of pelitic samples.

Sample	M_1 assemblage (c. 930 Ma)	M_2 assemblage (c. 530 Ma)
Northern Prince Charles Mountains (nPCM)		
DP-7	gt + sill + bi + ksp + sp_1 + ilm_1 + qz_1	cd + sp_2 + ilm_2 + pl + qz_2 (+ gt + sill + ksp)
PCM-83	gt + sill + bi + ksp + sp_1 + ilm_1 + qz	cd + sp_2 + ilm_2 (+ gt + sill)
77090	-	gt + sill + cd + bi + ilm + qz
77102B	-	gt + sill + cd + bi + ksp + ilm + pl + qz
77079	-	gt + bi + pl + ilm + qz
East Amery Ice Shelf (EAIS)		
72046A	gt + sill + bi + sp_1 + ilm_1 + qz	cd + sp_2 + ilm_2 + ksp + pl (+ gt + sill)
77223	gt + sill + bi_1 + ksp_1 + ilm_1 + ru + pl_1 + qz_1	cd + bi_2 + ksp_2 + ilm_2 + pl_2 + qz_2 (+ gt)

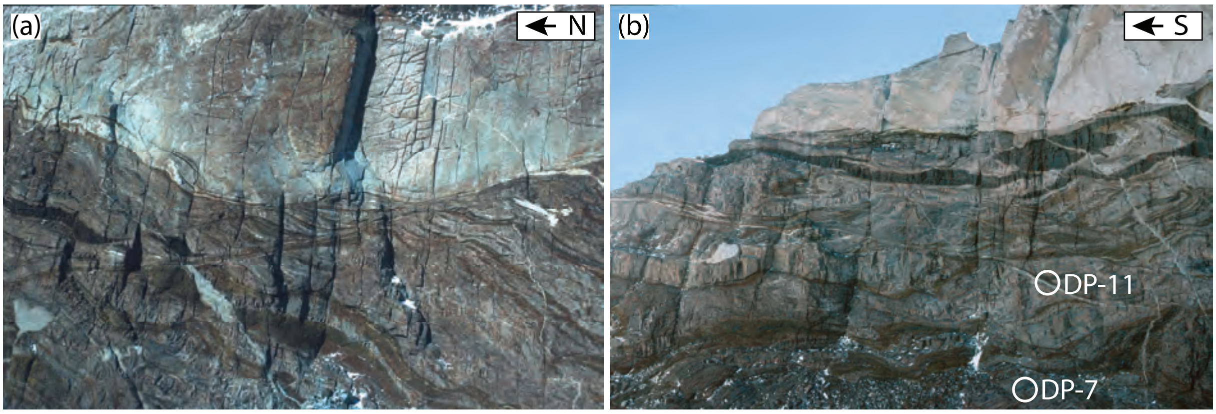

Figure 2: Outcrop photos from Depot Peak. The sampling locations for DP-11 and DP-7 are shown on Fig. 3b. The sampling location for DP-1 does not occur in these images.

provide some constraints on the timing of high temperature deformation. The petrography of pelitic samples is summarised in Table 3.

3.1. Northern Prince Charles Mountains

3.1.1. DP-1: Depot Peak

DP-1 is a pegmatite vein 20 cm wide located within a shear zone. These shear zones were described by Stüwe and Hand (1992). They are 1–5 m wide, shallowly north-dipping and post-date the two pervasive ductile deformation phases. They contain a strong north-plunging lineation. The shear zone movement changes from normal to reverse along dip, but the majority of kinematics suggest normal movement (Stüwe and Hand, 1992). Sample DP-1 is dominantly comprised of coarse-grained K-feldspar and quartz (5–10 mm). Plagioclase (up to 1 mm) occurs in areas containing finer-grained quartz and unoriented biotite. Anhedral garnet (up to 1 mm) occurs in the comparatively biotite-rich areas. The margin of the pegmatite contains coarse-grained cordierite, biotite and garnet.

3.1.2. DP-11: Depot Peak

DP-11 is a cross-cutting pegmatite which post-dates all deformation at Depot Peak (Fig. 2b). The mineral assemblage in DP-11 is K-feldspar, quartz, biotite, plagioclase and garnet. K-feldspar is perthitic, porphyritic and in some cases is up to 15 mm in diameter. Garnet is euhedral, varies in size from 3–15 mm in diameter and contains inclusions of quartz. It

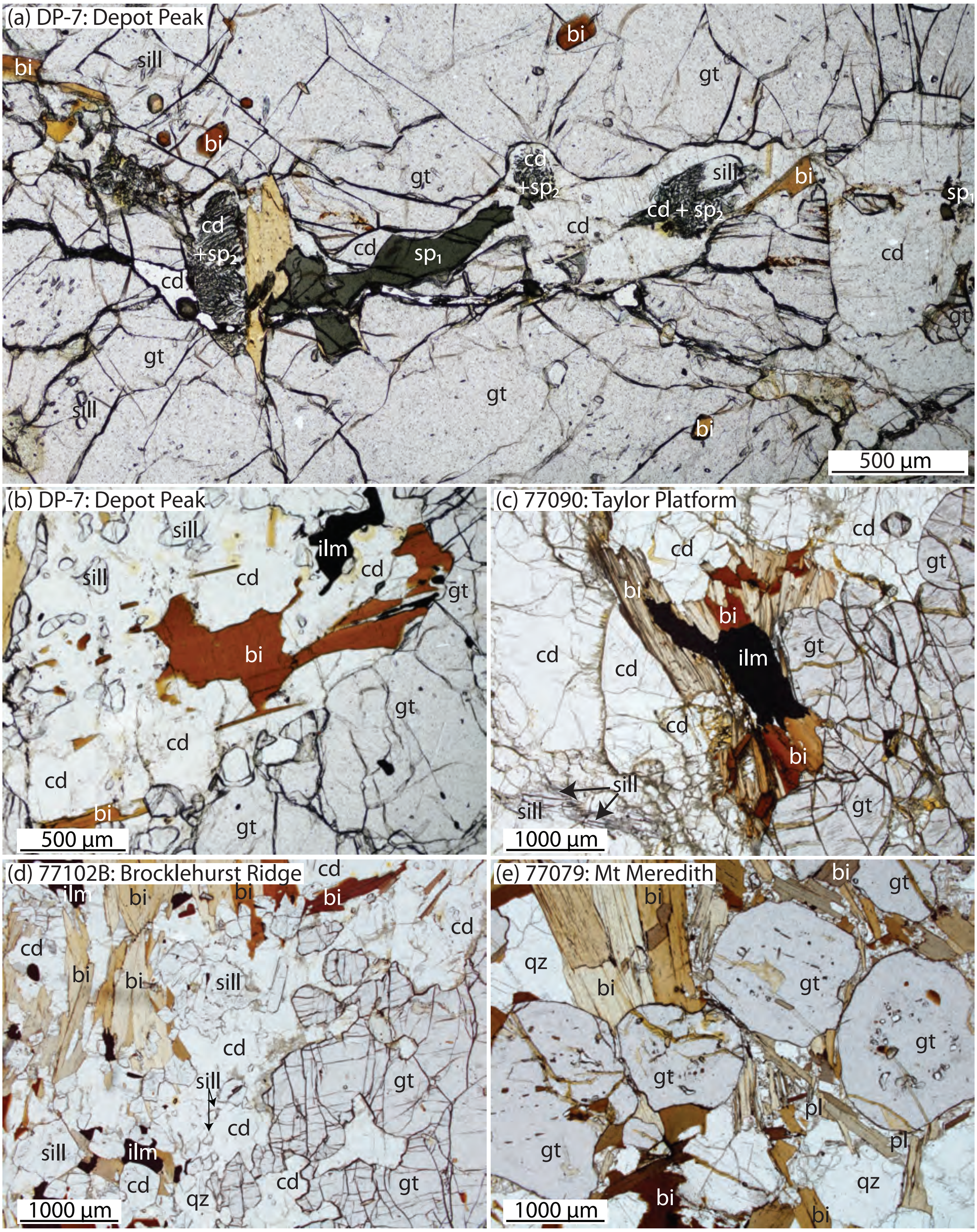

Figure 3: Photomicrographs. (a) Sample DP-7. Coarse-grained M_1 spinel is separated from M_1 garnet and sillimanite, whereas M_2 cordierite–spinel symplectites replace sillimanite. (b) Sample DP-7. Biotite inclusions within cordierite are optically continuous over length scales of >1 mm, suggesting cordierite replaced biotite. (c) Sample 77090. (d) Sample 77102B. (e) Sample 77079.

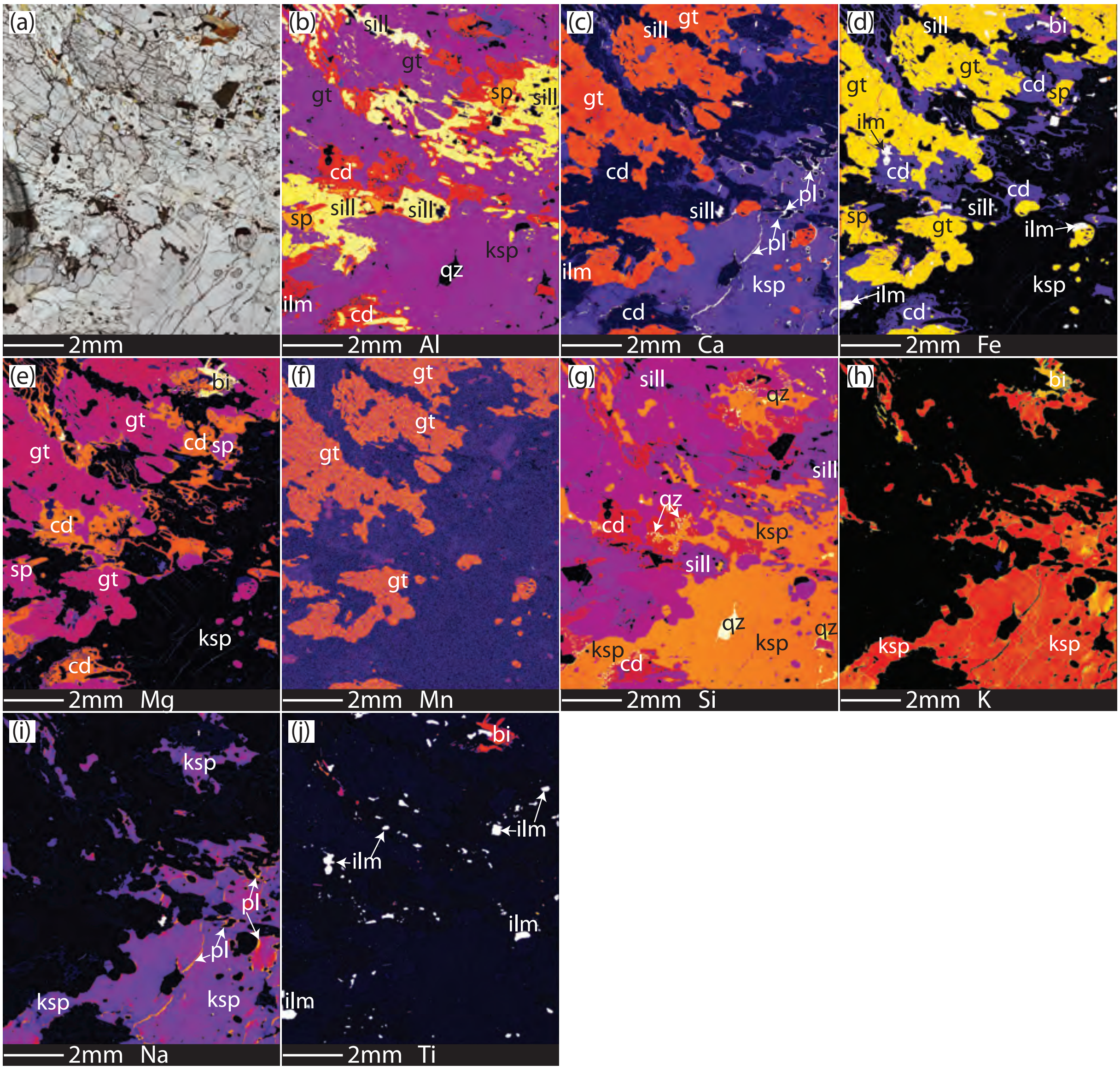

Figure 4: Compositional maps of DP-7 (Depot Peak), used to calculate the domain composition for phase equilibria modelling. The compositional maps also highlight important mineralogical relationships. (a) Photomicrograph of map area. (b) Al map: cordierite coronas separating coarse-grained garnet and sillimanite; cordierite coronas on coarse-grained spinel. (c) Ca map: plagioclase coronas (shown in white) on sillimanite and as veins separating K-feldspar grains. (d) Fe map: ilmenite occurs as inclusions within garnet and sillimanite and also within cordierite coronas. (e) Mg map: biotite (shown in white) occurs as uncommon, anhedral grains in the matrix. (f) Mn map. (g) Si map: quartz (shown in white) occurs as inclusions in K-feldspar and also as intergrowths with cordierite at the margin of K-feldspar grains. (h) K map. (i) Na map. (j) Ti map.

occurs throughout the sample. Biotite is scarce and occurs as anhedral grains up to 2 mm. Opaques, apatite, monazite and zircon make up the accessory minerals in DP-11.

3.1.3. DP-7: Depot Peak

Sample DP-7 contains garnet, sillimanite, K-feldspar, cordierite, spinel and ilmenite, with minor plagioclase, quartz and biotite. Garnet porphyroblasts (up to 15 mm in diameter) make up ~25% of the sample. These contain abundant inclusions of fine-grained sillimanite, as well as coarser sillimanite, biotite, ilmenite and occasionally K-feldspar (Figs. 3a, b and 4).

The K-feldspar inclusions in garnet contain rare inclusions of quartz (Fig. 4g). The matrix contains alternating domains that are rich in sillimanite and domains which are rich in K-feldspar. In sillimanite-rich domains, sillimanite (up to 2 mm in length) defines the foliation. Ilmenite and rare spinel occur in these domains. K-feldspar-rich domains comprise coarse (5 mm) K-feldspar grains that contain inclusions of ilmenite, small garnet and quartz. Biotite is uncommon in sample DP-7, and forms small tabular flakes included in garnet and cordierite and rare, anhedral grains in the matrix (Figs. 3a, b and 4). Where flakes of biotite are included in cordierite, they are commonly in optical continuity over length scales in excess of 1.5 mm, suggesting that the small flakes are relics of a larger grain (Fig. 3b). Quartz is rare and mainly occurs as inclusions in K-feldspar or as intergrowths separating K-feldspar from cordierite (Fig. 4g). Cordierite occurs as coronas on ilmenite and sillimanite and also separates spinel from the other phases (Figs. 3a and 4). Spinel occurs as grains up to 500 μm, as well as fine-grained, symplectitic intergrowths with cordierite (Fig. 3a). Plagioclase is rare and only occurs as very thin coronas on sillimanite and between K-feldspar grains (Fig. 4c and i).

3.1.4. PCM-83: Else Platform

Sample PCM-83 displays similar mineral assemblages and relationships to DP-7. Coarse-grained garnet (~ 3 mm) and sillimanite (2–5 mm) are separated by coronas of cordierite and spinel (Fig. 5a). Ilmenite occurs as inclusions in garnet but also as a matrix phase, where it occurs as anhedral, coarse grains (up to 1.5 mm; Fig. 5j). Spinel occurs as spinel–cordierite symplectites but also as coarser grains (~100 μm) in diameter (Fig. 5). It can occur in contact with ilmenite but does not occur in contact with garnet or sillimanite (Fig. 5). The majority of the matrix is made up of cordierite. Quartz (up to 1 mm) and K-feldspar (~500 μm) occur in contact with garnet but do not occur as part of the cordierite–spinel symplectites.

3.1.5. 77090: Taylor Platform

Sample 77090 contains garnet, biotite, cordierite, sillimanite, ilmenite and quartz. The rock is unfoliated and is dominantly composed of garnet and cordierite. Garnet grains are euhedral, ~1 mm and commonly form larger aggregates of garnet that are up to 10 mm in size (Fig. 3c). Garnet grains are commonly inclusion free. Cordierite is abundant and makes up the main mineral in the matrix (Fig. 3c). It contains fine-grained inclusions of sillimanite that do not have a preferred orientation. It also contains inclusions of euhedral–subhedral biotite (up to 400 μm) and small grains of quartz. In some cases, large cordierite grains also contain small, euhedral garnet grains. Where cordierite occurs in sillimanite-rich domains, it is very coarse-grained (up to 20 mm). The margins of some cordierite grains are decorated with fine-grained fibrolite, and where cordierite occurs near garnet or within fractures in garnet it has been pinitised. Sillimanite occurs as inclusions in cordierite and also as coarser grains (500–1000 μm) in the matrix (Fig. 3c). Biotite occurs as fine-grained, euhedral inclusions within cordierite and garnet and also as a matrix phase, where it forms coarser (up to 1 mm) anhedral grains commonly at the boundaries of cordierite or within fractures within garnet (Fig. 3c). Ilmenite usually occurs in contact with biotite, and biotite may be coronitic on ilmenite grains (Fig. 3c). Ilmenite also occurs along grain boundaries of garnet and cordierite.

3.1.6. 77102B: Brocklehurst Ridge

Sample 77102B contains garnet, biotite, cordierite, K-feldspar, sillimanite, ilmenite, quartz and minor plagioclase. It has a gneissic

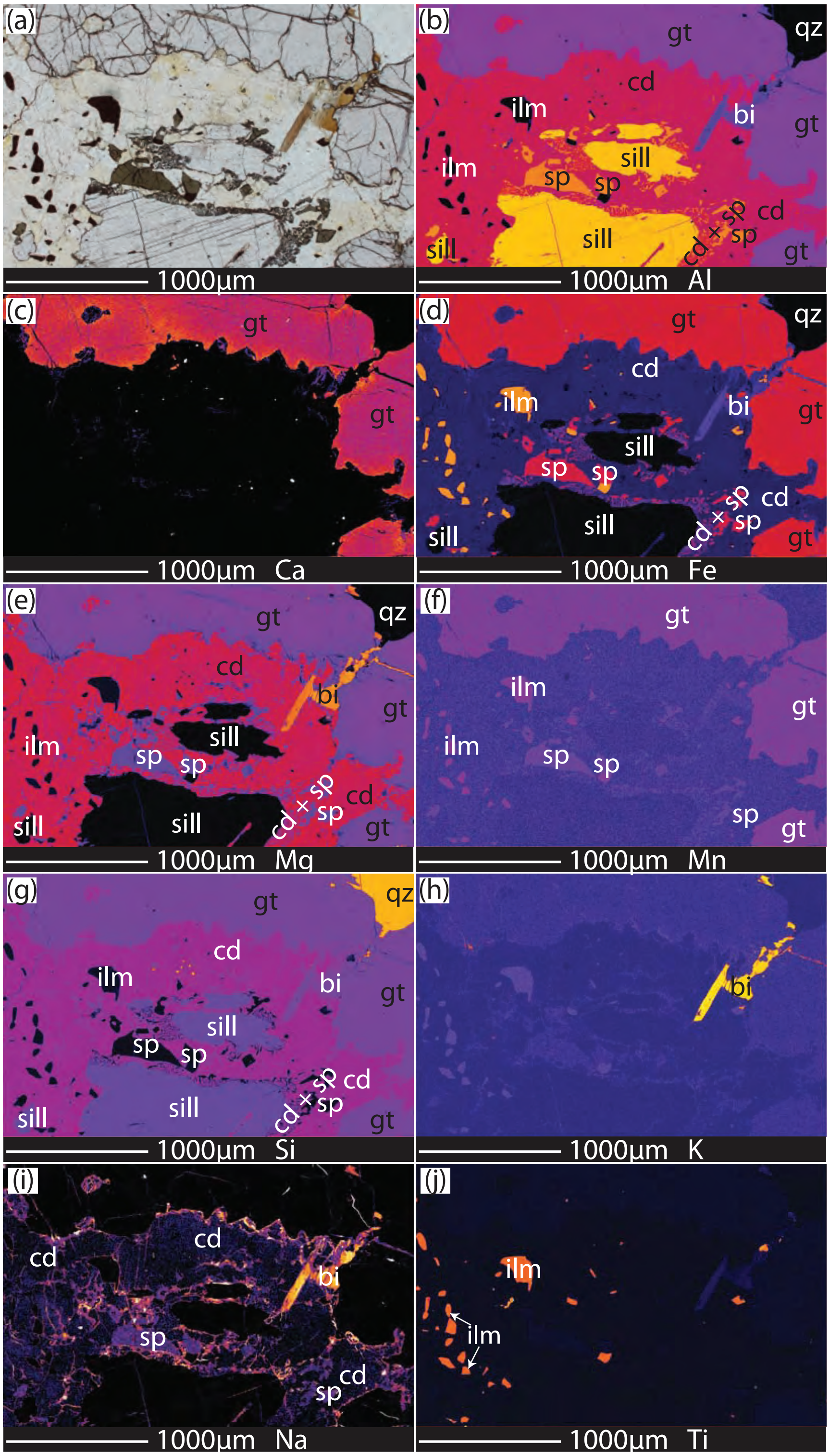

Figure 5: Compositional maps of PCM-83 (Else Platform), used to calculate the domain composition for phase equilibria modelling. The compositional maps also highlight important mineralogical relationships. (a) Photomicrograph of map area. (b) Al map: cordierite–spinel symplectites and cordierite moats separate sillimanite and garnet. (c) Ca map: garnet shows minor enrichment in calcium at the rims. (d) Fe map: ilmenite occurs within the cordierite moat and in contact with spinel. (e) Mg map. (f) Mn map. (g) Si map. (h) K map. (i) Na map: cordierite, spinel and biotite contain minor amounts of Na. (j) Ti map.

foliation defined by biotite, sillimanite and quartzo-feldspathic segregations. Garnet grains are up to 1 mm, anhedral and contain rare fine-grained biotite and quartz. Garnet occurs throughout the sample, except in the quartzo-feldspathic segregations. Sillimanite is up to 1.5 mm in length, defines a foliation and occurs preferentially in areas of the sample that are high in biotite. The sample contains three morphologies of biotite. One occurs as inclusions in garnet, the second comprises grains up to 1.5 mm that define the foliation (Fig. 3d) and the third generation comprises anhedral grains (up to 2 mm) with no clear preferred orientation. Cordierite is abundant and occurs throughout the sample, however, it is coarser grained (up to 1.5 mm) in areas that are rich in biotite. It contains inclusions of fine-grained sillimanite, biotite and quartz (Fig. 3d). Plagioclase is rare and is only found in the quartzofeldspathic domains of the sample. Quartz and K-feldspar occur throughout but are coarser-grained in the quartzofeldspathic segregations (up to 2 mm). They also occur throughout the sample as finer grains. Ilmenite forms anhedral grains which are commonly in contact with biotite and less commonly in contact with sillimanite.

3.1.7. 77079: Mt Meredith

Sample 77079 is a biotite-garnet granofels. It contains garnet, biotite, quartz and minor plagioclase and ilmenite. The sample does not have a foliation. Biotite occurs as euhedral grains (up to 4 mm in length; Fig. 3e) and contains inclusions of zircon, monazite and rare quartz. Garnet grains are euhedral, 2–5 mm in diameter and contain inclusions of fine-grained biotite (up to 200 μm), rare quartz and ilmenite (Fig. 3e). Quartz occurs as coarse, anhedral grains (up to 5 mm, commonly 1–3 mm). Plagioclase occurs as fine, anhedral grains (up to 200 μm), intergrown around coarse biotite crystals near garnet (Fig. 3e). Ilmenite occurs along some biotite grain boundaries or along cleavage planes and also as fine-grained (<100 μm) inclusions within garnet.

3.2. East Amery Ice Shelf

3.2.1. 72046A: Reinbolt Hills

Sample 72046A displays similar a mineral assemblage and spatial relationship to samples DP-7 and PCM-83 in the nPCM. The sample contains K-feldspar rich domains as well as domains dominantly comprised of coarse-grained garnet and sillimanite. In these domains, garnet and sillimanite comprise ~ 80% of the assemblage. Garnet contains inclusions of fine-grained sillimanite, but coarse garnet and sillimanite are separated by double coronas of cordierite and cordierite-spinel symplectites (Fig. 6). Garnet also contains inclusions of euhedral biotite, ilmenite and rare quartz (Fig. 6e). Plagioclase is rare and occurs as anhedral grains, often in contact with K-feldspar (Fig. 6i). Biotite occurs as euhedral inclusions within garnet (up to 500 μm) and also as anhedral grains in the matrix in contact with K-feldspar, though this is uncommon (Fig. 6e and h). It does not have a preferred orientation. Coarser-grained quartz (~500 μm) occurs as inclusions within K-feldspar in the K-feldspar-rich domains, and as finer-grains in contact with K-feldspar in the garnet–sillimanite-rich domains (Fig. 6g). Spinel occurs as coarser grains in direct contact with ilmenite and as fine-grained symplectites intergrown with cordierite (Fig. 6a and d).

3.2.2. 77223: McKaskle Hills

Sample 77223 contains garnet, biotite, plagioclase, K-feldspar, cordierite, quartz, ilmenite and rutile. The sample comprises domains of differing mineralogy. Some domains are mainly comprised of quartz, plagioclase and minor K-feldspar. These domains contain euhedral rutile crystals,

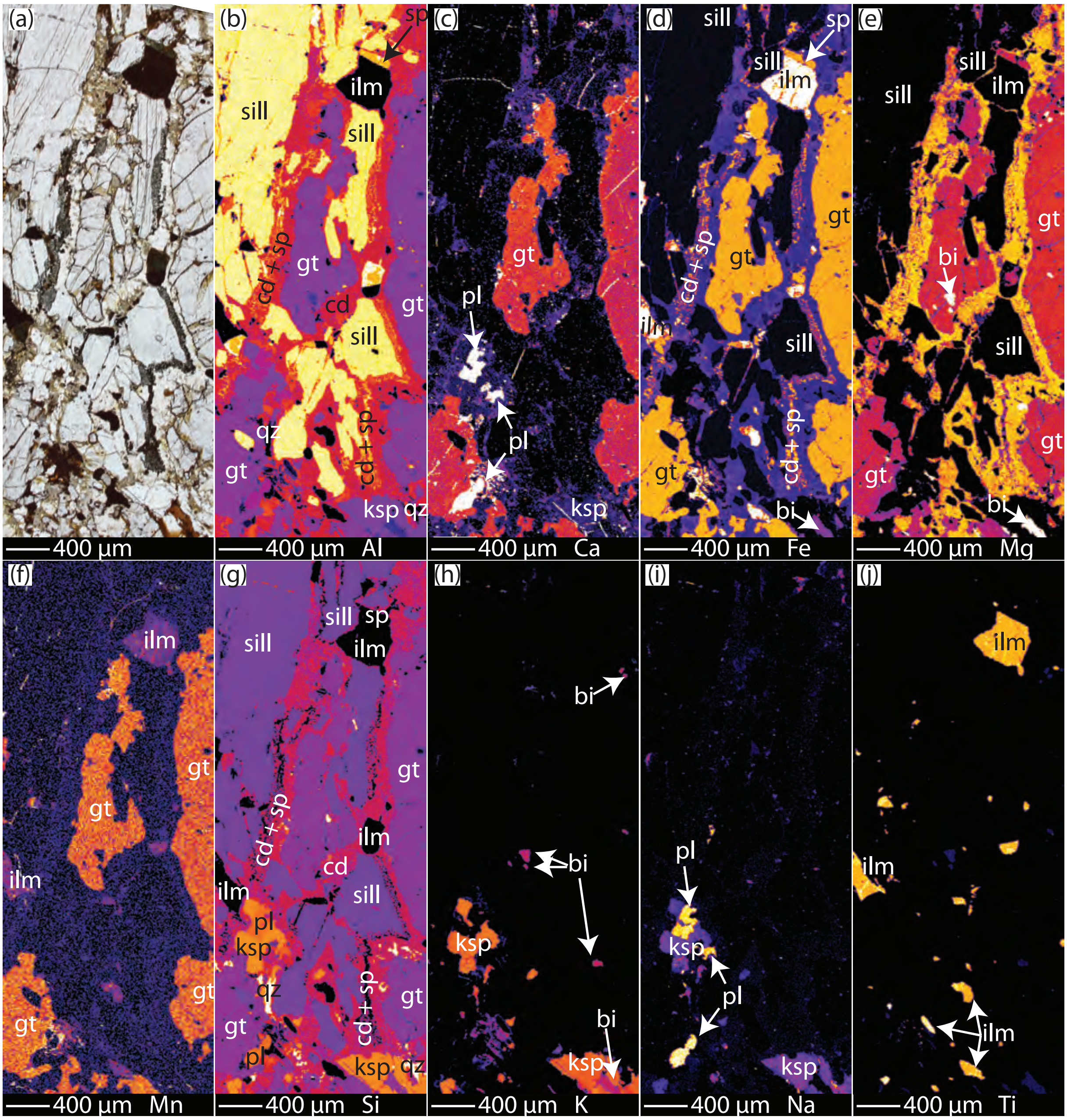

Figure 6: Compositional maps of 72046A (Reinbolt Hills), used to calculate the domain composition for phase equilibria modelling. The compositional maps also highlight important mineralogical relationships. (a) Photomicrograph of map area. (b) Al map: sillimanite and garnet separated by cordierite and cordierite-spinel reaction textures. (c) Ca map: anhedral plagioclase (shown in white) occurs in contact with garnet or K-feldspar. Garnet shows minor enrichment at the rims. (d) Fe map: ilmenite is separated from sillimanite by a corona of cordierite but can occur in contact with spinel. (e) Mg map: biotite occurs as small grains included in garnet. (f) Mn map. (g) Si map: quartz (shown in white) occurs as anhedral grains, usually in contact with K-feldspar. (h) K map: there is a general paucity of biotite, it occurs as inclusions in garnet and K-feldspar. (i) Na map. (j) Ti map.

but very little biotite. Other domains are richer in ferromagnesian minerals. In these domains, garnet porphyroblasts are commonly surrounded by cordierite–quartz symplectites, which can be up to 700 µm wide (Fig. 7b and e). These are commonly in contact with finer-

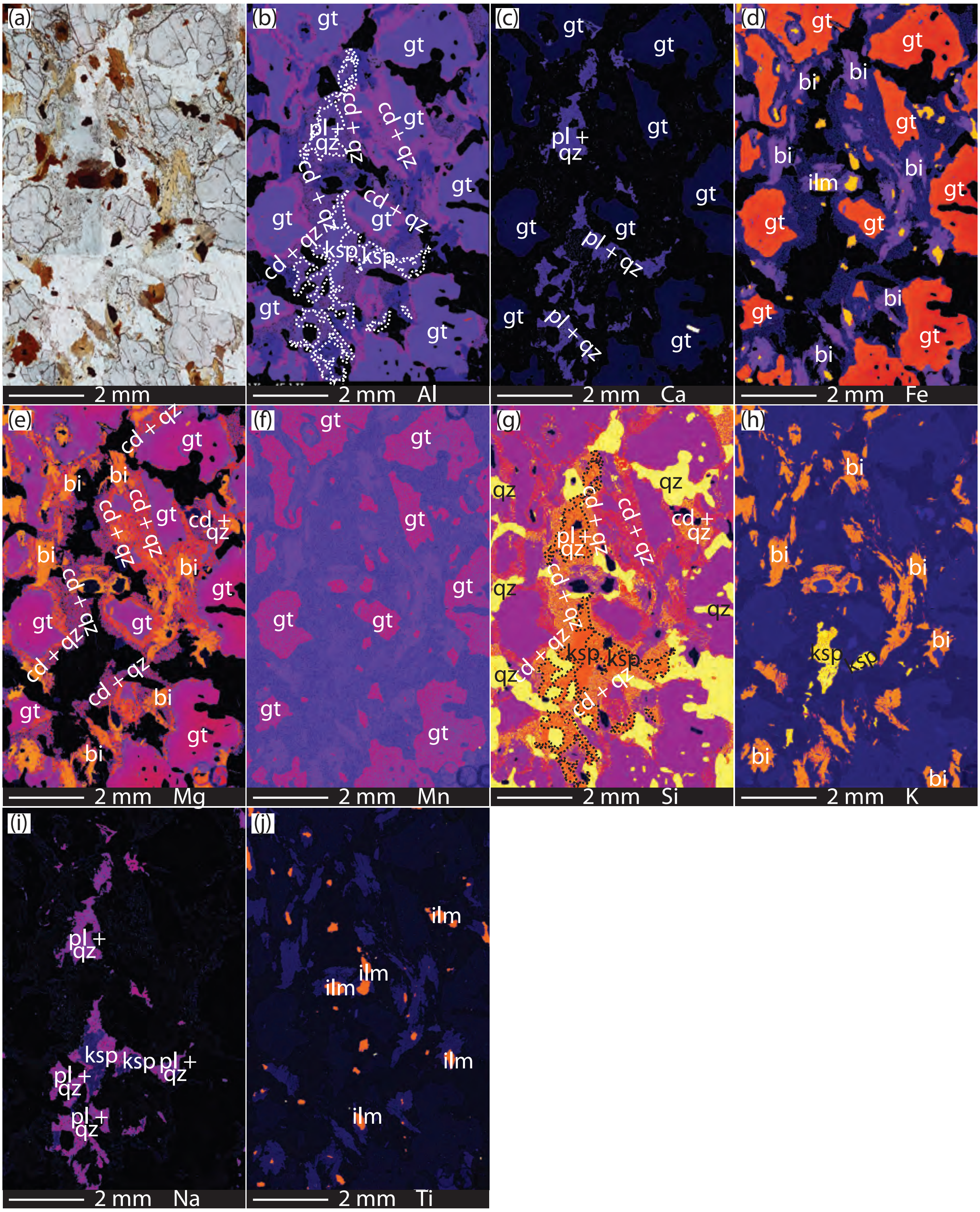

Figure 7: Compositional maps of 77223 (McKaskle Hills), used to calculate the domain composition for phase equilibria modelling. The compositional maps also highlight important mineralogical relationships. (a) Photomicrograph of map area. (b) Al map: double cordierite–quartz symplectites surround garnet, with cordierite-rich symplectites adjacent to garnet and more quartz-rich symplectites as a second layer. Plagioclase–quartz symplectites occur with K-feldspar and are outlined in white dashed lines. (c) Ca map: highlighting the plagioclase–quartz symplectites. (d) Fe map. (e) Mg map. (f) Mn map. (g) Si map. (h) K map: biotite occurs as coarse grains on ilmenite grains as well as intergrown with quartz. (i) Na map. (j) Ti map.

grained symplectites of quartz and cordierite in a second corona structure (Fig. 7b and e). K-feldspar is commonly separated from other minerals by plagioclase–quartz symplectites, and rarely by cordierite–quartz symplectites (Fig. 7c and i). Cordierite occurs as part of a quartz-cordierite symplectite and not as coarse grains. Biotite is abundant in the garnet-cordierite-quartz domains. In some cases, the edges of biotite grains are intergrown with quartz or biotite is included in cordierite–quartz symplectites (Fig. 7h). Ilmenite (up to 500 μm) often occurs included in or in contact with biotite (Fig. 7j). It occurs commonly in the ferromagnesian domains, but is less common in the domains containing quartz and plagioclase. Rutile occurs in the quartz–plagioclase-rich domains and as inclusions in garnet. It may occur in contact with ilmenite, where the two minerals appear to form a single euhedral grain. Rare sillimanite inclusions occur in garnet but sillimanite does not occur in the matrix.

4. Methods

4.1. Monazite U–Pb LA–ICP–MS geochronology

U–Pb isotopic data was collected using Laser Ablation–Inductively Coupled Plasma–Mass Spectrometry (LA–ICP–MS) on in situ monazite grains in thin section. Prior to LA–ICP–MS analysis, monazite grains were imaged using a back-scattered electron detector on a Phillips XL30 SEM to determine their microstructural locations and any compositional variations. For samples containing mineral reaction microstructures, monazite grains were qualitatively mapped using a Cameca SXFive electron microprobe, to determine variations in REE concentrations.

LA-ICP-MS analyses were performed at the University of Adelaide, following the method of Payne et al. (2008). U–Pb isotopic analyses were acquired using a New Wave 213 nm Nd–YAG laser coupled with an Agilent 7500cs ICP-MS. Ablation of monazites was performed in a He-ablation atmosphere at a frequency of 4 Hz. A spot size of 12 μm was used for all samples. The total acquisition time of each analysis was 100 s. This included 40 s of background measurement, 10 s of the laser firing with the shutter closed to allow for beam stabilisation, and 50 s of sample ablation. Isotopes measured were ^{204}Pb, ^{206}Pb, ^{207}Pb and ^{238}U for dwell times of 10, 15, 30 and 15 ms, respectively.

Monazite data were reduced using Glitter software (Griffin et al., 2004). Elemental fractionation and mass bias was corrected using the monazite standard MAdel (TIMS normalisation data: ^{207}Pb/^{206}Pb = 491.0 ± 2.7 Ma, ^{206}Pb/^{238}U = 518.37 ± 0.99 Ma and ^{207}Pb/^{235}U = 513.13 ± 0.19 Ma: updated from Payne et al. (2008) with additional TIMS analyses). Throughout the course of this study, MAdel yielded weighted mean ages of ^{207}Pb/^{206}Pb = 491 ± 4 Ma, ^{206}Pb/^{238}U = 519 ± 1 Ma, and ^{207}Pb/^{235}U = 513 ± 1 Ma (n = 218). Data accuracy was monitored using monazite standard 94-222/Bruna-NW (c. 450 Ma: Payne et al., 2008). As a secondary standard, 94-222 yielded weighted mean ages of ^{207}Pb/^{206}Pb = 463 ± 7 Ma, ^{206}Pb/^{238}U = 450 ± 2 Ma, ^{207}Pb/^{235}U = 452 ± 2 Ma (n = 83).

4.2. Mineral chemistry

X-ray compositional maps and chemical analyses of minerals were obtained using a Cameca SXFive electron microprobe at the University of Adelaide. The SXFive is equipped with 5 WDS X-Ray detectors, with four utilising large diffracting crystals. Beam conditions of 15kV and 20 nA with a focussed spot were used for all point analyses, and settings of 15kV and 150 nA used for compositional mapping. Calibration was performed on certified synthetic and natural mineral standards from Astimex Ltd

Table 4: Mineral composition and modal proportions used for bulk composition calculations.

	Sample DP-7: Depot Peak									**Sample PCM-83: Else Platform**						
	gt	sill	bi	cd	ilm	sp	qz	pl	ksp	gt	sill	bi	cd	ilm	sp	qz
Mode %	29	17	1	15	2	1	1	1	33	24	16	2	48	2	4	4
SiO_2	38.15	36.88	37.65	48.27	0.01	0.02	98.54	67.86	63.43	36.96	36.65	37.13	48.65	0	0.01	99.90
TiO_2	0.02	0.02	4.30	0.01	50.55	0.04	0.06	0.02	0.04	0.02	0.03	4.89	0	52.95	0.04	0.05
Al_2O_3	21.69	62.37	13.54	31.89	0.00	58.18	0.05	20.62	18.18	21.28	62.54	16.41	32.98	0.00	57.99	0.04
Fe_2O_3	1.17	0.38	-	-	5.05	1.78	-	-	-	2.48	1.14	-	-	0	4.26	0
FeO	29.15	0.00	10.78	6.42	42.67	30.80	0.02	0.02	0	31.12	0	9.84	6.08	46.68	27.61	0.05
MgO	8.37	0	17.72	10.09	1.49	6.65	0.03	0	0	5.92	0.02	16.34	10.06	0.08	6.33	0.02
CaO	0.92	0	0	0.02	0	0.01	0.01	5.04	0.69	1.23	0	0.01	0	0	0	0.02
Na_2O	0	0	0.18	0.03	0.01	0.06	0	6.92	3.32	0.02	0.02	0.14	0.03	0	0.12	0
K_2O	0.01	0	9.77	0	0	0	0	0.04	10.81	0	0	8.70	0	0.02	0.01	0
H_2O	0	0	3.50	1.50	0	0	0	0	0	0	0	3.50	1.50	0	0	0
Total	**99.47**	**99.65**	**97.44**	**98.23**	**99.79**	**97.55**	**98.71**	**100.52**	**96.47**	**99.02**	**100.40**	**96.96**	**99.30**	**99.73**	**96.37**	**100.08**

	Sample 72046A: Reinbolt Hills									**Sample 77223: McKaskle Hills**						
	gt	sill	bi	cd	ilm	sp	qz	pl	ksp	gt	bi	cd	ilm	q	pl	ksp
Mode %	25	35	1	27	3	3	1	2	3	28	11	20	3	27	8	3
SiO_2	38.42	36.65	38.15	49.43	0.06	0.02	99.90	61.56	64.88	38.00	35.12	48.77	0.00	98.28	57.96	64.20
TiO_2	0.01	0.03	5.81	0.03	51.33	0.04	0.05	0.00	0.02	0.00	3.67	0.00	54.24	0.06	0.01	0.00
Al_2O_3	21.70	62.54	14.76	33.38	0	58.64	0.04	24.49	19.00	21.44	14.88	33.57	0.03	0.02	25.95	18.84
Fe_2O_3	0.39	1.14	-	-	3.51	3.96	-	-	-	1.65	0.57	-	0.57	-	-	-
FeO	29.29	0	9.87	4.96	42.90	27.47	0.05	0.18	0.02	28.88	13.92	5.02	42.76	0.17	0.02	0.00
MgO	7.86	0.02	17.44	11.24	1.38	7.78	0.02	0	0.02	7.98	13.60	10.96	1.24	0.02	0.01	0.00
CaO	1.42	0	0	0.02	0.02	0.01	0.02	5.85	0.15	1.52	0.02	0.00	0.01	0.03	7.37	0.03
Na_2O	0	0.02	0.26	0.05	0.05	0.09	0	8.17	1.94	0.00	0.07	0.01	0.00	0.03	7.78	1.33
K_2O	0.01	0	9.61	0.00	0.01	0	0	0.15	13.62	0.00	8.84	0.00	0.02	0.00	0.12	14.05
H_2O	0	0	3.50	1.50	0	0	0	0	0	0.00	3.50	1.50	0.00	0.00	0.00	0.00
Total	**99.09**	**100.40**	**99.39**	**100.61**	**99.25**	**98.01**	**100.08**	**100.40**	**99.66**	**99.47**	**94.19**	**99.83**	**98.87**	**98.61**	**99.21**	**98.46**

and P&H Associates. Data calibration and reduction was carried out in Probe for EPMA, distributed by Probe Software Inc.

4.3. Phase equilibria modelling

Samples DP-7, PCM-83, 72046A and 77223 preserve localised mineral reaction microstructures. Therefore, chemical compositions for phase equilibria modelling were determined by combining measured mineral chemistry with estimates of the mineral modal abundances (Table 4) derived from qualitative element maps of a region interpreted to be relevant to the formation of the mineral reaction textures (Figs. 4–7). Modal abundances were determined by thresholding chemical maps in the software ImageJ. Although a whole-rock geochemical analysis may also provide a valid chemical composition for the purposes of phase equilibria modelling, we adopt a conservative view that targets domains in the rock that record the growth of new minerals, and the bulk chemistry is herein referred to as a 'domain composition' (see Kelsey and Hand, 2015) in order to distinguish it from whole-rock geochemistry. We accept that this 2D compositional determination is necessarily limited, but nonetheless have assumed for the purposes of modelling that this is a realistic composition.

The Fe^{3+} content of minerals was calculated from microprobe analyses using the assumed stoichiometric method of Droop (1987). As mineral chemistry is used in the derivation of the domain composition, Fe_2O_3 is constrained by the abundance of the Fe^{3+} bearing minerals. The amount of Fe_2O_3 may affect the stability of the oxides such as magnetite$_{(ss)}$, ilmenite$_{(ss)}$ and rutile as well as some silicate minerals, but small variations in Fe_2O_3 are not interpreted to significantly affect the topology of the pseudosections (e.g. Boger et al., 2012; Diener and Powell, 2010; Johnson and White, 2011; Morrissey et al., 2015). H_2O was constrained by the abundance of H_2O-bearing minerals (biotite and cordierite) and a conservative estimate of the H_2O content of biotite and cordierite in granulites (e.g. Bose et al., 2005; Cesare et al., 2008; Deer et al., 1992; Rigby and Droop, 2011). The samples preserve low-H_2O mineral assemblages with almost no matrix biotite, consistent with dehydration due to melt loss (Fyfe, 1973; Powell and Downes, 1990; White and Powell, 2002). We cannot unequivocally prove that melt was present in the samples. However, biotite is interpreted to be relict, and in samples such as PCM-83 no newly formed K-feldspar occurs within the reaction microstructures. This suggests that melt may have been generated and was subsequently removed from the sample. This interpretation is consistent with the presence of structurally late Cambrian-aged pegmatite veins in some locations (this study; Hand et al., 1994a) that contain garnet and cordierite, suggesting they were derived from the melting of metasediments. In order to reflect the likely composition prior to final melt loss in samples DP-7, PCM-83, 72046A and 77223, a small amount of melt (7 mol%; equivalent to the melt percolation threshold; e.g. Rosenberg and Handy, 2005) was integrated into the composition using the method of Anderson et al. (2013). This method involves calculating a T–M_{melt} section from the currently preserved, residual domain composition (at $M = 0$) to the composition of an average leucogranite (at $M = 1$). Based on the residual composition, the pressure for the T–M_{melt} section for each sample was set at 6 kbar after a first pass estimate of metamorphic conditions for the cordierite-spinel bearing assemblages. The integration of 7 mol% melt reflects the probability that melt was still present in minor amounts at the metamorphic peak, and was subsequently crystallised or lost (e.g. Brown and Korhonen, 2009; Korhonen et al., 2013a; White and Powell, 2011). It also allows for an assessment of the sensitivity of the mineral assemblages to the effect of melt and H_2O content (e.g. Anderson et al., 2013; Morrissey et al., 2013).

4.3.1. Samples with dominantly Cambrian monazite populations

Samples 77090, 77102B and 77079 do not contain localised mineral reaction microstructures. Therefore, the whole-rock chemical composition was considered to be representative of the equilibration volume at the time of metamorphism. Whole-rock chemical compositions were obtained from Franklin and Marshall College, Pennsylvania. The composition was determined by crushing up a representative amount of the rock and homogenising the sample using a tungsten carbide mill. Major elements were analysed by fusing a 0.4 g portion of the powdered sample with lithium tetraborate for analysis by XRF. Trace elements are analysed by mixing 7 g of crushed rock power with Copolywax powder and measurement by XRF. For these samples, Fe_2O_3 was estimated at 5%, based on the observed mineral assemblage, the modal abundance of Fe^{3+} bearing minerals and an appraisal of ferric iron content of those minerals as determined for measured mineral compositions using the method of Droop (1987). H_2O was also estimated based on the observed mineral assemblage in the rock, the modal abundances of H_2O bearing minerals and a conservative estimate of the H_2O content of biotite and cordierite in granulites.

Mineral equilibria for the samples were calculated using THERMOCALC v3.33, using the internally consistent data set of Powell and Holland (1988; dataset tcds55 November 2003 update), for the geologically realistic system NCKFMASHTO (Na_2O–CaO–K_2O–FeO–MgO–Al_2O_3–SiO_2–H_2O–TiO_2–Fe_2O3). The following activity–composition (*a–x*) relationships were used: silicate melt, garnet and biotite (White et al., 2007); cordierite (Holland and Powell, 1998); spinel, orthopyroxene and magnetite (White et al., 2002); ilmenite and hematite (White et al., 2000); muscovite (Coggon and Holland, 2002) and plagioclase and K-feldspar (Holland and Powell, 2003). Rutile, the aluminosilicates and H_2O are pure end member phases. The whole-rock or domain composition for each sample used in the calculation of the mineral equilibria pseudosections is given above each pseudosection.

5. Results

5.1. Monazite U–Pb geochronology

U–Pb data for all monazite analyses, as well as information on grain size and textural location, are presented as Supplementary Data S7.1. All samples are plotted on Tera–Wasserburg plots to assist with visualisation of the effects of common lead in some samples. The weighted average age is the $^{206}Pb/^{238}U$ age. Dashed ellipses denote analyses that have been excluded as outliers using linearized probability plots, but are shown for completeness. For some samples, ages are calculated using isochrons anchored to a model common Pb composition (single stage; Stacey and Kramers, 1975) at the approximate age of formation.

5.1.1. Northern Prince Charles Mountains

5.1.1.1. DP-1: Depot Peak

In sample DP-1, monazite is preferentially located near the biotite-rich areas of the pegmatite. Monazite grains are coarse-grained (commonly 100–200 μm in diameter, with some grains 20–50 μm), and some grains display patchy zoning (Fig. 8a). Thirty-three analyses were collected from 10 grains. One analysis

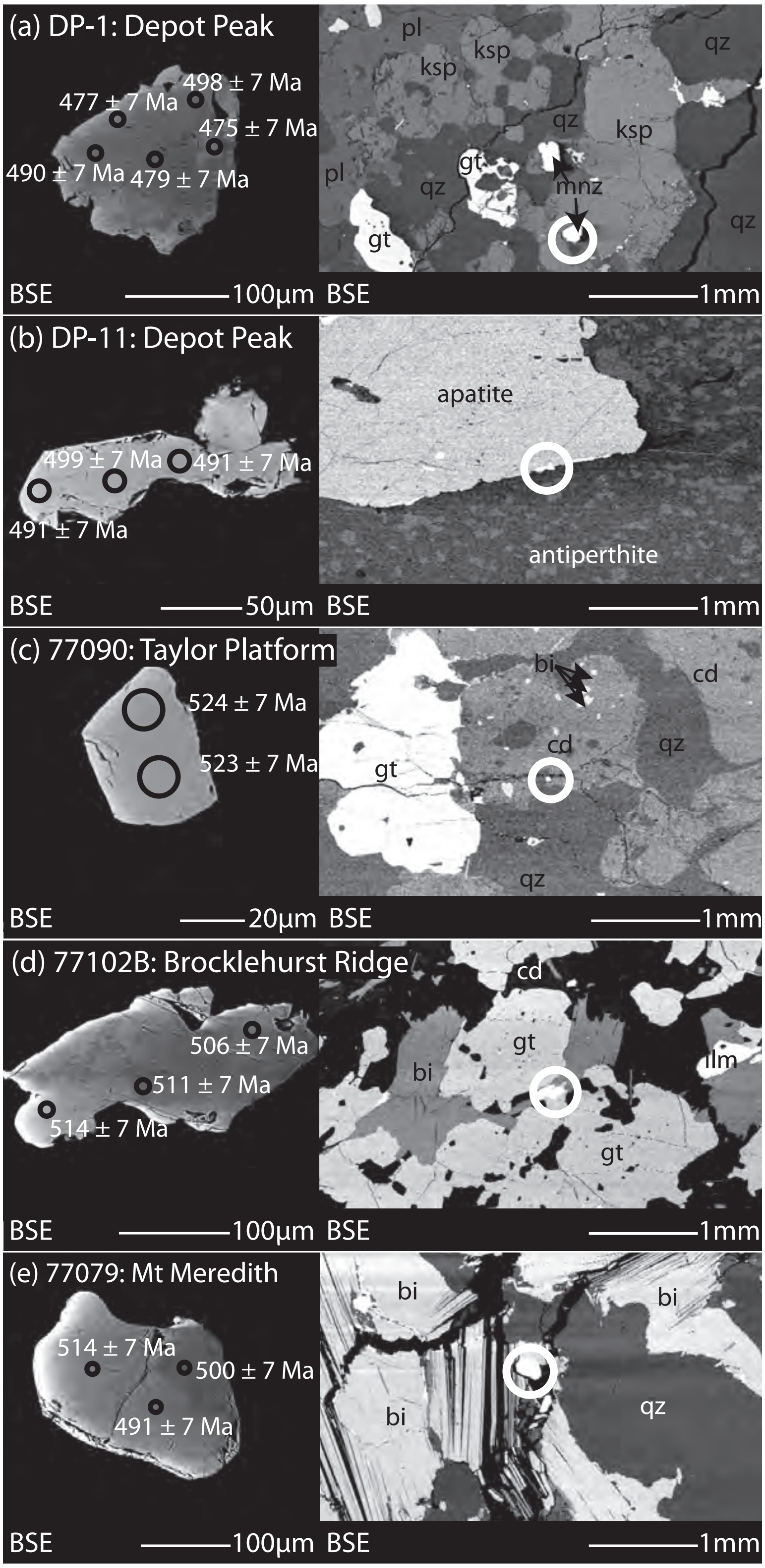

Figure 8: BSE images of representative monazite grains from each sample, and their textural location. The ages shown are the $^{206}Pb/^{238}U$ age. For the samples with localised mineral reaction textures, compositional maps of representative monazite grains that yield Cambrian ages are also shown. In the compositional maps, red denotes areas of higher concentration. (a) Sample DP-1. (b) Sample DP-11. (c) Sample 77090. (d) Sample 77102B. (e) Sample 77079. (f) Sample DP-7. (g) Sample PCM-83. (h) Sample 72046A. (i) Sample 77223.

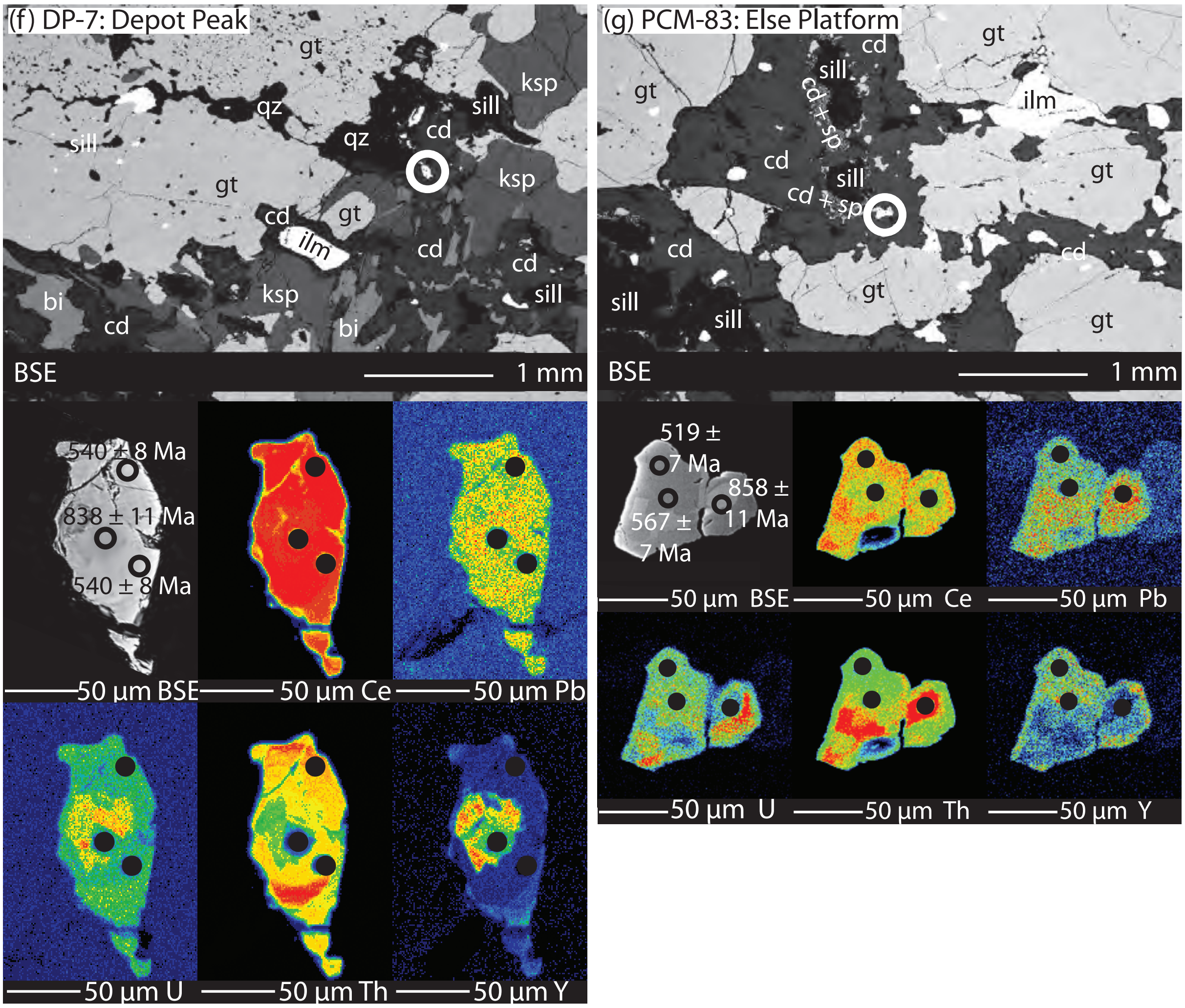

Figure 8 (continued).

was excluded from further calculations using a linearized probability plot. The remaining 32 analyses yield a $^{206}Pb/^{238}U$ weighted average age of 487 ± 3 Ma (MSWD = 1.30). This is identical to the age calculated from an isochron anchored to the single stage Pb age of 487 ± 3 Ma (Fig 9a; MSWD = 1.20).

5.1.1.2. DP-11: Depot Peak

In sample DP-11, monazite is distributed throughout the sample but is coarsest and most abundant in contact with garnet or apatite. Grains are anhedral, unzoned and predominantly vary in size from 20–50 µm in diameter, with some grains elongate and up to 200 µm in length (Fig. 8b). Twenty-two analyses were collected from 10 grains. Two discordant analyses were excluded from the calculation of the weighted average age (Fig. 9b). The remaining 20 analyses yield a $^{206}Pb/^{238}U$ weighted average age of 499 ± 3 Ma (MSWD = 1.01). This is identical to the age calculated from an isochron anchored to the single stage Pb age of 499 ± 3 Ma (MSWD = 1.05).

5.1.1.3. DP-7: Depot Peak

In sample DP-7, monazite is abundant and occurs as inclusions within garnet, within cordierite–spinel–ilmenite reaction textures and along grain boundaries in the matrix. Monazite grains are 50–100 µm in diameter

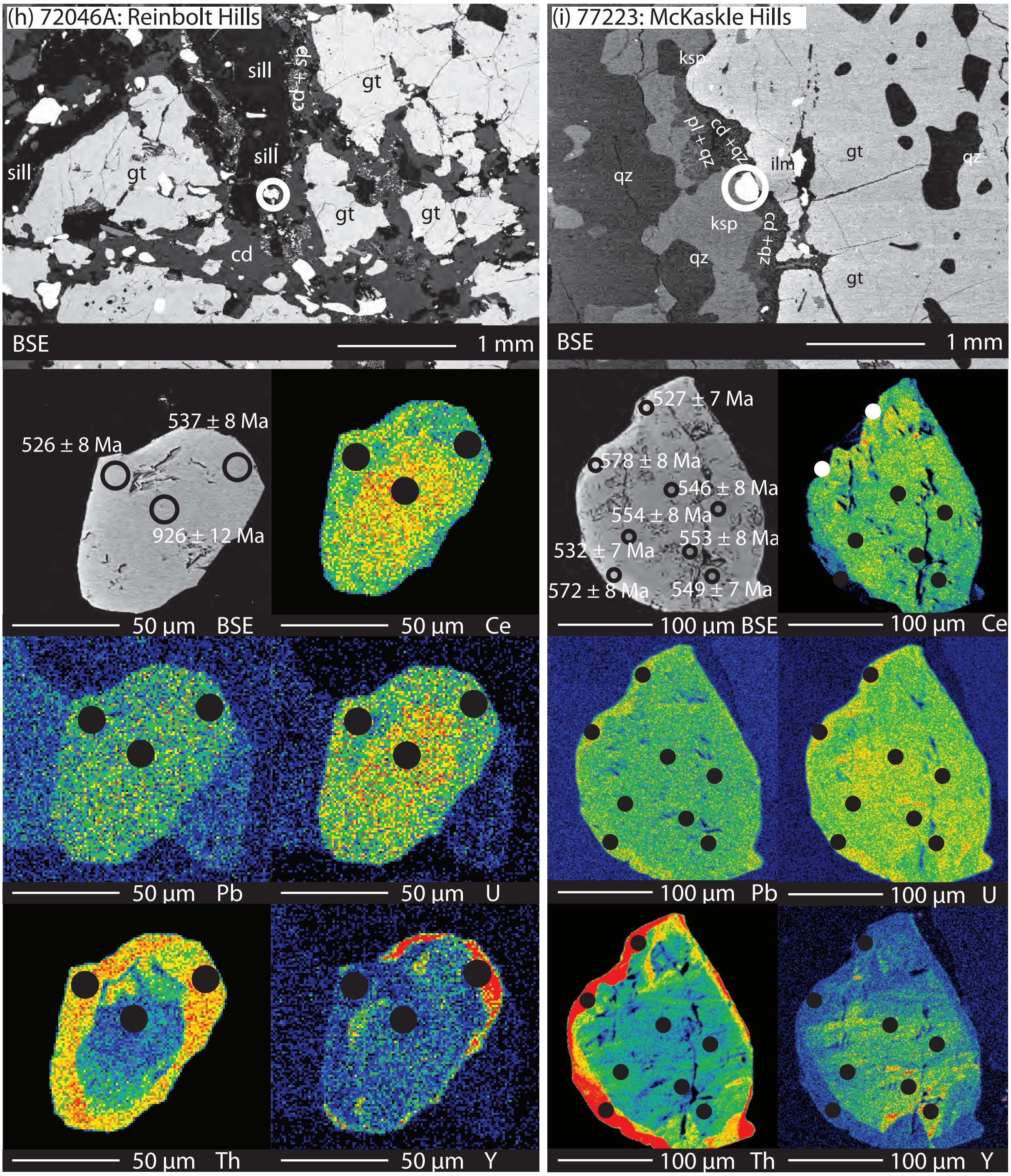

Figure 8 (continued).

and some grains display patchy zoning (Fig. 8f). Forty-two analyses were collected from 16 grains. Monazite grains hosted within coarse-grained, M_1 minerals are denoted as filled grey ellipses in Fig. 9c. The analyses define an older, discordant population and a younger, more clustered population (Fig. 9c). Many grains, including those hosted in garnet, yielded multiple ages in different domains. However, the monazite grains hosted in garnet that yielded younger ages are located on microfractures and so are therefore not isolated from the matrix. There is a link between monazite zoning and age. Areas with high Th and low Y tended to

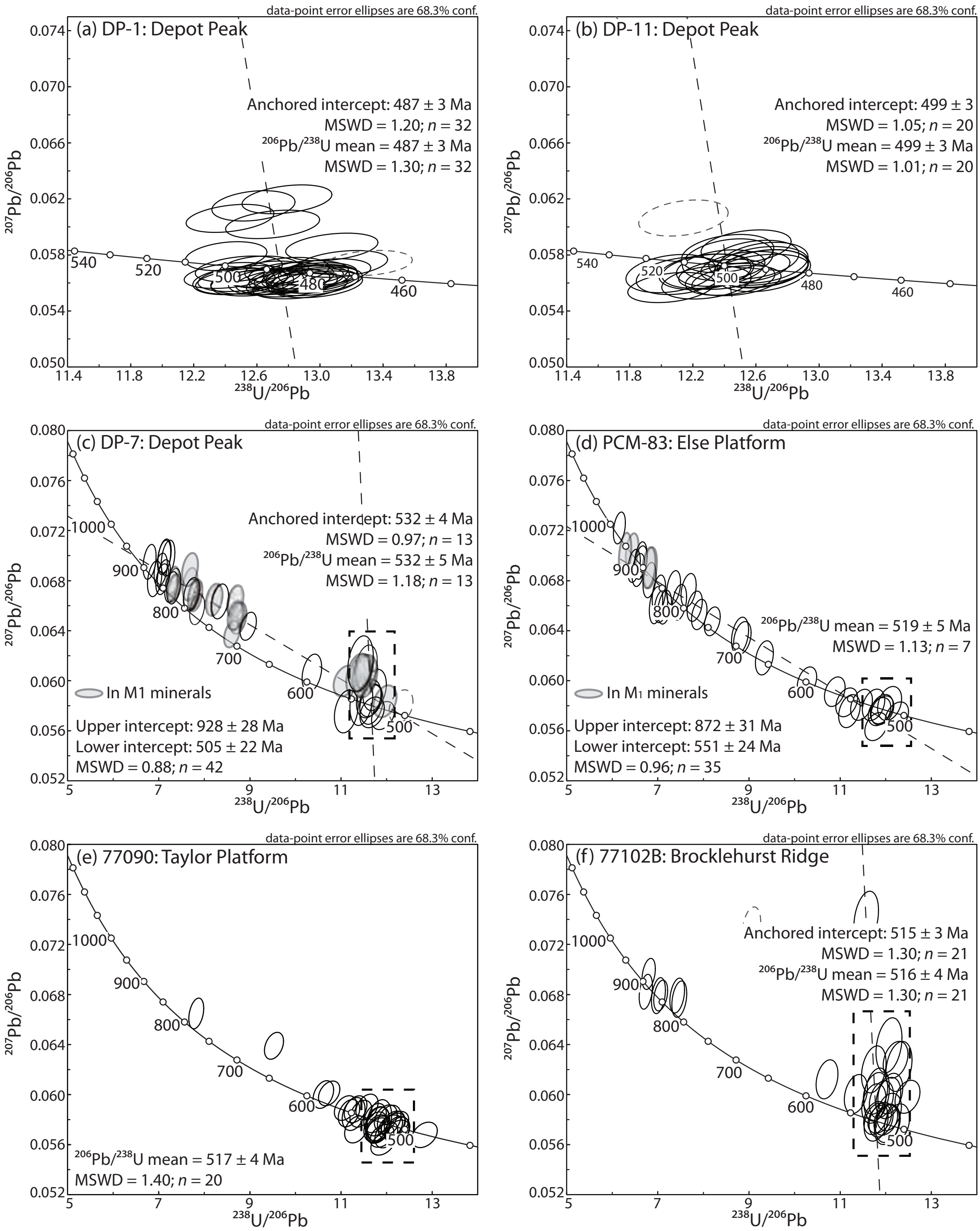

Figure 9: Tera–Wasserburg concordia plots for each of the samples in the study. Analyses denoted as dashed, grey ellipses are excluded from the calculation of weighted averages and intercept ages. The dashed boxes show the populations used for the calculation of weighted average ages. (a) sample DP-1. (b) sample DP-11. (c) sample DP-7. (d) sample PCM-83. (e) sample 77090. (f) sample 77102B. (g) sample 77079. (h) sample 72046A. (i) sample 77223.

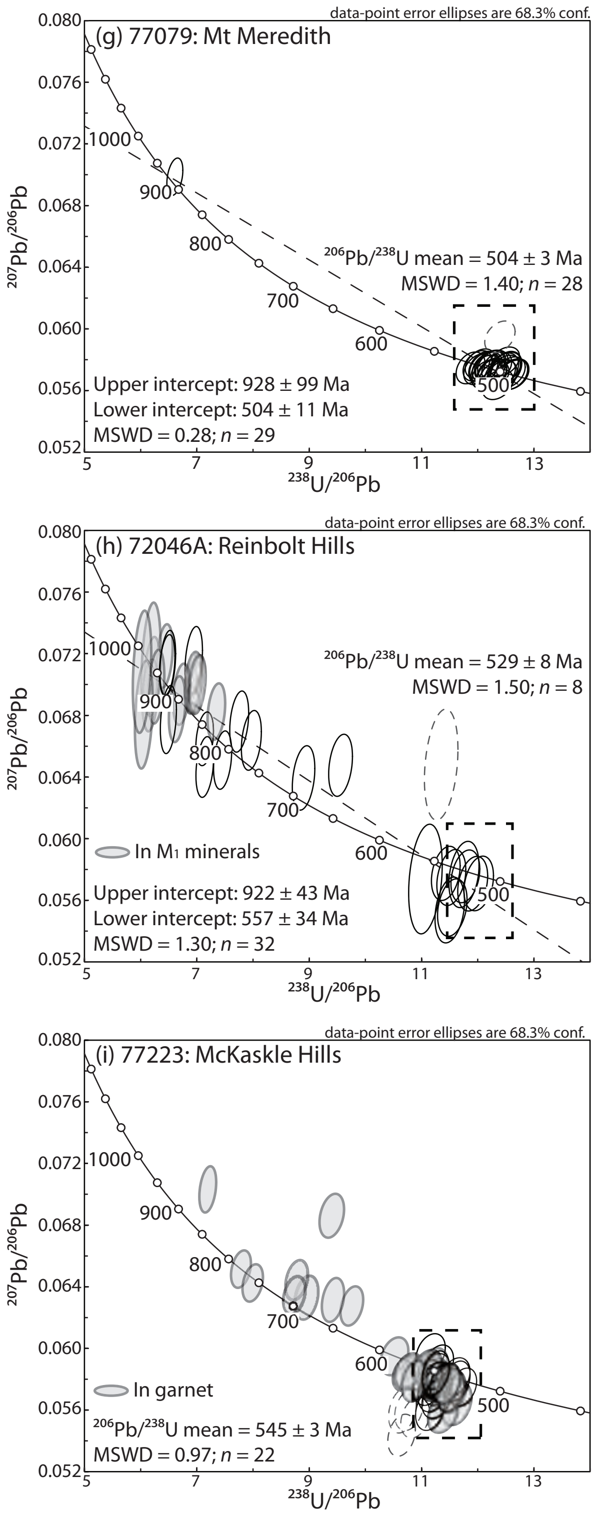

Figure 9 (continued).

yield younger ages (Fig. 8f). A Tera–Wasserburg plot yields a lower intercept of 505 ± 22 Ma and an upper intercept of 928 ± 28 Ma (Fig. 9c; MSWD = 0.88; *n* = 42). The $^{206}Pb/^{238}U$ weighted average age for the 13 analyses making up the younger population (outlined in the dashed box) is 532 ± 5 Ma (MSWD = 1.18). This is identical to the age calculated from an isochron anchored to the single stage Pb age of 532 ± 4 Ma (MSWD = 0.97).

5.1.1.4. PCM-83: Else Platform

In sample PCM-83, monazite is distributed throughout the sample, including within coarse-grained garnet and sillimanite, within cordierite and adjacent to ilmenite in the reaction microstructures. Monazite grains are 20–70 μm in diameter, with some grains showing well defined, patchy zoning patterns (Fig. 8g). Thirty-five analyses were collected from 17 grains. Monazite grains hosted within coarse-grained, M_1 minerals are denoted as filled grey ellipses in Fig. 9d. A Tera–Wasserburg plot of all analyses yields a poorly defined discordia with an upper intercept age of 872 ± 31 Ma and a lower intercept age of 551 ± 24 Ma (Fig. 9d; MSWD = 0.96). The seven analyses making up the younger population (outlined in the dashed box) yield a $^{206}Pb/^{238}U$ weighted average age of 519 ± 5 Ma (MSWD = 1.13). The younger ages come from grains located within cordierite or adjacent to ilmenite in the reaction textures, whereas all grains located within coarse-grained, M_1 minerals yield older ages. However, some older grains, or grains preserving older domains, are also located in the cordierite–spinel reaction textures, and grains which yield younger ages may also yield older ages in other domains (Fig. 8g). Unlike DP-7, younger ages appear to come from zones that are lower in Th and higher in Y (Fig. 8g).

5.1.1.5. 77090: Taylor Platform

In sample 77090, the majority of monazite grains occur throughout the matrix. One grain occurs within garnet, although it is located along a microfracture. Monazite grains are 20–50 μm in diameter and the majority of grains are unzoned (Fig. 8c). Thirty-two analyses were collected from 17 grains. The grain hosted within garnet yields an age of c. 513 Ma. However, as the majority of the grains are unzoned and located within the matrix it is difficult to draw links between age and textural location, or morphology. A younger population was inferred using a linearized probability plot (outlined in the dashed box; Fig. 9e). This population has a weighted average age of 517 ± 4 Ma (MSWD = 1.40; *n* = 20).

5.1.1.6. 77102B: Brocklehurst Ridge

In sample 77012B, monazite occurs within the matrix as well as within garnet grains. Analysed grains vary in size from 20–200 μm in diameter, with the majority of grains displaying patchy zoning (Fig. 8d). Thirty analyses were collected from 15 grains. The analyses fall within two populations. The younger population yields a $^{206}Pb/^{238}U$ weighted average age of 516 ± 4 Ma (Fig. 9f; MSWD = 1.30; *n* = 21). The age of this population calculated from an isochron anchored to the single stage Pb age is 515 ± 3 Ma (MSWD = 1.30). The older population is discordant but is c. 900 Ma. Monazite grains hosted within garnet yield both older and younger ages (Supplementary Data S7.1), and patchy zoning makes it difficult to identify core-rim relationships. However, the older ages are commonly from monazite grains >200 μm in diameter.

5.1.1.7. 77079: Mt Meredith

In sample 77079, the majority of monazite grains occur within biotite or adjacent to biotite grain boundaries, but some are located within quartz. No monazite was observed in garnet. Monazite grains have variable sizes, from 20–200 μm in diameter (Fig. 8e). Some grains display weak zoning but the majority are unzoned (Fig. 8e). Thirty analyses were collected from 14 grains. One discordant analysis was excluded from the calculations. A Tera–Wasserburg plot of the remaining 29 analyses yields a lower intercept of 504 ± 11 Ma and a poorly defined upper intercept of 928 ± 99 Ma (Fig. 9g; MSWD = 0.28). This upper intercept is defined by one old, near concordant analysis with a $^{206}Pb/^{238}U$ age of 908 ± 12 Ma. This analysis is from a grain located within quartz. The remaining 28 analyses define a younger population with a $^{206}Pb/^{238}U$ weighted average age of 504 ± 3 Ma (MSWD = 1.4).

5.1.2. East Amery Ice Shelf

5.1.2.1. 72046A: Reinbolt Hills

In sample 72046A, monazite is located within the cordierite–spinel–ilmenite symplectites, along grain boundaries and armoured within porphyroblasts of garnet, sillimanite and K-feldspar. Grains vary from 20 to 100 μm in diameter. The majority of grains are unzoned, although in rare cases they display REE zoning (Fig. 8h). Thirty-three analyses were collected from 18 grains. Monazite grains hosted within coarse-grained, M_1 minerals are denoted as filled grey ellipses in Fig. 9h. Analyses define two populations with an array of discordant analyses between them. A Tera–Wasserburg plot of all analyses yields an upper intercept of 922 ± 43 Ma and a lower intercept of 557 ± 34 Ma (Fig. 9h; MSWD = 1.30; *n* = 32). The eight analyses making up the younger population (outlined in the dashed box) yield a $^{206}Pb/^{238}U$ weighted average age of 529 ± 8 Ma (MSWD = 1.50). Grains located within M_1 minerals such as garnet, sillimanite, coarse-grained ilmenite or K-feldspar yield older ages, whereas the cordierite–spinel symplectites commonly yield partially reset or younger ages (Fig. 9h). As the

Table 5: Representative electron microprobe analyses for each mineral.

	DP-7: Depot Peak										PCM-83: Else Platform					
Mineral	gt rim	gt core	bi	cd	ksp	pl	qz	sill	ilm	sp	gt rim	gt core	bi	cd	ksp	qz
SiO_2	37.68	38.12	38.22	48.85	64.28	58.82	98.54	36.15	0.15	0.00	37.05	38.34	38.32	48.89	66.48	99.90
TiO_2	0.04	0.05	4.58	0.00	0.04	0.02	0.06	0.02	51.71	0.04	0.02	0.02	3.74	0.00	0.00	0.05
Al_2O_3	21.44	21.46	14.64	32.78	17.28	26.32	0.05	61.14	0.08	58.78	21.33	21.21	16.00	33.05	18.37	0.04
Cr_2O_3	0.02	0.03	0.04	0.00	0.03	0.01	0.00	0.45	0.06	0.49	0.10	0.06	0.20	0.00	0.00	0.01
FeO	31.33	30.53	10.27	6.80	0.15	0.09	0.02	0.21	44.29	30.43	33.43	30.37	11.24	5.51	0.00	0.05
MnO	0.44	0.39	0.02	0.04	0.01	0.01	0.01	0.02	0.14	0.04	0.88	0.75	0.04	0.02	0.00	0.04
MgO	7.49	8.04	17.50	9.78	0.00	0.00	0.03	0.00	1.57	6.56	5.93	7.48	17.42	10.47	0.00	0.02
ZnO	0.01	0.03	0.08	0.07	0.05	0	0.00	0.00	0.01	2.43	0.00	0.00	0.04	0.04	0.00	0.00
CaO	0.99	0.93	0.00	0.00	0.27	7.86	0.01	0.00	0.00	0.01	1.23	1.02	0.00	0.02	0.00	0.02
Na_2O	0.01	0.00	0.18	0.04	2.26	7.25	0.00	0.00	0.03	0.02	0.02	0.02	0.30	0.04	1.69	0.00
K_2O	0.01	0.00	10.39	0.00	14.03	0.10	0.00	0.00	0.00	0.00	0.00	0.00	8.86	0.02	13.69	0.00
Total	**99.45**	**99.57**	**95.95**	**98.36**	**98.40**	**100.48**	**98.72**	**97.99**	**98.03**	**98.81**	**99.99**	**99.27**	**96.17**	**98.06**	**100.23**	**100.13**
No. Oxygens	12	12	11	18	8	8	2	5	3	4	12	12	11	18	8	2
Si	2.96	2.98	2.75	4.99	3.01	2.62	1.00	1.00	0.00	0.00	2.93	3.02	2.75	4.98	3.03	1.00
Ti	0.00	0.00	0.25	0.00	0.00	0.00	0.00	0.00	0.95	0.00	0.00	0.00	0.20	0.00	0.00	0.00
Al	1.99	1.98	1.24	3.95	0.95	1.38	0.00	1.99	0.00	1.95	1.99	1.97	1.35	3.97	0.99	0.00
Cr	0.00	0.00	0.00	0.00	0.00	0.00	0.00	0.01	0.00	0.01	0.01	0.00	0.01	0.00	0.00	0.00
Fe^{3+}	0.08	0.05	-	-	-	-	-	0.01	0.10	0.03	0.15	0.00	-	-	-	-
Fe^{2+}	1.97	1.95	0.62	0.58	0.01	0.00	0.00	0.00	0.89	0.69	2.06	2.00	0.67	0.47	0.00	0.00
Mn^{2+}	0.03	0.03	0.00	0.00	0.00	0.00	0.00	0.00	0.00	0.00	0.06	0.05	0.00	0.00	0.00	0.00
Mg	0.88	0.94	1.87	1.49	0.00	0.00	0.00	0.00	0.06	0.27	0.70	0.88	1.86	1.59	0.00	0.00
Zn	0.00	0.00	0.00	0.01	0.00	0.00	0.00	0.00	0.00	0.05	0.00	0.00	0.00	0.00	0.00	0.00
Ca	0.08	0.08	0.00	0.00	0.01	0.38	0.00	0.00	0.00	0.00	0.10	0.09	0.00	0.00	0.00	0.00
Na	0.00	0.00	0.03	0.01	0.21	0.63	0.00	0.00	0.00	0.00	0.00	0.00	0.04	0.01	0.15	0.00
K	0.00	0.00	0.95	0.00	0.84	0.01	0.00	0.00	0.00	0.00	0.00	0.00	0.81	0.00	0.79	0.00
Total Cations	**8.00**	**7.93**	**11.01**	**5.00**	**4.99**	**1.00**	**3.00**	**2.01**	**8.02**	**8.02**	**7.89**	**11.03**	**5.01**	**1.00**	**3.00**	**3.00**

Table 5 (continued).

	PCM-83			77090: Taylor Platform						77102B: Brocklehurst Ridge						
Mineral	ilm	sp	sill	gt	bi	cd	qz	sill	ilm	gt rim	gt core	bi	cd	ksp	pl	qz
SiO_2	0.00	0.01	36.87	36.95	33.72	46.57	98.95	35.82	0.03	37.36	37.27	34.88	47.63	64.55	63.22	99.82
TiO_2	53.05	0.04	0.03	0.01	3.37	0.02	0.02	0.01	52.90	0.00	0.01	3.25	0.02	0.03	0.00	0.01
Al_2O_3	0.00	58.16	62.92	21.14	17.50	30.88	0.02	60.77	0.25	21.42	21.27	18.68	31.97	18.89	23.04	0.02
Cr_2O_3	0.08	0.00	0.09	0.06	0.28	0.03	0.04	0.04	0.09	0.07	0.03	0.09	0.01	0.00	0.05	0.00
FeO	46.76	31.53	0.50	35.54	20.23	9.56	0.01	0.23	45.14	37.13	36.69	20.82	9.18	0.08	0.03	0.28
MnO	0.19	0.05	0.00	1.53	0.00	0.13	0.00	0.01	0.38	0.53	0.42	0.03	0.02	0.00	0.00	0.00
MgO	0.08	6.35	0.02	3.28	7.61	7.15	0.00	0.01	0.12	2.73	3.58	7.91	7.56	0.01	0.00	0.00
ZnO	0.00	3.02	0.00	0.14	0.10	0.00	0.05	0.04	0.15	0.00	0.02	0.06	0.05	0.00	0.01	0.00
CaO	0.00	0.00	0.00	0.96	0.00	0.01	0.00	0.00	0.01	0.75	0.90	0.00	0.00	0.01	3.83	0.00
Na_2O	0.00	0.12	0.02	0.02	0.17	0.14	0.02	0.00	0.02	0.00	0.00	0.12	0.15	2.04	9.38	0.00
K_2O	0.02	0.01	0.00	0.01	9.31	0.00	0.01	0.01	0.00	0.00	0.00	9.11	0.01	12.87	0.08	0.00
Total	**100.18**	**99.29**	**100.46**	**99.64**	**92.29**	**94.51**	**99.11**	**96.94**	**99.08**	**99.98**	**100.19**	**94.95**	**96.60**	**98.47**	**99.65**	**100.13**
No. Oxygens	3	4	5	12	11	18	2	5	3	12	12	11	18	8	8	2
Si	0.00	0.00	0.99	2.99	2.68	5.03	1.00	1.00	0.00	3.02	2.99	2.68	5.01	2.99	2.80	1.00
Ti	1.01	0.00	0.00	0.00	0.20	0.00	0.00	0.00	1.01	0.00	0.00	0.19	0.00	0.00	0.00	0.00
Al	0.00	1.91	1.99	2.01	1.64	3.93	0.00	1.99	0.01	2.04	2.01	1.69	3.97	1.03	1.20	0.00
Cr	0.00	0.00	0.00	0.00	0.02	0.00	0.00	0.00	0.00	0.00	0.00	0.01	0.00	0.00	0.00	0.00
Fe^{3+}	0.00	0.09	0.02	0.02	-	-	-	0.01	0.00	0.00	0.01	-	-	-	-	-
Fe^{2+}	0.99	0.65	0.00	2.39	1.35	0.86	0.00	0.00	0.96	2.51	2.46	1.34	0.81	0.00	0.00	0.00
Mn^{2+}	0.00	0.00	0.00	0.11	0.00	0.01	0.00	0.00	0.01	0.04	0.03	0.00	0.00	0.00	0.00	0.00
Mg	0.00	0.26	0.00	0.40	0.90	1.15	0.00	0.00	0.00	0.33	0.43	0.91	1.19	0.00	0.00	0.00
Zn	0.00	0.06	0.00	0.01	0.01	0.00	0.00	0.00	0.00	0.00	0.00	0.00	0.00	0.00	0.00	0.00
Ca	0.00	0.00	0.00	0.08	0.00	0.00	0.00	0.00	0.00	0.07	0.08	0.00	0.00	0.00	0.18	0.00
Na	0.00	0.01	0.00	0.00	0.03	0.03	0.00	0.00	0.00	0.00	0.00	0.02	0.03	0.18	0.81	0.00
K	0.00	0.00	0.00	0.00	0.94	0.00	0.00	0.00	0.00	0.00	0.00	0.89	0.00	0.76	0.00	0.00
Total Cations	**2.00**	**2.99**	**3.01**	**8.00**	**7.77**	**11.02**	**1.00**	**3.00**	**2.00**	**8.00**	**8.00**	**7.73**	**11.02**	**4.97**	**5.00**	**1.00**

Table 5 (continued).

	77102B		77079: Mt Meredith					72046A: Reinbolt Hills								
Mineral	sill	ilm	gt rim	gt core	bi	pl	qz	gt rim	gt core	bi	cd	ksp	pl	qz	sill	ilm
SiO_2	36.18	0.06	36.01	35.15	34.12	60.16	98.55	38.41	38.58	38.15	48.92	64.77	61.56	99.90	36.87	0.06
TiO_2	0.00	52.71	0.00	0.00	2.80	0.01	0.00	0.00	0.02	5.81	0.00	0.05	0.00	0.05	0.03	50.90
Al_2O_3	62.22	0.01	20.65	20.36	19.01	23.23	0.01	21.82	21.84	14.76	32.55	18.77	24.49	0.04	62.92	0.00
Cr_2O_3	0.03	0.09	0.01	0.02	0.00	0.05	0.00	0.10	0.01	0.06	0.00	0.01	0.03	0.01	0.09	0.10
FeO	0.26	46.72	37.48	37.03	23.47	0.07	0.01	30.41	28.95	9.87	5.93	0.00	0.18	0.05	0.50	45.67
MnO	0.00	0.08	2.05	1.51	0.06	0.01	0.00	0.81	0.73	0.01	0.09	0.00	0.06	0.04	0.00	0.19
MgO	0.00	0.15	1.83	2.81	5.94	0.00	0.00	8.25	8.97	17.44	9.99	0.00	0.00	0.02	0.02	1.36
ZnO	0.00	0.00	0.06	0.02	0.09	0.02	0.00	0.06	0.07	0.08	0.19	0.03	0.00	0.00	0.00	0.20
CaO	0.00	0.00	0.93	1.05	0.02	5.63	0.00	0.94	0.90	0.00	0.00	0.18	5.85	0.02	0.00	0.02
Na_2O	0.01	0.00	0.02	0.02	0.37	8.29	0.00	0.00	0.00	0.26	0.14	2.51	8.17	0.00	0.02	0.05
K_2O	0.00	0.00	0.01	0.00	9.06	0.06	0.00	0.04	0.00	9.61	0.06	12.84	0.15	0.00	0.00	0.01
Total	**98.70**	**99.82**	**99.04**	**97.99**	**94.94**	**97.53**	**98.57**	**100.86**	**100.07**	**96.04**	**97.88**	**99.17**	**100.49**	**100.13**	**100.46**	**98.56**
No. Oxygens	5	3	12	12	11	8	2	12	12	11	18	8	8	2	5	3
Si	0.99	0.00	3.01	2.99	2.68	5.01	2.99	2.99	2.98	2.76	5.01	2.98	2.72	1.00	0.99	0.00
Ti	0.00	1.00	0.00	0.00	0.19	0.00	0.00	0.00	0.00	0.32	0.00	0.00	0.00	0.00	0.00	0.97
Al	2.00	0.00	2.03	2.01	1.69	3.97	1.03	1.99	1.99	1.26	3.93	1.02	1.28	0.00	1.99	0.00
Cr	0.00	0.00	0.00	0.00	0.01	0.00	0.00	0.01	0.00	0.00	0.00	0.00	0.00	0.00	0.00	0.00
Fe^{3+}	0.02	0.00	-	-	-	-	-	0.02	0.05	-	-	-	-	-	0.02	0.07
Fe^{2+}	0.00	0.99	2.50	2.46	1.34	0.81	0.00	1.91	1.82	0.60	0.51	0.00	0.01	0.00	0.00	0.90
Mn^{2+}	0.00	0.00	0.04	0.03	0.00	0.00	0.00	0.05	0.05	0.00	0.01	0.00	0.00	0.00	0.00	0.00
Mg	0.00	0.01	0.33	0.43	0.91	1.19	0.00	0.91	1.03	1.88	1.53	0.00	0.00	0.00	0.00	0.05
Zn	0.00	0.00	0.00	0.00	0.00	0.00	0.00	0.00	0.00	0.00	0.01	0.00	0.00	0.00	0.00	0.00
Ca	0.00	0.00	0.07	0.08	0.00	0.00	0.00	0.12	0.07	0.00	0.00	0.01	0.28	0.00	0.00	0.00
Na	0.00	0.00	0.00	0.00	0.02	0.03	0.18	0.00	0.00	0.04	0.03	0.22	0.70	0.00	0.00	0.00
K	0.00	0.00	0.00	0.00	0.89	0.00	0.76	0.00	0.00	0.89	0.01	0.75	0.01	0.00	0.00	0.00
Total Cations	**3.00**	**2.00**	**7.97**	**8.00**	**7.73**	**11.02**	**4.97**	**8.00**	**8.00**	**7.75**	**11.04**	**4.99**	**4.99**	**1.00**	**3.01**	**1.99**

Table 5 (continued).

	72046A	**77223: McKaskle Hills**								
Mineral	sp	gt rim	gt core	bi	cd	ksp	pl	ru	qz	ilm
SiO_2	0.02	36.88	2.97	35.12	48.77	64.20	57.96	0.00	98.28	0.00
TiO_2	0.04	0.08	0.00	4.67	0.00	0.06	0.01	100.8	0.06	54.24
Al_2O_3	58.69	20.99	1.97	14.88	33.57	18.84	25.95	0.06	0.02	0.03
Cr_2O_3	0.31	0.05	0.00	0.05	0.00	0.00	0.00	0.13	0.05	0.05
FeO	31.06	30.33	1.94	13.92	5.02	0.13	0.02	0.05	0.17	42.76
MnO	0.09	0.84	0.04	0.02	0.01	0.00	0.00	0.02	0.07	0.19
MgO	7.79	7.19	0.94	13.60	10.96	0.00	0.01	0.01	0.02	1.24
ZnO	1.38	0.12	0.00	0.08	0.00	0.00	0.01	0.00	0.05	0.12
CaO	0.01	1.24	0.13	0.02	0.00	0.03	7.37	0.00	0.03	0.01
Na_2O	0.09	0.00	0.00	0.07	0.01	1.33	7.78	0.00	0.03	0.00
K_2O	0.00	0.00	0.00	8.84	0.00	14.05	0.12	0.00	0.00	0.02
Total	**99.48**	**97.72**	**8.00**	**91.27**	**98.34**	**98.65**	**99.23**	**101.15**	**98.78**	**98.66**
No. Oxygens	4	12	12	11	18	8	8	2	2	3
Si	0.00	2.95	2.97	2.72	4.95	3.00	2.61	0.00	1.00	0.00
Ti	0.00	0.00	0.00	0.27	0.00	0.00	0.00	0.99	0.00	1.02
Al	1.91	1.98	1.97	1.36	4.01	1.04	1.38	0.00	0.00	0.00
Cr	0.01	0.00	0.00	0.00	0.00	0.00	0.00	0.00	0.00	0.00
Fe^{3+}	0.08	0.10	0.06	0.03	-	-	-	-	-	0.01
Fe^{2+}	0.64	1.93	1.88	0.90	0.43	0.01	0.00	0.00	0.00	0.89
Mn^{2+}	0.00	0.06	0.04	0.00	0.00	0.00	0.00	0.00	0.00	0.00
Mg	0.32	0.86	0.94	1.57	1.66	0.00	0.00	0.00	0.00	0.05
Zn	0.03	0.01	0.00	0.00	0.00	0.00	0.00	0.00	0.00	0.00
Ca	0.00	0.11	0.13	0.00	0.00	0.00	0.36	0.00	0.00	0.00
Na	0.00	0.00	0.00	0.01	0.00	0.12	0.68	0.00	0.00	0.00
K	0.00	0.00	0.00	0.87	0.00	0.84	0.01	0.00	0.00	0.00
Total Cations	**3.00**	**8.00**	**8.00**	**7.75**	**11.04**	**5.00**	**5.04**	**0.99**	**1.00**	**1.98**

Table 6: range of values for mineral chemistry of selected minerals.

	DP-7	PCM-83	77090	77102B	77079	72046A	77223
Garnet core							
X_{alm}	0.65–0.67	0.64–0.65	0.80–0.82	0.82–0.83	0.82–0.83	0.62–0.63	0.61–0.65
X_{py}	0.29–0.32	0.30–0.32	0.14	0.10–0.11	0.10–0.11	0.33–0.34	0.34–0.35
X_{grs}	0.025–0.028	0.029–0.030	0.023–0.030	0.027–0.030	0.026–0.030	0.023–0.026	0.022–0.030
X_{sps}	0.008–0.010	0.015	0.033–0.039	0.034–0.036	0.034–0.036	0.013–0.020	0.011–0.018
Garnet rim							
X_{alm}	Unzoned	0.66–0.71	Unzoned	0.85–0.86	0.85	0.64–0.65	0.68–0.69
X_{py}	Unzoned	0.26–0.29	0.11	0.07–0.08	0.07	0.29–0.31	0.26–0.28
X_{grs}	Unzoned	0.035–0.037	Unzoned	Unzoned	Unzoned	0.032–0.040	Unzoned
X_{sps}	Unzoned	0.017–0.019	Unzoned	0.045–0.047	0.046–0.047	Unzoned	0.017–0.022
Biotite							
Ti cpfu	0.24–0.27	0.09–0.23	0.14–0.20	0.18–0.22	0.14–0.20	0.27–0.33	0.22–0.31
X_{Fe}	0.25	0.22–0.28	0.57–0.62	0.58–0.62	0.68–0.70	0.20–0.30	0.34–0.38
Cordierite							
X_{Fe}	0.20–0.28	0.23–0.26	0.41–0.44	0.40–0.42	-	0.20–0.25	0.17–0.23
K-Feldspar							
X_{Or}	0.67–0.82	0.78–0.84	-	0.81–0.90	-	0.76–0.82	0.89
Plagioclase							
X_{Ab}	0.47–0.58	-	-	0.82	0.72–0.74	0.69–0.77	0.59–0.74
Spinel							
Cr cpfu	0.01	0–0.03	-	-	-	0–0.01	-
Zn cpfu	0.05	0.06–0.08	-	-	-	0.03	-
Ilmenite							
Ti cpfu	0.99–1.00	0.99–1.02	1.01–1.04	1.00–0.01		0.97–0.98	1.01–1.02
Mn cpfu	0.002–0.003	0.002–0.007	0.008–0.012	0.002–0.004		0.004–0.006	0.004–0.006

X_{alm} = Fe/(Fe + Mg + Ca + Mn) X_{Fe} = Fe/(Fe + Mg)
X_{py} = Mg/(Fe + Mg + Ca + Mn) X_{or} = K/(K + Na + Ca)
X_{grs} = Ca/(Fe + Mg + Ca + Mn) X_{ab} = Na/(Na + Ca)
X_{sps} = Mn/(Fe + Mg + Ca + Mn)

majority of grains were unzoned in REE, it is difficult to link the younger ages to specific compositional variations. However, in rare grains that do show zoning, the younger or reset ages appear to come from zones that are higher in Th (Fig. 8h).

5.1.2.2. 77223: McKaskle Hills

In sample 77223, monazite occurs within the matrix as well as included within garnet. Monazite grains vary in size from small grains (20 μm in diameter) to large grains up to 200 μm in diameter. Some grains show patchy zoning, others have rims that appear brighter under BSE (Fig. 8i). Forty analyses were collected from 15 grains. Monazite grains hosted within garnet are denoted as filled grey ellipses (Fig. 9i). The analyses fall into two populations (Fig. 9i). Older analyses are discordant and do not define a population, but fall along a poorly defined discordia with an upper intercept of c. 900 Ma. Older analyses are from grains included within garnet porphyroblasts, though grains hosted within garnet also yield younger ages (Fig. 9i). The younger population (defined using a linearized probability plot) yields a $^{206}Pb/^{238}U$ weighted average age of 545 ± 3 Ma (MSWD = 0.97;

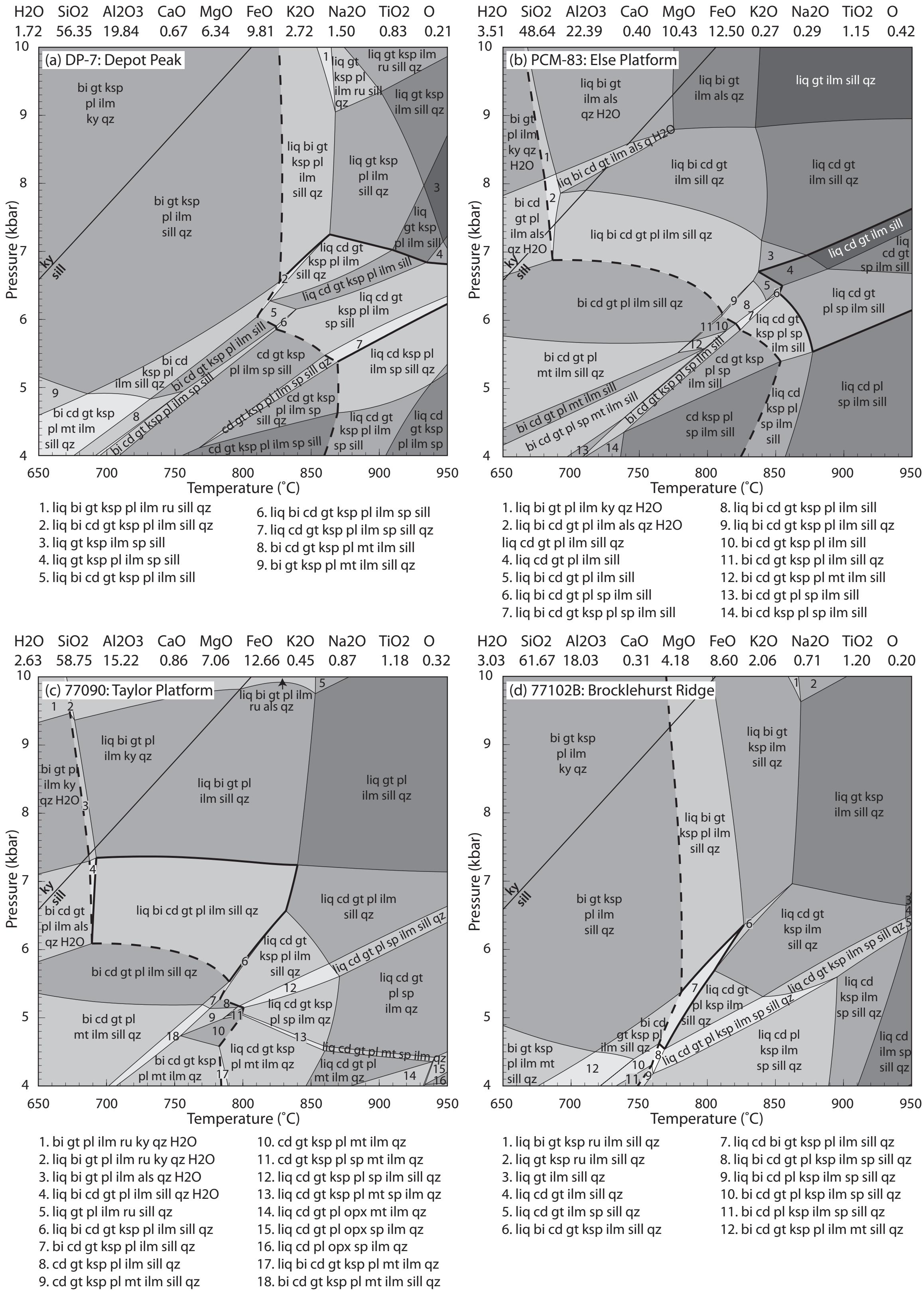

Figure 10: Calculated *P–T* pseudosections using THERMOCALC. The composition is given above each pseudosection. The bold dashed line in each pseudosection is the solidus and fields outlined in bold are the fields of interest. (a) Sample DP-7. (b) Sample PCM-83. (c) Sample 77090. (d) Sample 77102B. (e) Sample 77079. (f) Sample 72046A. (g) Sample 77223. (h) Interpreted peak fields for all samples overlain.

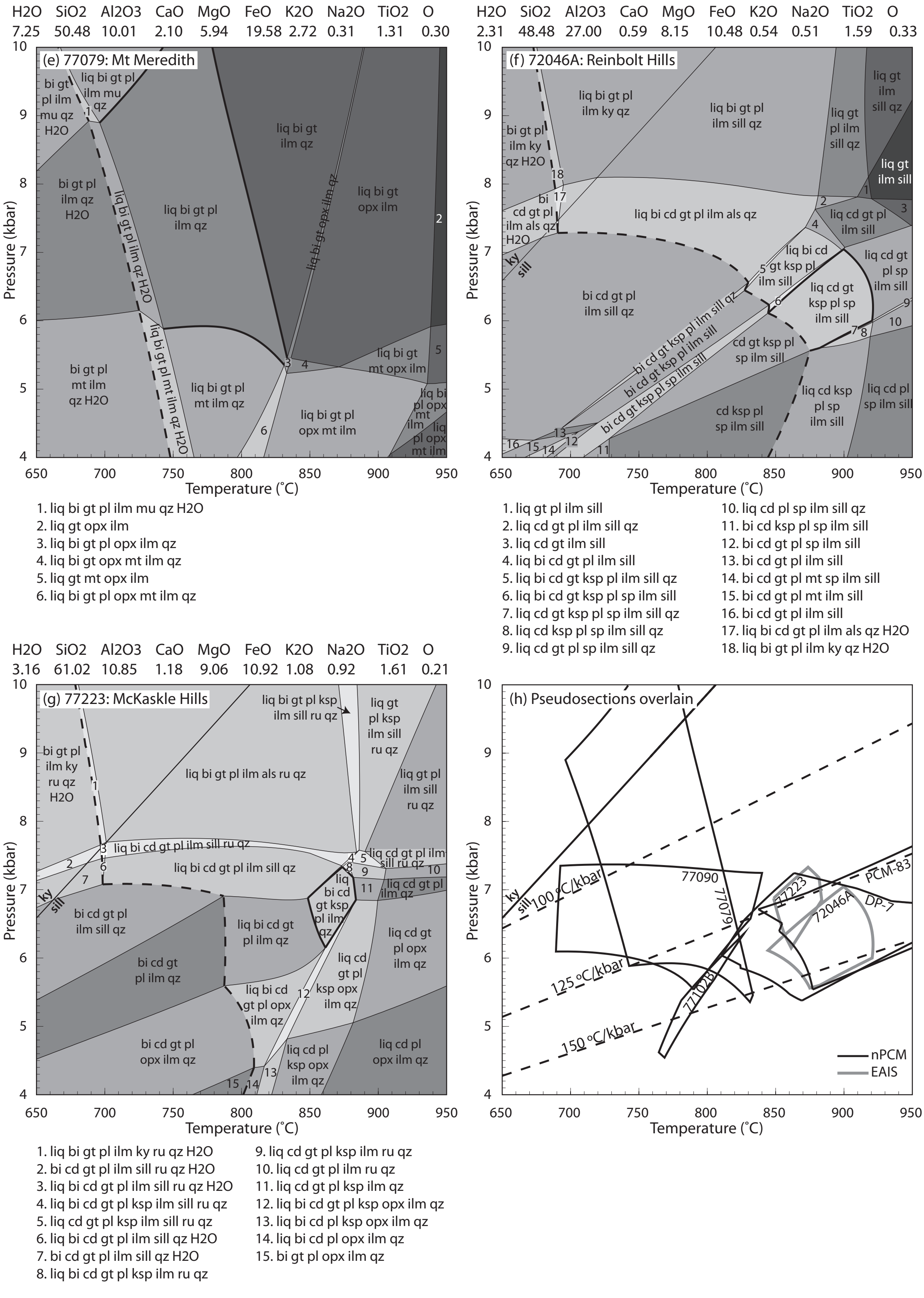

Figure 10 (continued).

n = 22).

5.2. Mineral chemistry

Representative electron microprobe analyses of all minerals are given in Table 5. The range of chemistry for selected minerals is given in Table 6.

5.2.1. Garnet

Garnet grains in samples DP-7, 72046A, PCM-83 and 77223 have X_{alm} values between 0.61–0.67 and X_{py} values between 0.29–0.35. Garnet grains in samples 77079, 77102B and 77079 are more almandine rich, with X_{alm} values between 0.80–0.83 and X_{py} values between 0.10–0.14. All samples have X_{grs} values between 0.02–0.03 and X_{sps} values between 0.01–0.04. Garnet grains in sample DP-7 and 77090 are unzoned in X_{alm}; the other samples show an increase in X_{alm} from core to rim. Sample DP-7 is unzoned in X_{py}; the other samples show a decrease in X_{py} from core to rim. Samples 72046A and PCM-83 display X_{grs} zoning, with an increase from core to rim; the other samples are unzoned in X_{grs}. Samples PCM-83, 77102B, 77079 and 77223 show minor increases in X_{sps} from core to rim, while the other samples are unzoned in X_{sps}.

5.2.2. Biotite

TiO_2 content of biotite in all samples varies from 0.09–0.33 cations pfu, with most analyses falling between 0.15–0.27 cations pfu. Biotite in samples DP-7, PCM-83 and 72046A have X_{Fe} of 0.20–0.30, samples 77090 and 77102B have X_{Fe} of 0.57–0.62, sample 77079 has X_{Fe} of 0.68–0.70 and sample 77223 has X_{Fe} of 0.34–0.38.

5.2.3. Spinel

Spinel in samples DP-7, 72046A and PCM-83 contains 0.03–0.08 Zn cations pfu and 0–0.03 Cr cations pfu.

5.2.4. Cordierite

Samples DP-7, PCM-83, 72046A and 77223 have similar X_{Fe} of 0.17–0.28, whereas samples 77090 and 77102B have higher X_{Fe} of 0.40–0.44.

5.2.5. Ilmenite

Ilmenite in all samples has Ti values between 0.97–1.04 cations pfu and Mn values between 0.002–0.012 cations pfu.

5.2.6. Feldspars

Samples DP-7, 77102B, 77079, 72046A and 77223 contain plagioclase. Sample DP-7 has a lower X_{Ab} range of 0.47–0.58, whereas samples 77079, 72046A and 77223 have X_{Ab} values falling between 0.59–0.77. Sample 77102B has high X_{Ab} of 0.82. Samples DP-7, PCM-83 and 72046A have X_{Or} values of 0.67–0.84 whereas samples 77102B and 77223 have higher X_{Or} values of 0.81–0.90.

5.3. T–M and P–T pseudosections

P–T pseudosections were calculated for metapelitic samples from each of the locations used for geochronology. The fields containing the assemblages of interest for each sample are outlined in bold (Fig. 10). In at least some samples, the mineral reactions probably developed during two high-grade events (Fig. 9). Therefore, mineral assemblages are described in terms of M_1 and M_2 relationships (Table 3).

The samples containing mineral reaction microstructures (DP-7, PCM-83, 72046A and 77223) contain low amounts of H_2O and an elevated solidus, consistent with melt loss. Therefore, *T–M*$_{melt}$ sections were calculated for each of the samples to investigate the effect of melt on the system (Supplementary Data S7.2). The *T–M*$_{melt}$ sections vary from the anhydrous composition of each sample at M_{melt} = 0 to M_{melt} = 0.5 (50 mol% added melt). These samples have similar mineral relationships so the T–M_{melt} sections show similar phase relationships. The effect of adding increasing amounts of melt to the system is to contract the spinel-bearing fields to higher temperatures in the spinel-bearing samples and to lower the temperature of the solidus in all four samples until it becomes water saturated at 660–680 °C (Supplementary Data S7.2). The P–T pseudosections for these samples (described below) were calculated with 7 mol% melt reintegrated into the composition, shown in the T–M_{melt} sections as a bold vertical line. This corresponds to the likely maximum amount of melt in the system at any point, after which melt extraction occurs (e.g. Brown, 2010; Rosenberg and Handy, 2005; Yakymchuk et al., 2013).

5.3.1. Interpretation of mineral reaction microstructures

Samples DP-7, PCM-83, 72046A preserve localised mineral reaction microstructures that are characterised by the partial replacement of garnet–sillimanite-bearing assemblages by cordierite–spinel-bearing assemblages (Table 3). Similarly, sample 77223 preserves a garnet-bearing assemblage that is partially replaced by cordierite–quartz and plagioclase–quartz symplectites (Table 3). Reaction microstructures such as these could be interpreted in several ways. One interpretation is that the microstructures reflect an arrested attempt of the rock to produce a new equilibrium assemblage, with the partially replaced minerals comprising disequilibrium relics (Kelsey and Hand, 2015). An alternative interpretation is that the newly formed minerals were in effective equilibrium with the relict minerals, producing a composite mineral assemblage in which the modal proportion of the reactants was simply reduced (Kelsey and Hand, 2015). We favour the latter interpretation for the following reason. The phase equilibria modelling for samples DP-7, PCM-83, 72046A and 77223 (Fig. 10) shows that replacement of one mineral assemblage by another generally occurs via a series of assemblages that record the progressive decrease in the modal proportion of reactants and the increase in proportion of new minerals. However, implicit in this process is that at each stage, an equilibrium assemblage will exist that comprises a mix of the residual (M_1) assemblage and the newly formed (M_2) minerals. Furthermore, if the reaction microstructures in samples DP-7, PCM-83, 72046A and 77223 represent an arrested attempt to completely replace the M_1 assemblage by the assemblage solely within the symplectites, there should be a calculated phase assemblage field that comprises only the minerals of the symplectites. This is not the case for any of the samples, suggesting that the symplectite assemblages must form part of an assemblage that also comprises one or more of the M_1 reactant minerals.

5.3.2. Northern Prince Charles Mountains

5.3.2.1. DP-7: Depot Peak

Sample DP-7 was likely to have contained an M_1 garnet + sillimanite + biotite + K-feldspar + spinel + ilmenite + quartz assemblage, probably with silicate melt. This was overprinted by a structurally late cordierite–spinel–ilmenite-bearing assemblage. The presence of optically continuous biotite inclusions in the cordierite suggests biotite was present as an M_1 mineral, but has been replaced and the remaining biotite is relict. The former presence of biotite is also suggested by the growth of ilmenite, which requires a source of Ti. Quartz and plagioclase both form fine-grained intergrowths and are interpreted to be part of the M_2 assemblage. We interpret the abundance of garnet and sillimanite in the sample, and the lack of compositional zoning in the garnet, to mean that garnet and sillimanite form part of the M_1 as well as M_2 assemblages. In outcrop, the presence of thin veins of structurally late Cambrian-aged garnet–cordierite-bearing pegmatite also implies that melt was present. We therefore interpret the M_2 mineral assemblage in sample DP-7 to be garnet + sillimanite + K-feldspar + cordierite + spinel + ilmenite + plagioclase + quartz + silicate melt.

The coexistence of spinel and melt means that the minimum temperature is 825 °C (Fig. 10a). However, spinel in this sample contains small amounts of Zn and Cr (Table 6), which are not included in the *a–x* models for spinel but are known to increase spinel stability to lower temperatures and higher pressures (e.g. Nichols et al., 1992; Tajcmanová et al., 2009). Instead, the absence of biotite and presence of quartz can be used to constrain temperatures to between 820–910 °C and the presence of cordierite and garnet constrain pressures to be between 5.4–7.2 kbar (Fig. 10a).

5.3.2.2. PCM-83: Else Platform

Sample PCM-83 is interpreted to have contained an M_1 garnet + sillimanite + biotite + K-feldspar + spinel + ilmenite + quartz assemblage, probably with silicate melt. This has been overprinted by a structurally late M_2 assemblage that involved the formation of cordierite, spinel and ilmenite at the expense of biotite, garnet and sillimanite. There now is a paucity of biotite in the sample. However, its former presence is suggested by small relict grains within the sample and the abundance of ilmenite in the cordierite–spinel-bearing symplectites, which requires the breakdown of a Ti-bearing mineral. The paucity of biotite suggests it may have been the limiting reactant. The presence of silicate melt is inferred based on the presence of Cambrian-aged felsic dykes and pegmatites (Hand et al., 1994b; Manton et al., 1992). Additionally, the lack of newly formed K-feldspar in the M_2 assemblage, despite the implied breakdown of biotite, suggests that melt was likely to have been produced and subsequently lost. Plagioclase is modelled to occur throughout a wide region of *P–T* space but does not occur in this sample. Electron microprobe analyses and X-ray mapping show that sodium is present in cordierite, spinel and biotite (Tables 4 and 5; Fig. 6h), but it is not incorporated in the current *a–x* models for these phases. The minor amounts of sodium in the domain composition result in the over-prediction of plagioclase stability in the sample. Therefore, the absence of plagioclase is not used as a pressure constraint for this sample (Fig. 10b).

The presence of coexisting spinel and silicate melt and the absence of K-feldspar in the reaction domains suggests temperatures are above 850 °C (Fig. 10b). This assemblage does not provide an upper temperature constraint. However, as above, spinel in this sample contains small amounts of Zn and Cr, which may expand the spinel stability field to lower temperatures and higher pressures. Therefore, the fields which best represent the stable mineral assemblage are defined by the absence of biotite and K-feldspar and the presence of garnet, and occur above 820 °C and between 5.4–7.3 kbar (Fig. 10b).

5.3.2.3. 77090: Taylor Platform

The assemblage in sample 77090 is interpreted to have consisted of garnet + sillimanite + cordierite + biotite + ilmenite + quartz + silicate melt. Plagioclase does not occur in this sample, but is present in modally small amounts in the pseudosection. This may be due to the large volume of cordierite in this sample, which contains minor amounts of sodium (as above; Table 5). The presence of cordierite suggests pressures of less than 7.3 kbar (Fig. 10c). The solidus provides a lower temperature constraint of 690 °C at pressures above 6 kbar (Fig. 10c). Biotite is interpreted to form part of the assemblage, but the paucity of biotite suggests that temperatures were near the biotite-out boundary at 830–840 °C (Fig. 10c).

5.3.2.4. 77102B: Brocklehurst Ridge

The assemblage in sample 77102B is interpreted to have consisted of garnet + sillimanite + cordierite + biotite + K-feldspar + ilmenite + quartz + silicate melt. Plagioclase is rare, but does occur in the quartzo-feldspathic regions of the rock, and is therefore also interpreted to form part of the peak assemblage. The coexisting presence of cordierite and biotite constrains peak conditions to a narrow field between 765–825 °C and 4.6–6.3 kbar (Fig. 10d).

5.3.2.5. 77079: Mt Meredith

The assemblage in sample 77079 is interpreted to have consisted of garnet + biotite + plagioclase + ilmenite + quartz + silicate melt. This assemblage is stable over a wide range of conditions (Fig. 10e). However, the absence of magnetite provides a lower pressure constraint of 5.4 kbar, whereas the presence of plagioclase provides an upper temperature constraint of 835 °C. The wet solidus provides a lower temperature constraint of 700 °C. Therefore, the assemblage is stable over temperatures of 700–835 °C and pressures of 5.4–10 kbar (Fig. 10e).

5.3.3. East Amery Ice Shelf

5.3.3.1. 72046A: Reinbolt Hills

Sample 720476A was likely to have contained an M_1 garnet + sillimanite + biotite + spinel + ilmenite + quartz assemblage, probably with silicate melt. The M_2 assemblage is structurally late and contains cordierite–spinel–ilmenite–plagioclase–K-feldspar-bearing domains that developed within the garnet–sillimanite-dominated part of the rock. The abundance of garnet and sillimanite in the sample is interpreted to reflect that they form part of the M_2 assemblage, but in reduced abundance relative to the M_1 assemblage. Therefore, we interpret the M_2 assemblage to comprise garnet + sillimanite + cordierite + spinel + ilmenite + K-feldspar + plagioclase. The additional presence of silicate melt in the M_2 assemblage is inferred based on the presence of Cambrian-aged aluminous pegmatite in the Reinbolt Hills (Ziemann et al., 2005). For the modelled domain composition, the M2 assemblage in sample 72046A is stable at 845–920 °C and 5.5–7 kbar (Fig. 10f).

5.3.3.1. 77223: McKaskle Hills

The M_1 assemblage for the McKaskle Hills is interpreted to be garnet + sillimanite + biotite + K-feldspar + ilmenite + rutile + plagioclase + quartz + silicate melt. The presence of sillimanite, rutile and biotite within garnet suggests that these minerals were part of an earlier stable assemblage. Rutile commonly occurs in the plagioclase–quartz-rich parts of the sample, suggesting they also formed part of the assemblage. Rutile is stable above pressures of 7.2 kbar and temperatures of 810 °C (Fig. 10i). However, as the domain composition is only appropriate for modelling the M_2 assemblage, the conditions of the M_1, probably higher-pressure rutile-bearing assemblage cannot be adequately determined.

The M_2 assemblage is interpreted to involve garnet + cordierite + biotite K-feldspar + ilmenite + plagioclase + quartz + silicate melt. Cordierite–quartz symplectites occur as double coronas on garnet grains, and quartz–plagioclase coronas commonly occur associated with K-feldspar. The symplectites occur in areas that are rich in biotite (Fig. 4f). Rutile is uncommon in these areas; instead biotite and ilmenite are the Ti-bearing minerals. Garnet grains preserve very minor X_{sps} zoning, suggesting that despite the apparent replacement of garnet by the symplectites, a large part of the garnet grain was part of the equilibration volume. The M_2 assemblage occurs between 6.1–7.3 kbar and temperatures of 850–880 ºC.

6. Discussion

6.1. Geochronology

All metapelitic samples preserve geochronological evidence for two episodes of metamorphism; an older population of monazite reflecting growth during the c. 1000–900 Ma Rayner Orogeny and another recording Cambrian-aged reworking. The expression of the overprint as recorded by monazite growth is variable between samples. Samples from Depot Peak, Else Platform and the Reinbolt Hills (samples DP-7, PCM-83 and 72046A) each have poorly defined Rayner-aged populations at c. 920 Ma, with a large number of analyses falling along a chord to a smaller concordant population at c. 530 Ma (Fig. 9c, d and h). Samples from Taylor Platform, Brocklehurst Ridge, Mount Meredith and the McKaskle Hills (samples 77090, 77012B, 77079 and 77223) have dominantly Cambrian-aged populations, with minor inheritance and/or discordance suggesting the samples also experienced a Rayner-aged event (Fig. 9e–g and i). The syn- and post-deformational pegmatite veins from Depot Peak (samples DP-1 and DP-11) are both Cambrian in age (Fig. 9a and b).

Interpreting monazite ages and linking them to the *P*–*T* evolution or development of a tectonic fabric can be difficult (e.g. Cubley et al., 2013; Foster and Parrish, 2003; Gasser et al., 2012; Gervais and Hynes, 2013; Morrissey et al., 2011; Vance et al., 2003). Monazite can be quite unreactive in the absence of fluids or melts and its closure temperature can exceed 900 ºC (Cherniak, 2010; Cherniak et al., 2004). Natural studies on high-temperature and ultrahigh-temperature granulite facies rocks seem to lend support to the preservation of growth ages or inheritance even at very high temperatures (e.g. Clark et al., 2011; Cutts et al., 2013; Goncalves et al., 2004; Kelsey et al., 2007; Kelsey et al., 2003a; Sajeev et al., 2010; Schmitz and Bowring, 2003; Walsh et al., 2015). Temperatures reached in the nPCMs–EAIS region during the Cambrian are not interpreted to exceed monazite closure temperatures (Fig. 10). Instead, natural and experimental studies have suggested that monazite is far more reactive in the presence of fluid or melt (e.g. Harlov et al., 2011; Högdahl et al., 2012; Kelly et al., 2012; Kelsey et al., 2008a; Rapp and Watson, 1986; Rubatto et al., 2013; Stepanov et al., 2012; Williams et al., 2011; Yakymchuk and Brown, 2014). The preservation of monazite during later melting or fluid flow events depends on factors such as the composition of the fluid and monazite grain size, with larger grains more likely to be left residual (Harlov et al., 2011; Rapp and Watson, 1986; Williams et al., 2011). There are minor volumes of pegmatite emplaced during the Cambrian throughout the nPCM–EAIS region, suggesting melt was present within at least some of the metamorphic assemblages (e.g. this study; Boger et al., 2002; Carson et al., 2000; Manton et al., 1992; Ziemann et al., 2005), and the replacement of biotite by cordierite in some samples is also interpreted to suggest that minor amounts of melting occurred. The rocks with residual chemical compositions that preserve localised domains of mineral reaction microstructures (such as samples DP-7 and 72046A and PCM-83) contain very little biotite and abundant monazite that is commonly coarse-grained. These samples also contain large numbers of Rayner-aged or partially reset Rayner-aged monazite grains. The older ages generally come from grains hosted in coarse-grained, M_1 minerals (Fig. 9), or from the cores of large monazite grains, whereas younger or discordant analyses come from the cordierite-bearing reaction microstructures.

Whereas our preferred interpretation is that the Cambrian-aged monazite reflects high-grade Cambrian metamorphism, it is possible that the younger monazite ages are due to coupled dissolution–reprecipitation as a result of a low-temperature fluid flow event that did not impact the major mineral assemblages in the rock (e.g. Harlov et al., 2011; Kelly et al., 2012; Williams et al., 2011). However, all the samples in this study lack the typical evidence for low-temperature (subsolidus) hydrous retrogression, such as abundant mica and pinitisation of cordierite, and preserve largely anhydrous rock compositions and mineralogy consistent with granulite-facies metamorphism and melt loss. Taken together, these suggest that the high temperature mineral assemblages were not subject to a later, lower-temperature fluid flow event that reset the monazite ages. Therefore, the evidence points to the high-temperature formation of new monazite and new mineral assemblages. This suggests that the cordierite–spinel-bearing assemblages are Cambrian in age and grew as a result of the breakdown of garnet–sillimanite–biotite-bearing assemblages at granulite-facies temperatures. The presence of biotite as a reactant is supported by its texturally relict nature within the M_2 assemblages, and the abundance of secondary ilmenite in some samples. The interpreted *P–T* conditions of the formation of the M_2 assemblages, and the lack of retrogression of the cordierite, suggest instead that melt produced during biotite breakdown was the likely fluid that aided the resetting of monazite. A second alternative is that the younger monazite ages are the result of monazite resetting due to prolonged exposure to moderate (< 600 °C) temperatures, perhaps to due a long residence time in the mid-crust following the Rayner Orogeny. The discordant age arrays in some samples could be interpreted to reflect diffusional resetting. However, elsewhere in the nPCM, granulite-facies metapelites do not show evidence for Cambrian-aged resetting of monazite (Morrissey et al., 2015) as would be the case if the Cambrian ages in the samples in this study were the result of diffusional Pb-loss. We therefore interpret the age discordia in some samples to reflect mixing of different age micro-domains within the laser ablation pit.

Further evidence for high temperatures during the Cambrian is provided by variable resetting of Sm–Nd systems in garnet from leucogneiss, charnockite and mafic granulite in the eastern nPCM (Hensen et al., 1997). Garnet up to 2–3 mm in diameter yields isochron ages of 630–555 Ma. These are slightly older than the 550–500 Ma ages in the Rayner Complex attributed to Cambrian tectonism (e.g. Boger et al., 2002; Liu et al., 2009b; Liu et al., 2007b; Phillips et al., 2009), suggesting partial to almost complete resetting of the Rayner-aged Sm–Nd system in garnet. The fastest published REE diffusivities suggest that a 2 mm diameter garnet would need to be heated to at least 750 °C for 10 Myr, or 850 °C for 1 Myr to reset the age (Baxter and Scherer, 2013; Tirone et al., 2005). If the slower REE diffusivities of Carlson (2012) are used, the time scale required to reset the garnets is up to 10 times longer for similar temperatures (Baxter and Scherer, 2013; Carlson, 2012). Therefore, the presence of significantly reset Sm–Nd systematics in garnet suggests that the terrane reached granulite-facies conditions during the Cambrian.

Greenschist-facies mylonites have previously been interpreted to record the *P–T* conditions of Cambrian-aged reworking in the nPCM. These greenschist-facies mylonites have not been directly dated, but post-date 550–500 Ma pegmatites and predate the closure of the Rb–Sr system in biotite at c. 475 Ma (Boger et al., 2002). Similar, but undated, mylonite zones occur in the Reinbolt Hills (Nichols, 1995; Nichols and Berry, 1991). Therefore, if our interpretation of high-temperatures during the Cambrian is correct, the mylonites would have formed during post-peak temperature cooling between c. 530 Ma and c. 475 Ma.

6.2. Metamorphic conditions

6.2.1. Modelled metamorphic conditions

Samples 77090, 77102B and 77079 are located west of the Lambert Glacier in the nPCM and contain dominantly Cambrian monazite and no reaction microstructures, and therefore the mineral assemblages are interpreted to dominantly or entirely record one metamorphic event. In these cases, it is likely that the samples experienced the Rayner Orogeny, but were completely recrystallised during the Cambrian. The mineral assemblages in samples 77090, 77102B and 77079 occur over a wide range of conditions, but overlap at temperatures of 790–830 °C and 5.5–6.3 kbar (Fig. 10c–e and h).

Sample 77223 is located east of the Lambert Glacier in the EAIS and contains dominantly Cambrian monazite, but has mineral reaction microstructures. The M_2 assemblage for this sample is interpreted to have formed at conditions of 850–880 °C and 6.1–7.3 kbar, at slightly higher conditions than those inferred for the dominantly Cambrian-aged samples west of the Lambert Glacier. Samples DP-7, PCM-83 and 72046A are from both east and west of the Lambert Glacier and contain essentially identical mineral assemblages and bimodal monazite populations. The presence of older monazite in garnet and sillimanite porphyroblasts suggests that they may be relics of Rayner-aged metamorphism (Fig. 9). The presence of younger monazite in the cordierite–spinel–ilmenite reaction microstructures suggests the reaction microstructures are likely to be Cambrian in age. The cordierite–spinel–ilmenite reaction microstructures present in these rocks are volumetrically minor, suggesting that only a small amount of the rock was reactive during Cambrian reworking. The modelled pseudosections suggest that temperatures required to form the cordierite–spinel-bearing assemblages were in the range 820–900 ºC, with pressures of 5.4–6.4 kbar (Fig. 10a–f and h). These are higher temperatures than those of the non-spinel-bearing samples, and reflect that the spinel stability field is probably extended to lower temperatures and higher pressures due to the presence of Zn and Cr (e.g. Nichols et al., 1992; Tajcmanová et al., 2009).

6.2.2. Controls on recording of Cambrian metamorphism in nPCM

Despite the interpretation of high temperatures in the nPCM during the Cambrian, and the apparent general similarities in mineral assemblages and chemical compositions in rocks throughout the region, some areas in the nPCM appear to have been metamorphically responsive, whereas others were not (Morrissey et al., 2015). There are numerous examples of previously metamorphosed terranes that record little evidence of later high temperature events (e.g. Drüppel et al., 2012; Korhonen et al., 2012; Tenczer et al., 2006; Wang et al., 2008). Dehydration during previous high-grade metamorphism not only hinders resetting of geochronometers such as monazite and zircon, it also hinders the formation of new mineral assemblages unless rocks experience significant strain (e.g. Harlov et al., 2011; Phillips et al., 2007a; Sajeev et al., 2010; Tenczer et al., 2006; Williams et al., 2011). Previous geochronology from the nPCM shows very little evidence for zircon growth during the Cambrian (e.g. Boger et al., 2000; Carson et al., 2000; Kinny et al., 1997). However, there are few geochronology studies from the nPCM and most of these studies have focused on samples of granite and charnockite, which are unlikely to have reactive chemical compositions. There have been no zircon studies from rocks such as metapelites that may have more reactive compositions.

Studies of polymetamorphic terranes suggest that if melting is limited, it is possible to reach granulite–UHT conditions without significant new zircon growth, even where other chronometers such as monazite or xenotime may be reactive (e.g. Drüppel et al., 2012; Högdahl et al., 2012; McFarlane et al., 2006; Rubatto et al., 2013; Wang et al., 2008). In Prydz Bay, several samples from both the Larsemann Hills and the Rauer Group show very little evidence for zircon growth at c. 500 Ma, despite the attainment of granulite–UHT conditions (Table 2; e.g. Grew et al., 2012; Harley, 1998; Kinny et al., 1993). Similarly, in the EAIS region, U–Pb zircon ages from high-grade rocks and charnockites show that some outcrops are dominated by Cambrian zircon, whereas adjacent outcrops show little evidence for it (Liu et al., 2009b; Wang et al., 2008). In the Mawson Escarpment, some samples contain Cambrian monazite but no Cambrian zircon (Corvino et al., 2008; Corvino et al., 2011; Phillips et al., 2009). The record of Cambrian reworking in these regions has been suggested to relate to rock fertility and the availability of free fluid (Liu et al., 2009b; Phillips et al., 2009; Phillips et al., 2007a). Conceivably, the patchy nature of the Cambrian reworking in the nPCM reflects a control exerted by the retrograde stage of the Rayner Orogeny. Many granulite terranes contain domains of hydrous retrogression associated with melt crystallisation or down-temperature deformation, and there is no logical reason why the nPCM should not also have contained areas of hydrous retrograde mineral growth. Hydrous domains may be sharply bounded by essentially anhydrous, residual granulite chemical compositions (for example shear zones) or be recorded by diffuse patchy retrogression at the grain scale enclosing relict granulite minerals. During a subsequent thermal event, these retrogressed domains will be reactive and effectively undergo a renewed cycle of prograde metamorphism, whereas the original, anhydrous granulites will remain largely unreactive. Rocks that were extensively retrogressed will completely recrystallise leaving no evidence for the former event, whereas rocks that contained volumetrically minor grain-scale retrogression may develop composite mineral assemblages that comprise newly grown prograde minerals and minerals inherited from the earlier granulite assemblage. In either case, the result will be the terrane exhibiting uniformly granulite-grade rocks, which may only be distinguished by geochronology. Therefore we suggest that the patchy record of Cambrian metamorphism in the nPCM reflects rock reactivity caused by patterns of retrogression associated with the earlier Rayner Orogeny.

6.2.3. Cambrian P–T paths

It is difficult to infer *P–T* evolutions in polymetamorphic terranes (e.g. Hand et al., 1992; Kelsey et al., 2003b; Vernon, 1996). Samples 77090, 77102B and 77079 have no reaction microstructures that suggest a likely prograde or retrograde evolution, making it difficult to infer a Cambrian-aged *P–T* path. Sample 77223 (from the McKaskle Hills) contains dominantly Cambrian monazite, and it also contains two separate mineral assemblages: an apparent higher pressure garnet + quartz + plagioclase + rutile + sillimanite assemblage, and an apparent lower pressure cordierite + quartz + plagioclase + biotite assemblage (Fig. 10g). However, sample 77223 contains evidence for older monazite, which has been variably reset (Fig. 9i). These older analyses come from monazite hosted within garnet, suggesting that at least part of the mineral assemblage may be older. Samples DP-7, PCM-83 and 72046A contain volumetrically minor reaction microstructures and do not provide obvious information on the Cambrian *P–T* path. The interpreted M_1 garnet–sillimanite–biotite-bearing assemblage could have formed the cordierite–spinel assemblage by either prograde heating during the Cambrian or decompression. However, given the temporal separation between the Rayner Orogeny and the Cambrian reworking, it is seemingly inevitable that the Cambrian event involved reheating rather than simply decompression.

6.2.4. Preconditioning to reach high temperatures during the Cambrian

Metamorphic conditions during Cambrian reworking in the Rayner Complex involved high apparent thermal gradients of approximately ~115–150 °C/kbar and granulite-facies conditions (Fig. 10h). Attainment of these conditions may have been facilitated by pre-conditioning of the crust that occurred as a result of melt loss and dehydration (e.g. Brown and Korhonen, 2009; Vielzeuf et al., 1990) during the high-temperature c. 1000–900 Ma Rayner Orogeny. The Rayner Orogeny is interpreted to have reached temperatures of 850–900 °C in the nPCM and MacRoberston Land and temperatures of 870– 990 °C in Kemp Land (Boger and White, 2003; Halpin et al., 2007a; Halpin et al., 2007b; Morrissey et al., 2015), and involved significant melt loss. Voluminous granitic and charnockitic magmatism occurred between c. 1150–900 Ma (Halpin et al., 2012). Charnockitic rocks along the Mawson Coast are interpreted to cross-cut the high-grade fabrics in the basement gneisses, suggesting they intruded after peak metamorphism (Halpin et al., 2007a). Modelling of the effect of melt loss shows that it has the capacity to significantly elevate the solidus of the residual rock (e.g. Korhonen et al., 2013a; Korhonen et al., 2010; White and Powell, 2002). Geochemistry from high-temperature granitic and charnockitic rocks that comprise the majority of outcrop in the Rayner Complex shows that they have low H_2O contents, and would therefore have elevated solidii (e.g. Kinny et al., 1997; Munksgaard et al., 1992; Zhao et al., 1997). Thus, by the end of the Rayner Orogeny, the majority of the Rayner Complex was comprised of rocks with 'infertile', mature compositions that would have inhibited significant melting in subsequent events. The infertile nature of the rocks post-Rayner Orogeny means that thermal buffering associated with partial melting would have played a much less significant role during subsequent events, compared to metamorphism of a hydrous terrane (Brown and Korhonen, 2009; Stüwe, 1995; Thompson and Connolly, 1995). As a result, the rocks could have attained higher temperatures (e.g. UHT) much more easily in subsequent events if an appropriate heat source existed (Brown and Korhonen, 2009; Clark et al., 2011; Morrissey et al., 2014; Stüwe, 1995; Vielzeuf et al., 1990; Walsh et al., 2015).

The heat source for Cambrian metamorphism in the nPCM–EAIS region is not well defined. Mikhalsky and Kamenev (2013) suggested

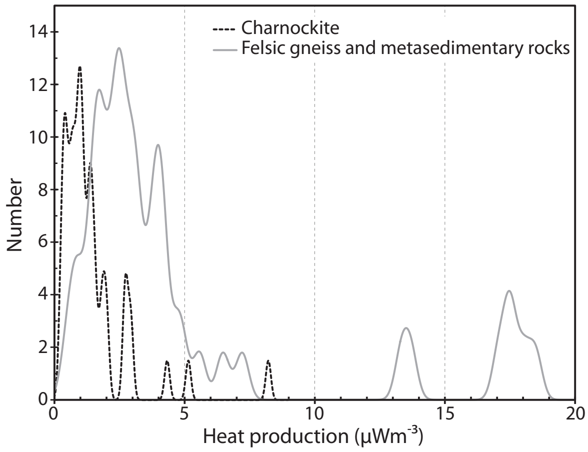

Figure 11: Heat production rates at 550 Ma determined from geochemistry for charnockite and felsic and associated metapelitic lithologies. Data sourced from this study, Munksgaard et al. (1992), Stephenson & Cook (1997), Manton et al. (1992), Young et al. (1997); Kinny et al. (1997), Zhao et al. (1997). Regional geophysical interpretations suggest that ~30% of the nPCM region may comprise felsic and metasedimentary lithologies (Golynsky et al., 2006).

that the Cambrian event was mostly thermal, involving emplacement of charnockite as a result of mafic underplating. The tectonic setting of the Rayner Complex during the Cambrian is uncertain, with some workers interpreting it to be intracratonic (e.g. Kelsey et al., 2008b; Mikhal'sky, 2008; Phillips et al., 2009; Phillips et al., 2007b; Wilson et al., 2007), whereas others have interpreted it to be the result of continent–continent collision (Boger et al., 2008; Boger et al., 2001; Fitzsimons, 1996; Liu et al., 2007a; Liu et al., 2013). If the continent–continent collision model is accepted, the nPCM–EAIS region may have been located in a back-arc extensional setting, which would have provided a thermal driver. Such a setting would logically be associated with comparatively high heat flows, although the geometry and existence of such a system is not well resolved.

Although a back-arc setting may have provided a thermal driver, it also worth noting that charnockites and pelitic granulites in the formerly contiguous Eastern Ghats terrane in India have internal crustal heat production values of about 3 μWm^{-3}, which is high when compared globally to other Archean and Proterozoic granulites (Kumar et al., 2007). It has been suggested that the heat production from these rocks may have resulted in elevated crustal temperatures at 550 Ma in the Eastern Ghats system, and is therefore a possible cause for the metamorphism recorded during the Cambrian (Kumar et al., 2007). Proterozoic rocks in the Rayner Complex have average crustal heat production values of ~2 μWm^{-3} (Carson and Pittard, 2012). Published geochemistry from the nPCM (e.g. Kinny et al., 1997; Manton et al., 1992; Mikhalsky et al., 2001b; Munksgaard et al., 1992; Stephenson and Cook, 1997; Zhao et al., 1997) suggests that the majority of felsic gneisses and metasediments have heat production values of ~2–5 μWm^{-3}, similar to the rocks in the Eastern Ghats Province (Fig. 11), and high by global standards. The proportion of metasedimentary rocks within the nPCM is not defined. However, regional geophysical interpretations (Golynsky et al., 2006; McLean et al., 2009) suggest that significant amounts of the nPCM, extending to Depot Peak, comprise metasedimentary lithologies. If this is the case, the heat production from the metasediments and felsic gneisses (Fig. 11) may have played a significant role in heating the terrane during the Cambrian, particularly given the anhydrous nature of the rocks. Burial of heat-producing rocks may be a thermal source for high-grade metamorphism (e.g. Anderson et al., 2013; Clark et al., 2011; McLaren et al., 2005; Morrissey et al., 2014; Sandiford and Hand, 1998). The lack of a clearly defined Cambrian *P–T* evolution in the Rayner Complex means that burial of high heat producing rocks as a mechanism for the metamorphism is speculative. Nonetheless, the compositions of the Rayner Complex charnockites and metasedimentary rocks are thermally energetic for rocks that have experienced deep crustal metamorphism.

6.3. Links with the Eastern Ghats

There is general agreement that paleogeographic reconstructions within Gondwana support a contiguous Rayner–Eastern Ghats terrane (e.g. Boger, 2011; Fitzsimons, 2000; Mezger and Cosca, 1999), and it therefore seems that the now separate regions were once part of a large, high-grade province. Both regions share a similar Neoproterozoic history, with high-temperature metamorphism and extensive charnockitic magmatism between c. 1150–900 Ma (e.g. Bose et al., 2011; Carson et al., 2000; Gupta, 2012; Halpin et al., 2012; Korhonen et al., 2013b; Mezger and Cosca, 1999). Therefore, given the evidence for Cambrian-aged reworking in parts of the Rayner Complex, it is also possible that the Eastern Ghats experienced a similar high-*T* overprint during the Cambrian.

Cambrian-aged tectonism is thought to have modified the internal structure of the Eastern Ghats Province (Dobmeier and Raith, 2003; Simmat and Raith, 2008). Cambrian reworking involved N–NW directed deformation focused along the boundary between the Eastern Ghats Province and the older cratons to the west (Gupta, 2012; Simmat and Raith, 2008). Electron Probe Micro-Analysis (EPMA) monazite ages of 530–470 Ma from sheared granulites and the growth of new monazite rims has been associated with hydration during this event (Gupta, 2012; Mezger and Cosca, 1999; Simmat and Raith, 2008), as has new growth of zircon in aplite veins (Mezger and Cosca, 1999; Simmat and Raith, 2008). Undeformed pegmatite dykes at c. 515–500 Ma have also been observed in the central migmatite domain (Simmat and Raith, 2008). Low-*T* chronometers such as titanite and isotopic systems such as Ar–Ar, Sm–Nd and Rb–Sr have been variably reset to c. 500 Ma (Crowe et al., 2001; Dobmeier et al., 2006; Mezger and Cosca, 1999; Shaw et al., 1997). The thermal regime associated with the Cambrian overprint in the Eastern Ghats has been interpreted to have been mid-amphibolite facies (Crowe et al., 2001; Mezger and Cosca, 1999). However, some samples from high-grade granulites in the central Eastern Ghats show bimodal distributions in monazite age data, which are similar to those observed in the samples from this study that contain localised mineral reaction microstructures presented in this study (Korhonen et al., 2013b; Simmat and Raith, 2008). Therefore, it seems plausible that the Eastern Ghats may have experienced similar Cambrian-aged reworking to the Rayner Complex.

7. Conclusions

In situ monazite U–Pb geochronology combined with calculated phase diagrams from samples throughout the nPCM–EAIS area of the Rayner Complex suggest that parts of the Rayner–Eastern Ghats terrane experienced high temperature metamorphism between 540–500 Ma. Temperatures were in the range 800–850 ºC with pressures of 5.5–6.5 kbar. This study extends the footprint of Cambrian reworking into the nPCM. This approach shows the importance of careful interpretation of mineral assemblages and *P*–*T* paths when identifying polymetamorphic terranes. Multiple high-grade events may produce a terrane that appears to preserve granulite-facies assemblages formed at similar conditions, when they may be recording temporally different events. Secondary events may only be recorded in spatially restricted locations, where there is an availability of free fluid that allows resetting of geochronometers and the formation of new mineral assemblages. These terranes may be preconditioned to reach high temperatures by previous high-grade metamorphism, which dehydrates the terrane and leaves behind rocks with elevated solidi that are unable to thermally buffer temperatures by melting. High crustal heat production in the Rayner–Eastern Ghats terranes may have further facilitated the attainment of high temperatures.

Acknowledgments

Isabella von Lichtan at the rock library at the University of Tasmania is thanked for providing some of the samples for this study. The staff at Adelaide Microscopy are thanked for their help with analytical work. Jacqueline Halpin, Xiaochun Liu and Steven Boger are thanked for thorough and constructive reviews. Contribution to Antarctic Science Advisory Council project 4191. This manuscript forms TRaX Record #334.

References

Anderson, J.R., Kelsey, D.E., Hand, M., Collins, W.J., 2013. Conductively driven, high-thermal gradient metamorphism in the Anmatjira Range, Arunta region, central Australia. Journal of Metamorphic Geology 31, 1003–1026.

Baxter, E.F., Scherer, E.E., 2013. Garnet Geochronology: Timekeeper of Tectonometamorphic Processes. Elements 9, 433–438.

Beliatsky, B.V., Laiba, A.A., Mikhalsky, E.V., 1994. U–Pb zircon age of the metavolcanic rocks of Fisher Massif (Prince Charles Mountains, East Antarctica). Antarctic Science 6, 355–358.

Boger, S.D., 2011. Antarctica — Before and after Gondwana. Gondwana Research 19, 335–371.

Boger, S.D., Carson, C.J., Fanning, C.M., Hergt, J.M., Wilson, C.J.L., Woodhead, J.D., 2002. Pan-African intraplate deformation in the northern Prince Charles Mountains, east Antarctica. Earth and Planetary Science Letters 195, 195–210.

Boger, S.D., Carson, C.J., Wilson, C.J.L., Fanning, C.M., 2000. Neoproterozoic deformation in the Radok Lake region of the northern Prince Charles Mountains, east Antarctica; evidence for a single protracted orogenic event. Precambrian Research 104, 1–24.

Boger, S.D., Maas, R., Fanning, C.M., 2008. Isotopic and geochemical constraints on the age and origin of granitoids from the central Mawson Escarpment, southern Prince Charles Mountains, East Antarctica. Contributions to Mineralogy and Petrology 155, 379–400.

Boger, S.D., White, R.W., 2003. The metamorphic evolution of metapelitic granulites from Radok Lake, northern Prince Charles Mountains, east Antarctica; evidence for an anticlockwise *P–T* path. Journal of Metamorphic Geology 21, 285–298.

Boger, S.D., White, R.W., Schulte, B., 2012. The importance of iron speciation (Fe^{+2}/Fe^{+3}) in determining mineral assemblages: an example from the high-grade aluminous metapelites of southeastern Madagascar. Journal of Metamorphic Geology 30, 997–1018.

Boger, S.D., Wilson, C.J.L., 2005. Early Cambrian crustal shortening and a clockwise *P–T–t* path from the southern Prince Charles Mountains, East Antarctica: implications for the formation of Gondwana. Journal of Metamorphic Geology 23, 603–623.

Boger, S.D., Wilson, C.J.L., Fanning, C.M., 2001. Early Paleozoic tectonism within the East Antarctic craton: The final suture between east and west Gondwana? Geology 29, 463–466.

Bose, S., Das, K., Fukuoka, M., 2005. Fluorine content of biotite in granulite-grade metapelitic assemblages and its implications for the Eastern Ghats granulites. European Journal of Mineralogy 17, 665–674.

Bose, S., Dunkley, D.J., Dasgupta, S., Das, K., Arima, M., 2011. India–Antarctica–Australia–Laurentia connection in the Paleoproterozoic–Mesoproterozoic revisited: Evidence from new zircon U–Pb and monazite chemical age data from the Eastern Ghats Belt, India. Geological Society of America Bulletin 123, 2031–2049.

Brown, M., 2010. Melting of the continental crust during orogenesis: the thermal, rheological, and compositional consequences of melt transport from lower to upper continental crust. Canadian Journal of Earth Sciences 47, 655–694.

Brown, M., Korhonen, F.J., 2009. Some Remarks on Melting and Extreme Metamorphism of Crustal Rocks Physics and Chemistry of the Earth's Interior, in: Gupta, A.K., Dasgupta, S. (Eds.). Springer New York, pp. 67–87.

Carlson, W.D., 2012. Rates and mechanism of Y, REE, and Cr diffusion in garnet. American Mineralogist 97, 1598–1618.

Carson, C.J., Boger, S.D., Fanning, C.M., Wilson, C.J.L., Thost, D.E., 2000. SHRIMP U–Pb geochronology from Mount Kirkby, northern Prince Charles Mountains, East Antarctica. Antarctic Science 12, 429–442.

Carson, C.J., Dirks, P.G.H.M., Hand, M., Sims, J.P., Wilson, C.J.L., 1995. Compressional and extensional tectonics in low-medium pressure granulites from the Larsemann Hills, East Antarctica. Geological Magazine 132, 151–170.

Carson, C.J., Fanning, C.M., Wilson, C.J.L., 1996. Timing of the progress granite, Larsemann hills: Additional evidence for early Palaeozoic orogenesis within the east Antarctic Shield and implications for Gondwana assembly. Australian Journal of Earth Sciences 43, 539–553.

Carson, C.J., Pittard, M., 2012. A reconnaissance crustal heat production assessment of the Australian Antarctic Territory (AAT). Geoscience Australia, Canberra.

Carson, C.J., Powell, R., Wilson, C.J.L., Dirks, P.H.G.M., 1997. Partial melting during tectonic exhumation of a granulite terrane: an example from the Larsemann Hills, East Antarctica. Journal of Metamorphic Geology 15, 105–126.

Cesare, B., Satish-Kumar, M., Cruciani, G., Pocker, S., Nodari, L., 2008. Mineral chemistry of Ti-rich biotite from pegmatite and metapelitic granulites of the Kerala Khondalite Belt (southeast India): Petrology and further insight into titanium substitutions. American Mineralogist 93, 327–338.

Cherniak, D.J., 2010. Diffusion in Accessory Minerals: Zircon, Titanite, Apatite, Monazite and Xenotime. Reviews in Mineralogy and Geochemistry 72, 827–869.

Cherniak, D.J., Watson, E.B., Grove, M., Harrison, T.M., 2004. Pb diffusion in monazite: a combined RBS/SIMS study. Geochimica et Cosmochimica Acta 68, 829–840.

Clark, C., Fitzsimons, I.C.W., Healy, D., Harley, S.L., 2011. How Does the Continental Crust Get Really Hot? Elements 7, 235–240.

Clarke, G.L., 1988. Structural constraints on the Proterozoic reworking of Archaean crust in the Rayner Complex, Macrobertson and Kemp Land coast, East Antarctica. Precambrian Research 40–41, 137–156.

Coggon, R., Holland, T.J.B., 2002. Mixing properties of phengitic micas and revised garnet-phengite thermobarometers. Journal of Metamorphic Geology 20, 683–696.

Corvino, A.F., Boger, S.D., Henjes-Kunst, F., Wilson, C.J.L., Fitzsimons, I.C.W., 2008. Superimposed tectonic events at 2450 Ma, 2100 Ma, 900 Ma and 500 Ma in the North Mawson Escarpment, Antarctic Prince Charles Mountains. Precambrian Research 167, 281–302.

Corvino, A.F., Wilson, C.J.L., Boger, S.D., 2011. The structural and tectonic evolution of a Rodinian continental fragment in the Mawson Escarpment, Prince Charles Mountains, Antarctica. Precambrian Research 184, 70–92.

Crowe, W.A., Cosca, M.A., Harris, L.B., 2001. $^{40}Ar/^{39}Ar$ geochronolgy and Neoproterozoic tectonics along the northern margin of the Eastern Ghats Belt in north Orissa, India. Precambrian Research 108, 237–266.

Cubley, J.F., Pattison, D.R.M., Tinkham, D.K., Fanning, C.M., 2013. U–Pb geochronological constraints on the timing of episodic regional metamorphism and rapid high-*T* exhumation of the Grand Forks complex, British Columbia. Lithos 156–159, 241–267.

Cutts, K.A., Kelsey, D.E., Hand, M., 2013. Evidence for late Paleoproterozoic (ca 1690–1665 Ma) high- to ultrahigh-temperature metamorphism in southern Australia: Implications for Proterozoic supercontinent models. Gondwana Research 23, 617–640.

Deer, W.A., Howie, R.A., Zussman, J., 1992. An introduction to the rock-forming minerals- 2nd edition. Longman, United Kingdom.

Diener, J.F.A., Powell, R., 2010. Influence of ferric iron on the stability of mineral assemblages. Journal of Metamorphic Geology 28, 599–613.

Diener, J.F.A., White, R.W., Powell, R., 2008. Granulite facies metamorphism and subsolidus fluid-absent reworking, Strangways Range, Arunta Block, central Australia. Journal of Metamorphic Geology 26, 603–622.

Dirks, P.H.G.M., Hand, M., 1995. Clarifying temperature-pressure paths via structures in granulite from the Bolingen Islands, Antarctica. Australian Journal of Earth Sciences 42, 157–172.

Dirks, P.H.G.M., Wilson, C.J.L., 1995. Crustal evolution of the East Antarctic mobile belt in Prydz Bay: continental collision at 500 Ma? Precambrian Research 75, 189–207.

Dobmeier, C., Lütke, S., Hammerschmidt, K., Mezger, K., 2006. Emplacement and deformation of the Vinukonda meta-granite (Eastern Ghats, India)—Implications for the geological evolution of peninsular India and for Rodinia reconstructions. Precambrian Research 146, 165–178.

Dobmeier, C.J., Raith, M.M., 2003. Crustal architecture and evolution of the Eastern Ghats Belt and adjacent regions of India, in: Yoshida, M., Windley, B.F., Dasgupta, S. (Eds.), Proterozoic East Gondwana: Supercontinent Assembly and Breakup. Geological Society of London Special Publications, pp. 145–168.

Droop, G.T.R., 1987. A general equation for estimating Fe^{3+} concentrations in ferromagnesian silicates and oxides from microprobe analyses, using stoichiometric criteria. Mineralogical Magazine 51, 431–435.

Drüppel, K., Elsäßer, L., Brandt, S., Gerdes, A., 2012. Sveconorwegian Mid-crustal Ultrahigh-temperature Metamorphism in Rogaland, Norway: U–Pb LA-ICP-MS Geochronology and Pseudosections of Sapphirine Granulites and Associated Paragneisses. Journal of Petrology.

Dutch, R.A., Hand, M., Clark, C., 2005. Cambrian reworking of the southern Australian Proterozoic Curnamona Province: constraints from regional shear-zone systems. Journal of the Geological Society 162, 763–775.

Fitzsimons, I.C.W., 1996. Metapelitic Migmatites from Brattstrand Bluffs, East Antarctica—Metamorphism, Melting and Exhumation of the Mid Crust. Journal of Petrology 37, 395–414.

Fitzsimons, I.C.W., 2000. A review of tectonic events in the East Antarctic Shield and their implications for Gondwana and earlier supercontinents. Journal of African Earth Sciences 31, 3–23.

Fitzsimons, I.C.W., Harley, S.L., 1991. Geological relationships in high-grade gneiss of the Brattstrand Bluffs coastline, Prydz Bay, East Antarctica. Australian Journal of Earth Sciences 38, 497–519.

Fitzsimons, I.C.W., Harley, S.L., 1992. Mineral reaction textures in high-grade gneisses: evidence for contrasting pressure-temperature paths in the Proterozoic Complex of East Antarctica, in: Yoshida, M., Kaminuma, K., Shiraishi, K. (Eds.), Recent Progress in Antarctic Earth Science. Terra Scientific Publishing, Tokyo, pp. 103–111.

Fitzsimons, I.C.W., Kinny, P.D., Harley, S.L., 1997. Two stages of zircon and monazite growth in anatectic leucogneiss: SHRIMP constraints on the duration and intensity of Pan-African metamorphism in Prydz Bay, East Antarctica. Terra Nova 9, 47–51.

Fitzsimons, I.C.W., Thost, D.E., 1992. Geological relationships in high-grade basement gneiss of the northern Prince Charles Mountains, East Antarctica. Australian Journal of Earth Sciences 39, 173–193.

Foster, G., Parrish, R.R., 2003. Metamorphic monazite and the generation of *P–T–t* paths. Geological Society, London, Special Publications 220, 25–47.

Fyfe, W.S., 1973. The Granulite Facies, Partial Melting and the Archaean Crust. Philosophical Transactions of the Royal Society of London. Series A, Mathematical and Physical Sciences 273, 457–461.

Gasser, D., Bruand, E., Rubatto, D., Stüwe, K., 2012. The behaviour of monazite from greenschist facies phyllites to anatectic gneisses: An example from the Chugach Metamorphic Complex, southern Alaska. Lithos 134–135, 108–122.

Gervais, F., Hynes, A., 2013. Linking metamorphic textures to U–Pb monazite in-situ geochronology to determine the age and nature of aluminosilicate-forming reactions in the northern Monashee Mountains, British Columbia. Lithos 160–161, 250–267.

Golynsky, A., Masolov, V., Volnukhin, V., Golynsky, D., 2006. Crustal Provinces of the Prince Charles

Mountains Region and Surrounding Areas in the Light of Aeromagnetic Data, in: Fütterer, D., Damaske, D., Kleinschmidt, G., Miller, H., Tessensohn, F. (Eds.), Antarctica. Springer Berlin Heidelberg, pp. 83–94.

Goncalves, P., Nicollet, C., Montel, J.-M., 2004. Petrology and in situ U–Th–Pb Monazite Geochronology of Ultrahigh-Temperature Metamorphism from the Andriamena Mafic Unit, North–Central Madagascar. Significance of a Petrographical *P–T* Path in a Polymetamorphic Context. Journal of Petrology 45, 1923–1957.

Grew, E.S., Carson, C.J., Christy, A.G., Maas, R., Yaxley, G.M., Boger, S.D., Fanning, C.M., 2012. New constraints from U–Pb, Lu–Hf and Sm–Nd isotopic data on the timing of sedimentation and felsic magmatism in the Larsemann Hills, Prydz Bay, East Antarctica. Precambrian Research 206–207, 87–108.

Griffin, W.L., Belousova, E.A., Shee, S.R., Pearson, N.J., O'Reilly, S.Y., 2004. Archean crustal evolution in the northern Yilgarn Craton: U–Pb and Hf-isotope evidence from detrital zircons. Precambrian Research 131, 231–282.

Gupta, S., 2012. Strain localization, granulite formation and geodynamic setting of 'hot orogens': a case study from the Eastern Ghats Province, India. Geological Journal 47, 334-351.

Halpin, J.A., Clarke, G.L., White, R.W., Kelsey, D.E., 2007a. Contrasting *P–T–t* paths for Neoproterozoic metamorphism in MacRobertson and Kemp Lands, east Antarctica. Journal of Metamorphic Geology 25, 683–701.

Halpin, J.A., Daczko, N.R., Clarke, G.L., Murray, K.R., 2013. Basin analysis in polymetamorphic terranes: An example from east Antarctica. Precambrian Research 231, 78–97.

Halpin, J.A., Daczko, N.R., Milan, L.A., Clarke, G.L., 2012. Decoding near-concordant U–Pb zircon ages spanning several hundred million years: recrystallisation, metamictisation or diffusion? Contributions to Mineralogy and Petrology 163, 67–85.

Halpin, J.A., White, R.W., Clarke, G.L., Kelsey, D.E., 2007b. The Proterozoic *P–T–t* Evolution of the Kemp Land Coast, East Antarctica; Constraints from Si-saturated and Si-undersaturated Metapelites. Journal of Petrology 48, 1321–1349.

Hand, M., Dirks, P., Powell, R., Buick, I.S., 1992. How well established is isobaric cooling in Proterozoic orogenic belts? An example from the Arunta Inlier, central Australia. Geology 20, 649–652.

Hand, M., Scrimgeour, I., Powell, R., Stüwe, K., Wilson, C.J.L., 1994a. Metapelitic granulites from Jetty Peninsula, east Antarctica: formation during a single event or by polymetamorphism? Journal of Metamorphic Geology 12, 557–573.

Hand, M., Scrimgeour, I., Stuwe, K., Arne, D., Wilson, C.J.L., 1994b. Geological observations in high-grade mid-Proterozoic rocks from Else Platform, northern Prince Charles Mountains region, east Antarctica. Australian Journal of Earth Sciences 41, 311–329.

Harley, S.L., 1998. Ultrahigh temperature granulite metamorphism (1050 °C, 12 kbar) and decompression in garnet (Mg70)–orthopyroxene–sillimanite gneisses from the Rauer Group, East Antarctica. Journal of Metamorphic Geology 16, 541–562.

Harlov, D.E., Wirth, R., Hetherington, C.J., 2011. Fluid-mediated partial alteration in monazite: the role of coupled dissolution–reprecipitation in element redistribution and mass transfer. Contributions to Mineralogy and Petrology 162, 329–348.

Hensen, B.J., Zhou, B., 1995a. A Pan-African granulite facies metamorphic episode in Prydz Bay, Antarctica: Evidence from Sm–Nd garnet dating. Australian Journal of Earth Sciences 42, 249–258.

Hensen, B.J., Zhou, B., 1995b. Retention of isotopic memory in garnets partially broken down during an overprinting granulite-facies metamorphism: Implications for the Sm-Nd closure temperature. Geology 23, 225–228.

Hensen, B.J., Zhou, B., Thost, D.E., 1997. Recognition of Multiple High Grade Metamorphic Events with Garnet Sm–Nd Chronology in the Northern Prince Charles Mountains, Antarctica, in: Ricci, C.A. (Ed.), The Antarctic Region: Geological Evolution and Processes. Terra Antarctica Publication, Sienna, pp. 97–104.

Högdahl, K., Majka, J., Sjöström, H., Nilsson, K., Claesson, S., Konecný, P., 2012. Reactive monazite and robust zircon growth in diatexites and leucogranites from a hot, slowly cooled orogen: implications for the Palaeoproterozoic tectonic evolution of the central Fennoscandian Shield, Sweden. Contributions to Mineralogy and Petrology 163, 167–188.

Holland, T.J.B., Powell, R., 1998. An internally consistent thermodynamic dataset for phases of petrological interest. Journal of Metamorphic Geology 16, 309–343.

Holland, T.J.B., Powell, R., 2003. Activity-composition relations for phases in petrological calculations: an asymmetric multicomponent formulation. Contributions to Mineralogy and Petrography 145, 492–501.

Johnson, T.E., White, R.W., 2011. Phase equilibrium constraints on conditions of granulite-facies metamorphism at Scourie, NW Scotland. Journal of the Geological Society 168, 147-158.

Kamenev, E.N., 1972. Geological structure of Enderby Land, in: Adie, R.J. (Ed.), Antarctic Geology and Geophysics. Oslo: International Union of Geologial Sciences (IUGS), pp. 579–583.

Kelly, N.M., Clarke, G.L., Fanning, C.M., 2002. A two-stage evolution of the Neoproterozoic Rayner Structural Episode: new U–Pb sensitive high resolution ion microprobe constraints from the Oygarden Group, Kemp Land, East Antarctica. Precambrian Research 116, 307–330.

Kelly, N.M., Harley, S.L., 2004. Orthopyroxene-corundum in Mg–Al-rich granulites from the Oygarden Islands, east Antarctica. Journal of Petrology 45, 1481–1512.

Kelly, N.M., Harley, S.L., Möller, A., 2012. Complexity in the behavior and recrystallization of monazite during high-*T* metamorphism and fluid infiltration. Chemical Geology 322–323, 192–208.

Kelsey, D.E., Clark, C., Hand, M., 2008a. Thermobarometric modelling of zircon and monazite growth in melt-bearing systems: examples using model metapelitic and metapsammitic granulites. Journal of Metamorphic Geology 26, 199–212.

Kelsey, D.E., Hand, M., 2015. On ultrahigh temperature crustal metamorphism: phase equilibria, trace element thermometry, bulk composition, heat sources, timescales and tectonic settings. Geoscience Frontiers 6, 311–356.

Kelsey, D.E., Hand, M., Clark, C., Wilson, C.J.L., 2007. On the application of in situ monazite chemical geochronology to constraining *P–T–t* histories in high-temperature (>850 °C) polymetamorphic granulites from Prydz Bay, East Antarctica. Journal of Geological Society, London 164, 667–683.

Kelsey, D.E., Powell, R., Wilson, C.J.L., Steel, D.A., 2003a. (Th+U)-Pb monazite ages from Al–Mg-rich metapelites, Rauer Group, east Antarctica. Contributions to Mineralogy and Petrography 146, 326–340.

Kelsey, D.E., Wade, B.P., Collins, A.S., Hand, M., Sealing, C.R., Netting, A., 2008b. Discovery of a Neoproterozoic basin the in Prydz Belt in East Antarctica and its implications for Gondwana assembly and ultrahigh temperature metamorphism. Precambrian Research 161, 355–388.

Kelsey, D.E., White, R.W., Powell, R., 2003b. Orthopyroxene–sillimanite–quartz assemblages: distribution, petrology, quantitative *P–T–X* constraints and *P–T* paths. Journal of Metamorphic Geology 21, 439–453.

Kelsey, D.E., White, R.W., Powell, R., Wilson, C.J.L., Quinn, C.D., 2003c. New constraints on metamorphism in the Rauer Group, Prydz Bay, east Antarctica. Journal of Metamorphic Geology 21, 739–759.

Kinny, P.D., Black, L.P., Sheraton, J.W., 1993. Zircon ages and the distribution of Archaean and Proterozoic rocks in the Rauer Islands. Antarctic Science 5, 193–206.

Kinny, P.D., Black, L.P., Sheraton, J.W., 1997. Zircon U–Pb ages and geochemistry of igneous and metamorphic rocks in the northern Prince Charles Mountains, Antarctica. AGSO Journal of Australian Geology and Geophysics 16, 637–654.

Korhonen, F.J., Brown, M., Clark, C., Bhattacharya, S., 2013a. Osumilite–melt interactions in ultrahigh temperature granulites: phase equilibria modelling and implications for the *P–T–t* evolution of the Eastern Ghats Province, India. Journal of Metamorphic Geology 31, 881–907.

Korhonen, F.J., Brown, M., Grove, M., Siddoway, C.S., Baxter, E.F., Inglis, J.D., 2012. Separating metamorphic events in the Fosdick migmatite–

granite complex, West Antarctica. Journal of Metamorphic Geology 30, 165–192.

Korhonen, F.J., Clark, C., Brown, M., Bhattacharya, S., Taylor, R., 2013b. How long-lived is ultrahigh temperature (UHT) metamorphism? Constraints from zircon and monazite geochronology in the Eastern Ghats orogenic belt, India. Precambrian Research 234, 322–350.

Korhonen, F.J., Saito, S., Brown, M., Siddoway, C.S., 2010. Modeling multiple melt loss events in the evolution of an active continental margin. Lithos 116, 230–248.

Kumar, P.S., Menon, R., Reddy, G.K., 2007. The role of radiogenic heat production in the thermal evolution of a Proterozoic granulite-facies orogenic belt: Eastern Ghats, Indian Shield. Earth and Planetary Science Letters 254, 39–54.

Liu, X., Hu, J., Zhao, Y., Lou, Y., Wei, C., Liu, X., 2009a. Late Neoproterozoic/Cambrian high-pressure mafic granulites from the Grove Mountains, East Antarctica: *P–T–t* path, collisional orogeny and implications for assembly of East Gondwana. Precambrian Research 174, 181–199.

Liu, X., Jahn, B.-m., Zhao, Y., Li, M., Li, H., Liu, X., 2006. Late Pan-African granitoids from the Grove Mountains, East Antarctica: Age, origin and tectonic implications. Precambrian Research 145, 131–154.

Liu, X., Jahn, B.-m., Zhao, Y., Liu, J., Ren, L., 2014. Geochemistry and geochronology of Mesoproterozoic basement rocks from the Eastern Amery Ice Shelf and southwestern Prydz Bay, East Antarctica: Implications for a long-lived magmatic accretion in a continental arc. American Journal of Science 314, 508–547.

Liu, X., Jahn, B.-M., Zhao, Y., Zhao, G., Liu, X., 2007a. Geochemistry and geochronology of high-grade rocks from the Grove Mountains, East Antarctica: Evidence for an Early Neoproterozoic basement metamorphosed during a single Late Neoproterozoic/Cambrian tectonic cycle. Precambrian Research 158, 93–118.

Liu, X., Zhao, Y., Hu, J., 2013. The c. 1000–900 Ma and c. 550–500 Ma tectonothermal events in the Prince Charles Mountains–Prydz Bay region, East Antarctica, and their relations to supercontinent evolution, in: Harley, S.L., Fitzsimons, I.C.W., Zhao, Y. (Eds.), Antarctica and Supercontinent Evolution. Geological Society, London, Special Publications, pp. 95–112.

Liu, X., Zhao, Y., Song, B., Liu, J., Cui, J., 2009b. SHRIMP U–Pb zircon geochronology of high-grade rocks and charnockites from the eastern Amery Ice Shelf and southwestern Prydz Bay, East Antarctica: Constraints on Late Mesoproterozoic to Cambrian tectonothermal events related to supercontinent assembly. Gondwana Research 16, 342–361.

Liu, X., Zhao, Y., Zhao, G., Jian, P., Xu, G., 2007b. Petrology and Geochronology of Granulites from the McKaskle Hills, Eastern Amery Ice Shelf, Antarctica, and Implications for the Evolution of the Prydz Belt. Journal of Petrology 48, 1443–1470.

Manton, W.I., Grew, E.S., Hofmann, J., Sheraton, J.W., 1992. Granitic rocks of the Jetty Peninsula, Amery Ice Shelf area, East Antarctica, in: Yoshida, Y., Kaminuma, K., Shiraishi, K. (Eds.), Recent Progress in Antarctic Earth Science. Terra Scientific Publishing Company, Tokyo, pp. 179–189.

McFarlane, C.R.M., Connelly, J.N., Carlson, W.D., 2006. Contrasting response of monazite and zircon to a high-*T* thermal overprint. Lithos 88, 135–149.

McLaren, S., Sandiford, M., Powell, R., 2005. Contrasting styles of Proterozoic crustal evolution: A hot-plate tectonic model for Australian terranes. Geology 33, 673–676.

McLean, M.A., Wilson, C.J.L., Boger, S.D., Betts, P.G., Rawling, T.J., Damaske, D., 2009. Basement interpretations from airborne magnetic and gravity data over the Lambert Rift region of East Antarctica. Journal of Geophysical Research: Solid Earth 114, B06101.

Meert, J.G., 2003. A synopsis of events related to the assembly of eastern Gondwana. Tectonophysics 362, 1–40.

Mezger, K., Cosca, M.A., 1999. The thermal history of the Eastern Ghats Belt (India) as revealed by U–Pb and $^{40}Ar/^{39}Ar$ dating of metamorphic and magmatic minerals: implications for the SWEAT correlation. Precambrian Research 94, 251–271.

Mikhal'sky, E.V., 2008. Main stages and geodynamic regimes of the Earth's crust formation in East

Antarctica in the Proterozoic and Early Paleozoic. Geotecton. 42, 413–429.

Mikhalsky, E., Laiba, A., Beliatsky, B., 2006a. Tectonic Subdivision of the Prince Charles Mountains: A Review of Geologic and Isotopic Data, in: Fütterer, D., Damaske, D., Kleinschmidt, G., Miller, H., Tessensohn, F. (Eds.), Antarctica. Springer Berlin Heidelberg, pp. 69–81.

Mikhalsky, E.V., Beliatsky, B.V., Sheraton, J.W., Roland, N.W., 2006b. Two distinct Precambrian terranes in the Southern Prince Charles Mountains, East Antarctica: SHRIMP dating and geochemical constraints. Gondwana Research 9, 291–309.

Mikhalsky, E.V., Kamenev, I.A., 2013. Recurrent transitional group charnockites in the east Amery Ice Shelf coast (East Antarctica): Petrogenesis and implications on tectonic evolution. Lithos 175–176, 230–243.

Mikhalsky, E.V., Sheraton, J.W., Beliatsky, B.V., 2001a. Preliminary U–Pb Dating of Grove Mountains Rocks: Implications for the Proterozoic to Early Palaeozoic Tectonic Evolution of the Lambert Glacier–Prydz Bay Area (East Antarctica). Terra Antartica 8, 3–10.

Mikhalsky, E.V., Sheraton, J.W., Laiba, A.A., Beliatsky, B.V., 1996. Geochemistry and origin of Mesoproterozoic metavolcanic rocks from Fisher Massif, Prince Charles Mountains, East Antarctica. Antarctic Science 8, 85–104.

Mikhalsky, E.V., Sheraton, J.W., Laiba, A.A., Tingey, R.J., Thost, D.E., Kamenev, I.A., Fedorov, L.V., 2001b. Geology of the Prince Charles Mountains, Antarctica. AGSO- Geoscience Australia Bulletin 247.

Morrissey, L., Payne, J.L., Kelsey, D.E., Hand, M., 2011. Grenvillian-aged reworking in the North Australian Craton, central Australia: Constraints from geochronology and modelled phase equilibria. Precambrian Research 191, 141–165.

Morrissey, L.J., Hand, M., Kelsey, D.E., 2015. Multi-stage metamorphism in the Rayner-Eastern Ghats Terrane: *P–T–t* constraints from the northern Prince Charles Mountains, east Antarctica. Precambrian Research 267, 137–163.

Morrissey, L.J., Hand, M., Raimondo, T., Kelsey, D.E., 2014. Long-lived high-temperature, low-pressure granulite facies metamorphism in the Arunta Region, central Australia. Journal of Metamorphic Geology 32, 25–47.

Morrissey, L.J., Hand, M., Wade, B.P., Szpunar, M., 2013. Early Mesoproterozoic metamorphism in the Barossa Complex, South Australia: links with the eastern margin of Proterozoic Australia. Australian Journal of Earth Sciences 60, 769–795.

Munksgaard, N.C., Thost, D.E., Hensen, B.J., 1992. Geochemistry of Proterozoic granulites from northern Prince Charles Mountains, East Antarctica. Antarctic Science 4, 59–69.

Nichols, G., Berry, R., Green, D., 1992. Internally consistent gahnitic spinel-cordierite-garnet equilibria in the FMASHZn system: geothermobarometry and applications. Contributions to Mineralogy and Petrology 111, 362–377.

Nichols, G.T., 1995. The role of mylonites in the uplift of an oblique lower crustal section, East Antarctica. Journal of Metamorphic Geology 13, 223–238.

Nichols, G.T., Berry, R.F., 1991. A decompressional *P–T* path, Reinbolt Hills, East Antarctica. Journal of Metamorphic Geology 9, 257–266.

Payne, J.L., Hand, M., Barovich, K.M., Wade, B.P., 2008. Temporal constraints on the timing of high-grade metamorphism in the northern Gawler Craton: implications for assembly of the Australian Proterozoic. Australian Journal of Earth Sciences 55, 623-640.

Phillips, G., Kelsey, D.E., Corvino, A.F., Dutch, R.A., 2009. Continental Reworking during Overprinting Orogenic Events, Southern Prince Charles Mountains, East Antarctica. Journal of Petrology 50, 2017–2041.

Phillips, G., White, R.W., Wilson, C.J.L., 2007a. On the roles of deformation and fluid during rejuvenation of a polymetamorphic terrane: inferences on the geodynamic evolution of the Ruker Province, East Antarctica. Journal of Metamorphic Geology 25, 855–871.

Phillips, G., Wilson, C.J.L., Campbell, I.H., Allen, C.M., 2006. U–Th–Pb detrital zircon geochronology from the southern Prince Charles Mountains, East Antarctica—Defining the Archaean to Neoproterozoic Ruker Province. Precambrian Research 148, 292-306.

Phillips, G., Wilson, C.J.L., Phillips, D., Szczepanski, S.K., 2007b. Thermochronological ($^{40}Ar/^{39}Ar$) evidence of Early Palaeozoic basin inversion within the southern Prince Charles Mountains, East Antarctica: implications for East Gondwana. Journal of the Geological Society 164, 771–784.

Powell, R., Downes, J., 1990. Garnet porphyroblast-bearing leucosomes in metapelites: mechanisms, phase diagrams, and an example from Broken Hill, Australia, in: Ashworth, J.R., Brown, M. (Eds.), High-temperature Metamorphism and Crustal Anatexis. Springer Netherlands, pp. 105–123.

Powell, R., Holland, T., 1988. An internally consistent thermodynamic dataset with uncertainties and correlations: 3. Application methods, worked examples and a computer program. Journal of Metamorphic Geology 6, 173–204.

Rapp, R., Watson, E.B., 1986. Monazite solubility and dissolution kinetics: implications for the thorium and light rare earth chemistry of felsic magmas. Contributions to Mineralogy and Petrology 94, 304–316.

Rigby, M.J., Droop, G.T.R., 2011. Fluid-absent melting versus CO_2 streaming during the formation of pelitic granulites: A review of insights from the cordierite fluid monitor, in: van Reenen, D.D., Kramers, J.D., McCourt, S., Perchuck, L.L. (Eds.), Origin and Evolution of Precambrian High-Grade Gneiss Terranes, with Special Emphasis on the Limpopo Complex of Southern Africa. Geological Society of America Memoirs, pp. 39–60.

Rosenberg, C.L., Handy, M.R., 2005. Experimental deformation of partially melted granite revisited: implications for the continental crust. Journal of Metamorphic Geology 23, 19–28.

Rubatto, D., Chakraborty, S., Dasgupta, S., 2013. Timescales of crustal melting in the Higher Himalayan Crystallines (Sikkim, Eastern Himalaya) inferred from trace element-constrained monazite and zircon chronology. Contributions to Mineralogy and Petrology 165, 349–372.

Sajeev, K., Williams, I.S., Osanai, Y., 2010. Sensitive high-resolution ion microprobe U–Pb dating of prograde and retrograde ultrahigh-temperature metamorphism as exemplified by Sri Lankan granulites. Geology 38, 971–974.

Sandiford, M., Hand, M., 1998. Australian Proterozoic high-temperature, low-pressure metamorphism in the conductive limit. Geological Society, London, Special Publications 138, 109–120.

Schmitz, M.D., Bowring, S.A., 2003. Ultrahigh-temperature metamorphism in the lower crust during Neoarchean Ventersdorp rifting and magmatism, Kaapvaal Craton, southern Africa. Geological Society of America Bulletin 115, 533–548.

Scrimgeour, I., Hand, M., 1997. A metamorphic perspective on the Pan African overprint in the Amery area of Mac. Robertson Land, East Antarctica. Antarctic Science 9, 313–335.

Shaw, R.K., Arima, M., Kagami, H., Fanning, C.M., Shiraishi, K., Motoyoshi, Y., 1997. Proterozoic Events in the Eastern Ghats Granulite Belt, India: Evidence from Rb–Sr, Sm–Nd Systematics, and SHRIMP Dating. The Journal of Geology 105, 645–656.

Simmat, R., Raith, M.M., 2008. U–Th–Pb monazite geochronometry of the Eastern Ghats Belt, India: Timing and spatial disposition of poly-metamorphism. Precambrian Research 162, 16–39.

Stacey, J.S., Kramers, J.D., 1975. Approximation of terrestrial lead isotope evolution by a two-stage model. Earth and Planetary Science Letters 26, 207–221.

Stepanov, A.S., Hermann, J., Rubatto, D., Rapp, R.P., 2012. Experimental study of monazite/melt partitioning with implications for the REE, Th and U geochemistry of crustal rocks. Chemical Geology 300–301, 200–220.

Stephenson, N.C.N., Cook, N., 1997. Metamorphic evolution of calcsilicate granulites near Battye Glacier, northern Prince Charles Mountains, East Antarctica. Journal of Metamorphic Geology 15, 361–378.

Stüwe, K., 1995. Thermal buffering effects at the solidus. Implications for the equilibration of partially melted metamorphic rocks. Tectonophysics 248, 39–51.

Stüwe, K., Hand, M., 1992. Geology and structure of Depot Peak, MacRobertson Land. More evidence for the continous extent of the 1000 Ma event of East Antarctica. Australian Journal of Earth Sciences 39, 211–222.

Tajcmanová, L., Konopásek, J., Košler, J.,

2009. Distribution of zinc and its role in the stabilization of spinel in high-grade felsic rocks of the Moldanubian domain (Bohemian Massif). European Journal of Mineralogy 21, 407–418.

Tenczer, V., Powell, R., Stüwe, K., 2006. Evolution of H_2O content in a polymetamorphic terrane: the Plattengneiss Shear Zone (Koralpe, Austria). Journal of Metamorphic Geology 24, 281–295.

Thompson, A.B., Connolly, J.A.D., 1995. Melting of the continental crust: Some thermal and petrological constraints on anatexis in continental collision zones and other tectonic settings. Journal of Geophysical Research: Solid Earth 100, 15565–15579.

Thost, D.E., Hensen, B.J., 1992. Gneisses of the Porthos and Athos Ranges, northern Prince Charles Mountains, East Antarctica: Constraints on the prograde and retrograde *P–T* path, in: Yoshida, Y., Kaminuma, K., Shiraishi, K. (Eds.), Recent Progress in Antarctic Earth Science. Terra Scientific Publishing Company, Tokyo, pp. 93–102.

Tingey, R.J., 1991. The regional geology of Archaean and Proterozoic rocks in Antarctica, in: Tingey, R.J. (Ed.), The Geology of Antarctica. Oxford University Press, U.S.A.

Tirone, M., Ganguly, J., Dohmen, R., Langenhorst, F., Hervig, R., Becker, H.-W., 2005. Rare earth diffusion kinetics in garnet: Experimental studies and applications. Geochimica et Cosmochimica Acta 69, 2385–2398.

Tong, L., Wilson, C.J.L., 2006. Tectonothermal evolution of the ultrahigh temperature metapelites in the Rauer Group, east Antarctica. Precambrian Research 149, 1–20.

Vance, D., Müller, W., Villa, I.M., 2003. Geochronology: linking the isotopic record with petrology and textures — an introduction. Geological Society, London, Special Publications 220, 1-24.

Vernon, R.H., 1996. Problems with inferring *P–T–t* paths in low-*P* granulite facies rocks. Journal of Metamorphic Geology 14, 143–153.

Vielzeuf, D., Clemens, J.D., Pin, C., Moinet, E., 1990. Granites, Granulites, and Crustal Differentiation, in: Vielzeuf, D., Vidal, P. (Eds.), Granulites and Crustal Evolution. Springer Netherlands, pp. 59-85.

Walsh, A., Kelsey, D.E., Kirkland, C., Hand, M., Smithies, R.H., Clark, C., Howard, H., 2015. *P–T–t* evolution of a large, long-lived, ultrahigh-temperature Grenvillian belt in central Australia. Gondwana Research 24, 969–983.

Wang, Y., Liu, D., Chung, S.-L., Tong, L., Ren, L., 2008. SHRIMP zircon age constraints from the Larsemann Hills region, Prydz Bay, for a late Mesoproterozoic to early Neoproterozoic tectono-thermal event in East Antarctica. American Journal of Science 308, 573–617.

White, R.W., Powell, R., 2002. Melt loss and the preservation of granulite facies mineral assemblages. Journal of Metamorphic Geology 20, 621–632.

White, R.W., Powell, R., 2011. On the interpretation of retrograde reaction textures in granulite facies rocks. Journal of Metamorphic Geology 29, 131–149.

White, R.W., Powell, R., Clarke, G.L., 2002. The interpretation of reaction textures in Fe-rich metapelitic granulites of the Musgrave Block, central Australia: constraints from mineral equilibria calculations in the system K_2O–FeO–MgO–Al_2O_3–SiO_2–H_2O–TiO_2–Fe_2O_3. Journal of Metamorphic Geology 20, 41–55.

White, R.W., Powell, R., Holland, T.J.B., 2007. Progress relating to calculation of partial melting equilibria for metapelites. Journal of Metamorphic Geology 25, 511–527.

White, R.W., Powell, R., Holland, T.J.B., Worley, B.A., 2000. The effect of TiO_2 and Fe_2O_3 on metapelitic assemblages at greenschist and amphibolite facies conditions: mineral equilibria calculations in the system K_2O–FeO–MgO–Al_2O_3–SiO_2–H_2O–TiO_2–Fe_2O_3. Journal of Metamorphic Geology 18, 497–511.

Williams, M.L., Jercinovic, M.J., Harlov, D.E., Budzyn, B., Hetherington, C.J., 2011. Resetting monazite ages during fluid-related alteration. Chemical Geology 283, 218–225.

Wilson, C.J.L., Quinn, C.D., Tong, L., Phillips, D., 2007. Early Palaeozoic intracratonic shears and post-tectonic cooling in the Rauer Group, Prydz Bay, East Antarctica constrained by $^{40}Ar/^{39}Ar$ thermochronology. Antarctic Science 19, 339–353.

Yakymchuk, C., Brown, M., 2014. Behaviour of zircon and monazite during crustal melting. Journal of the Geological Society 171, 465–479.

Yakymchuk, C., Brown, M., Clark, C., Korhonen, F.J., Piccoli, P.M., Siddoway, C.S., Taylor, R.J.M., Vervoort, J.D., 2015. Decoding polyphase migmatites using geochronology and phase equilibria modelling. Journal of Metamorphic Geology 33, 203–230.

Yakymchuk, C., Brown, M., Ivanic, T.J., Korhonen, F.J., 2013. Leucosome distribution in migmatitic paragneisses and orthogneisses: A record of self-organized melt migration and entrapment in a heterogeneous partially-molten crust. Tectonophysics 603, 136-154.

Young, D.N., Zhao, J.-x., Ellis, D.J., McCulloch, M.T., 1997. Geochemical and Sr–Nd isotopic mapping of source provinces for the Mawson charnockites, east Antarctica: implications for Proterozoic tectonics and Gondwana reconstruction. Precambrian Research 86, 1–19.

Zhao, J.-x., Ellis, D.J., Kilpatrick, J.A., McCulloch, M.T., 1997. Geochemical and Sr-Nd isotopic study of charnockites and related rocks in the northern Prince Charles Mountains, East Antarctica: implications for charnockite petrogenesis and proterozoic crustal evolution. Precambrian Research 81, 37–66.

Zhao, Y., Liu, X.H., Liu, X.C., Song, B., 2003. Pan-African events in Prydz Bay, East Antarctica, and their implications for East Gondwana tectonics. Geological Society, London, Special Publications 206, 231–245.

Zhou, B., Hensen, B.J., 1995. Inherited Sm/Nd isotope components preserved in monazite inclusions within garnets in leucogneiss from East Antarctica and implications for closure temperature studies. Chemical Geology 121, 317–326.

Ziemann, M.A., Forster, H.-J., Harlov, D.E., Frei, R., 2005. Origin of fluorapatite–monazite assemblages in a metamorphosed, sillimanite-bearing pegmatoid, Reinbolt Hills, East Antarctica. European Journal of Mineralogy 17, 567–579.

	Isotopic Ratios						Age Estimates							Morphology and location	
Spot name	$^{207}Pb/^{206}Pb$	±1σ	$^{206}Pb/^{238}U$	±1σ	$^{207}Pb/^{235}U$	±1σ	$^{207}Pb/^{206}Pb$	±1σ	$^{206}Pb/^{238}U$	±1σ	$^{207}Pb/^{235}U$	±1σ	Conc. (%)	Grain size (μm)	Textural location
Sample DP-1: Depot Peak															
1A	0.05656	0.00061	0.08047	0.00123	0.62726	0.00971	474	24	499	7	494	6	101	135x80	Along crack
1B	0.05615	0.00061	0.07998	0.00123	0.61886	0.00961	458	23	496	7	489	6	101	135x80	Along crack
2A	0.05634	0.00061	0.07988	0.00123	0.62025	0.00966	465	24	495	7	490	6	101	185x70	Included in qz
2B	0.05613	0.00061	0.07834	0.00121	0.60593	0.00947	457	24	486	7	481	6	101	185x70	Included in qz
2C	0.05582	0.00061	0.07768	0.00120	0.59752	0.00936	445	24	482	7	476	6	101	185x70	Included in qz
3A	0.05632	0.00061	0.07761	0.00120	0.60242	0.00944	464	24	482	7	479	6	101	295x130	Along crack in ksp grain
3B	0.05641	0.00062	0.07731	0.00120	0.60102	0.00945	468	24	480	7	478	6	100	295x130	Along crack in ksp grain
3C	0.05630	0.00063	0.07782	0.00120	0.60381	0.00956	464	25	483	7	480	6	101	295x130	Along crack in ksp grain
12A	0.06021	0.00067	0.07874	0.00122	0.65335	0.01036	611	24	489	7	511	6	96	95x40	Along crack in ksp grain
7A	0.05607	0.00064	0.07935	0.00122	0.61311	0.00978	455	25	492	7	486	6	101	75x40	Along crack
11A	0.05702	0.00061	0.08009	0.00117	0.62939	0.00938	492	24	497	7	496	6	100	225x85	Along crack, near gt
11B	0.05593	0.00063	0.07703	0.00113	0.59373	0.00908	449	24	478	7	473	6	101	225x85	Along crack, near gt
11C	0.05623	0.00062	0.07704	0.00113	0.59698	0.00904	461	24	478	7	475	6	101	225x85	Along crack, near gt
11D	0.05739	0.00063	0.07611	0.00111	0.60193	0.00908	506	24	473	7	479	6	99	225x85	Along crack, near gt
10A	0.06064	0.00066	0.08045	0.00119	0.67228	0.01012	627	23	499	7	522	6	96	185x150	Along boundary of qz and pl
10B	0.05653	0.00062	0.07725	0.00114	0.60183	0.00908	473	24	480	7	478	6	100	185x150	Along boundary of qz and pl
10C	0.06200	0.00068	0.07818	0.00115	0.66798	0.01013	674	23	485	7	520	6	93	185x150	Along boundary of qz and pl
8A	0.05860	0.00065	0.07648	0.00113	0.61761	0.00944	552	24	475	7	488	6	97	190x150	Boundary of ksp
8B	0.05679	0.00063	0.07675	0.00114	0.60075	0.00919	483	25	477	7	478	6	100	190x150	Boundary of ksp
8C	0.05608	0.00063	0.07718	0.00114	0.59644	0.00915	455	24	479	7	475	6	101	190x150	Boundary of ksp
9A	0.05632	0.00063	0.07721	0.00115	0.59930	0.00920	464	25	480	7	477	6	101	265x155	Boundary of ksp and qz
9B	0.05600	0.00064	0.07799	0.00116	0.60186	0.00930	452	25	484	7	478	6	101	265x155	Boundary of ksp and qz
3A1	0.05608	0.00067	0.07955	0.00110	0.61475	0.00914	455	26	493	7	487	6	101	295x130	Along crack in ksp grain
3A2	0.05675	0.00068	0.07746	0.00107	0.60577	0.00904	481	27	481	6	481	6	100	295x130	Along crack in ksp grain
14A1	0.05654	0.00079	0.07802	0.00109	0.60793	0.00992	473	31	484	7	482	6	100	65x40	Included in ksp
9A1*	0.05745	0.00071	0.07515	0.00104	0.59496	0.00902	508	27	467	6	474	6	99	265x155	Boundary of ksp and qz
9A2	0.05694	0.00070	0.07818	0.00108	0.61342	0.00929	489	27	485	6	486	6	100	265x155	Boundary of ksp and qz
9A3	0.05612	0.00070	0.07883	0.00109	0.60966	0.00931	457	27	489	7	483	6	101	265x155	Boundary of ksp and qz
8A1	0.05663	0.00071	0.07892	0.00109	0.61583	0.00937	476	28	490	7	487	6	101	190x150	Boundary of ksp
8A2	0.05617	0.00072	0.08029	0.00111	0.62143	0.00961	459	28	498	7	491	6	101	190x150	Boundary of ksp
4A1	0.05795	0.00074	0.08061	0.00111	0.64368	0.00991	528	28	500	7	505	6	99	280x135	Included in ksp
4A2	0.06154	0.00080	0.07950	0.00110	0.67415	0.01052	658	28	493	7	523	6	94	280x135	Included in ksp

	Isotopic Ratios						Age Estimates							Morphology and location	
Spot name	$^{207}Pb/^{206}Pb$	±1σ	$^{206}Pb/^{238}U$	±1σ	$^{207}Pb/^{235}U$	±1σ	$^{207}Pb/^{206}Pb$	±1σ	$^{206}Pb/^{238}U$	±1σ	$^{207}Pb/^{235}U$	±1σ	Conc. (%)	Grain size (μm)	Textural location
Sample DP-1 (continued)															
4A3	0.05685	0.00090	0.07922	0.00111	0.62050	0.01100	485	35	492	7	490	7	100	280x135	Included in ksp
Sample DP-11: Depot Peak															
19A1	0.05654	0.00088	0.08248	0.00127	0.64264	0.01193	473	34	511	8	504	7	101	235x35	Included in apatite
19A2	0.05670	0.00090	0.08292	0.00129	0.64792	0.01224	479	35	514	8	507	8	101	235x35	Included in apatite
19A3*	0.07594	0.00112	0.08341	0.00131	0.87283	0.01582	1094	29	516	8	637	9	81	235x35	Included in apatite
19B1	0.05687	0.00081	0.08133	0.00127	0.63736	0.01143	486	32	504	8	501	7	101	55x25	Included in apatite
19C1*	0.06067	0.00085	0.08237	0.00127	0.68865	0.01205	628	30	510	8	532	7	96	45x20	Along boundary of apatite and ksp
30A1	0.05718	0.00096	0.07915	0.00124	0.62366	0.01229	498	37	491	7	492	8	100	40x30	Along crack in matrix
30B1	0.05697	0.00073	0.07915	0.00123	0.62143	0.01048	490	28	491	7	491	7	100	70x25	Included in ksp
41A1	0.05692	0.00099	0.07908	0.00124	0.62019	0.01252	488	38	491	7	490	8	100	70x60	Included in apatite
41A2	0.05683	0.00084	0.08145	0.00128	0.63783	0.01174	484	33	505	8	501	7	101	70x60	Included in apatite
41B1	0.05815	0.00090	0.08051	0.00125	0.64495	0.01199	535	34	499	7	505	7	99	170x60	Boundary of apatite and antiperthite
57A1	0.05769	0.00098	0.08051	0.00123	0.64013	0.01244	518	37	499	7	502	8	99	55x35	Included in ksp
6A1	0.05606	0.00078	0.08139	0.00124	0.62883	0.01093	455	30	504	7	495	7	102	50x40	Included in ksp
25A1	0.05570	0.00071	0.08290	0.00125	0.63638	0.01045	440	28	513	7	500	6	103	320x145	Included in apatite
25A2	0.05665	0.00071	0.08070	0.00121	0.62999	0.01027	477	28	500	7	496	6	101	320x145	Included in apatite
25A3	0.05619	0.00071	0.08015	0.00120	0.62068	0.01012	459	28	497	7	490	6	101	320x145	Included in apatite
25A4	0.05770	0.00091	0.07945	0.00119	0.63174	0.01158	518	34	493	7	497	7	99	320x145	Included in apatite
25B1	0.05709	0.00086	0.08080	0.00121	0.63573	0.01137	495	33	501	7	500	7	100	325x50	Along boundary of apatite and antiperthite
25B2	0.05629	0.00075	0.08041	0.00121	0.62373	0.01046	463	29	499	7	492	7	101	325x50	Along boundary of apatite and antiperthite
25B3	0.05716	0.00074	0.07979	0.00119	0.62846	0.01037	497	29	495	7	495	6	100	325x50	Along boundary of apatite and antiperthite
25B4	0.05862	0.00079	0.07976	0.00120	0.64435	0.01084	553	29	495	7	505	7	98	325x50	Along boundary of apatite and antiperthite
41B2	0.05748	0.00096	0.07910	0.00119	0.62653	0.01193	510	37	491	7	494	7	99	170x60	Along boundary of apatite and antiperthite
41B3	0.05704	0.00090	0.07909	0.00118	0.62165	0.01141	492	35	491	7	491	7	100	170x60	Along boundary of apatite and antiperthite
Sample DP-7: Depot Peak															
8A1	0.05724	0.00074	0.08388	0.00117	0.66174	0.01027	500	28	519	7	516	6	101	120x50	Boundary between cd and bi
19A1	0.05815	0.00106	0.08571	0.00124	0.68686	0.01365	535	40	530	7	531	8	100	170x70	Boundary between gt and ksp
19A2	0.05929	0.00109	0.08520	0.00123	0.69617	0.01393	578	39	527	7	537	8	98	170x70	Boundary between gt and ksp
29B1	0.06573	0.00080	0.12752	0.00176	1.15511	0.01735	798	25	774	10	780	8	99	95x65	Included in gt (on crack)
31A1	0.05838	0.00084	0.08358	0.00117	0.67248	0.01125	544	31	518	7	522	7	99	55x30	Boundary of garnet
32A1	0.06775	0.00086	0.13011	0.00180	1.21477	0.01868	861	26	789	10	807	9	98	95x45	Boundary of sill and cd
33A1	0.05844	0.00084	0.08583	0.00120	0.69120	0.01154	546	31	531	7	534	7	99	165x95	In cd corona

Spot name	Isotopic Ratios $^{207}Pb/^{206}Pb$	±1σ	$^{206}Pb/^{238}U$	±1σ	$^{207}Pb/^{235}U$	±1σ	Age Estimates $^{207}Pb/^{206}Pb$	±1σ	$^{206}Pb/^{238}U$	±1σ	$^{207}Pb/^{235}U$	±1σ	Conc. (%)	Morphology and location Grain size (μm)	Textural location
Sample DP-7 (continued)															
33A2	0.06760	0.00094	0.13642	0.00191	1.27076	0.02063	856	29	824	11	833	9	99	165x95	In cd corona
33B1	0.06954	0.00092	0.14707	0.00204	1.40935	0.02215	915	27	885	11	893	9	99	200x110	In cd corona
33G1	0.05797	0.00088	0.08119	0.00114	0.64859	0.01118	528	33	503	7	508	7	99	30x20	In cd corona
33C1	0.06890	0.00087	0.14196	0.00193	1.34818	0.02040	896	26	856	11	867	9	99	95x60	In cd corona
33C2	0.06691	0.00081	0.12991	0.00176	1.19800	0.01773	835	25	787	10	800	8	98	95x60	In cd corona
37A1	0.06983	0.00095	0.13879	0.00190	1.33564	0.02121	923	28	838	11	861	9	97	110x70	In cd corona
37A2	0.05836	0.00126	0.08737	0.00126	0.70270	0.01588	543	47	540	7	540	9	100	110x70	In cd corona
38A1	0.06072	0.00094	0.08744	0.00121	0.73174	0.01273	629	33	540	7	558	7	97	165x285	Included in gt
38A2	0.06686	0.00084	0.12819	0.00173	1.18120	0.01779	833	26	778	10	792	8	98	165x285	Included in gt
38B1	0.06503	0.00083	0.11432	0.00154	1.02454	0.01558	775	27	698	9	716	8	97	120x235	Included in gt
38B2	0.06638	0.00086	0.11518	0.00155	1.05367	0.01614	819	27	703	9	731	8	96	120x235	Included in gt
33F1	0.07000	0.00090	0.14028	0.00189	1.35324	0.02061	928	26	846	11	869	9	97	70x70	Boundary of bi and ksp
33F2	0.06989	0.00091	0.14048	0.00189	1.35306	0.02069	925	26	847	11	869	9	98	70x70	Boundary of bi and ksp
33E1	0.06814	0.00081	0.14125	0.00187	1.32658	0.01904	873	25	852	11	857	8	99	80x50	In cd corona
39A1	0.06377	0.00071	0.11618	0.00153	1.02101	0.01406	734	23	709	9	714	7	99	55x60	Included in gt
39A2	0.06522	0.00074	0.11518	0.00151	1.03539	0.01438	782	24	703	9	722	7	97	55x60	Included in gt
39B1	0.06065	0.00099	0.09652	0.00132	0.80684	0.01442	627	35	594	8	601	8	99	150x80	Boundary between cd and sill
39B2	0.06438	0.00074	0.11156	0.00147	0.98989	0.01380	754	24	682	9	699	7	98	150x80	Boundary between cd and sill
39B3	0.06848	0.00081	0.14059	0.00186	1.32682	0.01892	883	24	848	11	858	8	99	150x80	Boundary between cd and sill
48A1	0.06800	0.00075	0.13693	0.00180	1.28340	0.01756	869	23	827	10	838	8	99	95x45	Sill inclusion in gt
48A2	0.06743	0.00074	0.13622	0.00179	1.26605	0.01724	851	23	823	10	831	8	99	95x45	Sill inclusion in gt
19A3	0.06112	0.00116	0.08656	0.00120	0.72914	0.01471	643	40	535	7	556	9	96	170x70	Boundary between gt and ksp
33A3	0.06752	0.00081	0.13740	0.00182	1.27861	0.01837	854	25	830	10	836	8	99	165x95	In cd corona
29B2	0.06000	0.00081	0.09016	0.00136	0.74558	0.01257	604	29	557	8	566	7	98	95x65	Included in gt (on crack)
32A2	0.06891	0.00087	0.13010	0.00195	1.23572	0.02010	896	26	789	11	817	9	97	95x45	Boundary of sill and cd
33A4	0.05859	0.00101	0.08615	0.00132	0.69570	0.01371	552	37	533	8	536	8	99	165x95	In cd corona
33A5	0.06696	0.00086	0.12948	0.00194	1.19505	0.01951	837	26	785	11	798	9	98	165x95	In cd corona
33B3	0.05750	0.00081	0.08560	0.00129	0.67831	0.01175	510	30	529	8	526	7	101	200x110	In cd corona
33F3	0.06817	0.00094	0.14469	0.00218	1.35950	0.02325	874	28	871	12	872	10	100	70x70	Boundary of bi and ksp
38A3	0.06039	0.00112	0.08675	0.00134	0.72204	0.01500	617	40	536	8	552	9	97	165x285	Included in gt
38A4	0.06040	0.00118	0.08783	0.00137	0.73119	0.01572	618	42	543	8	557	9	97	165x285	Included in gt

	Isotopic Ratios						Age Estimates							Morphology and location	
Spot name	$^{207}Pb/^{206}Pb$	±1σ	$^{206}Pb/^{238}U$	±1σ	$^{207}Pb/^{235}U$	±1σ	$^{207}Pb/^{206}Pb$	±1σ	$^{206}Pb/^{238}U$	±1σ	$^{207}Pb/^{235}U$	±1σ	Conc. (%)	Grain size (μm)	Textural location
Sample DP-7 (continued)															
38B3	0.06651	0.00085	0.12171	0.00180	1.11567	0.01817	822	27	740	10	761	9	97	120x235	Included in gt
39B4	0.06637	0.00092	0.11986	0.00179	1.09637	0.01864	818	29	730	10	752	9	97	150x80	Boundary between cd and sill
39B5	0.05757	0.00113	0.08997	0.00139	0.71381	0.01538	513	43	555	8	547	9	102	150x80	Boundary between cd and sill
37A3	0.06142	0.00146	0.08751	0.00142	0.74060	0.01852	654	50	541	8	563	11	96	110x70	In cd corona
Sample PCM-83: Else Platform															
14A1	0.06598	0.00080	0.12806	0.00180	1.16451	0.01761	806	25	777	10	784	8	99	125x85	Boundary between sill and cd
14A2	0.06478	0.00076	0.12204	0.00172	1.08948	0.01628	767	25	742	10	748	8	99	125x85	Boundary between sill and cd
14A3	0.06954	0.00084	0.15094	0.00214	1.44652	0.02202	915	25	906	12	908	9	100	125x85	Boundary between sill and cd
31A1	0.07225	0.00084	0.16243	0.00229	1.61722	0.02415	993	24	970	13	977	9	99	70x50	In cd corona
30B1	0.07037	0.00095	0.15537	0.00221	1.50679	0.02438	939	28	931	12	933	10	100	70x55	Included in sill
18A1	0.06921	0.00087	0.15440	0.00218	1.47274	0.02285	905	26	926	12	919	9	101	145x70	In cd corona, in contact with ilm
18A2	0.06533	0.00080	0.12644	0.00179	1.13831	0.01743	785	25	768	10	772	8	99	145x70	In cd corona, in contact with ilm
18A3	0.06889	0.00087	0.15211	0.00215	1.44402	0.02249	895	26	913	12	907	9	101	145x70	In cd corona, in contact with ilm
7C1	0.05831	0.00076	0.08973	0.00127	0.72094	0.01143	541	29	554	8	551	7	100	110x70	In cd corona
7C2	0.06346	0.00086	0.11293	0.00161	0.98758	0.01610	724	28	690	9	698	8	99	110x70	In cd corona
7C3	0.06728	0.00088	0.13029	0.00186	1.20789	0.01932	846	27	790	11	804	9	98	110x70	In cd corona
7C4	0.05821	0.00090	0.08274	0.00119	0.66370	0.01184	537	34	513	7	517	7	99	110x70	In cd corona
33A1	0.05757	0.00074	0.08429	0.00116	0.66862	0.01038	513	28	522	7	520	6	100	40x25	In cd corona
33B1	0.05997	0.00077	0.09735	0.00133	0.80450	0.01233	603	27	599	8	599	7	100	85x50	In cd corona
33B2	0.06749	0.00089	0.13612	0.00186	1.26592	0.01976	853	27	823	11	831	9	99	85x50	In cd corona
35B1	0.05811	0.00082	0.08719	0.00120	0.69818	0.01136	533	31	539	7	538	7	100	110x50	In cd corona
39C1	0.05766	0.00076	0.08384	0.00116	0.66621	0.01050	517	29	519	7	518	6	100	80x105	In cd corona
39C2	0.06697	0.00100	0.14236	0.00198	1.31379	0.02222	837	31	858	11	852	10	101	80x105	In cd corona
39C3	0.05916	0.00078	0.09189	0.00126	0.74908	0.01178	573	29	567	7	568	7	100	80x105	In cd corona
42A1	0.05776	0.00077	0.08395	0.00116	0.66824	0.01053	520	29	520	7	520	6	100	155x75	In cd corona
42A2	0.06598	0.00086	0.14146	0.00195	1.28629	0.02001	806	27	853	11	840	9	102	155x75	In cd corona
42A3	0.06591	0.00089	0.13987	0.00193	1.27046	0.02014	804	28	844	11	833	9	101	155x75	In cd corona
42A4	0.05810	0.00083	0.08523	0.00118	0.68241	0.01127	533	32	527	7	528	7	100	155x75	In cd corona
51A1	0.05760	0.00087	0.08926	0.00124	0.70853	0.01214	514	33	551	7	544	7	101	135x70	In cd corona, in contact with ilm
51A2	0.05719	0.00075	0.08167	0.00113	0.64374	0.01005	499	29	506	7	505	6	100	135x70	In cd corona, in contact with ilm
51A3	0.05636	0.00074	0.08483	0.00117	0.65892	0.01032	466	29	525	7	514	6	102	135x70	In cd corona, in contact with ilm

	Isotopic Ratios						Age Estimates							Morphology and location	
Spot name	$^{207}Pb/^{206}Pb$	±1σ	$^{206}Pb/^{238}U$	±1σ	$^{207}Pb/^{235}U$	±1σ	$^{207}Pb/^{206}Pb$	±1σ	$^{206}Pb/^{238}U$	±1σ	$^{207}Pb/^{235}U$	±1σ	Conc. (%)	Grain size (μm)	Textural location
Sample PCM-83 (continued)															
53B1	0.06808	0.00093	0.14665	0.00203	1.37582	0.02210	871	28	882	11	879	9	100	80x145	In cd corona
53B2	0.06964	0.00099	0.15097	0.00211	1.44888	0.02393	918	29	906	12	909	10	100	80x145	In cd corona
45B1	0.06607	0.00098	0.14366	0.00201	1.30807	0.02212	809	31	865	11	849	10	102	100x45	Mostly surrounded by coarse ilm
7D1	0.07015	0.00113	0.15919	0.00226	1.53886	0.02770	933	33	952	13	946	11	101	50x50	Included in sill
7B1	0.06907	0.00108	0.14635	0.00206	1.39293	0.02445	901	32	881	12	886	10	99	160x65	Included in gt (on crack)
7B2	0.06906	0.00108	0.14700	0.00207	1.39911	0.02466	901	32	884	12	889	10	99	160x65	Included in gt (on crack)
30A1	0.06186	0.00090	0.10709	0.00149	0.91291	0.01535	669	31	656	9	659	8	100	40x30	In cd corona
32A1	0.06631	0.00094	0.13381	0.00186	1.22274	0.02016	816	29	810	11	811	9	100	95x70	In cd corona, in contact with ilm
32A2	0.06364	0.00097	0.11359	0.00159	0.99624	0.01725	730	32	694	9	702	9	99	95x70	In cd corona, in contact with ilm
Sample 77090: Taylor Platform															
10A1	0.05733	0.00065	0.08456	0.00121	0.66799	0.01001	504	25	523	7	520	6	101	50x35	Along crack in cd
10A2	0.05716	0.00067	0.08468	0.00122	0.66696	0.01015	497	26	524	7	519	6	101	50x35	Along crack in cd
14A1	0.05746	0.00079	0.08502	0.00124	0.67308	0.01126	509	30	526	7	523	7	101	130x80	Included in qz
14A2	0.05795	0.00111	0.08447	0.00128	0.67449	0.01419	528	42	523	8	523	9	100	130x80	Included in qz
14A3	0.05791	0.00077	0.08477	0.00123	0.67637	0.01107	526	29	525	7	525	7	100	130x80	Included in qz
20A1	0.05762	0.00094	0.08473	0.00126	0.67261	0.01256	515	36	524	7	522	8	100	105x55	Along crack in cd
20A2	0.05848	0.00087	0.08868	0.00130	0.71467	0.01249	548	32	548	8	548	7	100	105x55	Along crack in cd
21A1*	0.05681	0.00067	0.07794	0.00113	0.61017	0.00936	484	26	484	7	484	6	100	50x25	Boundary between qz and bi
28D1	0.05733	0.00072	0.08471	0.00123	0.66912	0.01068	504	28	524	7	520	7	101	55x45	Boundary between qz and bi
28D2	0.05725	0.00071	0.08826	0.00129	0.69623	0.01112	501	27	545	8	537	7	102	55x45	Boundary between qz and bi
8A1	0.05761	0.00062	0.08233	0.00119	0.65358	0.00956	515	23	510	7	511	6	100	40x30	Included in cd
36A1	0.05896	0.00065	0.09012	0.00130	0.73216	0.01083	566	24	556	8	558	6	100	70x55	Along crack in cd
36A2*	0.06013	0.00065	0.09311	0.00134	0.77152	0.01127	608	23	574	8	581	6	99	70x55	Along crack in cd
39A1	0.05746	0.00062	0.08275	0.00120	0.65525	0.00962	509	24	513	7	512	6	100	50x40	Included in gt (on crack)
39B1*	0.06393	0.00071	0.10494	0.00152	0.92458	0.01373	739	23	643	9	665	7	97	60x25	Boundary between qz and bi
41A1	0.05674	0.00060	0.08404	0.00121	0.65699	0.00953	481	23	520	7	513	6	101	55x35	Included in cd
42A1*	0.05609	0.00059	0.08393	0.00121	0.64867	0.00942	456	23	520	7	508	6	102	65x40	Included in bi
42A2	0.05708	0.00060	0.08174	0.00118	0.64295	0.00934	494	23	507	7	504	6	100	65x40	Included in bi
42C1	0.05887	0.00071	0.08834	0.00128	0.71653	0.01105	562	26	546	8	549	7	99	75x50	Boundary between qz and gt
42C2	0.05772	0.00064	0.08185	0.00118	0.65110	0.00970	519	25	507	7	509	6	100	110x105	Boundary between qz and gt
42C3	0.05904	0.00068	0.08643	0.00120	0.70315	0.01036	504	25	523	7	520	6	99	110x105	Boundary between qz and gt

Spot name	Isotopic Ratios $^{207}Pb/^{206}Pb$	±1σ	$^{206}Pb/^{238}U$	±1σ	$^{207}Pb/^{235}U$	±1σ	Age Estimates $^{207}Pb/^{206}Pb$	±1σ	$^{206}Pb/^{238}U$	±1σ	$^{207}Pb/^{235}U$	±1σ	Conc. (%)	Morphology and location Grain size (μm)	Textural location
Sample 77090 (continued)															
42C3	0.05904	0.00068	0.08643	0.00120	0.70315	0.01036	568	25	534	7	541	6	99	110x105	Boundary between qz and gt
42C4*	0.06004	0.00073	0.09423	0.00132	0.77960	0.01180	605	26	581	8	585	7	99	110x105	Boundary between qz and gt
52A1	0.05800	0.00078	0.08294	0.00117	0.66287	0.01068	529	30	514	7	516	7	99	100x60	Boundary of cd and qz inclusion
52A2	0.05766	0.00069	0.08235	0.00115	0.65442	0.00981	517	26	510	7	511	6	100	100x60	Boundary of cd and qz inclusion
61A1	0.05728	0.00067	0.08180	0.00113	0.64564	0.00956	502	26	507	7	506	6	100	160x75	Included in cd
61A2	0.05855	0.00072	0.08949	0.00124	0.72202	0.01095	550	27	553	7	552	6	100	160x75	Included in cd
86A1	0.05711	0.00073	0.08162	0.00113	0.64243	0.00995	495	28	506	7	504	6	100	75x75	Included in cd
86A2	0.05850	0.00071	0.08744	0.00121	0.70492	0.01060	548	26	540	7	542	6	100	75x75	Included in cd
81A1*	0.06652	0.00081	0.12781	0.00176	1.17164	0.01758	823	25	775	10	787	8	98	65x50	Included in cd
Sample 77102B: Brocklehurst Ridge															
17A1	0.05803	0.00091	0.08404	0.00123	0.67194	0.01205	530	34	520	7	522	7	100	115x85	Boundary of gt and cd
17A2	0.06282	0.00097	0.08186	0.00120	0.70865	0.01263	702	33	507	7	544	8	93	115x85	Boundary of gt and cd
21A1	0.05816	0.00087	0.08493	0.00123	0.68069	0.01185	535	33	526	7	527	7	100	50x30	Boundary of gt and qz
25A1	0.06013	0.00110	0.08492	0.00127	0.70368	0.01410	608	39	525	8	541	8	97	110x70	Included in cd
25A2	0.06205	0.00124	0.08519	0.00129	0.72843	0.01555	676	42	527	8	556	9	95	110x70	Included in cd
25B1	0.06796	0.00092	0.13468	0.00193	1.26117	0.02046	867	28	815	11	828	9	98	245x20	Included in cd
25B2	0.06795	0.00095	0.14259	0.00205	1.33512	0.02220	867	29	859	12	861	10	100	245x20	Included in cd
25B3	0.06826	0.00092	0.14844	0.00212	1.39626	0.02261	876	28	892	12	887	10	101	245x20	Included in cd
17A3*	0.06008	0.00103	0.08814	0.00130	0.72972	0.01392	606	37	545	8	556	8	98	115x85	Boundary of gt and cd
17B1	0.05783	0.00100	0.08482	0.00125	0.67590	0.01298	523	38	525	7	524	8	100	80x40	Included in cd
8A1	0.05806	0.00074	0.08426	0.00121	0.67429	0.01072	532	28	522	7	523	7	100	380x20	Included in gt (on crack)
8A2	0.05931	0.00104	0.08518	0.00127	0.69631	0.01361	579	38	527	8	537	8	98	380x20	Included in gt (on crack)
8A3	0.06795	0.00081	0.14159	0.00202	1.32592	0.02022	867	25	854	11	857	9	100	380x20	Included in gt (on crack)
82A1	0.06228	0.00132	0.08136	0.00125	0.69833	0.01578	684	45	504	7	538	9	94	65x25	Included in gt
82A2	0.06003	0.00140	0.08475	0.00133	0.70111	0.01714	605	50	524	8	540	10	97	65x25	Included in gt
63A1*	0.06125	0.00103	0.09335	0.00138	0.78796	0.01491	648	36	575	8	590	8	98	35x25	Included in sill
60A1	0.06398	0.00145	0.08284	0.00129	0.73037	0.01733	741	47	513	8	557	10	92	165x17	In contact with bi and sill
25C2	0.06767	0.00096	0.13385	0.00193	1.24808	0.02092	858	29	810	11	823	9	98	235x13	In contat with ilm and cd
23B1	0.05976	0.00109	0.08293	0.00123	0.68291	0.01368	595	39	514	7	529	8	97	75x35	Included in gt (on crack)
23A1	0.05800	0.00080	0.08332	0.00119	0.66594	0.01104	529	30	516	7	518	7	100	85x45	Boundary of bi and cd
28A1	0.05964	0.00098	0.08400	0.00123	0.69041	0.01282	591	35	520	7	533	8	98	95x60	Included in qz

	Isotopic Ratios						Age Estimates							Morphology and location	
Spot name	$^{207}Pb/^{206}Pb$	±1σ	$^{206}Pb/^{238}U$	±1σ	$^{207}Pb/^{235}U$	±1σ	$^{207}Pb/^{206}Pb$	±1σ	$^{206}Pb/^{238}U$	±1σ	$^{207}Pb/^{235}U$	±1σ	Conc. (%)	Grain size (μm)	Textural location
Sample 77102B (continued)															
28A2	0.05766	0.00107	0.08316	0.00124	0.66075	0.01343	516	40	515	7	515	8	100	95x60	Included in qz
28A3*	0.05985	0.00087	0.08014	0.00116	0.66101	0.01136	598	31	497	7	515	7	96	95x60	Included in qz
28B1	0.05864	0.00099	0.08282	0.00122	0.66924	0.01272	554	36	513	7	520	8	99	50x55	Included in gt
8A4	0.06968	0.00082	0.14707	0.00208	1.41227	0.02134	919	24	885	12	894	9	99	380x200	Included in gt
22A1	0.05771	0.00100	0.08300	0.00123	0.66014	0.01282	519	38	514	7	515	8	100	280x125	Between two gt grains, in contact with bi
22A2	0.06011	0.00107	0.08264	0.00123	0.68458	0.01351	608	38	512	7	530	8	97	280x125	Between two gt grains, in contact with bi
22A3	0.05772	0.00103	0.08166	0.00122	0.64961	0.01292	519	39	506	7	508	8	100	280x125	Between two gt grains, in contact with bi
Sample 77079: Mt Meredith															
18B1	0.05755	0.00065	0.08250	0.00119	0.65428	0.00976	512	24	511	7	511	6	100	135x70	Along crack in sample
22B1	0.05762	0.00065	0.08191	0.00118	0.65043	0.00975	515	24	508	7	509	6	100	135x40	Along crack in biotite
22B2	0.05753	0.00065	0.08000	0.00115	0.63425	0.00948	512	24	496	7	499	6	99	135x40	Along crack in biotite
30A1	0.05770	0.00062	0.08152	0.00118	0.64828	0.00947	518	23	505	7	507	6	100	105x115	Included in qz
30A2	0.05791	0.00062	0.08019	0.00116	0.63997	0.00933	526	24	497	7	502	6	99	105x115	Included in qz
30A3	0.05718	0.00063	0.08163	0.00117	0.64324	0.00946	498	24	506	7	504	6	100	105x115	Included in qz
34A1	0.05744	0.00075	0.07994	0.00116	0.63270	0.01015	508	28	496	7	498	6	100	60x40	Included in bi
22A1	0.05741	0.00066	0.08325	0.00119	0.65868	0.00988	507	25	516	7	514	6	100	530x185	Included in bi
22A2	0.05725	0.00071	0.08234	0.00119	0.64957	0.01011	501	27	510	7	508	6	100	530x185	Included in bi
36A1*	0.05952	0.00068	0.08068	0.00116	0.66167	0.00994	586	25	500	7	516	6	97	140x40	Included in qz (on crack)
40A1	0.05696	0.00062	0.08137	0.00116	0.63882	0.00930	490	24	504	7	502	6	101	170x75	Boundary between qz and bi
40A2	0.05707	0.00062	0.08224	0.00117	0.64681	0.00943	494	24	510	7	507	6	101	170x75	Boundary between qz and bi
40A3	0.05763	0.00065	0.08336	0.00118	0.66205	0.00972	515	24	516	7	516	6	100	170x75	Boundary between qz and bi
54A1	0.05755	0.00065	0.08105	0.00115	0.64276	0.00950	512	24	502	7	504	6	100	150x140	Included in qz
54A2	0.05739	0.00070	0.08027	0.00114	0.63498	0.00978	506	27	498	7	499	6	100	150x140	Included in qz
54A3	0.05709	0.00065	0.07912	0.00112	0.62252	0.00924	495	25	491	7	491	6	100	150x140	Included in qz
59A1	0.06990	0.00080	0.15131	0.00215	1.45772	0.02167	926	23	908	12	913	9	99	50x40	Included in qz
9A1	0.05751	0.00070	0.08265	0.00117	0.65507	0.01003	511	26	512	7	512	6	100	35x25	Included in bi (aligned with cleavage)
19A1	0.05750	0.00068	0.08423	0.00120	0.66741	0.01014	510	26	521	7	519	6	100	130x70	Boundary between qz and bi
19A2	0.05704	0.00069	0.08161	0.00116	0.64152	0.00983	492	27	506	7	503	6	100	130x70	Boundary between qz and bi
18A1	0.05778	0.00063	0.08303	0.00121	0.66105	0.00984	521	24	514	7	515	6	100	250x145	Boundary of bi
18A2	0.05713	0.00062	0.08066	0.00117	0.63496	0.00940	496	24	500	7	499	6	100	250x145	Boundary of bi
18A3	0.05706	0.00063	0.07917	0.00115	0.62249	0.00932	493	25	491	7	491	6	100	250x145	Boundary of bi

	Isotopic Ratios						Age Estimates							Morphology and location	
Spot name	$^{207}Pb/^{206}Pb$	±1σ	$^{206}Pb/^{238}U$	±1σ	$^{207}Pb/^{235}U$	±1σ	$^{207}Pb/^{206}Pb$	±1σ	$^{206}Pb/^{238}U$	±1σ	$^{207}Pb/^{235}U$	±1σ	Conc. (%)	Grain size (μm)	Textural location
Sample 77079 (continued)															
33A1	0.05753	0.00064	0.08217	0.00119	0.65146	0.00971	512	24	509	7	509	6	100	220x130	Included in bi
33A2	0.05732	0.00066	0.08009	0.00116	0.63260	0.00959	503	25	497	7	498	6	100	220x130	Included in bi
33A3	0.05720	0.00066	0.07956	0.00115	0.62726	0.00950	499	25	494	7	494	6	100	220x130	Included in bi
33B1	0.05641	0.00064	0.08093	0.00118	0.62917	0.00949	468	25	502	7	496	6	101	130x80	Included in bi
33B2	0.05692	0.00071	0.08048	0.00117	0.63139	0.01001	488	28	499	7	497	6	100	130x80	Included in bi
36A2	0.05707	0.00066	0.07931	0.00116	0.62375	0.00953	494	26	492	7	492	6	100	140x40	Included in qz (on crack)
30A4	0.05757	0.00070	0.08175	0.00119	0.64869	0.01011	513	26	507	7	508	6	100	105x115	Included in qz
Sample 72046A: Reinbolt Hills															
98B1	0.06652	0.00115	0.14006	0.00203	1.28379	0.02440	823	36	845	11	839	11	101	105x55	In cd corona
98B2	0.06642	0.00128	0.12546	0.00185	1.14823	0.02363	820	40	762	11	776	11	98	105x55	In cd corona
83A1	0.05778	0.00116	0.08748	0.00129	0.69655	0.01487	521	44	541	8	537	9	101	90x55	In cd/sp symplectite
83A2	0.05556	0.00123	0.08660	0.00130	0.66304	0.01530	435	48	535	8	517	9	104	90x55	In cd/sp symplectite
83A3	0.05752	0.00120	0.08673	0.00128	0.68737	0.01506	511	46	536	8	531	9	101	70x30	In cd/sp symplectite
90C1	0.05711	0.00117	0.08396	0.00124	0.66075	0.01429	495	45	520	7	515	9	101	70x30	In cd/sp symplectite, in contact with ilm
89A1	0.07189	0.00136	0.15557	0.00227	1.54122	0.03114	983	38	932	13	947	12	98	40x30	Included in sill
83B1	0.07160	0.00146	0.14399	0.00213	1.42061	0.03029	975	41	867	12	898	13	97	110x50	Boundary of sill and cd
83B2	0.06397	0.00138	0.11236	0.00167	0.99058	0.02212	741	45	686	10	699	11	98	110x50	Boundary of sill and cd
83D1	0.07015	0.00133	0.14421	0.00208	1.39421	0.02798	933	38	868	12	887	12	98	40x35	Included on gt (on crack)
69B1	0.05759	0.00113	0.08489	0.00122	0.67366	0.01405	514	43	525	7	523	9	100	70x50	Boundary of gt and cd
69B2	0.05713	0.00117	0.08321	0.00120	0.65504	0.01407	496	44	515	7	512	9	101	70x50	Boundary of gt and cd
69B3*	0.06480	0.00133	0.10462	0.00153	0.93417	0.02008	768	43	641	9	670	11	96	70x50	Boundary of gt and cd
89B1	0.06987	0.00119	0.16216	0.00228	1.56148	0.02891	925	35	969	13	955	11	101	90x60	Included in gt
89B2	0.07055	0.00170	0.16117	0.00247	1.56696	0.03865	945	49	963	14	957	15	101	90x60	Included in gt
82A1	0.06941	0.00131	0.14870	0.00213	1.42229	0.02850	911	38	894	12	898	12	99	65x60	Included in gt
82A2	0.06827	0.00121	0.13610	0.00192	1.28059	0.02450	877	36	823	11	837	11	98	65x60	Included in gt
82A3	0.07003	0.00126	0.14271	0.00202	1.37726	0.02653	929	36	860	11	879	11	98	65x60	Included in gt
82B1	0.06468	0.00130	0.14004	0.00203	1.24830	0.02635	764	42	845	11	823	12	103	50x40	In cd/sp symplectite
76A1	0.06844	0.00141	0.15039	0.00219	1.41840	0.03047	882	42	903	12	897	13	101	60x40	Boundary of coarse ilmenite and cd
76A2	0.06990	0.00158	0.15926	0.00238	1.53411	0.03571	926	46	953	13	944	14	101	60x40	Boundary of coarse ilmenite and cd
81A1	0.07119	0.00276	0.16169	0.00297	1.58593	0.06030	963	77	966	16	965	24	100	25x20	Included in sill
81A2	0.06810	0.00231	0.16513	0.00284	1.54932	0.05191	872	69	985	16	950	21	104	65x40	Included in sill

	Isotopic Ratios						Age Estimates							Morphology and location	
Spot name	$^{207}Pb/^{206}Pb$	±1σ	$^{206}Pb/^{238}U$	±1σ	$^{207}Pb/^{235}U$	±1σ	$^{207}Pb/^{206}Pb$	±1σ	$^{206}Pb/^{238}U$	±1σ	$^{207}Pb/^{235}U$	±1σ	Conc. (%)	Grain size (μm)	Textural location
Sample 72046A (continued)															
81A3	0.07088	0.00262	0.16597	0.00299	1.62086	0.05878	954	74	990	17	978	23	101	65x40	Included in sill
95A1	0.06765	0.00131	0.12896	0.00185	1.20193	0.02459	858	40	782	11	802	11	98	120x45	In cd/sp symplectite
95A2	0.06515	0.00125	0.13407	0.00191	1.20336	0.02443	779	40	811	11	802	11	101	120x45	In cd/sp symplectite
65A1*	0.06486	0.00238	0.08811	0.00153	0.78729	0.02836	770	75	544	9	590	16	92	105x50	In cd/sp symplectite
65A2	0.05743	0.00235	0.09034	0.00161	0.71473	0.02875	508	87	558	9	548	17	102	105x50	In cd/sp symplectite
69A1	0.05773	0.00142	0.08507	0.00128	0.67652	0.01699	519	53	526	8	525	10	100	95x70	In cd/sp symplectite, in contact with ilm
69A2	0.05542	0.00141	0.08694	0.00131	0.66374	0.01709	429	55	537	8	517	10	104	95x70	In cd/sp symplectite, in contact with ilm
69A3	0.07135	0.00130	0.15452	0.00218	1.51841	0.02955	967	37	926	12	938	12	99	95x70	In cd/sp symplectite, in contact with ilm
71B1	0.06782	0.00146	0.15400	0.00224	1.43812	0.03198	863	44	923	13	905	13	102	75x65	Ksp-qz-rich domain, adjacent to qz
71B2	0.07147	0.00140	0.15425	0.00220	1.51842	0.03135	971	40	925	12	938	13	99	75x65	Ksp-qz-rich domain, adjacent to qz
Sample 77223: McKaskle Hills															
1A1*	0.05605	0.00089	0.09280	0.00143	0.71681	0.01351	454	34	572	8	549	8	104	240x190	In cd-qz symplectite, in contact with gt and ksp
1A2	0.05902	0.00082	0.08845	0.00136	0.71930	0.01262	568	30	546	8	550	7	99	240x190	In cd-qz symplectite, in contact with gt and ksp
1A3	0.05972	0.00084	0.08959	0.00138	0.73724	0.01294	594	30	553	8	561	8	99	240x190	In cd-qz symplectite, in contact with gt and ksp
8A1*	0.05952	0.00081	0.09506	0.00146	0.77970	0.01342	586	29	585	9	585	8	100	230x140	Included in gt
8A2	0.05884	0.00080	0.08926	0.00137	0.72372	0.01246	561	29	551	8	553	7	100	230x140	Included in gt
8A3	0.05783	0.00080	0.08865	0.00136	0.70646	0.01236	523	30	548	8	543	7	101	230x140	Included in gt
7A1*	0.05553	0.00087	0.09185	0.00142	0.70294	0.01320	434	34	567	8	541	8	105	235x130	Included in gt (on crack)
7A2*	0.06864	0.00094	0.10636	0.00163	1.00613	0.01738	888	28	652	9	707	9	92	235x130	Included in gt (on crack)
7A3	0.06332	0.00094	0.11168	0.00173	0.97462	0.01767	719	31	683	10	691	9	99	235x130	Included in gt (on crack)
7A4	0.05801	0.00091	0.08912	0.00136	0.71256	0.01327	530	34	550	8	546	8	101	235x130	Included in gt (on crack)
2A1	0.06518	0.00080	0.12844	0.00193	1.15367	0.01857	780	26	779	11	779	9	100	110x50	Included in gt
2A2	0.05840	0.00074	0.09320	0.00140	0.75008	0.01228	545	27	574	8	568	7	101	110x50	Included in gt
2A3	0.06428	0.00080	0.12508	0.00188	1.10801	0.01802	751	26	760	11	757	9	100	110x50	Included in gt
3A1	0.06447	0.00085	0.11392	0.00172	1.01223	0.01700	757	28	696	10	710	9	98	95x65	Included in gt
3A2	0.06348	0.00080	0.11449	0.00172	1.00165	0.01633	725	26	699	10	705	8	99	95x65	Included in gt
4A1*	0.05602	0.00097	0.09380	0.00143	0.72401	0.01431	453	38	578	8	553	8	105	70x55	Boundary of gt and cd-qz symplectite
4A2	0.05760	0.00083	0.08862	0.00134	0.70343	0.01237	514	32	547	8	541	7	101	70x55	Boundary of gt and cd-qz symplectite
5A1	0.05645	0.00092	0.08605	0.00131	0.66945	0.01269	470	36	532	8	520	8	102	90x45	Included in gt
5A2	0.05579	0.00081	0.08791	0.00133	0.67583	0.01197	444	32	543	8	524	7	104	90x45	Included in gt
9A1	0.05824	0.00096	0.08885	0.00136	0.71310	0.01370	538	36	549	8	547	8	100	70x40	In cd-qz symplectite

	Isotopic Ratios						Age Estimates							Morphology and location	
Spot name	$^{207}Pb/^{206}Pb$	±1σ	$^{206}Pb/^{238}U$	±1σ	$^{207}Pb/^{235}U$	±1σ	$^{207}Pb/^{206}Pb$	±1σ	$^{206}Pb/^{238}U$	±1σ	$^{207}Pb/^{235}U$	±1σ	Conc. (%)	Grain size (μm)	Textural location
Sample 77223 (continued)															
9A2	0.05780	0.00097	0.08995	0.00138	0.71648	0.01397	522	37	555	8	549	8	101	70x40	In cd-qz symplectite
6A1	0.05880	0.00074	0.09006	0.00135	0.72979	0.01190	560	27	556	8	556	7	100	115x75	Included in gt
6A2	0.05858	0.00075	0.09285	0.00138	0.74960	0.01221	552	28	572	8	568	7	101	115x75	Included in gt
11A1	0.05803	0.00073	0.08878	0.00132	0.70999	0.01153	531	28	548	8	545	7	101	130x80	Boundary of gt and cd-qz symplectite
11A2	0.05780	0.00085	0.08760	0.00132	0.69784	0.01245	522	32	541	8	538	7	101	130x80	Boundary of gt and cd-qz symplectite
10A1	0.05726	0.00089	0.08931	0.00136	0.70483	0.01297	501	34	552	8	542	8	102	70x20	In cd-qz symplectite
12A1	0.05676	0.00083	0.08878	0.00134	0.69439	0.01233	481	32	548	8	535	7	102	50x30	Boundary of ksp and qz
12A2	0.05818	0.00082	0.08623	0.00130	0.69137	0.01193	536	31	533	8	534	7	100	50x30	Boundary of ksp and qz
1A4*	0.05439	0.00090	0.09394	0.00143	0.70416	0.01349	387	36	579	8	541	8	107	240x190	In cd-qz symplectite, in contact with gt and bi
1A5	0.05607	0.00090	0.08967	0.00137	0.69293	0.01307	455	35	554	8	535	8	104	240x190	In cd-qz symplectite, in contact with gt and bi
1A8	0.05753	0.00081	0.08520	0.00116	0.67543	0.01099	512	31	527	7	524	7	101	240x190	In cd-qz symplectite, in contact with gt and bi
1A6	0.05793	0.00085	0.08604	0.00118	0.68678	0.01151	527	32	532	7	531	7	100	240x190	In cd-qz symplectite, in contact with gt and bi
4A3	0.05734	0.00091	0.08690	0.00120	0.68669	0.01211	504	34	537	7	531	7	101	70x55	Boundary of cd-qz symplectite and gt
15A1	0.06279	0.00084	0.10247	0.00140	0.88660	0.01396	701	28	629	8	645	8	98	50x40	Included in gt
16A1	0.07035	0.00099	0.13899	0.00191	1.34757	0.02198	939	29	839	11	867	10	97	40x25	Included in gt
13A1	0.05723	0.00089	0.08665	0.00120	0.68334	0.01195	500	34	536	7	529	7	101	140x100	Included in gt
13A2	0.05774	0.00086	0.08734	0.00120	0.69497	0.01179	520	33	540	7	536	7	101	140x100	Included in gt
13A3	0.05790	0.00087	0.09191	0.00127	0.73334	0.01256	526	33	567	8	559	7	101	140x100	Included in gt
3A3	0.06318	0.00094	0.10612	0.00147	0.92393	0.01570	714	31	650	9	664	8	98	95x65	Included in gt
1A7	0.05846	0.00093	0.08884	0.00124	0.71574	0.01271	547	34	549	7	548	8	100	240x190	In cd-qz symplectite, in contact with gt and bi

* Analyses marked with a star are shown as dashed grey ellipses on the concordia diagrams, and were excluded from the calculation of weighted average ages or intercept ages

H2O	SiO2	Al2O3	CaO	MgO	FeO	K2O	Na2O	TiO2	O	
0.87	55.31	20.69	0.66	6.79	10.49	2.75	1.33	0.89	0.23	(0)
6.99	62.70	14.63	0.74	3.60	5.65	2.58	2.51	0.47	0.12	(0.5)

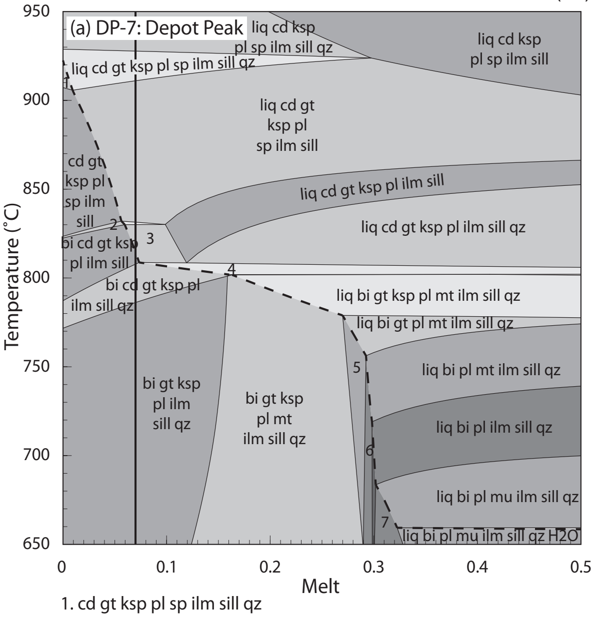

1. cd gt ksp pl sp ilm sill qz
2. bi cd gt ksp pl sp ilm sill qz
3. liq bi cd gt ksp pl ilm sill
4. liq bi cd gt ksp pl ilm sill qz
5. bi gt pl mt ilm sill qz
6. bi pl mt ilm sill qz
7. bi pl mu ilm sill qz

H2O	SiO2	Al2O3	CaO	MgO	FeO	K2O	Na2O	TiO2	O	
2.80	47.03	23.43	0.37	11.19	13.38	0.11	0.03	1.23	0.45	(0)
7.95	58.55	16.00	0.59	5.80	7.10	1.27	1.86	0.66	0.24	(0.5)

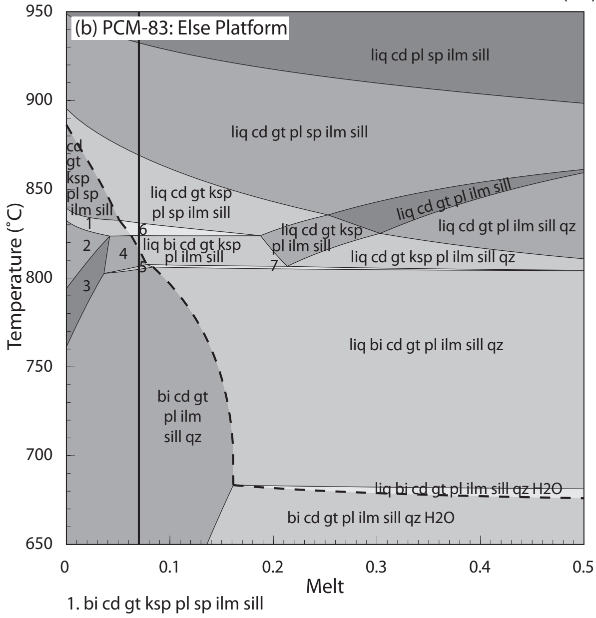

1. bi cd gt ksp pl sp ilm sill
2. bi cd gt pl sp ilm sill
3. bi cd gt pl ilm sill
4. bi cd gt ksp pl ilm sill
5. bi cd gt ksp pl ilm sill qz
6. liq bi cd gt ksp pl sp ilm sill
7. liq bi cd gt ksp pl silm sill qz

H2O	SiO2	Al2O3	CaO	MgO	FeO	K2O	Na2O	TiO2	O	
1.50	46.86	28.39	0.58	8.74	11.21	0.40	0.27	1.71	0.36	(0)
7.30	58.46	18.48	0.70	4.57	6.01	1.41	1.98	0.90	0.19	(0.5)

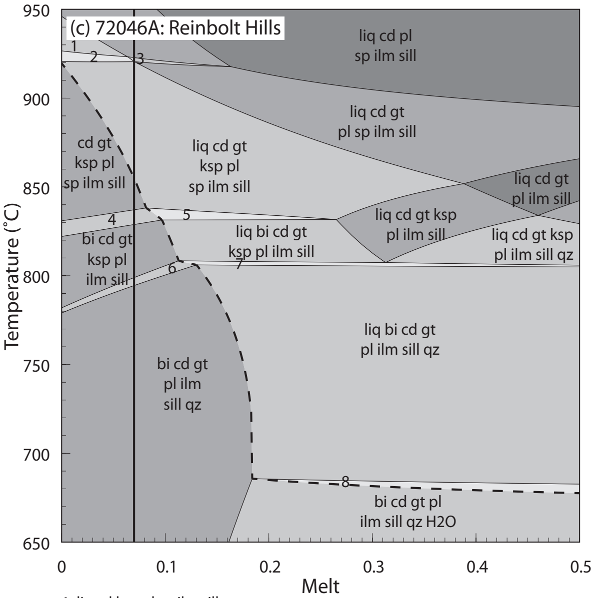

1. liq cd ksp pl sp ilm sill qz
2. liq cd gt ksp pl sp ilm sill qz
3. liq cd gt pl sp ilm sill qz
4. bi cd gt ksp pl sp ilm sill
5. liq bi cd gt ksp pl sp ilm sill
6. bi cd gt ksp pl ilm sill qz
7. liq bi cd gt ksp pl ilm sill qz
8. liq bi cd gt pl ilm sill qz H2O

H2O	SiO2	Al2O3	CaO	MgO	FeO	K2O	Na2O	TiO2	O	
2.41	60.34	11.02	1.20	9.71	11.69	0.98	0.71	1.72	0.23	(0)
7.76	65.21	9.79	1.01	5.06	6.24	1.70	2.20	0.90	0.12	(0.5)

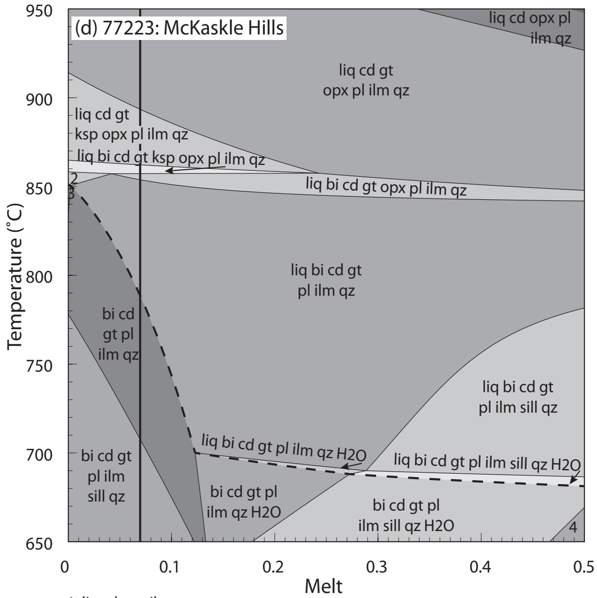

1. liq cd opx ilm qz
2. liq bi cd gt ksp pl ilm qz
3. bi cd gt ksp pl ilm qz
4. bi gt pl ilm sill qz H2O

CHAPTER 8

Conclusions and future research directions

This thesis endeavoured to characterise the metamorphic evolution of high thermal gradient terranes, from the tectonic settings required for the attainment of regional high temperatures to the consequences of high thermal gradient metamorphism and melt loss on the bulk compositions and reactivity of the terrane during subsequent metamorphic events. Each of the chapters in this thesis also investigated ways to overcome some of the major difficulties and limitations in the understanding of high thermal gradient terranes. These include uncertainties relating to the determination of the timescales of metamorphism and difficulties in the determination of an effective bulk composition in rocks that have experienced melt loss. The three main aims of the thesis are discussed below with relation to the key outcomes of each of the chapters of this study. Potential areas for further research are also discussed.

8.1. Tectonic settings required to achieve and maintain long-lived, elevated temperatures.

Chapters 2–5 used a combination of techniques, including zircon U–Pb and Lu–Hf isotopes from metasedimentary and magmatic rocks, in situ U–Pb monazite geochronology and calculated metamorphic phase diagrams with the aim of characterising the tectonic settings of metamorphism in three terranes that record high to ultrahigh thermal gradients. A secondary aim was to create a general framework for the investigation of the *P–T–t* conditions of high thermal gradient terranes. These chapters demonstrate the importance of in situ geochronology and selecting samples that record different stages of the overall *P–T* evolution when attempting to unravel complex metamorphic evolutions.

The metasedimentary protoliths in the Windmill Islands (**Chapters 2 and 3**) were deposited in the interval 1350–1320 Ma and contain zircon detrital age peaks that correspond to events in neighbouring terranes, including the West Australian Craton, Musgrave Province and the Loongana Arc of the Madura Province. This suggests that the three were contiguous at the time of sediment deposition. Deposition was shortly followed by regional, high thermal gradient metamorphism (M_1) at c. 1320–1300 Ma, which occurred at conditions of 3.5–4 kbar and 700–730 ºC and was associated with the formation of a horizontal fabric. The high thermal gradients and horizontal fabric suggest that M_1 was an extensional event. After M_1 metamorphism, voluminous juvenile granitic magmatism occurred between c. 1250–1210 Ma. Monazite ages of c. 1180 Ma from throughout the Windmill Islands record the timing of the second phase of metamorphism. The effects of M_2 are more localised and increase progressively to the south, to conditions of 4 kbar and temperatures of >850 ºC. M_2 was coeval with the intrusion of isotopically juvenile charnockite between 1200–1170 Ma, interpreted to reflect another period of extension. The charnockitic magmatism and high temperatures during M_2 may reflect that the crust was dehydrated during the previous events. **Chapters 2 and 3** show that combined detrital zircon, Lu–Hf isotopes and metamorphic phase diagrams can provide detailed constraints on the metamorphic evolution. The combination of arc- and craton-derived sedimentary sources and the short interval between deposition of the sediments and high thermal gradient metamorphism suggests that the Windmill Islands may have formed in a back-arc setting in a highly extended part of the West Australian Craton. In addition, the relatively juvenile Hf isotopic signature of the 1250–1210 Ma and 1200–1170 Ma magmatic rocks is consistent with the location of the Windmill Islands above thin crust that contains little evolved material. Therefore, the overall tectonic setting of high temperature metamorphism in the Windmill Islands was extensional. M_1 metamorphism records a period of accelerated extension, whereas the voluminous 1250–1210 Ma granitic magmatism may record thickening of this extensional system.

The central Aileron Province (**Chapter 4**) records suprasolidus high thermal gradient conditions for >60–80 Myr. Peak conditions of 850 °C and 6.5–7.5 kbar were followed by a retrograde evolution that involved minor decompression and slow cooling in the order of 2.5–4 °CMa^{-1} along a high thermal gradient. These constraints were achieved by collecting geochronology data from a number of samples that each record a different part of the overall *P*–*T* evolution. The slow cooling and the high thermal gradient retrograde *P*–*T* path implies that exhumation potential was limited and that metamorphism occurred in crust of relatively normal thickness. Therefore, the central Aileron Province may have remained relatively topographically neutral for c. 80 Ma. There is no evidence for external magmatic inputs or long-lived extension. Instead, the long-lived high thermal gradient metamorphism may have been driven to a significant extent by the burial of voluminous high heat-producing granitic rocks emplaced 250–180 Myr prior to metamorphism.

The Rayner Complex (**Chapter 5**) records a complex metamorphic evolution, with episodic charnockitic magmatism occurring between 1140 and 900 Ma and discrete periods of monazite growth between c. 1020–900 Ma, suggesting an extremely long-lived elevated thermal regime. Metamorphism at c. 1020 Ma is poorly recorded but is interpreted to have involved pressures of >7.4 kbar and temperatures of 840–880 °C, based on the presence of rutile in one sample from the southern Rayner Complex that preserves an older monazite population. Monazite growth at c. 940–900 Ma occurs throughout the Rayner Complex and was associated with metamorphism at conditions of 850–880 °C and 6–7 kbar. The formation of late biotite in all samples suggests that the post-peak evolution was dominated by cooling. The monazite ages in this study are similar to ages observed in the Eastern Ghats Province in India. It is proposed that the elevated thermal structure of the Rayner–Eastern Ghats terrane was inherited from an extensional basin or back-arc setting inboard of a long-lived continental arc which was then overprinted by shortening. However, an early higher pressure phase of metamorphism has not been recognised in the Rayner Complex or the Eastern Ghats and therefore the regional significance of the c. 1020 Ma event is unclear. Detrital zircon data from throughout the Rayner Complex may determine whether the localised record of the c. 1020 Ma event is due to metasedimentary packages with different depositional ages or is spatially controlled, and therefore provide more information on the tectonic setting. The use of coupled zircon U–Pb and Lu–Hf analyses and geochemistry with metamorphic constraints may also provide more information on the role of mantle magmatism in the Rayner–Eastern Ghats terrane and further constrain the tectonic setting.

Chapters 2–5 therefore suggest that long-lived high thermal gradients can be attained in both collisional and extensional settings. The primary thermal driver in the Windmill Islands and the Rayner Complex was likely to have been the thinned lithosphere resulting from back-arc extension, whereas in the central Aileron Province, the primary thermal driver was likely to have been anomalously high heat producing crust. However, common to all three terranes is that metamorphism did not involve the formation of significant topography, which **limited exhumation** and allowed the maintenance of high temperatures for prolonged periods. A second important requirement is that the **crust was preconditioned (dehydrated)** by prior melt loss events, inhibiting further melting and allowing the attainment of high temperatures and high thermal gradients.

Constraining the tectonic setting of high thermal gradient metamorphism is an important aspect of understanding the evolution of high thermal gradient terranes. Another aim of constraining metamorphic conditions is to investigate secular changes in lithospheric geodynamic regimes throughout Earth's history (e.g. Brown, 2006, 2014). A number of recent studies have noted that there appears to be a temporal relationship between the formation of ultrahigh temperature granulites and the amalgamation of supercontinents (e.g. Brown, 2007; Clark et al., 2015; Cutts et al., 2013). The timing of metamorphism in both the Windmill Islands and the Rayner Complex corresponds to the amalgamation of Rodina (e.g. Li et al., 1995, 2008; Smits et al., 2014), and at least in these two terranes, it appears to be have been associated with back-arc closure. A number of other Rodinian-aged orogenic belts also record high thermal gradient metamorphism and voluminous, juvenile magmatism consistent with thickened back-arcs, including Namaqua Land, southern Africa (Diener et al., 2013), the Musgrave Province, central Australia (Tucker et al., 2015; Walsh et al., 2015) and the Eastern Ghats (Korhonen et al., 2014). In addition, this period involved an unprecedented level of crustal recycling, proposed to be due in part to the addition of large volumes of juvenile crust in back-arcs prior to Rodinian orogenesis (Van Kranendonk and Kirkland, 2013). Constraints on the tectonic setting, isotopic character and *P–T–t* evolutions of other Rodinian-aged orogenic belts are necessary to explore this trend further. However, it suggests that determining the metamorphic character of temporally similar orogenic belts may be a useful constraint on mechanisms of supercontinent reorganisation.

8.2. To explore the effect of granulite facies metamorphism and melt loss on the bulk composition, metamorphic reactivity and the way economic mineral systems can be augmented via high temperature metamorphic processes.

Chapter 6 explored the effects of step-wise melt loss using forward modelling of a package of iron-rich metasedimentary rocks in the southern Gawler Craton that range in grade from greenschist facies phyllite to granulite facies gneisses. Phase equilibria forward modelling from two samples of the greenschist facies protoliths suggests that volume reduction as a result of melt loss is a mechanism to enrich the Fe-oxide content and the amount of $Fe_2O_{3(TOTAL)}$ in the bulk composition. The specific extent of enrichment is controlled by the melt fertility of the rock. Muscovite-rich horizons lose more melt and therefore experience more enrichment in Fe-oxides, with a relative increase of ~90% in the modelled sample. More Fe-rich, muscovite-poor horizons produce less melt and therefore do not show the same increase, with the total amount of Fe-oxides increasing by a relative ~40%. Therefore, **Chapter 6** shows that melt loss associated with progressive metamorphism to granulite facies is a mechanism to concentrate iron in the residual rock package up to economic grades. In addition, high-grade metamorphism will typically increase grain size, improving crushing and concentration processes. This suggests that high temperature terranes may be prospective for magnetite-dominated iron ore deposits.

The interplay between metamorphism and economic ore deposits is an interesting future research direction. There are comparatively few examples of magnetite deposits analogous to the type explored in **Chapter 6**, where mineralisation is hosted in a Fe-rich, clastic sediment. However, the recognition of this deposit type may have important implications for iron ore exploration in high temperature (>650–700 °C) metamorphic terranes that have undergone partial melting. Melt loss is also likely to be a way of enriching other economic elements and therefore the methodology developed in **Chapter 6** is not limited to iron ore. Challenger (Au) and Broken Hill (Pb–Zn) are examples of deposits where the redistribution and concentration of metals is proposed to be the result of partial melting (e.g. Frost et al., 2005; Tomkins and Mavrogenes, 2002). However, the melting temperatures in ore deposits are likely to be different than those of typical silicate rocks, depending on the sulphide minerals present (Tomkins et al., 2007). Therefore, metamorphic modelling of a variety of ore deposits that have experienced high temperature metamorphism is necessary to understand the requirements for the generation of economic ore deposits in metamorphic terranes. An understanding of the effects of melt generation and melt loss may also be useful for exploration in high temperature granulite facies regions that have historically not been considered prospective.

An additional implication of melt loss modelling is the potential to integrate the phase equilibria modelling in THERMOCALC with other thermodynamic modelling programs such as MELTS (Asimow and Ghiorso, 1998; Ghiorso and Sack, 1995) to further understand the processes of granite genesis. A suite of activity–composition relations for modelling partial melting in metabasic rocks is also soon to be released (White et al., 2015), opening up opportunities to explore crust formation and differentiation using mafic bulk compositions. This development will allow modelling of the generation of TTGs and reworking of arc lower crust during ongoing or renewed subduction, which are fundamental processes in the generation and evolution of the continents. It will also allow for the exploration of the changing composition of magmas throughout Earth's history as a function of primary mantle composition. Thermodynamic modelling has significantly increased our understanding of the process of partial melting in metasedimentary rocks, and similarly this new dataset will provide opportunities for exploration of high temperature processes in mafic bulk compositions.

8.3. To explore the way in which metamorphic reworking is recorded in compositionally resistant terranes.

Chapter 7 provided a framework for recognising the effects of high temperature reworking in a refractory residual terrane that has undergone extensive melt loss and metamorphism. Detailed petrography was combined with in situ U–Pb monazite geochronology and *P–T* pseudosections to demonstrate that parts of the Rayner Complex record a high temperature metamorphic event at 540–500 Ma. This event reached temperatures of 800–850 °C and pressures of 5.5–6.5 kbar. **Chapter 7** shows that multiple high temperature events may produce a terrane that exhibits uniformly granulite-grade rocks that can only be distinguished by geochronology and careful interpretation of mineral assemblages and *P–T* paths. The record of subsequent reworking is likely to be related to the presence of fluid, and therefore may highlight those areas that underwent hydrous retrogression or low-*T* shearing at the end of the first high temperature event. The tectonic setting for the attainment of high temperatures in the Rayner Complex is still unclear. However, there is limited magmatism of this age in the Rayner Complex, making advective heat transfer unlikely. An alternative is that high crustal heat production may have provided a thermal driver, similar to cause of metamorphism in **Chapter 4**. As in **Chapters 2–5**, the attainment of high temperatures at c. 540–500 Ma is likely to have been facilitated by the high temperature metamorphism during the Rayner Orogeny, which dehydrated the terrane and created rocks with elevated solidi that are unable to thermally buffer temperature increase by melting.

The Rayner Complex provides an example of a region where the controls on monazite and zircon growth are poorly understood. Some regions in the Rayner Complex are dominated by 540–500 Ma monazite ages whereas other regions record only ages corresponding to the Rayner Orogeny. However, throughout the Rayner Complex there is very little evidence for 540–500 Ma zircon. This may be a function of sampling bias, as much of the zircon geochronology comes from magmatic rocks emplaced during the Rayner Orogeny that are unlikely to have reactive compositions, but it may also be the result of differences in monazite and zircon reactivity. Polymetamorphic terranes that reach granulite to UHT conditions without significant new zircon growth are not uncommon, even where other chronometers such as monazite may be reactive. Although this phenomenon has been noted in other regions and has been explored theoretically (Kelsey et al., 2008; Yakymchuk and Brown, 2014), there remains scope for further research using samples that specifically contain metamorphic monazite but no metamorphic zircon. This would allow for an exploration of the effects of the melt fertility of the sample on monazite and zircon reactivity, as well as a consideration of the effects of differing concentrations of Zr and REE.

References

Asimow, P.D., Ghiorso, M.S., 1998. Algorithmic modifications extending MELTS to calculate subsolidus phase relations, American Mineralogist, p. 1127.

Brown, M., 2006. Duality of thermal regimes is the distinctive characteristic of plate tectonics since the Neoarchean. Geology 34, 961–964.

Brown, M., 2007. Metamorphism, Plate Tectonics, and the Supercontinent Cycle. Earth Science Frontiers 14, 1–18.

Brown, M., 2014. The contribution of metamorphic petrology to understanding lithosphere evolution and geodynamics. Geoscience Frontiers 5, 553–569.

Clark, C., Healy, D., Johnson, T., Collins, A.S., Taylor, R.J., Santosh, M., Timms, N.E., 2015. Hot orogens and supercontinent amalgamation: A Gondwanan example from southern India. Gondwana Research 28, 1310–1328.

Cutts, K.A., Kelsey, D.E., Hand, M., 2013. Evidence for late Paleoproterozoic (ca 1690–1665 Ma) high- to ultrahigh-temperature metamorphism in southern Australia: Implications for Proterozoic supercontinent models. Gondwana Research 23, 617–640.

Diener, J.F.A., White, R.W., Link, K., Dreyer, T.S., Moodley, A., 2013. Clockwise, low-*P* metamorphism of the Aus granulite terrain, southern Namibia, during the Mesoproterozoic Namaqua Orogeny. Precambrian Research 224, 629–652.

Frost, B.R., Swapp, S.M., Gregory, R.W., 2005. Prolonged existence of sulfide melt in the Broken Hill orebody, New South Wales, Australia. The Canadian Mineralogist 43, 479–493.

Ghiorso, M.S., Sack, R.O., 1995. Chemical mass transfer in magmatic processes IV. A revised and internally consistent thermodynamic model for the interpolation and extrapolation of liquid-solid equilibria in magmatic systems at elevated temperatures and pressures. Contributions to Mineralogy and Petrology 119, 197–212.

Kelsey, D.E., Clark, C., Hand, M., 2008. Thermobarometric modelling of zircon and monazite growth in melt-bearing systems: examples using model metapelitic and metapsammitic granulites. Journal of Metamorphic Geology 26, 199–212.

Korhonen, F.J., Clark, C., Brown, M., Taylor, R.J.M., 2014. Taking the temperature of Earth's hottest crust. Earth and Planetary Science Letters 408, 341–354.

Li, Z.-X., Zhang, L., Powell, C.M., 1995. South China in Rodinia: Part of the missing link between Australia–East Antarctica and Laurentia? Geology 23, 407–410.

Li, Z.X., Bogdanova, S.V., Collins, A.S., Davidson, A., De Waele, B., Ernst, R.E., Fitzsimons, I.C.W., Fuck, R.A., Gladkochub, D.P., Jacobs, J., Karlstrom, K.E., Lu, S., Natapov, L.M., Pease, V., Pisarevsky, S.A., Thrane, K., Vernikovsky, V., 2008. Assembly, configuration, and break-up history of Rodinia: A synthesis. Precambrian Research 160, 179–210.

Smits, R.G., Collins, W.J., Hand, M., Dutch, R., Payne, J.L., 2014. A Proterozoic Wilson cycle identified by Hf isotopes in central Australia: Implications for the assembly of Proterozoic Australia and Rodinia. Geology, 42, 231–234.

Tomkins, A.G., Mavrogenes, J.A., 2002. Mobilization of Gold as a Polymetallic Melt during Pelite Anatexis at the Challenger Deposit, South Australia: A Metamorphosed Archean Gold Deposit. Economic Geology 97, 1249–1271.

Tomkins, A.G., Pattison, D.R.M., Frost, B.R., 2007. On the Initiation of Metamorphic Sulfide Anatexis. Journal of Petrology 48, 511–535.

Tucker, N.M., Hand, M., Kelsey, D.E., Dutch, R.A., 2015. A duality of timescales: Short-lived ultrahigh temperature metamorphism preserving a long-lived monazite growth history in the Grenvillian Musgrave–Albany–Fraser Orogen. Precambrian Research 264, 204–234.

Van Kranendonk, M.J., Kirkland, C.L., 2013. Orogenic climax of Earth: The 1.2–1.1 Ga Grenvillian superevent. Geology 41, 735-738.

Walsh, A.K., Kelsey, D.E., Kirkland, C.L., Hand, M., Smithies, R.H., Clark, C., Howard, H.M., 2015. *P–T–t* evolution of a large, long-lived, ultrahigh-temperature Grenvillian belt in central Australia. Gondwana Research 28, 531–564.

White, R.W., Green, E., Palin, R.M., Diener, J.F.A., Powell, R., Holland, T., 2015. Partial melting of metabasic rocks, Granulite and Granulites Conference 2015: Granulites, melting and melt extraction from the mid- and lower crust, Windhoek, Namibia.

Yakymchuk, C., Brown, M., 2014. Behaviour of zircon and monazite during crustal melting. Journal of the Geological Society 171, 465–479.

APPENDIX 1

Morrissey, L.J., Hand, M., Wade, B.P., Szpunar, M., 2013. Early Mesoproterozoic metamorphism in the Barossa Complex, South Australia: links with the eastern margin of Proterozoic Australia. *Australian Journal of Earth Sciences*, **60**, 769–795.

Wong, B., Morrissey, L.J., Hand, M., Fields, C., Kelsey, D.E., 2015. Grenvillian-aged reworking of late Paleoproterozoic crust of the southern North Australian Craton, central Australia: implications for the assembly of Mesoproterozoic Australia. *Precambrian Research*, **270**, 100–123.

Morrissey, L.J., Hand, M., Wade, B.P. & Szpunar, M. (2014). Early Mesoproterozoic metamorphism in the Barossa Complex, South Australia: links with the eastern margin of Proterozoic Australia.
Australian Journal of Earth Sciences, 60(8), 769–795.

Precambrian Research 270 (2015) 100–123

Contents lists available at ScienceDirect

Precambrian Research

journal homepage: www.elsevier.com/locate/precamres

Grenvillian-aged reworking of late Paleoproterozoic crust of the southern North Australian Craton, central Australia: Implications for the assembly of Mesoproterozoic Australia

Belinda L. Wong, Laura J. Morrissey*, Martin Hand, Courtney E. Fields, David E. Kelsey

Department of Physical Sciences, University of Adelaide, Adelaide 5005, South Australia, Australia

A R T I C L E I N F O

Article history:
Received 13 April 2015
Received in revised form 3 September 2015
Accepted 4 September 2015
Available online 12 September 2015

Keywords:
Grenvillian-aged deformation
North Australian Craton
Mesoproterozoic suture
Monazite and zircon geochronology
Phase equilibria modelling

A B S T R A C T

LA–ICP–MS U–Pb monazite and zircon geochronology from metapelites and migmatitic orthogneiss along the central southern margin of the North Australia Craton (NAC), central Australia, reveal the presence of a regional-scale Grenvillian-aged (ca. 1130 Ma) deformation system. Grenvillian-aged deformation extends over a strike length of over 110 km from the southern Aileron Province in the vicinity of Alice Springs to the Teapot Granite Complex within the Warumpi Province. There is also evidence for Grenvillian-aged migmatisation and resetting of monazite further west in the Mount Liebig area, which may extend the Grenvillian-aged footprint to a strike-length of at least 250 km. Deformation associated with Grenvillian-aged reworking produced map-scale east–west trending folds and strongly foliated, steeply dipping shear zones that define the structural architecture of the interface region between the Aileron and Warumpi Provinces. Shallow, westerly-plunging folds associated with partial melting have evolved into shear zones and mylonites that record south-side up movement. Phase equilibria modelling of age-constrained garnet–biotite ± sillimanite ± cordierite-bearing metapelites from the southern Aileron and Warumpi Provinces suggest Grenvillian-aged metamorphism reached temperatures in the range of 775–820 °C and pressures of 5–5.5 kbar, corresponding to thermal gradients of ~130–165 °C kbar^{-1}. The extensive Grenvillian-aged system reworks and overprints late Paleoproterozoic (ca. 1650–1630 Ma) high-grade metamorphic rocks. The Grenvillian-aged system occurs above a south dipping lithospheric-scale interface that has been geophysically imaged to depths of at least 200 km. This feature was interpreted to represent a fossil subduction zone of late Paleoproterozoic age. However, the presence of regional-scale Grenvillian-aged deformation in the crust above this feature suggests that it may instead be Grenvillian-aged. If that is the case, deformation along the southern margin of the NAC may record suturing of the NAC with the Grenvillian-aged Musgrave Province to the south. This would effectively place the long-lived, Late Mesoproterozoic ultrahot orogen that is the Musgrave Province in southern central Australia in an upper plate tectonic setting, linked to the convergence of the NAC with the South Australian Craton.

1. Introduction

The Precambrian evolution of the North Australian Craton (NAC; Fig. 1) has long been considered to reflect Paleoproterozoic-aged processes of crustal growth and reworking. However, there has been significant debate regarding the geodynamic setting of these processes, with intracratonic and plate margin settings both proposed (Betts et al., 2002; Cawood and Korsch, 2008; Giles et al., 2002, 2004; McLaren et al., 2005; Myers et al., 1996; Oliver et al., 1991; Payne et al., 2009; Smits et al., 2014; Wade et al., 2006; Wyborn, 1992). The evolution of the southern margin of the NAC is of particular significance, as in many tectonic models it is proposed to have been located at or close to a convergent margin (e.g. Betts and Giles, 2006; Betts et al., 2008; Cawood and Korsch, 2008; Giles et al., 2004; Hoatson et al., 2005; Maidment et al., 2005; Scott et al., 2000; Scrimgeour et al., 2005b). Although late Mesoproterozoic (Grenvillian) ages have been known from the southern NAC and Warumpi Province for many years, they have been previously attributed little geodynamic significance and instead the metamorphic and structural architecture of the southern margin of the NAC has been interpreted to be a result of Paleoproterozoic–Early Mesoproterozoic processes (e.g. Collins and Shaw, 1995; Biermeier et al., 2003; Scrimgeour et al., 2005b; Teyssier et al., 1988). However, a Grenvillian-aged (ca. 1130 Ma) system of deformation and

* Corresponding author. Tel.: +61 418 851 623.
E-mail address: laura.morrissey@adelaide.edu.au (L.J. Morrissey).

http://dx.doi.org/10.1016/j.precamres.2015.09.001
0301-9268/

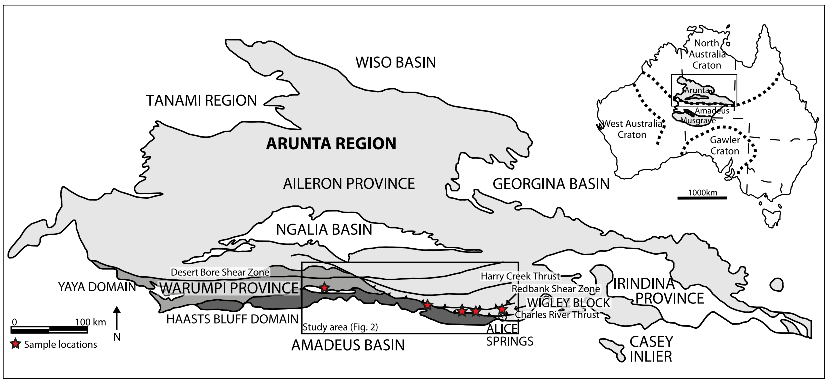

Fig. 1. Simplified geological map of the Arunta Region, central Australia illustrating the location of the Warumpi Province, Southern Aileron Province and Irindina Province (adapted from Scrimgeour et al., 2005b). Within the study area, the Warumpi Province and the southern Aileron Province make up the southern margin of the NAC. The location of the Arunta Region with respect to the NAC and Musgrave Province is inset (adapted from Wade et al., 2008).

metamorphism has recently been recognised along the exposed southern margin of the NAC in the eastern Warumpi Province (Fig. 1; Morrissey et al., 2011). The timing of this Grenvillian-aged tectonism is contemporaneous with the latter stages of long-lived and ultrahot tectonism in the Musgrave Province to the south (Morrissey et al., 2011; Smithies et al., 2011; Walsh et al., 2015). This challenges the proposition that the current day geology of the southern NAC wholly reflects the effects of late Paleoproterozoic convergence and suggests that a reappraisal of the tectonic evolution of the southern NAC may be warranted.

This study focuses on the exposed southern NAC, namely the southern Aileron Province and the adjacent rocks of the northern Warumpi Province (Fig. 1), to provide quantitative constraints on the timing and tectono-metamorphic evolution. Samples from an approximately 250 km east–west strike length are used to evaluate the extent of Grenvillian-aged metamorphism and deformation (Fig. 2). U–Pb monazite geochronology from metapelites and migmatitic orthogneiss and U–Pb zircon geochronology from igneous rocks are used to determine the age of magmatism and metamorphism. Calculated metamorphic phase diagrams for

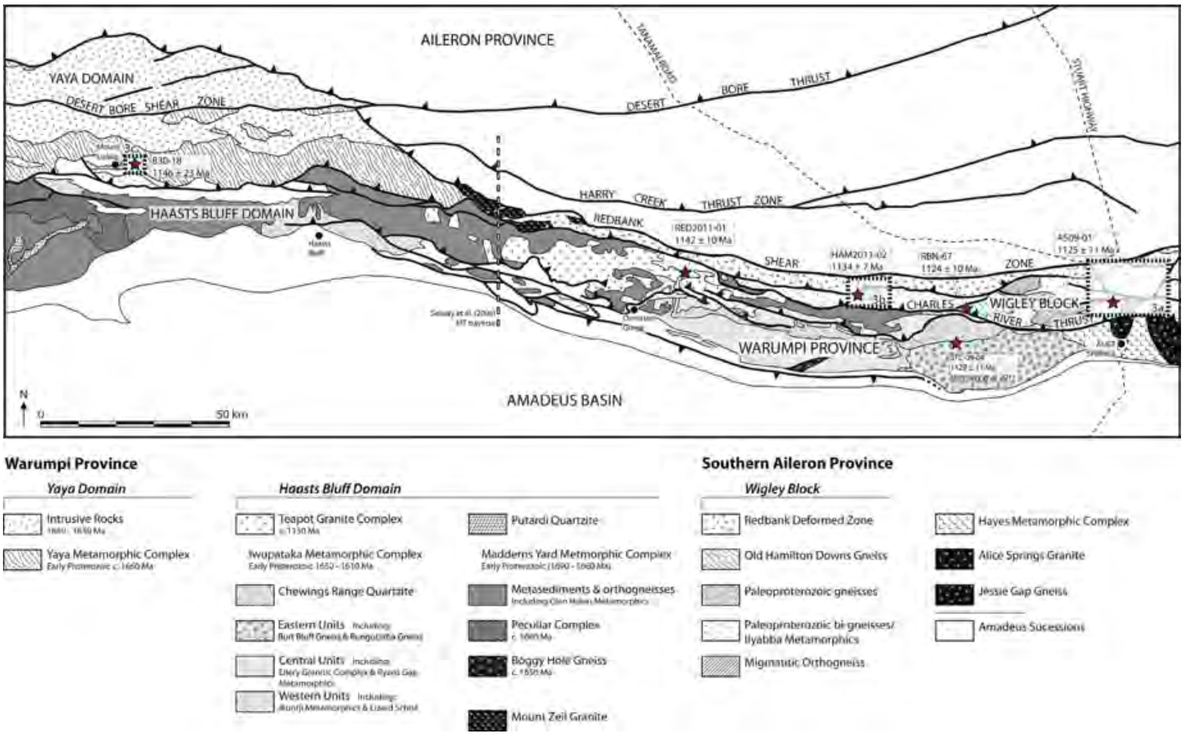

Fig. 2. Simplified geological map of the central southern margin of the NAC, which includes the Warumpi Province and southern Aileron Province of the Arunta Region. The series of east–west trending, crustal scale faults that separate the Warumpi and Aileron Provinces are also shown. Samples were collected from a strike length of ~250 km from Mount Liebig to Alice Springs. Three areas of significance are shown in more detail in Fig. 3.

metapelitic rock samples are used to constrain the conditions of metamorphism. The results of this study suggest that the dominant structural and metamorphic character of the southern margin of the NAC is a consequence of ca. 1130 Ma Grenvillian-aged deformation. Grenvillian-aged deformation overprints an earlier late Paleoproterozoic event at ca. 1650–1630 Ma that is recorded in zircon ages from migmatitic rocks and granitic gneisses and in monazite from metapelites in the west of the area examined in this study.

2. Regional setting

The southern margin of the NAC comprises the Warumpi and southern Aileron Provinces, which are part of the larger Arunta Region (Fig. 1). The Arunta Region exposes approximately 200,000 km^2 of Paleoproterozoic to early Paleozoic rock (Claoué-Long and Edgoose, 2008; Hand and Buick, 2001) and preserves an extensive and protracted tectono-metamorphic history from the ca. 1810–1800 Ma Stafford Event through to the ca. 400–300 Ma Alice Springs Orogeny (e.g. Claoué-Long and Edgoose, 2008; Collins and Shaw, 1995; Hand and Buick, 2001). Historically the Arunta Region was subdivided into three distinct geological provinces (largely bound by east–west trending faults) on the basis of differing protolith ages and tectono-metamorphic histories recognised at the time (Fig. 1; e.g. Collins and Shaw, 1995; Scrimgeour, 2004; Scrimgeour et al., 2005b; Stewart et al., 1984). These provinces are the Aileron, Warumpi and Irindina (Fig. 1). The Irindina Province comprises Neoproterozoic–Cambrian-aged protoliths that record high-grade Paleozoic metamorphism (Buick et al., 2001; Maidment and Hand, 2002). The southern Aileron and Warumpi Provinces have Paleoproterozoic protoliths and are the focus of this study.

The Aileron Province is the largest of the three provinces and is predominantly comprised of variably metamorphosed sedimentary units, with depositional ages between 1840 and 1710 Ma (Claoué-Long et al., 2008; Collins and Williams, 1995; Dirks and Wilson, 1990; Scrimgeour et al., 2005b), intruded by abundant felsic magmatic rocks and less abundant mafic to ultramafic rocks (e.g. Claoué-Long and Hoatson, 2005; Collins and Shaw, 1995). In the southern part of the Aileron Province, the Wigley Block comprises an east–west trending belt of well-exposed feldspathic migmatitic gneisses and metasediments, bounded by the Redbank Shear Zone to the north and the Charles River Thrust to the south (Fig. 2; Offe and Shaw, 1983; Warren and Shaw, 1995).

The Warumpi Province trends east–west along the southern margin of the NAC, and is separated from the Aileron Province by a series of crustal scale, east–west trending shear zones including the Charles River Thrust, Redbank Shear Zone and the Desert Bore Shear Zone (Figs. 1 and 2). From the few studies done to date, the Warumpi Province has known igneous and sedimentary protolith ages between ca. 1690–1610 Ma (Close et al., 2004; Scrimgeour et al., 2005b), in part derived from the Aileron Province (Kirkland et al., 2013). It has been subdivided into two fault-bound domains based on differing protolith ages and metamorphic grades (Fig. 2; Close et al., 2003). The Haasts Bluff Domain is comprised of ca. 1680 Ma felsic volcanics, and a ca. 1630–1610 Ma amphibolite facies grade metasedimentary cover sequence (Fig. 2; Black and Shaw, 1995; Warren and Shaw, 1995). The ca. 1680 Ma felsic volcanics are overlain by the 1660–1640 Ma granulite facies metasediments of the Yaya Domain to the north (Fig. 2; Scrimgeour et al., 2005a). The Warumpi Province has been considered exotic to the NAC (Scrimgeour, 2003; Scrimgeour et al., 2005a,b). However, Hf isotopic data show that at least the western parts of the Warumpi Province are indistinct from the Aileron Province, implying the Warumpi Province is not an exotic terrane (Hollis et al., 2013; Kirkland et al., 2013).

2.1. Tectono-metamorphic evolution of the southern NAC

The southern NAC experienced numerous tectono-metamorphic events in the Paleoproterozoic (Table 1). The majority of the events summarised in Table 1 have been inferred to relate to larger scale processes of continental assembly (e.g. Betts and Giles, 2006; Giles et al., 2004; Myers et al., 1996; Payne et al., 2009; Scrimgeour et al., 2005b; Wade et al., 2006). The events that are common to the southern Aileron and Warumpi Provinces are discussed below.

The Strangways Event in the southern Aileron Province has been subdivided into two discrete events, the Early Strangways Event (ca. 1730–1715 Ma) and Late Strangways Event (ca. 1700–1670 Ma; Claoué-Long et al., 2008). The Early Strangways Event is characterised by upper-amphibolite to granulite facies high thermal gradient metamorphism (Claoué-Long et al., 2008; Collins and Shaw, 1995; Diener et al., 2008; Maidment et al., 2005). The latter event was associated with the development of kilometre-scale sheath folds, and granulite facies mylonite systems that record east and northeast directed apparent extensional movement (M. Hand unpub. data; Goscombe, 1991).

The ca. 1640 Ma Liebig Orogeny involved localised (as far is currently known) high grade metamorphism at conditions up to ~9 kbar and ~900 °C (Scrimgeour et al., 2005b). It was accompanied by syn-tectonic felsic and mafic–ultra mafic magmatism in both the Warumpi and Aileron Provinces (Claoué-Long and Hoatson, 2005; Young et al., 1995). The Liebig Orogeny has been interpreted to record collisional suturing of the exotic Warumpi Province with the NAC (Scrimgeour et al., 2005b), in which the NAC was thrust beneath the overriding Warumpi Province (Scrimgeour et al., 2005b; Selway et al., 2006, 2009).

The 1580–1520 Ma Chewings Orogeny has been interpreted to have significantly affected the Arunta Region, including the Warumpi Province and the southern Aileron Province, as part of a larger scale regional event (Anderson et al., 2013; Claoué-Long and Edgoose, 2008; Claoué-Long and Hoatson, 2005; Collins and Shaw, 1995; Morrissey et al., 2014; Rubatto et al., 2001; Williams et al., 1996). However, the effects of the Chewings Orogeny in the southern part of the Aileron Province and much of the Warumpi Province are inferred rather than demonstrated (e.g. Teyssier et al., 1988).

The un-named Grenvillian-aged event reworked the region at ca. 1130 Ma (Morrissey et al., 2011). Metamorphism associated with ca. 1130 Ma deformation involved a clockwise *P*–*T* evolution, from pressures of 4–4.5 kbar at 530 °C to pressures of ~3.5 kbar at 570 °C, corresponding to thermal gradients of ~120–165 °C kbar^{-1}. Throughout the southern Arunta region, K–Ar and $^{40}Ar/^{40}Ar$ isotopic systems were reset to ca. 1130 Ma (Biermeier et al., 2003; Shaw et al., 1992). Emplacement of the alkaline and ultramafic Mordor Complex occurred at ca. 1130 Ma in the eastern Aileron Province, coeval with the generation of syn-deformation migmatite complexes in the Haasts Bluff and Yaya Domains of the Warumpi Province (Biermeier et al., 2003; Black and Shaw, 1995; Claoué-Long and Hoatson, 2005; Collins and Shaw, 1995; Scrimgeour et al., 2005b; Shaw and Langworthy, 1984). These ages coincide with the later stages of the Musgrave Orogeny, several hundred kilometres to the south (e.g. Smithies et al., 2011; Wade et al., 2008; Walsh et al., 2015). However, Grenvillian-aged reworking does not appear to continue north of the Redbank Shear Zone (Lawson-Wyatt, 2012). Following this, extensive mafic dykes were emplaced at ca. 1080 Ma (Collins and Shaw, 1995; Zhao and McCulloch, 1993), coeval with voluminous mafic and ultramafic magmatism in the Musgrave Province, that has been suggested to have occurred in a failed intra-plate rift setting (Edgoose et al., 2004; Evins et al., 2010; Smithies et al., 2015; Wingate et al., 2004).

Table 1
Summary of Proterozoic tectonic events that have created and shaped the Arunta region.

Event	Age (Ma)	Regional distribution	Magmatism	Metamorphic character	Deformation	Studies
Stafford Event	1810–1800	Aileron Province north of the Redbank Shear Zone	Felsic and mafic	*P–T* 850 °C abd 3 kbar (∼285 °C/kbar)	Predominantly thermal event	Claoué-Long and Hoatson (2005)
Yambah Event	1780–1760	Central and southern Aileron Province	Felsic and mafic	*P–T* poorly known but possible ∼3.5 kbar, 550 °C (andalusite–cordierite-bearing; ∼160 °C/kbar)	Likely compressional	Claoué-Long and Hoatson (2005) and Hand and Buick (2001)
Inkamulla Igneous Event	1760–1740	South-eastern Aileron Province	Felsic and mafic. Includes apparent arc-related and A-type magmatism	Unknown	Unknown	Scrimgeour (2003)
Early Strangways Event	1730–1715	South-eastern and southern Aileron Province	Minor felsic magmatism	*P–T* poorly known but possible >800 °C and 8 kbar	Regional high-grade deformation-assumed to be compressional	Claoué-Long et al. (2008) and Diener et al. (2008)
Late Strangways Event	1700–1670	South-eastern and southern Aileron Province	Abundant mafic dykes	*P–T* up to 800 °C and 7 kbar (∼115 °C/kbar)	Regional-scale mylonites and large scale sheath folds associated with east-directed extension	Claoué-Long et al. (2008) and Claoué-Long and Hoatson (2005)
Argilke Igneous Event	1690–1670	Southern Warumpi Province	Voluminous felsic magmatism	Poorly known- up to amphibolite facies	Unknown	Scrimgeour et al. (2005a)
Leibig Orogeny	1640–1630	Central Warumpi Province and southern Aileron Province	Voluminous felsic magmatism, minor mafic to ultramafic magmatism	*P–T* up to 900 °C and 9 kbar (∼100 °C/kbar)	Unknown, but shallow low-strain fabrics in southern Aileron Province interpreted to represent extension	Scrimgeour et al. (2005b) and Claoué-Long and Hoatson (2005)
Chewings Orogeny	1580–1520	Central Warumpi Province and southern and central Aileron Province	Minor felsic magmatism in central Aileron Province	*P–T* > 850 °C and 6 kbar (∼140 °C/kbar)	Compressional, associated with top to the south transport	Hand and Buick (2001), Morrissey et al. (2014) and Anderson et al. (2013)
Teapot Event	1160–1130	Warumpi Province and southern Aileron Province	Felsic to mafic and ultramafic	Eastern Warumpi: *P–T* up to 570 °C and 4.5 kbar (∼130°/kbar) Northern Warumpi: *P–T* up to 840 °C and 6.3 kbar (∼130 °C/kbar) Southern Aileron: *P–T* up to 835 °C and 6.4 kbar (∼130 °C/kbar)	Compressional with regional-scale E–W trending isoclinal folding and south up shear systems	Black and Shaw (1995), Claoué-Long and Hoatson, (2005), Morrissey et al. (2011) This study

The final event to have affected the southern NAC is the ca. 400–300 Ma Alice Springs Orogeny, which is expressed by large scale east–west striking mylonite zones, associated with the south-vergent exhumation of the Arunta region and deformation of the northern margin of the Centralian Superbasin (Flöttmann and Hand, 1999; Sandiford and Hand, 1998; Shaw et al., 1992; Teyssier, 1985).

3. Sample selection and description

This study aims to investigate the spatial extent of the footprint of Grenvillian-aged deformation along the southern margin of the NAC. Therefore, samples were collected from various structurally constrained locations widely distributed throughout the southern Aileron Province and the Warumpi Province over an ~250 km strike length in order to provide tight spatial and temporal constraints on metamorphism and deformation within the region. Samples collected for this study are described in Table 2 and shown in Figs. 1–3.

3.1. Structure of the southern margin of the NAC

Combined satellite imagery and outcrop-scale mapping of the southern margin of the NAC reveals the presence of three distinct structural elements (Fig. 3a). The oldest fabric system (S_1) is parallel to lithological layering and has locally undergone kilometre-scale folding with roughly north-trending fold axes and currently easterly reclined axial planes (Fig. 3a). These folds have been subsequently overprinted by regionally pervasive and contiguous east–west trending shear systems and associated folds (S_2–F_2; Figs. 3a and 4a). Within the D_2 high strain zones, three generations of foliation development with varying degrees of migmatisation occur (Fig. 4a and b). Highly strained migmatitic fabrics (S_{2a}) with near-horizontal westerly plunging mineral lineations (L_{2a}) are overprinted by co-planar S_{2b} and steeply plunging lineations (L_{2b}) associated with south-side up movement, and local post-S_{2b} migmatisation (Fig. 4c). The system is overprinted by a series of pervasive east–west trending fine-grained (S_{2c}) mylonites and ultramylonites up to 60 m wide with vertical mineral lineations (L_{2c}), which are also associated with south side up movement. The D_{2c} mylonites are cross cut by undeformed ca. 1080 Ma mafic dykes of the Stuart Dyke Swarm (Warren and Shaw, 1995; Zhao and McCulloch, 1993). However, in some areas including the Teapot Granite Complex within the Haasts Bluff Domain, F_2 folds are relatively subordinate and a low angle pre-F_2 foliation is the predominate structure within rocks that have ca. 1150 Ma intrusive ages (Black and Shaw, 1995; Warren and Shaw, 1995).

Table 2
Summary of samples and U–Pb geochronology.

Sample	Location (UTM, GDA94)	Province	Rocktype description	Field context	Predominant age	Subordinate age
Monazite U–Pb geochronology						
Pre-D_2 fabric						
AS2010-63D	53J 0380898 7387482	Southern Aileron	gt-sil-cd-bearing pelitic gneiss	Older fabric which folds into the E–W high strain belt	1085 ± 16 Ma	1633 ± 24 Ma
AS2010-66D	53J 0382933 7386196	Southern Aileron	gt-sil-bearing migmatitic gneiss	Older fabric which folds into the E–W high strain belt	1083 ± 17 Ma	1720 ± 17 Ma
AS2010-67A2	53 J 0383622 7386185	Southern Aileron	gt-sil-bearing migmatitic metapelite	Older fabric which folds into the E–W high strain belt	1133 ± 17 Ma	1569 ± 21 Ma
D_2 Fabric						
830-10G	52K 0762237 7426363	Warumpi	gt-bearing migmatitic metapelite	E–W high strain belt with westerly plunging open folds	1650 ± 44 Ma	
830-18	52K 0761079 7424632	Warumpi	gt-sil-bearing metapelite		1617 ± 11 Ma	1146 ± 23 Ma*
AS09-01	53J 0382941 7388186	Southern Aileron	gt-sil-cd bearing migmatitic metapelite	Boundary of E–W high strain belt	1125 ± 11 Ma	
AS2010-65J	53J 0385454 7389461	Southern Aileron	gt-sil-bearing migmatitic metapelite	E–W high strain belt	1138 ± 14 Ma	
AS2010-72D	53J 0385790 7388832	Southern Aileron	bi-ksp-pl-bearing ultramylonite	60 m wide E–W south side up shear zone	1126 ± 8 Ma	
RED2011-01	53K 0275184 7397376	Warumpi	gt-sil-bearing metapelite	E–W high strain belt with westerly plunging open folds	1143 ± 10 Ma	
RED2011-02			gt-cd-bearing metapelite			
AS2010-66J	53J 0385454 7389461	Southern Aileron	Microgranite	E–W high strain belt	1117 ± 10 Ma	
RBN-43	53K 0347748 7383931	Warumpi	Undeformed pegmatite	Cross cuts regional E–W gneissic fabric	1070 ± 26 Ma	
RBN-67	53K 0348649 7385840	Southern Aileron	Quartzofeldspathic gneiss	E–W high strain belt	1122 ± 12 Ma	
RBN-71	53K 0352800 7387700	Southern Aileron	Granitic gneiss	Periphery of a low strain zone within the E–W high strain belt	1126 ± 14 Ma	
RBN-54	53K 0328349 7386229	Warumpi	Granitic bi-gneiss	Low strain zone enveloped by E–W trending shears	1098 ± 12 Ma	
Zircon U–Pb Geochronology						
HAM2011-02	53J 0330270 7388919	Southern Aileron	Pegmatite	Periphery of a kilometre scale low strain boudin enveloped by regional E–W fabric	1136 ± 8 Ma	
HAM2011-08	53J 0329884 7390901	Southern Aileron	Migmatitic melt vein	Periphery of a kilometre scale low strain boudin enveloped by regional E–W fabric	1625 ± 8 Ma	1139 ± 19 Ma
AS2012-1	53K 384435 7394616	Southern Aileron	Migmatitic granitic gneiss	Older fabric which folds into the E–W high strain belt	1638 ± 8 Ma	1115 ± 25 Ma*
AS2012-2	53K 385668 7389949	Southern Aileron	Migmatitic orthogneiss	Older fabric which folds into the E–W high strain belt	1631 ± 7 Ma	1152 ± 34 Ma

Ages quoted are $^{206}Pb/^{207}Pb$, *denotes single analysis.

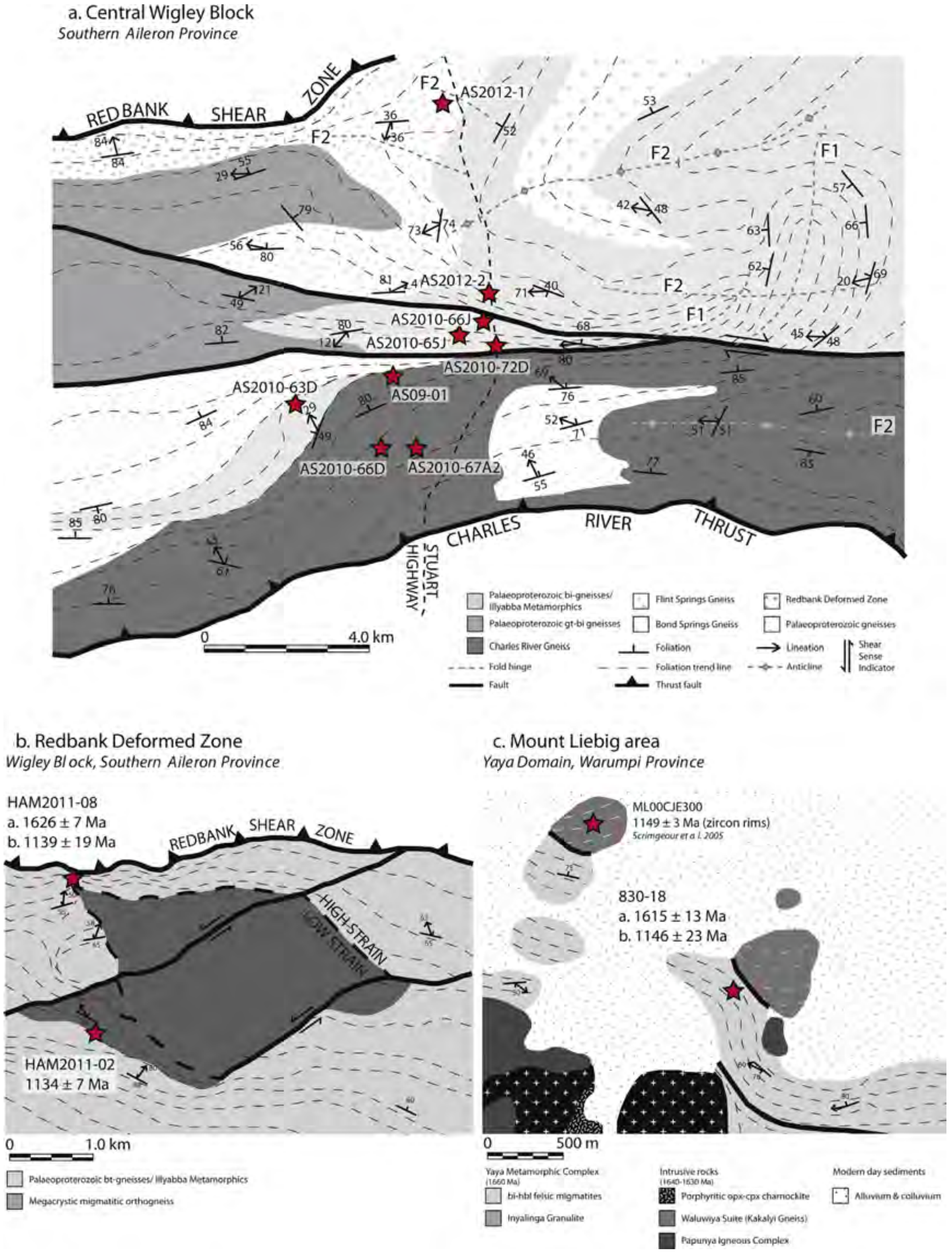

Fig. 3. Schematic diagrams highlighting significant geological features along the southern margin of the NAC. Diagrams were constructed in conjunction with satellite imagery and 1:250,000 scale regional geological maps. (a) Central Wigley Block of the southern Aileron Province ~10 km north of Alice Springs. The region is characterised by north-trending, kilometre-scale folding which has been overprinted by a pervasive east–west D_2 fabric. (b) Western Wigley Block of the southern Aileron province ~50 km west-northwest of Alice Springs. A kilometre-scale, low strain 'mega boudin' is enveloped by an east–west D_2 fabric. (c) Approximately 20 km east-northeast of Mount Liebig on the southern margin of the Yaya Domain, Warumpi Province. The region is characterised by a dominant northwest-southeast D_2 foliation which cross-cuts an older roughly east–west striking foliation recorded in the ca. 1150 Ma Kakalyi Gneiss.

Fig. 4. Field photographs from the southern Aileron Province and Mount Liebig region (d) demonstrating the key structural relationships. (a) Felsic melt veins cross-cutting S_{2a}. (b) Interboudin pegmatitic accumulation within S_{2a}. (c) S–C fabrics showing south-side up movement from S_{2a} shear fabric. (d) Metapelite from the Mt Liebig region.

The southern Aileron Province is also characterised by relatively low D_2 strain domains enclosed by the D_2 shear zones. This overprinting is best expressed ~50 km west of Alice Springs in the region bounded by the Redbank Shear Zone and the Charles River Thrust, where mapping and satellite imagery reveals the presence of a kilometre-scale 'megaboudin' enveloped by D_2 shear zones (Fig. 3b). Further west in the Mt Liebig area of the Warumpi Province, megaboudins of ca. 1640 Ma granulite and coeval metagabbro are enclosed by strongly foliated and mylonitic upper-amphibolite facies mineral fabrics. These are associated with south over north transport and overprint migmatites dated at 1150 Ma (Figs. 3c and 4d; Scrimgeour et al., 2005b).

3.2. Metamorphic petrography

Four samples of variably migmatised garnet–biotite ± sillimanite ± cordierite metapelites were selected for mineral equilibria modelling. Three of the four samples were also used for U–Pb monazite geochronology. Spatial locations of all samples are provided in Table 2.

3.2.1. AS09-01

Sample AS09-01 is a garnet–sillimanite–cordierite-bearing migmatitic metapelite from near the margin of a major D_2 belt in the southern Aileron Province. It contains intensely foliated biotite–sillimanite domains which form part of a layered composite fabric with granoblastic K-feldspar–plagioclase–quartz-bearing leucosomes that contain garnet and minor cordierite. Garnet porphyroblasts are euhedral and range in size between 2 and 10 mm. They contain inclusions of biotite and quartz up to 1 mm in length (Fig. 5a). Cordierite may partially envelop garnet. Uncommonly, chlorite (up to 2 mm in length) occurs within large fractures and on the boundaries of large garnet grains. Perthitic K-feldspar contains sillimanite inclusions when it is located within the biotite–sillimanite domains in the sample. Ilmenite occurs in the biotite–sillimanite-rich domains, along biotite cleavages or biotite grain boundaries. The peak metamorphic assemblage is interpreted to be garnet + biotite + sillimanite + cordierite + K-feldspar + plagioclase + ilmenite + quartz + inferred silicate melt.

3.2.2. AS2010-65J

Sample AS2010-65J is a porphyroblastic garnet–biotite–sillimanite-bearing migmatitic gneiss from a D_2 zone in the southern Aileron Province and contains the S_{2a} fabric. The sample preserves stromatic leucosomes and a shallow west-plunging lineation defined by sillimanite. Garnet grain sizes range between 3 and 9 mm and contain inclusions of biotite, sillimanite and quartz (Fig. 5b). In general the inclusions are unoriented or weakly

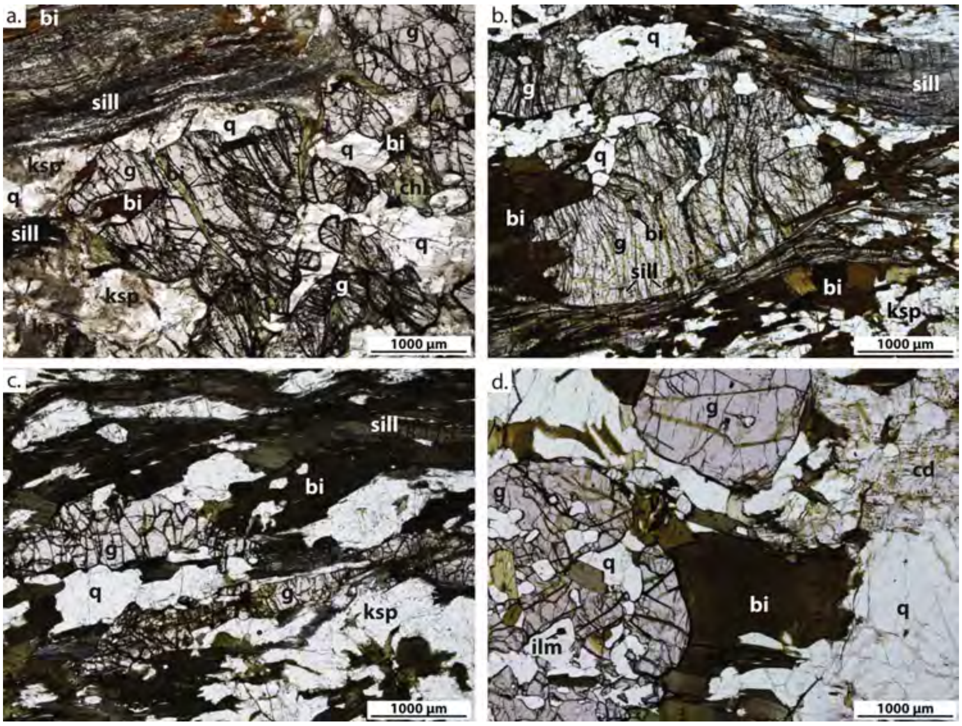

Fig. 5. Key petrological relationships for samples used for phase equilibria modelling: (a) AS09-01: Garnet porphyroblasts cluster along the boundary of a leucosome which is wrapped by intensely foliated biotite–sillimanite. Garnet grains are highly fractured and contain inclusions of biotite and quartz. (b) AS2010-65J: Garnet porphyroblasts wrapped by a fabric comprising of biotite and prismatic sillimanite. (c) RED2011-01: Elongate garnet parallel to the biotite–sillimanite fabric. (d) RED2011-02: Poikiloblastic garnet with inclusions of quartz, biotite and ilmenite. Biotite defines a weak foliation. Cordierite is abundant throughout the matrix.

oriented, but rarely form well defined inclusion trails that parallel the trace of the matrix foliation. The rims of garnet rarely also contain large inclusions of monazite (~250 µm). The strongly developed foliation is defined by biotite and sillimanite which forms a fabric domain interlayered with quartz and plagioclase and lesser microcline-dominated layers (Fig. 5b). The fabric layers of different composition and mineralogy are typically 3–5 mm wide, with elongate quartz up to 3 by 1 mm and plagioclase and microcline <1 mm. Biotite tends to be more strongly concentrated around garnet with typically larger crystals forming in strain shadows on garnet (Fig. 5b). Sillimanite occurs in bundles defined by aggregates of elongate fine-grained prismatic sillimanite. Both sillimanite and garnet are overprinted by a well-developed fracture fabric that is orthogonal to the foliation (in 2-D), and approximately orthogonal to the lineation in hand sample. When these fractures occur in sillimanite included in plagioclase and quartz, the fractures terminate in the quartz and plagioclase host (Fig. 5b), with occasional fine-grained trails of ilmenite in the quartz–plagioclase matrix that mark the former continuation of the fracture. These annealed fractures suggest the extension of the sillimanite aggregates was associated with the deformation recorded by the fabric and its associated lineation. The peak metamorphic assemblage is interpreted to be garnet + biotite + sillimanite + K-feldspar + plagioclase + ilmenite + quartz + inferred silicate melt.

3.2.3. RED2011-01

Sample RED2011-01 is a garnet–biotite–sillimanite-bearing metapelite, layered within migmatitic felsic gneiss that forms part of the Teapot Granite Complex in the Warumpi Province. The sample is located along strike of the D_2 high strain belt identified in the southern Aileron Province. It comes from a set of shallow, open, westerly plunging F_2 folds that fold a flat lying S_1 foliation defined by sillimanite and biotite that envelopes garnet and parallels migmatitic layers composed of K-feldspar, plagioclase and quartz. Garnet grains are anhedral and commonly elongate (<6 × 1.5 mm; Fig. 5c). Early, coarse grained, tabular biotite is abundant throughout the matrix and rarely occurs as inclusions within coarser quartz and feldspar grains. As well as being intergrown with biotite, sillimanite occurs in dense aggregates of fine-grain prismatic crystals. Some of the sillimanite and biotite grains exhibit well developed micro-boudinage with the inter-boudin necks occasionally filled with fine-grained magnetite. The sample contains abundant monazite. The peak metamorphic assemblage is interpreted to be garnet + biotite + sillimanite + K-feldspar + magnetite + quartz + inferred silicate melt.

3.2.4. RED2011-02

Sample RED2011-02 is from the same location as RED2011-01, but instead contains a cordierite-bearing, K-feldspar-absent assemblage. The pre-F_2 foliation is defined by coarse grained, platy biotite up to 4 mm in length which occurs as discontinuous domains between granoblastic quartz–cordierite–plagioclase-bearing domains. Garnet occurs as euhedral grains commonly up to 2 mm with sparse inclusions of quartz and ilmenite, and as anhedral poikiloblastic grains with abundant inclusions of quartz, biotite and lesser ilmenite (Fig. 5d). Garnet preferentially occurs near biotite rich areas. Fine-grained, anhedral magnetite (<0.2 mm) occurs along the boundaries of foliated biotite domains and within biotite cleavages, and as rare coarser euhedral grains (<2.5 mm). Sillimanite does not occur in thin section of this sample

Table 3
Whole rock geochemistry.

	AS09-01	AS2010-65J	RED2011-01	RED2011-02
Major elements (wt%)				
SiO	44.58	59.13	67.26	68.01
TiO_2	1.11	0.98	0.57	0.72
Al_2O_3	29.51	15.65	13.80	12.06
Fe_2O_3	12.66	14.63	10.74	9.17
MnO	0.17	0.23	0.15	0.12
MgO	4.70	3.01	1.91	4.21
CaO	0.76	1.00	0.28	0.98
Na_2O	0.65	0.72	0.09	0.79
K_2O	3.43	3.73	3.05	2.35
P_2O_5	0.05	0.19	0.13	0.21
LOI	3.16	1.72	2.58	2.03

except for one cluster of matted fibrolite included in coarse grained cordierite. Minor chlorite occurs on the boundaries of some biotite grains. The sample contains abundant monazite throughout the matrix. The peak metamorphic assemblage is interpreted to be garnet + cordierite + biotite + plagioclase + magnetite + ilmenite + quartz + inferred silicate melt.

4. Analytical methods

4.1. Whole rock and mineral chemistry

Whole rock chemical compositions for the construction of metamorphic phase diagrams for samples AS09-01, AS2010-65J, RED2011-01 and RED2011-02 were obtained by XRF at Franklin and Marshall College, Pennsylvania (Table 3). A representative portion of each sample (approximately 20–50 g) was crushed up using a ceramic mill for homogenisation. Major elements were analysed by mixing a 0.4 g portion of the powdered sample with 3.6 g of lithium tetraborate before being presented for analysis by XRF. Trace elements were analysed by mixing 7 g of whole rock powder with 1.4 g of high purity Copolywax powder before XRF analysis. Representative compositions of minerals were obtained using a Cameca SX51 Electron Microprobe with a beam current of 20 nA and an accelerating voltage of 15 kV at the University of Adelaide.

4.2. Geochronology

4.2.1. U–Pb monazite LA–ICP–MS geochronology

In situ monazite geochronology was collected from grains in thin section for nine samples (samples AS2010-63D, AS2010-66D, AS2010-67A2, 830-10G and 830-18, AS09-01, AS2010-65J, AS2010-72D, RED2011-01); and on separated monazite grains mounted in epoxy resin (method outlined in section 4.2.2 below) for five samples (samples AS2010-66J, RBN-43, RBN-67, RBN-71 and RBN-54). Prior to analysis, monazite grains were imaged by BSE on a Phillips XL30 Scanning Electron Microscope (SEM) in order to identify internal compositional variability, and in the case of in situ analysis, to determine their microstructural location.

U–Pb isotopic analyses were done using a New Wave 213 nm Nd–YAG laser coupled to an Agilent 7500cs ICP–MS for 11 monazite samples at the University of Adelaide following the method of Payne et al. (2008). Ablation was performed in a helium atmosphere, with a beam diameter of 15 μm and a repetition rate of 5 Hz. Each analytical run had a total acquisition time of 90 s, comprising 20 s of background measurement, 10 s of laser firing with the shutter closed to allow for beam stabilisation and 60 s of sample ablation.

Monazite U–Pb age data was also collected using a Resonetics M-50 laser ablation system attached with an Agilent 7700s ICP-MS for three samples AS09-01, 830-10G and 830-18. A beam diameter of approximately 20 μm was used for samples AS09-01 and 830-18, whereas a beam diameter of 10 μm was used for sample 830-10G due to the small size of monazite grains. Ablation of monazite grains was done with a frequency of 5 Hz. The total acquisition time for each analysis was 60 s, which included 30 s of background measurement and 30 s of sample ablation. For both methods, isotope masses measured were ^{204}Pb, ^{206}Pb, ^{207}Pb and ^{238}U for 10 ms, 15 ms, 30 ms and 15 ms respectively.

Monazite data was processed using 'GLITTER' software (Griffin et al., 2008). U–Pb fractionation in all samples was corrected using the internal monazite standard MAdel (TIMS normalisation data: $^{207}Pb/^{206}Pb$ age = 491.0 ± 2.7 Ma; $^{206}Pb/^{238}U$ age = 518.37 ± 0.99 Ma; $^{207}Pb/^{235}U$ age = 513 ± 0.19 Ma: Payne et al., 2008; updated with additional TIMS data), with the exception of AS2010-66D, where the external monazite standard 44069 was used (TIMS normalisation data: $^{207}Pb/^{206}Pb$ age = 425.3 ± 1.1 Ma; $^{206}Pb/^{238}U$ = 426.86 ± 0.36 Ma; $^{207}Pb/^{235}U$ age = 424.86 ± 0.35 Ma: Aleinikoff et al., 2006). The accuracy of data correction was monitored by repeated analysis of the in-house monazite standard 94-222/Bruna NW (450 ± 3.5 Ma; Payne et al., 2008), with the exception of AS2010-66D where data accuracy was monitored by the internal monazite standard MAdel. Common lead (proxied by ^{204}Pb) was not corrected for during data reduction, but analyses were not used in age calculations if $^{204}Pb/^{206}Pb$ ratios were above 0.0003 (approximately equivalent to a non-radiogenic ^{206}Pb proportion of 0.5% at 1.6 Ga). Background subtracted $^{204}Pb/^{206}Pb$ ratios for each analysis are provided in Appendix A. Analyses were also not used for age calculations if discordance exceeded 5%. Throughout the study MAdel yielded weighted mean ages of $^{207}Pb/^{206}Pb$ = 491 ± 5 Ma, $^{206}Pb/^{238}U$ = 518 ± 1 Ma and $^{207}Pb/^{235}Pb$ = 513 ± 1 Ma (n = 136) and standard 94-222 yielded weighted mean ages of $^{207}Pb/^{206}Pb$ = 464 ± 11 Ma, $^{206}Pb/^{238}U$ = 448 ± 5 Ma and $^{207}Pb/^{235}Pb$ = 450 ± 5 Ma (n = 31). Standard 44069 yielded weighted mean ages of $^{207}Pb/^{206}Pb$ = 420 ± 14 Ma, $^{206}Pb/^{238}U$ = 427 ± 4 Ma and $^{207}Pb/^{235}Pb$ = 426 ± 5 Ma (n = 27).

4.2.2. U–Pb zircon LA–ICP–MS geochronology

Zircon U–Pb age data was collected from samples HAM2011-02, HAM2011-08, AS2012-1 and AS2012-2. Zircons were extracted from whole rock samples of approximately 2 kg using a jaw crusher, tungsten carbide mill and conventional magnetic and heavy liquid separation techniques. Individual zircons were then handpicked, mounted in 2.5 cm diameter circular epoxy grain mounts and the mount was hand polished until the centre of the zircons were revealed. Prior to LA–ICP–MS analysis, all zircon grains were imaged by backscatter electron (BSE) and cathodoluminescence (CL) on a Phillips XL20 Scanning Electron Microscope (SEM) in order to study their internal structure, determine if multiple age components were present and to select homogeneous areas for age determination.

U–Pb isotopic analyses of zircons were collected using a similar methodology to monazite geochronology. Laser ablation was performed with a beam diameter of 30 μm at the sample surface and a repetition rate of 5 Hz. Each analysis consisted of a total acquisition time of 100 s, comprising 20 s of background measurement, 10 s of laser firing with the shutter closed to allow for beam stabilisation and 70 s of sample ablation. Isotopes measured were ^{204}Pb, ^{206}Pb, ^{207}Pb, ^{208}Pb, ^{232}Th and ^{238}U for 10 ms, 15 ms, 30 ms, 10 ms, 10 ms and 15 ms respectively.

U–Pb fractionation was corrected using the external zircon standard GJ (TIMS normalisation data: $^{207}Pb/^{206}Pb$ age = 607.7 ± 4.3 Ma; $^{206}Pb/^{238}U$ age = 600.7 ± 1.1 Ma; $^{207}Pb/^{235}U$ age = 602.0 ± 1.0 Ma: Jackson et al., 2004). The accuracy of data correction was monitored by repeated analysis of the internal zircon standard Plešovice (ID–TIMS normalisation data: $^{206}Pb/^{238}U$ age = 337.13 ± 0.37 Ma: Sláma et al., 2008).

Raw data was reduced using 'GLITTER' software as outlined above, and was not corrected for common lead. Throughout the study, the weighted averages obtained for GJ were $^{207}Pb/^{206}Pb = 608.0 \pm 6.9$ Ma, $^{206}Pb/^{238}U = 600.7 \pm 1.6$ Ma and $^{207}Pb/^{235}Pb = 602.3 \pm 1.8$ Ma ($n = 84$) and Plešovice $^{207}Pb/^{206}Pb = 323 \pm 15$ Ma, $^{206}Pb/^{238}U = 337 \pm 5$ Ma and $^{207}Pb/^{235}Pb = 335 \pm 4$ Ma ($n = 16$).

4.3. Mineral equilibria modelling

Calculated phase equilibria techniques were employed to determine the physical and thermal (i.e. *P–T*) conditions of metamorphism over a ~110 km strike length of the southern margin of the NAC. Samples were selected from the east (samples AS09-01 and AS2010-65J) in the southern Aileron Province and west (samples RED2011-01 and RED2011-02) in the Warumpi Province. *P–T* pseudosections were calculated using the phase equilibria forward modelling programme THERMOCALC v3.40, using the internally consistent dataset, ds62, of Holland and Powell (2011) and the activity–composition (*a–x*) models re-parameterised for metapelitic rocks in the system MnNCKFMASHTO ($MnO–Na_2O–CaO–K_2O–FeO–MgO–Al_2O_3–SiO_2–H_2O–TiO_2–Fe_2O_3$) (Powell et al., 2014; White et al., 2014a,b).

It has been widely recognised that variations in the H_2O and Fe_2O_3 components of the bulk composition may affect the stability of phase assemblages in *P–T* space (e.g. Johnson and White, 2011; White et al., 2000). Determination of Fe_2O_3 by titration may overestimate the amount of Fe_2O_3 in the whole rock geochemistry due to low-*T* oxidation during weathering, or oxidation during sample preparation for geochemical analysis (e.g. Johnson and White, 2011; Kelsey and Hand, 2015; Lo Pò and Braga, 2014). Therefore, in this study, the proportion of Fe_2O_3 to FeO was estimated through the consideration of the modal abundance of Fe^{3+} bearing minerals and the stoichiometric evaluation of the Fe_2O_3 content of those minerals within each sample (e.g. Kelsey and Hand, 2015). For these samples, the main effect of varying oxidation state is to expand the stability of magnetite to higher pressures in the more oxidised compositions. However, small variations in the oxidation state do not significantly affect the topology or *P–T* conditions of the fields on the pseudosections. Similarly, LOI may not provide an appropriate estimation of H_2O at peak conditions due to hydration of the sample during weathering, as well as the presence of other volatiles such as CO_2, F and Cl. Therefore, the H_2O content for each sample was estimated based on the proportion of H_2O bearing minerals (i.e. biotite and/or cordierite; Kelsey and Hand, 2015) and an estimate of the H_2O content of these minerals. For biotite, the H_2O content was determined by calculating the difference between the electron microprobe totals including Cl and F for each sample (in the range ~95–97.5 wt%) and 100%. Cordierite H_2O contents were estimated at 0.5–1% based on electron microprobe totals and the likelihood that some of the volatile content of cordierite is CO_2 (Rigby and Droop, 2011). Small variations in H_2O do not significantly affect the interpreted peak conditions. The main effect of decreasing the H_2O content of the bulk composition is to elevate the solidus, whereas increasing the amount of H_2O favours the stability of silicate melt at the expense of diminishing K-feldspar stability. In all samples, the H_2O content of the bulk composition results in an elevated solidus at peak conditions, reflecting the fact that the samples have lost melt and preserve residual, granulite-facies assemblages.

5. Results

5.1. Mineral chemistry

Representative compositions of selected minerals in samples used for *P–T* modelling are summarised below and the ranges in values given in Table 4. A representative analysis for each mineral identified in each sample is given in Table 5.

Table 4
Chemistry ranges for selected minerals.

	AS09-01	AS2010-65J	RED2011-01	RED2011-02
Garnet core				
X_{alm}	0.67–0.71	0.73–0.75	0.82–0.84	0.69–0.71
X_{py}	0.23–0.28	0.16–0.17	0.10–0.13	0.22–0.23
X_{grs}	0.03–0.05	0.06–0.07	0.03	0.04–0.04
X_{sps}	0.02	0.02–0.03	0.02–0.03	0.03
Garnet rim				
X_{alm}	0.67–0.80	0.76–0.80	0.85–0.86	0.71–0.73
X_{py}	0.12–0.23	0.13–0.15	0.07–0.09	0.20–0.22
X_{grs}	Unzoned	0.036–0.040	Unzoned	Unzoned
X_{sps}	0.02–0.04	Unzoned	0.03-0.04	Unzoned
Biotite				
F (wt%)	0.24–0.38	0.26–0.35	0.45–0.55	0.39–0.72
TiO_2 (wt%)	3.63–4.77	2.22–3.87	1.52–1.91	1.32–2.52
X_{Fe}	0.49–0.52	0.49–0.58	0.64–0.66	0.28–0.65
Cordierite				
X_{Fe}	0.29–0.30	–	–	0.29–0.31
K-feldspar				
X_{Or}	0.77–0.91	0.67–0.96	0.62–0.91	–
Plagioclase				
X_{Ab}	0.67–0.71	0.66–0.67	–	0.63–0.72
Ilmenite				
MnO (wt%)	0.42–1.68	–	–	0.19–0.26
Magnetite				
Cr_2O_3 (wt%)	–	–	0–0.03	0–0.10
Al_2O_3 (wt%)	–	–	0.33–2.83	0.15–0.50

X_{alm} = Fe/(Fe + Mg + Ca + Mn); X_{py} = Mg/(Fe + Mg + Ca + Mn); X_{grs} = Ca/(Fe + Mg + Ca + Mn).
X_{sps} = Mn/(Fe + Mg + Ca + Mn); X_{Fe} = Fe/(Fe + Mg); X_{Or} = K/(K + Na + Ca); X_{Ab} = Na/(Na + Ca).

5.1.1. Garnet

Throughout all samples, garnet grains exhibit similar zoning patterns. X_{alm} (=$Fe^{2+}/(Fe^{2+} + Mg + Ca + Mn)$) and X_{py} (=$Mg/(Fe^{2+} + Mg + Ca + Mn)$) values are weakly zoned in all samples, whereas X_{sps} (=$Mn/(Fe^{2+} + Mg + Ca + Mn)$) and X_{grs} (=$Ca/(Fe^{2+} + Mg + Ca + Mn)$) values exhibit very weak to no zoning. Where zoning occurs, the largest variation in values occurs in the outer rim, before plateauing towards the centre of the grains.

In samples AS09-01, AS2010-65J and RED2011-02, X_{alm} core values increase from 0.67–0.75 to 0.67–0.80 at the rim. Sample RED2011-01 has notably higher X_{alm} values, increasing from 0.82–0.84 in the core to 0.85–0.86 at the rim. X_{py} values are variable between samples. Samples AS09-01 and RED2011-02 have the highest X_{py} values, decreasing from 0.22–0.28 in the core to 0.12–0.23 at the rim. Sample AS2010-65J has lower X_{py} values, decreasing from 0.16–0.17 in the core to 0.13–0.15 at the rim. The lowest values occur in RED2011-01, where values decreased from 0.10–0.13 in the core to 0.07–0.09 at the rim. Samples AS09-01, RED2011-01 and RED2011-02 do not display X_{grs} zoning, with values between 0.03–0.05, whereas sample AS2010-65J is very weakly zoned, with X_{grs} values decreasing from 0.06 to 0.07 in the core to 0.04 in the rim. Samples AS09-01 and RED2011-01 show a weak increase in X_{sps} from 0.02–0.03 in the core to 0.02–0.04 at the rim. Samples AS2010-65J and RED2011-02 are unzoned and have X_{sps} values between 0.02 and 0.03.

5.1.2. Biotite

Biotite compositions vary between samples and grain locations within samples. Sample RED2011-02 has the lowest X_{Fe} (=$Fe^{2+}/(Fe^{2+} + Mg)$) values ranging between 0.28 and 0.45, with

Table 5
Electron microprobe representative mineral chemistry.

	AS09-01									AS2010-65J							
	g rim	g core	bi	cd	ksp	pl	ilm	sill	q	g rim	g core	bi	ksp	pl	ilm	sill	q
SiO_2	37.92	38.59	35.95	48.16	65.66	60.48	0.04	36.37	102.45	37.07	37.46	34.54	65.23	59.53	0.05	36.27	100.71
TiO_2	0.02	0.01	3.63	0.00	0.03	0.01	51.49	0.25	0.00	0.01	0.01	3.77	0.00	0.00	49.42	0.00	0.01
Al_2O_3	20.25	20.34	17.50	32.57	17.91	24.28	0.00	59.59	0.00	20.76	20.96	18.51	18.22	24.56	0.00	59.45	0.03
Cr_2O_3	0.00	0.00	0.05	0.00	0.01	0.00	0.03	0.05	0.00	0.02	0.01	0.07	0.00	0.00	0.02	0.06	0.00
FeO	34.39	31.42	17.66	6.93	0.00	0.01	44.01	0.53	0.02	34.91	33.25	19.61	0.00	0.02	41.60	0.57	0.02
MnO	1.07	1.01	0.05	0.06	0.01	0.00	1.68	0.00	0.00	1.17	1.09	0.02	0.00	0.00	1.02	0.00	0.00
MgO	4.36	6.68	10.53	9.17	0.00	0.01	0.04	0.02	0.01	3.62	4.28	7.98	0.00	0.00	0.02	0.00	0.00
ZnO	0.00	0.00	0.01	0.02	0.00	0.00	0.01	0.02	0.00	0.00	0.00	0.06	0.06	0.00	0.10	0.04	0.02
CaO	1.17	1.17	0.06	0.02	0.08	6.70	0.12	0.08	0.01	1.29	2.22	0.00	0.06	6.95	0.04	0.00	0.00
Na_2O	0.00	0.01	0.22	0.08	1.57	7.72	0.01	0.01	0.00	0.02	0.00	0.02	2.04	7.85	0.08	0.00	0.00
K_2O	0.00	0.00	9.92	0.01	14.80	0.16	0.01	0.01	0.01	0.00	0.01	10.02	13.74	0.09	0.02	0.01	0.03
OF_2	0.09	0.06	0.38	0.00	0.00	0.00	0.17	0.00	0.00	0.06	0.04	0.27	0.00	0.00	0.18	0.00	0.00
Cl_2O	0.00	0.00	0.10	0.00	0.00	0.00	0.00	0.01	0.00	0.01	0.00	0.00	0.07	0.00	0.00	0.01	0.00
Total	99.28	99.28	96.06	97.02	100.07	99.37	97.62	96.94	102.50	98.92	99.32	94.89	99.43	98.98	92.56	96.41	100.83
No. oxygens	12	12	11	18	8	8	3	5	2	12	12	11	8	8	3	5	2
Si	3.05	3.06	2.71	5.00	3.02	2.71	0.00	1.02	1.00	3.01	3.01	2.66	3.01	2.68	0.00	1.02	1.00
Ti	0.00	0.00	0.21	0.00	0.00	0.00	1.00	0.01	0.00	0.00	0.00	0.22	0.00	0.00	1.01	0.00	0.00
Al	1.92	1.90	1.55	3.98	0.97	1.28	0.00	1.96	0.00	1.99	1.98	1.68	0.99	1.30	0.00	1.97	0.00
Cr	0.00	0.00	0.00	0.00	0.00	0.00	0.00	0.00	0.00	0.00	0.00	0.00	0.00	0.00	0.00	0.00	0.00
Fe^{3+}	–	–	–	–	–	–	0.00	0.01	–	–	–	–	–	–	0.00	0.00	–
Fe^{2+}	2.31	2.08	1.11	0.60	0.00	0.00	0.95	0.00	0.00	2.37	2.23	1.26	0.00	0.00	0.95	0.01	0.00
Mn^{2+}	0.07	0.07	0.00	0.01	0.00	0.00	0.04	0.00	0.00	0.08	0.07	0.00	0.00	0.00	0.02	0.00	0.00
Mg	0.52	0.79	1.18	1.42	0.00	0.00	0.00	0.00	0.00	0.44	0.51	0.92	0.00	0.00	0.00	0.00	0.00
Zn	0.00	0.00	0.00	0.00	0.00	0.00	0.00	0.00	0.00	0.00	0.00	0.00	0.00	0.00	0.00	0.00	0.00
Ca	0.10	0.10	0.00	0.00	0.00	0.32	0.00	0.00	0.00	0.11	0.19	0.00	0.00	0.34	0.00	0.00	0.00
Na	0.00	0.00	0.03	0.02	0.14	0.67	0.00	0.00	0.00	0.00	0.00	0.00	0.18	0.69	0.00	0.00	0.00
K	0.00	0.00	0.95	0.00	0.87	0.01	0.00	0.00	0.00	0.00	0.00	0.99	0.81	0.01	0.00	0.00	0.00
F	0.02	0.01	0.06	0.00	0.00	0.00	0.01	0.00	0.00	0.01	0.01	0.05	0.00	0.00	0.01	0.00	0.00
Cl	0.00	0.00	0.01	0.00	0.00	0.00	0.00	0.00	0.00	0.00	0.00	0.00	0.00	0.00	0.00	0.00	0.00
Total cations	8.00	8.00	7.76	11.02	5.00	4.99	2.01	3.00	1.00	8.01	8.01	7.79	5.00	5.01	2.00	3.00	1.00
X_{Fe}	0.82	0.73	0.49	0.30	–	–	0.99	–	–	0.84	0.81	0.58	–	–	0.99	–	–
X_{alm}	0.77	0.69	–	–	–	–	–	–	–	0.79	0.74	–	–	–	–	–	–
X_{py}	0.17	0.26	–	–	–	–	–	–	–	0.15	0.17	–	–	–	–	–	–
X_{grs}	0.03	0.03	–	–	–	–	–	–	–	0.04	0.06	–	–	–	–	–	–
X_{spss}	0.02	0.02	–	–	–	–	–	–	–	0.03	0.03	–	–	–	–	–	–

	RED2011-01							RED2011-02							
	g rim	g core	bi	ksp	mt	sill	q	g rim	g core	bi	cd	pl	mt	ilm	q
SiO_2	37.58	38.01	34.68	65.24	1.08	36.66	99.83	37.69	38.06	36.70	49.00	59.77	0.05	0.00	100.10
TiO_2	0.00	0.00	1.79	0.00	0.08	0.00	0.00	0.01	0.00	2.44	0.00	0.00	0.08	49.20	0.00
Al_2O_3	21.58	21.45	19.99	19.02	0.98	62.72	0.06	21.36	21.50	18.15	33.00	25.33	0.15	0.00	0.03
Cr_2O_3	0.00	0.00	0.01	0.00	0.03	0.04	0.00	0.02	0.00	0.01	0.00	0.00	0.00	0.01	0.01
FeO	36.40	35.78	23.05	0.11	84.40	0.89	0.02	32.53	31.59	16.66	7.19	0.02	89.92	46.38	0.00
MnO	1.21	0.83	0.03	0.01	0.00	0.00	0.00	1.41	1.36	0.03	0.08	0.01	0.01	0.22	0.01
MgO	2.54	2.99	6.78	0.00	0.06	0.01	0.00	5.63	5.92	13.15	9.64	0.00	0.00	0.77	0.00
ZnO	0.09	0.00	0.00	0.00	0.04	0.02	0.02	0.00	0.00	0.05	0.01	0.03	0.10	0.09	0.00
CaO	1.11	1.09	0.02	0.08	0.03	0.02	0.00	1.48	1.46	0.02	0.01	7.11	0.04	0.02	0.01
Na_2O	0.00	0.01	0.12	2.54	0.05	0.00	0.01	0.01	0.02	0.57	0.22	7.73	0.00	0.00	0.00
K_2O	0.01	0.00	10.00	13.10	0.18	0.01	0.00	0.00	0.00	9.00	0.01	0.06	0.04	0.00	0.01
OF_2	0.06	0.08	0.55	0.00	0.31	0.00	0.00	0.05	0.02	0.55	0.00	0.00	0.47	0.14	0.00
Cl_2O	0.00	0.00	0.05	0.02	0.01	0.00	0.00	0.00	0.00	0.00	0.00	0.00	0.01	0.00	0.00
Total	100.58	100.24	97.07	100.12	87.24	100.38	99.94	100.19	99.92	97.34	99.14	100.07	90.85	96.83	100.17
No. oxygens	12	12	11	8	4	5	2	12	12	11	18	8	4	3	2
Si	3.01	3.04	2.65	2.98	0.04	0.99	1.00	2.98	3.00	2.70	4.98	2.66	0.00	0.00	1.00
Ti	0.00	0.00	0.10	0.00	0.00	0.00	0.00	0.00	0.00	0.14	0.00	0.00	0.00	0.95	0.00
Al	2.04	2.02	1.80	1.02	0.05	1.99	0.00	1.99	2.00	1.57	3.95	1.33	0.01	0.00	0.00
Cr	0.00	0.00	0.00	0.00	0.00	0.00	0.00	0.00	0.00	0.00	0.00	0.00	0.00	0.00	0.00
Fe^{3+}	–	–	–	–	1.90	0.04	–	–	–	–	–	–	1.94	0.10	–
Fe^{2+}	2.44	2.39	1.47	0.00	0.96	−0.02	0.00	2.15	2.08	1.02	0.61	0.00	1.04	0.90	0.00
Mn^{2+}	0.08	0.06	0.00	0.00	0.00	0.00	0.00	0.09	0.09	0.00	0.01	0.00	0.00	0.00	0.00
Mg	0.30	0.36	0.77	0.00	0.00	0.00	0.00	0.66	0.70	1.44	1.46	0.00	0.00	0.03	0.00
Zn	0.01	0.00	0.00	0.00	0.00	0.00	0.00	0.00	0.00	0.00	0.00	0.00	0.00	0.00	0.00
Ca	0.10	0.09	0.00	0.00	0.00	0.00	0.00	0.13	0.12	0.00	0.00	0.34	0.00	0.00	0.00
Na	0.00	0.00	0.02	0.22	0.00	0.00	0.00	0.00	0.00	0.08	0.04	0.67	0.00	0.00	0.00
K	0.00	0.00	0.98	0.76	0.01	0.00	0.00	0.00	0.00	0.84	0.00	0.00	0.00	0.00	0.00
F	0.01	0.02	0.09	0.00	0.03	0.00	0.00	0.01	0.00	0.09	0.00	0.00	0.04	0.01	0.00
Cl	0.00	0.00	0.00	0.00	0.00	0.00	0.00	0.00	0.00	0.00	0.00	0.00	0.00	0.00	0.00
Total cations	7.98	7.96	7.89	5.00	3.00	3.00	1.00	8.02	8.00	7.80	11.06	5.01	3.04	2.00	1.00
X_{Fe}	0.89	0.87	0.66	–	0.99	–	–	0.76	0.75	0.42	0.30	–	1.00	0.97	–
X_{alm}	0.84	0.83	–	–	–	–	–	0.71	0.70	–	–	–	–	–	–
X_{py}	0.10	0.12	–	–	–	–	–	0.22	0.23	–	–	–	–	–	–
X_{grs}	0.03	0.03	–	–	–	–	–	0.04	0.04	–	–	–	–	–	–
X_{spss}	0.03	0.02	–	–	–	–	–	0.03	0.03	–	–	–	–	–	–

one outlying analysis of 0.65. Sample RED2011-01 has the highest X_{Fe} values ranging between 0.64 and 0.66. Samples AS09-01 and AS201-65J has mid-range values occurring between 0.4 and 0.58, with biotite grains next to garnet exhibiting X_{Fe} values in the lower range. Throughout all samples, F values range between 0.24 and 0.72 wt% and TiO_2 values range between 1.32 and 4.77 wt%. In general, samples RED2011-01 and RED2011-02 have higher F and lower TiO_2 values than AS2010-65J and AS09-01.

5.1.3. Cordierite

Cordierite commonly occurs as coarse grains in leucosomes in samples AS09-01 and RED2011-02. X_{Fe} (=Fe^{2+}/(Fe^{2+} + Mg)) values range between 0.28 and 0.30 in sample AS09-01 and 0.29–0.31 in sample RED2011-02.

5.1.4. Feldspar

Samples AS09-01, AS2010-65J and RED2011-01 contain K-feldspar. Sample AS09-01 has the lowest range of X_{Or} (=K/(K + Na + Ca)) with values between 0.78–0.91. Sample AS201-65J and RED2011-01 have a broad range of X_{Or} values between 0.67–0.96 and 0.62–0.91 respectively, with generally no X_{Or} values in the range of AS09-01. Samples AS09-01, AS2010-65J and RED2011-02 contain Na-rich plagioclase. Sample RED2011-02 has a broad range of X_{Ab} (=Na/(Na + Ca)) values between 0.63 and 0.71. Samples AS2010-65J and AS09-01 have X_{Ab} ranges between 0.60–0.67 and 0.67–0.71 respectively.

5.1.5. Ilmenite

Ilmenite occurs in samples AS09-01 and RED2011-02. Sample AS09-01 has TiO_2 contents from 51.24 to 68.65 wt% and MnO contents of 0.42–1.68 wt%, whereas sample RED2011-02 has TiO_2 contents of 48.88–49.40 wt% and MnO contents of 0.19–0.26%.

5.1.6. Magnetite

Magnetite in sample RED2011-01 has TiO_2 contents of 0.08–0.18 wt%; Cr_2O_3 contents of 0–0.03 wt% and Al_2O_3 contents of 0.33–2.83 wt%, whereas in sample RED2011-02 magnetite has TiO_2 contents of 0.04–0.08 wt%, Cr_2O_3 contents of 0–0.1 wt% and Al_2O_3 contents of 0.15–0.50 wt%.

5.2. Monazite geochronology

Monazite age data are presented in Appendix A, with sample locations and brief structural descriptions given in Table 1. Ages quoted throughout the study are $^{207}Pb/^{206}Pb$ ages. All errors stated in data tables and on the concordia diagrams are at the 1σ level. Unless specified, monazite grains are unzoned in BSE. Analyses that are excluded from the calculations of weighted average ages or intercepts on the basis of $^{204}Pb/^{206}Pb$ ratios or discordance are shown in Fig. 7 as grey ellipses for completeness.

5.2.1. Pre-D2 fabrics

Results from samples which structurally pre-date the dominant D_2 fabric (Fig. 3a) are shown in Table 1 and Fig. 7a.

5.2.2. AS2010-63D

Twenty-three analyses were collected from 14 monazite grains situated within the biotite–sillimanite fabric, cordierite-bearing leucosomes and along the grain boundaries of garnet. Monazite grains are generally euhedral with round or elongate shapes and 30–60 μm long (Fig. 6a). Nine analyses were excluded from the calculations. The remaining 14 analyses produce a discordant array with an unpopulated upper intercept 1732 ± 46 Ma and a well-defined lower intercept of 1103 ± 33 Ma (MSWD = 0.96, Fig. 7a). The population defining the lower intercept (outlined in the dashed box) yields $^{207}Pb/^{206}Pb$ weighted average age of 1085 ± 16 Ma (n = 6, MSWD = 0.34; Fig. 7a). The older analyses define a discordant population with a $^{207}Pb/^{206}Pb$ weighted average age of 1633 ± 24 Ma (n = 6, MSWD = 1.60; Fig. 7a). Monazite grains associated with the garnet-bearing domains in the sample typically preserve older (ca. 1630 Ma) ages whereas the overprinting cordierite-bearing assemblage preserves younger (ca. 1100) ages.

5.2.3. AS2010-66D

Forty-four analyses were collected from 27 monazite grains situated within the biotite–sillimanite fabric and garnet-bearing, quartzo-feldspathic leucosomes. Monazite grains range in length between 20 and 250 μm and occur as both rounded and elongate grains preferentially oriented parallel to the fabric (Fig. 6b). Sixteen analyses were excluded from the calculations. The remaining 28 analyses produce an array of data along a discord with an upper intercept of 1726 ± 32 Ma and a lower intercept of 1121 ± 24 Ma (MSWD = 0.67, Fig. 7a). The upper intercept age is defined by an older population (outlined in the dashed box) with a $^{207}Pb/^{206}Pb$ weighted average age of 1720 ± 17 Ma (n = 10, MSWD = 1.60), and are from monazite grains within the leucosomes. Twelve younger analyses define a younger population (outlined in the dashed grey box) with a $^{207}Pb/^{206}Pb$ weighted average age of 1083 ± 17 Ma (MSWD = 1.30), and are from smaller monazite grains within the biotite–sillimanite fabric.

5.2.4. AS2010-67A2

Twenty-seven analyses were collected from 10 monazite grains situated within quartzo-feldspathic leucosomes, the biotite–sillimanite fabric and along grain boundaries and microfractures of garnet porphyroblasts. Monazite grains range in length between 60 and 120 μm, exhibit fracturing or pitting and are typically subhedral with rounded and elongate shapes (Fig. 6c). Nine analyses were excluded from the calculations. A Terra Wasserburg plot of the remaining 24 analyses yields an upper intercept of 1598 ± 49 Ma and lower intercept age of 1140 ± 47 Ma (MSWD = 0.48; Fig. 7a). Ten older analyses make up an older population (outlined in the dashed box) that yields a $^{207}Pb/^{206}Pb$ weighted average age of 1569 ± 21 Ma (MSWD = 2.30), and are from monazite grains along the grain boundaries of biotite and garnet. Seven younger analyses (outlined in the dashed box) yield a $^{207}Pb/^{206}Pb$ weighted average age of 1133 ± 17 Ma (MSWD = 0.80), and include monazite grains hosted within biotite and garnet.

5.2.5. D2 fabrics

Results from samples from the structurally younger D2 fabrics (Fig. 3a and c) are shown in Table 1 and summarised in Figs. 7a–c.

5.2.6. 830-10G

Eighteen analyses were collected from six monazite grains situated within the biotite–sillimanite–quartz–K-feldspar-bearing fabric that surrounds garnet porphyroblasts. Monazite grains are typically 20 μm in diameter, but may be up to ∼75 μm, and exhibit euhedral, spherical shapes (Fig. 6d). Nine analyses were excluded from concordia age calculations. The remaining nine analyses produce an array of scattered data. Eight older analyses yield a $^{207}Pb/^{206}Pb$ weighted average age of 1646 ± 27 Ma (MSWD = 4.40). The youngest concordant analysis has a $^{207}Pb/^{206}Pb$ age of 1230 ± 48 Ma (Fig. 7a).

5.2.7. 830-18

Thirty-five analyses were collected from seven monazite grains situated within the biotite–sillimanite fabric that encloses abundant garnet porphyroblasts and quartzo-feldspathic layers. Monazite grains are typically euhedral, rounded and range in length

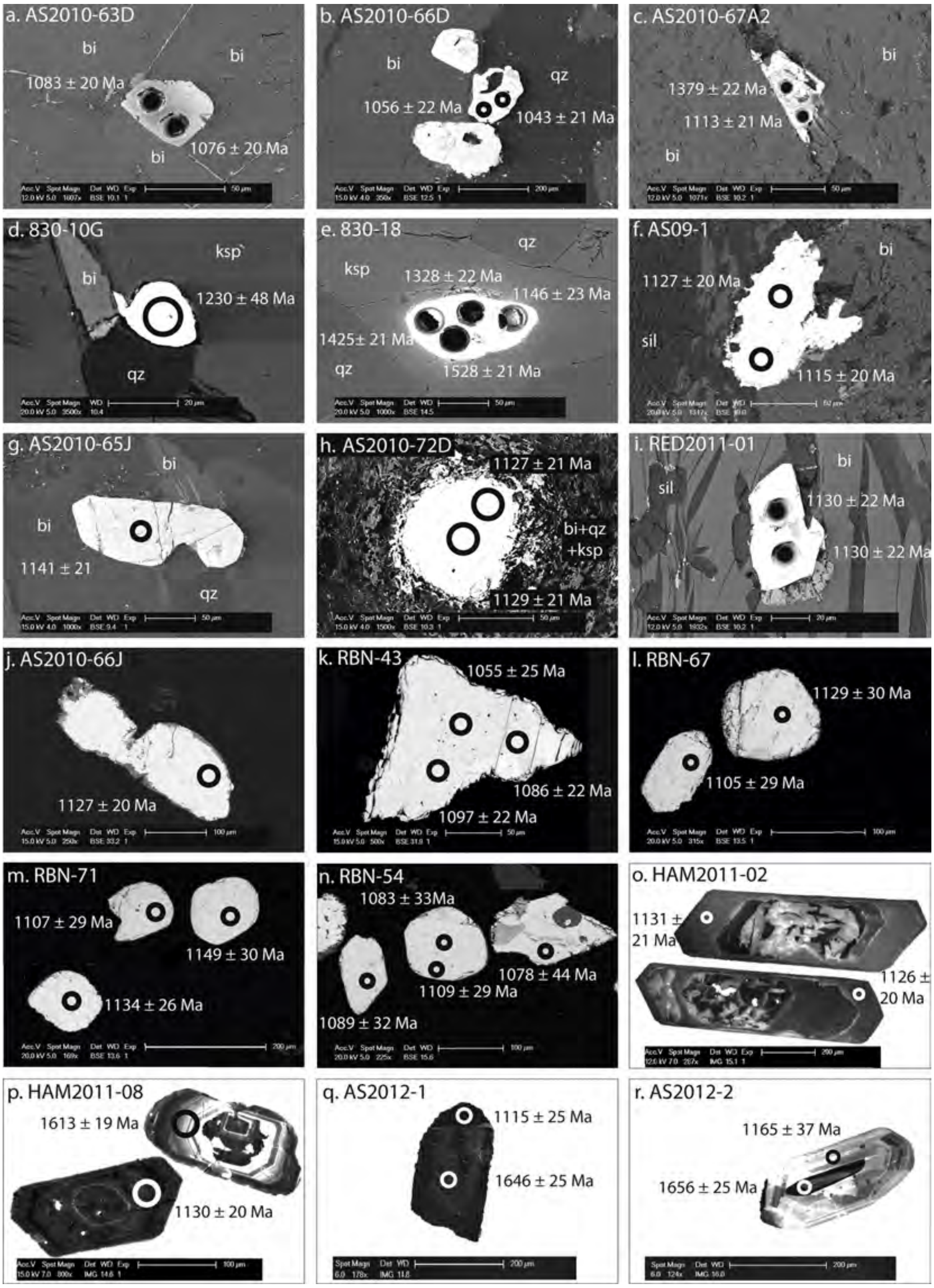

Fig. 6. BSE and CL images of representative monazite (a–n) and zircon (o–r) grains from each sample are shown. All ages given are $^{207}Pb/^{206}Pb$ ages. Monazite geochronology was collected from samples a–i in situ. Samples j–r are grain mounts.

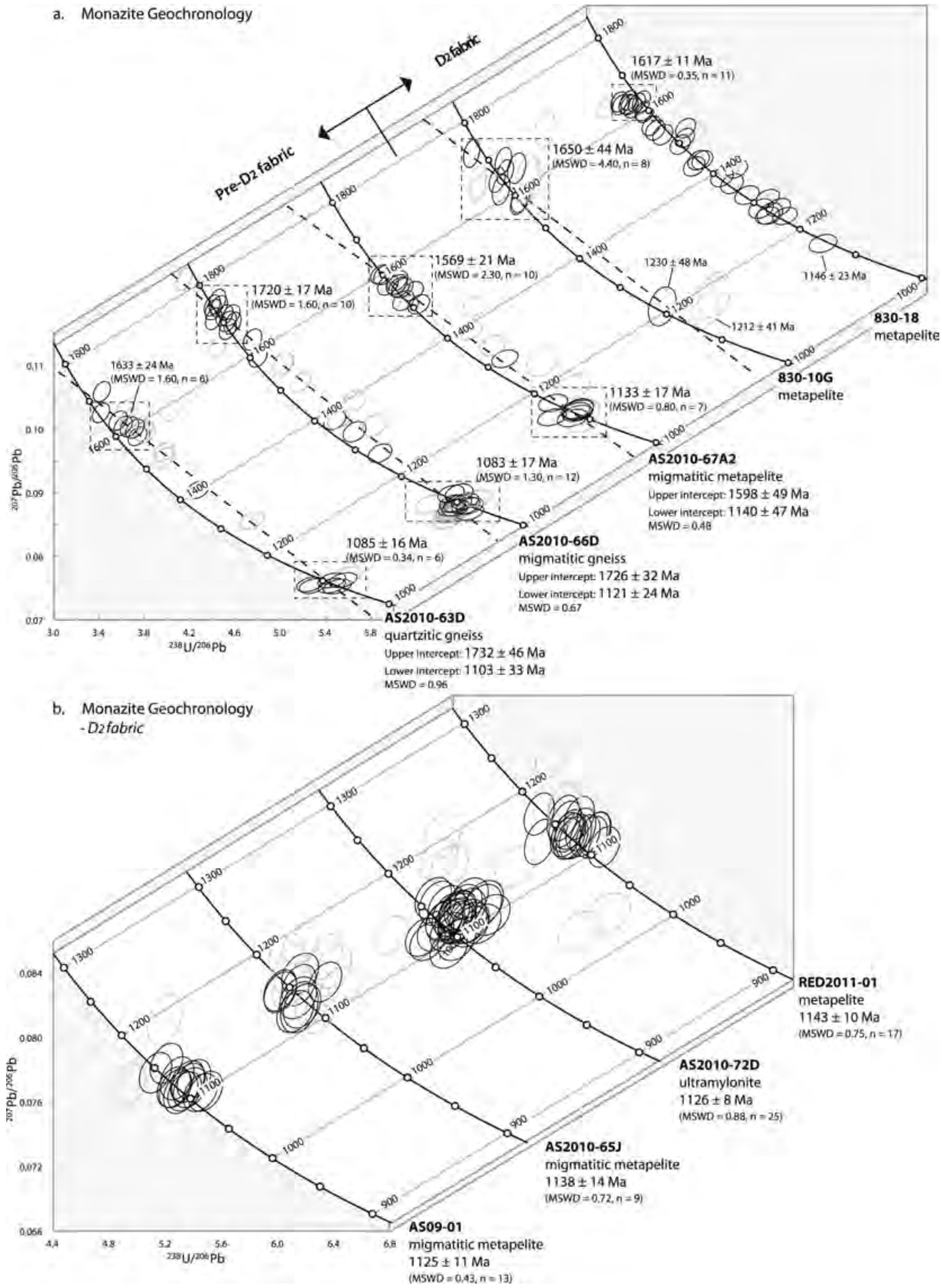

Fig. 7. (a–c) Stacked Terra-Wasserburg concordia diagrams for LA–ICP–MS monazite U–Pb geochronology. The $^{207}Pb/^{206}Pb$ weighted average ages are quoted for each sample. Error ellipses are shown at the 1-sigma level. Analyses which were excluded from the calculations appear as grey ellipses. For samples which exhibit two concordant age populations, analyses included in weighted average age calculations are highlighted by the dashed box. (d) LA–ICP–MS zircon U–Pb geochronology. The $^{207}Pb/^{206}Pb$ weighted average ages are quoted for each sample. Analyses which were excluded from the calculations appear as grey ellipses. For samples which exhibit two concordant age populations, analyses included in weighted average age calculations are highlighted by the dashed box.

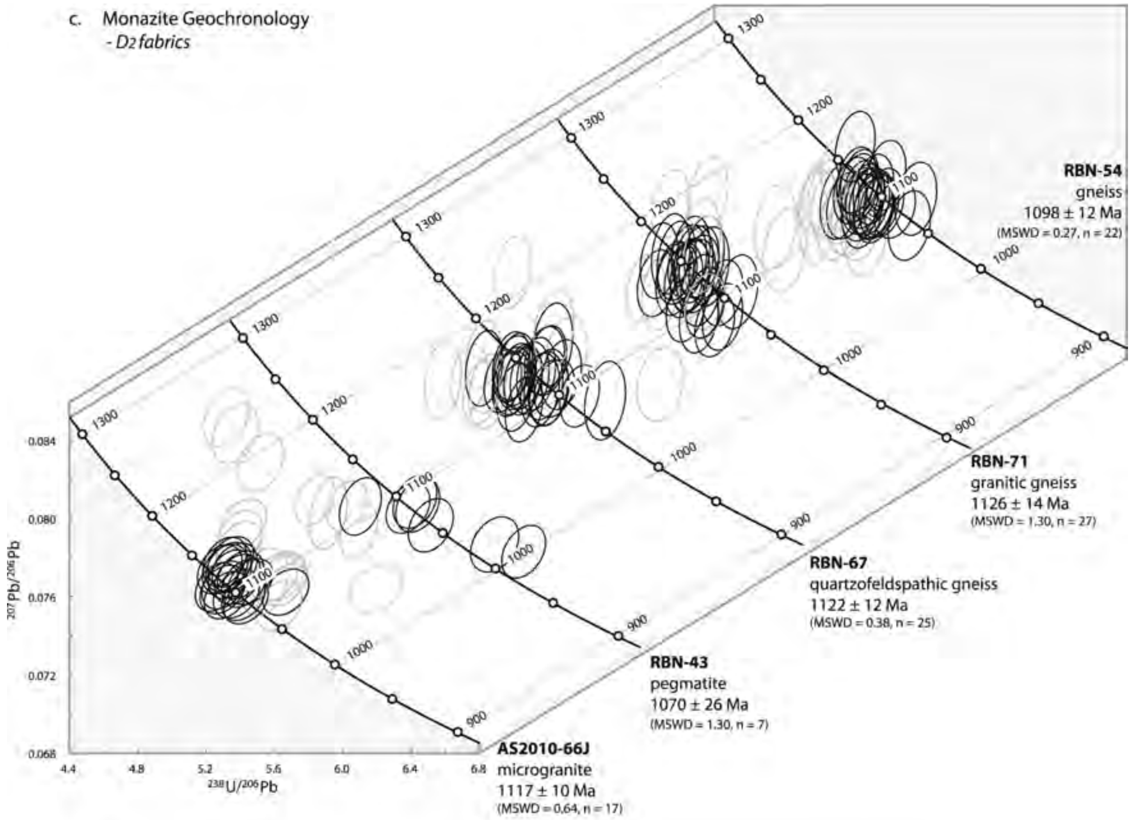

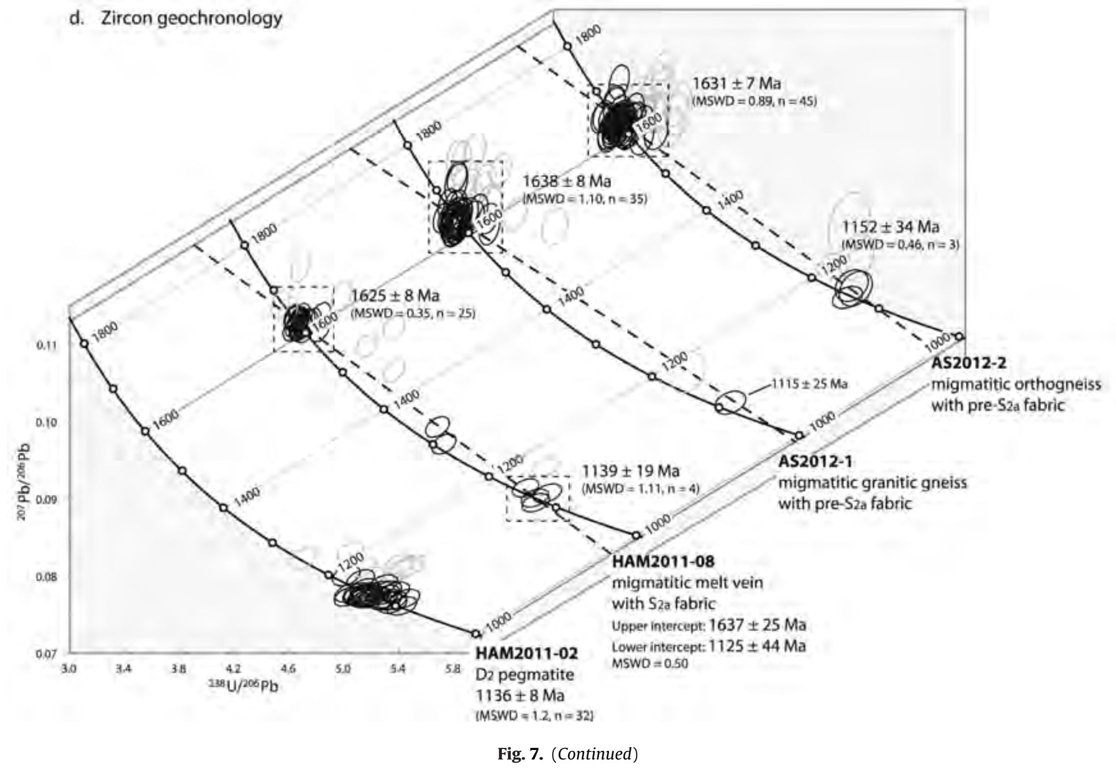

Fig. 7. (*Continued*)

from 150 to 350 μm, with an aspect ratio of 1:2 parallel to the fabric (Fig. 6e). Four analyses were excluded from the calculations. The remaining 31 analyses produce an array of ages from ca. 1630 Ma to ca. 1150 Ma (Fig. 7a). Eleven older analyses (outlined in the dashed box) define a population with a $^{207}Pb/^{206}Pb$ weighted average age of 1617 ± 11 Ma (MSWD = 0.35). The youngest analysis yields a concordant age of 1146 ± 23 Ma.

5.2.8. AS09-01

Fifteen analyses were collected from 11 monazite grains situated throughout the foliated biotite–sillimanite matrix as well as from grains hosted within garnet. Monazite grains are typically anhedral and 120–200 μm long, with an aspect ratio of 1:4 parallel to the fabric (Fig. 6f). Two discordant analyses were excluded from age calculations and appear as grey ellipses in Fig. 7b. The remaining 13 concordant grains form one population and yield a $^{207}Pb/^{206}Pb$ weighted average age of 1125 ± 11 Ma (MSWD = 0.43; Fig. 7b).

5.2.9. AS2010-65J

Eighteen analyses were collected from 13 monazite grains situated within leucosomes, the biotite–sillimanite fabric and within and at the grain boundaries of garnet porphyroblasts. Monazite grains range in length between 20 and 240 μm, and are typically euhedral and elongate parallel to the fabric. However, a small population exhibits anhedral, fractured and angular shapes (Fig. 6). Nine analyses were excluded from age calculations and appear as grey ellipses on the concordia plot. The two groups of monazite give a single concordant population with a $^{207}Pb/^{206}Pb$ weighted average age of 1138 ± 14 Ma (*n* = 9, MSWD = 0.72; Fig. 7b).

5.2.10. AS2010-72D

Thirty-six analyses were collected from 16 monazite grains situated throughout the mylonitic, quartzo-feldspathic fabric. Monazite grains are commonly 50–120 μm in length, and exhibit euhedral to spherical morphologies with resorbed grain boundaries (Fig. 6h). Eleven analyses were excluded from age calculations. The remaining 25 concordant grains yield a $^{207}Pb/^{206}Pb$ weighted average age of 1126 ± 8 Ma (MSWD = 0.88; Fig. 7b).

5.2.11. RED2011-01

Twenty analyses were collected from 11 monazite grains situated within the biotite–sillimanite fabric (Fig. 6i) and quartzo-feldspathic domains. Grains range in length between 40 and 80 μm, are typically euhedral and elongate parallel to the fabric. Three analyses were excluded from the calculation. The remaining 17 analyses define a population with a $^{207}Pb/^{206}Pb$ weighted average age of 1143 ± 10 Ma (MSWD = 0.75; Fig. 7b).

5.2.12. AS2010-66J

Thirty-three analyses were collected from 23 monazite grains mounted in epoxy resin. Monazite grains typically range in length between 50 and 400 μm and occasionally exhibit zoning, with dark domains forming around the rims and within microfractures of the grains (Fig. 6j). Initial analyses of these domains provided noisy and largely discordant ages associated with high levels of common Pb and they were therefore avoided during further analysis. Sixteen analyses were excluded from age calculations. The remaining 17 analyses form a concordant population with a $^{207}Pb/^{206}Pb$ weighted average age of 1117 ± 10 Ma (MSWD = 0.64; Fig. 7c).

5.2.13. RBN-43

Eleven analyses were collected from 4 monazite grains mounted in epoxy resin. Monazite grains ranged in diameter between 80 and 150 μm, are typically anhedral and internally fractured parallel to the long edge of the grain (Fig. 6k). Four reversely discordant analyses were excluded from the calculations. The remaining seven analyses yield a $^{207}Pb/^{206}Pb$ weighted average age of 1070 ± 26 Ma (MSWD = 1.30; Fig. 7c).

5.2.14. RBN-67

Thirty-five analyses were collected from 23 monazite grains mounted in epoxy resin. Monazite grains range in diameter between 80 and 150 μm, and are typically subhedral with spherical to elliptical morphologies (Fig. 6l). Nine analyses were excluded from age calculations. The remaining 25 analyses yield a $^{207}Pb/^{206}Pb$ weighted average age of 1122 ± 12 Ma (MSWD = 0.38, Fig. 7c).

5.2.15. RBN-71

Thirty-six analyses were collected from 25 monazite grains mounted in epoxy resin. Monazite grains range in diameter between 80 and 250 μm and are typically euhedral with spherical shapes (Fig. 6m). Nine analyses were excluded from age calculations. The remaining 27 analyses yield a $^{207}Pb/^{206}Pb$ weighted average age of 1126 ± 14 Ma (MSWD = 1.30, Fig. 7c).

5.2.16. RBN-54

Thirty-six analyses were collected from 35 monazite grains mounted in epoxy resin. Monazite grains exhibit two distinguishing morphologies; the first are grains ranging in diameter between 80 and 100 μm and are typically euhedral to subhedral spherical shaped (Fig. 6n). The second population range in length between 100 and 200 μm and exhibit anhedral fractured shapes (Fig. 6n). Fourteen analyses were excluded from the calculations. The remaining 22 analyses yield a single age population with a $^{207}Pb/^{206}Pb$ weighted average age of 1098 ± 12 Ma (MSWD = 0.27, Fig. 7c).

5.3. Zircon geochronology

U–Pb Zircon LA–ICP–MS geochronology was collected from four samples. Zircon age data, including documentation of core and rim analysis locations, are presented in Appendix A and brief structural descriptions of each sample given in Table 1. As for the monazite samples, analyses that were excluded on the basis of high $^{204}Pb/^{206}Pb$ ratios or discordance are shown as grey ellipses on Fig. 7d for completeness.

5.3.1. HAM2011-02

Forty analyses were collected from 24 grains zircon obtained from an inter-boudin pegmatitic segregation within the S_{2a} fabric (Fig. 4b). Zircon grains are euhedral, internally fractured and range in length between 0.4 and 1.7 mm, with aspect ratios of 1:4. Under CL, the vast majority of grains exhibit weakly luminescent, weak to moderate oscillatory and sector zoning of the rims, and moderately luminescent chaotic internal zoning (Fig. 6o). Most grains possess weakly luminescent metamict cores and metamorphic overgrowths. Metamict zones were avoided during analysis as they produced highly discordant data. Nine discordant analyses were excluded from calculations. The remaining 32 analyses yield a $^{207}Pb/^{206}Pb$ weighted average age of 1136 ± 8 Ma (MSWD = 0.77, Fig. 7d). Of the 32 analyses, three were from cores and the remaining 29 were from rims.

5.3.2. HAM2011-08

Forty-one analyses were collected from 39 zircon grains obtained from a migmatitic granitic gneiss containing the S_{2a} fabric. Zircon grains typically range in length between 80 and 300 μm with aspect ratios of 1:3, and exhibit two distinguishing morphologies. The first population encompasses 90% of all grains and is characterised by subhedral, rounded crystals which exhibit highly luminescent strong oscillatory and domain zoning, particularly within the centre of grains (Fig. 6p). The remaining population is defined by euhedral angular zones which exhibit weakly luminescent oscillatory zoning of the rims and chaotic metamict cores (Fig. 6p). Metamict cores and overgrowths were avoided during analysis as they produced highly discordant data. Six analyses were excluded from concordia calculations. The remaining 31 analyses produce an array of data along a discord with an upper intercept of 1637 ± 25 Ma and a lower intercept of 1125 ± 44 Ma (MSWD = 0.50, Fig. 7d). Twenty-five older analyses (defined by the dashed grey box) yield a $^{207}Pb/^{206}Pb$ weighted average age of 1625 ± 8 Ma (MSWD = 0.35), and come from the first population of zircons. Four concordant younger analyses (defined by the dashed grey box) yield a $^{207}Pb/^{206}Pb$ weighted average age of 1139 ± 19 Ma (MSWD = 1.11), and come from the second, smaller population of zircons (rim analyses).

5.3.3. AS2012-1

Fifty analyses were collected from 33 zircon grains hosted by a pre-S_2 fabric that defines outcrop-scale upright F_2 folds. Zircon grains are typically euhedral to subhedral with rounded edges and range in length between 120 and 400 μm with aspect ratios of 1:3. Most grains are fractured and exhibit weak to highly luminescent oscillatory zoning and variable, strongly to weakly luminescent rims (Fig. 6q). Fourteen discordant analyses were excluded from calculations. Thirty-five analyses produce an older population (outlined by the dashed grey box) with a $^{207}Pb/^{206}Pb$ weighted average age of 1638 ± 8 Ma (MSWD = 1.10, Fig. 7d). A single concordant analysis from a weakly luminescent overgrowth on the rim of a ca. 1646 Ma core yields an age of 1115 ± 25 Ma (Fig. 6q).

5.3.4. AS2010-2

Sixty-seven analyses were collected from 20 zircon grains hosted by a pre-S_2 fabric that outlines F_2 folds. Zircon grains are typically euhedral to subhedral with rounded edges and range in length between 80 and 400 μm with aspect ratios of 1:3. Most grains are fractured and exhibit weak to highly luminescent oscillatory zoning with variable, strong to weakly luminescent rims (Fig. 6r). Nineteen discordant analyses were excluded from calculations. Forty-five concordant older analyses (outlined in the dashed grey box) produce a $^{207}Pb/^{206}Pb$ weighted average age of 1631 ± 7 Ma (MSWD = 0.89, Fig. 7d). Three concordant younger analyses (outlined in the dashed grey box) give a $^{206}Pb/^{207}Pb$ weighted average age of 1152 ± 34 Ma (MSWD = 0.46), and come from rim overgrowths which exhibit variably luminescent oscillatory zoning.

5.4. Pressure–temperature conditions

Pressure–temperature (*P–T*) pseudosections were calculated for four age-constrained metapelites from two regions ~110 km apart in order to provide an understanding of style and conditions of regional metamorphism along the southern margin of the NAC. Samples AS09-01 and AS2010-65J were selected from within a major east–west trending D_2 high strain zone in the southern Aileron Province (eastern study area; Figs. 2 and 3a), and contain single-aged ca. 1130 Ma monazite populations. Approximately 110 km west along the D_2 structural strike in the northern Warumpi Province, Samples RED2010-01 and RED2010-02 were selected from a gently folded westerly plunging outcrop (Fig. 2). RED2010-01 has a single-aged monazite population of ca. 1140 Ma, and RED2010-02 has a different bulk chemical composition from the same outcrop.

5.4.1. AS09-01

The S_2 peak metamorphic assemblage is interpreted to have been garnet + plagioclase + K-feldspar + biotite + cordierite + ilmenite + sillimanite + quartz + silicate melt. Quartz and K-feldspar occur together in the leucosomes, whereas K-feldspar occurs in the biotite–sillimanite-rich domains. Therefore, the coexistence of quartz and K-feldspar within the mineral assemblage constrains the peak conditions to 775–840 °C and 4.8–6.6 kbar (Fig. 8a). The elevated solidus provides a minimum temperature constraint of 775–790 °C. Texturally, cordierite is interpreted to postdate the development of garnet, suggesting that the sample may have evolved down pressure during the development of the S_2 fabric.

5.4.2. AS2010-65J

The peak S_2 metamorphic assemblage is interpreted to have been garnet + plagioclase + K-feldspar + biotite + ilmenite + sillimanite + quartz + silicate melt. The presence of biotite provides an upper temperature constraint of 815 °C, whereas the elevated solidus provides a lower temperature constraint of 750 °C (Fig. 8b). The peak metamorphic assemblage occurs over a large pressure interval. The absence of cordierite in the sample provides a minimum pressure constraint of ~5 kbar, whereas the presence of sillimanite rather than kyanite provides an upper pressure constraint of ~9 kbar.

5.4.3. RED2011-01

The peak metamorphic assemblage is interpreted to have been garnet + K-feldspar + biotite + magnetite + sillimanite + quartz + silicate melt. Ilmenite is not present in this sample, but occurs throughout *P–T* space in modally small amounts (<0.6 mol%) in the peak field. As it occurs in small amounts, its presence is not interpreted to significantly affect the topology of the pseudosection. The presence of magnetite and absence of plagioclase and cordierite from the assemblage broadly constrain peak temperatures to between ~750 and 830 °C and peak pressures to between ~4.4 and 7.6 kbar (Fig. 8c).

5.4.4. RED2011-02

The peak metamorphic assemblage is interpreted to have been garnet + cordierite + biotite + plagioclase + magnetite + ilmenite + quartz + silicate melt. The sample does not contain K-feldspar, but this occurs in the modelled pseudosection in modally small amounts (<3 mol%). The elevated solidus provides a lower temperature constraint of 800–810 °C. The presence of magnetite and absence of orthopyroxene within the assemblage suggests peak temperatures did not exceed ~830 °C and peak pressures were 4–5.4 kbar (Fig. 8d). Although the modelled bulk composition is not appropriate for making definitive inferences about the prograde evolution, the presence of rare sillimanite included within cordierite suggests that the rock may have had a comparatively high-*P* prograde evolution.

6. Discussion

The southern NAC preserves a protracted history of tectonometamorphic events in the Proterozoic (Table 1). The following discussion aims to interpret the timing and conditions of the metamorphism and deformation that produced the dominant structural character of the interpreted southern margin of the NAC. The timing and *P–T* constraints on metamorphism and magmatic events within the southern Aileron and Warumpi Provinces have significant implications for redefining the Proterozoic evolution of the southern margin of the NAC.

6.1. Interpretation of U–Pb monazite geochronology

Nine monazite-bearing samples from various upper amphibolite to granulite facies rocks in different structural and lithological contexts each record single U–Pb age populations ranging between

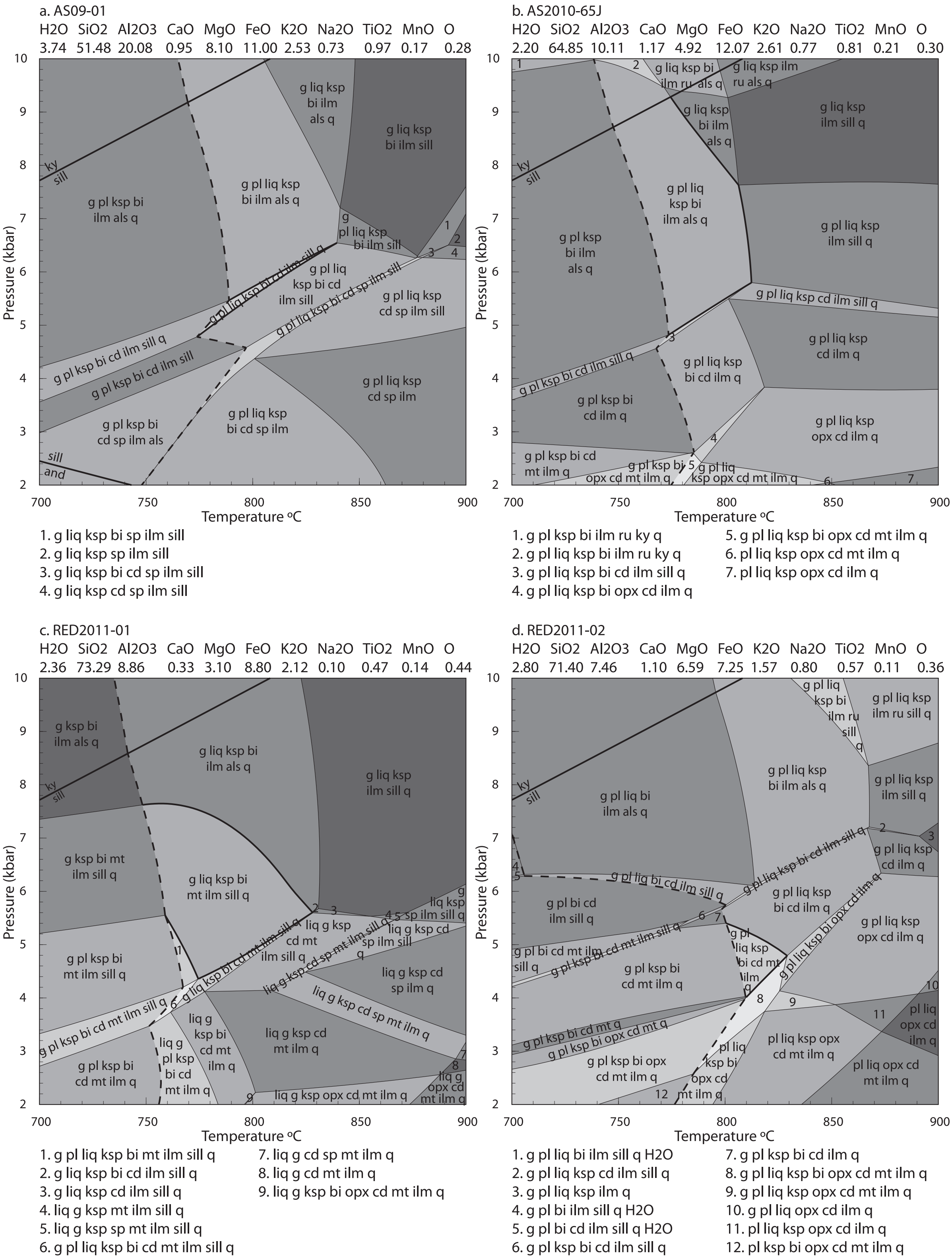
a. AS09-01
H2O SiO2 Al2O3 CaO MgO FeO K2O Na2O TiO2 MnO O
3.74 51.48 20.08 0.95 8.10 11.00 2.53 0.73 0.97 0.17 0.28
Pressure (kbar)
Temperature °C
1. g liq ksp bi sp ilm sill
2. g liq ksp sp ilm sill
3. g liq ksp bi cd sp ilm sill
4. g liq ksp cd sp ilm sill
b. AS2010-65J
H2O SiO2 Al2O3 CaO MgO FeO K2O Na2O TiO2 MnO O
2.20 64.85 10.11 1.17 4.92 12.07 2.61 0.77 0.81 0.21 0.30
Pressure (kbar)
Temperature °C
1. g pl ksp bi ilm ru ky q
2. g pl liq ksp bi ilm ru ky q
3. g pl liq ksp bi cd ilm sill q
4. g pl liq ksp bi opx cd ilm q
5. g pl liq ksp bi opx cd mt ilm q
6. pl liq ksp opx cd mt ilm q
7. pl liq ksp opx cd ilm q
c. RED2011-01
H2O SiO2 Al2O3 CaO MgO FeO K2O Na2O TiO2 MnO O
2.36 73.29 8.86 0.33 3.10 8.80 2.12 0.10 0.47 0.14 0.44
Pressure (kbar)
Temperature °C
1. g pl liq ksp bi mt ilm sill q
2. g liq ksp bi cd ilm sill q
3. g liq ksp cd ilm sill q
4. liq g ksp mt ilm sill q
5. liq g ksp sp mt ilm sill q
6. g pl liq ksp bi cd mt ilm sill q
7. liq g cd sp mt ilm q
8. liq g cd mt ilm q
9. liq g ksp bi opx cd mt ilm q
d. RED2011-02
H2O SiO2 Al2O3 CaO MgO FeO K2O Na2O TiO2 MnO O
2.80 71.40 7.46 1.10 6.59 7.25 1.57 0.80 0.57 0.11 0.36
Pressure (kbar)
Temperature °C
1. g pl liq bi ilm sill q H2O
2. g pl liq ksp cd ilm sill q
3. g pl liq ksp ilm q
4. g pl bi ilm sill q H2O
5. g pl bi cd ilm sill q H2O
6. g pl ksp bi cd ilm sill q
7. g pl ksp bi cd ilm q
8. g pl liq ksp bi opx cd mt ilm q
9. g pl liq ksp opx cd mt ilm q
10. g pl liq opx cd ilm q
11. pl liq ksp opx cd ilm q
12. pl ksp bi opx cd mt ilm q

ca. 1143 and 1070 Ma. Metapelitic samples AS2010-63D, AS2010-66D and AS2010-67A2 have two monazite age populations, with a common young population at ca. 1110 Ma and older populations varying between ca. 1720 and 1569 Ma. Samples 830-10G and 830-18 dominantly record monazite growth at ca. 1630 Ma, with an array of discordant analyses and minor growth of monazite at ca. 1145 Ma. Therefore, samples containing Grenvillian-aged monazite occur over an east–west strike distance ~250 km along the southern margin of the NAC (Fig. 2).

All the samples with single, Grenvillian-aged monazite populations come from east–west trending, high strain regional-scale D_2 fabrics (Figs. 3 and 7, Table 2). Metapelitic samples contain Grenvillian-aged monazite grains that are included in biotite aligned with the D_2 fabric and located within the foliated rock matrix, suggesting that the formation of the biotite–sillimanite-bearing S_2 fabrics occurred at ca. 1130 Ma. In addition, the timing of deformation associated with the development of the pervasive D_2 foliation is constrained by samples AS2010-66J, AS2010-72D and RBN-4. Sample AS2010-66J, which is a microgranite that intruded intensely S_2-foliated augen gneiss, but which also contains an S_2-parallel foliation, has an age 1117 ± 10 Ma. Monazite analysed from a regional south-up D_2 mylonite (AS2010-72D), preserves an age of 1126 ± 8 Ma. Therefore, these two samples give a maximum age of deformation. Similarly, a late, undeformed pegmatite (RBN-43) which cross cuts the regional east–west gneissic fabric provides a minimum age on the development of the foliation at 1070 ± 26 Ma.

In contrast to the samples discussed above that have single age populations, samples AS2010-63D, AS2010-66D, AS2010-67A2 in the southern Aileron Province are more complex. Each are located within pre-D_2 fabric domains which are deformed by the D_2 structures (Fig. 3a), and each display a discordia with a lower intercept at ca. 1130–1090 Ma. In situ analysis reveals that the older age population in all three samples typically come from monazite grains within garnet-bearing, quartzo-feldspathic leucosomes whereas the concordant younger populations are from monazite located within the biotite–sillimanite foliated matrix. This may reflect that monazite is extremely resistant to resetting in an anhydrous environment, such as in quartzo-feldspathic leucosomes (e.g. Korhonen et al., 2013; Sajeev et al., 2010; Walsh et al., 2015), whereas it is more reactive in the presence of a fluid or melt (e.g. Harlov et al., 2011; Rapp and Watson, 1986; Rubatto et al., 2013; Stepanov et al., 2012; Williams et al., 2011; Yakymchuk and Brown, 2014). The monazite grains do not preserve zoning in BSE, and therefore the ages cannot be linked specific compositional domains. However, as the peak temperatures in this study (Fig. 8) are not interpreted to exceed monazite closure temperatures (>900 °C; Cherniak, 2010; Cherniak et al., 2004), we interpret that the discordant ages reflect either coupled dissolution–reprecipitation of older monazite at ca. 1130 Ma, or mixing of younger and older monazite domains during analysis. The significance of the older monazite ages is ambiguous. It is possible that the older monazite ages may be detrital. However, the older monazite populations correspond to the timing of events seen elsewhere in the southern NAC (Table 1). The older monazite population in sample AS2010-66D yields a weighted age of 1720 ± 17 Ma, corresponding to the age of the Early Strangways Event (e.g. Claoué-Long et al., 2008), whereas the weighted average of 1569 ± 21 Ma in sample AS2010-67A2 corresponds to the age of the Chewings Orogeny (Anderson et al., 2013; Morrissey et al., 2014; Rubatto et al., 2001; Vry et al., 1996; Williams et al., 1996). In sample AS2010-63D, one concordant analysis occurs at 1669 ± 18 Ma, but the majority of ages are discordant and occur at ca. 1630 Ma, broadly corresponding to the age of the Liebig Orogeny in the western Warumpi Province and the timing of zircon growth in the southern Aileron Province (this study; Scrimgeour et al., 2005b). Therefore, we prefer the interpretation that the older monazite ages reflect the age of events that predate the Grenvillian-aged reworking.

Approximately 250 km west of the central southern Aileron Province, samples 830-10G and 830-18 were collected from a garnet–sillimanite–biotite-bearing fabric domain in the Warumpi Province that encloses a 5 km-scale low-strain domain containing 1640–1630 Ma granulite and metagabbro (Fig. 3c; Scrimgeour et al., 2005b), and contains a record of top to the N to NE-directed tectonic transport, which is compatible with the south-up movement kinematics on steeply dipping D_2 fabrics further east. Samples 830-10G and 830-18 contain monazite populations at 1650 ± 44 Ma and 1617 ± 11 Ma respectively (corresponding to the age of the Liebig Orogeny; Scrimgeour et al., 2005b), and an array of younger discordant data (Fig. 7a). Sample 830-18 yields a young concordant analysis of 1146 ± 23 Ma, whereas sample 830-10G contains several younger analyses with variable concordance at ca. 1220 Ma, but no ca. 1130 Ma analyses. Although these younger ages do not define a population, they do suggest the occurrence of a younger disturbance in this region. This is observed in Fig. 6e, where analyses from a single unzoned monazite grain produce four distinct ages over a span of 400 Ma. Airphoto imagery shows the fabric that hosts these disturbed populations truncates migmatitic felsic gneiss that gives an age of 1147 ± 3 Ma (Scrimgeour et al., 2005b), indicating that whereas the monazite populations contain only a small proportion of late Mesoproterozoic grains, the deformation is almost certainly late Mesoproterozoic in age.

6.2. Interpretation of U–Pb zircon geochronology

All samples contain ca. 1130 Ma zircons, consistent with the monazite ages observed throughout this study (Fig. 7d). Sample HAM2011-02 contains a single zircon age population at 1136 ± 8 Ma; whereas the remaining three samples (migmatitic gneisses) are dominated by ca. 1630 Ma ages, with minor growth of zircon at ca. 1130 Ma.

Sample HAM2011-02 was obtained from a pegmatitic segregation located in an inter-boudin neck within the D_2 fabric (Fig. 3b). Very weakly luminescent oscillatory and sector zoned zircon rims from this sample yield a single Grenvillian-aged population (Fig. 6o). Samples HAM2011-08, AS2012-01 and AS2012-02 contain an older, dominant ca. 1633–1626 Ma population, with an array of analyses falling along a discord to ca. 1130 Ma (Fig. 7d). Although an attempt was made to ensure that the analysis spot did not straddle different domains, the possibility that the discord is due to mixed analyses cannot be discounted. If this is the case, the discord should not be taken to provide insight into the conditions of Pb diffusion in zircon. The lower intercept of the discord is defined by less common, concordant analyses with ages between 1152 and 1115 Ma. The older ca. 1630 Ma zircon ages in samples HAM2011-08, AS2012-1 and AS2012-2 come from highly luminescent cores with strongly oscillatory and sector zoning that appear to preserve a magmatic character (Corfu et al., 2003). Smaller, weakly luminescent zircon rims with oscillatory zoning in sample HAM2011-08 produced a smaller, younger population with an age of 1139 ± 19 Ma (Figs. 6p and 7d). Therefore, it is probable that the rims of the younger zircons preserve the age of crystallisation of the melt vein, and the older ages are inherited (Rubatto

Fig. 8. Calculated *P–T* pseudosections for metapelitic samples (a) AS09-01 and (b) AS2010-65J from the Wigley Block of the southern Aileron Province and samples (c) RED2011-01 and (d) RED2011-02 from the Haasts Bluff Domain of the Warumpi Province. The bulk compositions in mol% are given above each diagram. The interpreted peak field is depicted in bold. The solidus is highlighted by a bold dashed line.

et al., 2001; Schaltegger et al., 1999) and therefore, the age of the foliation that confines the melt vein. Similarly, ca. 1130 Ma rim overgrowths on zircons with ca. 1640 Ma cores from migmatitic gneisses AS2012-1 and AS2012-2 (Fig. 6q and r) are likely to represent the age of metamorphism and subsequent migmatisation. The Grenvillian ages identified within dated zircon samples are consistent with the ages recorded by monazite in adjacent metapelite and magmatic samples.

Therefore, monazite and zircon ages from the samples in this study also provide evidence for an older, wide-scale magmatic and metamorphic event at ca. 1630 Ma recorded within the southern Aileron Province. This age is approximately coeval with the timing of the 1640 Ma Liebig Orogeny observed in the western Warumpi Province (Table 1; Scrimgeour et al., 2005b). The ca. 1630 Ma zircon ages from this study suggest that magmatism associated with this event extends significantly further east than previously identified. Significantly, it appears that the Warumpi and southern Aileron Provinces have a shared tectonic history at 1640–1630 Ma. This is supported by the presence of detrital zircon ages in the Warumpi Province that are similar to ages in the Aileron Province (Cross et al., 2004), and therefore suggests that the Warumpi Province may not be exotic to the Aileron Province. The Liebig Orogeny was previously interpreted to reflect collision between the NAC and the exotic Warumpi Province (Scrimgeour et al., 2005b). However, the presence of significant volumes of syn-orogenic mafic and ultramafic magmatism instead suggests that the Liebig Orogeny may have been extensional in character (Claoué-Long and Hoatson, 2005; Young et al., 1995).

6.3. Pressure–temperature conditions

Whereas the preservation of older ages in some samples may suggest that the metamorphic assemblages relate to older events, the dominance of ca. 1130 Ma monazite, and the presence of ca. 1130 Ma zircon in structurally controlled settings suggests that the geochronology relates to the metamorphism and deformation that formed the foliated mineral assemblages. The samples chosen for *P*–*T* pseudosection modelling (samples AS09-01, AS2010-65J, RED2011-01 and RED2011-02) contain single, Grenvillian-aged monazite populations are were therefore modelled with the aim of providing constraints on the *P*–*T* conditions during Grenvillian-aged deformation and metamorphism. Although there are significant uncertainties in the determination of a bulk composition (particularly regarding Fe_2O_3, H_2O and the effect of melt loss; Kelsey and Hand, 2015), the aim of this study is to provide general constraints on the conditions of metamorphism. Therefore, the pseudosections were modelled using the currently preserved bulk compositions.

To compare the modelled conditions between samples, the interpreted conditions of the peak fields have been overlapped in Fig. 9. The samples: (a) exhibit similar petrography; (b) exhibit similar bulk compositions; (c) occur within the same D_2 structural system; and (d) yield similar ca. 1130 Ma monazite ages, within error, and are therefore broadly comparable. Samples RED2011-01 and RED2011-02 in the Warumpi Province of the central NAC are from the same location, but are slightly different chemical compositions, such that RED2011-01 contains sillimanite whereas RED2011-02 contains cordierite. Together, they suggest *P*–*T* conditions between ~795 and 820 °C and 4.9–5.5 kbar (Fig. 9; field B). These estimates on *P*–*T* conditions are comparable to samples AS09-01 and AS2010-65J, 110 km to the east in the southern Aileron Province, where the peak fields overlap in *P*–*T* space between ~775 and 815 °C and 5–6 kbar (Fig. 9; field A). The thermal gradient corresponding to these *P*–*T* conditions is in the range ~130–165 °C/kbar, which places it in a high to ultrahigh *T*/*P* regime (Brown, 2006, 2014; Kelsey and Hand, 2015; Stüwe, 2007).

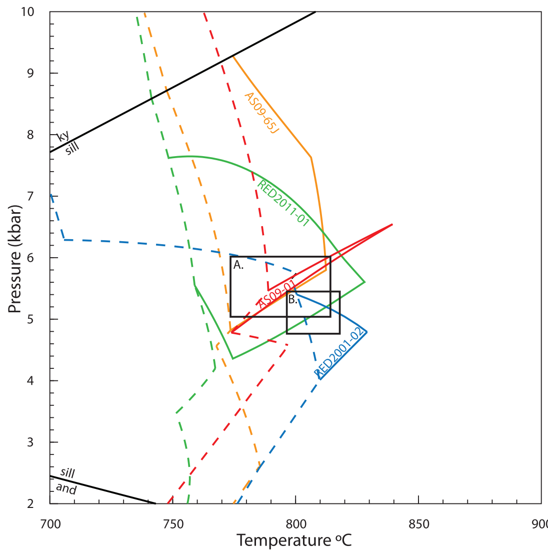

Fig. 9. 'Venn diagram' depicting the stability field of interpreted peak metamorphic assemblages for each sample. The solidus of each sample is represented by dashed lines.

The *P*–*T* conditions for Grenvillian-aged tectonism inferred in this study in the southern Aileron Province and northern margin of the Warumpi Province are higher than the conditions of 4–4.5 kbar and 570 °C suggested Morrissey et al. (2011) in the eastern Warumpi Province. However, those conditions correspond to a similarly high thermal gradient of ~125–140 °C/kbar (Table 1), consistent with different exposure levels within the same overall thermal environment.

6.4. Implications of the Grenvillian-aged reworking

6.4.1. Regional extent of Grenvillian-aged reworking

The Grenvillian-aged monazite and zircon observed in this study correspond to ages previously obtained from the southern NAC (e.g. Biermeier et al., 2003; Black and Shaw, 1995; Claoué-Long and Hoatson, 2005; Collins et al., 1995; Morrissey et al., 2011; Scrimgeour et al., 2005b; Shaw and Black, 1991). Most recently, Morrissey et al. (2011) argued that the formation of flat lying fabrics and regional-scale, east–west trending folds within the eastern Warumpi Province, originally attributed to the ca. 1580 Ma Chewings Orogeny, are Grenvillian in age. Further west in the Warumpi Province, zircons from the migmatitic Teapot Granite Complex preserve a $^{207}Pb/^{206}Pb$ crystallisation age of 1136 ± 6 Ma (Black and Shaw, 1995). The complex extends over a strike distance of distance of ~100 km (Fig. 2), and is interpreted to represent a large anatectic granite that formed by in situ partial melting of Paleoproterozoic rocks (Sun et al., 1995). Within the vicinity of the Teapot Granite Complex, the Rb–Sr system in micas from the Ormiston Pound Granite have been reset to 1100–1030 Ma (Collins et al., 1995). In the western extent of the present study area (i.e. Mount Liebig area), zircons from migmatites of the Kakalyi Gneiss preserve a crystallisation age of 1149 ± 3 Ma (Fig. 3c; Scrimgeour et al., 2005b). In the southern Aileron Province, monazite rims from deformed amphibolite to granulite facies metapelites north of the Redbank Shear Zone have an age of 1139 ± 25 Ma (Biermeier et al., 2003) and a pegmatite yields a Rb–Sr isotopic age of 1140 ± 56 Ma (Shaw and Black, 1991). Lastly, the undeformed mafic to ultramafic alkaline Mordor Complex in the south-eastern Aileron Province has a zircon crystallisation age of 1133 ± 5 Ma (Claoué-Long and Hoatson, 2005). The emplacement of the Teapot Granite Complex and mafic to ultramafic Mordor Complex suggests that the Grenvillian-aged event is significant and cannot simply reflect localised thermal reworking, or local activity related to the reactivation of the crustal-scale Redbank Shear Zone. However, despite the well-known occurrence of ca. 1140–1130 Ma ages in studies in the southern NAC over the last 30 years, with the exception of Morrissey et al. (2011), the event was largely considered to be thermal in nature with little or no associated deformation.

This study records high-grade Grenvillian-aged deformation over a strike length of more than 100 km, from the southern Aileron Province, from ~10 km north of Alice Springs (Wigley Block) to the migmatitic Teapot Granite Complex within the eastern Haasts Bluff Domain of the Warumpi Province. Grenvillian-aged deformation is associated with the development of a strongly developed, east–west trending deformation system that resulted in the formation of upright folds and associated shear fabrics. In the ca. 1130 Ma Teapot Granite Complex, the upright folds deform an earlier flat lying fabric which must also be Late Mesoproterozoic in age, similar to the structural evolution proposed by Morrissey et al. (2011). The migmatitic Mesoproterozoic high strain belts evolved into a pervasive set of south-side up mylonites (Fig. 4c). The minimum age of the east–west trending mylonitic system is constrained by the presence of cross cutting dolerite dykes of the ca. 1080 Ma Stuart Dyke Swarm. In the Mount Liebig region, tectonic fabrics that overprint the migmatitic ca. 1140 Ma Kakalyi Gneiss (Fig. 4d; Scrimgeour et al., 2005b) contain monazite age populations with evidence for late Mesoproterozoic disturbance, and show south side up reverse/thrust shear sense tectonic transport. The development of large-scale upright east–west trending folds (Morrissey et al., 2011) and shear fabrics that record either south-side up or N to NE-directed thrust transport point to late Mesoproterozoic contractional deformational regime where the Warumpi Province was located in the upper plate with respect to the Aileron Province. The high to ultrahigh thermal gradients suggest that the Grenvillian-aged thermal regime may have involved extension prior to the development of the contractional east–west trending fabrics. Conceivably, the late Mesoproterozoic flat-lying fabrics that developed prior to shortening were associated with this hypothesised extensional regime.

6.4.2. Geodynamic implications for the southern margin of the NAC

The timing of the late Mesoproterozoic tectonism in the southern NAC coincides with the latter stages of long-lived, high-*T* metamorphism, deformation and magmatism in the Musgrave Province several hundred kilometres to the south (Fig. 1; Howard et al., 2015; Smithies et al., 2011; Tucker et al., 2015; Walsh et al., 2015). The rocks in the Musgrave Province form part of the Musgrave–Albany Fraser Orogen (MAFO) which is a large belt that transects southern Australia and extends into Antarctica, and separates older lithosphere to the north and south (e.g. Kirkland et al., 2013). Additionally, regional aeromagnetic data shows that beneath younger cover sequences, the Musgrave system extends to the southern margin of the NAC (Aitken and Betts, 2008). This strengthens the case that the late Mesoproterozoic deformation in the southern NAC is tectonically linked to the development of the Musgrave–Albany Fraser Orogen.

Metamorphism in the Musgrave part of the MAFO is characterised by regionally developed, long-lived ultra-high temperatures (UHT) of up to 1000 °C in comparatively thin crust (Smithies et al., 2011; Walsh et al., 2015) and voluminous, predominantly felsic magmatism with intraplate geochemical affinities from ca. 1220 to 1140 Ma (Howard et al., 2015; Smithies et al., 2011). Smithies et al. (2011) and Howard et al. (2015) consider the Musgrave region to be a "hot zone" where asthenospheric mantle is focussed into a region of thin lithosphere that is bounded by regions of thicker lithosphere comprising the surrounding Paleoproterozoic to Archaean cratons. In this intraplate model, long-lived high temperatures are maintained by a high basal heat flux that leads to extensive high-temperature crustal melting and metamorphism. In contrast, Gorczyk et al. (2015) suggest a plate margin controlled system where the Musgrave Province is located in an upper plate setting, which may have been part of a larger continental system that included the South Australian Craton (SAC). In this model, lithosphere comprising the leading edge of the NAC is underthrust (subducted) beneath the Musgrave system, with extension of the upper plate (Musgrave system) providing the setting for high-temperature metamorphism and magmatism in comparatively thin crust that is geodynamically located in a back arc setting (Kelsey and Hand, 2015; Walsh et al., 2015). Convergence between the NAC and the SAC maintained an extensional upper plate setting, leading to the development of a long-lived, high thermal gradient regime recorded by the UHT metamorphism and associated magmatism in the Musgrave Province. Encroachment of the NAC resulted in the development of contractional structures along the southern margin of the NAC and also within the Musgrave Province (Gorczyk et al., 2015). Although evidence for the arc is not present, we note that the Amadeus Basin obscures ~250 km of the system between the NAC and the Musgrave Province, and conceivably the arc may lie obscured beneath the Amadeus Basin. Whereas the time scales in the model proposed by Gorczyk et al. (2015) appear to be shorter than the duration of high-temperature tectonism in the Musgrave Province, a generalised upper plate geodynamic scenario does appear to be compatible with the regional geophysics (see below) and the data presented in this study that suggests that the compressional structures are 1140–1130 Ma in age. The timing of these structures postdates much of the evolution of the Musgrave Province, as would be expected if the preceding convergence had maintained extension in the upper plate system.

Selway et al. (2006, 2009) used magnetotelluric imaging to infer the presence of a south-dipping lithospheric-scale structure extending to a depth at least 200 km from the surface interface between the Warumpi and Aileron Provinces (Fig. 10). They inferred this to represent the continuation of the NAC beneath the Warumpi Province and its southward continuation towards the Musgrave Province. This architecture was interpreted to record a fossilised subduction system associated with amalgamation of the NAC and the Warumpi Province at 1640 Ma. However, the regional extent of Grenvillian-aged deformation and magmatism associated with the Teapot and Mordor Complexes in the southern part of the NAC, combined with its equivalence in age to the deformation and metamorphism in the Musgrave Province, suggests that the structure imaged by Selway et al. (2006, 2009) may be late Mesoproterozoic in age. Although it cannot be definitively proven that the late Mesoproterozoic ages relate to the genesis of this geophysically defined structure, rather than reworking, the ca. 1130 Ma clockwise *P*–*T* evolutions recorded in the eastern Warumpi Province are consistent with a collisional regime (Morrissey et al., 2011). Garnet grains in that study with Sm–Nd ages of 1130–1100 Ma preserve prograde compositional zoning, suggesting that they relate to the first phase of metamorphism (Morrissey et al., 2011). Additionally, the kinematics associated with the 1140–1130 Ma compressional structures developed along the southern margin of NAC implies a downward movement of the NAC with respect to the Warumpi–Musgrave system, and are comparable with the kinematics of the large-scale geophysical architecture inferred by Selway et al. (2006, 2009). Therefore, we entertain that long-lived, late Mesoproteroic UHT metamorphism in the Musgrave Province was maintained within a back arc setting linked to the encroachment of the NAC, with termination of the

B.L. Wong et al. / Precambrian Research 270 (2015) 100–123 121

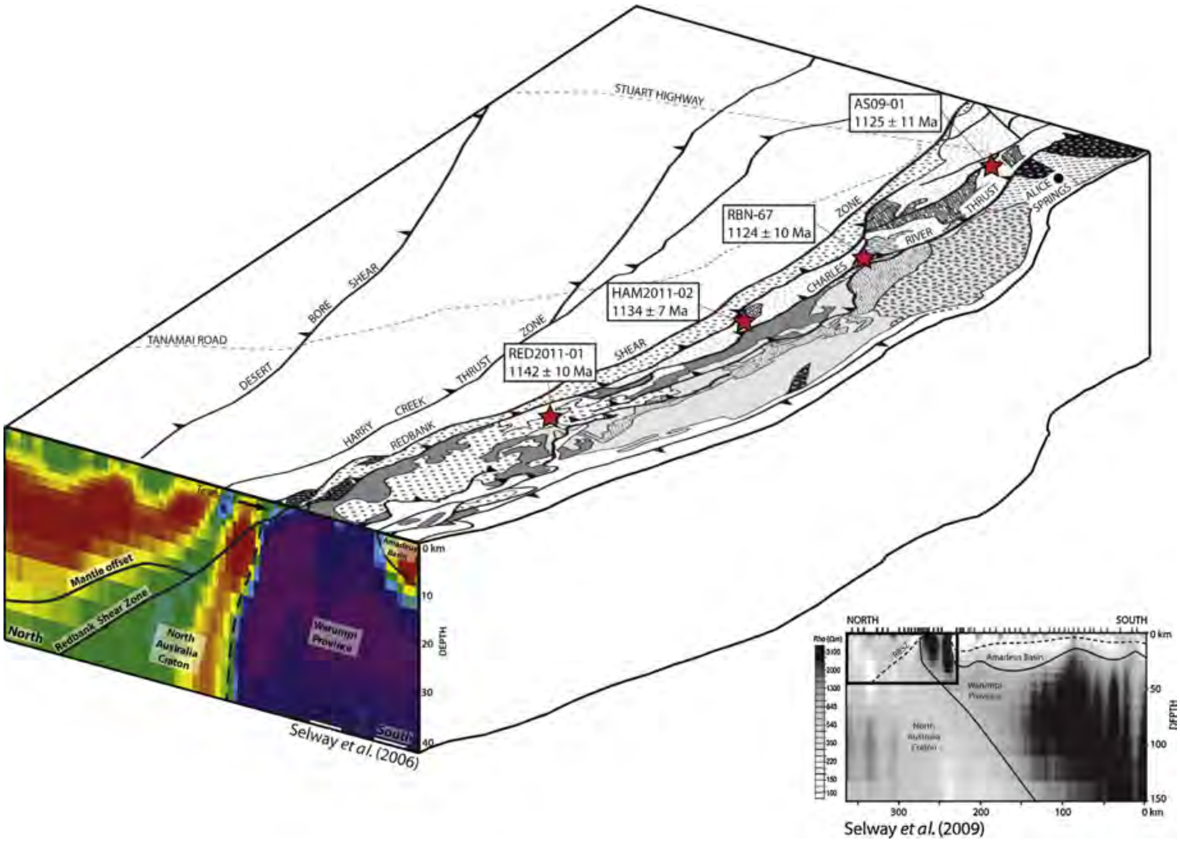

Fig. 10. A schematic 3-D diagram illustrating the correlation between surficial E–W trending structures along the southern margin of the NAC (including the Redbank Shear Zone) and the interpreted boundary between the NAC and the Warumpi Province imaged by magnetotellurics. The larger-scale MT image demonstrates the location of the Warumpi Province MT transect with respect to significant lithospheric scale structures including the Amadeus Basin and the interpreted fossilised subduction zone between the NAC and the Warumpi Province (Selway et al., 2009). It is noted that the Warumpi Province MT line imaged by Selway et al. (2006) was not collected along the exact surface transect shown in the diagram and is purely intended to provide insight into the sub-surface geology beneath the southern Aileron Province.

system being recorded by the development of contractional structures as the NAC came into contact with the Warumpi part of the upper plate, with collision occuring at ca. 1130 Ma.

7. Conclusions

U–Pb geochronology reveals the dominant structural architecture of the central southern margin of the North Australian Craton (NAC), central Australia, is unequivocally the result of Grenvillian-aged (ca. 1130 Ma) reworking. Deformation associated with this reworking initially produced a flat lying fabric which was overprinted by kilometre-scale east–west trending upright folds that evolved over time into shear zones and mylonites with south-side up movement. Phase equilibria modelling on garnet–biotite ± sillimanite ± cordierite-bearing metapelites from the southern Aileron and the Warumpi Provinces indicate peak metamorphic conditions during the Grenvillian occurred in a thermal regime of high to ultrahigh thermal gradients. The Grenvillian-aged deformation overprints an earlier, high-grade metamorphic event at ca. 1630 Ma, which is recorded by metapelites and by migmatitised granitic protoliths that intruded between 1650 and 1630 Ma. Monazite grains within the southern Aileron Province also record ages between ca. 1600 and 1720 Ma and suggest multiple, pre-Grenvillian metamorphic events along the southern margin of the NAC. The timing of deformation in the southern NAC coincides with the latter stages of long-lived, high to ultrahigh thermal gradient metamorphism and magmatism in the Musgrave Province, which forms the eastern extent of the continental-scale Musgrave–Albany Fraser Orogen to the south of the NAC. The locus of Grenvillian-aged deformation in the NAC coincides with the surface projection of a lithospheric-scale structure that places rocks of the Musgrave Province in an upper plate setting with respect to the NAC. We suggest that the Grenvillian-aged deformation records the amalgamation of the NAC with southern Australia. In this scenario, high to ultrahigh thermal gradient metamorphism in the Musgrave region between ca. 1220–1140 Ma was effectively maintained within a long-lived back arc setting.

Acknowledgements

B. Wade, A. Netting and A. McFadden at Adelaide Microscopy are thanked for their excellent technical support with analytical equipment. Stan Mertzman is thanked for geochemical analyses. The Central Lands Council is thanked for facilitating access to the Mt Liebig area. This work was supported by Australian Research Council Grant DP120104004 and Linkage Grant LP100200127.

Chris Kirkland and Fawna Korhonen are thanked for their constructive reviews.

Appendix A. Supplementary data

Supplementary data associated with this article can be found, in the online version, at http://dx.doi.org/10.1016/j.precamres.2015.09.001.

References

Aitken, A.R.A., Betts, P.G., 2008. High-resolution aeromagnetic data over central Australia assist Grenville-era (1300–1100 Ma) Rodinia reconstructions. Geophys. Res. Lett. 35, 1–6.

Aleinikoff, J.N., Schenck, W.S., Plank, M.O., Srogi, L.A., Fanning, C.M., Kamo, S.L., Bosbyshell, H., 2006. Deciphering igneous and metamorphic events in high-grade rocks of the Wilmington Complex, Delaware: morphology, cathodoluminescence and backscattered electron zoning, and SHRIMP U–Pb geochronology of zircon and monazite. Geol. Soc. Am. Bull. 118, 39–64.

Anderson, J.R., Kelsey, D.E., Hand, M., Collins, W.J., 2013. Conductively driven, high-thermal gradient metamorphism in the Anmatjira Range, Arunta region, central Australia. J. Metamorph. Geol. 31, 1003–1026.

Betts, P.G., Giles, D., 2006. The 1800–1100 Ma tectonic evolution of Australia. Precambrian Res. 144, 92–125.

Betts, P.G., Giles, D., Lister, G.S., Frick, L.R., 2002. Evolution of the Australian lithosphere. Aust. J. Earth Sci. 49, 661–695.

Betts, P.G., Giles, D., Schaefer, B.F., 2008. Comparing 1800–1600 Ma accretionary and basin processes in Australia and Laurentia: possible geographic connections in Columbia. Precambrian Res. 166, 81–92.

Biermeier, C., Stüwe, K., Foster, D.A., Finger, F., 2003. Thermal evolution of the Redbank thrust system, central Australia: geochronological and phase-equilibrium constraints. Tectonics 22, 1–23.

Black, L.P., Shaw, R.D., 1995. An assessment, based on U–Pb zircon data, of Rb–Sr dating in the Arunta Inlier, central Australia. Precambrian Res. 71, 3–15.

Brown, M., 2006. Duality of thermal regimes is the distinctive characteristic of plate tectonics since the Neoarchean. Geology 34, 961–964.

Brown, M., 2014. The contribution of metamorphic petrology to understanding lithosphere evolution and geodynamics. Geosci. Front. 5, 553–569.

Buick, I.S., Miller, J.A., Williams, I.S., Cartwright, I., 2001. Ordovician high-grade metamorphism of a newly recognised late Neoproterozoic terrane in the northern Harts Range, central Australia. J. Metamorph. Geol. 19, 373–394.

Cawood, P.A., Korsch, R.J., 2008. Assembling Australia: proterozoic building of a continent. Precambrian Res. 166, 1–35.

Cherniak, D.J., 2010. Diffusion in accessory minerals: zircon, titanite, apatite, monazite and xenotime. Rev. Mineral. Geochem. 72, 827–869.

Cherniak, D.J., Watson, E.B., Grove, M., Harrison, T.M., 2004. Pb diffusion in monazite: a combined RBS/SIMS study. Geochim. Cosmochim. Acta 68, 829–840.

Claoué-Long, J., Edgoose, C.J., 2008. The age and significance of the Ngadarunga Granite in Proterozoic central Australia. Precambrian Res. 166, 219–229.

Claoué-Long, J., Hoatson, D.M., 2005. Proterozoic mafic-ultramafic intrusions in the Arunta Region, central Australia Part 2: event chronology and regional correlations. Precambrian Res. 142, 134–158.

Claoué-Long, J., Maidment, D., Hussey, K., Huston, D., 2008. The duration of the Strangways Event in central Australia: evidence for prolonged deep crust processes. Precambrian Res. 166, 246–262.

Close, D.F., Scrimgeour, I., Edgoose, C., Cross, A., Clauoé-Long, J., Kinny, P., Meixner, T., 2003. Redefining the Warumpi Province. In: Annual Geoscience Exploration Seminar (AGES) 2003. Record of Abstracts, Northern Territory Geological Survey Record 2003–2011.

Close, D.F., Scrimgeour, I.R., Edgoose, C.J., Cross, A., 2004. Late Palaeoproterozoic development of the SW margin of the North Australian Craton. Geol. Soc. Aust. (Abstracts) 73, 149.

Collins, W.J., Shaw, R.D., 1995. Geochronological constraints on orogenic events in the Arunta Inlier: a review. Precambrian Res. 71, 315–346.

Collins, W.J., Williams, I., 1995. SHRIMP ionprobe dating of short-lived Proterozoic tectonic cycles in the northern Arunta Inlier, central Australia. Precambrian Res. 71, 69–89.

Collins, W.J., Williams, I.S., Shaw, R.D., McLaughlin, N.A., 1995. The age of the Ormiston Pound Granite: implications for Mesoproterozoic evolution of the Arunta Inlier, central Australia. Precambrian Res., 71.

Corfu, F., Hanchar, J.M., Hoskin, P.W.O., Kinny, P.D., 2003. In: Hanchar, J.M., Hoskin, P.W.O. (Eds.), Atlas of Zircon Textures. Zircon, Washington, DC, pp. 468–500.

Cross, A., Claoué-Long, J., Scrimgeour, I.R., Close, D.F., Edgoose, C.J., 2004. Summary of results. Joint NTGS-GA geochronology project southern Arunta region. NTGS Record 2004–2003.

Diener, J.F.A., White, R.W., Powell, R., 2008. Granulite facies metamorphism and subsolidus fluid-absent reworking, Strangways Range, Arunta Block, central Australia. J. Metamorph. Geol. 26, 603–622.

Dirks, P.H.G.M., Wilson, C.J.L., 1990. The geological evolution of the Reynolds Range, central Australia: evidence for three distinct structural-metamorphic cycles. J. Struct. Geol. 12, 651–665.

Edgoose, C.J., Scrimgeour, I.R., Close, D.F., 2004. Geology of the Musgrave Block, Northern Territory. Northern Territory Geological Survey.

Evins, P.M., Smithies, R.H., Howard, H.M., Kirkland, C., Wingate, M.T.D., Bodorkos, S., 2010. Devil in the detail; The 1150–1000 Ma magmatic and structural evolution of the Ngaanyatjarra Rift, west Musgrave Province, Central Australia. Precambrian Res. 183, 572–588.

Flöttmann, T., Hand, M., 1999. Folded basement-cored tectonic wedges along the northern edge of the Amadeus Basin, central Australia: evaluation of orogenic shortening. J. Struct. Geol., 21.

Giles, D., Betts, P.G., Lister, G.S., 2002. Far-field continental backarc setting for the 1.80–1.67 Ga basins of northeastern Australia. Geology.

Giles, D., Betts, P.G., Lister, G.S., 2004. 1.8-1.5-Ga links between the North and South Australian Cratons and the Early-Middle Proterozoic configuration of Australia. Tectonophysics 380, 27–41.

Gorczyk, W., Smithies, H., Korhonen, F., Howard, H., Quentin De Gromard, R., 2015. Ultra-hot Mesoproterozoic evolution of intracontinental central Australia. Geosci. Front. 6, 23–37.

Goscombe, B., 1991. Intense non-coaxial shear and the development of mega-scale sheath folds in the Arunta Block, Central Australia. J. Struct. Geol. 13, 299–318.

Griffin, W.L., Powell, W.J., Pearson, N.J., O'Reilly, S.Y., 2008. GLITTER: data reduction software for laser ablation ICP-MS. In: Sylvester, P. (Ed.), Laser Ablation ICP-MS in the Earth Sciences: Current Practices and Outstanding Issues. Mineralogical Association of Canada. Short Course Series 40. , pp. 308–311.

Hand, M., Buick, I.S., 2001. The Tectonic Evolution of the Reynolds-Anmatjira Ranges: A Case Study in Terrain Reworking from the Arunta Inlier, Central Australia. Geological Society of London, Special Publications 184, pp. 237–260.

Harlov, D.E., Wirth, R., Hetherington, C.J., 2011. Fluid-mediated partial alteration in monazite: the role of coupled dissolution–reprecipitation in element redistribution and mass transfer. Contrib. Mineral. Petrol. 162, 329–348.

Hoatson, D.M., Sun, S., Claoué-Long, J., 2005. Proterozoic mafic-ultramafic intrusions in the Arunta Region, central Australia Part 1: Geological setting and mineral potential. Precambrian Res. 142, 93–133.

Holland, T.J.B., Powell, R., 2011. An improved and extended internally consistent thermodynamic dataset for phases of petrological interest, involving a new equation of state for solids. J. Metamorph. Geol. 29, 333–383.

Hollis, J.A., Kirkland, C., Spaggiari, C.V., Tyler, I.M., Haines, P.W., Wingate, M.T.D., Belousova, E.A., Murphy, R.C., 2013. Zircon U–Pb–Hf Isotope Evidence for Links between the Warumpi and Aileron Provinces, West Arunta Region. Geological Survey of Western Australia, pp. 30.

Howard, H.M., Smithies, R.H., Kirkland, C.L., Kelsey, D.E., Aitken, A., Wingate, M.T.D., Quentin de Gromard, R., Spaggiari, C.V., Maier, W.D., 2015. The burning heart—the Proterozoic geology and geological evolution of the west Musgrave Region, central Australia. Gondwana Res. 27, 64–94.

Jackson, M.J., Pearson, N.J., Griffin, W.L., Belousova, E.A., 2004. The application of laser ablation-inductively coupled plasma-mass spectrometry to in situ U–Pb zircon geochronology. Chem. Geol. 211, 47–69.

Johnson, T.E., White, R.W., 2011. Phase equilibrium constraints on conditions of granulite-facies metamorphism at Scourie, NW Scotland. J. Geol. Soc. 168, 147–158.

Kelsey, D.E., Hand, M., 2015. On ultrahigh temperature crustal metamorphism: phase equilibria, trace element thermometry, bulk composition, heat sources, timescales and tectonic settings. Geosci. Front. 6, 311–356.

Kirkland, C.L., Smithies, R.H., Woodhouse, A.J., Howard, H.M., Wingate, M.T.D., Belousova, E.A., Cliff, J.B., Murphy, R.C., Spaggiari, C.V., 2013. Constraints and deception in the isotopic record; the crustal evolution of the west Musgrave Province, central Australia. Gondwana Res. 23, 759–781.

Korhonen, F.J., Clark, C., Brown, M., Bhattacharya, S., Taylor, R., 2013. How long-lived is ultrahigh temperature (UHT) metamorphism? Constraints from zircon and monazite geochronology in the Eastern Ghats orogenic belt, India. Precambrian Res. 234, 322–350.

Lawson-Wyatt, M., 2012. Regional Inkamulla-Aged (ca. 1740–1755 Ma) Tectonism Along Strike of the Mt. Hay-Redbank Hill Region, Southern Aileron Province, Central Australia. Center for Tectonics, Resources and Exploration, The University of Adelaide (unpublished).

Lo Pò, D., Braga, R., 2014. Influence of ferric iron on phase equilibria in greenschist facies assemblages: the hematite-rich metasedimentary rocks from the Monti Pisani (Northern Apennines). J. Metamorph. Geol. 32, 371–387.

Maidment, D., Hand, M., 2002. The extent od Cambrian metasediments and the Ordovician Larapinta Event, eastern Arunta Province, central Australia. In: Geological Society of Australia (Abstracts) 67.

Maidment, D., Hand, M., Williams, I.S., 2005. Tectonic cycles in the Strangways Metamorphic Complex, Arunta Inlier, central Australia: geochronological evidence for exhumation and basin formation between two high-grade metamorphic events. Aust. J. Earth Sci. 52, 205–215.

McLaren, S., Sandiford, M., Powell, R., 2005. Contrasting styles of Proterozoic crustal evolution: a hot-plate tectonic model for Australian terranes. Geology.

Morrissey, L., Payne, J.L., Kelsey, D.E., Hand, M., 2011. Grenvillian-aged reworking in the North Australian Craton, central Australia: constraints from geochronology and modelled phase equilibria. Precambrian Res., 191.

Morrissey, L.J., Hand, M., Raimondo, R., Kelsey, D.E., 2014. Long-lived high-T, low-P granulite facies metamorphism in the Arunta Region, central Australia. J. Metamorph. Geol. 32, 25–47.

Myers, J.S., Shaw, R.D., Tyler, I.M., 1996. Tectonic evolution of Proterozoic Australia. Tectonics 15, 1431–1446.

Offe, L.A., Shaw, R.D., 1983. Alice springs region, Northern Territory. 1:100 000 Map Commentary. Bureau of mineral resources. Geol. Geophys.

Oliver, N.H.S., Holcombe, R.J., Hill, E.J., Pearson, P.J., 1991. Tectono-metamorphic evolution of the Mary Kathleen Fold Belt, northwest Queensland: a reflection of mantle plume processes? Aust. J. Earth Sci. 38, 425–455.

Payne, J.L., Hand, M., Barovich, K.M., Reid, A., Evans, D.A.D., 2009. Correlations and reconstruction models for the 2500–1500 Ma evolution of the Mawson Continent. In: Geological Society London, Special Publications 323., pp. 319–355.

Payne, J.L., Hand, M., Barovich, K.M., Wade, B.P., 2008. Temporal constraints on the timing of high-grade metamorphism in the northern Gawler Craton; implications for assembly of the Australian Proterozoic. Aust. J. Earth Sci. 55, 623–640.

Powell, R., White, R.W., Green, E.C.R., Holland, T.J.B., Diener, J.F.A., 2014. On parameterizing thermodynamic descriptions of minerals for petrological calculations. J. Metamorph. Geol. 32, 245–260.

Rapp, R., Watson, E.B., 1986. Monazite solubility and dissolution kinetics: implications for the thorium and light rare earth chemistry of felsic magmas. Contrib. Mineral. Petrol. 94, 304–316.

Rigby, M.J., Droop, G.T.R., 2011. Fluid-absent melting versus CO_2 streaming during the formation of pelitic granulites: a review of insights from the cordierite fluid monitor. Geol. Soc. Am. Mem. 207, 39–60.

Rubatto, D., Chakraborty, S., Dasgupta, S., 2013. Timescales of crustal melting in the Higher Himalayan Crystallines (Sikkim, Eastern Himalaya) inferred from trace element-constrained monazite and zircon chronology. Contrib. Mineral. Petrol. 165, 349–372.

Rubatto, D., Williams, I.S., Buick, I.S., 2001. Zircon and monazite response to prograde metamorphism in the Reynolds Range, central Australia. Contrib. Mineral. Petrol. 140, 458–468.

Sajeev, K., Williams, I.S., Osanai, Y., 2010. Sensitive high-resolution ion microprobe U–Pb dating of prograde and retrograde ultrahigh-temperature metamorphism as exemplified by Sri Lankan granulites. Geology 38, 971–974.

Sandiford, M., Hand, M., 1998. Controls on the locus of intraplate deformation in central Australia. Earth Planet. Sci. Lett. 162, 97–110.

Schaltegger, U., Fanning, C.M., Günther, D., Maurin, J.C., Schulmann, K., Gebauer, D., 1999. Growth, annealing and recrystallization of zircon and preservation of monazite in high-grade metamorphism: conventional and in-situ U–Pb isotope, cathodoluminescence and microchemical evidence. Contrib. Mineral. Petrol. 134, 186–201.

Scott, D.L., Rawlings, D.J., Page, R.W., Tarlowski, C.Z., Idnurm, M., Jackson, M.J., Southgate, P.N., 2000. Basement framework and geodynamic evolution of the Palaeoproterozoic superbasins of north-central Australia: an integrated review of geochemical, geochronological and geophysical data. Aust. J. Earth Sci. 47, 341–380.

Scrimgeour, I.R., 2003. Developing a revised framework for the Arunta Region, Annual Geoscience Exploration Seminar (AGES) 2003. In: Record of Abstract. Northern Territory Geological Survey Record 2003-001.

Scrimgeour, I.R., 2004. A revised province definition and Palaeoproterozoic framework for the Arunta region, central Australia. Geol. Soc. Aust. (Abstracts) 73, 185.

Scrimgeour, I.R., Close, D.F., Edgoose, C.J., 2005a. Mount Liebig, Northern Territory. 1:250 000 geological map series explanatory notes, SF 52-16. In: Northern Territory Geological Survey, Darwin and Alice Springs.

Scrimgeour, I.R., Kinny, P.D., Close, D.F., Edgoose, C.J., 2005b. High-T granulites and polymetamorphism in the southern Arunta Region, central Australia: evidence for a 1.64 Ga accretional event. Precambrian Res. 142, 1–27.

Selway, K., Hand, M., Heinson, G., Payne, J.L., 2009. Magnetotelluric constraints on subduction polarity: reversing reconstruction models for Proterozoic Australia. Geology.

Selway, K., Heinson, G., Hand, M., 2006. Electrical evidence of continental accretion: steeply dipping crustal-scale conductivity contrast. Geophys. Res. Lett., 33.

Shaw, R.D., Black, L.P., 1991. The history and tectonic implications of the Redbank Thrust Zone, central Australia, based on structural, metamorphic and Rb-Sr isotopic evidence. Aust. J. Earth Sci. 38, 307–332.

Shaw, R.D., Langworthy, A.P., 1984. Strangways Region, Northern Territory. 1:100 000 Map Commentary. Bureau of Mineral Resources Australia, Canberra.

Shaw, R.D., Zeitler, P.K., Mcdougall, I., Tingate, P.R., 1992. The Paleozoic history of an unusual intracratonic thrust belt in central Australia based on $^{40}Ar/^{39}Ar$, K–Ar and fission-track dating. J. Geol. Soc. 149, 937–954.

Sláma, J., Košler, J., Condon, D.J., Crowley, J.L., Gerdes, A., Hanchar, J.M., Horstwood, S.A., Morris, G.A., Nasdala, L., Norberg, N., Schaltegger, U., Schoene, B., Tubrett, M.N., Whitehouse, M.J., 2008. Plešovice zircon – a new natural reference material for U–Pb and Hf isotopic microanalysis. Chem. Geol. 249, 1–35.

Smithies, R.H., Howard, H.M., Evins, P.M., Kirkland, C., Kelsey, D.E., Hand, M., Wingate, M.T.D., Collins, A.S., Belousova, E.A., 2011. High-temperature granite magmatism, crust-mantle interaction and the Mesoproterozoic intracontinental evolution of the Musgrave Province, central Australia. J. Petrol. 52, 931–958.

Smithies, R.H., Kirkland, C.L., Korhonen, F.J., Aitken, A.R.A., Howard, H.M., Maier, W.D., Wingate, M.T.D., Quentin de Gromard, R., Gessner, K., 2015. The Mesoproterozoic thermal evolution of the Musgrave Province in central Australia—Plume vs. the geological record. Gondwana Res. 27, 1419–1429.

Smits, R.G., Collins, W.J., Hand, M., Dutch, R., Payne, J., 2014. A Proterozoic Wilson cycle identified by Hf isotopes in central Australia: implications for the assembly of Proterozoic Australia and Rodinia. Geology 42, 231–234.

Stepanov, A.S., Hermann, J., Rubatto, D., Rapp, R.P., 2012. Experimental study of monazite/melt partitioning with implications for the REE. Th and U geochemistry of crustal rocks. Chem. Geol. 300–301, 200–220.

Stewart, A.J., Shaw, R.D., Black, L.P., 1984. The Arunta Inlier: a complex ensialic mobile belt in central Australia. Part 1: Stratigraphy, correlations and origin. Aust. J. Earth Sci. 31, 445–455.

Stüwe, K., 2007. Geodynamics of the Lithosphere: An Introduction. Springer Berlin, Heidelberg.

Sun, S.-S., Warren, R.G., Shaw, R.D., 1995. Nd isotope study of granites from the Arunta Inlier, central Australia: constraints on geological models and limitation of the method. Precambrian Res. 71, 301–314.

Teyssier, C., 1985. A crustal system in an intracratonic tectonic environment. J. Struct. Geol. 7, 689–700.

Teyssier, C., Amri, C., Hobbs, B.E., 1988. South Arunta Block: the internal zones of a Proterozoic overthrust in Central Australia. Precambrian Res. 40/41, 157–173.

Tucker, N.M., Hand, M., Kelsey, D.E., Dutch, R.A., 2015. A duality of timescales: short-lived ultrahigh temperature metamorphism preserving a long-lived monazite growth history in the Grenvillian Musgrave–Albany–Fraser Orogen. Precambrian Res. 264, 204–234.

Vry, J., Compston, W., Cartwright, I., 1996. SHRIMP II dating of zircons and monazites: reassessing the timing of high-grade metamorphism and fluid flow in the Reynolds Range, northern Arunta Block, Australia. J. Metamorph. Geol. 14, 335–350.

Wade, B.P., Barovich, K.M., Hand, M., Scrimgeour, I.R., Close, D.F., 2006. Evidence for Early Mesoproterozoic arc magmatism in the Musgrave Block, central Australia: implications for Proterozoic crustal growth and tectonic reconstructions of Australia. Geology.

Wade, B.P., Kelsey, D.E., Hand, M., Barovich, K.M., 2008. The Musgrave Province: stitching north, west and south Australia. Precambrian Res. 166, 370–386.

Walsh, A.K., Kelsey, D.E., Kirkland, C.L., Hand, M., Smithies, R.H., Clark, C., Howard, H.M., 2015. P–T–t evolution of a large, long-lived, ultrahigh-temperature Grenvillian belt in central Australia. Gondwana Res. 28, 531–564.

Warren, R.G., Shaw, R.D., 1995. Hermansburg, Northern Territory (second ed.) 1:250 000 Geological Map Series Explanatory Notes. Darwin, Northern Territory Geological Survey.

White, R.W., Powell, R., Holland, T.J.B., Johnson, T.E., Green, E.C.R., 2014a. New mineral activity–composition relations for thermodynamic calculations in metapelitic systems. J. Metamorph. Geol. 32, 261–286.

White, R.W., Powell, R., Holland, T.J.B., Worley, B.A., 2000. The effect of TiO_2 and Fe_2O_3 on metapelitic assemblages at greenschist and amphibolite facies conditions: mineral equilibria calculations in the system $K_2O–FeO–MgO–Al_2O_3–SiO–H_2O–TiO–Fe_2O_3$. J. Metamorph. Geol. 18, 497–511.

White, R.W., Powell, R., Johnson, T.E., 2014b. The effect of Mn on mineral stability in metapelites revisited: new *a–x* relations for manganese-bearing minerals. J. Metamorph. Geol. 32, 809–828.

Williams, I.S., Buick, I.S., Cartwright, I., 1996. An extended episode of early Mesoproterozoic metamorphic fluid flow in the Reynolds Range, central Australia. J. Metamorph. Geol. 14, 29–47.

Williams, M.L., Jercinovic, M.J., Harlov, D.E., Budzyn, B., Hetherington, C.J., 2011. Resetting monazite ages during fluid-related alteration. Chem. Geol. 283, 218–225.

Wingate, M.T.D., Pirajno, F., Morris, P.A., 2004. Warakurna large igneous province: a new Mesoproterozoic large igneous province in west-central Australia. Geology 32, 105–108.

Wyborn, L., 1992. Proterozoic granite types in Australia – implications for lower crust composition, structure and evolution. Trans. R. Soc. Edinburgh Earth Sci., 83.

Yakymchuk, C., Brown, M., 2014. Behaviour of zircon and monazite during crustal melting. J. Geol. Soc. 171, 465–479.

Young, D.N., Fanning, C.M., Shaw, R.D., Edgoose, C.J., Blake, D.H., Page, R.W., Camacho, A., 1995. U–Pb zircon dating of tectonomagmatic events in the northern Arunta Inlier, central Australia. Precambrian Res. 71, 45–68.

Zhao, J., McCulloch, M.T., 1993. Sm-Nd mineral isochron ages of Late Proterozoic dyke swarms in Australia – evidence for 2 distinctive events of mafic magmatism and crustal extension. Chem. Geol. 109, 341–354.